Theoretical Geochemistry: Application of Quantum Mechanics in the Earth and Mineral Sciences

---

JOHN A. TOSSELL
DAVID J. VAUGHAN

Theoretical Geochemistry: Applications of Quantum Mechanics in the Earth and Mineral Sciences

This page intentionally left blank

Theoretical Geochemistry: Applications of Quantum Mechanics in the Earth and Mineral Sciences

JOHN A. TOSSELL
Professor of Chemistry
University of Maryland

DAVID J. VAUGHAN
Professor of Mineralogy
University of Manchester

New York Oxford
OXFORD UNIVERSITY PRESS
1992

Oxford University Press

Oxford New York Toronto
Delhi Bombay Calcutta Madras Karachi
Petaling Jaya Singapore Hong Kong Tokyo
Nairobi Dar es Salaam Cape Town
Melbourne Auckland

and associated companies in
Berlin Ibadan

Published by Oxford University Press, Inc.,
200 Madison Avenue, New York, New York 10016

Library of Congress Cataloging-in-Publication Data
Tossell, John A.
Theoretical geochemistry : applications of quantum mechanics
in the earth and mineral sciences / John A. Tossell, David J Vaughan.
p. cm. Includes bibliographical references and index.
ISBN 0-19-504403-7
1. Analytical geochemistry. 2. Quantum chemistry.
3. Mineralogical chemistry 4. Chemical bonds.
I. Vaughan, David J., 1946– . II. Title.
QE516.3.T67
1991 551.9—dc20
90-21551

9 8 7 6 5 4 3 2 1

Printed in the United States of America
on acid-free paper

PREFACE

Geochemistry is most obviously defined as the "study of the chemistry of the Earth." In the broadest sense, the subject attempts to describe and understand the distribution of the elements (and their isotopes) in all parts of the Earth; the atmosphere, and hydrosphere, the Earth's crust, and its deeper interior (mantle and core). However, geochemists have traditionally concentrated their attention on the solid Earth and on surface or near-surface processes involving fluids, leaving the atmosphere and hydrosphere to other specialists such as the atmospheric scientists and chemical oceanographers. Geochemists have also concerned themselves with the chemistry of extraterrestrial matter (strictly termed *cosmochemistry*) because of its importance in understanding the origin and history of the solar system and hence of the Earth. A recent, and very welcome, development is the growth of interdisciplinary fields (such as biogeochemistry) and a return to attempts to view the chemical systems of the Earth (lithosphere, hydrosphere, biosphere, and atmosphere) as a whole.

The great Norwegian geochemist V.M. Goldschmidt formulated the tasks of geochemistry as: (1) to establish the terrestrial abundance relationships of the elements; (2) to account for the terrestrial distribution of elements in the geochemical spheres (such as the minerals and rocks of the lithosphere); (3) to detect the laws governing the abundance relationships and the distribution of the elements. Since the past century, a very large body of data on the chemical compositions of mineral and rocks has been accumulated, and much has been learned about the crystal structures of minerals. A reasonable "data base" apparently exists with which one could tackle the "tasks of geochemistry," although it is important to note that direct information is almost entirely limited to the Earth's crust. Our knowledge of the Earth beneath this thin skin comes chiefly from the gross physical parameters of the Earth (mass, moment of inertia, magnetic field, etc.), from earthquake shock waves and from the analogies drawn with meteorites and other solar-system bodies.

Although many of the early advances in chemistry were achieved by scientists who were as much mineralogists, crystallographers, and geologists as chemists, the more recent history of geochemistry has commonly seen the later application to geological problems of techniques or theories developed by chemists (and physicists). This is particularly true of various spectroscopic methods used to study chemical bonding (see Chapter 2) and of chemical bonding theories that may be applied to understanding mineralogical and geochemical systems (see Chapters 1 and 3). The application of quantum mechanics to chemical systems, enabling the crystal structures, stabilities, reactivities, and certain physical properties of phases to be understood or predicted, is a well-established branch of chemistry, sometimes called *quantum chemistry*. The application of quantum mechanics to minerals and other geochemical systems has developed rapidly over the past 15 years. This major branch of *theoretical geochemistry,* which might be termed *quantum geochemistry,* forms the subject of this book. (Note that much of the subject matter could be described, at least in part, by a variety of other terms, some currently in use, including "mineral physics," "physics and chemistry of minerals," or "quantum mineralogy.")

It is the thesis of this book that further major advances in geochemistry, particularly in understanding the rules that govern the ways in which elements come together to form minerals and rocks, require application of the theories of quantum mechanics. This is particularly the case in gaining further knowledge of the geochemistry of the interior of the Earth.

In the following chapters the elements of quantum mechanics are outlined, and various models that may be used to describe bonding in geochemical systems are discussed. Chapter 2 provides a brief account of experimental techniques that can be used to study bonding in geochemical systems. Although the emphasis in this text is not on experimentation, it is important to understand how theoretical models can be tested and refined using such methods. Chapter 3 is used to outline the theoretical background and the various quantum-mechanical models and methods that can be employed, whereas in the first part of Chapter 4 high-level applications of these methods to simple molecules or compounds of relevance to mineralogy and geochemistry are considered. The latter part of Chapter 4 and the whole of Chapters 5 and 6 describe the applications of various bonding models to major groups of minerals—the oxides, silicates, carbonates, borates, and sulfides. The applications of bonding models to more general problems in mineral physics and chemistry, geophysics, and geochemistry form the subject matter of Chapters 7 and 8. These problems include structure, stereochemistry, bond strengths and stabilities of minerals, physical properties (including elastic properties) of minerals, crystal–melt equilibria and partitioning of elements, behavior of minerals at elevated pressure, prediction of solution species and mineral–solution equilibria, surface properties of minerals, and overall geochemical distribution of the elements.

Although the emphasis in the text is chemical and geochemical, the subject matter is so fundamental to all aspects of the Earth and Mineral

Sciences, that we hope it will appeal to the wider audience of mineralogists, petrologists, and geophysicists. It is also hoped that physicists, chemists, and materials scientists with major interests outside the Earth Sciences will find it a useful source of information and ideas. Indeed, several topics that link the mineral sciences with broader aspects of materials science are discussed in Chapter 7. An attempt has been made to cover key references up to the end of 1990, although where, as is commonly the case, the number of references is too great to include them all, the reader is directed to major review articles. The appendices provide not only information on relevant symbols, units, constants, and conversion factors, but also a guide to both experimental and calculational methods for studying structure and bonding and to the numerous acronyms employed to refer to these methods.

Many people have contributed directly or indirectly to the completion of this book. Particular thanks are due to Professor R.G. Burns, who offered advice and encouragement in the early stages; Professor G.V. Gibbs, who read and commented upon the final text; and Professor C.M.B. Henderson, who gave advice on studies of glasses and melts. Numerous colleagues responded to requests for their most recent work. In the preparation of the manuscript, Mrs. Catherine Hardy and Mrs. Dorothy Thomas devoted many hours to careful work, and in the preparation of figures much help was provided by Mr. Richard Hartley and Miss Susan Maher. In recent years the authors have benefitted from the financial support of funding agencies in the completion of original work cited in the text (the National Science Foundation and both the Natural Environment and Science and Engineering Research Councils). Particular thanks are due to NATO, which provided funds for collaborative research by the authors.

Finally, we wish to thank our wives, Julia and Heather, for their continuing support and encouragement over the years spent preparing this text.

College Park, Md. J.A.T.
Manchester, Eng. D.J.V.
November 1990

CONTENTS

Theoretical Geochemistry: Applications of Quantum Mechanics in the Earth and Mineral Sciences

1

INTRODUCTION

1.1. Historical perspective—ionic and atomistic approaches

The early descriptions of chemical bonding in minerals and geological materials utilized purely ionic models. Crystals were regarded as being made up of charged atoms or ions that could be represented by spheres of a particular radius. Based on interatomic distances obtained from the early work on crystal structures, ionic radii were calculated for the alkali halides (Wasastjerna, 1923) and then for many elements of geochemical interest by Goldschmidt (1926). Modifications to these radius values by Pauling (1927), and others took account of such factors as different coordination numbers and their effects on radii. The widespread adoption of ionic models by geochemists resulted both from the simplicity and ease of application of these models and from the success of rules based upon them. Pauling's rules (1929) enabled the complex crystal structures of mineral groups such as the silicates to be understood and to a limited extent be predicted; Goldschmidt's rules (1937) to some degree enabled the distribution of elements between mineral phases or mineral and melt to be understood and predicted. Such rules are further discussed in later chapters. Ionic approaches have also been used more recently in attempts to simulate the structures of complex solids, a topic discussed in detail in Chapter 3.

Chemical bonding theory has, of course, been an important component of geochemistry and mineralogy since their inception. Any field with a base of experimental data as broad as that of mineralogy is critically dependent upon theory to give order to the data and to suggest priorities for the accumulation of new data. Just as the bond with predominantly ionic character was the first to be quantitatively understood within solid-state science, the ionic bonding model was the first used to interpret mineral properties. Indeed, modern studies described herein indicate that structural and energetic properties of some minerals may be adequately understood using this model. However, there are numerous indications that an ionic model is inadequate to explain many mineral properties. It also appears that some properties that may be rationalized within an ionic model may also be rationalized assuming other limiting bond types. It has long been recognized that mineral properties may be affected by departures from complete ionicity and that such covalent components of the chemical bond are correlated with purely atomic properties such as ionization potential and electron affinity. In the early 1950s, a number of researchers developed interpretations of mineral structures and energetics by establishing a correlation with some atomic properties (Ahrens, 1952, 1953; Fyfe, 1954; Ramberg, 1952; Ringwood, 1955; Verhoogen, 1958). Such work provided a framework for systematizing a vast body of experimental data, which was its primary intent. Understanding the nature of chemical bonding in minerals was not the focus of this research. In any case, quantum-mechanical theory, computational techniques, and experimental capabilities were inadequate for the study of the chemical bonds occurring in minerals. Reasonably accurate solutions to the quantum-mechanical equations had been obtained for a number of atoms, for H_2, and for some alkali halide solids, but it was not until the early 1950s that the fundamental theory needed for the quantum-mechanical studies of molecules was developed and not until the late 1950s that automatic computer programs were developed for doing the necessary computations (Schaefer, 1984). Since that time, quantum-mechanical computational capabilities have greatly increased, although there are still fairly strict limitations on the complexity of systems that can be treated.

The early attempts to determine bond type also foundered on a number of obstacles. First, while precise numerical results could be obtained within an ionic model, molecular quantum theory could only be applied in a qualitative, and often ambiguous, way. Accurately calculating even the properties of free atoms was difficult. Most molecular quantum-mechanical arguments utilized atomic ionization potentials or electronegativities and calculated atomic-orbital overlap integrals to obtain only approximate molecular orbitals. Second, the properties considered were generally structural and energetic in nature (e.g., bond distances and heats of formation). Properties inherently quantum mechanical in nature and that could not be considered using atomistic approaches, such as spectral properties arising from the existence of quantized energy states, were often ignored. As we shall see in our discussion of *ab initio* molecular-orbital (MO) theory (see Chapter 3), accurate calculation of bond distances requires an *ab initio* approach, and accurate calculation of energies demands high-level *ab initio* calculations. Since the 1950s the development of new spectroscopic methods has demanded knowledge of the allowed electronic states of mineral systems, often approximated semiquantitatively utilizing an energy-level diagram (or specifically an "eigenvalue spectrum," see sections 3.1 and 3.5) of the molecular orbitals of the material. Such an increased emphasis upon spectral properties has encouraged more researchers to use molecular quantum-mechanical approaches. Nonetheless, many of the basic questions concerning the effect of bond type on geologic processes, such as those raised by Ramberg's (1952) study of trace-element fractionation between the different silicate structure types, cannot at present be directly answered by quantum-mechanical calculation. Experimental and theoretical studies of silicate properties have, however, given us a deeper understanding of changes in silicate bond type with degree of polymerization. Rather than estimating bond type based on atomic properties such as electron affinities, we can now accurately calculate electronic structures of many different materials. Finally, some of the difficulties encountered in the 1950s arose from an attempt to define quantities such as "charge" and "covalency," which cannot be uniquely defined. It is now clear that such quantities must be used with care and that relative values are much more meaningful than absolute ones. For example, we might convincingly say that NO_3^- shows more evidence of covalency than BO_3^{3-} (from the experimental evidence of photoemission spectra; see Chapter 5), without attempting to give some absolute number to represent the covalency of either.

It is worth noting that the referenced works from the 1950s addressed very large, important, and general questions in geochemistry. Such studies are currently uncommon in mineralogy and geochemistry.

1.2. Crystal-field theory and the geochemistry of the transition metals

A great advance in understanding the geochemistry of transition-metal systems occurred in the 1950s when crystal field theory (Bethe, 1929; Orgel, 1966) was applied to them. The partly filled *d* shell of transition elements is responsible for their anomalous geochemical, crystal chemical, thermodynamic, magnetic, and spectral properties. Experimental studies, particularly of optical absorption ("crystal-field spectra") could be interpreted using crystal-field theory and used to provide information on the chemistry of transition elements in different crystalline environments. In mineralogy and geochemistry, crystal-field theory and spectral measurements were used to understand color and pleochroism in certain minerals, the distribution of transition metals between different sites in crystals and between minerals in the Earth, properties of the Earth's mantle, and, more recently, of the surfaces of other planets (Burns, 1970, 1985, 1989). Crystal-field theory thus provided a framework for relating a number of different structural, energetic, spectroscopic, and magnetic properties of transition-metal compounds. Perhaps its most important contribution was in providing a connection between spectral properties, of interest to a relatively small number of scientists, and energetic properties, a fundamental concern of a very much larger group of scientists.[1] It also established that properties associated at a certain level of approximation with the occupation of single-electron orbitals could be used to interpret changes of the total internal energy of complex many-electron systems. A similar theoretical advance occurred in organic chemistry in the 1960s when simple semiquantitative molecular-orbital calculations were used to relate the electron-density distributions in single electron orbitals to the overall reactivities of the compounds in which they occur. In both cases, the significant properties of the material are strongly dependent upon symmetry properties of the crystal site or molecular point group, so that a highly accurate description of the chemical bonding is not crucial.

Crystal field theory was quickly applied to a wide range of problems in transition-metal chemistry, including that of the partitioning of transition elements between solid silicates and silicate magma. A central concept in these interpretations was the crystal field stabilization energy (CFSE), which is dependent upon the number of metal $3d$ electrons, site symmetry, and to a lesser extent the identity of atoms in the first coordination sphere. Reasonable assumptions about the nature of coordination sites in magmas together with crystallographic knowledge of the site symmetry in silicate crystals yielded CFSE differences between magma and solid consistent with observed element fractionations in slowly cooled magma chambers. To understand the partitioning of elements between closely related sites in solids required more detailed information on the dimensions of the crystallographic sites and on the energetic splittings of the metal *d* orbitals. Such energy splittings were acquired from experimental electronic (ir–visible) absorption spectral data (see Burns, 1970) for a wide variety of silicate minerals and were shown to give CFSE values in qualitative agreement with known metal site partitionings. Refinement of this model has, however, proved to be difficult. Direct calculation of metal *d*-orbital energies using a purely ionic crystal field model does not generally give good results. In fact, experimental data attesting to the limited accuracy of the ionic crystal field model are commonly cited in introductory inorganic chemistry textbooks. However, as we shall see, first-principles quantum-mechanical calculations can now give quite accurate values of metal *d*-orbital energies for simple molecules and molecular complexes. Simple, semiempirical molecular approaches such as the angular overlap model (AOM; see Appendix C) can also accurately reproduce *d*-orbital splittings. In fact, the only systematic calculations of *d*-orbital splitting from crystal site data in the mineralogical literature were actually obtained using a version of the AOM (Wood and Strens, 1972).

1.3. Quantum chemistry

In 1929 Dirac stated that

> The underlying physical laws necessary for the mathematical theory of a large part of physics and the whole of chemistry are thus completely known, and the difficulty is only that the exact appli-

> cation of these laws leads to equations which are much too complicated to be soluble. It therefore seems desirable that approximate practical methods of applying quantum mechanics should be developed, which can lead to an explanation of the main features of complex atomic systems without too much computation.

In 1972 Schaefer described the results of many approximate quantum-mechanical calculations on gas-phase atoms and small molecules that indicated that Dirac's goal was close to being achieved for such species. Around the same time, it became clear that quantum-mechanical theory could also be applied to many categories of more complicated chemical systems in a qualitative manner, leading to substantial advances in the understanding of the structure and reactivity of such complex materials. Contemporaneous with this improved capability of quantum-mechanical theory within chemistry was an expansion in experimental methods that yielded knowledge pertinent to the electronic structure of molecules.

Recently the beginning of the "third age of quantum chemistry" has been heralded (Richards, 1979). This is the age in which quantum-mechanical calculations yield properties with accuracies rivaling experiment for molecules of real interest to practicing chemists. Admittedly, the example molecule chosen by Richards was excited triplet-state ethyne, C_2H_2, which is relatively easy to study theoretically because of its small number of electrons and quite difficult to study experimentally because its C is coordinatively unsaturated and therefore very reactive. Nonetheless, the ability of the quantum-mechnical "computer experiment" to rival the accuracy of laboratory experiment was impressive. Since that time, both collaborations and healthy rivalries have arisen between laboratory and computer experimental descriptions of many molecules, including H_2SiCH_2 (Schaefer, 1982), isoelectronic with silanone, H_2SiO. Theoretical methods have also been usefully applied to difficult problems in surface chemistry and in catalysis (Goddard, 1985). Of course, quantum-mechanical studies can be quite valuable even if the accuracy of their calculated properties does not rival experiment. As Goddard (1985) has said:

> If theory could provide only exact results for any desired property of any system, it would not be any better than a collection of good experiments. What theory uniquely provides is the qualitative principles responsible for the results from a particular experiment or calculation. With proper understanding of the principles, one can predict how new systems will act in advance of either experiment or quantitative calculations.

In addition to those groups within quantum chemistry using very accurate and computationally demanding theoretical methods, there are other groups focusing upon simple semiempirical methods that rely upon symmetry arguments and qualitative models for atomic-orbital interactions. Although much of this research is interpretative in nature, identifying specific simple chemical interactions that correctly reproduce trends in chemical behavior, there is now an important predictive component to such research. Such work often focuses upon classes of molecules in which there is substantial synthetic research and suggests directions for further synthetic studies (see, for example, Hoffman, 1982).

1.4. Solid-state quantum physics (band theory and related approaches)

At the same time as the "third age of quantum chemistry" was commencing, a similar development was occurring in computational solid-state physics. The development of *ab initio* pseudopotentials (Cohen, 1979; see Section 3.11, Appendix C) allowed accurate calculation of ground-state equilibrium geometries for valence-electron-only systems, even those of low symmetry. Such success led to serious philosophical consideration of the best ways for such accurate band-theoretical approaches to be used. Since that time the *ab initio* pseudopotential methods have been used with great success to study materials with low symmetries, such as surfaces of solids, and to assess lattice-dynamic properties. The good agreement of calculation and experiment has established that the local-density approximations used in most band-theoretical approaches do not preclude an accurate determination of ground-state properties. Although pseudopotential approaches remain difficult for transition-metal compounds, due to the necessity for retaining valence character for the metal *d* electrons, other band-theoretical approaches such as augmented-plane-wave (APW) and the linear muffin-tin orbital (LMTO) methods (see Appendix C) have been successfully applied to the calculation of ground-state properties of transition metals and some of their compounds. Unfortunately, such local-density approaches give poor results for excited-state properties in some cases (e.g., greatly underestimating band gaps in semiconductors and insulators). Some workers are trying to avoid such problems by using nonlocal Hartree–Fock treatments of exchange and correlation (e.g., Dovesi et al., 1987), while others are trying to reformulate the local-density approach to deal with such excitations. In the recent development of high-temperature superconductors, experimentalists have clearly been the leaders, but several theoretical groups have made notable contributions. The present level of understanding of the theory of such materials has been reviewed by Pickett (1989).

At the same time that band-theoretical methods have been rapidly developing in accuracy and breadth of applicability, there has been substantial progress in qualitative or semiquantitative atomic-orbital-based methods, whether based upon accurate atomic potentials or upon parametrized interactions akin to the extended Hückel theory applied to molecules (see Appendix C). These approaches provide preliminary determinations of electronic structure for complicated materials and constitute a basis for qualitative discussions of the effect of orbital interactions on structural stability.

1.5. Quantum geochemistry

The early 1970s also saw the birth of a new subfield on the borderline of mineralogy, chemistry, and solid-state physics, the field we have called *quantum geochemistry* (although the basis for such a field was laid by researchers in the 1950s and 1960s, as we have described).

Quantum geochemistry exploits recent advances within molecular quantum chemistry and theoretical solid-state physics that have made possible accurate solutions of the quantum-mechanical equations of motion for complex materials. Its goal is to be both interpretive and predictive, both to rationalize known properties of well-characterized materials and to predict unmeasured properties of poorly characterized materials by "computer experiment." It provides a theoretical framework within which the relationships between different properties of a material may be elucidated. By virtue of the nonuniformity in the geochemical distribution of the elements, quantum geochemistry is more strongly concerned with some types of chemical bonds than with others. There is a difference in emphasis but no sharp boundaries between it and inorganic quantum chemistry or theoretical solid-state physics. Although it is predominantly theoretical in nature, it has an experimental component. An experiment designed to probe an aspect of the electronic structure of a mineral is just as much a part of quantum geochemistry as is a computation using, for example, some molecular-orbital method.

Most quantum geochemistry studies have so far been interpretive rather than predictive in nature. This is partly a consequence of the complexity of mineralogical systems, which makes the most accurate quantum-mechanical calculations extremely difficult. However, even a highly accurate quantum-mechanical calculation cannot really "predict" a property if that property has already been experimentally determined to high accuracy. Most of the structural properties of most minerals have been accurately determined experimentally at ambient temperature and pressure. Synthesis of compounds with new chemical compositions is not an important component of mineralogy, although we would argue that such research can be of value. There are, however, important regimes in which mineralogical and geochemical species are poorly characterized—in high-pressure and -temperature solids, in melts and solutions, and at surfaces. It is these species, difficult to study experimentally, for which quantum-mechanical calculations may have the greatest predictive value. Another area, more clearly identified with cosmochemistry, is that of condensation of solids from interplanetary media. In all of these regimes, at least the simplest of the species involved are susceptible to quantum-mechanical study, and we will give illustrative examples of each.

1.6. Models and methods

Quantum-mechanical calculations are concerned with the (approximate) solution of the quantum-mechnical equation of motion, the Schrödinger equation. This is the starting point in a series of choices of "model" and "method" emphasized in Fig. 1.1.

In quantum geochemistry, choice of a specific model for the system of interest is a step of more significance than in quantum chemistry or solid-state physics. Quantum-chemical studies typically consider either the molecule of interest or some "friendly" simplification of it in a "localized" electron model (see Fig. 1.1). For example, a large hydrocarbon group lying far from the bond of interest in a molecule might well be replaced by an H atom in a quantum-chemical calculation. Such a procedure is often thoroughly justified, but it certainly precludes any understanding of the differences at the particular bond produced by variations in the nature of the hydrocarbon fragment. In solid-state physics the model is generally of infinite extent (in at least one dimension) and is thus a "delocalized" electron model (see Fig. 1.1), although finite molecular-cluster models are finding increased use within this discipline. Many quantum-geochemical studies have also employed molecular models of infinite extent (although the resulting problem is not of infinite difficulty due to the simplifications of translational symmetry). However, it is more common to employ some finite molecular cluster (or even an isolated molecule) to describe the properties of the mineral solid (e.g., a tetrahedral SiO_4 "molecular" cluster to model quartz). Although such a procedure reduces the number of electrons to be treated, its disadvantage for a crystalline material is that it fails to take advantage of the translational symmetry, although it may well exploit the point-group symmetry of the smaller cluster. Of course, if the molecule or molecular cluster used as model for the mineral is a stable species, one may be able to compare calculated and experimental properties for the molecule and thus gain information relevant to the mineral itself. Indeed, we shall argue that a great deal can be learned about minerals by studies on nonmineral solids or gas-phase molecules with similar bond types. In principle, one can enlarge the molecular cluster somewhat so as to approach the bulk solid gradually. In practice, such enlarged clusters are very difficult to perform calculations upon, and the results are hard to interpret. Generally, enlarged clusters are studied by accurate methods only when specific interactions outside the simplest cluster are the focus of interest. For example,

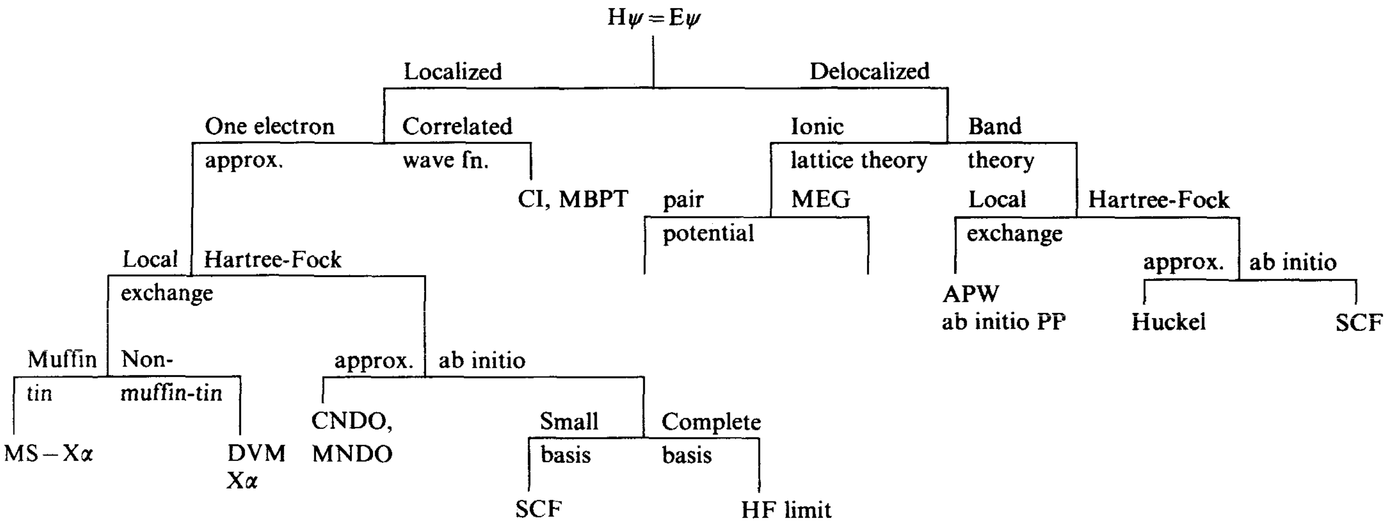

Fig. 1.1. Diagram to illustrate the principles involved in choosing a model and a method when performing quantum-mechanical calculations (to solve the Schrödinger equation shown at the apex of this figure) on geochemical (particularly mineral) species. See text (and also Appendix C) for discussion and explanation of abbreviations (from Tossell, 1987).

one might study the interaction of transition-metal atoms across a shared edge of two metal–oxygen polyhedra (e.g., an Fe_2O_{10} cluster involving two edge-sharing FeO_6 octahedra) with some expectation that the specific metal–metal interaction might be well described, but artifacts of the cluster truncation might give unreliable results for the other properties such as oxygen orbital energies. The cluster approximation to the bulk solid can be improved by imposing conditions on the electron density or other properties at the cluster boundary, but such conditions are not easy to formulate or to reduce to computer algorithms. Nonetheless, some important advances can be made in this area, which we will later describe (see also Sauer, 1989).

Once a model for the mineral has been chosen, one must adopt a particular method for the approximate solution of the Schrödinger equation. (A full account of the development of quantum-mechnical theory is given in Chapter 3.) Although this equation can be solved exactly only for one-electron systems, extremely accurate approximate solutions are now obtainable for systems with a small number of electrons (e.g., <120) with reasonable computational effort. In general, the computational effort involved increases rapidly with the degree of rigor of the calculation and even more rapidly with the number of electrons in the system. Thus, most quantum-geochemical studies have utilized quantum-mechanical methods with rather low levels of rigor.

If we follow the localized (left-hand) route of Fig. 1.1 and thus choose some form of molecular cluster, we find that the most common description of many-electron systems employs the independent-electron approximation, in which the many-electron wave function is written as a product of one-electron wave functions or orbitals, modified so as to satisfy the Pauli exclusion principle (the "one-electron approximation," Fig. 1.1). Only a few calculations on geochemically important materials have gone beyond this level of approximation and employed correlated wave functions, but procedures for doing so using the methods of configuration-interaction (CI) and many-body pertubation theory (MBPT) have only recently become widely available. The best possible one-electron wave function is known as the Hartree–Fock wave function. If a Hartree–Fock level wave function is deemed adequate for the study, one must then decide how closely it is necessary to approach this wave function [and the "Hartree–Fock (HF) limit"], which requires, in principle, an infinite set of analytical functions for its representation. The difficulty of the calculation increases approximately as the fourth power of the number of such functions. Thus, for systems with large numbers of atoms, the set of analytical expansion functions, known as the *basis set,* is generally not complete, and a self-consistent-field (SCF) calculation is carried out using a small basis set (Fig. 1.1). Much simpler but thereby much cruder than such *ab initio* Hartree–Fock methods are the approximate Hartree–Fock methods that involve some gross assumptions, such as the complete neglect of differential overlap (CNDO) or modified neglect of differential overlap (MNDO) methods. Alternatives to the Hartree–Fock approach involve more approximate methods of calculating the exchange energy ("local-exchange" methods) such as the various types of X_α methods discussed fully in Chapter 3.

The delocalized (right-hand) side of Fig. 1.1 involves some form of calculation on the full lattice such as a band-theory calculation. Again, the Hartree–Fock wave function may be employed in an *ab initio* method or some approximate method such as Hückel band theory, or the local-exchange approximations employed leading to augmented-plane-wave or *ab initio* pseudopotential (PP) methods. As an alternative to band theory, the development of the ionic approach using pair potentials or modified electron-gas (MEG) theory has proved effective for certain crystalline species.

Both in chemistry and in solid-state physics the connection between computation and experiment has become considerably closer in recent years, with computations being critically important in the interpretation of new experimental data and in guiding the experimentalists towards interesting and informative experiments. It is initially surprising that so much time has been required since the development of quantum mechanics in the 1920s to reach this stage. Slater (1975) has noted that political developments and the growth of new areas in physics have retarded computational solid-state physics, but he regards the overwhelming intractability of the quantum-mechanical equations and the need for enormous computational speed and storage capacity in their solution as the main cause of this slow development. Computer-determined limitations have now been overcome to a large extent, and both sophisticated quantum-mechanical software and supercomputers are becoming routinely available. Thus, the stage is set for general application in the Earth Sciences and Solid-State Sciences of the techniques discussed in this book.

Note

1. It is interesting to note that a connection has more recently been made between macroscopic thermodynamic data and vibrational spectra (Kiefer, 1979). Although it has long been known that heat capacities of minerals are directly related to vibrational spectra, quantification of this relationship has been hampered by inadequate experimental knowledge. Systematic studies of the spectra, along with clever interpolations into inaccessible spectral regions, have now made possible accurate calculations of heat capacities—hence linking a microscopic property of limited interest to a macroscopic property of wide interest.

2

EXPERIMENTAL METHODS

An understanding of chemical bonding in a system can be gained through calculations based on the theoretical approaches outlined in the previous chapter, or through experimentation. In a much more limited way, it is also possible to gain some understanding of the bonding in a system by a "phenomenological" application of (qualitative) theory given certain properties of the system (e.g., chemical composition, crystal or molecular structure, magnetic and electrical behavior, etc.). Ideally these approaches should be combined so as to gain a unified understanding of the bonding in a particular system. It is very important that the results of quantum-mechanical calculations are compared with experimental data so as to assess their validity. Conversely, the results of calculations may be used in the interpretation of the data from experiments.

In this chapter, the wide range of experimental methods that can provide information on chemical bonding in geochemical systems is reviewed. Following a very brief summary of the principles of each technique, some examples are given of its application to minerals (or other systems of geochemical interest, such as melts, glasses, or aqueous solutions). The objective is to draw attention to techniques of importance and to show their relevance to bonding studies and their relationships both to quantum-mechanical calculations and to other experimental methods. No attempt is made to explain the theoretical background of these techniques fully or the practical problems involved in their application. Indeed, each of them has spawned a substantial literature, including books and review articles, some of which are cited here for the reader requiring further details.

The experimental methods to be discussed have been divided into five major categories—diffraction effects, electron and x-ray spectroscopies, optical (uv–visible–near-ir) spectroscopy, vibrational spectroscopy, and nuclear spectroscopy. A number of techniques are also discussed in the sixth category—"other methods." Nevertheless, the range of techniques discussed is very far from complete, and a fuller listing is given in Appendix B. This Appendix also serves to provide some useful references on each technique and a key to the numerous acronyms and abbreviations used throughout the literature to refer to these techniques. General references dealing with the applications of experimental methods to the understanding of chemical bonding in geochemical and mineralogical systems include Berry and Vaughan (1985) and Hawthorne (1988).

2.1. Diffraction effects

X-rays, electrons, and neutrons all have wavelike as well as particle nature, and each can be generated as a beam of a very limited energy (and therefore of a specific, or "monochromatic," wavelength). X-rays and electrons are scattered when they hit electrons, and neutrons are scattered when they hit nuclei. If these electrons and nuclei are arranged in the three-dimensional regular array of a crystal lattice, scattering takes place only in specific directions; that is, diffraction occurs.

2.1.1. X-ray diffraction

Highly monochromatic x-rays of wavelengths (typically ~0.5–2.3 Å) suitable to produce diffraction effects in crystalline solids are easily generated. Since the first recording of x-ray diffraction patterns on photographic plates in the early part of the twentieth century, techniques for making diffraction measurements have evolved to ever-greater sophistication, and throughout this period very large numbers of crystalline solids have been studied. The recording of diffraction effects by powder and single-crystal samples enables the crystal symmetry to be determined; in the case of detailed studies of single crystals (or very high-resolution powder diffraction), a crystal structure analysis can be performed. Details of the experimental methods and of interpretation and analysis of the data are given in numerous texts (e.g., Buerger, 1960; Arndt and Willis, 1966; Stout and Jensen, 1972). Earlier methods of recording the angles (relative to the incident beam) and the intensities of diffracted x-rays on photographic film have largely been superseded by the use of single-crystal diffractometers. In such instruments, a detector (scintillation or proportional counter) is used to measure very accurately the intensity of diffracted x rays with angles being varied by rotation of counter and crystal. Because the whole system is automated (computer controlled), large amounts of data of high quality may be obtained in a very short time.

Accurate data on interatomic distances (to ±0.0001 Å) and bond angles to ±0.01°) are therefore now available for large numbers of minerals. As well as being the source of accurate crystal structure data, modern x-ray crystallography can also provide information on the distribution of electron density in crystalline solids. This is because it is the electrons within an atom that are responsible for scattering an incident x-ray wave, and scattered amplitude falls off progressively with increasing scattering angle in a way that depends on the distribution of electron density in the atom, the falloff being less rapid the more centrally concentrated is the electron density. This, expressed in terms of scattering factor (*f*) as a function of diffraction angle and wavelength of x-rays employed [(sin θ)/λ}, appears in the expression for the amplitude of x-rays diffracted by a particular plane (*hkl*) of atoms in the crystal—the structure factor:

$$F_{hkl} = \sum_i f_i \cos 2\pi(hx_i + ky_i + lz_i) \qquad (2.1)$$

where F_{hkl} is the structure factor for the set of diffracting planes *hkl,* and f_i is the scattering factor for the atoms of the type *i* occurring in the position given by coordinates *x,y,z* of the unit cell (where the summation is taken over all atoms in the unit cell and the crystal is centrosymmetric). Thus, from the measured structure factor (derived from x-ray intensities) can be derived the information on scattering of x-rays by particular atoms and how this varies in different directions (i.e., the spacial distribution of electron density). Electron density data can be presented in the form of a diagram of the type shown in Fig. 2.1 (an early example from the classic work of M. J. Buerger). Such data can be directly compared with the results of quantum-mechanical calculations and the results of other spectroscopic measurements.

In making comparisons with theoretically determined electron densities (also referred to as *electronic charge distributions* or as *charge densities*), a number of other approaches are commonly used in addition to presenting the total charge density for a molecule or cluster (Smith, 1977). Because total charge densities for a molecule may be quite similar for different models, the alternative approaches make use of *difference (charge) densities* (Δρ). Essentially this involves considering the difference between the molecular density (ρ_{mol}) and the density of superimposed free atoms (ρ_{SFA}) at the molecular geometry (i.e., $\Delta\rho = \rho_{\text{mol}} - \rho_{\text{SFA}}$). Various workers have, in fact, used different approachs to the calculation of ρ_{SFA}. Some use the superposition of the spherically averaged ground-state atoms (the *promolecule*); others superpose the dissociated free atoms but directionally prepare them for molecular formation (i.e., an F atom would be in the configuration $(1s^22s^22p_z2p^2_{\pi x}2p^2_{\pi y})$, where *z* refers to the bond axis). Yet another approach, in cases where the bonding is assumed to be highly ionic, is to use the sum of the superposed free ions (whether entirely free or stabilized by counterions). In Fig. 2.2 are shown contour maps of total charge density and difference charge density for LiF using both superposed directionally prepared free atoms and superposed free ions. A critical discussion of the different approaches is provided by Smith (1977).

2.1.2. Neutron diffraction

Quantum effects require that neutrons have a wavelike as well as particle nature with wavelengths dependent on the velocity ($\lambda = h/mv$, where *m* is the mass of the neutron and v its velocity). Neutrons emerging from a nuclear reactor, after many atomic collisions in passing through a graphite

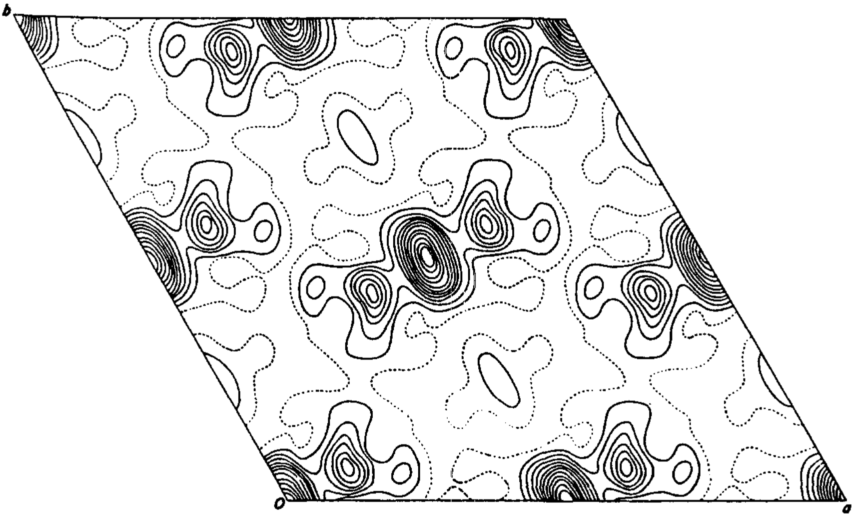

Fig. 2.1. Electron density projection $\rho_{(xy)}$ (projected parallel to c) for coesite (SiO_2) obtained from x-ray data.

or other moderator, have energies corresponding to wavelengths of the order of 1.3 Å, which are ideal for diffraction by crystals. "Reflection" of these neutrons from a crystal plate can provide a neutron beam that is effectively monochromatic. The principles of the diffraction of neutrons by crystals are entirely analogous to those of x-ray diffraction.

The disadvantages of neutron diffraction compared with x-ray diffraction are that the equipment required to generate a neutron beam is vastly more expensive and the beams provided are relatively weak and interact much more weakly with matter. As a result, much larger specimens have to be used to obtain measurable effects. The advantages of neutron diffraction are that the neutrons interact with nuclei instead of electrons, and neutrons suffer additional scattering by atoms with magnetic moments. The scattering of the neutrons by nuclei enables determination of the structural positions of light elements such as hydrogen to be determined; these atoms have so few electrons that their scattering by x-rays is negligible. It also enables atoms of neighboring atomic number, which therefore have very similar scattering amplitudes for x-rays, to be distinguished, since scattering powers of nuclei generally vary considerably from one element to another. It is also true, of course, that, whereas a neutron-diffraction experiment locates the position of the atom (nucleus), an x-ray-diffraction experiment locates the center of the electron density of the atom, and these two may well be different. The additional scattering of neutrons by atoms with magnetic moments enables the magnetic structures of solids to be studied, since coherent diffraction peaks arise for ferromagnetic and antiferromagnetic materials. A detailed account of

ρ MOL

LiF

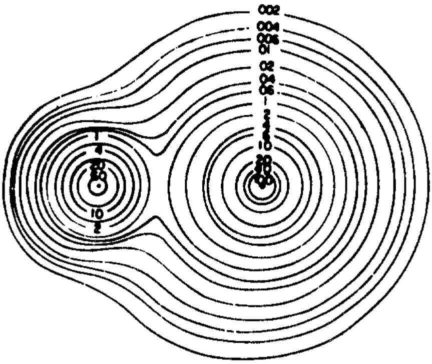

$\Delta\rho$ ATOMS

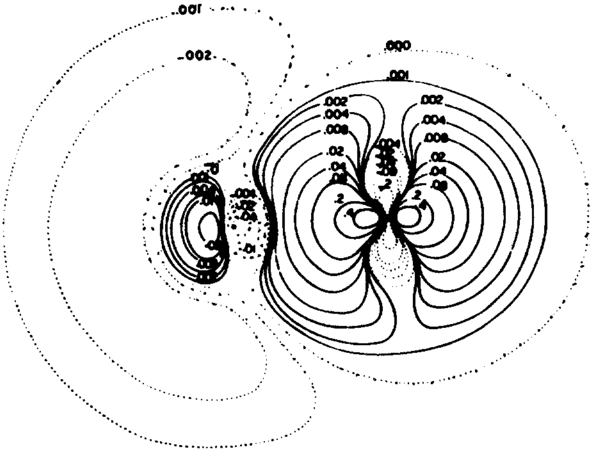

$\Delta\rho$ IONS

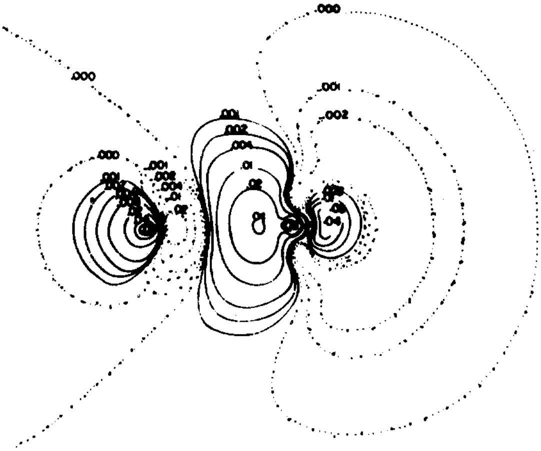

the theory, experimental techniques, and applications of neutron diffraction is given by Bacon (1962).

2.1.3. Electron diffraction and associated phenomena

Electron beams are generated and can be accelerated and focused in the electron microscope. The wavelike nature of such a beam of electrons means that it can be diffracted by crystals. However, at the high acceleration voltages employed, wavelengths are much shorter than those used in x-ray diffraction (e.g., at 50 kV, the electron wavelength is 0.0535 Å; at 1000 kV, the electron wavelength is 0.0087 Å). Electrons also interact with matter much more strongly than x-rays, and an electron beam is seriously attenuated in passing through a crystal. In fact, diffraction effects can only be observed in a transmission electron microscope (TEM), provided very thin crystals (a few hundred angstroms thick) or thin areas of crystal (as at the edges) are used. The strong interaction of electrons with matter leads to more complex diffraction effects than those observed in x-ray diffraction, so that electron diffraction is poorly suited to detailed crystal structure determination. Electron diffraction does enable very small particles or small areas of crystals (as in intergrowths) to be examined and characterized by determination of their cell dimensions and possible space-group types. With modern electron microscopes of very high resolution, it is also possible to take the information from certain "reflections" and use them to obtain a high-resolution image showing the unit cells of a crystal, or even a certain amount of detail within the unit cells. Such direct imaging of the crystal structure enables irregularities at the level of the unit cell (e.g., stacking disorder, polytypes, defects and dislocations, twinning, and fine-scale intergrowths) to be studied. Electron microscopes may also now be equipped with facilities for the chemical analysis of very small areas. Electron diffraction, direct imaging, and microanalysis are discussed in numerous references (e.g., Andrews et al., 1971; White, 1985).

Focused electron beams can also be rapidly scanned across surfaces of very small area to obtain a greatly magnified image of that surface as in scanning electron microscopy (SEM). There are also electron diffraction techniques such as reflection high-energy electron diffraction (RHEED) and low-energy electron diffraction (LEED), which are employed in obtaining structural information about the surfaces of solids (see Appendix B and Chapter 8).

←

Fig. 2.2. Contour maps of the total molecular charge density (ρ_{mol}) and the difference densities with respect to the superposition of the directionally prepared free atoms ($\Delta\rho_{ATOMS}$) and free ions ($\Delta\rho_{IONS}$) for LiF (after Smith, 1977, and Bader, 1964; reproduced with the publisher's permission).

2.2. Electron and x-ray spectroscopy

When matter is irradiated with high-energy photons, electrons can be ejected from their orbitals. If monoenergetic photons are used to cause the ejection of electrons from a material, then, to a first approximation, the kinetic energy of the emitted electrons will equal the energy of the incident radiation less the binding energy (i.e., the difference of neutral and cation total energies). In x-ray photoelectron spectroscopy (XPS, also known as ESCA, electron spectroscopy for chemical analysis), the binding energies of electrons in solids may be obtained by measuring the kinetic energies of electrons ejected by a monochromatic beam of x-rays (see Fig. 2.3). When an incident high-energy photon ejects an electron from one of the inner orbitals of an atom in the material being bombarded, the resulting vacancy can be filled by an electron from an outer orbital dropping into the inner orbital hole, with the energy lost by this electron being emitted as an x-ray photon (Fig. 2.3). The energy of this x-ray emission corresponds to the difference in ionization energies between the two orbitals. Measurement of the energies and intensities of the emitted x-rays (in x-ray emission spectroscopy, XES) can therefore provide information on the energy separation of inner orbitals and less tightly bound orbitals, including the valence orbitals. It is also possible for the energy lost by an outer electron undergoing "relaxation," so as to fill a core orbital vacancy, to be internally converted. Here the energy is used to eject one of the outer electrons rather than being emitted as x-rays (Fig. 2.3). Measurement of the kinetic energies of these electrons is the basis of Auger electron spectroscopy (AES). It is also possible to measure the absorption of a range of incident x-ray energies in the process of exciting valence electrons into higher-energy vacant orbitals. This is the basis of x-ray absorption spectroscopy and related spectroscopies.

2.2.1. Photoelectron spectroscopy (and Auger electron spectroscopy)

If a sample is bombarded with radiation of frequency ν, then photoemission will occur for electrons with ionization energies of less than $h\nu$ (where h is Planck's constant). If the binding energy of the electron is E_b, then the ejected photoelectron will have a kinetic energy of E_k, where $E_k = h\nu - E_b$ for a free atom in the gas phase (subject to a very minor correction for the recoil energy of the positive ion). However, in a solid, further corrections are required in the form of a work function (C), which is a constant for the sample and spectrometer concerned. This takes account of effects such as positive charging of the surface following removal of photoelectrons; this charge will attract the emerging photoelectrons and degrade their kinetic energies. Thus we have:

$$E_k = h\nu - E_b - C \qquad (2.2)$$

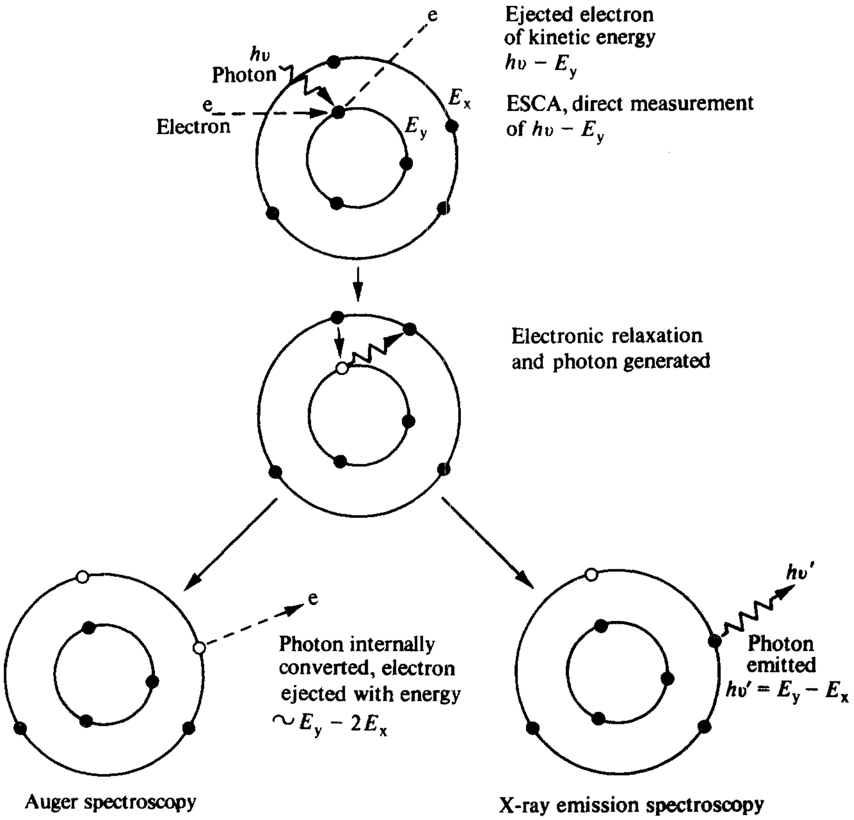

Fig. 2.3. Schematic illustration of the mechanisms of electron and x-ray generation in x-ray emission, ESCA, and Auger spectroscopies (after Urch, 1971, reproduced with the publisher's permission).

The probability that an incident photon will cause the ejection of a particular electron is proportional to an integral of the type:

$$\int \Psi_i P \, \Psi_f \, d\tau \tag{2.3}$$

where $d\tau$ is a differential volume element, Ψ_i and Ψ_f are wave functions for the initial and final states of the system and P is the transition operator. This integral can be simplified by approximations involving replacing Ψ_i and Ψ_f by the wave function for the "atomic" orbital from which the photoelectron was ejected (Φ_i) and a plane-wave function for a free electron Φ_f, and using the electric dipole approximation for P, which yields:

$$\int \Phi_i(er)\Phi_f \, d\tau \tag{2.4}$$

where e is the electronic charge and r the electron coordinate. No forbidden transitions arise from this integral, and the probability of photoemission will depend on the magnitude of the integral, which depends in turn largely on the spatial overlap of Φ_i and Φ_f.

Experimentally, photoelectron spectroscopy requires a source of monochromatic radiation. In x-ray photoelectron spectroscopy the sources normally used are the Mg $K\alpha_{1,2}$ peak (1253.6 eV) and the Al $K\alpha_{1,2}$ peak (1486.6 eV). Although the peak widths are effectively 0.7 and 0.8 eV, respectively, resolution is adequate to gain useful chemical information. Noble-gas discharge radiation sources are employed in the experimentally distinct form of photoelectron spectroscopy known as ultraviolet photoelectron spectroscopy (UPS). Most commonly, the He I resonance line (21.22 eV) has been employed, with the radiation being generated in a gas discharge lamp. The reason for using the lower energies of UPS is that, whereas x-rays will cause ejection of core- and valence-region electrons, the more intense photoemission will arise from core electrons. On the other hand, valence-shell electrons will most efficiently be ejected by far-ultraviolet light (or soft x-rays). Synchrotron radiation (see Section 2.2.3) may also be used as an excitation source, allowing tuning of the excitation energy within certain limits.

A typical x-ray photoelectron spectrometer is shown schematically in Fig. 2.4. The sample, on the end of a long rod, is irradiated by x-rays in the vacuum chamber (at $\sim 10^{-9}$ torr)—there may also be provision for an ultraviolet light source. The photoelectrons pass into an energy analyzer and detector system. Because electrons with relatively low kinetic energies are being studied (<1500 eV), the maximum depth of the sample from which such electrons emerge is only about 10 nm. Photoelectron spectroscopy is therefore a surface-sensitive technique, and, if interest is in the bulk material, great care must be taken to avoid surface contamination. Hence the use of a high vacuum and techniques such as ion (usually argon ion) bombardment to remove contaminated surface layers.

An x-ray photoelectron spectrum is typically presented as a plot of electron binding energies against intensities, and an example is shown in Fig. 2.5. This valence-region spectrum of PbS (galena) reported by McFeely et al. (1973) can be interpreted in terms of published band-structure calculations and calculations based on molecular-orbital methods. As further discussed in Chapter 6, the peaks labeled 1 and 1′ at the top of the valence band arise from electrons in orbitals of essentially sulfur 3*p* character (nonbonding molecular orbitals). Below these in energy lie the main bonding orbitals (peak 2) of chiefly lead 6*s* plus sulfur 3*p* character. Peak 3 arises from the sulfur 3*s* orbitals, which are not involved in bonding. The intense double peak at ~20 eV binding energy comes from electrons in the lead 5*d* orbitals. These more tightly bound, compact, and "core-like" orbitals give rise to much more intense photoemission.

Auger electrons will also be detected in the same spectrometer as used for x-ray photoelectron spectroscopy. The ejection of a second electron

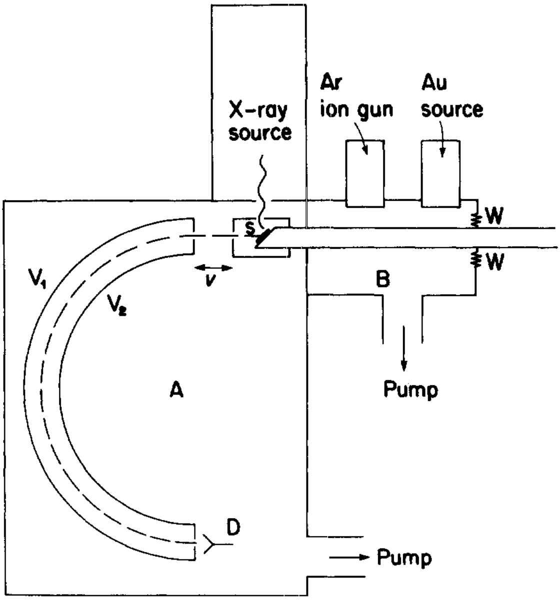

Fig. 2.4. Diagrammatic representation of an x-ray photoelectron spectrometer. The sample S is at the end of the long rod that can be moved from the analysis chamber A into the sample preparation chamber B by means of the bellows W. The sample can be treated in a variety of ways in B; two possibilities are indicated in the diagram — argon ion bombardment for sample "cleaning" or depth profiling and gold decoration for calibration. Once in position in the analyzer the sample is irradiated by x rays (〰) and emits photoelectrons (---). The energy of the photoelectrons is measured by having a retarding potential (*V*) between the sample and the entrance to the hemicylindrical energy analyzer. Electrons of a specific energy are brought to a focus at the detector D by the presence of a potential difference (V_1–V_2) between the two plates of the analyzer. Spectra are scanned by varying *V* with time and observing the change in the number of photoelectrons arriving at D (after Urch, 1985, reproduced with the publisher's permission).

by the process of internal conversion (Fig. 2.3) leaves a doubly ionized atom. The energy of this second ejected electron—the Auger electron—will be approximately:

$$E(\text{Auger}) = E_b - E_c - E_d \tag{2.5}$$

where E_b is the binding energy of the original photoelectron [as in Eq. (2.2)], E_c is the binding energy of the electron involved in the process of relaxation and generation of an x-ray photon, and E_d is the binding energy for an electron from orbital *d* in the atom with an atomic number that is 1 greater than the atom under consideration. In Fig. 2.6 are shown Auger spectra of PbS, the interpretation of which is more fully discussed in Chapter 6.

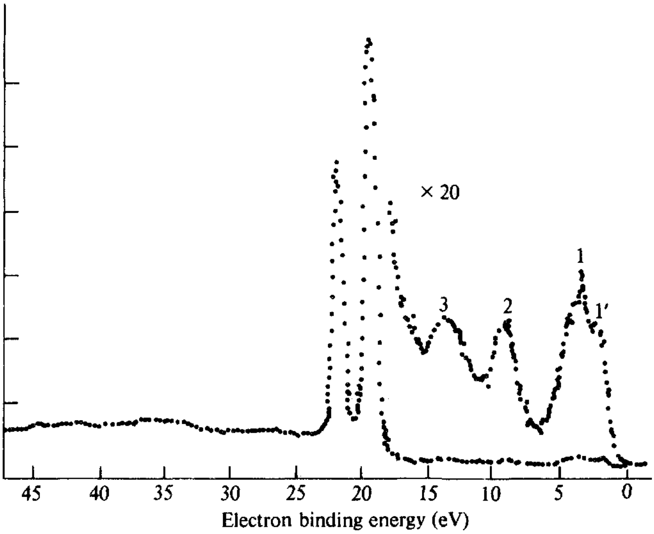

Fig. 2.5. Valence-region x-ray photoelectron spectrum of galena, PbS (after McFeely et al., 1973).

2.2.2. *X-ray emission spectroscopy*

In x-ray emission spectroscopy, the energy lost by relaxation of an outer electron (binding energy E_c) into a hole created in a more tightly bound orbital (binding energy E_b) is emitted as an x-ray photon of energy $h\nu'$. Thus the frequency ν of the emitted x-radiation is:

$$\nu = \frac{E_b - E_c}{h} \tag{2.6}$$

X-ray emission spectra are subject to an electric-dipole selection rule that requires that the orbital angular momentum quantum number (l) changes only one unit during the transition; hence:

$$\Delta l = \pm 1 \tag{2.7}$$

Permitted x-rays ("diagram lines") will only be generated by the transitions: $s \leftarrow p$, $p \leftarrow s$ or d, $d \leftarrow p$ or f, $f \leftarrow d$ or g. Although this is essentially an "atomic" selection rule, it can be applied to transitions involving "molecular" orbitals in the valence band. Thus, x-ray spectra can provide valuable information about the atomic contributions to molecular orbitals. X-ray emission peaks are classified according to the orbital (or "shell"—K, L, M, etc.) in which the initial vacancy was created, a familiar system summarized in Fig. 2.7.

The intensity (I) of x-ray emission is given by an equation of the form:

$$I = \text{constants} \times \nu^3 \left(\int \Psi_i P \Psi_f d\tau\right)^2 \tag{2.8}$$

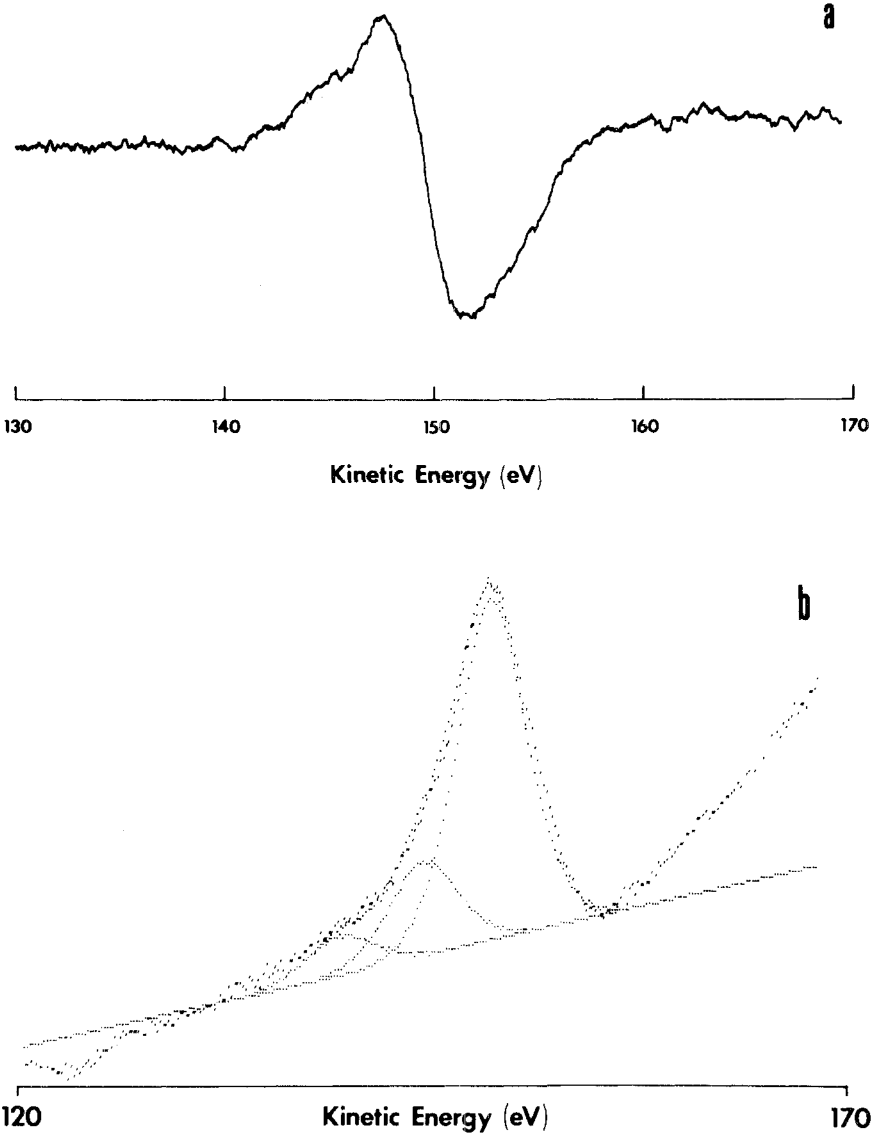

Fig. 2.6. Sulfur *LMM* Auger electron spectra of PbS obtained from a natural specimen of high purity: (a) differentiated spectrum; (b) undifferentiated spectrum showing computer fit of the data points (dashes) to three-component peaks (dots) at 140, 145.2, and 149.5 eV, respectively. Data were obtained using a Kratos XSAM 800 instrument (after Tossell and Vaughan, 1987, reproduced with the publisher's permission).

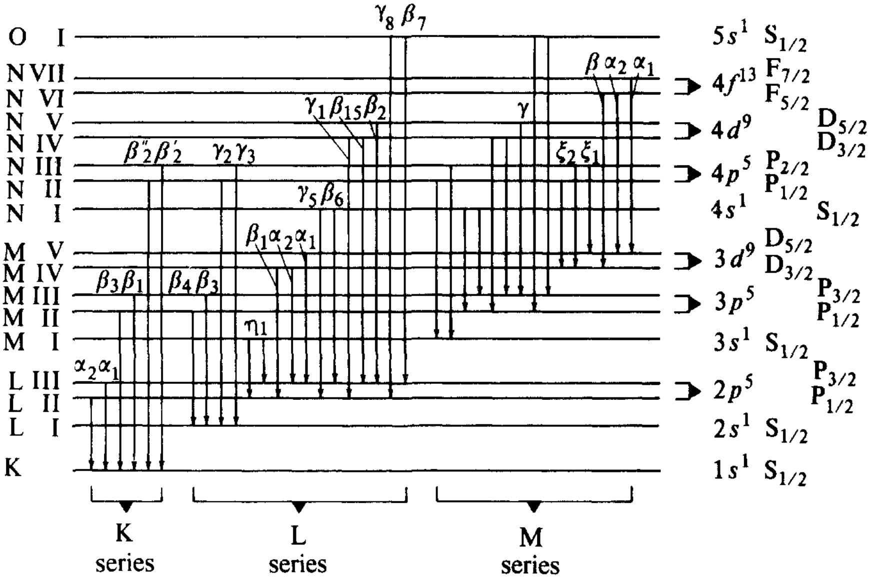

Fig. 2.7. Permitted x-ray emission transitions. Electron configurations and the corresponding spectroscopic state are indicated on the right (after Urch, 1971, reproduced with the publisher's permission).

where Ψ_i and Ψ_f are the wave functions for initial and final states, before and after x-ray emission, and P is the transition operator. If a one-electron (or "frozen-orbital") approach is used in which only the orbitals involved in the transition are considered and the others regarded as unaffected, Ψ_i will be replaced by the atomic orbital for the initial vacancy (Φ_i) and Ψ_f by the (atomic or molecular) orbital having the final vacancy. If a molecular orbital has to be used, the simplest form will be a linear combination of atomic orbitals, $\Sigma_r a_{rf}\Phi_r$ where Φ_r is an atomic orbital at atom r. If P is also assumed to be dominated by the electric-dipole term, then we can write:

$$I \propto \int \Phi_i(er)\left(\sum_r a_{rf}\Phi_r\right) d\tau \qquad (2.9)$$

If, for example, the final-state molecular orbital is composed of s and p orbitals from atoms X and Y, and the initial vacancy is an s orbital on atom X (written Xs' to distinguish it from other s orbitals on X), then the above integral becomes:

$$\int \Phi_{Xs'}\,(er)a_{Ys}\Phi_{Ys}\,d\tau + \int \Phi_{Xs'}\,(er)a_{Yp}\Phi_{Yp} + \int \Phi_{Xs'}\,(er)a_{Xs}\Phi_{Xs} \qquad (2.10)$$
$$+ \int \Phi_{Xs'}\,(er)a_{Xp}\Phi_{Xp}$$

The first term corresponds to a forbidden transition $s' \leftarrow s$ on atom X and is hence zero. The second term is an allowed transition on X, and the third and fourth terms are "crossover" transitions from orbitals on Y to the vacancy on X. Examination of the magnitudes of valence orbitals of $Y(\Phi_{Ys}, \Phi_{Yp})$ in the region of $\Phi_{Xs'}$ shows that they will be very small, so that the third and fourth terms above can be ignored. Thus we have:

$$I = \text{constants} \times \nu^3 (a_{Xp})^2 \left(\int \Phi_{Xs'} \, (er) \Phi_{Xp} \right)^2 d\tau \qquad (2.11)$$

showing that the intensity of an x-ray emission peak from a valence orbital is dominated by the atomic transition term, modified by the square of the appropriate molecular-orbital coefficient. If two or more molecular orbitals have Xp character, then the transitions to a vacancy in a core Xs' orbital will produce two or more x-ray peaks, the relative intensities of which would be determined by the magnitudes of the $(a_{Xp})^2$ terms in the different orbitals. Thus, the relative intensities of x-ray peaks resulting from valence-band–to–core transitions can be used to measure the contributions of specific atomic orbitals in different molecular orbitals.

X-ray emission spectra are generated from solids in a number of instruments widely used for the chemical (elemental) analysis of materials. In the x-ray fluoresence spectrometer, the source of ionizing radiation is x-rays from an x-ray tube, and in the electron probe microanalyzer the source is a beam of electrons. Both instruments can be used to record x-ray emission spectra, although the former is usually employed. In practice, the use of spectrometers for chemical bonding studies requires higher resolution than for routine analysis, and this may require some modifications to commercial instruments as well as special care in recording the data. The essential features of an x-ray spectrometer are shown in Fig. 2.8. More sophisticated systems leading to improved resolution may employ such features as a double-crystal spectrometer, a curved-crystal spectrometer, or a diffraction grating. Long-wavelength ("soft") x-rays have the greatest potential for bonding studies since the small changes involved in chemical shifts (a few electron volts) are more readily observed when the overall transition energies are of the order of hundreds rather than thousands of volts. However, the soft-x-ray region is also the most difficult experimentally, requiring an intense radiation source, good vacuum conditions, and especially sensitive detectors.

Although valuable information may be revealed in a single x-ray emission spectrum, much more information can be gained if all possible x-ray emission spectra, along with the x-ray photoelectron spectrum of the material, can be assembled and put on a common energy scale. Given XPS and XES data, this is possible because core ionization energies are measured directly using XPS. This approach, and the application of XES in

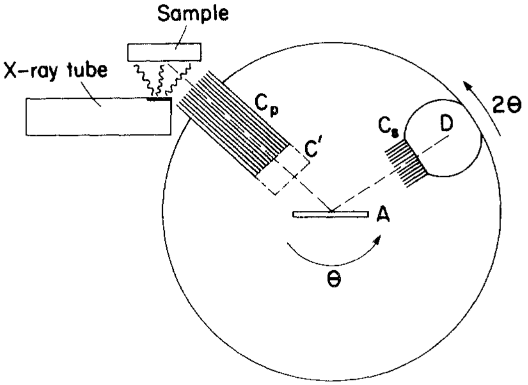

Fig. 2.8. Diagrammatic representation of an x-ray emission spectrometer. Characteristic x rays from the sample (---) are stimulated by irradiating it with radiation from a sealed (or open-window) x-ray tube (〰). A parallel beam of characteristic x rays is generated by passage through the primary collimator C_p. Those x rays that are diffracted by the crystal A according to Bragg's equation are detected in a gas-filled proportional counter (or scintillation counter) D after having passed through the secondary collimator C_s. Spectra are scanned by rotating A through θ and D through 2θ. C′ is a convenient position for extra collimation, at right angles to C_p, to improve resolution and peak profile (after Urch, 1985, reproduced with the publisher's permission).

the study of minerals, can be illustrated by considering the spectra of MgO (periclase)—a simple oxide with the rocksalt-type crystal structure.

In Fig. 2.9 are shown the x-ray photoelectron spectrum and the Mg $K\beta$, Mg $L_{2,3}M$, and O K_α x-ray emission spectra of periclase from the work of Nicholls and Urch (1975). Essentially, the magnesium $K\beta$ spectra arise from Mg $3p \rightarrow 1s$ transitions, magnesium $L_{2,3}M$ from Mg $3s$ and possibly $3d \rightarrow 2p$, and oxygen K_α from O $2p \rightarrow 1s$ transitions. Alignment of the spectra on a common energy scale enables the relative energies of these transitions and hence of the orbitals involved to be compared. A first point of note from these spectra is the actual existence of the Mg $K\beta$ spectrum (i.e., the presence of electrons in orbitals expected to be empty in Mg^{2+}), and an indication of the covalent character of the Mg–O bond. Similarly, the structure of the O $K\beta$ spectrum, indicating splitting of the $2p$ level, shows a covalent interaction between Mg and O. Nicholls and Urch (1975) suggest that the bonding between magnesium and oxygen is best understood using just one cube of the MgO lattice with its four magnesiums and four oxygen atoms at alternate corners. From the magnesium atoms can be constructed a_1 and t_2 orbitals from p orbitals on the oxygen atoms. Interaction is also possible between the e, t_1, and t_2 orbitals of the remaining magnesium p orbitals and orbitals of the same irreducible representations from the other oxygen p orbitals. These interactions provide a qualitative explanation for the splitting of Mg $K\beta$, O $K\alpha$, and Mg $L_{2,3}M$ peaks. The main peak in the XPS is due to oxygen $2s$ character

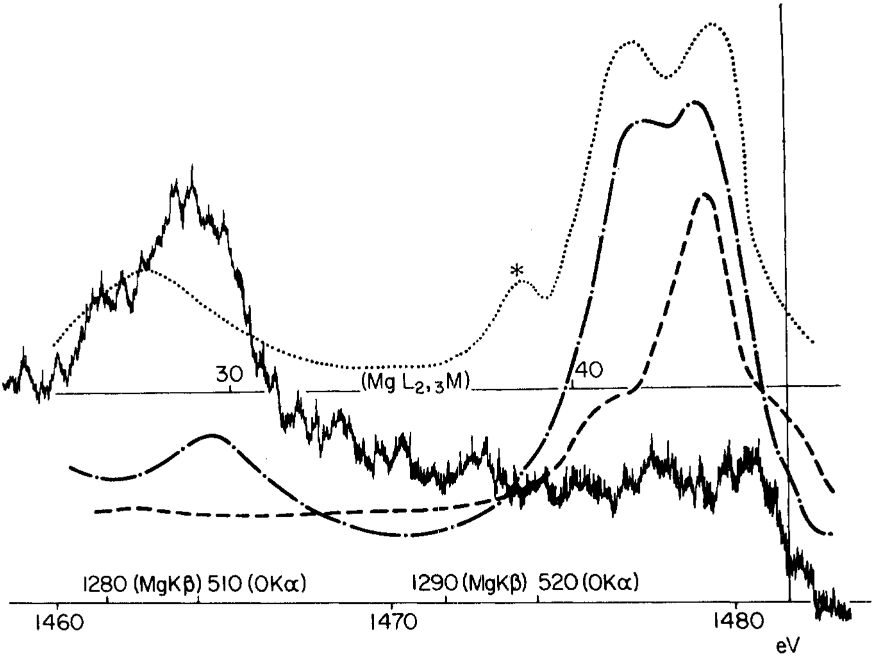

Fig. 2.9. X-ray emission (Mg Kβ —·—, $L_{2,3}M$ ···, O Kα – – –) and x-ray photoelectron spectra for periclase (MgO). Photoelectron kinetic energies are given on the lower scale, x-ray emission energies on the upper scales, as indicated. The asterisk marks the Mg $L_{I}L_{2,3}$ x-ray line (after Urch, 1985, reproduced with the publisher's permission).

orbitals and lines up with Mg Kβ′, showing that this peak originates from a small amount of Mg 3*p* character present in molecular orbitals that are mostly oxygen 2*s* in character. A fuller discussion of the electronic structure of MgO is given in Chapter 4.

2.2.3. X-ray absorption spectroscopy (including EXAFS and XANES)

The absorption of x rays by materials has been studied for many years, but x-ray absorption spectroscopy has only become an important tool in structure and bonding studies over the past decade. This has been partly because of advances in theory, but chiefly because of the availability of synchrotron radiation sources providing x rays three or more orders of magnitude more intense than those from the standard x-ray tube. Spectral measurements formerly taking a week or more can now be completed in minutes.

Synchrotron radiation is emitted when relativistic charged particles travel in curved paths in magnetic fields (and hence is a byproduct of high-energy physics experiments). Although x-ray absorption spectra can be recorded as an excitation spectrum of one of the secondary processes (uv–visible or x-ray fluorescence, secondary- or Auger-electron yield), they are most simply measured using the single-beam transmission method illustrated in Fig. 2.10.

The absorption of an x-ray photon of energy E by a sample of thickness x is given by:

$$I_t(E) = I_0(E)e^{-\mu_{\mathrm{total}}(E)x} \tag{2.12}$$

where $I_t(E)$ and $I_0(E)$ are the transmitted and incident photon intensities, and $\mu_{\mathrm{total}}(E)$ is the total absorption coefficient of the sample. When the x-ray photon energy (E) is tuned to the binding energy of some core level of an atom in the material, an abrupt increase in the absorption coefficient occurs (giving an absorption edge). For an isolated atom, a spectrum of x-ray absorption as a function of energy around and beyond the absorption edge shows little or no fine structure; after the sharp increase at the edge, the absorption coefficient decreases monotonically (Fig. 2.11). For atoms in a molecule or in a condensed phase, the variations of absorption coefficient around the absorption edge and above the absorption edge display complex fine structure (see Fig. 2.11). The former is studied in x-ray absorption near-edge structure (XANES) and the latter in extended x-ray absorption fine structure (EXAFS). The energy regions studied in each of these techniques are shown in Fig. 2.12. Near or below the edge, there also generally appear absorption peaks due to excitation of core electrons to some bound states [e.g., $1s \rightarrow nd$, $(n+1)s$, or $(n+1)p$ orbitals for the K edge]. The processes occurring here, which are akin to those studied in x-ray emission spectroscopy, can provide valuable bonding information, such as the energetics of virtual orbitals and the electronic configuration.

For x-ray absorption of a metal atom embedded in a solid, $\mu_{\mathrm{total}}(E)$ beyond the absorption edge is made up of: (1) absorption of the matrix $[\mu_{\mathrm{B}}(E)]$ in which the metal atom is embedded, and (2) absorption due to the metal atom under study $[\mu_{\mathrm{A}}'(E)]$. Hence:

$$\mu_{\mathrm{total}}(E) = \mu_{\mathrm{B}}(E) + \mu_{\mathrm{A}}'(E) \tag{2.13}$$

where $\mu_{\mathrm{A}}'(E)$ again is composed from three contributions. The first is reminiscent absorption from the preceding absorption edges. $[\mu_{\mathrm{L}}(E)]$; the second is atomic absorption of the atom under study $[\mu_{\mathrm{A}}(E)]$; and the third is the modulation on the second due to the electron backscattering from the neighboring atoms $[\mu_{\mathrm{EXAFS}}(E)]$. Thus:

$$\mu_{\mathrm{A}}'(E) = \mu_{\mathrm{L}}(E) + \mu_{\mathrm{A}}(E) + \mu_{\mathrm{EXAFS}}(E) \tag{2.14}$$

Within the first 20–30 eV of the edge, a further contribution due to multiple scattering, $\mu_{\mathrm{XANES}}(E)$, is present. Both μ_{XANES} and μ_{EXAFS} are small contributions to the total absorption by the sample.

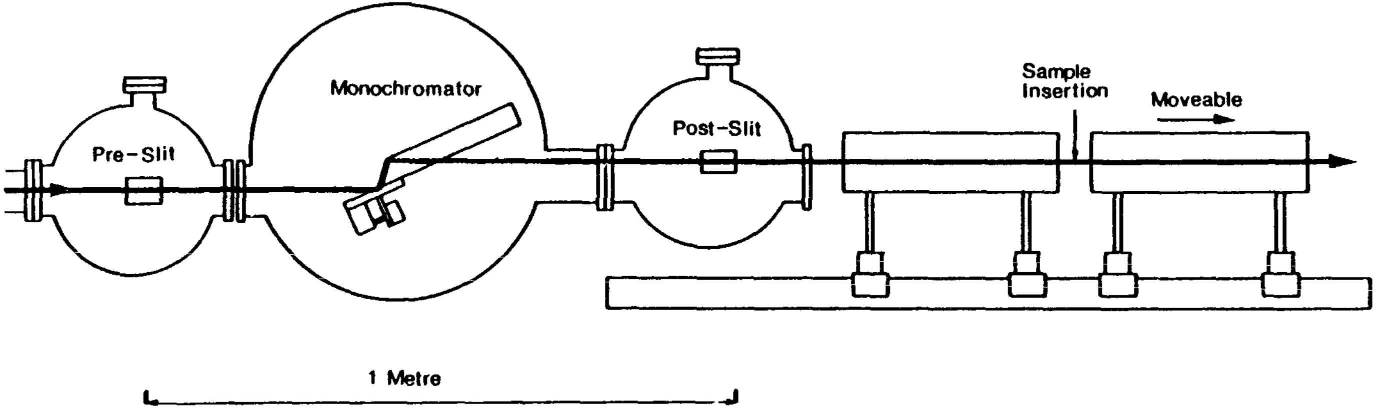

Fig. 2.10. Experimental arrangement for measuring EXAFS and XANES in transmission mode (after Hasnain, 1981, reproduced with the publisher's permission).

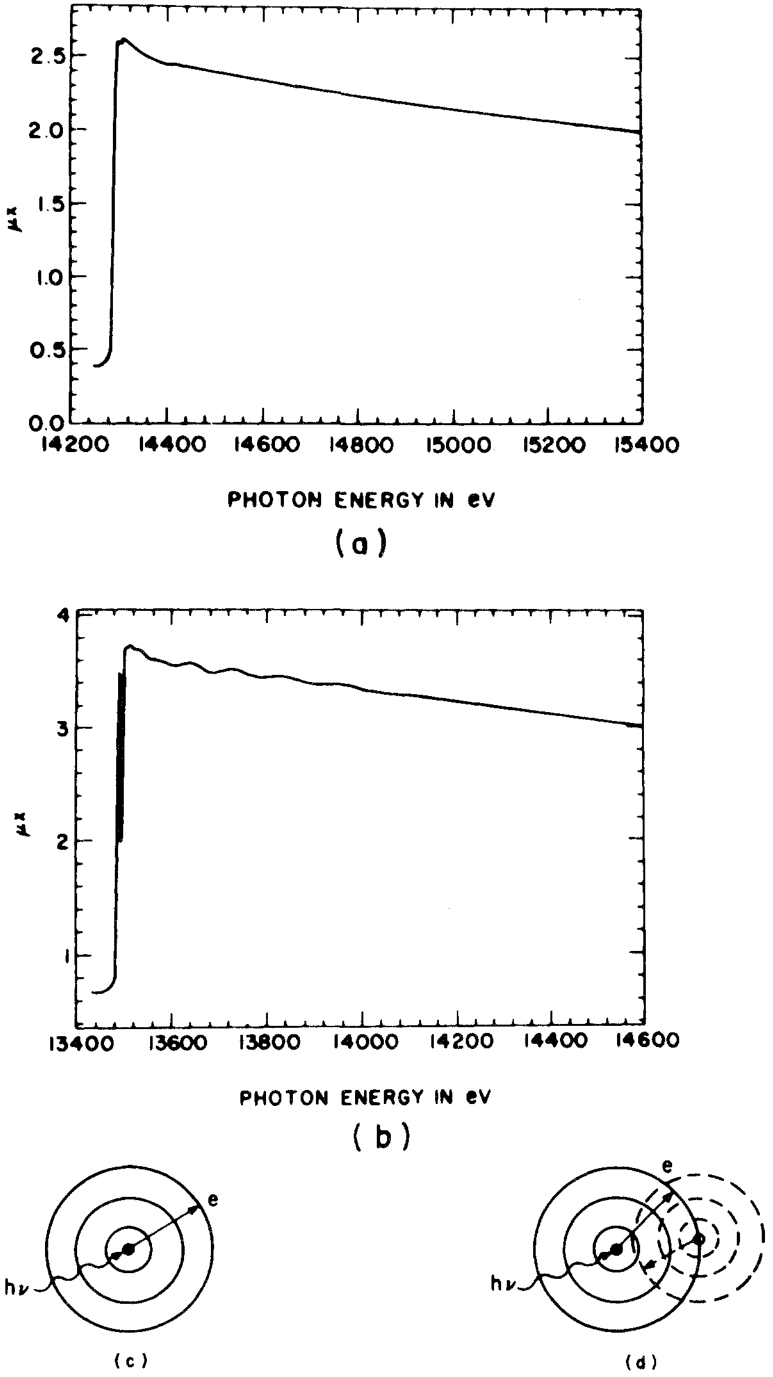

Fig. 2.11. Qualitative rationalization of the absence of EXAFS in a monatomic gas such as K [(a) and (c) above], and the presence of EXAFS in a diatomic gas such as Br_2 [(b) and (d) above] (after Teo and Joy, 1981, reproduced with the publisher's permission).

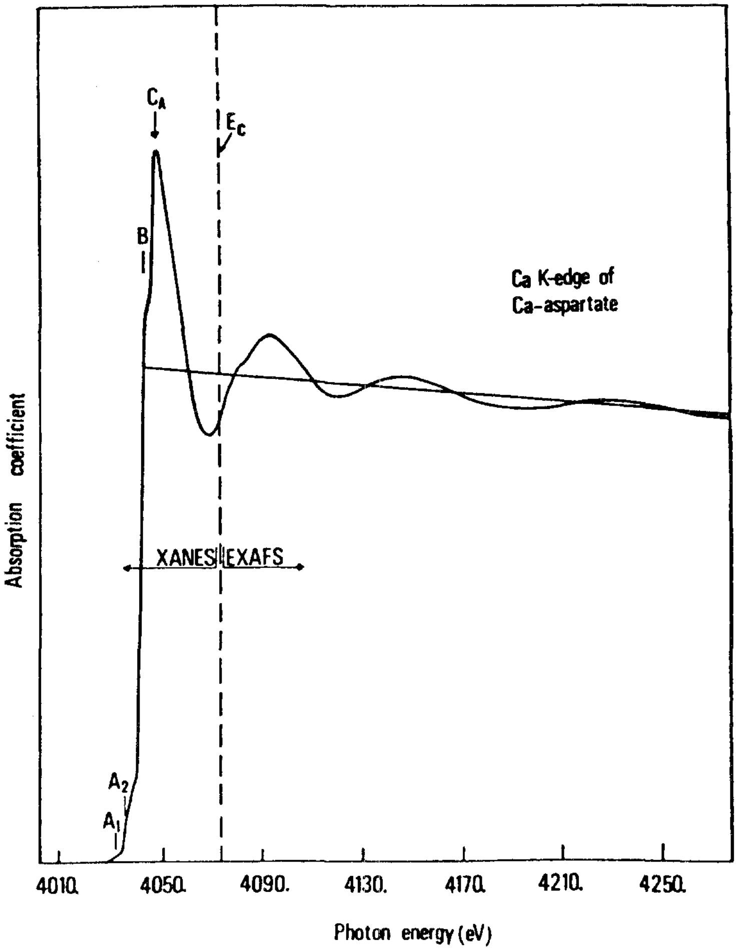

Fig. 2.12. X-ray absorption spectrum of a calcium complex showing the weak simple EXAFS oscillations and the strong near-edge (XANES) resonances (after Bianconi, 1981, reproduced with the publisher's permission).

EXAFS is thus a final-state interference effect involving scattering of the outgoing photoelectron from the neighboring atoms, as simply illustrated in Fig. 2.11. Hence, whereas in a monatomic gas the photoelectron ejected by absorption of an x-ray photon will travel outwards unimpeded and the x-ray absorption curve simply decays smoothly, in the presence of neighboring atoms, this outgoing photoelectron can be backscattered, producing an incoming wave that can interfere either constructively or destructively with the outgoing wave near the origin. The result is oscillatory behavior of the absorption rate (Fig. 2.11), and the amplitude and frequency of this modulation depend on the type and bonding of the neighboring atoms and their distances from the absorber. The distinction between XANES and EXAFS can be simply pictured as shown in Fig. 2.13. The XANES are determined by multiple-scattering resonances (MSR), where the final-state wave function in the continuum is localized inside the molecule; EXAFS oscillations are a product of scattering processes in the single-scattering regime.

Both XANES and EXAFS spectroscopies are being widely applied to materials of mineralogical and geochemical interest. For example, the $L_{2,3}$ edge (XANES) spectrum of Si in SiF_4 is shown in Fig. 2.14 (after Pittel et al., 1979; reproduced by Bianconi, 1988). This spectrum is characteristic of tetrahedrally coordinated species and shows a close similarity between the gaseous and solid forms of this compound. There are two strong peaks below E_0 (the continuum threshold, equivalent to the energy of the core ionization potential) and two strong peaks above E_0; the former have been assigned to unoccupied valence orbitals. The L_3 XANES of Si in solid SiO_2 (Fig. 2.15, after Bianconi, 1979) are also very similar to SiF_4 gas, suggesting that the spectra are chiefly determined by multiple scattering inside the first coordination shell, and also lending weight to arguments for using SiF_4 and SiO_4 tetrahedral clusters in modeling the electronic structures of more complex silicates.

Because the information from EXAFS concerns the local structure surrounding a particular atom, it is especially useful in studying materials

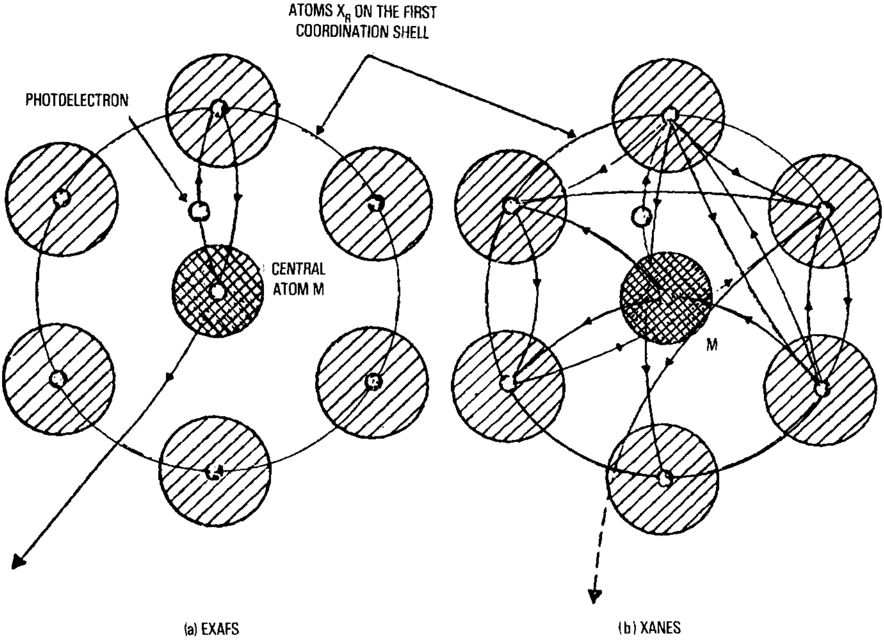

Fig. 2.13. Pictorial view of the scattering processes of the excited internal photoelectron determining the EXAFS oscillations (single-scattering regime) and the XANES (multiple-scattering regime) (after Bianconi, 1981, reproduced with the publisher's permission).

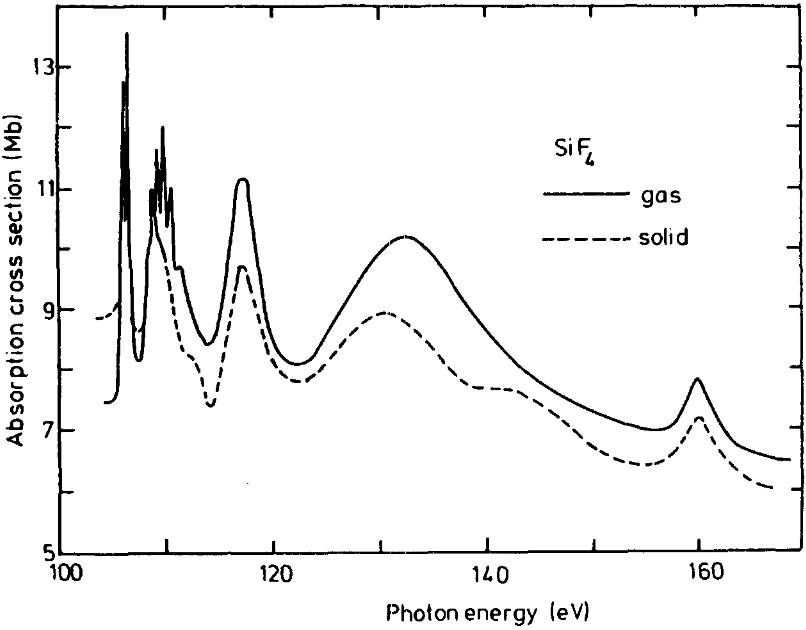

Fig. 2.14. The $L_{2,3}$ edge of Si in the SiF_4 molecule, a spectrum typical of a tetrahedral molecule (after Bianconi, 1981, reproduced with the publisher's permission).

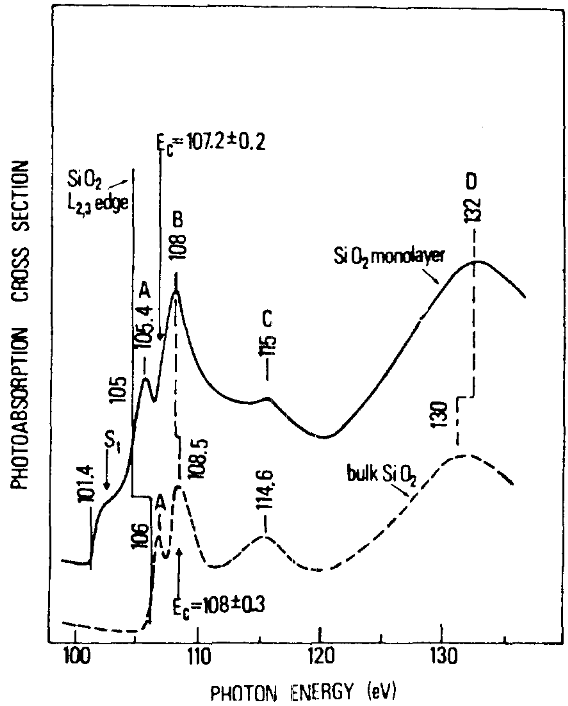

Fig. 2.15. The L_3 XANES of Si in SiO_2 together with the surface L_3 XANES of a thin SiO_2 layer (~5 Å in thickness "monolayer") (after Bianconi, 1981, reproduced with the publisher's permission).

lacking long-range order, such as glasses. Studies of α-quartz, amorphous silica, and silicate and borate glasses (Greaves et al., 1981) have provided new information on the local structure. Thus, in Fig. 2.16 are shown EXAFS spectra above the sodium K edge in sodium disilicate, soda–lime–silica, and sodium diborate glasses. Simulation of the spectra (dotted curves in Fig. 2.16) yields the information that the sodium in the disilicate is 5-coordinate to the oxygen, in the diborate it is 6-coordinate, and in the soda–lime glass only 2-coordinate.

2.3. Optical (uv–visible–near-ir) spectroscopy

Electromagnetic radiation in the visible and near-ir and uv regions of the spectrum, particularly with energies between approximately 33,000 and 4,000 cm^{-1} (3,000–25,000 Å, ~4–0.5 eV) interacts with the electrons in solids (or liquids and gases). These interactions give rise to the processes of absorption and reflection qualitatively observed in minerals as the properties of color and luster. The quantitative measurement of such absorption and reflection processes forms the basis of electronic (optical) absorption spectroscopy. The absorption and reflection phenomena arise from electronic excitation processes involving the valence electrons, excitation processes that may be of several kinds:

1. *Crystal-field (or d-d) transitions.* Splitting of the *d*-orbital energy levels of a transition-metal ion by the crystal (or ligand) field of the surrounding anions gives rise to the possibility of electronic transitions between these levels. Such *d-d* transitions are responsible for the colors of many transition-metal-bearing minerals and are best treated within the formalism of crystal-field theory.
2. *Charge-transfer transitions.* Electrons may be transferred between filled (or partly filled) orbitals and empty orbitals on adjacent anion (or ligand) and cation (commonly a metal) or between adjacent cations (usually metals). Such ligand–metal and metal–metal charge-transfer transitions are best treated within the formalism of molecular-orbital theory.
3. *Electronic transitions involving color center or other "imperfections."* The presence of interstitial impurities, of vacancies or of other imperfections, can introduce electrons that may absorb electromagnetic energy in transitions to various excited states.
4. *Electron transitions involving energy bands.* In metals and in semiconductors in which the energy gap between large numbers of filled and vacant energy levels is small (<2 eV as in many metal oxides and sulfides), intense absorption and reflection of light will occur, resulting in a metallic appearance. The absorption resulting from transitions between such adjacent filled and

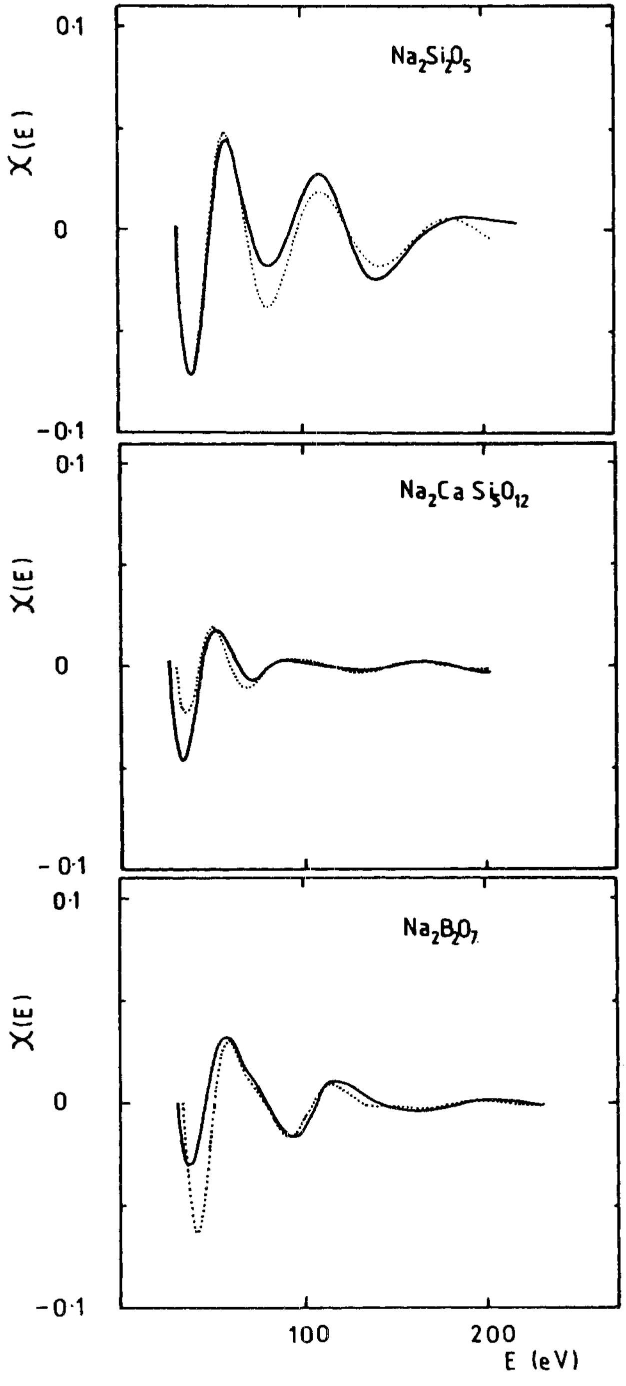

Fig. 2.16. Normalized EXAFS spectra, $\chi(E)$, above the sodium K edge in three glasses: $Na_2Si_2O_5$, $Na_2CaSi_5O_{12}$, and $Na_2B_4O_7$. Solid lines are experimental data, dotted lines are simulated spectra (after Greaves et al., 1981, reproduced with the publisher's permission).

vacant energy levels is best treated within the formalism of band theory (or a molecular-orbital/band model).

The electronic excitation processes listed as (1) to (3) are generally localized and give rise to color in minerals that nevertheless remain translucent (such as the silicates, carbonates, and many of the oxides). The processes listed under (4) commonly result in opaque minerals since the availability of large numbers of vacant energy levels into which the electrons may be excited causes very strong absorption. When this happens, reflectance is also high because light is re-emitted when the electrons return to the ground state. Translucent phases may be studied using the methods of electronic (optical) absorption spectroscopy and opaque phases using diffuse and specular reflectance spectroscopy.

2.3.1. Electronic (optical) absorption spectroscopy

Absorption spectral measurements of transparent solids can be undertaken using standard spectrophotometers. Although early work in this field was hampered by the lack of crystals of a suitable size, the development of microscope accessories for spectrophotometers (Burns, 1970; Mao and Bell, 1973; Langer and Fentrup, 1979) means that natural or synthetic crystals only tens of micrometers in diameter can now be measured using systems of the type illustrated in Fig. 2.17. Such systems also permit the routine measurement of the absorption spectra of oriented single crystals using polarized light. Using the high-pressure diamond anvil cell and laser heating systems, it is also possible to measure such spectra at elevated temperatures and at high pressures. One disadvantage of microscope photometry is that, whereas accurate measurements of the energies of absorption bands are possible, intensity determinations are subject to error due to the convergent light introduced by the optical system of the microscope.

Crystal-field transitions originate when electrons are excited by light between incompletely filled 3*d* orbital energy levels within a transition-metal ion. The principal parameters derived from measuring the positions of the absorption bands in crystal-field spectra are the crystal-field splitting parameter (Δ) and the Racah parameters (B and C), which provide a measure of the degree of covalent character of the cation–anion bonds. Such spectra also afford a means of identifying the oxidation state and coordination of transition metals in mineral structures, given favorable circumstances.

An example of a "crystal-field" spectrum is shown in Fig. 2.18. This is the optical absorption spectrum of a crystal of andradite garnet [$Ca_3Fe_2(SiO_4)_3$] and is typical of the profile arising from crystal-field transitions in Fe^{3+} ions octahedrally coordinated to oxygen. Assignment of the features in such a spectrum is normally undertaken using an energy-level diagram of the type shown in Fig. 2.19. Here, the energies of the

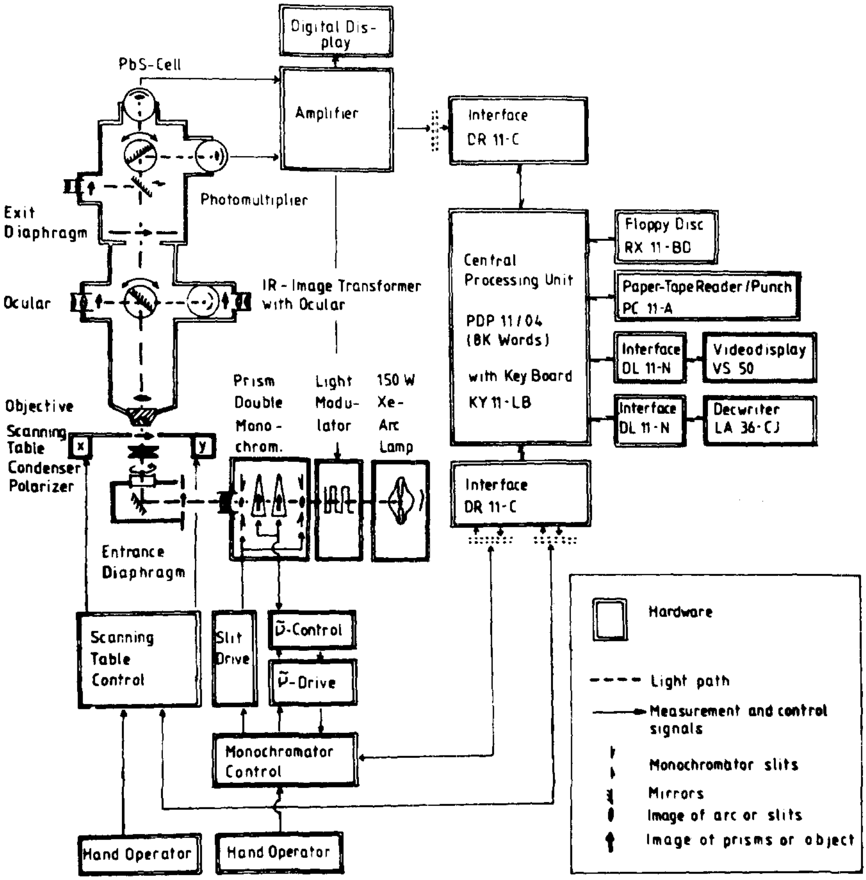

Fig. 2.17. Schematic layout of a microscope spectrophotometer system used to measure polarized absorption spectra of very small mineral crystals. The computer-operated, single-beam instrument shown here comprises a polarizing microscope equipped with a stabilized light source (xenon arc lamp or tungsten lamp cover the range 250–2000 nm), a modulator that chops the light beam with a frequency of 50 Hz (the amplifier for the photodetector signals is modulated with the same phase and frequency), and a Zeiss prism double monochromator. Single crystals as small as 10 μm diameter may be measured with this system. A diamond-windowed high-pressure cell can be readily mounted on the microscope scanning table for spectral measurements at very high pressures (after Burns, 1985, reproduced with the publisher's permission).

possible *d*-electron excited-state configurations have been calculated in an octahedral field of increasing strength, using the formalisms of crystal-field theory. Thus, in order of increasing energy (decreasing wavelength), the peaks here can be assigned as ${}^6A_{1g}$ to ${}^4T_{1g}$, ${}^4T_{2g}$, ${}^4E_g + {}^4A_{1g}$, ${}^4T_{2g}$, ${}^4E_g$ transitions. The intensities of all of these transitions are weak since, in this d^5 ion, a change of spin multiplicity (number of unpaired electrons) is involved in the transition. The intensity of an absorption band is, in fact,

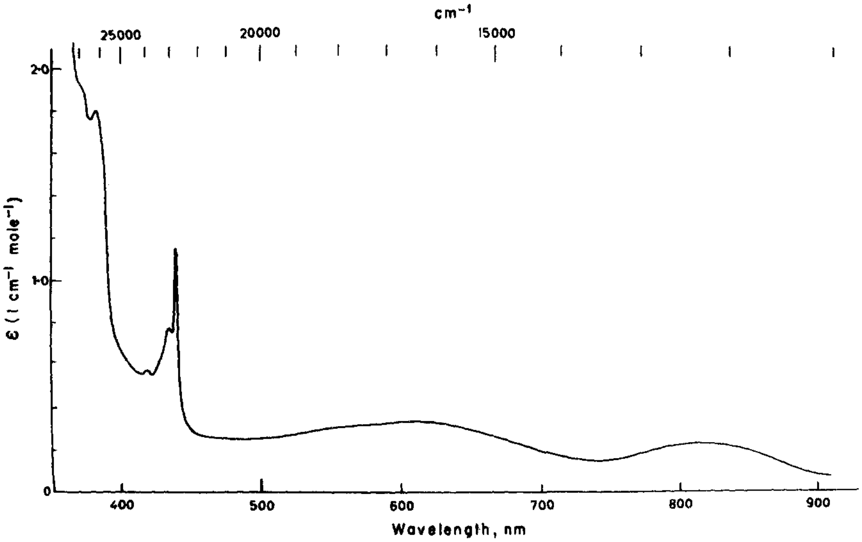

Fig. 2.18. Electronic (optical) absorption spectrum of andradite $Ca_3Fe_2(SiO_4)_3$. The spectrum shows the typical profile of crystal-field transitions in Fe^{3+} ions.

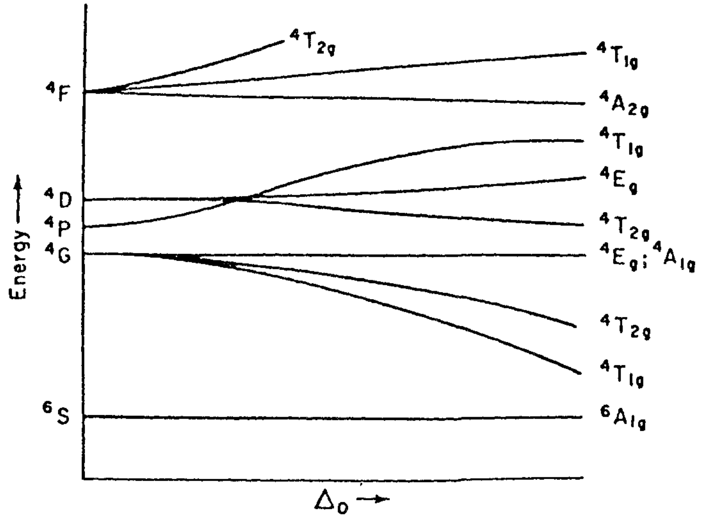

Fig. 2.19. Partial energy-level diagram for transition-metal ions with d^5 configurations in high-spin states in an octahedral crystal field. Only sextet and quartet spectroscopic and crystal-field states are shown (after Burns, 1970, reproduced with the publisher's permission).

related to the probability of the transition that is proportional to the transition moment (Q), where:

$$Q = \left| \int_{-\infty}^{+\infty} \psi_G \, \mu \, \psi_E \, d\tau \right|^2 \tag{2.15}$$

and ψ_G and ψ_E are the wave functions of ground and excited states, μ is the electric dipole moment operator, and $d\tau$ the volume element. A transition is forbidden when $Q = 0$. The transition moment can be expressed in terms of spacial and spin components:

$$Q = \int_{-\infty}^{+\infty} \psi_G \, \mu \, \psi_E \, d\tau_{\text{space}} \int_{-\infty}^{+\infty} \psi_G \, \mu \, \psi_E \, d\tau_{\text{spin}} \tag{2.16}$$

Unless $(\psi_G)_{\text{spin}} = (\psi_E)_{\text{spin}}$, then the spin component is zero and the transition is spin-forbidden. Nevertheless, spin-forbidden transitions are observed as weak features (as in Fig. 2.18) typically with 10^{-3}–10^{-5} the intensity of fully allowed transitions. This is because of the interaction between the electron spin magnetic moment and the magnetic moment due to the orbital motion of the electron (spin-orbit coupling). The Laporte selection rule, furthermore, states that only transitions between wave functions with one having gerade and the other ungerade character are allowed (hence all *d-d* transitions are Laporte forbidden). This arises since the spatial component can be further broken down:

$$\psi_{\text{space}} = \psi_{\text{electronic}} \, \psi_{\text{vibrational}} \, \psi_{\text{rotational}} \, \psi_{\text{translational}} \tag{2.17}$$

The last two remain unchanged over the time span of an electronic transition and integrate out to unity, so that:

$$Q_{\text{space}} = \int_{-\infty}^{+\infty} (\psi_G)_{\text{electronic}} \, (\psi_G)_{\text{vibrational}} \, \mu (\psi_E)_{\text{electronic}} \, (\psi_E)_{\text{vibrational}} \, d\tau \tag{2.18}$$

The dipole moment operator (μ) has associated with it ungerade character; so the integral will be zero if ψ_E and ψ_G are both either gerade or ungerade. Again, Laporte-forbidden transitions do occur (with 10^{-2}–10^{-3} the intensity of fully allowed transitions) because of mixing of the orbitals in the excited state in noncentrosymmetric sites, and even in centrosymmetric sites as a result of vibrations of the metal atoms away from the center of symmetry (vibronic coupling).

Both spin-allowed and spin-forbidden transitions in Fe^{2+} ions are seen in the polarized absorption spectra of a lunar olivine shown in Fig. 2.20 (after Bell and Mao, 1972). This ferromagnesian silicate has cations in two kinds of distorted octahedral sites (*M*1 and *M*2). The broad bands at 8680 and 11,210 cm^{-1} are attributed to Fe^{2+} ions in *M*1 positions, while the more intense 9500 cm^{-1} band originates from Fe^{2+} ions in noncentrosymmetric *M*2 positions. There is debate over assignment of the abundant

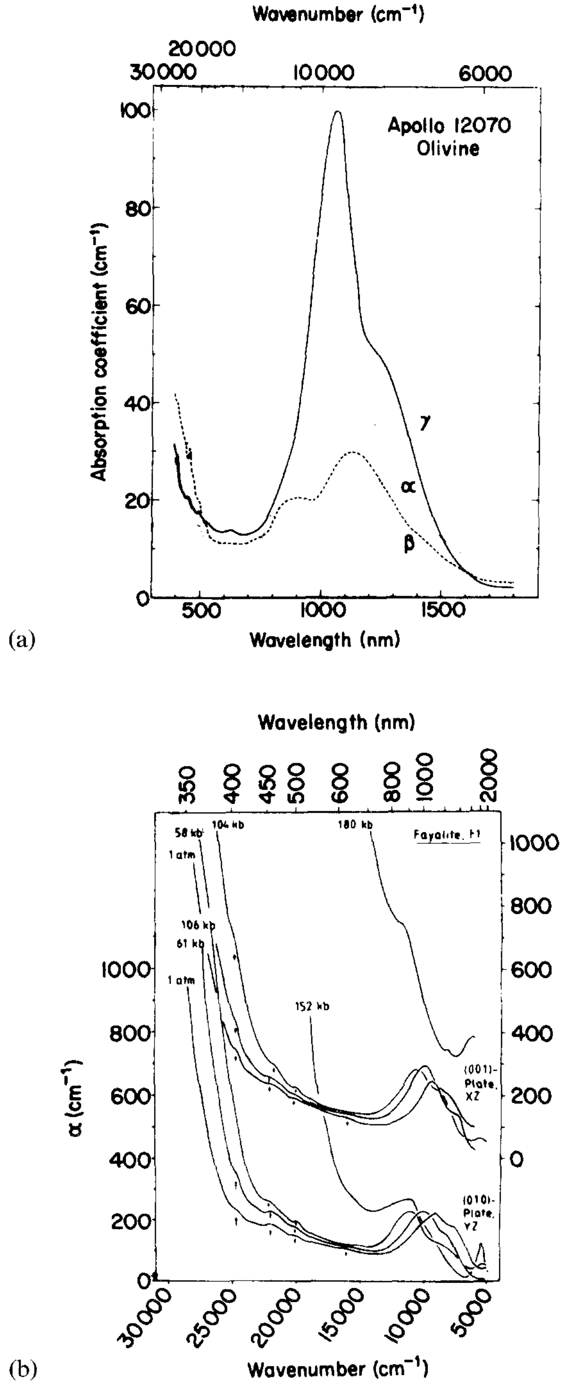

Fig. 2.20. Electronic (optical) absorption spectra of olivines: (a) polarized spectra of a lunar olivine containing 32 mol % Fe_2SiO_4 (after Hazen et al., 1977); (b) unpolarized spectra of orientated sections of fayalite at high pressures (after Smith and Langer, 1982).

features in the visible-region spectra of olivines. Peaks at 16,800 and 22,000 cm^{-1} have been variously assigned to Fe^{2+} spin-forbidden transitions, Fe^{3+} spin-forbidden transitions, $\mathrm{Fe}^{2+} \rightarrow \mathrm{Fe}^{3+}$ charge transfer (see below), or, in certain cases, Cr^{3+} spin-allowed transitions.

For an ion such as Cr^{3+} in an octahedral site (in garnet or olivine) the lowest-energy spin-allowed transition gives an absorption band with frequency ν_1 that is equivalent to the crystal-field splitting parameter (Δ_0). The second spin-allowed transition gives rise to an absorption band ν_2 the energy of which is given by:

$$\nu_2 = \tfrac{1}{2}(15B + 30\Delta_0) - \tfrac{1}{2}[(15B - 10\Delta_0)^2 + 12B\Delta_0]^{1/2} \qquad (2.19)$$

(Konig, 1971) from which the B Racah parameter may be evaluated

$$B = [(2\nu_1 - \nu_2)(\nu_2 - \nu_1)]/(27\nu_1 - 15\nu_2) \qquad (2.20)$$

Metal–metal charge transfer or intervalence transitions occur in many mixed-valence compounds and may involve cations of the same metal (e.g., $\mathrm{Fe}^{2+} \rightarrow \mathrm{Fe}^{3+}$, $\mathrm{Ti}^{3+} \rightarrow \mathrm{Ti}^{4+}$) or different metals (e.g., $\mathrm{Fe}^{2+} \rightarrow \mathrm{Ti}^{4+}$). The majority of intervalence transitions take place between octahedrally coordinated cations where the octahedra are edge-sharing; the transitions are strongly polarization dependent and occur only when the electric vector is oriented along the appropriate metal–metal axis in the crystal structure. The absorption peaks are often located in the visible region.

A good example of a mixed-valence mineral showing an $\mathrm{Fe}^{2+} \rightarrow \mathrm{Fe}^{3+}$ intervalence transition is vivianite $\mathrm{Fe_3(PO_4)_2 \cdot 8H_2O}$. Freshly cleaved vivianite crystals are pale green, but they eventually turn blue when exposed to air. In the polarized absorption spectra of a vivianite crystal shown in Fig. 2.21 the peaks centered around 8,300 and 11,400 cm^{-1} originate from transitions to components of the ^5E_g crystal-field state of Fe^{2+} ions located in distorted ($\mathrm{FeO_6}$) octahedra in the structure. The weak peak at 22,200 cm^{-1} is also a *d-d* transition, a spin-forbidden transition in $\mathrm{Fe}^{3+}(^6A_{1g} \rightarrow {}^4A_{1g}, {}^4E_g)$. However, the absorption peak at 15,800 cm^{-1} occurs only when light is polarized along the *b* vector lying parallel to the *y* crystallographic axis and intensifies when the vivianite crystals are allowed to undergo oxidation (Fig. 2.20). This peak arises from electron transfer between adjacent Fe^{2+} and Fe^{3+} ions separated by only 2.85 Å in dimers of edge-shared octahedra in the vivianite structure.

Other mineralogically important examples of metal–metal charge transfer include $\mathrm{Fe}^{2+} \rightarrow \mathrm{Ti}^{4+}$, known to occur in certain pyroxenes (Burns and Vaughan, 1975; Burns, 1981) and the $\mathrm{Ti}^{3+} \rightarrow \mathrm{Ti}^{4+}$ charge-transfer transitions believed to occur in lunar and meteoritic pyroxenes. $\mathrm{Fe}^{2+} \rightarrow \mathrm{Fe}^{3+}$ transitions also occur in the alkali amphiboles of the glaucophane–riebeckite series, which contain these cations in infinite bands of edge-shared octahedra. Such intervalence transitions cannot be treated within the formalism of crystal-field theory, but calculations using molec-

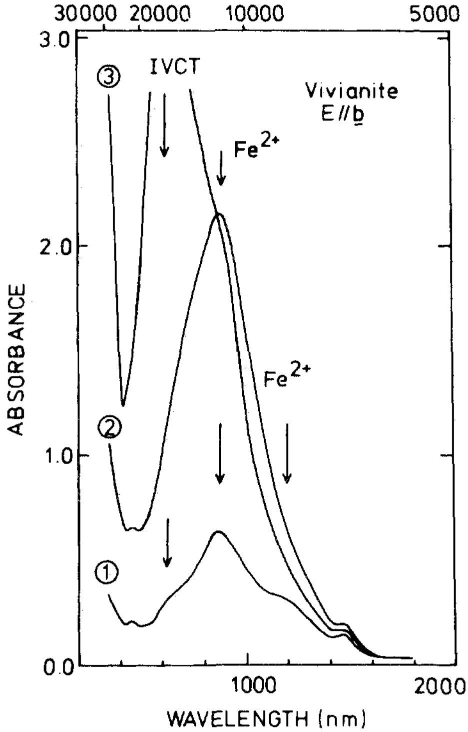

Fig. 2.21. Polarized electronic (optical) absorption spectra of a vivianite crystal with zones (labeled 1, 2, 3) exhibiting three different degrees of oxidation. The arrows identify Fe^{2+} crystal-field bands at 8,300 and 11,400 cm^{-1}, and the $Fe^{2+} \rightarrow Fe^{3+}$ intervalence charge-transfer transition at 15,800 cm^{-1} (after Amthauer and Rossman, 1984; reproduced with the publisher's permission).

ular-orbital theory (notably the scattered-wave $X\alpha$ method) on linked clusters have been used to describe such transitions (Burns and Vaughan, 1975; Sherman, 1984; see also Chapter 4). Because spectral features arising from metal–metal charge-transfer transitions occur in complex spectra along with *d-d* transitions, and because models enabling their prediction are not well established, their assignment has often been controversial.

Ligand (commonly oxygen)–metal charge-transfer transitions also occur in mineral systems with electrons being transferred between cations and their coordinated oxygens. Such transitions generally occur at relatively high energies, often in the ultraviolet, although edges or shoulders may extend into the visible region. This can be seen in many spectra, for example, in the spectrum of octahedrally coordinated Fe^{2+} ions in the periclase structure shown in Fig. 2.22. Here, the peaks at around 10,000 and 11,600 cm^{-1} arise from the spin-allowed *d-d* ($^5T_{2g} \rightarrow {}^5E_g$) transition in Fe^{2+} and the weaker peaks at 21,300 and 26,200 cm^{-1} from spin-forbidden *d-d* transitions. The intensity of the latter is enhanced by the onset of the intense oxygen → Fe^{2+} charge-transfer transition.

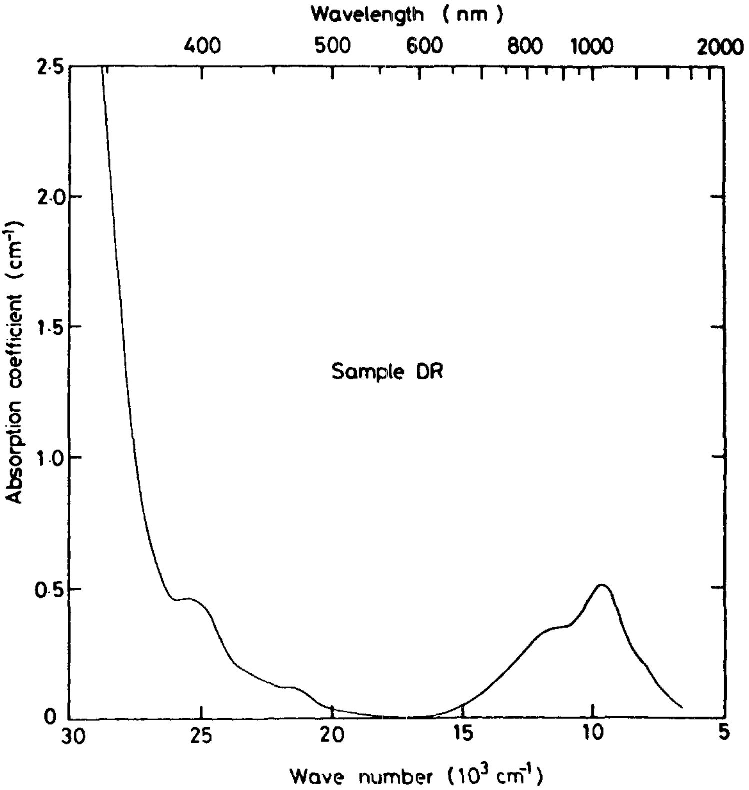

Fig. 2.22. Electronic (optical) absorption spectrum of octahedrally coordinated Fe^{2+} ions in the periclase (MgO) structure (after Goto et al., 1980; reproduced with the publisher's permission).

Interpretation and prediction of oxygen → metal charge-transfer transitions have been attempted using molecular-orbital theory; for example, using the molecular-orbital diagram for the FeO_6^{10-} cluster obtained from MS-SCF-$X\alpha$ calculations (see Appendix C and Chapter 3) shown in Fig. 2.23 (after Loeffler et al., 1974). In this diagram, which shows the effects of a spin polarization in splitting the energy levels into spin-up and spin-down sets, the highest occupied orbital is the $2t_{2g\downarrow}$, which contains one electron. The lowest-energy fully allowed $O^{2-} \rightarrow Fe^{2+}$ charge-transfer transition is from the $6t_{1u\downarrow}$ orbital (a nonbonding orbital of largely O $2p$ character) to the $2t_{2g\downarrow}$ ("crystal-field-type") orbital. The calculated transition state energy is 37,500 cm^{-1}, which seemed to agree well with experimental data (Runciman et al., 1973). Calculations and experiments suggested that the energies of oxygen → metal charge-transfer bands decrease in the order oct. Cr^{3+} > oct. Ti^{3+} > oct. Fe^{2+} > oct. Ti^{4+} > tet. Fe^{2+} > oct. Fe^{3+} spanning a range from approximately 60,000 cm^{-1} (166 nm) down to 25,000 cm^{-1} (400 nm) in Fe^{3+}-bearing oxides and silicates. Recent MS-SCF-$X\alpha$ calculations using an improved overlapping-sphere

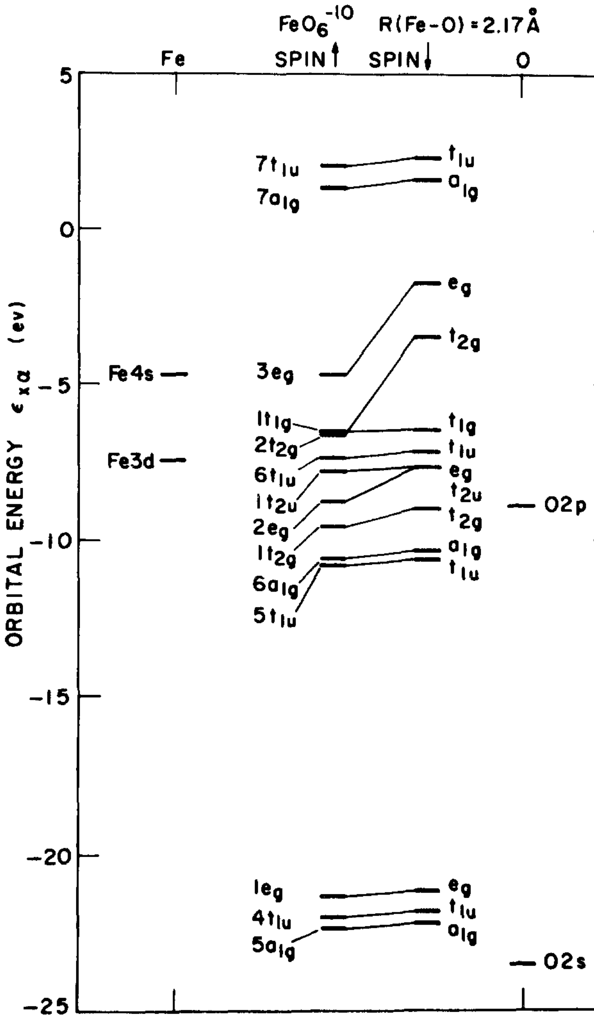

Fig. 2.23. Molecular-orbital diagram for the FeO_6^{10-} cluster (at Fe-O distance of 2.17 Å) calculated using the MS-SCF-$X\alpha$ method (see Section 3.10). The highest occupied orbital is the $2t_{2g\downarrow}$, containing one electron (after Loeffler et al., 1974; reproduced with the publisher's permission).

version of the method have yielded larger O $2p$–Fe $3d$ separations (Sherman, 1985a), giving a $6t_{1u\downarrow}$–$2t_{2g\downarrow}$ transition energy of 38100 cm^{-1} for the Fe^{3+} case, in agreement with experiment for well-characterized materials such as Fe^{3+}:MgO. The experimental results of Runciman et al. (1973) then presumably correspond to the spectra of small concentrations of Fe^{3+} in materials with predominant Fe^{2+}. The general trends in oxygen → metal charge-transfer energy calculated by Loeffler et al. (1974) seem still to be sound; that is, the early (touching-sphere) MS-SCF-$X\alpha$ calculations exaggerated the stabilities of metal $3d$ orbitals versus O $2p$ orbitals by roughly 1 eV for all the metals considered. This revision does, however, show how difficult it is to calculate such energies accurate to within a few thousands of cm^{-1}.

2.3.2. *Reflectance (diffuse and specular) spectroscopy*

Light (or near-ir and uv radiation) that is incident on opaque minerals is partly absorbed and partly reflected by them. There are two kinds of reflection processes: that occurring when light is reflected from a flat polished surface of the mineral (specular reflectance) and that occurring when the light is reflected from the mineral after it has been finely powdered (diffuse reflectance). The latter arises from radiation that has penetrated the crystals (as in an electronic absorption spectrum) and reappeared at the surface after multiple scatterings; in this case there will also be a specular component to the reflectance from light that is reflected from the surfaces of the particles. The specular reflectance of a flat polished surface of an opaque mineral measured at normal incidence can be related to the n and k terms of the complex refractive index (N) in which:

$$N = n + ik \tag{2.21}$$

where n is the refractive index, k the absorption coefficient, $i = \sqrt{-1}$. The refractive index terms are related to reflectance through the Fresnel equation, which for reflection at normal incidence in air is:

$$R = \frac{(n-1)^2 + k^2}{(n+1)^2 + k^2} \tag{2.22}$$

where $R = 1 = 100\%$ reflectance. More complex equations describe the relationship for non-normal incidence. Using specular reflectance data obtained at different angles of incidence, the values of n and k as a function of wavelength (λ) can be obtained through a Kramers–Kronig calculation (see Wendlandt and Hecht, 1966). The plot of k against λ approximates the information obtained from a transmission measurement on a translucent solid. The variations in n and k as a function of λ for the pyrite-structure disulfide minerals are illustrated in Fig. 2.24. As described in greater detail in Section 6.4, the features in the plot of k against λ can be interpreted using MO and band models for the electronic structure of pyrite and the other disulfides. Thus, feature E_1 can be attributed to the onset of $t_{2g} \rightarrow e_g^*$ transitions and peaks E_2, E_3, E_4 to similar transitions or transitions from the σ (valence band) to e_g^* levels.

The commercial spectrometers designed primarily for undertaking transmittance measurements in the near-ir–visible–near-uv range commonly have attachments that enable specular reflectance measurements to be made on polished blocks (see Wendlandt and Hecht, 1966; Hedelman and Mitchell, 1968). Specular reflectance measurements of small

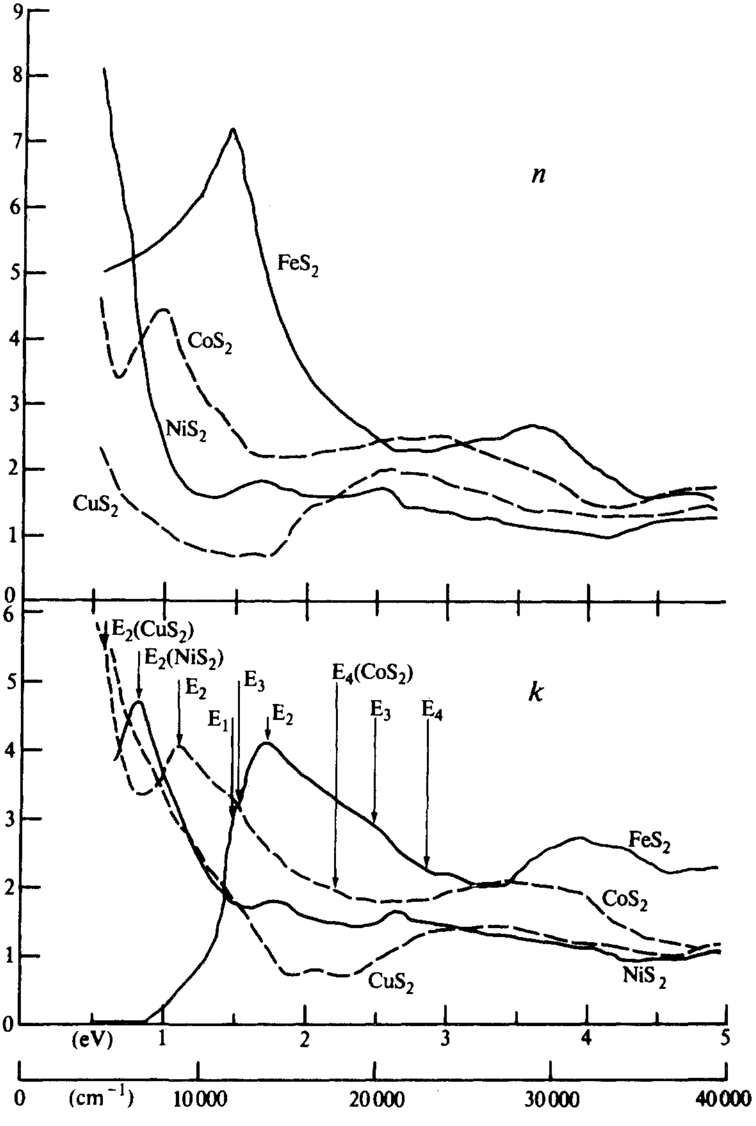

Fig. 2.24. Relative refractive index (*n*) and absorption coefficient (*k*) — the real and imaginary parts of the complex refractive index (*N*) — as a function of energy for the pyrite-type compounds FeS_2, CoS_2, NiS_2, and CuS_2 (after Bither et al., 1968; reproduced with the publisher's permission).

grains at normal incidence can be made in air and other media using photometer attachments to the reflected light microscope (see Craig and Vaughan, 1981; Piller, 1977). Such measurements are usually restricted to the visible range and from measurements made in air and under an immersion oil, it is possible to obtain values for *n* and *k* from the Fresnel equation. There are errors associated with such determinations, as pointed out by Embrey and Criddle (1978). Commercial spectrometers also commonly have attachments that enable diffuse reflectance spectra to be recorded. Such measurements are only, of course, possible on powder samples and involve finely grinding the mineral with a white powder such as MgO so as to suppress the specular component of the reflectance and compressing the mixture to form a pellet or disc. In diffuse reflectance spectroscopy, the approximate equivalent of an electronic absorption spectrum can be obtained by much simpler manipulation of the raw data. A commonly used method is to employ the Kubelka–Munk function $f(r)$, which provides a measure of the ratio of the absorption and scattering coefficients:

$$f(r) = \frac{(1-r)^2}{2r} = \frac{k}{s} \tag{2.23}$$

where r is the diffuse reflectance, k the absorption coefficient, and s is the scattering coefficient. For the types of material used in diffuse reflectance studies of minerals, the scattering coefficient is nearly independent of wavelength so that the Kubelka–Munk function approximates directly the absorption coefficient. Diffuse reflectance spectra of the pyrite-type disulfides are illustrated in Fig. 2.25 and clearly show the absorption edge in FeS_2 due to the onset of $t_{2g} \rightarrow e_g^*$ transitions. These data are also further discussed in section 6.4.

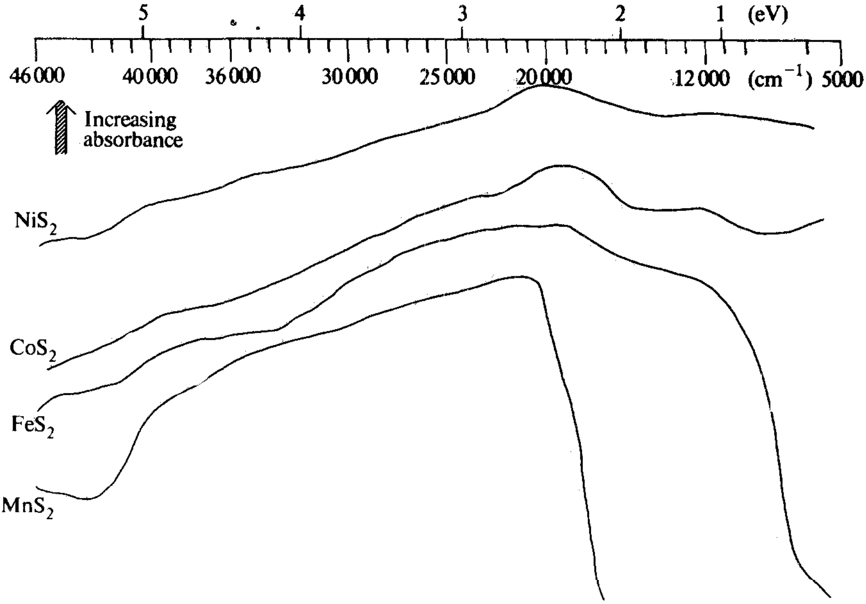

Fig. 2.25. Diffuse reflectance spectra of pyrite-type disulfides (after Vaughan, 1971).

2.4. Vibrational spectroscopy

Electromagnetic energy is absorbed by molecules in the gas phase through vibrations of the atoms or rotations of the molecular system. Such energies are generally in the microwave (~100 μm–10 cm wavelength) and infrared (~0.75–100 μm) regions of the spectrum and studied using infrared and microwave spectroscopies. In the case of crystalline solids and glasses, although the "molecule" is no longer able to rotate, vibrational spectra can still be recorded. Vibrational transitions can also be studied using the Raman effect, which involves recording the energies and intensities of light (visible or ultraviolet) scattered on passing through a translucent material. Infrared and Raman spectroscopies are powerful means of studying the structure and bonding in materials, including minerals and other geologically important substances.

2.4.1. Theoretical basis

The simplest system that can be studied by vibrational spectroscopy is the diatomic molecule, and the simplest model for its vibration is the harmonic oscillator. If the atoms have masses m_1 and m_2 and are connected by an "ideal spring," at rest they have an equilibrium separation r_0 and on extension or compression ($r_0 \pm \Delta r$) the masses are subject to a restoring force proportional to the displacement:

$$F = -k\,\Delta\,r \qquad (2.24)$$

where k is the force constant. The classical equation of motion for the harmonic oscillator is:

$$\mu \frac{d^2\,\Delta r}{dt^2} = -k\Delta r \qquad (2.25)$$

where μ is the reduced mass:

$$\mu = \frac{m_1 m_2}{m_1 + m_2} \qquad (2.26)$$

The classical model does not explain the interaction of molecular vibrations with light; this requires consideration of the quantum-mechanical oscillator for which the wave equation is:

$$\frac{d^2\,\psi}{dr^2} + 4\frac{\pi^2\mu}{h}\,[2E - k(\Delta r)^2]\psi = 0 \qquad (2.27)$$

Solution of this equation provides a set of vibrational eigenfunctions ψ_n and their associated energies E_n, where the subscripts n are all integers—the vibrational quantum numbers. The vibrational energy levels are found to be:

$$E_n = (n + ½) \frac{h}{2\pi} \sqrt{k/\mu} \\ = (n + ½)h\nu_0, \tag{2.28}$$

where ν_0 is the harmonic-oscillator frequency $[\nu_0 = (1/2\pi)\sqrt{k/\mu}]$.

These form a sequence of equidistant energy levels separated by $\Delta E = h\nu_0$ and bounded by the potential energy curve $V = ½k(\Delta r)^2$, as shown in Fig. 2.26. The lowest (ground-state) level with $n = 0$ has an energy $E_0 = ½h\nu_0$, known as the zero-point energy. The vibrational eigenfunctions are usually interpreted in terms of probability density functions $|\psi_n|^2$ of the type shown in Fig. 2.26.

Although the harmonic oscillator is a useful starting model, true interatomic potentials are not harmonic. The repulsive forces resisting bond compression vary more rapidly with distance than the attractive forces resisting separation. The two effects combine to give a minimum in energy at the equilibrium bond distance, r_e, but, whereas the potential rises steeply at small r, it flattens off to zero energy at large r, as shown in Fig. 2.27. These potentials may be approximated using empirical functions or by adding higher-order terms in r to the harmonic potential function:

$$V = ½\, kr^2 + ⅓\, gr^3 + \cdots \tag{2.29}$$

This anharmonic function has energy levels:

$$E_n = h\nu_e\,[(n + ½) - x_e\,(n + ½)^2 + y_e\,(n + ½)^3 - \cdots] \tag{2.30}$$

where ν_e, x_e, y_e are the anharmonicity constants.

For a molecular system containing N atoms, the equations of motion give $3N$ solutions corresponding to the total degrees of freedom of its constituent atoms. Three of these solutions always correspond to translations of the entire system, and three (or two for linear molecules) to its

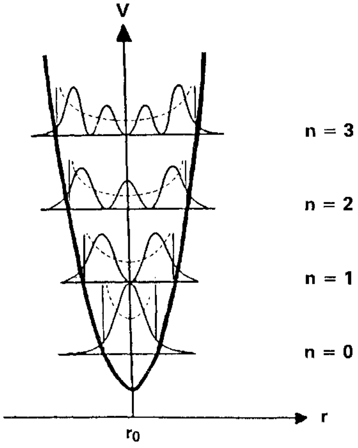

Fig. 2.26. The harmonic oscillator: energy levels and wave functions. The potential is bounded by the curve $V = ½k(\Delta r)^2$ (heavy solid line). The quantum-mechanical probability density functions $|\phi_n|^2$ are shown as light solid lines for each energy level, while the corresponding classical probabilities are shown as dashed lines (after McMillan, 1985; reproduced with the publisher's permission).

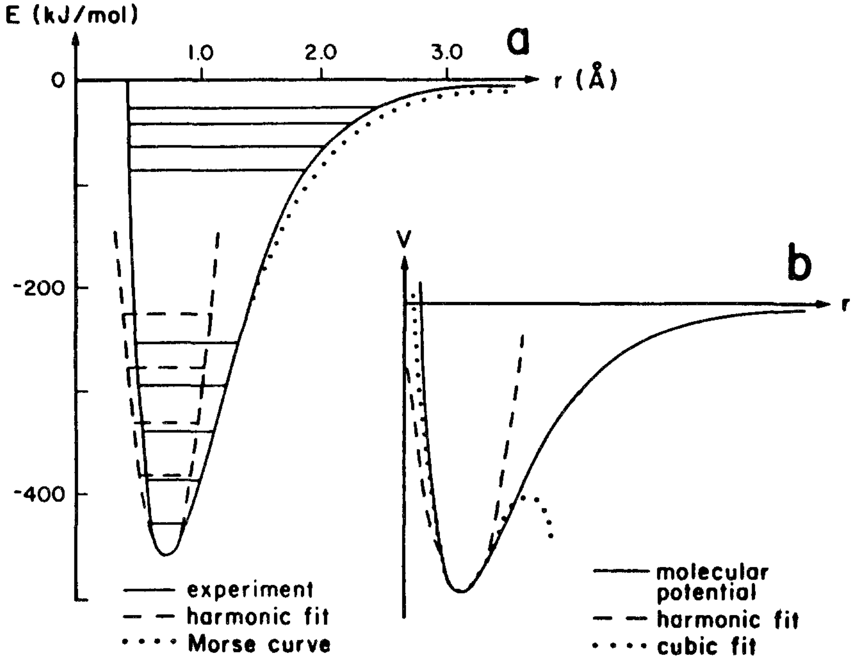

Fig. 2.27. (a) The experimental potential curve for H_2 (full curve); the dotted curve represents a Morse fit to the data, and the dashed curve shows a harmonic-oscillator function with the force constant taken at $r = r_c$ (0.7414 Å). The first five energy levels are drawn for the harmonic (dashed lines) and the observed (full lines) potential functions. (b) Comparison of a typical molecular potential function (full curve), a harmonic fit (dashed curve), and a cubic anharmonic fit (dotted curve) (after McMillan, 1985; reproduced with the publisher's permission).

rotations. The remaining $3N-6$ (or $3N-5$ for linear molecules) solutions are the *vibrational normal modes* for the system. The first stage in a vibrational analysis of a system is the calculation of the number of vibrational normal modes; for example, $3N-5 = 4$ for CO_2 (a linear molecule), $3N-6 = 3$ for H_2O. For crystalline systems N is taken as the number of atoms in the primitive unit cell and rotational degrees of freedom ignored to give $3N - 3$ normal modes; for example, forsterite (Mg_2SiO_4) has $N = 28$ hence 81 normal modes.

The quantum-mechanical description of a polyatomic system may be extrapolated from the treatment of the diatomic molecule. Starting again with the harmonic oscillator, the energy levels for the entire system (E) can be given in terms of the characteristic frequencies (ν_t) and quantum numbers (n_t) of a series of independent harmonic oscillators:

$$E = (n_1 + ½)\,h\nu_1 + (n_2 + ½)\,h\nu_2 + (n_3 + ½)\,h\nu_3 + \cdots \quad (2.31)$$

The effects of anharmonicity in polyatomic systems are similar to the diatomic case; the zero-point level drops in energy, energy levels close up, and spacings decrease for higher quantum numbers. However, a further effect is that, whereas in the harmonic model each mode of vibration is independent and discrete, in the anharmonic case the oscillators are no longer independent and energy transfer between modes is possible. So, for example, when vibrational modes are excited by light, some of the incident light energy resonating with a particular vibration may be dissipated through anharmonic effects and appear as heat.

The dynamics of crystals can be treated similarly to polyatomic molecules, taking into account the periodicity of the crystal. Generally, a crystal contains n primitive unit cells with N atoms per cell. If each unit cell is treated as a molecule, it will have $3N$ normal modes, since molecular translations and rotations become vibrational modes when the "molecule" is embedded in a crystal structure. The atomic motions take the form of waves traveling through the crystal (lattice vibrations or *phonons*) with their wavelengths determined by the phase relationships between adjacent unit cells. Phonons may be completely described by their energy (wavelength) and the wave vector k in the direction of propagation, between which there is a dispersion relation (see Fig. 2.28).

The dispersion relationships of lattice waves may be simply described within the first Brillouin zone of the crystal. When all unit cells are in phase, the wavelength of the lattice vibration tends to infinity and k approaches zero. Such "zero-phonon" modes are present at the center of the Brillouin zone. The variation in phonon frequency as reciprocal (k) space is traversed is what is meant by dispersion, and each set of vibrational modes related by dispersion is a *branch*. For each unit cell, three modes correspond to translation of all the atoms in the same direction. A lattice wave resulting from such displacements is similar to propagation of a sound wave; hence these are *acoustic branches* (Fig. 2.28). The remaining $3N-3$ branches involve relative displacements of atoms within each cell and are known as *optical branches*, since only vibrations of this type may interact with light.

2.4.2. *Infrared spectroscopy*

When infrared light interacts with the fluctuating electric dipole caused by the vibration of the constituent atoms in molecules or crystals, absorption may occur when the energy of the radiation matches that of the vibration. This fluctuating electric dipole can be considered to arise if two centers (atoms) of equal and opposite charge ($\pm Q$) are separated by a distance r, when the dipole moment (μ) will be:

$$\mu = Qr \tag{2.32}$$

Such a dipole moment may be defined between any two atoms of differing electronegativity. If $r = r_0$ and the atoms are at rest, then $\mu = \mu_0$, the equilibrium dipole moment. For a polyatomic molecule, each atom pair defines a dipole moment, and these bond dipole moments may be

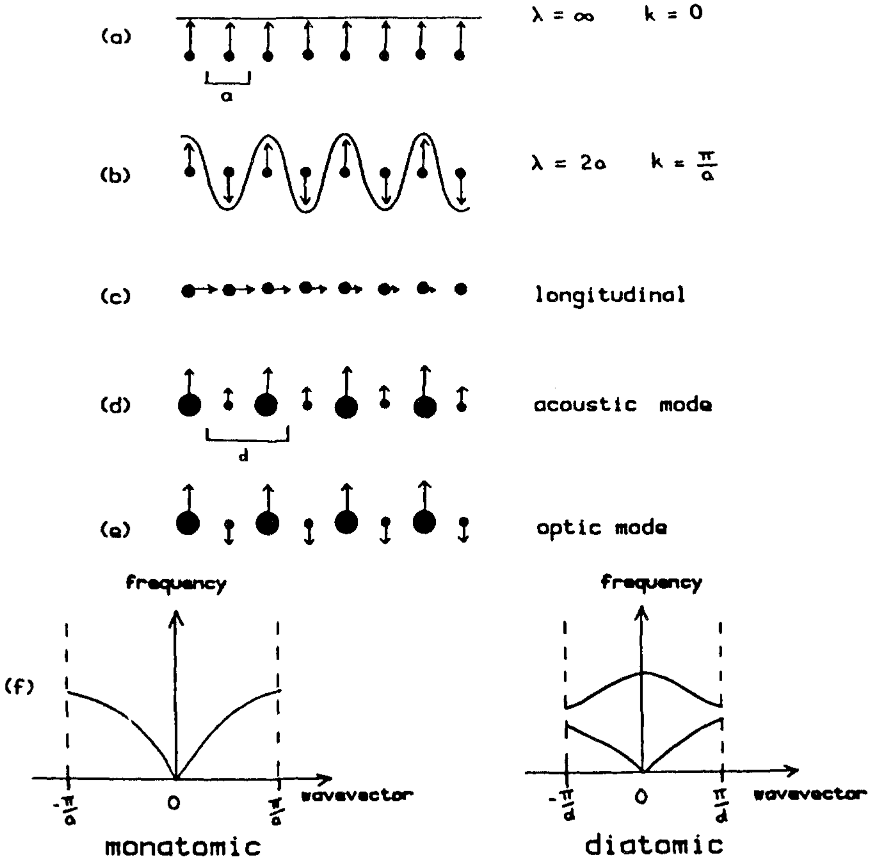

Fig. 2.28. (a) and (b). Transverse modes for a monatomic chain of atoms with lattice spacing a [(a) shows a mode of infinite wavelength, hence zero wave vector; (b) shows the mode with wavelength $\lambda = 2a$; hence $k = \pi/a$ at the edge of the first Brillouin zone]. (c) Longitudinal mode with $\lambda \sim 14a$ for the monatomic chain. (d) and (e) Transverse modes at $k = 0$ for a diatomic chain with lattice spacing d. The mode in (d) has both atoms within the unit cell moving in the same direction, hence is an *acoustic mode*. The mode in (e) has the atoms within the unit cell moving in opposite directions hence is an *optic mode*. (f) The dispersion curves for the monatomic and diatomic chains. (After McMillan, 1985; reproduced with the publisher's permission.)

summed vectorially to give a net molecular dipole moment. The relative motion of the nuclei during a vibrational mode may cause a change in the net dipole moment:

$$\mu(r) = \mu_0 + \frac{d\mu}{dr}\Delta r \tag{2.33}$$

As the vibrational motion is oscillatory, this creates a fluctuating electric field that may interact with the electric part of the electromagnetic radiation. Generally, the probability of a transition between vibrational states n and n' is proportional to the square of the transition moment $M_{n'n}$, where:

$$M_{n'n} = \mu_0 \int_0^\infty \psi_{n'}{}^* \psi_n \, dr + \int_0^\infty \psi_{n'}{}^* Q^* \Delta r \, \psi_n \, dr \qquad (2.34)$$

The first of these two terms is zero, since the wavefunctions $\psi_{n'}$ and ψ_n are defined as orthogonal; hence vibrations are only infrared active when $Q \neq 0$. If the harmonic model is assumed, the transition moment is only nonzero for transitions where $\Delta n = \pm 1$; although this restriction is lifted for the anharmonic oscillator, transitions where $\Delta n = \pm 2, \pm 3$, etc., are still much weaker than $\Delta n = \pm 1$.

Interaction of infrared radiation with molecules and crystals to produce absorption (or reflectance) bands can be predicted using group theory (see Orchin and Jaffé, 1971; Cotton, 1971), and the same approach is used in the prediction and interpretation of other vibrational spectra (such as Raman spectra).

Infrared spectra may be studied in reflection or in absorption using single-crystal or powdered samples of solids (or, in the case of absorption, of gases and liquids). The classical description of these phenomena employs the same concept as outlined for optical spectroscopy (the refractive index, Fresnel equation, etc.; see Section 2.3.2). Instrumentation is also very similar to that employed in the study of optical spectra, the same commercial spectrometer often being used to measure visible and parts of the infrared regions. The most common methods involve passing an infrared beam through the sample and observing the transmission minima corresponding to absorption by vibrational transitions in the sample; rarely this involves a slice of crystalline material; more commonly a solid is ground up and dispersed in a supporting matrix that may then be pressed into a disc. In detailed work, polarized spectra may be obtained from single crystals.

Figure 2.29 shows the powder transmission infrared spectrum of forsterite, Mg_2SiO_4 (after Akaogi et al., 1984). A detailed discussion of the interpretation of these (and of single-crystal polarized) spectra is also given by McMillan (1985). The modes between 820 and 1100 cm^{-1} are assigned to silicon–oxygen stretching motions. This is supported by comparison with simple silicates and by *ab initio* molecular-orbital calculations of silicon–oxygen stretching force constants (O'Keeffe et al., 1980). Studies involving calculations and chemical and isotopic substitutions (Paques-Ledent and Tarte, 1973; Iishi, 1978) indicate modes at 364 cm^{-1} arising from vibrations of the MgO_6 octahedral group, and suggestions that peaks at 466, 425, 415, 320, 300, and 277 cm^{-1} chiefly involve the MgO_6 units. Other peaks may arise from the complex vibrations involving both magnesium and silicon displacements, and the understanding of the crystalline dynamics of forsterite is still far from complete.

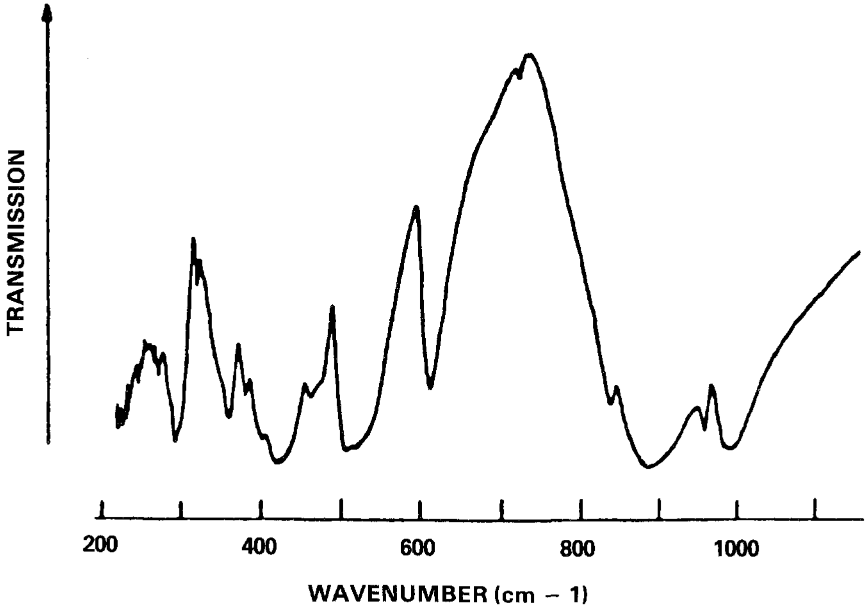

Fig. 2.29. Powder transmission infrared spectrum of forsterite, Mg_2SiO_4 (after Akaogi et al., 1984; reproduced with the publisher's permission).

2.4.3. *Raman spectroscopy*

In Raman spectroscopy, based on the phenomenon discovered by Raman and Krishnan in 1928, monochromatic light from a suitable source is directed through a translucent sample (gas, liquid, glass, crystalline solid, or powder), and the light scattered at 90° or 180° is collected, analyzed by a suitable optical system, and recorded. A schematic diagram of a Raman spectrometer is shown in Fig. 2.30. The availability of powerful monochromatic laser sources in the 1960s produced a renaissance and further development of the technique after a lull following the early work. Furthermore, by using polarized incident light (from a laser), a scattered beam that is polarized is produced, increasing the variety of possible spectra from a single sample. For an anisotropic crystal, the sample can be cut and measured in different crystallographic orientations. Even in isotropic crystals, glasses, or liquids, spectra can be measured with polarization of the incoming and scattered beams parallel (as in *VV* spectra; see the following) or crossed (as in *VH* spectra, see the following).

The scattering of monochromatic light (the "exciting line") of frequency ν by molecules or crystals to which the light is transparent (i.e., electronic excitation does not occur) is of two kinds: Raman and Rayleigh. In Rayleigh scattering, which accounts for most of the intensity of scattered light, no frequency change occurs. The Raman effect involves a change of frequencies, and the new frequencies (ν') are found on either

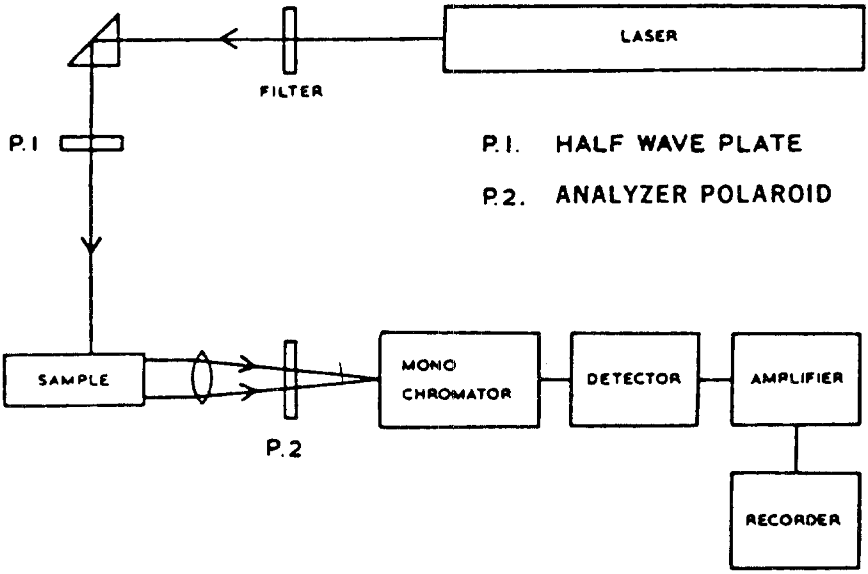

Fig. 2.30. Schematic diagram of a Raman spectrometer with 90° scattering. P_1 and P_2 are half-wave and polarizing plates, respectively, to study the state of polarization of scattered light (after Griffith, 1975; reproduced with the publisher's permission).

side of the exciting line (see Fig. 2.31). The differences ($\nu + \nu'$) are independent of ν and are, in the case of solids, lattice (acoustic) or vibrational modes. Combinations and overtones of these constitute the much weaker second-order Raman effect. The new frequencies on the low-frequency side of the exciting line (the so-called Stokes line) are generally more intense than those on the high-frequency side (so-called anti-Stokes lines). Only about 10^{-6} of the incident radiation is observed as Raman scattering. Raman spectra are studied with light sources in the visible or ultraviolet region of the spectrum. For example, the Stokes and anti-Stokes Raman spectra for α-quartz shown in Fig. 2.32 were produced using the blue line of an argon-ion gas laser (with an incident energy of 20,027 cm^{-1} corresponding to the visible wavelength 487.986 nm). Here, the intense line on the Stokes side at 20,027 cm^{-1} corresponds to the Raman shift of 465 cm^{-1}, and the weaker anti-Stokes spectrum at 20,957 cm^{-1} to a Raman shift of -465 cm^{-1}.

The origin of the Raman effect can be seen by considering the interaction of photons of energy $h\nu$ (ν being the frequency of the exciting line) with the "molecules" in the sample. Photons may be scattered elastically without loss of energy (the Rayleigh effect) or inelastically, whereby energy is given up to the molecule or taken from the molecule (the Raman effect). The energy exchanged must be in quanta $h\nu' = E_1 - E_2$, the energy difference between two stationary states E_1 and E_2 of the "mole-

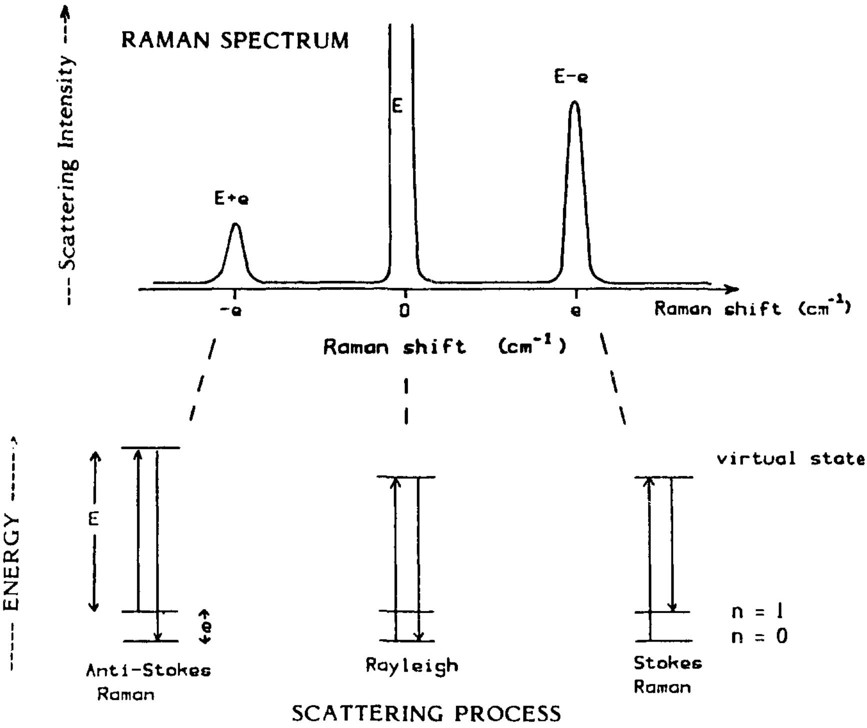

Fig. 2.31. The Raman scattering process. The incident beam (usually a laser) has energy E. Rayleigh scattering is an inelastic scattering process and gives rise to a strong central peak at the incident frequency (zero Raman shift). Raman scattering is accompanied by a change in vibrational energy level to give peaks at $E - e$ (Stokes shift) or $E + e$ (anti-Stokes shift), where e is the vibrational-level separation. At normal temperatures, the ground state is more populated than higher vibrational states; hence the Stokes spectrum is more intense than the anti-Stokes (after McMillan, 1985; reproduced with the publisher's permission).

cule" (e.g., two definite vibrational energy levels). If the molecule is in the ground state, it may extract energy $h\nu'$ from the incident photons ($h\nu$) to raise itself to an excited state (ν' being a fundamental rotational, vibrational, or lattice mode). The photon released has energy $h(\nu - \nu')$ and frequency $(\nu - \nu')$ and is thus a Stokes line. Conversely, if the molecule is in an excited state, it may impart energy $h\nu'$ to the incident photon to give an anti-Stokes line of frequence $(\nu + \nu')$. The great intensity of Stokes lines arises because more "molecules" will be in the ground state than in excited states.

Raman scattering occurs as a result of a dipole moment induced in the "molecule" by incident light. Thus, if an atom or molecule is placed in a static electric field (E) such as is produced by passage of light, a dipole moment (μ) will be induced as a result of the displacement of the nucleus

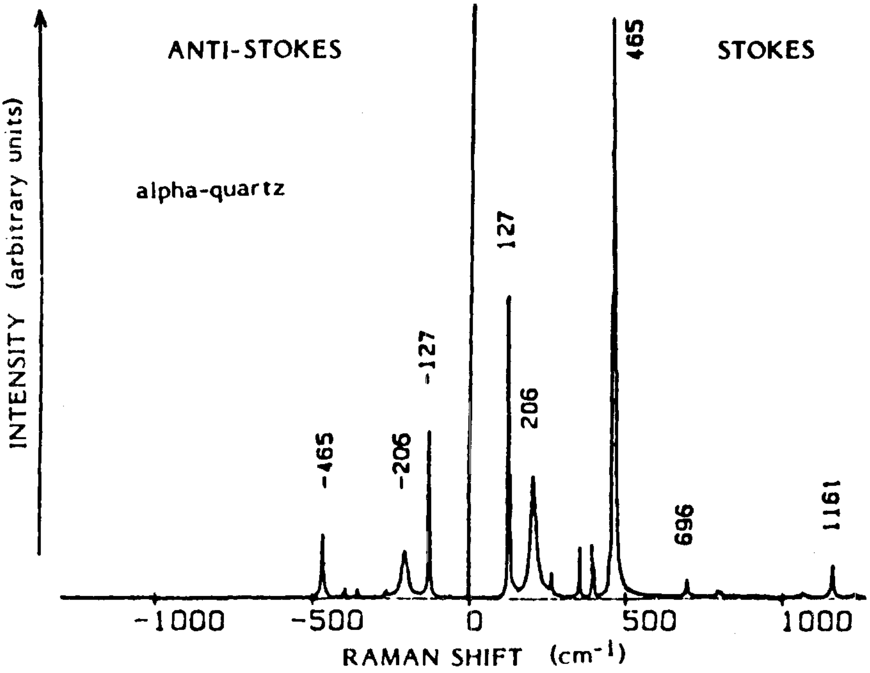

Fig. 2.32. Stokes and anti-Stokes Raman spectra for α-quartz (after McMillan, 1985; reproduced with the publisher's permission).

within its electron cloud (such a dipole is independent of any permanent dipole the molecule may possess). Then, to a first approximation:

$$\mu = \alpha E \tag{2.35}$$

where α is the polarizability of the molecule (and dependent on the electron density). The transition probability for the Raman effect is:

$$|\mu|_{nm} = |E| \int \psi_n{}^* \alpha \psi_m \, d\tau \tag{2.36}$$

where n and m are the two energy states and ψ_n and ψ_m their respective wave functions. If α is constant, this integral vanishes because of the orthogonality of the wave functions. In order that a vibration or rotation be Raman active, therefore, the polarizability must change during the rotation or vibration.

In the study of minerals and other geological materials, Raman spectroscopy has been applied for chemical analysis and in studies of molecular and crystal structure, and of elastic and thermodynamic properties. A particularly important field for the application of Raman spectroscopy in chemical analysis is in the study of fluid inclusions in minerals, where the Raman microprobe has been developed to enable nondestructive *in* *situ* analysis of inclusions as small as a few micrometers in diameter (see, for example, Rosasco and Roedder, 1979). In structural studies, Raman spectroscopy has been used to understand the mechanisms involved in phase transformations such as the atom displacements required to transform α-quartz to β-quartz (e.g., Iishi, 1978) or the order–disorder processes occurring in many mineral systems (e.g., Al-Si ordering in cordierite, McMillan et al., 1984).

A major area of application of Raman spectroscopy in geochemistry has been in structural studies of silicate melts and glasses. Much of the work in this area has been reviewed by McMillan (1984a), who has also studied glasses in the system CaO-MgO-SiO_2 (McMillan, 1984b), a system that provides good examples to illustrate this application. Polarized Raman spectra of glasses in the series SiO_2-$CaMgSiO_4$ are shown in Fig. 2.33, which also gives their compositions in terms of component oxides. Curve fitting of the spectra shows bands at 862, 906, 972, and 1056 cm^{-1} varying in intensity along the series. In line with the suggestions of previous workers, these bands are attributed to symmetric silicon–oxygen stretching vibrations in silicate tetrahedral units with 4, 3, 2, and 1 nonbridging oxygens, respectively. These are shown schematically in Fig. 2.34 and labeled by McMillan (1984b) as SiO_4, $-SiO_3$, $=SiO_2$, and $\equiv SiO$ groups, where the number of horizontal lines specifies the number of bridging oxygens. Such assignments are largely made by studying the appearance and shifting of bands in a series of phases of related compositions, although calculations have been used with some success to aid in assignment (see Section 8.1).

A band that varies in position from 704 to 620 cm^{-1} with increasing silica content has generally been associated with bridging oxygens corner-sharing between adjacent SiO_4 tetrahedra. In the middle region of the spectra, a band around 780 cm^{-1} in the *VH* spectra and seen as a weak shoulder in the *VV* spectra may be predominantly associated with the motion of silicon against its oxygen cage. The bands at high frequency (~850–1050 cm^{-1}) show variations in intensity with composition (Fig. 2.33) consistent with a decrease in average polymerization of the silicate units as the silica content is decreased. McMillan (1984b) suggests that the major high-frequency bands are highly localized within a given silicate tetrahedral unit and are relatively insensitive to the nature of adjacent tetrahedral units.

The effects of substitution of the different metals on the distribution of silicate species has been investigated not only for Ca/Mg substitution in the CaO-MgO-SiO_2 system, but also for a wide range of other silicate

→

Fig. 2.33. Polarized (*VV* and *VH*) Raman spectra of SiO_2 (above) and of glasses (of compositions 1 to 10 on the inset compositional triangular diagram) near the SiO_2-$CaMgSiO_4$ join (after McMillan, 1984b; reproduced with the publisher's permission).

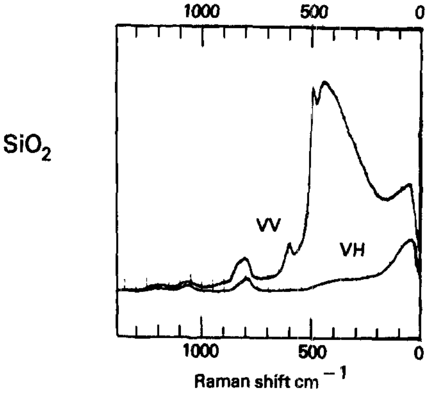
SiO2
1000
500
0
VV
VH
Raman shift cm⁻¹

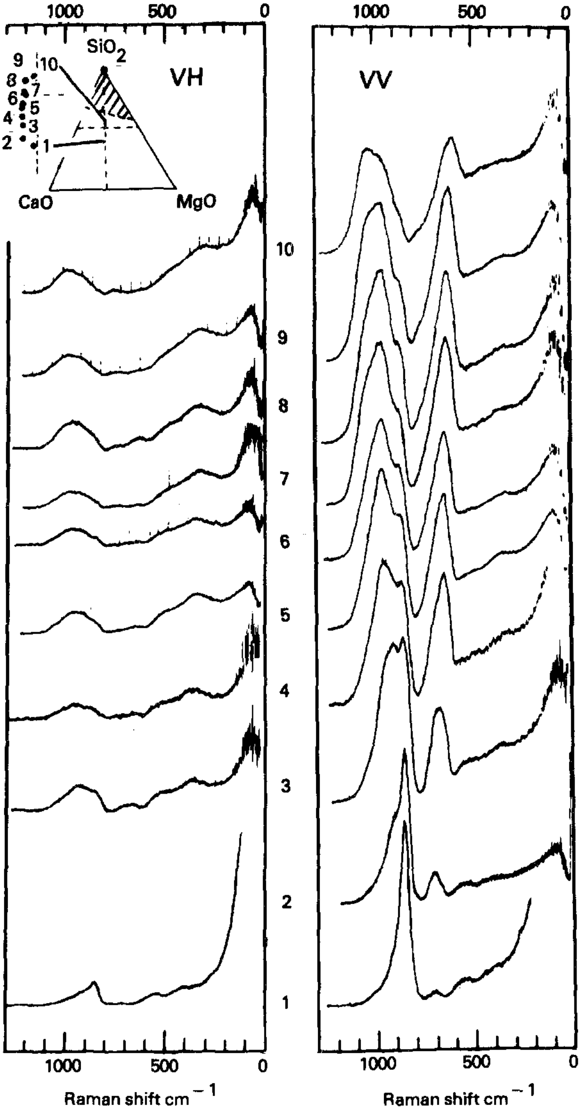
1000
500
0
VH
VV
SiO2
CaO
MgO
9
10
8
7
6
5
4
3
2
1
Raman shift cm⁻¹
Raman shift cm⁻¹

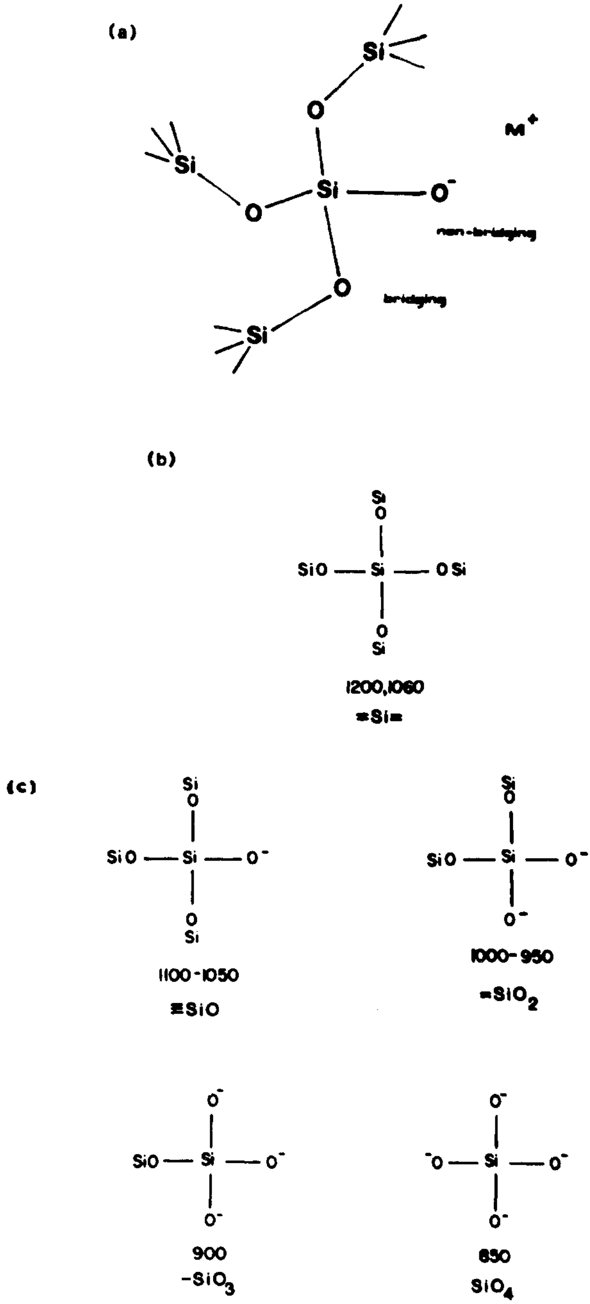

Fig. 2.34. (a) Schematic illustration of silicate structural units indicating the nature of bridging and nonbridging oxygens (M^+ may also refer to $0.5M^{2+}$ as in the alkaline earth series). (b) The weak, depolarized bands at 1200 and 1060 cm^{-1} are assigned to asymmetric silicon–oxygen stretching vibrations within a fully polymerized tetrahedral network =Si=. (c) The four major polarized high-frequency bands are generally assigned to symmetric stretching vibrations of tetrahedral silicate units with one, two, three, and four nonbridging oxygens as shown (after McMillan, 1984b; reproduced with the publisher's permission).

glass systems. In the case of Ca/Mg substitution, the spectra suggest that the relative proportion of $=\mathrm{SiO}_2$ to $\equiv\mathrm{SiO}$ groups increases as magnesium is substituted for calcium in the glass structure. Trends interpreted from the data on other systems such as increases in the proportions of $=\mathrm{SiO}_2$ and $=\mathrm{Si}=$ units relative to $\equiv\mathrm{SiO}$ groups with substitution of Ca or Mg for Na (Brawer and White, 1975) have been rationalized using a "molecular site model" (McMillan, 1981; McMillan and Piriou, 1983).

As described by McMillan (1984b), if it is assumed that all oxygen is coordinated to silicon and that local electrostatic charge balance must be satisfied, then a given metal cation will have an appropriate combination of bridging and nonbridging oxygens in its coordination sphere. For systems with high silica content, $=\mathrm{SiO}_2$, $\equiv\mathrm{SiO}$, and uncharged $=\mathrm{Si}=$ units predominate. Assuming the cation species are either M^+ or M^{2+}, then a single-site $\equiv\mathrm{SiO}$ defines a site for one M^+ cation, and a coupled site $(\equiv\mathrm{SiO})_2$ may be formulated to house a single M^{2+} or two M^+ cations. The unit $=\mathrm{Si}=$ has no associated cation. At a given silica content, the relative proportion of these sites will be a function of metal cation. Large cations should prefer the single-site $\equiv\mathrm{SiO}$, while smaller M^+ cations should allow a higher proportion of $=\mathrm{SiO}_2$ sites. Large M^{2+} cations should prefer the more open coupled $(\equiv\mathrm{SiO})_2$ site and smaller M^{2+} cations the $=\mathrm{SiO}_2$ sites. At constant silica content the overall distribution is governed by the "reaction":

$$2(\equiv\mathrm{SiO}) \rightleftharpoons {=\mathrm{Si}=} + {=\mathrm{SiO}_2} \tag{2.37}$$

which will be driven to the right for small doubly charged cations and to the left for large singly charged cations. This is consistent with experimental observations, where bands for $=\mathrm{SiO}_2$ and $=\mathrm{Si}=$ units become more prominent at the expense of $\equiv\mathrm{SiO}$ groups (at similar silica content) in the order of $\mathrm{Cs}^+ < \mathrm{Rb}^+ < \mathrm{K}^+ < \mathrm{Na}^+ < \mathrm{Li}^+$ and $\mathrm{Ca}^{2+} < \mathrm{Mg}^{2+}$. Since the $=\mathrm{Si}=$ unit has no associated cation, the formation of $=\mathrm{Si}=$ and $=\mathrm{SiO}_2$ units from $\equiv\mathrm{SiO}$ groups can be regarded as a charge concentration effect, and the clustering induced by it may be regarded as incipient immiscibility. The model suggests that the tendency for unmixing should increase in the order $\mathrm{Cs} < \mathrm{Rb} < \mathrm{K} < \mathrm{Na} < \mathrm{Li}$ for the alkali silicates, and $\mathrm{Ca} < \mathrm{Mg}$ for alkaline earth silicates, a prediction consistent with available experimental data.

2.4.4. Reporting of data

Studies of the vibrational spectra of various materials are reported later in the text; for example, in Table 5.22 are given calculated and experimental vibrational frequencies for the borate ion in aqueous solution. The labeling of vibrational frequencies (ν_1, ν_2, ν_3, etc.) follows the convention in standard texts linked to the nomenclature of normal vibrational modes (see, for example, Drago, 1977). Thus, it may be recalled that for a particular "molecule" a vibration is designated by the letter A if it is symmetric with respect to the highest-fold rotation axis, B if it is antisymmetric. E stands for a doubly degenerate vibration, T (or F) for a triply degenerate mode. Subscripts g and u refer to symmetry with respect to inversion through a center of symmetry; if a vibration is symmetric with respect to the horizontal plane of symmetry, this is designated by a prime, while a double prime indicates antisymmetry with respect to this plane. Subscripts 1 and 2 indicate symmetry and antisymmetry, respectively, toward a twofold axis that is perpendicular to the principal axis.

2.5. Nuclear spectroscopy

Protons and neutrons both have a spin quantum number of ½, and, depending on how these particles are combined in the nucleus, that nucleus may, or may not, have a net nonzero nuclear spin quantum number I. If the spins of all the particles are paired, there will be no net spin and the value of I will be zero (Fig. 2.35a). When $I = ½$, there is one net unpaired spin, and this unpaired spin imparts a nuclear magnetic moment (μ_N) to the nucleus. The distribution of positive charge in such a nucleus is spherical, as symbolized in Fig. 2.35b. When $I > 1$, the nucleus has a spin and the nuclear charge distribution is nonspherical (Fig. 2.35c). The nucleus is said to have a quadrupole moment eQ, where e is the unit of electrostatic charge and Q is a measure of the deviation of the nuclear charge distribution from spherical symmetry. Whereas eQ is zero for a spherical nucleus, a positive value of Q means that charge is oriented along the direction of the principal axis (Fig. 2.35c), and a negative value of Q means that charge is concentrated in the plane perpendicular to the principal axis (Fig. 2.35d).

Unpaired nuclear spin leads to a nuclear magnetic moment (μ_N). The allowed orientations of the nuclear magnetic moment vector in a magnetic field are given by the nuclear-spin angular-momentum quantum number (m_I). This quantum number can take on values of I, $I-1$, . . . , $(-I + 1)$, $-I$. When $I = ½$, then $m_I = \pm ½$, corresponding to alignments of the magnetic moment with and opposed to the field. When $I = 1$, m_I can take values of 1, 0, and -1, corresponding, respectively, to alignments with,

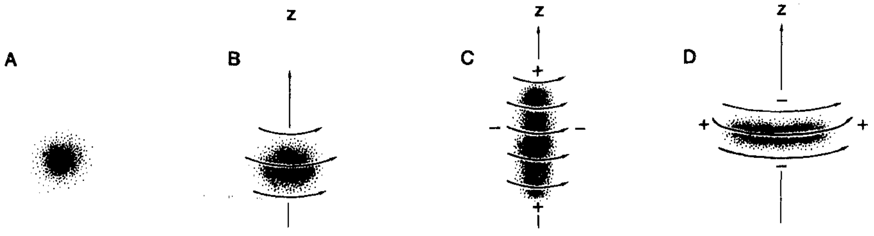

$I=0,\ \mu=0$ $I=1/2,\ \mu\neq 0,\ eQ=0$ $I\geqslant 1,\ \mu\neq 0, eQ>0$ $I\geqslant 1, \mu\neq 0, eQ<0$

Fig. 2.35. Representations of nuclei with different properties.

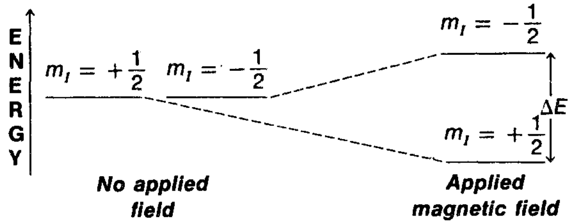

Fig. 2.36. Splitting of the $m = \pm \frac{1}{2}$ states of the nucleus in a magnetic field.

perpendicular to, and opposed to the field. In the absence of a magnetic field, all orientations of the nuclear magnetic moment are degenerate, but, in the presence of an external field, this degeneracy is removed. For a nucleus with $I = \frac{1}{2}$, the $m_I = \frac{1}{2}$ state will be lower in energy and the $-\frac{1}{2}$ higher, as shown in Fig. 2.36. In nuclear magnetic resonance (NMR), an external field is applied, and the resonant absorption of electromagnetic radiation directed at the sample and causing transitions between these energy states is studied. In nuclear quadrupole resonance (NQR), the degeneracy of the nuclear-spin angular moments (where $I > \frac{1}{2}$) is removed simply by the electric field created by the charge distribution surrounding the nucleus in the material under study. Resonant absorption of electromagnetic radiation, resulting in transitions between these energy states, is again studied, but without the need to apply an external magnetic field. In Mössbauer spectroscopy, the nucleus under study is actually excited to a higher-energy spin state, with resonant absorption of very much greater electromagnetic radiation taking place. In all of these spectroscopic methods, the exact energies of the transitions and nature of fine structure in the spectra resulting from partial or complete removal of the degeneracy of energy states is affected by the molecular or crystalline environment in which the atom (and hence nucleus) is placed. They are powerful probes of the nature of bonding associated with particular atoms in a molecule or crystal.

2.5.1. Nuclear quadrupole resonance

Nuclear quadrupole resonance spectroscopy depends on the interaction between the quadrupole moment of the nucleus (eQ) and the electric-field gradients at the nucleus arising from the charge distribution in a *solid* (molecular motion averages the electric-field gradients in gases and liquids so that quadrupole splitting does not occur). In theory, it is a technique applicable to all atoms with a nuclear spin greater than ½, because all such nuclei have a quadrupole moment greater than zero. In practice, however, a nucleus must have reasonably large values for the nuclear quadropole moment and be reasonably abundant to be suitable for NQR studies. It is also necessary for the electric-field gradient to be quite large for the resonance to be observable. There are about 130 different isotopes, the nuclei of which can be detected by NQR spectroscopy. In Table 2.1 are listed some more frequently studied NQR-active nuclides of interest in geochemistry.

The quadrupole moment is a measure of deviation of a nucleus from spherical symmetry and is defined as:

$$eQ = \int \rho(3z_m^2 - r^2)\, dx\, dy\, dz \tag{2.38}$$

where ρ is the density distribution of the charge in the nucleus, $r^2 = x^2 + y^2 + z^2$, and z_m is an axis coincident with the direction of the nuclear-spin vector I (the principal axis in Fig. 2.35). eQ is positive if the nucleus is elongated along this axis and negative if the nucleus is shortened in that direction. The value of eQ is constant for a particular isotope.

Nuclei of atoms bonded together in molecules or crystals may be subject to an inhomogeneous electric field produced by an asymmetric electron distribution—this is defined by the electric field gradient (q) at the nucleus. This gradient is a tensor quantity. If q is axially symmetric with respect to Z and the coordinate axes are selected such that the tensor for q takes a diagonal form, then the tensor can be represented by six irreducible components. Those about the X, Y, and Z axes are q_{zz}, q_{yy}, and q_{xx} (with $q_{zz} > q_{yy} > q_{xx}$). By Laplace's equation, the sum of the tensor components equals zero, so that only two parameters are required to specify the field-gradient tensor. By convention, these two quantities are q_{zz} and the asymmetry parameter (η). If $q_{zz} = q_{yy} = q_{xx}$, the field gradient is spherical and there is no splitting of quadrupole energy levels. If $q_{zz} \neq$

Table 2.1. NQR-active nuclides of geochemical interest

Nuclide	**Natural abundance (%)**	**Nuclear spin *I***	**Quadrupole moment ($Qe \times 10^{-24}$ cm^2)**
$^{9}Be_{4}$	100.0	3/2	2×10^{-2}
$^{10}B_{5}$	18.83	3	11.1×10^{-2} (8.6×10^{-2})
$^{11}B_{5}$	81.17	3/2	3.55×10^{-2} (3.6×10^{-2})
$^{27}Al_{13}$	100.0	5/2	0.149
$^{35}Cl_{17}$	75.4	3/2	-7.97×10^{-2} (-8.5×10^{-2})
$^{37}Cl_{17}$	24.6	3/2	-6.21×10^{-2} (-6.7×10^{-2})
$^{59}Co_{27}$	100.0	7/2	0.5
$^{63}Cu_{29}$	69.1	3/2	−0.15 (−0.16)
$^{75}As_{33}$	100.0	3/2	(−0.3) 0.27
$^{121}Sb_{51}$	57.25	5/2	−0.8 (−0.5)(−1.2)
$^{123}Sb_{51}$	42.75	7/2	−1.0 (−0.7)(−1.5)
$^{209}Bi_{83}$	100.0	9/2	−0.4

$q_{xx} = q_{yy}$, the maximum field gradient q_{zz} lies along the highest-fold symmetry axis (Z) and there is axial symmetry. When $q_{zz} \neq q_{xx} \neq q_{yy}$, the field gradients are nonsymmetric and

$$\eta = (q_{xx} - q_{yy})/q_{zz} \tag{2.39}$$

When a nucleus with a quadrupole moment is situated in an inhomogeneous electric field, there is a quadrupole splitting of nuclear energy states directly proportional to the quantity e^2Qq, the nuclear quadrupole coupling constant. In an axially symmetric field ($\eta = 0$), the energy arising from the quadrupole moment (eQ) in an electric-field gradient (q) is:

$$E_m = \frac{e^2qQ\,[3m^2 - I\,(I + 1)]}{4I\,(2I - 1)} \tag{2.40}$$

where m is the nuclear magnetic quantum number. For a nuclear spin of $I = 3/2$, m can take values of $3/2$, $1/2$, $-1/2$, $-3/2$. Substitution of $m = 3/2$ into Eq. (2.40) gives the result $E_{3/2} = e^2Qq/4$, and because m is squared in Eq. (2.40), the same value is obtained for $m = -3/2$. Substitution of $m = 1/2$ gives $E_{1/2} = -e^2Qq/4$ and the result for $m = -1/2$ is again identical. Hence, for a nucleus with a spin $I = 3/2$ in an axially symmetric field, there are two doubly degenerate quadrupole energy states, as shown in Fig. 2.37, separated by an energy ΔE corresponding to $e^2Qq/4 - (-e^2Qq/4) = e^2\,Qq/2$. A single transition is observed, resulting in absorption of electromagnetic energy:

$$h\nu = \Delta E = e^2Qq/2 \tag{2.41}$$

It is this absorption of electromagnetic energy that is measured in NQR spectroscopy. Radiation in the radio-frequency region is actually employed to effect transitions among the various orientations of a quadrupolar nucleus in a nonspherical field. In the experiment, which is generally carried out on a powder sample, one set of resonances is exposed for each chemically or crystallographically inequivalent quadrupolar nucleus

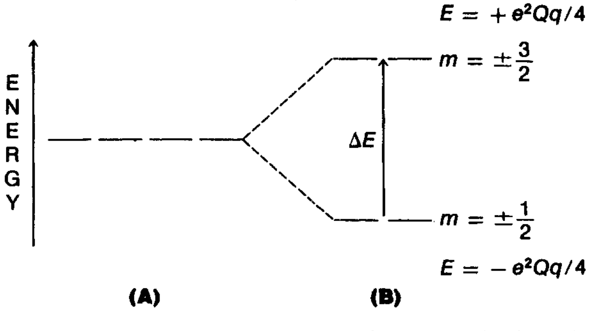

Fig. 2.37. Nuclear-quandrupole energy levels in (a) a spherical field and (b) an axially symmetric field.

(further experimental details are provided by such works as Das and Hahn, 1958). The quantity e^2qQ that is measured in NQR experiments is commonly expressed as a frequency in megahertz (although strictly this should be e^2qQ/h).

For nuclei with values of I other than $\frac{3}{2}$, splittings and transition energies in an axially symmetric field can be similarly calculated using Eq. (2.40). Thus for $I = \frac{7}{2}$, four energy levels result, as shown in Fig. 2.38. Three transitions are allowed between these energy levels, governed by the selection rule $\Delta m = \pm 1$ (see Fig. 2.38). In measured spectra, deviations from the energies (frequencies) predicted when $\eta = 0$ are attributable to deviations from axial symmetry of the field gradient surrounding the nucleus in the sample (Fig. 2.38).

When a nucleus with a quadrupole moment is situated in an inhomogeneous field that is not axially symmetric (i.e., $\eta \neq 0$), the energies of the various quadrupole levels are no longer given by Eq. (2.40). For $I = \frac{3}{2}$, the following equations can be derived for the energies of the two states:

$$E_{\pm 3/2} = \frac{3e^2Qq\sqrt{1 + \eta^2/3}}{4I\,(2I - 1)} \tag{2.42}$$

$$E_{\pm 1/2} = \frac{-3e^2Qq\sqrt{1 + \eta^2/3}}{4I\,(2I - 1)} \tag{2.43}$$

One transition is thus expected, with an energy corresponding to the difference of Eqs. (2.42) and (2.43) (i.e., $\Delta E = e^2Qq\sqrt{1 + \eta^2/3}$). As there are two unknowns (η and q), the value of e^2Qq cannot be obtained from measuring this energy (frequency). For nuclei with values of I other than $\frac{3}{2}$, more than one absorption line is often observed in the spectrum, and

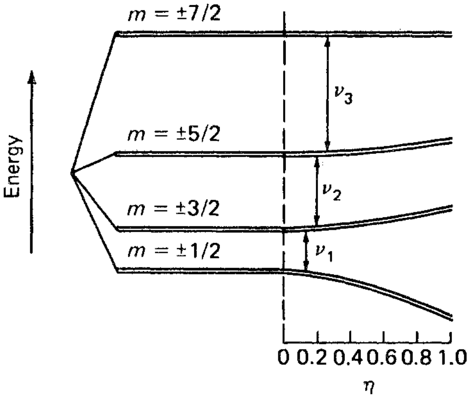

Fig. 2.38. Nuclear-quadrupole energy-level diagram for $I = \frac{7}{2}$.

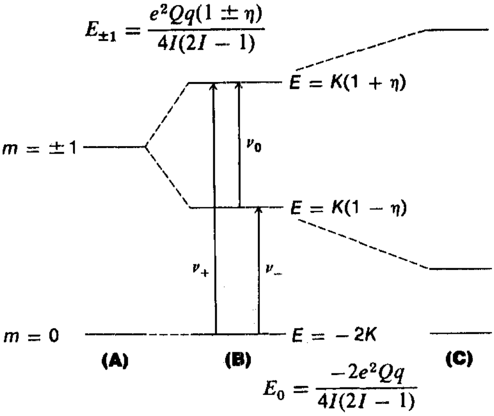

Fig. 2.39. Nuclear energy-level diagram for $I = 1$ under different conditions; (a) $\eta = 0$ and applied magnetic field $H_0 = 0$; (b) $\eta \leqslant 0$ and $H_0 = 0$; (c) $\eta \neq 0$ and $H_0 \neq 0$ but constant.

both η and e^2Qq can be obtained from the experimental measurements. The case of nuclei with $I = 1$ is illustrated and the equations shown in Fig. 2.39. The evaluation of q and η in a case such as that where $I = 3/2$ and only one transition is observed can be achieved by applying a static magnetic field to remove the degeneracy of the $\pm 1/2$ and $\pm 3/2$ levels and measuring the energies of the four transitions now allowed in addition to the transition in the absence of a field.

Having obtained values for q and η from NQR measurements, how can these values be related to molecular structure? Townes and Dailey (1949) applied a valence-bond approach to this problem and presented the formula:

$$e^2Qq_{\text{mol}} = [1 - s + d - i\,(1 - s - d)]\, e^2Qq_{\text{at}} \tag{2.44}$$

where e^2Qq_{mol} is determined by NQR measurements on the "molecule" under consideration, e^2Qq_{at} is the quadrupole coupling constant calculated for occupancy of the p_z orbital by a single electron in the isolated atom, s is the fraction of s character employed by the atom in the bond to its neighbor, d is the fraction of d character in this bond, and i is the fraction of ionic character (for a molecule A-B, $\psi^0 = c\,\psi_A + d\,\psi_B$, and $i = c^2 - d^2$). This approach is based on the argument that, provided the atom being studied is not the least electronegative in the "molecule," the maximum field gradient at this atom in the molecule (q_{mol}) is the field gradient for a single electron in a p_z orbital of the isolated atom (q_{at}). A modified form of Eq. (2.44) includes the term π to represent the extent of π bonding:

$$e^2Qq_{\text{mol}} = (1 - s + d - i - \pi)\, e^2Qq_{\text{at}} \tag{2.45}$$

A molecular-orbital approach to the problem has also been developed, since the electronic wave function and the field gradient at atom A in a molecule are related by:

$$q^{A}_{\mathrm{mol}} = e\left(\sum_{B\neq A}[Z_B(3\cos^2\theta_{AB}-1)/R^3_{AB}] - \int\psi^*\sum_n[(3\cos^2\theta_{An}-1)/r^3_{An}]\psi\, d\tau\right) \tag{2.46}$$

The first term in the equation is a summation over all nuclei external to the quadrupolar nucleus, and the second term is a summation over all electrons. If the crystal (or molecular) structure is known, the first term is easily evaluated since Z_B is just the nuclear charge of any atom in the crystal (or molecule) other than A, and θ_{AB} is the angle between the bond axis for A and the radius vector from A to B, R_{AB}. The second term, which represents the contribution to the field gradient in the crystal (or molecule) from the electron density, is an integral that is much more difficult to evaluate. Here, ψ is the ground-state wave function and θ_{An} is the angle between the bond axis and the radius vector r_{An} to the nth electron. Various semiempirical methods have been proposed for evaluating this integral. One such approach leads to the following expression:

$$\frac{e^2Qq}{h} = -\frac{e^2Qq_{\mathrm{at}}}{h}[P_z - \tfrac{1}{2}P_x - \tfrac{1}{2}P_y] \tag{2.47}$$

where e^2Qq/h is the quadrupole coupling constant, e^2Qq_{at}/h is the coupling constant for a single electron in the p orbital, and P_z,P_x,P_y are the gross atomic populations of each of the p orbitals. Equation (2.47) is a simplified molecular-orbital analog of Eq. (2.44).

NQR has been used to study structure and chemical properties of certain minerals; for example, the spectra of As, Sb, and Bi in sulfosalts and in minerals such as antimonite, orpiment, and realgar. Thus in realgar (As_4S_4) the values of e^2Qq are 178.44, 182.10, 184.10, 189.92 MHz (Pen'kov and Safin, 1963) arising from four nonequivalent As atoms in the structure. Their differing field gradients can be attributed to varying contributions from donor–acceptor and van der Waals bonds. Order–disorder phenomena have also been studied in mineral systems by NQR of a variety of nuclides, notably ^{27}Al, and the approach has been similar to that applied in the NMR studies discussed in the following.

As with many spectroscopic techniques, NQR data are most useful when compared with quantum-mechanical calculations for the mineral or system under study. Thus, Vaughan and Tossell (1973) compared the quadrupole coupling constants for ^{11}B in BO_3 (2.5–2.6 MHz) and BO_4 (0.5–0.7 MHz) polyhedra in borate minerals to the results of calculations on $[BO_3]^{3-}$ and $[BO_4]^{5-}$ clusters using an approximate molecular-orbital method. The Townes and Dailey formula [Eq. (2.44)] was used to relate the electric-field gradient at the ^{11}B nucleus to the anisotropy in B 2_p orbital populations given by the $[BO_3]^{3-}$ calculation. Using the measured atomic value of e^2qQ for the free boron atom with one unbalanced $2p$ electron (5.39 MHz), the predicted imbalance of σ and π B $2p$ orbital populations for trigonally coordinated boron (2.55 MHz) is 0.47 electrons. The calculation on $[BO_3]^{3-}$ gave a p-orbital imbalance of 0.43 electrons, in good agreement with the prediction of the Townes and Dailey model. However, as noted by Snyder et al. (1976), there are substantial difficulties associated with the Townes and Dailey treatment, including the neglect of the charge dependence of the r_{An}^{3} integral, the neglect of contributions from other nuclear centers, and the crudeness of the methods generally used to calculate charge distributions from electronegativities within the Townes and Dailey model. By contrast, the electric-field gradient can now be directly calculated using Hartree–Fock molecular-orbital methods. Semiquantitative values and trends seem to be obtained adequately for B-containing systems using routine Hartree–Fock methods (Snyder et al., 1976; Tossell and Lazzeretti, 1988c), although very accurate results require quite sophisticated wave functions.

2.5.2. *Nuclear magnetic resonance*

Spin quantum numbers (I) of nuclei of geochemical interest include ^{1}H($I=½$), ^{19}F($I=½$), ^{23}Na($I=\frac{3}{2}$), ^{27}Al($I=\frac{5}{2}$), ^{29}Si($I=½$), ^{31}P($I=½$). For nuclei in which $I \neq 0$, spinning of the positively charged nucleus gives rise to nuclear magnetism (paramagnetism), whereas, in cases where $I = 0$ (as in ^{16}O), the nucleus is nonmagnetic. For a nucleus with a spin I, the nuclear angular momentum is $[I(I+1)]^{1/2}(h/2\pi)$ and the magnitude of the nuclear magnetic moment (μ_N) is given by:

$$\mu_N = g_N\,[I(I+1)]^{1/2}\,\beta_N \tag{2.48}$$

where β_N is the nuclear magneton ($=eh/4\pi M$, where e and M are the charge and mass of the proton) and g_N is the nuclear g factor. If such a nucleus is placed in a uniform external magnetic field of flux B_o and with the nuclear magnetic moment vector (μ_N) inclined at an angle of θ to the Z axis of the external field, it will experience a torque L that tends to align it with the field, and it can be shown that:

$$L = \mu_N B_o \tag{2.49}$$

Since the nucleus is spinning, this torque causes μ_N to precess (in the way a spinning top precesses under the torque of a gravitational field) about $B_o(Z)$ at an angular frequency ν_o, where

$$\nu_o = \gamma_N B_o \tag{2.50}$$

and γ_N is the gyromagnetic ratio ($= g_N\mu_N$). The frequency ν_o is the Larmor frequency.

Quantum mechanics requires that the magnetic moment vector (μ_N) component in the direction of the field is restricted to values:

$$\mu_N = m_N g_N \beta_N \tag{2.51}$$

where m_N, the nuclear-magnetic quantum number, may take values of I, $I-1$, $I-2$, . . . , $-I$. For the simplest case, where $I = \frac{1}{2}$ (applicable to ^{1}H, ^{19}F, ^{29}Si), then m_N can take values of $+\frac{1}{2}$ and $-\frac{1}{2}$ and in the external magnetic field B_o the degeneracy of these states is removed and they are split in energy (see Fig. 2.40). This can be conceptualized as two possible orientations of the "nuclear magnet" in the external field and the energy difference ΔE between them is given by:

$$\Delta E = g_N \beta_N B_o \tag{2.52}$$

The frequency of the radiation corresponding to this energy (and that would be absorbed in bringing about the transition) would be:

$$\nu = \frac{\Delta E}{h} = \frac{g_N \beta_N B_o}{h} \tag{2.53}$$

and this turns out to be the same as the Larmor precession frequency (ν_o). This energy difference is very small and lies in the microwave region of the electromagnetic spectrum. Attempts to measure this energy by conventional absorption or emission spectroscopy were unsuccessful, but when an oscillating electromagnetic field of frequency equivalent to the Larmor frequency is applied, a resonance effect is observed that can be measured.

A simplified illustration of the apparatus used in NMR measurements is shown in Fig. 2.41. The magnet applies an external field, commonly of ~1.5 T (15 kG, although fields up to 50 kG are now used), the strength of

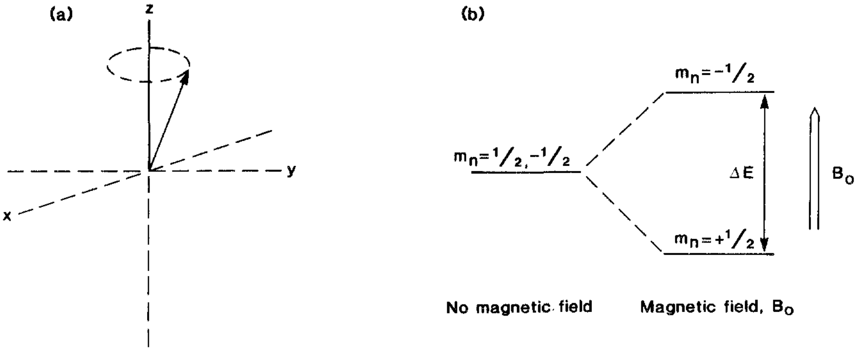

Fig. 2.40. Nuclear magnetic resonance (NMR): (a) precession of vector about z (the direction of B_o); (b) splitting of the $m = \pm\frac{1}{2}$ states in a magnetic field.

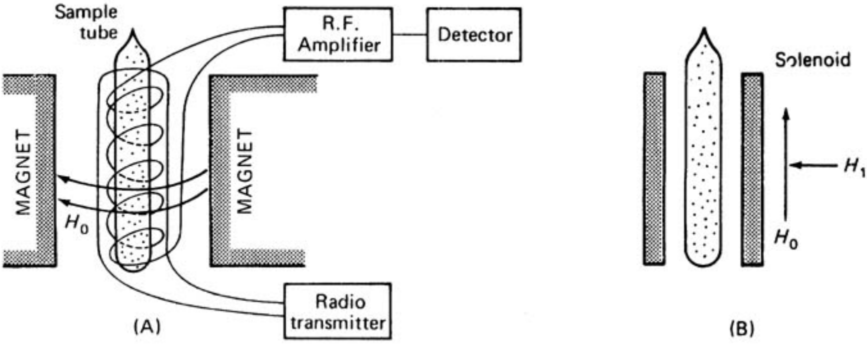

Fig. 2.41. Schematic illustration of a simple NMR spectrometer.

which can be varied, and this splits the nuclear energy levels (Fig. 2.40). The low-power radio-frequency transmitter (operating at, say, 60 MHz) applies a small oscillating electromagnetic field to the sample. This is, in fact, a fixed field, and it is the field of the large magnet that is varied to produce the resonance condition. When transitions occur in the sample, the fluctuations in the overall field are detected by a receiver coil.

The resonance frequency measured in NMR is normally expressed in terms of units independent of the spectrometer field strength and hence as a *chemical shift* (δ) in parts per million with respect to a reference compound [i.e., $\delta = (H_{\text{sample}} - H_{\text{reference}})/\nu_1(10^6)$, where H_{sample} and $H_{\text{reference}}$ are positions of the respective absorption lines (in Hz) and ν_1 is the spectrometer operating frequency].

Modern NMR spectrometers subject the spin system to a series of equally spaced pulses of radio-frequency energy, the objective being to examine the decay in magnetization of the specimen as a function of time between pulses rather than use continuous-wave excitation. If an external field B_0 is applied along the z axis of a cartesian coordinate set that rotates about z at the Larmor frequency ($\nu_0 = \gamma_N B_0$), the net magnetization vector M is invariant with time. B_1 (in Fig. 2.42) rotates at the Larmor frequency in the laboratory framework and is applied in the xy plane. At resonance, B_0 is cancelled along z, leaving only B_1 to interact with M. Since B_1 and the rotating cartesian set rotate at the same frequency, B_1 is considered directed along x, so that M will begin to precess about x. In t_p seconds it will precess through θ radians, where:

$$\theta = \gamma_N B_1 t_p \tag{2.54}$$

A pulse of radio-frequency energy is applied for t_p seconds, and the instrument is arranged to detect only the component of M along y so that maximum intensity is obtained if $\theta = \pi/2$ (the 90° pulse). After t_p seconds, B_1 returns to zero, and the system relaxes to equilibrium with M along the z axis. The component of magnetization along y decays to zero with a time constant T_2 (the spin–spin relaxation time) and the restoration of

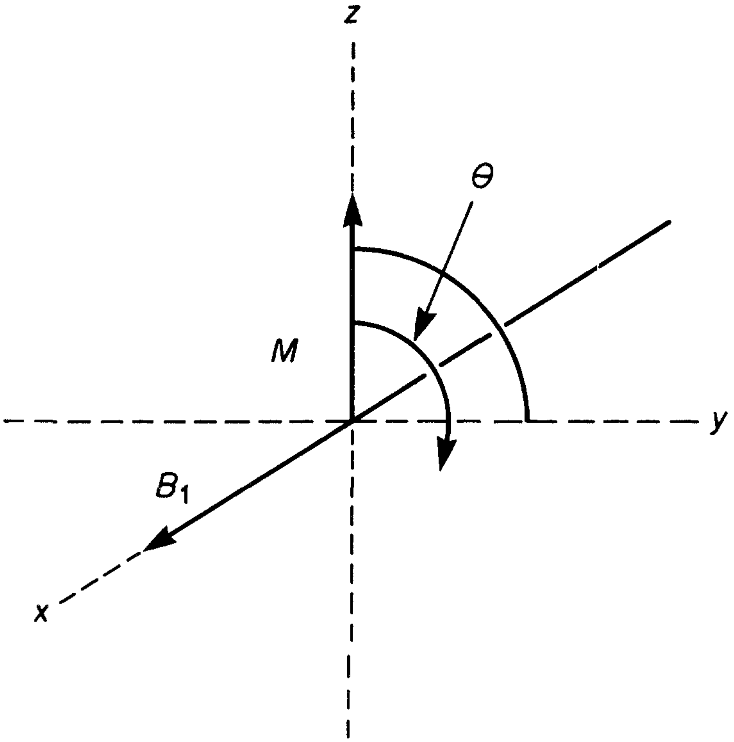

Fig. 2.42. Precession of *M* about *yx*.

the *z* component of *M* to the equilibrium value occurs with time constant T_1 (the spin–lattice relaxation time). The nuclei under investigation in a sample will likely have different chemical and magnetic environments, so that a spectrum of Larmor frequencies will be observed; excitation of all transitions can occur simultaneously, given appropriate radio-frequency pulses. The decay following the 90° pulse is now not a simple exponential decay but an interferogram containing all resonance frequencies. The spectroscopic information in this "time-domain" form can be processed to data in the more familiar "frequency-domain" form by a Fourier transformation.

NMR studies of solids have presented particular problems in that, using normal experimental procedures, very broad lines will be observed, masking details of the spectrum. This can be seen if we consider that the energy of interaction between the nuclear magnetic moment (μ_N) and the external magnetic field (B_o) can be expressed as the eigenvalues of a Hamiltonian operator $\bar{H}$:

$$\bar{H} = -\mu B_o \tag{2.55}$$

which can be, in turn, regarded as comprising:

$$\bar{H} = \bar{H}_{CS} + \bar{H}_J + \bar{H}_D + \bar{H}_Q \tag{2.56}$$

where $\bar{H}_{CS}$ relates to chemical shift, $\bar{H}_J$ to spin–spin coupling, $\bar{H}_D$ to dipolar terms, and $\bar{H}_Q$ to quadrupole terms. In liquids, $\bar{H}_D$ and $\bar{H}_Q$ are averaged to zero by molecular tumbling, whereas in solids they are very large terms (5×10^4 and $\sim 10^6$ MHz, respectively, compared to 10^3 MHz for $\bar{H}_{CS}$ and 10 MHz for $\bar{H}_J$ in both solids and liquids). Since the information of value regarding the chemical environment is contained in the $\bar{H}_{CS}$ term, ways have to be found to extract this or to modify the experiment and so suppress the other terms. One approach that has been particularly applied to minerals is magic-angle spinning (MAS). Here, rapid spinning of the sample about a rotation axis inclined at 54.7° with respect to the magnetic field results in the $\bar{H}_D$ term going to zero. For nuclei where $I = \frac{1}{2}$ (e.g., ^{29}Si) there are no quadrupolar terms, so that high-resolution information on chemical shifts can be obtained from ^{29}Si MAS NMR.

There are now numerous examples of the applications of NMR spectroscopy in mineralogy, certain of which will be further discussed later in the book. In Fig. 2.43, the ^{29}Si MAS NMR of zeolite Y is illustrated. Such studies have been used to determine the distribution of Si and Al within the framework structure of these minerals. The peaks with chemical shifts

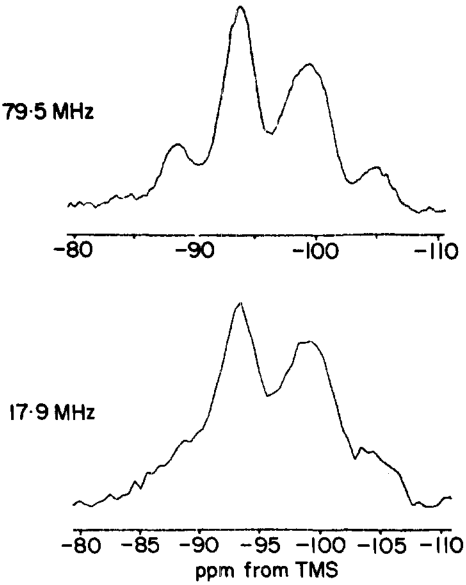

Fig. 2.43. ^{29}Si MAS NMR spectrum of zeolite Y (5858 scans at 79.5 MH_z, 3762 scans at 17.9 MH_z) (after Fyfe et al., 1982; reproduced with the publisher's permission).

centered around 88, 94, 99, and 105 can be assigned to SiO_4 (silicate) tetrahedra with, respectively, 3, 2, 1, and 0 AlO_4 (aluminate) tetrahedra as next-nearest neighbors. The areas under the resonance peaks provide data on the ratios of silicon atoms occupying these different tetrahedra in the structure. Lippmaa et al. (1980) have shown that ^{29}Si MAS NMR is a technique that can be applied to silicate minerals so as to identify a particular environment for a SiO_4 tetrahedron. High-resolution NMR studies have also been undertaken on ^{23}Na, ^{1}H, and ^{27}Al, and there is considerable potential for future work on these and rarer systems such as ^{17}O-enriched synthetic oxides. Broad-line (as opposed to "high-resolution") studies have chiefly involved ^{1}H and ^{2}D spectra in clays, micas, and other hydrated minerals. The considerable potential for further work is illustrated by the table of NMR properties of nuclei (Table 2.2). NMR is a technique of considerable versatility that has been developed for chemical applications through numerous adaptations and modifications of the basic methods. Many of these NMR-based methods are separately listed in Appendix B (including, for example, those referred to by the acronyms CP-MAS, COSY, DANTE, NMDR, and NOESY), but few of them have, as yet, been applied to geochemical problems.

Table 2.2. Some nuclides of potential use in NMR studies of solids

Nucleus	Readily observed	Spin	Quadrupole moment (10^{-24} cm^2)	Natural abundance (%)	Frequency (MHz) (11.7 T)
^{1}H	yes	1/2	—	99.985	500
^{2}H	yes	1	0.0028	0.015	76.8
^{7}Li	yes	3/2	−0.03	92.58	194.3
^{9}Be	yes	3/2	0.0512	100	70.3
^{10}B	yes	3	0.074	19.58	53.7
^{11}B	yes	3/2	0.0355	80.42	160.4
^{13}C	yes	1/2	—	1.1	125.7
^{14}N	yes	1	0.016	99.6	36.1
^{15}N	yes	1/2	—	0.37	50.7
^{17}O	yes	5/2	−0.026	0.037	67.8
^{19}F	yes	1/2	—	100	470.4
^{23}Na	yes	3/2	0.14	100	132.3
^{25}Mg	yes	5/2	ND	10.1	30.6
^{27}Al	yes	5/2	0.149	100	130.3
^{29}Si	yes	1/2	—	4.7	99.3

Table 2.2. Continued

Nucleus	Readily observed	Spin	Quadrupole moment (10^{-24} cm^2)	Natural abundance (%)	Frequency (MHz) (11.7 T)
^{31}P	yes	1/2	—	100	202.4
^{33}S	no	3/2	−0.064	0.76	38.4
^{35}Cl	yes	3/2	−0.0789	75.5	49.0
^{39}K	yes	3/2	0.11	93.1	23.3
^{45}Sc	yes	7/2	−0.22	100	121.5
^{49}Ti	no	7/2	ND	5.5	28.2
^{51}V	yes	7/2	−0.04	99.76	131.4
^{63}Cu	yes	3/2	0.16	69.1	132.5
^{67}Zn	yes	5/2	0.15	4.1	31.3
^{71}Ga	yes	3/2	0.112	39.6	152.5
^{73}Ge	yes	9/2	−0.2	7.8	17.4
^{77}Se	no	1/2	—	7.6	95.3
^{79}Br	yes	3/2	0.33	50.5	125.3
^{85}Rb	yes	5/2	0.27	71.25	48.3
^{87}Sr	no	9/2	0.2	7.0	21.7
^{89}Y	yes	1/2	—	100	24.5
^{91}Zr	no	5/2	ND	11.2	46.7
^{93}Nb	yes	9/2	−0.2	100	122.2
^{95}Mo	yes	5/2	0.12	15.7	32.6
^{109}Ag	yes	1/2	—	48.18	23.3
^{113}Cd	yes	1/2	—	12.26	110.9
^{115}In	yes	9/2	1.14	95.72	109.6
^{119}Sn	yes	1/2	—	8.58	186.4
^{125}Te	no	1/2	—	6.99	158.0
^{133}Cs	yes	7/2	−0.003	100	65.6
^{137}Ba	no	3/2	0.2	11.3	55.6
^{139}La	yes	7/2	0.21	99.9	70.6
^{171}Yb	no	1/2	—	14.3	88.1
^{195}Pt	no	1/2	—	33.8	107.5
^{199}Hg	yes	1/2	—	16.8	89.1
^{205}Tl	yes	1/2	—	70.5	288.5
^{207}Pb	yes	1/2	—	22.6	104.6

Many parameters that are accessible directly or indirectly by NMR experiment are also parameters that can be calculated quantum mechanically, as will be seen in the following chapters. Of particular interest are the NMR properties that are strongly and uniquely dependent upon local structure and that can be accurately measured; for example, the nuclear-quadrupole coupling constant (NQCC) due (as already explained in Section 2.5.1) to the interaction of the electric-field gradient, eq, at the nucleus with the nuclear quadrupole moment, eQ, so that NQCC $= e^2qQ/h$. Properties that contribute to the NQCC can also be calculated, such as the asymmetry parameter η, defined in Eq. (2.39) or specific components of the electric-field-gradient (EFG) tensor (q_{xx}, q_{yy}, q_{zz}). Also accessible from NMR spectra and by quantum-mechanical calculations are the NMR shielding constants σ, where the effective field at the nucleus (H_{eff}) is given by $H_{\mathrm{eff}} = (1 - \sigma)H_{\mathrm{applied}}$. Again, specific contributions to the average shielding constant (σ_{av}) such as diamagnetic (σ^{d}) or paramagnetic (σ^{p}) contributions, or contributions parallel ($\sigma_{\parallel}$) or perpendicular ($\sigma\perp$) to a major symmetry axis and their difference ($\Delta\sigma$, hence a shielding constant anisotropy) can also be calculated. NMR shielding constants relate directly to chemical shifts (δ) and like them are reported in ppm. Data of this type are presented in Chapters 4 and 5 (see, for example, Tables 5.4, 5.13, and 5.14).

2.5.3. The Mössbauer effect

As we have already seen (Section 2.3), the interaction of photons of light with the electrons in solids (or liquids and gases) can result in the resonant absorption of photons of particular energies. Measurement of such absorption effects as a function of the energy (wavelength) of the light yields an optical absorption spectrum. The absorption of energy quanta by excitation of electrons in atomic systems should have a parallel in the absorption of much greater energies in the excitation of nuclei. However, for many years attempts to observe resonant absorption of γ-ray photons (particularly with energies of $\sim 10^3$–10^5 eV) by their excitation of appropriate nuclei were frustated by the effects of recoil. The energies of γ-ray photons are so much greater than those of visible radiation that considerable energy is lost through recoil during emission and absorption processes in free-atom systems. Consequently, the γ-ray photons do not have sufficient energy to raise the nucleus from its ground state to an excited state. In 1958, Rudolf Mössbauer discovered that if decaying nuclei are *rigidly* held in a crystal lattice, certain γ rays may be emitted without recoil. Conversely, recoiless resonant absorption of these γ rays may also take place by appropriate nuclei in a solid. The recoilless emission and resonant absorption of nuclear γ rays in solids subsequently became known as the Mössbauer effect, and the measurement of Mössbauer spectra is now a routine laboratory procedure. Many excellent introductions to the theory and experimental methods of Mössbauer spectroscopy have been published (e.g., Wertheim, 1964; Greenwood and Gibb, 1971), including some dealing particularly with applications in mineralogy and geochemistry (Bancroft, 1973; Maddock, 1985; Hawthorne, 1988). Although the Mössbauer effect has been studied in isotopes of more than 20 of the chemical elements, it is only readily studied in a much smaller number. The vast majority of studies involving minerals and rocks concern the Mössbauer effect in the nucleus of ^{57}Fe (2% natural abundance). Discussion here will be confined to this isotope (although data of geochemical interest have also been obtained on systems such as ^{119}Sn, ^{125}Te, ^{121}Sb, ^{197}Au).

The stable isotope ^{57}Fe may be formed by the decay of the radioactive isotope ^{57}Co, as shown in Fig. 2.44. This process is accompanied by the emission of γ rays of various energies as the decaying ^{57}Co passes through various excited states of ^{57}Fe characterized by different nuclear spin quantum numbers (I). These are very short-lived species with half-lives ($t_{1/2}$) of 10^{-7} s or less. The 14.4-keV γ rays emitted when ^{57}Fe in the first excited state ($I = 3/2$) passes to the ground state ($I = 1/2$) are used in the Mössbauer-effect experiment. When γ rays of this energy are emitted without recoil, they may be absorbed resonantly (again without recoil) by the nuclei of ^{57}Fe atoms in a solid absorber such as a mineral. However, the precise energy at which this absorption occurs and the nature of the absorption is influenced by the environment of the ^{57}Fe nucleus, and thus a range of γ-ray energies must be provided by the source. This is achieved by making use of the Doppler effect and vibrating the source through a range of velocities. In the experimental system (Fig. 2.44) the sample is placed between the source, mounted on the vibrating system, and the γ-ray detector. As the source sweeps through a range of velocities, the counts from the detector pass into a range of counting cells in a multichannel analyzer. The resulting spectrum is a plot of γ-ray energies (expressed as velocity of the source in mm s^{-1}) versus absorption (see Fig. 2.44). The influence the environment of the nucleus exerts on the energies of the ground and first excited states of ^{57}Fe makes the Mössbauer effect a powerful tool in the study of the electronic structure of iron-bearing solids. The effects of the perturbations on the energy levels and their corresponding spectra are summarized in Fig. 2.44.

Differences in the electron density at the nucleus between source and absorber result in shifting of the relative energies of ground and excited states. This isomer shift (IS) results from the electrostatic interaction between the charge distribution of the nucleus and those electrons that have a finite probability of being found in the region of the nucleus. In fact, only *s* electrons have a finite probability of overlapping with the nuclear charge density, so that the isomer shift is a function of the *s*-electron density at the nucleus (although *p, d,* and *f* electrons can exert an influence by screening the *s* electrons). The nucleus is not, in fact, a point charge

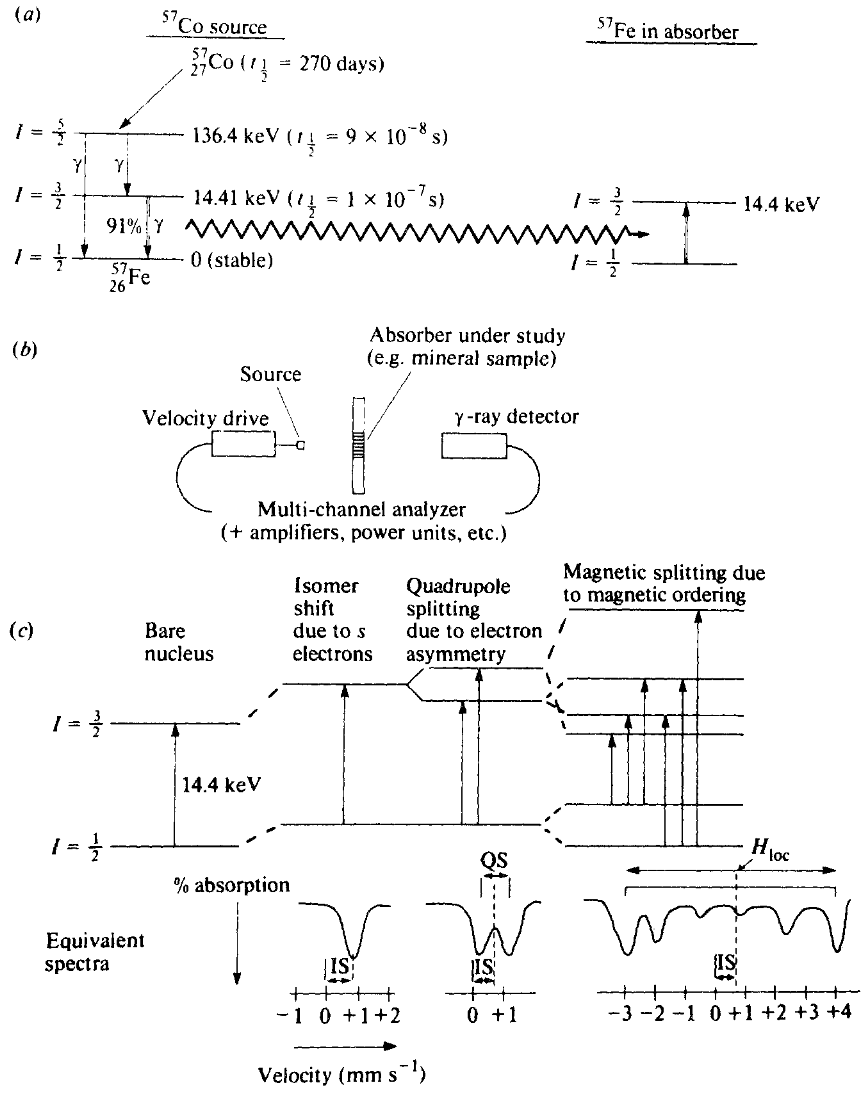

Fig. 2.44. Mössbauer spectroscopy: (a) nuclear transitions giving rise to the Mössbauer effect in ^{57}Fe; (b) principles involved in the Mössbauer spectrometer; (c) Mössbauer resonant absorption of iron in different crystal environments and the resulting spectral types. (After Vaughan and Craig, 1978; reproduced with the publisher's permission).

but has a radius (R) that differs in the excited state and ground state by an amount $\delta R = R_{\mathrm{ex}} - R_{\mathrm{gr}}$. This term, along with the nuclear charge (Z), electronic charge (e), and a term for the s-electron density at the nucleus $[\,|\psi(0)_s|^2]$, appears in the expression for isomer shift derived from first-order perturbation theory:

$$\mathrm{IS} = \frac{4\pi}{5} Ze^2R^2 \frac{\delta R}{R} [\ |\ \psi(0)_s\ |\ ^2_{\mathrm{absorber}} - \ |\ \psi(0)_s\ |\ ^2_{\mathrm{source}}] \tag{2.57}$$

For a given source material we can simplify this expression to:

$$\mathrm{IS} = \mathrm{const} \times R^2 \frac{\delta R}{R} [\ |\ \psi(0)_s\ |\ ^2_{\mathrm{absorber}} - C\ ] \tag{2.58}$$

where C is a constant for the source used. The nuclear factor ($R^2\ \delta R/R$) in the above expression is also constant for a given nucleus, which shows the direct dependence of isomer shift on s-electron density at the nucleus. Electron density in p or d orbitals directly affects the isomer shift because it can penetrate the s orbital and thus screen the s-electron density from the nuclear charge. Even in the early days following the discovery of the Mössbauer effect, the results of Hartree–Fock calculations (Duncan and Wigley, 1963; Watson and Freeman, 1960) demonstrated that a decrease in the number of d electrons causes a marked increase in the total s-electron density at the iron nucleus. In a well-known diagram reproduced in Fig. 2.45, isomer-shift values in various iron compounds are shown plotted against $3d$- and $4d$-electron charge density based on Hartree–Fock calculations for free ions of different configurations (after Walker et al., 1961).

If the electronic environment of the nucleus is not spherically symmetrical, the resulting electric-field gradient (q) may interact with nuclear states having a quadrupole moment (Q) (i.e., any nuclear state having a spin $I > ½$). In the case of ^{57}Fe, this results in splitting of the excited state ($I = 3/2$) so that two transitions can occur, producing a two-peak spectrum (see Fig. 2.44). This corresponds to alignment of the quadrupole moment of the "nonspherical" nucleus either with, or across, the electric-field gradient produced by, for example, a distorted coordination site or an asymmetric distribution of electrons in the orbitals. Allowed energies (E_{Q}) are given by the formula:

$$E_{\mathrm{Q}} = \frac{e^2qQ}{4I(2I-1)} [3m^2 - I(I+1)]\ (1 + \eta^2/3)^{1/2} \tag{2.59}$$

as discussed for NQR spectroscopy (Section 2.5.1, where the terms Q, q, m, and η are more fully explained). In the case where the excited state has $I = 3/2$ (as in ^{57}Fe), the allowed energies give rise to two transitions and hence two peaks separated by a quadrupole splitting (QS), where:

$$\mathrm{QS} = \mathrm{const} \times Qq \tag{2.60}$$

The Mössbauer nucleus can, therefore, be used as an "observer" or probe to obtain information about site symmetries and field gradients, much as in NQR spectroscopy. However, whereas in NQR transitions are observed directly between ground-state sublevels, in Mössbauer spectroscopy transitions between sublevels of the excited state and the ground-

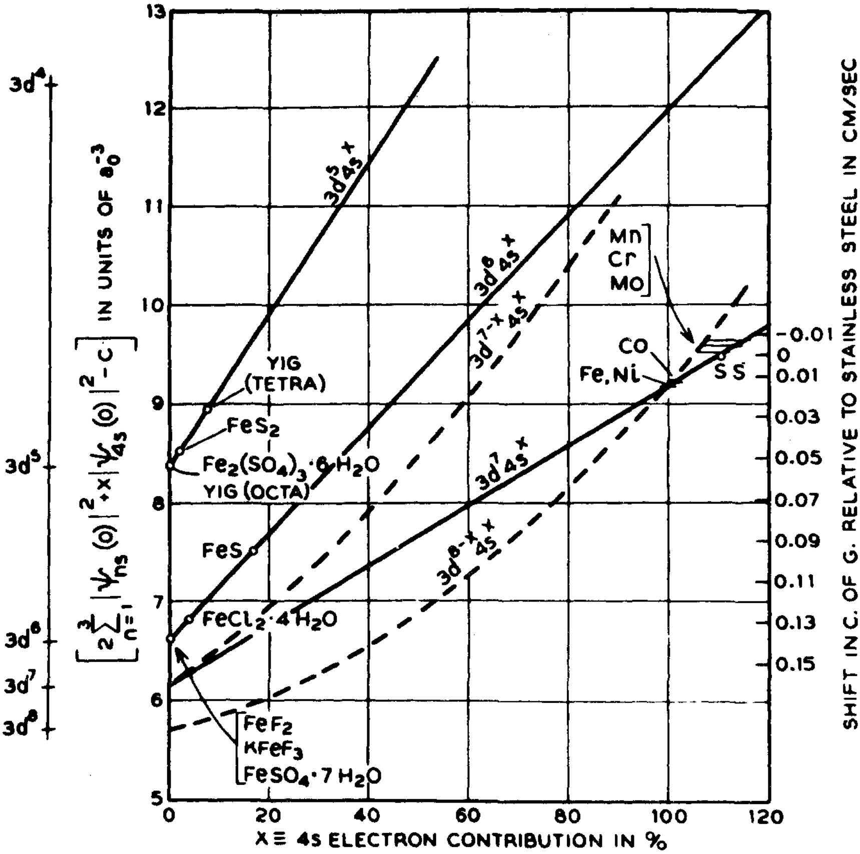

Fig. 2.45. The isomer shift of ^{57}Fe as a function of 3*d*- and 4*s*-electron charge density (after Walker et al., 1961; reproduced in Wertheim, 1964).

state level (or sublevels) are observed. Because of this, Mössbauer spectroscopy is applicable to a wider range of nuclei than NQR (not just those with ground-state spins $I > \frac{1}{2}$) and is easier to measure. It is also possible to obtain the sign as well as the magnitude of the field gradient, particularly through the use of an external magnetic field (as discussed in the following).

As noted in Section 2.5.2, a nucleus with a spin I has a nuclear magnetic moment (μ_N) given by:

$$\mu_N = g_N I \beta_N \tag{2.61}$$

Thus, if a magnetic field is applied to this nucleus in some way, there is an interaction between the field and the moment μ_N such that $(2I + 1)$ energy levels result with energies:

$$E = -g_N \, H_{int} \, m_I \, \beta_N \tag{2.62}$$

where H_{int} is the magnetic field at the nucleus and $m_I = I, I-1, \ldots, -I$. The result is that the degeneracy of the ground- and the excited-state energy levels is completely removed by this magnetic hyperfine splitting, as shown in Fig. 2.44. The origin of this magnetic field may be internal, as in a material that is magnetically ordered at the temperature of study, or it may be externally applied. If there is no quadrupole splitting in addition to the magnetic splitting, then the separations between the energy levels are identical (and equal to $g_N H_{\mathrm{int}} \beta_N$) and the magnitude of the splitting is directly proportional to H_{int} (and g_N). Because transitions can take place only if $\Delta m = \pm 1$ or 0, only six transitions are possible, giving rise to a six-peak spectrum. In a randomly oriented powder sample, the intensities of peaks 1 to 6 will vary in the ratios 3:2:1:1:2:3. The presence of quadrupole splitting in addition to magnetic splitting, as shown in Fig. 2.44, gives rise to an asymmetric six-peak spectrum. However, in this case the m_I value of each level (and spectral peak) is identifiable, so the sign of the quadrupole splitting can be obtained from the relative separations of peaks 1,2 and 5,6 (Fig. 2.44). Thus Mössbauer spectroscopy yields valuable information on the presence of magnetic ordering in a material, and the variation of this ordering can be studied as a function of temperature and pressure. The use of externally applied fields enables the sign of the quadrupole splitting to be determined.

The Mössbauer spectra of iron in numerous minerals have been studied, but a few examples will serve to illustrate this technique. In the rock-forming silicate minerals, Mössbauer spectroscopy has been used to study the oxidation state, spin state and coordination of iron, and its distribution between different sites in a structure. Thus, Fig. 2.46 (after Williams et al., 1971) shows the spectrum of an augite [essentially $(\mathrm{Ca,Mg,Fe})_2\mathrm{Si}_2\mathrm{O}_6$], the structure of which contains two kinds of sixfold-coordinate sites that may be occupied by iron (the *M*1 and *M*2 sites). The Mössbauer spectrum can be fitted to three quadrupole doublets: peaks 1 and 1′ have parameter characteristic of Fe^{3+} (in both *M*1 and *M*2 sites), peaks A and A′ have parameters characteristic of Fe^{2+} in *M*1, and peaks C and C′ of Fe^{2+} in the *M*2 sites. These assignments, based chiefly on comparisons with endmember compositions and related species, also enable estimates of site populations to be made on the basis of the areas under the peaks. Studies of the variation in site populations as a function of composition and thermal treatment have led to important advances in understanding intercrystalline order–disorder equilibria, as pioneered in the work of Virgo and Hafner (1970).

In the mineral pyrite (FeS_2), the isomer shift and quadrupole splitting values indicate that iron is present in one (octahedral) site as low-spin Fe^{2+} (Vaughan and Craig, 1978). However, small amounts (~2%) of iron impurity in the isostructural MnS_2 (hauerite) exhibit the larger isomer shift and quadrupole splitting parameters characteristic of high-spin Fe^{2+} (see Fig. 2.47). It was found by Bargeron et al. (1971) that, on subjecting

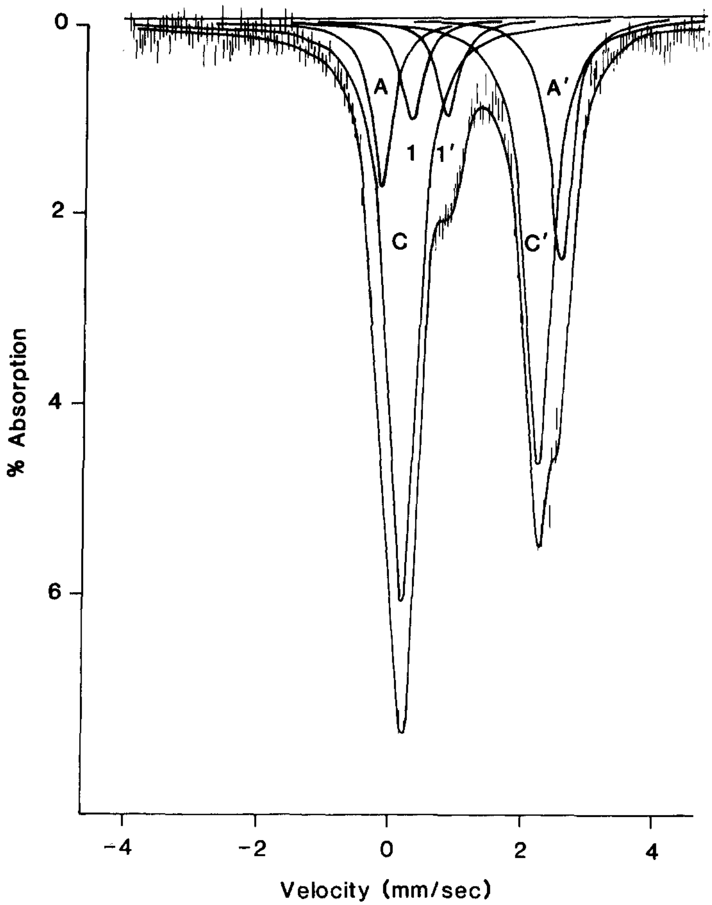

Fig. 2.46. The ^{57}Fe room-temperature Mössbauer spectrum of augite [~$(Ca,Mg,Fe)_2Si_2O_6$] (after Williams et al., 1971).

this material to high pressures, changes in the spectrum (as illustrated in Fig. 2.47) occur that indicate a progressive conversion of iron from the high-spin to the low-spin state. Complete conversion was achieved by 120–130 kbar and the process shown to be reversible with only slight hysteresis. In addition to such spin-pairing, high-pressure Mössbauer spectroscopy has led to observation of a wealth of other phenomena, including pressure-induced reduction of iron and pressure-induced magnetic transitions (many of which are reviewed by Drickamer and Frank, 1973).

The application of Mössbauer studies to magnetic materials is well illustrated by the spectra of magnetite (Fe_3O_4) shown in Fig. 2.48. Although this ferrimagnetically ordered material is an inverse spinel with nominally tetrahedral Fe^{3+} and both Fe^{2+} and Fe^{3+} on octahedral sites, at temperatures above 119 K (the Verwey transition temperature) only

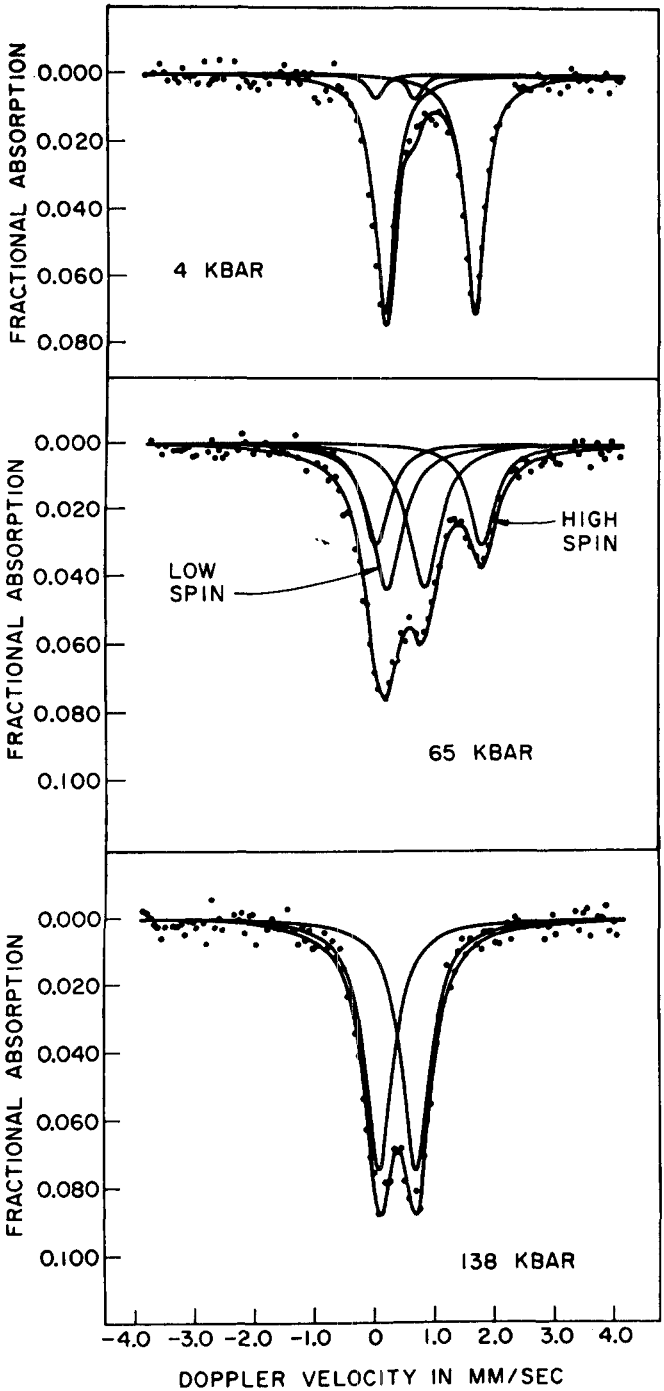

Fig. 2.47. The ^{57}Fe Mössbauer spectrum of (Fe,Mn)S_2 at 4 and 65 kbar, illustrating a pressure-induced high-spin → low-spin transition (after Bargeron et al., 1971).

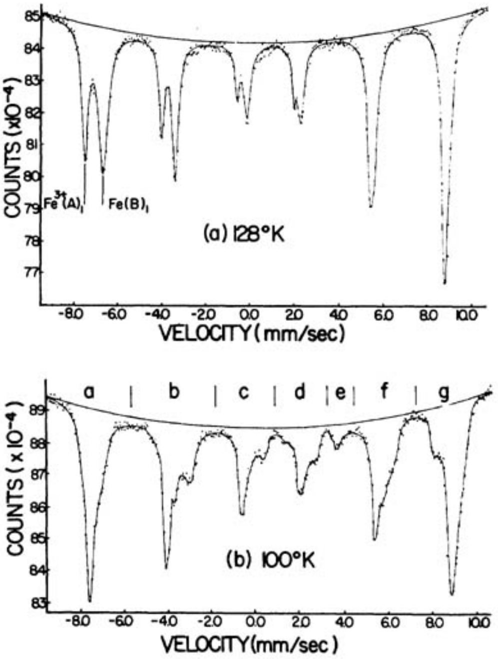

Fig. 2.48. The ^{57}Fe Mössbauer spectra of magnetite (Fe_3O_4) at temperatures (a) above and (b) below the Verwey transition (after Sawatzky et al., 1969).

two sets of superimposed six-peak spectra are observed. These arise from the tetrahedral Fe^{3+} and an averaged contribution from the octahedral sites due to electron hopping between Fe^{2+} and Fe^{3+}, which takes place more rapidly than the Mössbauer transition. However, on cooling below 119 K, this is no longer the case, and additional peaks (Fig. 2.48) arise from Fe^{2+} and Fe^{3+} species on octahedral sites, although matters are further complicated by subtle changes in crystal structure.

The Mössbauer-effect experiment can also be applied to the study of surfaces in the variation known as conversion electron Mössbauer spectroscopy (CEMS). Here, what is monitored as a function of incident γ-ray energy is not absorption, but the emission of electrons through a process of internal conversion (i.e., as a byproduct of the absorption of Mössbauer γ rays). Since the conversion electrons can only escape from the surface layers of the solid, data are selectively acquired for the surface region, arising from the Mössbauer effect in the (most commonly iron) atoms of the surface layers. The monitoring of emitted electrons results in a "mirror image" of the usual absorption spectrum. Transmission and CEM spectra of vivianite [$Fe_3(PO_4)_2 \cdot 8H_2O$] are illustrated in Fig. 2.49 (after Tricker et al., 1979].

It will be evident from the above discussion of the nature and origin of the Mössbauer effect that it should be possible to calculate Mössbauer parameters accurately using quantum-mechanical methods. This has not proved to be a straightforward matter, and the subject of the calculation

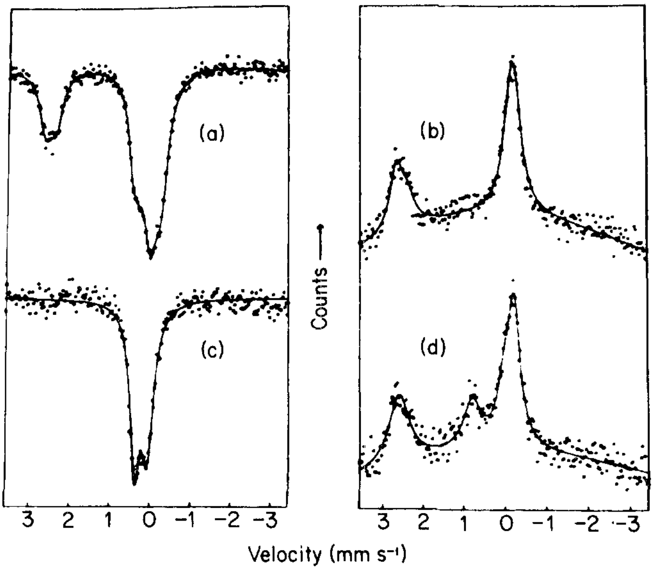

Fig. 2.49. (a) Transmission and (b) conversion electron ^{57}Fe Mössbauer spectra of a single crystal of vivianite. Spectra (c) and (d) represent transmission and CEM spectra, respectively, of the same material after heating at 120°C for 1 h and show that the bulk is largely Fe^{3+}, whereas the surface comprises largely Fe^{2+} species (after Tricker et al., 1979; reproduced with the publisher's permission).

of Mössbauer parameters is discussed in detail in Chapter 4, with particular reference to the iron oxides and related compounds (see Section 4.5).

2.6. Other methods

As noted in the introduction to this chapter, a very wide range of experimental methods is now available for the study of the electronic structures of earth materials. Many of the most important methods have been discussed in the preceding sections, and an attempt made in Appendix B to list all of the relevant methods, along with a very brief explanation of each technique and information on further reading. One major spectroscopic method was not discussed above but is worthy of inclusion in this chapter: electron spin resonance.

2.6.1. Electron spin resonance

Electron spin resonance (ESR) spectroscopy, also known as electron paramagnetic resonance (EPR) or electron magnetic resonance, involves the absorption of microwave-frequency radiation by molecules, ions, or atoms possessing electrons with unpaired spins. More detailed accounts of the technique are provided by Atherton (1973), Symons (1978), and

Abragam and Bleaney (1970), and McWhinnie (1985) has reviewed applications in mineral chemistry. ESR spectroscopy is possible because an electron has a spin together with an associated magnetic moment. Thus, for a "free electron," this electron will have a spin quantum number $S = \pm 1/2$ and a magnetic moment $\mu = B$ (the electronic Bohr magneton $= eh/4\pi mc$). If the electron is placed in a magnetic field B, the magnetic moment can align either parallel or antiparallel to the field, thus removing the spin degeneracy, as shown in Fig. 2.50. If the system is then irradiated with electromagnetic energy of the correct frequency, transitions can occur between the two spin orientations. Because the lower state is more "populated" than the upper energy state at thermal equilibrium, there is a net absorption of energy (and loss of power from the incident radiation) as absorptive transitions ($-1/2 \rightarrow +1/2$) outnumber radiative transitions ($+1/2 \rightarrow -1/2$). The transition energy (ΔE) or its observed frequency ($h\nu$) is given by

$$\Delta E(=h\nu) = g\beta B \tag{2.63}$$

where β is the electronic Bohr magneton, B is the applied field, and g is termed the "g value."

In a free multielectron atom or ion, the spin and orbital angular moments of the electrons couple to give a total angular momentum represented in the Russell–Saunders scheme by the quantum number J. Since J arises from vectorial addition of L (the total orbital quantum number) and S (total spin quantum number), it may take integral (or half-integral

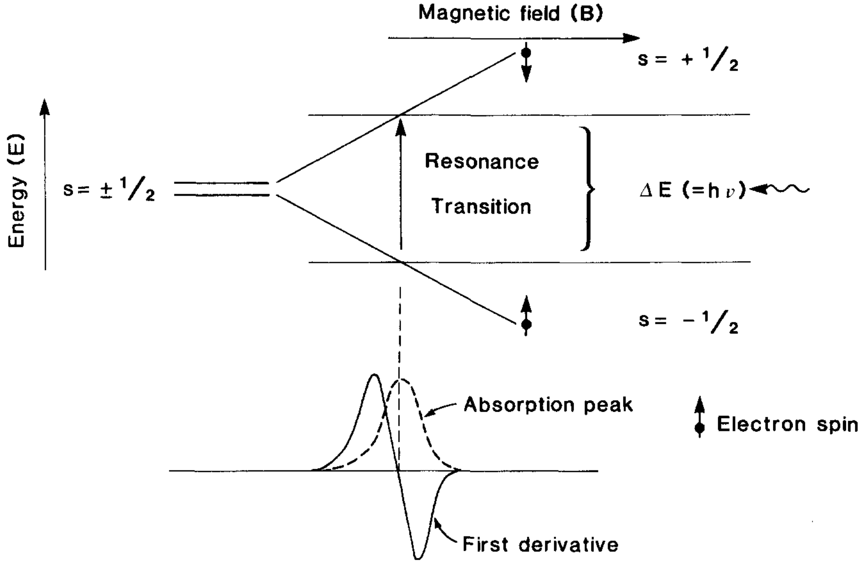

Fig. 2.50. The principles of electron spin resonance (ESR) spectroscopy.

if S is half-integral) values between $(L-S)$ and $(L+S)$. The resulting $(2J+1)$ states are degenerate in the free ion, but split into $(2J+1)$ equally spaced energy levels in a magnetic field (B). The energy of each state is given by $g_L \beta B M_J$, where M_J is the magnetic quantum number with integral or half-integral values of J, $(J-1)$ . . . , $-J$, and g_L is the Landé g factor,

$$g_L = 1 + \frac{J(J+1) - L(L+1) + S(S+1)}{2J(J+1)} \tag{2.64}$$

Thus, in a magnetic-resonance experiment performed on the free ion, transitions may be induced between these levels under the selection rule $M_J = \pm 1$, giving the resonance condition:

$$\Delta E = h\nu = g_L \beta\, B[M_J + 1) - M_J] = g_L \beta\, B \tag{2.65}$$

For a paramagnetic *molecule* or for an ion in a *crystal* (with a nondegenerate ground state), the orbital angular momentum of the unpaired electron is not free to respond to the aligning force of the external field, since it is likely to be strongly aligned along a specified molecular (or crystal) axis by the intramolecular (intracrystalline) electric field. This results in a "quenching" of the orbital contribution. If the quenching were total, the value of g would be 2 minus the free-electron value (actually 2.0023 after relativity effects are considered). In practice, it may not be total because spin–orbit coupling can produce some breakdown of the coupling between the orbital angular momentum and the electric field. This may be described by an admixture of various excited states that can be coupled to the ground state by components of the orbital-angular-momentum operator along various molecular axes.

The value of g and hence deviation (Δg) in its value from the free-electron value is measured in the ESR experiment. The small differences arising from location of the paramagnetic ion in differing "molecular" environments are readily detectable, enabling the technique to be used as a "probe" in crystal chemistry and bonding studies. Also, given the above, Δg may assume different values for each "molecular" or crystal axis if the symmetry is lower than cubic. Hence, the g value may be anisotropic and represented by a second-rank tensor with principal axes that may, or may not, coincide with the molecular axes. In axially symmetric "molecules," two values $g_{\parallel}$ and $g_{\perp}$ are given; for lower symmetry cases, three values are determined (g_{xx}, g_{yy}, g_{zz}).

Contributions to Δg can arise from many atoms in the molecule. Studies of minerals commonly involve metal ions in relatively weak ligand fields, where the major contribution is from the metal. The calculation of Δg in this case involves the Hamiltonian:

$$H = H_0 + H' \tag{2.66}$$

where the Zeeman interaction between the electron spin (S) and the magnetic field (B) is

$$H_0 = g_e\beta BS \tag{2.67}$$

where $g_e = 2.0023$, the free-electron value. The perturbation H' is the sum of orbital Zeeman interactions and the spin–orbit interaction:

$$H' = \Sigma_\mu(\beta Bl_\mu + \lambda_\mu l_\mu S_\mu) \tag{2.68}$$

where l_μ is the orbital angular momentum of the μth electron, which has spin S_μ, and λ_μ is the spatial part of the spin–orbit interaction. A first-order perturbation treatment shows that, for any nondegenerate electronic wave functions (e.g., the ground state, $|\,0>$), all matrix elements of the form $<0\,|\,l_\mu\,|\,0>$ vanish. This is a mathematical statement of the quenching of the orbital contribution. Hence calculation of the first contribution to Δg requires second-order perturbation theory. Terms linear in B and S are selected from the complete expression for the second-order energy, and this part of the energy is written as $\Delta g\beta BM_s$, where Δg is the g shift for a particular orientation of B and M_s is the projection of the total spin on B. If one particular excited state gives the major contribution to Δg, the result takes the form:

$$\Delta g = \left(\frac{2}{M_s}\right)\frac{<0\,|\,\lambda l_B \mathrm{S}_B\,|\,1><1\,|\,l_B\,|\,0>}{E_0 - E_1} \tag{2.69}$$

where $|\,1>$ denotes the wavefunction of the low-lying excited state of energy E_1, and L_B,S_B are the components of l_μ and S_μ along B.

For many of the transition-metal ions of geochemical interest, the number of unpaired electrons is greater than one, and several spin states are accessible. The field generated by the other electron adds a constant energy to all Zeeman terms in cubic symmetry, but, when the symmetry is low, polarization of the secondary field may occur, causing splitting in the absence of a magnetic field. Thus for Fe^{3+}, where $S = 5/2$, separation of the $\pm 1/2$, $\pm 3/2$, $\pm 5/2$ states may be caused by such *zero-field splitting* and result in the states known as *Kramers doublets*. Experimentally, ESR spectra are only readily observed in transition-metal ions if the ground state is a Kramers doublet (e.g., in Cu^{2+}, Mo^{5+}, V^{4+}, Cr^{3+}, Fe^{3+}, Mn^{2+}). In these cases, where crystal-field effects are of greater magnitude than magnetic effects, the spin Hamiltonian is:

$$H = g\beta BS_z + DS_z^2 + E\,(S_x^2 - S_y^2) \tag{2.70}$$

and D describes an axial distortion, E a rhombohedral distortion. In an example such as Fe^{3+} in an axial field, $E=0$, and the energy levels (W) are given by:

$$W = Dm^2 \tag{2.71}$$

where $m = \pm 5/2$, $\pm 3/2$, $\pm 1/2$. Small distortions result in a fine-line spectrum, whereas for large values of D a limiting case is reached where a "$g_\perp$" feature is seen close to 6, whereas "$g_\parallel$" remains at 2.

Hyperfine interactions between the electron and any magnetic nuclei ($I>0$) present (such as a proton, for example) produces hyperfine splitting, as illustrated in a very simple example in Fig. 2.51. This hyperfine interaction may be divided into an isotropic and an anisotropic component. The isotropic part arises from unpaired electron density at the nucleus and can only be nonzero for *s*-type orbitals. The anisotropic term corresponds to the classical part of the magnetic dipole interaction for which the Hamiltonian is:

$$H = IAS \tag{2.72}$$

where

$$A_{ij} = A_0\, \delta_{ij} + B_{ij} \tag{2.73}$$

A_0 is the isotropic component, and B is the anisotropic contribution. Commonly Eq. (2.63) may be modified to:

$$\Delta E = h\nu = g\beta\,(B + M_I A) \tag{2.74}$$

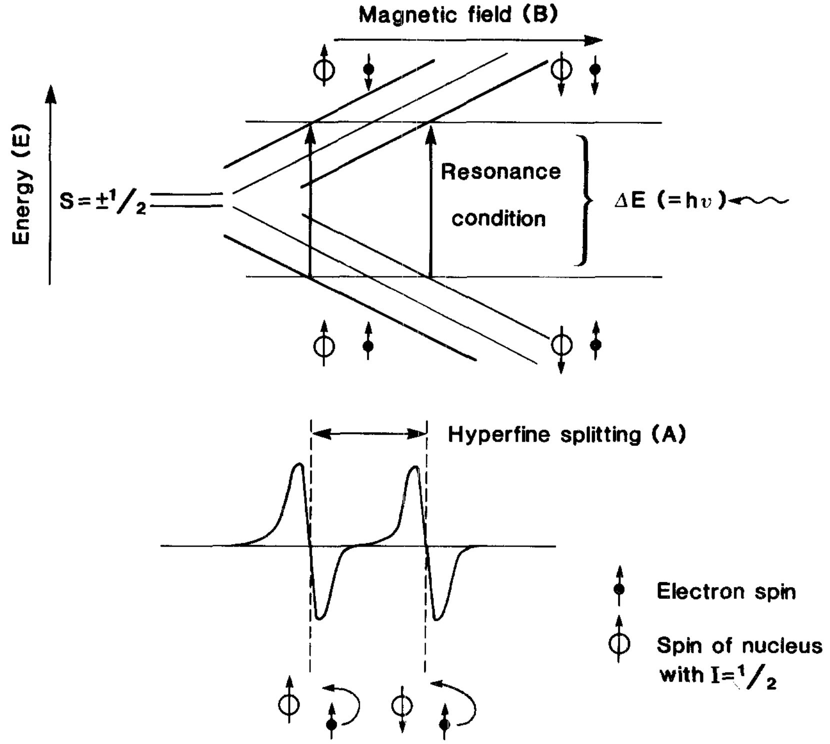

Fig. 2.51. Hyperfine interactions in electron spin resonance.

In fact, A is usually measured as the separation of peaks in an experimental spectrum (see Fig. 2.51). The selection rules governing hyperfine interactions are $\Delta M_s = \pm 1$, $\Delta M_I = 0$. Hence, a magnetic nucleus of spin I will split the resonance into $2I+1$ components, and when g is anisotropic all components will be split [e.g., in the axially symmetric case, $g_\perp$ and $g_\parallel$ will be split into $(2I+1)$ components separated by $A_\perp$ and $A_\parallel$, respectively, and the differences in $A_\perp$ and $A_\parallel$ will arise from the anisotropy of B in Eq. (2.74).

In an ESR experiment, the principal components of g and A are measured; linewidths and line shapes are also studied, as they can give insight into unresolved hyperfine splitting and to various relaxation phenomena whereby energy may be transferred to other parts of the system (e.g., the crystal lattice in spin–lattice relaxation). ESR spectra are recorded at a fixed microwave frequency by scanning the magnetic field, and usually it is the first derivative of the absorption versus the field that is recorded (see Figs. 2.50 and 2.51). Solutions, glasses, powders, and single crystals may be studied, and a wide variety of applications are relevant to mineralogy and geochemistry. In Fig. 2.50 are shown ESR spectra of powdered calcite ($CaCO_3$) containing Mn^{2+} impurity. This complex spectrum shows some g anisotropy and other fine structure. Heating to 800°C causes de-

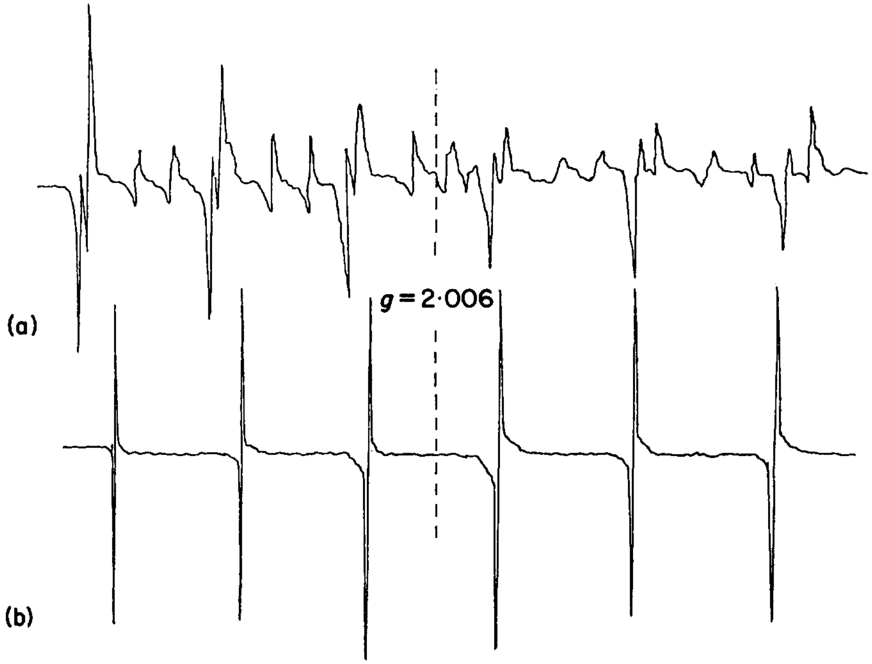

Fig. 2.52. (a) The ESR spectrum of powdered calcite ($CaCO_3$) containing Mn^{2+} as an impurity; (b) the same specimen as in (a) heated to 800°C. (After McWhinnie, 1985; reproduced with the publisher's permission).

composition to cubic calcium oxide with a simple isotropic six-line pattern as shown in Fig. 2.52. The ESR spectrum can thus be used to monitor such reactions. Among many other applications might be mentioned the use of ESR to characterize minor Fe^{3+} impurities in kaolinite (Meads and Malden, 1975) that occur in the octahedral layer, and to study the absorption of transition-metal ions into a range of other clay mineral structures.

2.7. Concluding remarks

In this chapter, the most important experimental methods available to study chemical bonding and crystal chemistry in geochemical systems have been briefly reviewed, and some examples provided of their applications. Numerous further examples will be considered in the following chapters. What is already evident, however, is that meaningful interpretation of the results obtained using these experimental methods is only possible using models of chemical bonding, models based on quantum-mechanical theories. The development and application of such models is further discussed in the next chapter, from which it will be evident that the bonding models in turn can only be properly tested by comparison with experiment.

3

THEORETICAL METHODS

In this chapter, the most important quantum-mechanical methods that can be applied to geological materials are described briefly. The approach used follows that of modern quantum-chemistry textbooks rather than being a historical account of the development of quantum theory and the derivation of the Schrödinger equation from the classical wave equation. The latter approach may serve as a better introduction to the field for those readers with a more limited theoretical background and has recently been well presented in a chapter by McMillan and Hess (1988), which such readers are advised to study initially. Computational aspects of quantum chemistry are also well treated by Hinchliffe (1988).

In the section that follows this introduction, the fundamentals of the quantum mechanics of molecules are presented first; that is, the "localized" side of Fig. 1.1 is examined, basing the discussion on that of Levine (1983), a standard quantum-chemistry text. Details of the calculation of molecular wave functions using the standard Hartree–Fock methods are then discussed, drawing upon Schaefer (1972), Szabo and Ostlund (1989), and Hehre et al. (1986), particularly in the discussion of the agreement between calculated versus experimental properties as a function of the size of the expansion basis set. Improvements on the Hartree–Fock wave function using configuration-interaction (CI) or many-body perturbation theory (MBPT), evaluation of properties from Hartree–Fock wave functions, and approximate Hartree–Fock methods are then discussed.

The focus then shifts to the "delocalized" side of Fig. 1.1, first discussing Hartree–Fock band-structure studies, that is, calculations in which the full translational symmetry of a solid is exploited rather than the point-group symmetry of a molecule. A good general reference for such studies is Ashcroft and Mermin (1976). Density-functional theory is then discussed, based on a review by von Barth (1986), and including both the multiple-scattering self-consistent-field $X\alpha$ method (MS-SCF-$X\alpha$) and more accurate basis-function–density-functional approaches. We then describe the success of these methods in calculations on molecules and molecular clusters. Advances in density-functional band theory are then considered, with a presentation based on Srivastava and Weaire (1987). A discussion of the purely theoretical modified electron-gas ionic models is followed by discussion of empirical simulation, and we conclude by mentioning a recent approach incorporating density-functional theory and molecular dynamics (Car and Parrinello, 1985).

Qualitative molecular-orbital theory approaches (and related qualitative treatments) are discussed throughout the text (particularly in Chapters 4 and 6), and a more detailed discussion of the contributions of such approaches presented in Chapter 8. As with the experimental methods discussed in Chapter 2, the topics presented in the present chapter are associated with numerous abbreviations and acronyms (and alternative titles). Both to serve as a key to these abbreviations, and as a source of reference to the numerous theoretical approaches now available, they are listed along with brief descriptions and references to further information in Appendix C.

3.1. Elements of quantum mechanics

Although the Schrödinger equation, the fundamental equation of quantum mechanics, may be derived from the classical wave equation by a heuristic approach, it is currently more common to present quantum mechanics as a set of postulates, such as those tabulated below (Levine, 1983).

Postulate 1. The state of a system is described by a function ψ of the coordinates and the time. This function, called the *state function* or *wave function,* contains all the information that can be determined about the system. ψ is single-valued, continuous, and quadratically integrable.

Postulate 2. To every physical observable there corresponds a linear Hermitian operator. To find this operator, write down the classical-mechanical expression for the observable in terms of Cartesian coordinates and corresponding linear-momentum components, and then replace each coordinate x by the operator $\hat{x}$ and each momentum component p_x by the operator $-i\hbar\,\partial/\partial x$.

Postulate 3. The only possible values that can result from measurements of the physical observable G are the eigenvalues g_i of the equation:

$$\hat{G}\phi_i = g_i\phi_i \tag{3.1}$$

where $\hat{G}$ is the operator corresponding to the property G.

Postulate 4. If $\hat{G}$ is any linear Hermitian operator that represents a physical observable, then the eigenfunctions ϕ_i of the eigenvalue equation above form a complete set.

Postulate 5. If $\psi(q,t)$ is the normalized state function of a system at time t, then the average value of a physical observable G at time t is:

$$<G> = \int \psi^* \hat{G} \psi \, dq \tag{3.2}$$

Postulate 6. The time development of the state of an undisturbed system is given by the Schrödinger time-dependent equation

$$-\frac{\hbar}{i}\frac{\partial \psi}{\partial t} = \hat{H}\psi \tag{3.3}$$

where $\hat{H}$ is the *Hamiltonian* (i.e., energy) *operator* of the system.

If the Hamiltonian is independent of time, the wave function as a function of coordinates and time may be written as:

$$\psi(q,t) = e^{-iEt/\hbar}\, \psi(q) \tag{3.4}$$

where the spatial part of the wave function satisfies the time-independent Schrödinger equation:

$$\hat{H}\psi\,(q) = E\psi\,(q) \tag{3.5}$$

This time-independent Schrödinger equation provides the theoretical foundation for the solution of virtually all problems in chemistry. Since the exact analytic solution of the Schrödinger equation is only possible for systems with one electron (see Levine, 1983), one must turn to approximate solutions to obtain information on systems of interest to chemists (or geochemists).

For molecules, a common simplification is the *Born–Oppenheimer separation* in which the slow-moving nuclei and the fast-moving electrons are treated separately. Using this approximation (and suppressing the q dependence), we first solve the electronic Schrödinger equation:

$$\hat{H}_e\, \psi_e = E_e\, \psi_e \tag{3.6}$$

for various positions of the N atoms within the molecule. The resulting electronic energies E_e form a potential energy surface $V(\mathbf{R}_1, \mathbf{R}_2, \ldots, \mathbf{R}_n)$ where $\boldsymbol{R}_A$ specifies the coordinates of atom A. This leads to a Schrödinger equation describing the motion of the nuclei:

$$\hat{H}_N\, \psi_N = E\psi_N \tag{3.7}$$

where:

$$\hat{H}_N = -\sum_A \frac{\nabla_A^2}{2M_A} + V(\mathbf{R}_1, \mathbf{R}_2, \ldots, \mathbf{R}_N) \tag{3.8}$$

in which $\frac{\nabla_A^2}{2M_A}$ is the quantum-mechanical operator expression for the kinetic energy of nucleus A. Equation (3.7) may then be solved to yield the approximate total wave function:

$$\psi = \psi_e \psi_N \tag{3.9}$$

and the total energy E.

The nonrelativistic Hamiltonian operator for a molecule in field-free space may be written as:

$$\hat{H}_e = \sum_A \sum_{B>A} \frac{Z_A Z_B}{R_{AB}} + \sum_i \left(\frac{\nabla_i^2}{2} - \sum_A \frac{Z_A}{\mathrm{r}_{iA}} \right) + \sum_i \sum_{j>i} r_{ij}^{-1} \tag{3.10}$$

where the first summation represents the repulsions between pairs of nuclei A and B with nuclear charges Z_A and Z_B; the second sum goes over all n electrons and includes the operators for electron kinetic energy and electron nuclear attraction (where r_{iA} is the separation of electron i and nucleus A); and the third term gives the repulsions between pairs of electrons i and j, r_{ij} being the distance between them.

In writing the Hamiltonian in Eq. (3.10) we have used atomic units, in which $\hbar$ (Planck's constant divided by 2π), the electronic charge (e), and the electron mass are all set to unity. Distances are then given in bohr (a_0), where 1 a_0 = 0.52918 Å. The atomic unit of energy is the hartree, with 1 hartree = 27.21 eV = 627.5 kcal/mol. The bohr is the most probable electron–nuclear separation in the ground state of the hydrogen (H) atom, while the hartree is twice the ionization potential (IP) of ground-state H (a related quantity, the Rydberg, is equal to the H-atom ionization potential, or one-half the hartree).

If we have a wave function ψ for the ground state of our system, then we can calculate the energy as the expectation value of the Hamiltonian operator

$$E = \int \psi^* \hat{H} \psi \, d\tau \tag{3.11}$$

If the wave function is the exact wave function, we obtain for E the exact (nonrelativistic) energy. If ψ is an approximate wave function, the *variational principle* (Levine, 1983) tells us that the lower the E the more closely ψ resembles the exact wave function, so long as it satisfies certain conditions, the most important being the Pauli exclusion principle. If ψ contains parameters, then that choice of parameters giving the lowest E will give the best wave function in the sense of maximum overlap with the true wave function.

A necessary and reasonable approximation in the generation of wave functions for many-electron systems is to represent the many-electron wave function using products of one-electron wave functions or orbitals, ϕ_i. To ensure compliance with the Pauli exclusion principle, the wave function for the n-electron system is written as a normalized antisymmetric product or *Slater determinant*:

$$\Phi_i = \frac{1}{\sqrt{n!}} \begin{vmatrix} \phi_1(1) & \phi_1(2) & \cdots & \phi_1(n) \\ \phi_2(1) & \phi_2(2) & \cdots & \phi_2(n) \\ \phi_n(1) & \phi_n(2) & \cdots & \phi_n(n) \end{vmatrix} \tag{3.12}$$

The one-electron orbital ϕ_i is, in turn, the product of a spatial part and a spin function α (for $m_s = +½$) or β (for $m_s = -½$). If the orbital ϕ_i has infinite variational flexibility, we obtain the best possible single determinant wave function, called the *Hartree–Fock wave function.*

By minimizing the energy of Φ_i in Eq. (3.12), we obtain a set of coupled integro-differential equations, the Hartree–Fock equations, which may be expressed in the following form for closed-shell systems (for open-shell cases see Szabo and Ostlund, 1989):

$$\hat{F}(1)\phi_i(1) = \varepsilon_i\phi_i(1), \qquad i = 1, \ldots, n \tag{3.13}$$

where $\hat{F}(1)$, the *Fock operator,* is given by:

$$\hat{F}(1) = -\frac{1}{2\nabla_1^2} - \sum_A \frac{Z_A}{r_{1A}} + \sum_{j=1}^{n/2} [2J_i(1) - K_j(1)] \tag{3.14}$$

and the *Coulomb operator* J_j and the exchange operator K_j are defined by:

$$\hat{J}_j(1)\phi_i(1) = \phi_i(1) \int \frac{[\phi_j(2)]^2}{r_{12}} \phi\tau_2 \tag{3.15}$$

$$\hat{K}_j(1)\phi_i(1) = \phi_j(1) \int \frac{\phi_j^*(2)\phi_i(2)}{r_{12}} d\tau_2 \tag{3.16}$$

The first term on the right of Eq. (3.14) is the operator for the kinetic energy of one electron; the second term is the potential-energy operator for the attractions between one electron and the nuclei. These two terms form the one-electron *core Hamiltonian;* the core Hamiltonian omits interactions with the other electrons. The Coulomb operator $J_j(1)$ is the potential energy of the interaction between electron 1 and a smeared-out electron with electronic density $[\phi_j(2)]^2$; the factor 2 occurs because for a closed-shell state there are two electrons in each spatial orbital. The exchange operator has no simple physical interpretation but arises from the requirement that the wave function be antisymmetric with respect to electron exchange. The Hartree–Fock molecular orbitals ϕ_i in Eq. (3.14) are eigenfunctions of the same operator $F(1)$, the eigenvalues being the orbital energies ε_i.

The true Hamiltonian operator and wave function involve the coordinates of all n electrons. The Hartree–Fock Hamiltonian operator F is a one-electron operator (i.e., it involves the coordinates of only one electron), and Eq. (3.12) is a one-electron differential equation. This has been indicated by writing F and Φ_i as functions of the coordinates of electron 1; of course, the coordinates of any electron could have been used. The operator F is peculiar in that it depends on its own eigenfunctions, which are not known initially. Hence the Hartree–Fock equations must be solved by an iterative process. One obtains approximate solutions for the ϕ_i and from these constructs the first approximation to F. Equation (3.13) is then solved to obtain a new set of ϕ_i (which are generally occupied according to their order of ε_i) and a new F is constructed. Such a process is called a *self-consistent-field* approach, and the process is terminated when the orbitals' output from one step are virtually identical to those that are input from the preceding step (in practice, the energy E is usually monitored).

A key development that helped make feasible the calculation of accurate SCF wave functions for molecules was Roothaan's (1951) proposal to expand the spatial orbitals as linear combinations of a set of basis functions χ_k:

$$\phi_i = \sum_k c_{ki}\chi_k \tag{3.17}$$

Substitution of this expansion into Eq. (2.9) gives:

$$\sum_k c_{ki}F\chi_k = \varepsilon_i \sum_k c_{ki}\chi_k \tag{3.18}$$

Multiplication by $\chi_j{}^*$ and integration gives:

$$\sum_k c_{ki}\,(F_{jk} - \varepsilon_i S_{jk}) = 0, \qquad j = 1, 2, 3, \ldots, \tag{3.19}$$

where:

$$F_{jk} = <\chi_j \mid F \mid \chi_k> \qquad S_{jk} = <\chi_j \mid \chi_k> \tag{3.20}$$

Equations (3.16) are a set of simultaneous linear homogeneous equations in the unknowns c_{ki}. For a nontrivial solution, we must have:

$$\det(F_{jk} = \varepsilon_i S_{jk}) = 0 \tag{3.21}$$

This is a *secular equation* whose roots give the orbital energies. These *Hartree–Fock–Roothaan* (HFR) equations must be solved by an interative process, since the F_{jk} integrals depend on the orbitals ϕ_i, which in turn depend on the unknown coefficients c_{ki}.

3.2. Details of Hartree–Fock–Roothaan calculations: Choice of basis set

To solve the HFR problem one must choose a *basis set*. The larger and more flexible the basis set, the better (in general) the calculated properties.

A basis set may be employed that is of the same form throughout the space of the system, or one in which the orbitals are expanded in different types of basis functions in different parts of space. Such partitioned bases are often used in solid-state calculations in which one must describe an overall wave function that is rapidly varying near the nuclei and slowly varying and "free-electron-like" when far from the nuclei. Such partitioned bases will be considered further in our discussion of band-theoretical calculations and the multiple-scattering $X\alpha$ molecular-orbital method.

Most molecular calculations employ nonpartitioned bases that are constructed either of *Slater orbitals* with the form:

$$Ar^{n-1}\, e^{-\alpha r} \tag{3.22}$$

where A is a normalizing factor, n the principal quantum number, r the electron–nucleus distance, and α the orbital exponent; or *Gaussian functions* with the form:

$$B\, r^{n}\, e^{-\alpha r^2} \tag{3.23}$$

where n is the analog of the principal quantum number and α the analog of the orbital exponent. Angular dependence may be introduced by multiplying these radial functions by spherical harmonics, but for the Gaussians it is often introduced by using a function of the form:

$$cx^{p}y^{q}z^{s}e^{-\alpha r^2} \tag{3.24}$$

where p, s, and q are integers, giving what are called *Cartesian Gaussians*.

In principle, one would prefer to use Slater functions for molecular calculations since they more closely resemble Hartree–Fock atomic orbitals in their functional form, and, thus, a small set of Slater orbitals gives the energy and other properties with much greater accuracy than a set of individual (or primitive) Gaussians of the small size. However, the integrals of electron–electron repulsion are much more difficult to evaluate over Slater orbitals since numerical integration is required. By contrast, the same integrals over Gaussians have closed analytic expressions, as shown by Boys (1950). Use of fixed linear combinations of the Gaussians (*contracted Gaussians*) reduces the number of integrals over variable basis functions, although it remains necessary to calculate all of the electron–electron repulsion integrals over the *primitive Gaussians*. Most modern quantum-chemical calculations employ Gaussian orbital basis sets.

3.2.1. Minimum basis sets

A *minimum basis set* (MBS) includes one expansion function for each orbital occupied in the ground states of the free atoms. For example, a minimum-basis-set calculation on diatomic MgO would employ 1*s*, 2*s*, 3*s*, and $2p$ functions on Mg and $1s$, $2s$, and $2p$ functions on O. A common slight extension of the basis would employ a Mg $3p$ function as well. Slater-type minimum basis functions are characterized by their orbital exponents, which may be obtained from various prescriptions, such as minimization of atomic energies. Alternatively, the best molecular exponents may be obtained by minimizing the total energy of a molecule with respect to the orbital exponents. A common procedure is to determine such optimum Slater orbital exponents from calculations on one or a few small molecules, and then to transfer these values to calculations on other molecules. If Gaussian functions are to be used in the molecular calculation, a fixed linear combination of Gaussians is used with coefficients chosen to give the best overlap of the contracted Gaussian and the Slater orbital whose behavior it is intended to mimic. A common Gaussian basis is designated STO-*L*G, where *L* is the number of primitive Gaussians (G) used in the contraction to simulate the STO (Slater-type orbitals). This basis has a number of special features for speeding integral evaluation, as described elsewhere (Hehre et al., 1986).

Prior to 1960, virtually all molecular electronic-structure calculations utilized minimum basis sets. Many calculations on complex molecular clusters of mineralogical significance still employ minimum bases. Minimum-basis-set calculations give qualitatively reasonable minimum energy geometries, eigenvalue spectra ("energy levels"), and electron distributions, but the results are not of quantitative accuracy. STO-3G calculations for compounds of first- and second-row elements give average errors in bond lengths of 0.02–0.03 Å and average errors in bond angles of 2–3°. For third-row elements, average errors in bond distances increase to about 0.06 Å (Hehre et al., 1986). Unfortunately, for compounds of transition metals, minimum-basis STO-3G calculations give somewhat erratic results, with errors in metal–ligand distance routinely ranging from 0.05 to 0.20 Å (Hehre et al., 1986).

3.2.2. *Extended basis sets: Double-ζ bases*

The usual next step in improvement upon the minimum basis set is the use of two functions in place of each minimum basis set function, a *double-ζ* basis. The orbital exponents or ζs of these two functions are generally chosen to be somewhat larger and somewhat smaller than the optimum minimum-basis-set exponent, allowing for expansion or contraction of the corresponding atomic orbital on molecule formation by variation of the expansion coefficients. In many cases, doubling of the core basis functions is unnecessary, and it is efficient to use a *valence double-ζ basis* or *split valence basis* (e.g., $1s$, $2s$, $3s$, $3s'$, $3p$, $3p'$ on Mg and $1s$, $2s$, $2s'$, $2p$, $2p'$ on O for MgO). Common sets of contracted Gaussians (G) for such calculations are the 4-31G, 6-31G, and 3-21G, where the first number gives the number of Gaussians in the core function, the second the number in the more contracted valence shell function, and the third the number in the more diffuse valence shell function. Since the 3-21G bases are cheaper to use and give results very similar to N-31G, they are generally preferable.

Equilibrium geometries calculated at the split valence level almost always show shorter bond distances than the minimum-basis-set results and are generally in better agreement with experiment. Split valence wave functions also give considerably better electron distributions, as evidenced by dipole moments and molecule–atom electron-density differences that compare better with experiment (Hehre et al., 1986; Szabo and Ostlund, 1989).

3.2.3. Extended basis sets: Polarized bases

To improve upon a double-ζ basis, one generally adds *polarization functions* whose l values correspond to orbitals unoccupied in the free atoms. For example, to expand upon a double-ζ basis for H_2O, one would add $2p$ functions on H and $3d$ functions on O. Such functions are called polarization functions since they describe the polarization of atomic electron density arising from molecule formation. For example, if a H atom is placed in the electrostatic field of an O atom, its electron density will be polarized along the O–H bond direction, a change that can be described by the mixing of H $2p$ character into the H $1s$ wave function.

Polarization-function exponents can be chosen by varying the exponent to obtain a minimum molecular energy. Optimum values for $3d$ polarization functions have been tabulated for both first- and second-row elements. Such functions are important for describing electron distribution properties, but they often have only small effects upon geometric properties, eigenvalues, and energetics. A common type of polarized basis set for hydrogen-containing molecules is designated 6-31G**. In addition to a split-valence 6-31G basis, it has $2p$ functions on the hydrogens and $3d$ functions on the other atoms.

3.2.4. Extended basis sets: Other approaches

Finally, to approach the Hartree–Fock limit, it is necessary to use even more flexible bases. In particular, one must use less severely contracted Gaussians (i.e., with more variable coefficients), more Gaussians, and functions with even higher l quantum numbers. Many properties require the inclusion of highly diffuse basis functions that do not contribute significantly to the molecular energy. An excellent discussion of basis-set selection for accurate calculations is given by Davidson and Feller (1986). When very large basis sets are employed, it is common to specify the number of primitive and contracted Gaussian functions of s, p, and d (or higher ℓ) type. For example, a calculation on SiO that used $13s$ and $9p$-type primitive Gaussian functions on Si contracted to $9s$ and $5p$-type functions, together with 9*s* and 5*p* primitive Gaussians on O contracted to 4*s* and 3*p* functions, then further augmented by two uncontracted 3*d* polarization functions on Si and one on O, would be designated as (13*s*9*p*2*d*/9*s*5*p*1*d*) → [9*s*5*p*2*d*/4*s*3*p*1*d*].

It is worth noting two promising improvements in atomic basis sets that have occurred in the past few years: (1) valence basis sets with the cores replaced by effective potentials (ECP bases) (e.g., Hay and Wadt, 1985), and (2) uncontracted Gaussian bases from atomic calculations incorporating electron correlation (Almlof and Taylor, 1987). The ECP bases open up the possibility of accurate calculations on systems with heavy atoms, even those with significant relativistic effects, while the Gaussian bases obtained from correlated atom calculations provide more accuracy both at the HF level and for later correlated calculations. Effective core potentials are now available for many atoms and in many SCF packages. Miyoshi and Sakai (1988) have recently shown good agreement of effective core potential and all-electron calculations for several transition-metal compounds.

3.2.5. *Basis set and calculated properties*

To give some idea of the effect of choice of basis set upon computed properties, we have taken results from Szabo and Ostlund (1989) for the series of 10-electron molecules CH_4, NH_3, H_2O, and HF (Table 3.1) and from Sauer (1983), Ernst et al. (1981), and Meier and Ha (1980) for the silicate models $Si(OH)_4$ and $H_3SiOSiH_3$ (Table 3.2). A more complete tabulation of basis-set effects is given in Sauer (1989). The trends in bond lengths and angles evident from Tables 3.1 and 3.2 are, in fact, quite general. For compounds of first-row elements, expansion of the basis from STO-3G to 4-31G (or 3-21G) almost always gives shorter bond distances, 6-31G** results are very close to the HF-limit results, and HF-limit bond distances are systematically shorter than experimentally determined values. The neglect of electron correlation in the HF calculation causes the

Table 3.1. Equilibrium bond lengths (in a_0) for a series of ten-electron molecules from (SCF) Hartree–Fock–Roothaan calculations using different basis sets, compared with experimental values

Molecule	CH_4	NH_3	H_2O	HF
Basis set				
STO-3G	2.047	1.952	1.871	1.807
4-31G	2.043	1.873	1.797	1.742
6-31G**	2.048	1.897	1.782	1.703
Near HF limit	2.048	1.890	1.776	1.696
Experimental value	2.050	1.912	1.809	1.733

Source: Data from Szabo and Ostlund, 1989.

Table 3.2. Equilibrium Si–O bond lengths [R(Si–O) in Å] for S_4 symmetry $Si(OH)_4$ and Si–O–Si angles (∢Si–O–Si) for $H_3SiOSiH_3$ from (SCF) Hartree–Fock–Roothaan calculations using different basis sets

Basis set	R(Si–O)[a]	∢Si–O–Si[b]
STO-3G	1.654[c]	145[d]
6-31G	1.635[c]	180[d]
6-31G + Si3*d*	1.640[c]	180[d]
6-31G*	1.635[c]	142[d]
STO-3G*	—	140[e]

[a] The average Si–O bond distance experimentally determined for the SiO_4 unit in olivine is 1.635 Å.

[b] The experimentally determined ∢Si–O–Si in α-quartz is 143.7°.

[c] Sauer (1983); Si–H distance = 0.938 Å; Si–O–H angle = 115.9° (fixed).

[d] Ernst et al. (1981); Si–O distance = 1.634 Å, Si–H distance = 1.486 Å (fixed).

[e] Meier and Ha (1980).

energy at short bond distances to be systematically too low compared to that at long bond distances, giving calculated bond lengths that are too short. For second-row elements (e.g., Al-Cl), the effect of inclusion of 3*d* polarization functions is more variable. In general, 3*d* polarization functions on the second-row atom give shorter bond distances, in better agreement with experiment. Indeed, STO-3G* bases (STO-3G plus 3*d* polarization functions) give better distances than 4-31G. However, the magnitude of the geometry effects changes through the second row, with 3*d* addition to SO_3^{2-}, for example, giving a very substantial equilibrium distance reduction, particularly if 3*d* functions with high orbital exponents are included (Stromberg et al., 1984).

3.3. Improvements on the Hartree–Fock wave function

In the Hartree–Fock approximation, the equation of motion of each electron is solved for in the presence of the average potential created by the remaining $n-1$ electrons. Thus, the HF approximation considers only the averaged, not the instantaneous, repulsions between pairs of electrons. The contribution to the total energy due to the difference between instantaneous and averaged repulsions is defined as the *correlation energy*. In general, the correlation energy contributes a significant percentage to bond dissociation energies, which are therefore not given accurately in the HF approximation.

If a wave function of higher accuracy than the single-determinant HF wave function is desired, a number of techniques are available. The most frequently used method is that of *configuration interaction*, in which the wave function has the form:

$$\psi_i = \sum_i C_i \Phi_i \tag{3.25}$$

where the Φ_i are an orthonormal set of Slater determinants. The coefficients C_i are determined so as to minimize the energy. This requirement leads to the eigenvalue equation:

$$(H - E\,1)\,C = 0 \tag{3.26}$$

where H is composed of matrix elements between configurations:

$$H_{ij} = \int \Phi_i^* H \Phi_j \, dr \tag{3.27}$$

From Brillouin's Theorem (Levine, 1983), we know that H_{ij} vanishes if i and j differ by a single one-electron excitation. A consequence is that the HF wave function gives one-electron properties (expectation values of an operator that is a sum of n terms, each depending on the coordinates of a single electron) that are correct to first order. A well-known one-electron property of a molecule is the dipole moment. The operator for the x component of the dipole moment is:

$$\mu_x = \sum_{A=1} Z_A X_A - \sum_{i=1} x_i \tag{3.28}$$

where X_A and x_i are the coordinates of nucleus A and electron i, respectively.

In principle, a CI approach provides an exact solution of the many-electron problem. In practice, however, only a finite set of Slater determinants can be handled in the linear expansion. A common procedure is to retain all Slater determinants that differ from the HF determinant by one or two excitations (although one-electron excitations do not couple directly to the ground state; they couple with two-electron excitations, which in turn affect the ground state indirectly). Unfortunately, such a procedure is not size consistent. For example, the energy of two highly separated monomers will not be twice that of a single monomer in such a truncated CI calculation. Fortunately, a slightly modified approach called quadratic *CI* has recently been developed (Pople et al., 1987) that is size consistent.

Various methods are available for improving the orbitals used in a truncated CI calculation. One is to variationally optimize both the CI mixing coefficients, C_i, and the form of the orbitals in Φ_i, yielding what is called a *multiconfiguration SCF* wave function. Another is to generate approximations to those orbitals that give the most rapidly convergent CI expansion of the electron density, called the *natural orbitals*. Almost no CI or multiconfiguration SCF approaches have yet been used within geochemistry.

An alternative method treats the effect of electron correlation according to *perturbation theory*. The perturbation is the difference between the

Table 3.3. Equilibrium bond distance [R(O–H) in a_0] for H_2O from an (SCF) Hartree–Fock–Roothaan calculation, and calculations using correlated wave functions (CI and MBPT) compared with experiment

Values	R(O–H)
Calculated values	
Hartree–Fock–Roothaan (near-HF limit)	1.766
Configuration interaction (CI)	1.800
Many-body perturbation theory (MBPT)	1.816
Experimental value	1.809

Source: Data from Szabo and Ostlund, 1989.

true Hamiltonian, with instantaneous electron repulsions, and the Hartree–Fock Hamiltonian, containing the averaged electron repulsions. Application of conventional perturbation theory leads to a result now commonly known as Moller–Plesset perturbation theory (Moller and Plesset, 1934; Hehre et al., 1986). Perturbations to the Hartree–Fock Hamiltonian may also be included using the many-body Green's-function method (in *many-body perturbation theory,*) an approach well adapted to calculation of ionization potentials and electron affinities of complex systems (Cederbaum et al., 1980).

The effects of including correlation on the calculated bond distance in H_2O is shown in Table 3.3, using data taken from Szabo and Ostlund (1989). Introduction of correlation effects generally results in increases in bond distance, and for H_2O the best correlated calculations give almost exact agreement with experiment.

3.4. Dependence of computation time on basis-set size (and property calculated) for Hartree–Fock–Roothaan and configuration-interaction calculations

It is apparent from our description of the HFR procedure (and has been well established numerically) that the time required for a HFR calculation increases as somewhere between the third and fourth power of the size of the basis set. Similarly, the time required for going beyond HFR by configuration interaction increases as about the sixth power of the basis-set size for conventional CI calculations. These important results explain why dramatic increases in computer speed lead only to modest increases in the size of systems treatable by such methods. For example, an increase of 1000 in computer speed increases the size of molecules tractable by CI by slightly more than a factor of three, and those accessible to HFR procedures by a factor of about six. Thus, it appears that CI techniques are directly applicable to only the simplest models of the species occurring in solid minerals. Even an approach to the Hartree–Fock limit wave function for such species requires heroic computation. Nonetheless, calculations at lower levels provide useful information. One may also be able to obtain correction factors from a few accurate calculations to improve systematically the values of properties calculated at a lower level.

Contemporary Gaussian HFR programs also have very efficient procedures for calculating minimum energy geometries of complicated molecules (and other stationary points of the energy) and for evaluating force constants and vibrational spectra (Pulay, 1977; see Appendix C by Zerner in Szabo and Ostlund, 1989). Such efficient optimization methods, along with techniques for speeding integral evaluation and for accelerating SCF convergence are common features of the various Gaussian HFR programs.

3.5. Prediction of properties other than equilibrium geometries from Hartree–Fock–Roothaan calculations

So far we have focused upon the geometric structures of molecules, that is, the arrangement of their nuclei, for which the predictions of Hartree–Fock–Roothaan calculations are in good agreement with experiment. From the total energies calculated by such methods for atoms and molecules, we may also calculate bond dissociation energies, but here the agreement is poorer due to correlation effects. For example, the dissociation energy calculated for SiO at the Hartree–Fock level is about 4.9 eV, compared with an experimental value of about 8.3 eV (see further discussion in Chapter 4). Such a discrepancy is fairly typical (e.g., see Schaefer, 1972). In most cases, however, we are interested in *reaction* energies, which may be calculated quite accurately if the reaction is homodesmic (containing the same number of bonds in reactants and products) or, even better, is isodesmic (containing the same number and types of bonds). Such energies are often obtained quite accurately (e.g., see Hehre et al., 1986). For example, we might wish to compare reaction energies for:

$$CO_2(g) + 2H_2O(g) \rightarrow H_4CO_4(g)$$

and

$$SiO_2(g) + 2H_2O(g) \rightarrow H_4SiO_4(g)$$

to probe the competition between multiply and single-bonded carbon and silicon oxides. The results to be expected and those calculated for these reactions are fully discussed in Chapter 4 and show multiple bonding in silicon oxides to be much weaker than in carbon oxides.

For reactions that are not isodesmic, we can obtain improved reaction energies by calculating total energies of reactant and products at a partly correlated level using geometries optimized at the HF level. For example, we might optimize geometries of reactants and products at the HF 3-21G level and do single calculations at these geometries using 3-21G* basis with second-order Moller–Plesset (MP2) corrections, a procedure indicated by the symbol MP2/3-21G*//HF/3-21G, as described in Hehre et al. (1986). This approach assumes that basis-set and correlation effects are approximately additive, and seems to be accurate so long as the basis used for the correlated correction is at least polarized split valence.

In addition to geometries and reaction energies, Hartree–Fock–Roothaan calculations yield data on the energies of occupied and unoccupied orbitals (an "eigenvalue spectrum"). According to Koopmans' (1933) theorem, the negative energies of the occupied orbital eigenvalues are approximately equal to the energies needed to remove electrons from these orbitals. Within the Hartree–Fock–Roothaan approximation, a more accurate method for calculating ionization potentials is to solve the SCF problem separately for both the neutral molecule and the cation, and take the energy difference (the so-called "ΔSCF method"). This approach includes the reorganization of electron density in the cation but ignores differences in correlation energy between molecule and ion. Finally, the effects of correlation can be incorporated through configuration interaction or many-body perturbation theory (Cederbaum et al., 1980).

For molecules containing only main-group atoms, Koopmans' Theorem applied to wave functions of split valence or better quality usually gives the right ordering of orbital ionizations, although for orbitals close in energy and of different symmetry or atomic-orbital composition, inversions in the order of ionization potentials occasionally occur. Koopmans' Theorem almost always overestimates ionization potentials in such materials, and empirical reduction factors (generally involving multiplication of the Koopmans' ionization potentials by around 0.9; Brundle et al., 1970) can be used to obtain better agreement with experiment. A one-electron orbital interpretation (in which, for example, each peak in a photoemission spectrum is associated with a single orbital) seems to be valid for the outermost valence orbitals, but the inner valence orbitals, for example, the O2*s*–type orbitals of CO_2, show large configuration mixing so that no simple correspondence between orbitals and cation states can be drawn (Cederbaum et al., 1980). The dependence of ionization potential upon method of calculation is shown for N_2 in Table 3.4 using results from Szabo and Ostlund (1989) and Ermler and McLean (1980). Further details are given by Ermler and McLean (1980).

Our discussion of Hartree–Fock–Roothaan calculations has so far focused upon main-group elements; such calculations for transition-metal-bearing molecules have been somewhat less successful. Although calculated bond distances seem to be about as accurate for transition-metal fluorides as for main-group fluorides (Schaefer, 1981; Pietro and Hehre, 1983; Barandiaran et al., 1986), serious discrepancies with experiment have appeared for many transition-metal organometallic compounds with π acceptor ligands. For ferrocene, $Fe(C_5H_5)_2$, poor agreement with ex-

Table 3.4. Comparison of the first ionization potentials (in eV) of the N_2 molecule calculated using different methods, along with the experimental values

Electronic state of N_2 ion	$3\sigma_g^{-1,2}\Sigma$	$1\pi_u^{-1,2}\Pi$
Calculated values		
Hartree–Fock–Roothaan (using Koopmans' Approximation)		
Basis Set: STO-3G	14.7	15.6
4-31G	17.1	16.9
6-31G*	17.1	16.9
near HF limit	17.3	16.8
Hartree–Fock–Roothaan (using ΔSCF approach)	15.9	15.3
Many-body perturbation theory (MBPT)	15.5	16.9
Configuration interaction (CI)	15.6	16.8
Experimental value	15.6	17.0

Source: Data from Szabo and Ostlund, 1989; Ermler and McLean, 1980.

perimental bond lengths was even obtained at the Hartree–Fock limit (Almlof et al., 1984). For transition-metal oxides and sulfides the accuracy of HF bond lengths is still somewhat uncertain. Double-ζ basis-set results for $M(OH_2)_6^{2+}$ (Table 3.5) and minimum-basis-set results for $M(OH_6)^{4-}$ species (Sano and Yamatera, 1982; Tossell, 1985b) are about as good as those for main-group compounds, but recent accurate studies of neutral-metal-atom–OH_2 complexes (Sauer et al., 1986) have indicated that correlation effects may be very important and that previous studies suffered from large errors due to basis-set superposition effects (Boys and Bernardi, 1970). There have been almost no studies of the geometries of metal sulfide systems, although Tossell (1990d) has calculated a Zn–S distance of 2.40 Å in $Zn(SH)_4^{2-}$ at the polarized split valence level (about 0.05 Å larger than experiment).

Table 3.5. Comparison of metal–water bond lengths and binding energies calculated using (SCF) Hartree–Fock–Roothaan methods with experimental values

	Hydration energy (kJ mol^{-1})		**Metal–water distance (Å)**	
Metal	**calc.**	**expt.**	**calc.**	**expt.**
Mg	1659	1997	2.07	
Ca	1272	1668	2.40	2.40
Cr	1529	1925	2.13, 2.32	
Mn	1510	1920	2.19	2.20
Fe	1577	2008	2.14	2.12
Co	(1588)	2105	2.09	2.08
Ni	1689	2170	2.05	2.04
Cu	1710	2174	2.00, 2.12	1.94, 2.43
Zn	1688	2120	2.04	2.08

Source: After Sano and Yamatera, 1982; see text and this reference for further details.

As described earlier in this section, one can obtain accurate orbital ionization energies through many-body perturbation theory (Cederbaum et al., 1980) or by using the ΔSCF method. Many-body perturbation theory has been extremely successful for small molecules, since it incorporates both electronic relaxation and correlation effects, while the ΔSCF method, incorporating relaxation alone, generally leads to substantial improvement in absolute ionization potentials and some improvement in relative ionization potentials. Unfortunately, both approaches require considerably more computation than that for the ground-state wave function. It is, therefore, still common to estimate ionization potentials directly from eigenvalues through Koopmans' Theorem.

Although this procedure generally gives correct assignments of orbitals to ionization potentials for main-group molecules, it fails disastrously for transition-metal compounds (Cowley, 1979), giving metal $3d$ orbitals too deeply bound with respect to ligand valence orbitals by many electron volts. For transition-metal compounds the ΔSCF method or correlated calculations are essential to give good agreement with experiment (Smit et al., 1978). Such deficiencies appear to extend also to Hartree–Fock band theory (Kunz and Surratt, 1978), where, in metal oxides, metal $3d$ levels are too tightly bound compared to oxygen $2p$ levels, again by many electron volts. It is worthwhile to note that such problems are not encountered within density-functional theory, where eigenvalues (particularly for transition states, as explained later) give proper relative ionization potentials for both main-group and transition-metal compounds.

3.6. Evaluation of spectral and other experimental parameters using Hartree–Fock–Roothaan calculations

Hartree–Fock–Roothaan methods have often been quite successful in the calculation of properties despite the fact that the variational principle upon which they are based ensures only the best total energy. In particular, other energetic properties such as force constants and charge-distribution properties such as electron-density distributions and electric-field gradients are well reproduced.

Many of the properties described in Chapter 2 can be rather routinely evaluated from ground-state wave functions for the equilibrium geometry. Such properties, P, can be expressed as a sum over molecular orbitals i as:

$$P = \sum_{i=1}^{n} C_{ij} \, C_{ik} \, P_{jk} \tag{3.29}$$

where P_{jk} is the value of the property for the j,k basis-function pair. Charge distribution properties such as electron-density contours (studied by x-ray or neutron diffraction), electron densities at the nucleus (determining Mössbauer isomer shifts), and electric-field gradients at nuclei (determining the nuclear quadrupole interaction seen in NQR or NMR) can be obtained in this way. Other spectral properties can be estimated in terms of their energies using ground-state eigenvalues and in terms of their intensities using ground-state electron distributions. For example, uv absorption spectra can be estimated from ground-state eigenvalues for many materials, although their accurate evaluation requires some approach incorporating changes in relaxation and correlation energy with orbital occupation. Similarly, atomic-orbital character in molecular orbitals can yield estimates of transition intensities. Direct calculations of intensities by perturbation theory, as described later, are necessary for obtaining accurate results but are often very difficult to perform. Vibrational spectra can be obtained from the variation of energy with nuclear coordinates at the energy minimum, requiring only slightly more calculation than the equilibrium geometry alone using present computer algorithms (Hehre et al., 1986).

One set of quantities often evaluated from the ground-state wave function that are *not* quantum-mechanical observables are the various components of the Mulliken population analysis (Mulliken, 1955, 1962). For example, we could define the net Mulliken charge on an atom A as:

$$q_A = Z_A - \sum_{i=1}^{n} \left(\sum_{\substack{j \text{ on} \\ A}} \sum_{\substack{k \text{ on} \\ A}} C_{ij} C_{ik} S_{jk} + \tfrac{1}{2} \sum_{\substack{j \text{ on} \\ A}} \sum_{\substack{l \text{ not} \\ \text{on } A}} C_{ij} C_{il} S_{jl} \right) \tag{3.30}$$

by dividing the charge arising from orbital overlap equally between pairs of atoms. Such a charge partitioning is not unique, and a number of other partitioning schemes have been devised (see discussion in Hehre et al., 1986). In general, comparison of net Mulliken charges between related molecules using comparable basis sets is meaningful. The Mulliken charges are, however, highly basis-set dependent and are by no means theoretically comparable with effective atomic charges determined from x-ray diffraction or other experimental studies. Thus, absolute numerical values of Mulliken charges are essentially meaningless, and we shall not use them within this book.

There are also properties for which the magnitude is dependent upon transition intensity and for which accurate results can be obtained only with perturbation theory; examples occur in currently much studied areas like NMR spectroscopy (described in Chapter 2), but also involve other properties like magnetic susceptibilities and refractive indices, which are not much studied from an electronic structure point of view (although we would argue that, due to advances in theory, such experimental techniques are ripe for further exploration). Within a Hartree–Fock approach the perturbation of a molecule by electric or magnetic fields can be calculated at a number of levels of theory. Coupled Hartree–Fock perturbation theory (Lipscomb, 1966; Ditchfield, 1974), which arrives at a self-consistent molecular energy distribution as a function of field strength, has been applied to some small molecular cluster models of minerals. Calculations based upon equation of motion theory (Oddershede, 1978) have also recently been used (Tossell and Lazzeretti, 1988b).

The interaction of an atom or molecule with radiation, or its collision with a particle, may also be treated using perturbation theory. If we define the Hamiltonian for the system in field-free space as H^O and the total Hamiltonian as:

$$H = H^O + H' \tag{3.31}$$

the H' is the perturbation. The theory may be developed to various orders in a parameter measuring the strength of the perturbation, but the most common approach yields a perturbed energy.

$$E = E^0 + \int \psi^0 H' \psi^0 \, d\tau + \sum_{i \neq 0} \int \frac{\psi^i H' \psi^0}{E^i - E^0} \, d\tau \tag{3.32}$$

where E^0 and ψ^0 are the energy and wave function in the absence of the perturbation and E^i and ψ^i are the energy and wave function for some excited state i. It is clear that application of a radiation field to an atom or molecule gives information on either its ground state [$\int \psi^0 H' \psi^0 \, d\tau$ in Eq. (3.32)] or on both its ground and excited states [the summation in Eq. 3.32)].

Perturbations may be divided into two categories on the basis of whether H and H^0 have a common set of eigenfunctions. If they do, then only the ground-state term on the right-hand side of Eq. (3.32) is nonzero and the perturbation can be evaluated from ψ^0 alone. An example is the case in which H' is the nuclear quadrupole moment. The first-order energy $\int \psi^0 H' \psi^0 \neq 0$ if and only if the electric field has a nonzero gradient at the nucleus of interest. The gradient of the electric field at this point may contain valuable information about the electron-density distribution and/or the spatial arrangement of nuclei. An example of the second type of perturbation is an electromagnetic field, the major effects of which may be described by an electronic dipole operator, er, for which H does not have common eigenfunctions with H^0. By applying such a perturbation to the system, we can study the properties of excited states of the system. In general, the energies of excited states may be described more accurately than the integrals of the perturbation Hamiltonian that determine the spectral intensities.

Information on particle and potential distributions within a system may also be obtained from particle (e.g., photon, electron, or neutron) scattering in which the initial and final energy momenta of the scattered particle are monitored. Such scattering processes may also be treated by perturbation theory. In some scattering arrangements, simple connections may be made between scattering intensities and ground-state properties. The best known example is elastic x-ray scattering, which may be used to study the electron distribution within the system.

3.7. Approximate Hartree–Fock methods

Calculation of the molecular Hamiltonian, the time-consuming step in the Hartree–Fock method, may be greatly simplified by ignoring or approximating either the component integrals making up the Hamiltonian matrix or the Hamiltonian matrix elements themselves. Methods making such approximations are usually designated as "semiempirical" or "approximate" molecular-orbital theories and require much less time than the *ab initio* methods discussed previously in which all integrals are calculated accurately (particularly as the size of the system increases and the number of electron repulsion integrals becomes overwhelming). In general, such methods either try to approximate an *ab initio* Hamiltonian as closely as possible (usually within a minimum basis set) or utilize parameters designed to fit certain types of experimental data for a class of reference molecules as closely as possible. The complete neglect of differential overlap (CNDO) and intermediate neglect of differential overlap (INDO) methods of Pople and Beveridge (1970) are methods in which electron repulsion integrals and some Hamiltonian matrix elements are approximated and the approximate Hartree–Fock equations are solved and iterated to self-consistency, with the goal of matching minimum-basis-set SCF calculations as closely as possible. Unfortunately, such calculations are less reliable than the minimum-basis-set SCF calculations they mimic, particularly for unusual bonding situations (e.g., see Thiel, 1978). Nonetheless, if minimum-basis-set SCF calculations give an acceptable description of a small version of the system and CNDO calculations adequately reproduce the minimum-basis-set SCF results, then CNDO calculations applied to a larger system should be accurate. However, when such methods give surprising results, inconsistent with those for smaller systems or with chemical intuition, it is prudent to doubt them. Lasaga (1982) has shown that it is virtually impossible to parametrize CNDO to reproduce minimum-basis-set SCF results for simple silicate clusters.

An approach in which parameters of the theory are adjusted to match experiment is exemplified by extended Hückel molecular-orbital (EHMO) theory (Hoffman and Lipscomb, 1962; Hoffman, 1963) and by modified INDO (MINDO) theory (Dewar and Thiel, 1977) and its decendents, like AM1 (Dewar et al., 1985). The EHMO theory is very simple, using diagonal matrix elements of the Hamiltonian matrix, H_{ii}, from atomic quantities called *valence-shell ionization energies* (VSIE) and simply setting the off-diagnoal matrix elements H_{ij} proportional to the product of overlap integrals S_{ij} and average diagonal elements. Through the use of VSIE's, relative orbital energies are well reproduced by extended Hückel calculations. In fact, such calculations often reproduce photoemission spectra and other aspects of valence-band structure better than do Hartree–Fock calculations (at the Koopmans'-theory level of approximation) for transition-metal systems. Effects arising from orbital symmetry and overlap are also well described by this method, so that angular properties are often well predicted. Since this method effectively employs a minimum-basis Hartree–Fock approach, it lends itself to simple population analysis in the same way as a minimum-basis-set SCF Hartree–Fock calculation, and this often proves valuable in interpretation. EHMO theory is weak in its prediction of bond distances, which actually depend on rather subtle competition between nuclear–electron attraction, electron–electron repulsion, and kinetic-energy terms, and the absolute values it generates for properties are only qualitatively correct. It is generally used for comparison of properties in related molecules rather than in assessing accurate values of properties for a single molecule.

MINDO is a much more powerful theory when properly parametrized, giving generally better predictions of structures and energies than minimum-basis-set Hartree–Fock calculations. We shall later describe applications of MINDO and similar approaches to borates (Uchida et al., 1985) and to defects in SiO_2 (Edwards and Fowler, 1985). However, some of the claims made for this semiempirical approach have been strongly criticized (e.g., Pople, 1975).

3.8. Hartree–Fock band-structure calculations

Hartree–Fock calculations on molecules commonly exploit the symmetry of the molecular point group to simplify calculations; such studies on perfectly ordered bulk crystalline solids are possible if one exploits the translational symmetry of the crystalline lattice (see Ashcroft and Mermin, 1976) as well as the local symmetry of the unit cell. From orbitals centered on various nuclei within the unit cell of the crystal *Bloch orbitals* are generated, as given by the formula (in one dimension):

$$\psi_{nk}(x) = e^{ikx}\, u_{nk}(x), \tag{3.33}$$

where k is the electron wave vector or crystal momentum and the function $u_{nk}(x)$ has the periodicity of the crystalline Bravais lattice. This allows solution of a Hamiltonian matrix equation of the order of the number of orbitals in the unit cell for each value of k, which is essentially a symmetry index for the infinite group of translation symmetry operations. Nonetheless, construction of this Hamiltonian matrix in an *ab initio* scheme requires consideration of orbitals (and nuclei) outside a single unit cell.

Hartree–Fock band calculations were performed by Euwema *et al.*

(1974) and others in the early 1970s, and extensive methodological studies were carried out in the mid- and late-1970s by a number of workers, but relatively few computations were reported until the method was revived by a group of Italian researchers (Pisani, 1987). We shall briefly mention their recent results for MgO (Causa et al., 1986a,b,c) and will describe in detail their SiO_2 studies (Dovesi et al., 1987). Hartree–Fock band calculations are computationally very demanding because of the enormous number of integrals that must be calculated and processed. An orbital on one atom in a crystal has finite electron repulsion integrals with orbitals on all other atoms, not just those in the same unit cell. Criteria must be carefully chosen for the neglect of integrals of small magnitude with proper consideration for the balancing of nuclear attraction, Coulomb, and exchange electron repulsion. In principle, Hartree–Fock calculations benefit from a sounder, or at least better defined, theoretical foundation than density-functional band methods, allowing more rigorous corrections for correlation. In practice, correlation corrections remain very difficult and have not yet been applied to Hartree–Fock band theory in an *ab initio* manner. The early painstaking work by Surratt et al. (1973) and Euwema et al. (1974) yielded lattice constants for C (diamond) and LiF that were about 1% smaller than experiment, and bulk moduli that were too high by 5–10%. These errors are of the same direction and magnitude as observed for Hartree–Fock calculations on gas molecules. Results for MgO are as good as those from density-functional methods, and the geometry calculated for SiO_2 is similar to that from Hartree–Fock–Roothaan calculations using a similar basis set on free molecules and is in reasonable agreement with experiment.

3.9. Elements of density-functional theory

An alternative to Hartree–Fock theory is density-functional (DF) theory in which certain elements in the Hamiltonian are evaluated at fixed points directly from the electron densities at those points. This can circumvent the need for calculating the enormous numbers of electron–electron repulsion integrals encountered in Hartree–Fock calculations. We here briefly describe density-functional theory based upon reviews by von Barth (1986) and Srivastava and Weaire (1987).

During the 1970s and 1980s, density-functional theory became an important tool for calculating static electronic and structural properties of solids. The theory represents in principle an exact formulation of the many-electron problem in terms of a single particle moving in the mean field of the other electrons. All the difficulties associated with the solution of the many-electron problem are enclosed in this mean field, for which some approximation must be adopted. In practice, most calculations have been carried out using the local-density approximation (LDA), which has proved to be surprisingly accurate. For example, bond distances in solids are predicted with an accuracy of the order of about 0.05 Å, and cohesive energies are accurate to within about 1 eV. In fact, the main problem in obtaining accurate results has not been associated with the LDA itself but with the difficulty of solving the one-particle problem in periodic solids with complicated geometries. Density-functional theory is based on a theorem by Hohenberg and Kohn (1964) that states that a knowledge of the one-particle position space density $\rho(r)$ in the ground state is sufficient to characterize completely a many-electron system. This means that the total ground-state energy is a functional[1] of $\rho(r)$. Hohenberg and Kohn (1964) also proved that this functional is minimized by the true ground-state density. Their proof relied on some assumptions that were later shown to be unnecessary. Generalization to a spin-density-functional theory, necessary for open-shell systems, was suggested in the original paper by Kohn and Sham (1965) and rigorously developed by von Barth and Hedin (1972).

The Hohenberg–Kohn theorem was of great importance for the development of density-functional theory, but a practical implementation of DF theory was first presented by Kohn and Sham (1965). This paper contains two important advances of the theory: (1) the exact conversion of the many-electron problem to an effective one-electron problem, and (2) the local-density approximation.

The conversion to a one-electron problem was achieved by a simple reshuffling of terms in the functional for the total energy normally written as:

$$E[\rho] = T[\rho] + U[\rho] + \int V(r)\rho(r)\, d^3r \tag{3.34}$$

Here, $T[\rho]$ is the total kinetic energy, $U[\rho]$ is the interelectronic Coulomb interaction, and the last term represents the interaction with the external potential $V(r)$. Introducing the kinetic energy $T_0[\rho]$ in the ground state of a fictitious system of noninteracting electrons also having the density $\rho(r)$, we can write:

$$\begin{aligned} E[\rho] = {} & T_0[\rho] + \frac{1}{2}\int\int \rho(r)\frac{1}{r-r'}\rho(r')\, d^3r\, d^3r' + E_{xc}[\rho] \\ & + \int v(r)\rho(r)\, d^3r \end{aligned} \tag{3.35}$$

so that the second term is the classical part of $U[\rho]$ and $E_{xc}[\rho]$ is simply the remainder, that is, what is needed to make the two energy expressions (3.34) and (3.35) equal. The quantity $E_{xc}[\rho]$ is referred to as the *exchange-correlation energy*. It has a kinetic contribution that, however, only originates in exchange and correlation, that is, $T-T_o$, but the dominant electrostatic interaction energy is not included in E_{xc}. The quantity E_{xc} is thus relatively small, and the simplest possible approximation to it, the LDA, gives the major part of it. The small value of E_{xc} is the most important reason for the success of density-functional theory.

As mentioned above, the total energy is minimized by the true density, and by rewriting $E[\rho]$ as in Eq. (3.35) the stationary property of $E[\rho]$ leads to the following equation:

$$\frac{\delta T_o}{\delta\rho(r)} + V_{\text{eff}}(r) = \mu \tag{3.36}$$

Here,

$$V_{\text{eff}}(r) = V(r) + \int \frac{1}{r-r'}\,\rho(r')\,d^3r' + V_{\text{xc}}(r) \tag{3.37}$$

and the exchange-correlation potential $V_{\text{xc}}(r)$ is obtained as the functional derivative of E_{xc} with respect to the density,

$$V_{\text{xc}}(r) = \frac{\delta E_{\text{xc}}}{\delta\rho(r)} \tag{3.38}$$

The constant μ, the chemical potential, is a Lagrange parameter that is introduced to ensure proper normalization, as in Hartree–Fock theory. At this stage, Kohn and Sham noted that Eq. (3.36) is the Euler equation for noninteracting electrons in the external potential V_{eff}. Thus, finding the total energy and the density of the system of electrons subject to the external potential V is equivalent to finding these quantities for a noninteracting system in the potential V_{eff}. Such a problem can in principle be solved exactly, but we have to know E_{xc} and the potential V_{xc}.

The one-particle problem can be solved as:

$$[-\tfrac{1}{2}\nabla^2 + V_{\text{eff}}(r)]\,\Phi_k(r) = \varepsilon_k\Phi(r) \tag{3.39}$$

with

$$\rho(r) = \sum_{e_k<\mu} |\Phi_k(r)|^2 \tag{3.40}$$

From the solution of these Kohn–Sham equations, we can evaluate the noninteracting kinetic energy T_0 needed in Eq. (3.34) for obtaining the total energy of the interacting system. The resulting density can then be used to obtain V_{eff}. Consequently, the many-electron problem has been reduced to a one-electron problem with self-consistency required. At this point, the theory outlined is an exact theory for obtaining the ground-state energy and the electron density. Exact excitation energies are, in principle, beyond the reach of the theory except in special cases, but this fact does not prevent us from obtaining approximate and sometimes rather accurate excitation energies.[2]

Since E_{xc} is unknown, it is fortunate that the simplest approximation to it, the local-density approximation, works quite well. The basic idea of the LDA is to view the inhomogeneous system as being made up of volumes so small that each can be considered to contain a homogeneous electron gas having a density equal to the local density of that volume. The total exchange-correlation energy is then the sum of the contributions from all these quasihomogeneous volumes:

$$E_{xc}[\rho] = \int \rho(r)\varepsilon_{xc}(\rho(r))\, d^3r \tag{3.41}$$

Here, $\varepsilon_{xc}(\rho)$ is the exchange-correlation energy per particle of a homogeneous but interacting electron gas of density ρ. Consequently, the LDA is defined in terms of formally exact but imprecisely known properties of the homogeneous electron gas. In applications of density-functional theory, a number of different electron-gas potentials are used, one of the most prominent being the Hedin and Lundquist (1971) potential. In all such calculations, the local-density approximation has been employed, and the different potentials normally have a negligible effect on the results. Knowledge of electron-gas energies has greatly improved lately, and it is generally believed that the data of Ceperley and Alder (1980) fitted by Perdew and Zunger (1981) are close to the exact results, and that their results should be used in the implementation of the LDA in density-functional theory.

One of the earliest representations of the exchange-correlation potential was given by Slater (1951, 1974) as:

$$V_{X\alpha} = -6\alpha\left(\frac{3}{4\pi}\rho\right)^{1/3} \tag{3.42}$$

In most formulations α is treated as essentially an atomic parameter that is chosen to give a local density or $X\alpha$ total energy identical to the Hartree–Fock value for each atom of the molecule (Schwarz, 1972, 1974), although other criteria for choice of α have been considered (Smith and Sabin, 1978). The value of α obtained by matching to atomic Hartree–Fock energies is around 0.7 for all atoms, and small variations in α cause little change in properties.

Calculation of the potential without further approximation within the LDA scheme is somewhat complex for molecules, and a number of schemes have been developed (e.g., Baerends et al., 1973; Sambe and Felton, 1975). The need for careful numerical procedures has been documented by Dunlap et al. (1979a). Equilibrium bond distance and bond dissociation from the various $X\alpha$ schemes (referred to as LCAO-$X\alpha$, LMTO-$X\alpha$, DV-$X\alpha$) compare with experiment almost as well as do Hartree–Fock calculations for first-row diatomic molecules (Table 3.6). It appears that the $X\alpha$ bond distances are less stable than the Hartree–Fock (compared to experiment) and have a slightly larger average error. Few geometrical optimizations have been done within the $X\alpha$ scheme for polyatomic molecules, due to the absence of methods for analytically calculating the derivatives of energy with respect to nuclear coordinates. The recent development of an analytical gradient procedure within the

Table 3.6. Comparison of the results of various types of (local) density-functional calculations (LCAO-$X\alpha$, LMTO-$X\alpha$, DV-$X\alpha$) with *ab initio* SCF Hartree–Fock and multiple-scattering $X\alpha$ calculations (using overlapping spheres, OS) and experimental data (expt.) for equilibrium bond distance [$R_e(a_0)$] and bond dissociation energy (D_e in eV) in the nitrogen molecule (N_2)

N_2	expt.[a]	HF[b]	LCAO-$X\alpha$[c]	LMTO-$X\alpha$[d]	DV-$X\alpha$[e]	MS-SCF-$X\alpha$[f] (OS)
$R_e(a_0)$	2.07	2.01	2.08	2.16	2.11	2.4
D_e(eV)	9.90	5.3	9.2	7.8	8.4	—

[a] Hubner (1972).

[b] Cade et al. (1966).

[c] Dunlap et al. (1979b).

[d] Gunnarrson et al. (1977).

[e] Heijser et al. (1976).

[f] Salahub et al. (1976).

DVM-$X\alpha$ approach (Versluis and Ziegler, 1988) promises greatly to expand the use of $X\alpha$ calculations for molecular geometry optimizations. For H_2O and NH_3, $X\alpha$ calculations with small orbital bases (Kitaura *et al.*, 1979) and with larger bases (Müller et al., 1983) give results in as good agreement with experiment as does the Hartree–Fock approach (Table 3.7). An advantage of the local-density-functional approach is that it is easily extended to heavier atoms. For example, spin-polarized LDF theory accurately predicts bond distances and energies for Cr_2 and Mo_2 (Delley et al., 1983; Bernholc and Holzwarth, 1983), which are very difficult to describe using Hartree–Fock methods, even with configuration interaction (Goodgame and Goddard, 1982).

Table 3.7. Calculated equilibrium structural properties of H_2O and NH_3 [bond lengths, R(O–H) and R(N–H) in Å, bond angles ∢H–O–H and ∢H–N–H in degrees] obtained using density-functional theory (local-density approximation, LCAO-$X\alpha$ method) and Hartree–Fock–Roothaan theory, compared with experimental data

	Density-functional theory (LCAO-$X\alpha$ method)		Hartree–Fock theory	
	Small basis set	Large basis set	Large basis set	Experimental value
H_2O R(O–H) (Å)	0.979	0.974	0.941	0.957
∢H–O–H (deg)	111	106	111	104.7
NH_3 R(N–H) (Å)	1.021	1.027	0.989	1.013
∢H–N–H (deg)	1.06	108	105	106.7

Source: After Kitaura et al., 1979; Muller et al., 1983; see text for other data sources.

3.10. The multiple-scattering or scattered-wave X-α method

Although local-density-approximation schemes utilizing expansion basis sets give accurate structures and energetics for both solids and molecules, further simplification of the potential to "muffin-tin" form (see below), as in the MS-$X\alpha$ method (Johnson, 1973), gives much poorer results for such properties. Through the use of overlapping atomic spheres (Rosch et al., 1973) one can obtain bond distances in modest agreement with experiment if there is not great ambiguity in the choice of atomic sphere radius (Salahub et al., 1976). Even calculated angular properties show qualitative agreement with experiment if overlapping atomic spheres and interstitial spheres (to reduce the volume of the interatomic region) are used (Weber and Geoffrey, 1979). However, it is apparent that the MS-$X\alpha$ method is not the most appropriate if equilibrium geometries are the primary focus of the study.

However, the multiple-scattering or scattered-wave (SW)-$X\alpha$ method has given accurate results for many spectral properties of both molecules and molecular cluster models for solids. Results for mineral systems have been reviewed by Tossell and Gibbs (1977b). More general reviews have been provided by Johnson (1975) and Case (1982). Although more accurate schemes, such as the discrete variation method $X\alpha$ (DVM-$X\alpha$; Baerends et al., 1973) are being increasingly applied to mineral systems, most of the spectral results for oxide and sulfide minerals presented in later chapters were obtained with the MS-$X\alpha$ method. This method has also recently been extended to the calculation of photoionization and x-ray absorption spectra (Dill and Dehmer, 1974; Kutzler et al., 1980), which requires the solution of an electron–molecule scattering problem and remains the only practical method for solving such scattering problems for complex molecules.

In the MS-$X\alpha$ method, the exchange correlation potential produced is approximated by the Slater, $X\alpha$ potential [Eq. (3.42)]. The easier Coulomb terms are obtained from electrostatics. Once the quantum-mechanical potential has been obtained, it is simplified to facilitate the solution of Schrödinger's equation. The molecular cluster is first divided into regions by surrounding each nucleus with an atomic sphere and the entire cluster with an outer sphere. Anionic clusters are neutralized by enclosing them in a uniformly charged positive sphere (the *Watson sphere*). The atomic sphere radii chosen are usually similar to the covalent radii of the atoms. The radii chosen will have a moderate impact on the results (Norman, 1976). Atomic regions, an interatomic region, and an outer-sphere region are thus defined. The potential in the atomic and outer-sphere regions is then spherically averaged, and the potential in the interatomic region volume averaged. The resultant potential has what is called a "muffin-tin" form. With this form for the potential, one can obtain solutions of the one-electron Schrödinger equations in each of the three spatial regions, the solutions being expressed in the form of radial functions times spherical harmonics of the angles. The equations to be solved depend implicitly upon the orbital energy ε_i, and solutions can be obtained for any ε_i. By setting boundary conditions that require the orbitals and their first derivatives to be continuous across the boundaries of the regions, one can generate a secular equation constraining the expansion coefficients for the solutions in the various regions. This equation can be solved to yield the orbital eigenvalue and expansion coefficients. This continuity requirement constitutes the scattered-wave component of the method. From the one-electron orbitals obtained (and their assumed occupations), a new charge distribution is generated, and from it, a new potential. This process is continued until self-consistency is obtained. One then has a set of one-electron orbitals describing the electronic structure of the material, with which one can interpret spectral data and the nature of the bonding. One-electron energies, total energies, and electron-density distributions may all be evaluated from this orbital set. To obtain accurate absolute binding energies or orbitals, the transition-state approach described below must be used.

Since the MS-SCF-$X\alpha$ eigenvalue is a partial derviative of the total energy with respect to occupation number,

$$\varepsilon_{iX\alpha} = \frac{\partial \langle E_{X\alpha} \rangle}{\partial_{n_i}} \tag{3.43}$$

it does not satisfy Koopmans' Theorem. If the total energy is expanded as a Taylor series in the occupation numbers, direct calculation shows that all terms beyond the second-order term are small. The ionization energy of an electron can then be expanded in a Taylor series and, if one defines a transition state (TS) midway between the initial and final states (with $n_i = n_{i_0} - \frac{1}{2}$), then $\Delta E = |\partial \langle E \rangle / \partial n_i|_{\mathrm{TS}}$ + third-order terms. Thus, the eigenvalue difference for this transition state accurately approximates the energy difference. In practice, the eigenvalue differences are sometimes only weakly dependent on occupation number.

The MS-$X\alpha$ method has been very successful for the calculation of ionization energies for both gas-phase molecules and molecular cluster models of solids. DeAlti et al. (1982) have employed both the MS-$X\alpha$ method and the LCAO-$X\alpha$ scheme of Sambe and Felton (1975) in the transition-state procedure for calculating ionization potentials for a number of molecules where the Koopmans approximation within Hartree–Fock theory gives the wrong ordering. They found that the LCAO-$X\alpha$ ionization potentials were more accurate than the Hartree–Fock Koopmans values, while the MS-$X\alpha$ results typically showed errors of one or two electron volts. Representative results are given for ozone (O_3) in Table 3.8.

Table 3.8. Calculated ionization potentials of ozone (O_3) obtained using MS-SCF-$X\alpha$, LCAO-$X\alpha$, and Hartree–Fock calculations

Molecular orbital	Experimental value	Calculated values				
		MS-SCF-$X\alpha$[a]		LCAO-$X\alpha$ method	Hartree–Fock method	Hartree–Fock + MBPT
		TS	OS			
$4a_1$	12.7	15.0	13.2	11.9	15.8	12.9
$3b_2$	13.0	14.6	13.2	12.2	16.3	13.3
$1a_2$	13.6	15.0	13.6	12.6	14.0	14.1
$2b_2$, $1b_1$, $3a_1$	20.0	20.0–20.7	19.4–20.7	18.2–18.9	21.9–23.3	19.4

[a] Results for touching sphere (TS) and overlapping sphere (OS) calculations.

3.11. Density-functional band theory

The local-density-approximation scheme may also be easily applied to calculations of the structural properties of solids using band theory. For example, an *ab initio* LDA pseudopotential method (discussed in the following) has been used to obtain lattice constants, cohesive energies, and bulk moduli of diamond structure C, Si, and Ge that are in very good agreement with experiment, as shown in Table 3.9 (Cohen, 1984). LDA band calculations may also be extended to the solid phases of heavier elements using the more approximate augmented-plane-wave (APW) method. Studies on the transition metals (Moruzzi et al., 1977) accurately reproduce trends in lattice constants, cohesive energies, and bulk moduli. Extension to simple solid compounds is also possible if the number of atoms in the unit cell is not too large. For example, LDA calculations on solid BeO correctly predict it to be most stable in a wurtzite-type structure and give accurate structural and energetic properties (Chang and Cohen, 1984) for the atmospheric-pressure structure.

There are a number of band-structure methods that make varying approximations in the solution of the Kohn–Sham equations. They are described in detail by Godwal et al. (1983) and Srivastava and Weaire (1987), and we shall discuss them only briefly. For each method, one must construct Bloch functions delocalized by symmetry over all the unit cells of the solid. The methods may be conveniently divided into: (1) pesudopotential methods, (2) linear combination of atomic orbital (LCAO) methods; (3) muffin-tin methods, and (4) linear band-structure methods. The pseudopotential method is described in detail by Yin and Cohen (1982); the linear muffin-tin orbital method (LMTO) is described by Skriver (1984); the most advanced of the linear methods, the full-potential linearized augmented-plane-wave (FLAPW) method, is described by Jansen

Table 3.9. Static structural properties for C, Si, and Ge obtained from the *ab initio* pseudopotential calculations of density-functional band theory compared with experiment

	Lattice constant (Å)	Cohesive energy (eV)	Bulk modulus (Mbar)
C: calc.	3.60	7.57	4.41
expt.	3.57	7.37	4.43
Si: calc.	5.45	4.67	0.98
expt.	5.43	4.63	0.99
Ge: calc.	5.66	4.02	0.73
expt.	5.65	3.85	0.77

Source: Cohen, 1984

and Freeman (1984); and the most accurate *ab initio* form of the LCAO method (within the LDA formalism) is described by Chelikowsky and Louie (1984).

The most difficult problems in solving the Kohn–Sham equations for solids arise from three sources: (1) the different rate of variation of the electron wave function in different regions of space; (2) the complicated angular variation of the potential about the nuclear centers; and (3) the energy dependence of the radial wave functions near the nuclei. Point (1) means that, although electron orbitals far from the nuclear centers can be well described by a modest number of plane waves, the core electrons and localized valence electrons must either be described by nuclear-centered functions expressed as localized radial functions multiplied by spherical harmonics, or must be omitted from the calculation. If omitted from the calculation, their effect upon the valence orbitals must be properly accounted for by subjecting the valence orbitals to a fictitious potential or "pseudopotential." If the more localized electrons are represented by basis functions, these must have adequate flexibility, and, if mixed sets of basis functions are used, they must connect continuously throughout space. Point (2) demands that one either make a shape approximation to the potential, for example retaining only its spherically symmetric component, or face the prospect of solving a much more complicated matrix equation for the orbital coefficients. Point (3) requires that the radial wave functions be treated as implicitly dependent upon the energy, considerably complicating the solution of the radial equations, or that some "linearization" of the radial wave functions be carried out, simplifying their energy dependence.

In the pseudopotential method, core states are omitted from explicit consideration, a plane-wave basis is used, and no shape approximations are made to the potentials. This method works well for complex solids of arbitrary structure (i.e., not necessarily close-packed) so long as an adequate division exists between localized core states and delocalized valence states and the properties to be studied do not depend upon the details of the core electron densities. For materials such as ZnO, and presumably other transition-metal oxides, the $3d$ orbitals are difficult to accommodate since they are neither completely localized nor delocalized. For example, Chelikowsky (1977) obtained accurate results for the O $2s$ and O $2p$ part of the ZnO band structure but treated the Zn $3d$ orbitals as a core, thus ignoring the Zn $3d$ participation at the top of the valence region found in MS-SCF-$X\alpha$ cluster calculations (Tossell, 1977) and, subsequently, in energy-dependent photoemission experiments (Disziulis et al., 1988).

The LCAO methods can treat all electrons and need not make shape approximations to the potential. However, as for Hartree–Fock band calculations, there is a very large number of electron–electron repulsion integrals, and care must be taken in truncating their sums. A number of different types of LCAO basis functions are possible, but their number must be fairly strictly controlled, with most calculations employing what are essentially minimum basis sets. Since the potential must be expanded over the basis at each iteration, it is common for such calculations to not fully iterate to self-consistency in the electron distribution, often constructing the potential from superimposed free-atom densities. The strengths of these methods lie in their generation of approximate electronic structures for complex materials containing heavy atoms, and in their ease of qualitative interpretation within an LCAO approach. Their weakness is in their computational difficulty, which generally forces the use of small bases and assumed charge distributions. Several LCAO studies of transition-metal oxides and sulfides will be described in later chapters, including work by Bullett (1980, 1987). It should be noted that the LCAO method is also well known as the "tight-binding method" and has a long history as an approximate method in which the atomic-orbital matrix elements of the Hamiltonian are approximated or estimated from atomic data. The simplest such approach is that of extended Hückel band theory (Burdett, 1984). This approach requires proper empirical input in order to reproduce relative atomic-orbital energies, and relies upon simple symmetry and overlap effects to explain qualitative features of electron distributions and geometries. Some examples of such calculations will be considered later.

In "muffin-tin" methods such as the augmented-plane-wave and Korringa–Kohn–Rostoker (KKR) methods, the electronic charge density is spherically averaged within spheres centered on the nuclei, and volume averaged in the interatomic region, much as in the MS-SCF-$X\alpha$ molecular method. Full energy dependence in the nuclear-centered basis functions is maintained, and the charge density is iterated to self-consistency. Such methods work well for close-packed high-symmetry solids, for which the shape approximations to the potential do not introduce serious error. In the discussion of transition-metal oxides, we will describe KKR calculations of equilibrium geometries and cohesive energies (after Yamashita and Asano, 1983a,b).

Finally, an important advance was made through the development of "linear" band-structure methods, starting with the work of Andersen (1975). The idea is to approximate energy-dependent basis functions as a linear combination of solutions to the radial Schrödinger equation inside the muffin-tin spheres and their energy derivatives at some carefully chosen fixed energy. The secular matrix equations then become linear in energy, and the computation is reduced by one or two orders of magnitude with little loss of accuracy. This advance has been developed in two directions, the linear muffin-tin orbital method, which has been widely and generally applied to many materials because of its lower computer cost (Skriver, 1984), and the full-potential linearized augmented-plane-wave method (Jansen and Freeman, 1984), which retains the full nonspherical potential within the "muffin tins." The FLAPW method is still very computationally demanding, and, aside from its initial test applications, it has been most commonly applied to problems at the forefront of solid-state physics, such as high-temperature superconductors or the structure of surfaces. Preliminary results have been presented for FeO (Mehl et al., 1987) and will be discussed along with the transition-metal oxides in Chapter 4. Results for metallic Fe obtained using a number of different methods (some of which have not been discussed) are summarized in Table 3.10 (Hathaway et al., 1985). Results of the different methods are very similar for this close-packed material and are in reasonably good agreement with experiment.

Although local-density-approximation results for equilibrium structures and other related properties such as phonon frequencies are in quite good agreement with experiment, it is well known that band gaps estimated from LDA ground-state eigenvalues are much lower than experimental values. Several groups are exploring corrections to the LDA in order to remove this difficulty (Perdew and Zunger, 1981; Pickett and Wang, 1984; Hybertsen and Louie, 1987). However, no feasible scheme for general application to complex materials has yet appeared.

Note that, in the above discussion, we have neglected methods that generate band structures from empirical data. Most band calculations before the 1970s were of this type. The considerable contributions to knowledge made through use of the empirical pseudopotential approach, for example, have been discussed by Cohen (1979). Such approaches have

Table 3.10. Comparison with experimental values of calculated properties for Fe obtained by different density-functional band-theory methods

	Lattice constant (a_0)	**Bulk modulus (Mbar)**	**Magnetic moment (μ_B)**	**Cohesive energy (eV)**
FLAPW (vBH)[a]	5.225 ± 0.005	2.5 ± 0.4	2.06 ± 0.01	6.56 ± 0.03
FLAPW (VWN)[a]	5.21	2.72	2.18	
FLAPW (KSG)[a]	5.35	1.90	2.29	
LMTO	5.30	2.43	2.16	6.38
Pseudopotential	5.17	2.00	1.72	
ASW[b]	5.33	2.1	2.18	6.11
KKR	5.27	2.17	2.15	6.26
KKR ASA[c]	5.28	2.60	2.17	
Experimental values	5.41	1.68–1.73	2.12	4.28

[a] Various forms of electron gas-potential (see Hathaway et al., 1985, for details).

[b] Augmented-spherical-wave method.

[c] Atomic sphere approximation (ASA) of the KKR method.

Source: From Hathaway et al., 1985; see text and Appendix C for information on methods.

now been superseded by *ab initio* band-structure methods, which yield the quantitative data of most value to earth and mineral scientists.

3.12. Theoretical ionic models—the modified electron-gas approach

Although the ionic model of solids has long been used in a qualitative form or as a parametric theory in which ion–ion repulsive parameters are fitted to experimental data (Tosi, 1964), such fitting procedures inevitably incorporate covalency effects, if such exist, through empirical parametrization. Thus, they do not provide a test of the ionic model per se (Gaffney and Ahrens, 1970). In the 1970s a model was developed by Gordon and co-workers (Gordon and Kim, 1972) in which the total energy of the crystal was calculated directly from an ionic-limit charge density, thus providing a much better test of the ionic model.

The details of the modified electron-gas (MEG) ionic model method have been fully described by Gordon and Kim (1972). The fundamental assumptions of the method are: (1) the total electron density at each point is simply the sum of the free-ion densities, with no rearangements or distortion taking place; (2) ion–ion interactions are calculated using Coulomb's law, and the free-electron gas approximation is employed to evaluate the electronic kinetic, exchange, and correlation energies; (3) the free ions are described by wave functions of Hartree–Fock accuracy. Note that this method does not iterate to a self-consistent electron density.

The Coulombic part of the interaction energy between ions a and b is given by the expression:

$$\begin{aligned} V_{\text{Coul}} = \frac{Z_a Z_b}{R} + \int\!\!\int \frac{\rho_a(r_1)\,\rho_b\,(r_2)}{r_{12}}\,dr_1\,dr_2 \\ -Z_b \int \frac{\rho_a(r_1)}{r_{1b}}\,dr_1 - Z_a \int \frac{\rho_b(r_2)}{r_{2a}}\,dr_2 \end{aligned} \qquad (3.44)$$

where Z_a and Z_b are nuclear charges, R the internuclear distance, r_{12} the separation of electrons 1 and 2, r_{1b} the separation of electron 1 and nucleus b, and $\rho_a(r_1)$ the electron density arising from ion a evaluated at a distance of r_1 from the nucleus of a. The Hartree–Fock portion of the energy density of an electron gas is given by:

$$E_{\text{HF}}(\rho) = \frac{3}{10}\,(3\pi^2)^{2/3}\,\rho^{2/3} - \frac{3}{4}\left(\frac{3}{\pi}\right)^{1/3}\rho^{1/3} \qquad (3.45)$$

where the terms represent kinetic energy and exchange energy, respectively. The energy arising from the correlation of electron motions is then added, using a form described by Gordon and Kim (1972). If we then define the total energy-density functional for an electron gas as:

$$E_{\mathrm{G}}(\rho) = E_{\mathrm{HF}}(\rho) + E_{\mathrm{corr}}(\rho) \tag{3.46}$$

the contribution of this term to the interaction energy becomes:

$$\begin{aligned} V_{\mathrm{G}} = \int dr\, \{[\rho_a(r_a) + \rho_b(r_b)]E_{\mathrm{G}}(\rho_a + \rho_b) \\ - \rho_a(r)E_{\mathrm{G}}(\rho_a) - \rho_b(r_b)E_{\mathrm{G}}(\rho_b)\} \end{aligned} \tag{3.47}$$

The total interaction energy is just the sum of V_{Coul} and V_{G}.

Once the ion–ion interaction energy has been calculated, it can be partitioned into the sum of a long-range point-charge Coulombic term and a short-range ion-pair repulsion term. The sum of the point-charge Coulombic terms for an entire solid may be obtained simply from the nearest-neighbor distance and the Madelung constant. The total lattice energy is then given by this Madelung energy plus the sum of the short-range ion-pair repulsions. Generally, short-range repulsions between cation pairs are small enough to be neglected, and cation–anion and anion–anion repulsions need to be included only out to second-nearest neighbors (Cohen and Gordon, 1976). For example, the total lattice energy of MgO in the NaCl (or *B*1) structure is given accurately by the sum of the Madelung energy, six times the $Mg^{2+} - O^{2-}$ short-range pair repulsion energy, six times the $O^{2-} - O^{2-}$ short-range repulsion, and eight times the short-range repulsion of Mg^{2+} and O^{2-} second-nearest neighbors. Thus, the total lattice energy is constructed as a sum of pairwise interaction energies.

Since its original formulation, the MEG method has been improved and has been extensively applied within solid-state physics (Mackrodt and Steward, 1979; Boyer, 1981), gas-phase inorganic chemistry (Tossell, 1979, 1981), mineralogy (Tossell, 1980b,c), and geophysics (Cohen et al., 1987, and references therein). Representative results for a number of gas-phase fluorides from Tossell (1979) are shown in Table 3.11 and for metal oxides (Mackrodt and Stewart, 1979) in Table 3.12. Although there have been some improvements in the form of the electron-gas energy functional, the most important improvements for oxides and sulfides have been in the evaluation of the ion densities. These developments have been reviewed by Cohen et al. (1987). Paschalis and Weiss (1969) showed that properties of anions were strongly dependent on the incorporation of the stabilizing effects of nearby cations. Cohen and Gordon (1976) studied oxides using an O^{2-} wave function stabilized by a fixed-radius sphere of positive charge, resulting in a stabilized rigid-ion model. Muhlhausen and Gordon (1981) introduced a self-consistency requirement on this stabilizing potential by requiring it to match the Madelung potential at the site. In a later version of this approach, often designated the shell-stabilized

Table 3.11. Values of bond distances (in Å) calculated (R_{calc}) using the modified electron-gas (MEG) method compared with experimental values (R_{exp}) and showing errors in calculated values (ΔR) for gas-phase halides

Compound	R_{calc}	R_{expt}	ΔR
BeF_2	1.36	1.40	−0.04
$BeCl_2$	1.83	1.75	0.08
BF_3	1.32	1.31	0.01
BCl_3	1.80	1.74	0.06
CF_4	1.33	1.32	0.01
CCl_4	1.80	1.77	0.03
MgF_2	1.70	1.77	−0.07
$MgCl_2$	2.15	2.18	−0.03
AlF_3	1.60	1.63	−0.03
$AlCl_3$	2.05	2.06	−0.01
SiF_4	1.53	1.56	−0.03
$SiCl_4$	1.99	2.02	−0.03
CaF_2	1.94	2.10	−0.16
$CaCl_2$	2.35	2.51	−0.16
TiF_4	1.72	1.70	0.02
$TiCl_4$	2.14	2.18	−0.04
MnF_2	1.94	1.73	0.21
$MnCl_2$	2.37	2.21	0.16
CuF	2.17	1.74	0.43
CuCl	2.60	2.16	0.44
ZnF_2	1.94	1.81	0.13
$ZnCl_2$	2.38	2.05	0.33

Source: After Tossell, 1979.

(SS) MEG, the energy of the component ions was corrected for the stabilizing effect (Hemley and Gordon, 1985). Finally, in an approach designated potential-induced breathing (PIB), Mehl *et al.* (1986) explicitly included the dependence of the ion self-energy and the ion–ion interaction energy on the Madelung site potential in the total-energy expression. A dramatic effect of this coupling of ion–ion interaction and site potential was an improvement in the elastic constants for oxides such as MgO. In particular, the Cauchy equality $C_{12} = C_{44}$ that held in all rigid-ion calculations but that was violated experimentally by about a factor of 2 was

Table 3.12. Calculated lattice energies (W_L) and lattice parameters (a_o) obtained for a range of metal oxides using the modified electron-gas approach, compared with experimental values

Oxide phase	W_L(eV)		a_0(Å)	
	Calculation	Experiment	Calculation	Experiment
Li_2O	−31.6	−30.1	2.30	2.31
BeO	−40.4	−46.9, −47.7	2.72	2.70
MgO	−40.75	−40.8, −40.4	2.18	2.11
α-Al_2O_3	−161.9	−160.4	13.2	13.0
CaO	−36.0	−37.0, −36.1	2.46	2.41
TiO_2	−122.4	−126.0	4.59	—
MnO	−37.49	−39.54	2.36	2.22
α-Fe_2O_3	−148.7	−156.3	14.3	13.7
Ga_2O_3	−149.7	−157.4, −161.8	14.3	13.4
SrO	−33.9	−34.3, −33.9	2.62	2.58
CdO	−34.7	−40.2	2.58	2.35
SnO_2	−113.6	−123.0, −177.8	4.87	4.74
BaO	−32.0	−32.4, −31.9	2.78	2.76
CeO_2	−107.7	−107.2	2.72	2.71
PbO_2	−109.7	−121.8, −119.9	5.05	4.95
ThO_2	−101.5	−103.0, −104.7	2.87	2.80
UO_2	−102.4	−106.7	2.84	2.73
$CaTiO_3$	−159.1	−161.9	3.90	3.84
BaTiO	−154.5	−158.2	4.04	4.01
$MgAl_2O_4$	−203.6	−200.7	4.12	4.04

Source: From Mackrodt and Stewart, 1979.

also violated to the proper degree in the PIB model calculations. Both the shell-stabilized MEG and the PIB models have since been used to evaluate the equilibrium structures and elastic properties of many oxides and silicates, and numerous applications of these methods will be discussed in later chapters.

The MEG method seems to be of considerable general utility even for compounds in which one would expect considerable covalency, so long as the structure is relatively compact and does not involve important angular variables. For example, the geometries of main-group sulfides and nitrides are predicted fairly accurately by this method (Muhlhausen and

Gordon, 1981). However, for Si oxides the SS-MEG method yields Si–O–Si angles that are too large. Models incorporating oxygen polarization are currently being developed to deal with such deficiencies (Jackson and Gibbs, 1988).

This method has a number of powerful features. First, it is very fast. Thus, one can calculate many structures and also study the effects of pressure and temperature upon the structures. Structures of low symmetry can be considered if covalency effects are small, so as to obtain a full set of elastic constants. Indeed, the most important applications of this method within geophysics have been in evaluating equations of state (volume as function of pressure and/or temperature) and elastic constants that can be related to seismic velocities.

3.13. Simulation methods

In addition to the quantum-mechanical studies using the ionic model charge distributions we have described in Section 3.12, there have been a number of illuminating studies of minerals and other condensed-phase systems employing techniques in which interatomic or interionic interaction potentials are "simulated." Such potentials may be obtained by fitting calculated quantities to experiment without any explicit consideration of quantum-mechanical calculations. Since the pioneering work of Rahman utilizing molecular dynamics and Metropolis developing the Monte Carlo method, enormous advances have been made in numerical methods, computer architecture, and in the construction of realistic pair potentials. Results of such studies have recently been reviewed by Woodcock (1975), Catlow and Mackrodt (1982), Klein (1985), and Matsui and Kawamura (1984). Such studies have related bulk properties to their atomistic details in a way that is extremely difficult to do experimentally. Nonetheless, as Klein (1985) has noted:

> [C]omputer studies on "real" systems, be they solid or liquid, have much in common with the modeling of the economy or the weather . . . although in principle one can now obtain exact numerical results, we cannot thereby evade the question of how faithfully the model mimics reality.

In this section, we will briefly describe the static and dynamic simulation methods and then give some results for the liquid of greatest geochemical importance: water. Applications of such methods to mineral structures will be discussed in later chapters.

Static simulations are generally based on an energy minimization procedure; that is, the energy of the system is written as a function of structural variables that include atomic coordinates and cell dimensions. The energy is generally described as a function of interatomic or interionic pair potentials, giving an equation of the form:

$$E = \sum_{i>j}\sum V_{ij}(r_{ij}) \tag{3.48}$$

where V_{ij} is an analytical or numerical function of the distance r_{ij} between particles i and j. More recent approaches to partially covalent materials such as SiO_2 have utilized angle-dependent or "three-body" terms as well (i.e., V_{ijk}), with a significant improvement in accuracy of description, but a concomitant increase in the difficulty of the calculation (Catlow et al., 1985).

The interparticle potential is generally written as the sum of a Coulombic interaction, a short-range repulsion of exponential or inverse power form, and sometimes an attractive short-range term arising from dispersion or covalence. Parameters in the interparticle potentials may be determined by fitting to the properties of known systems or by theoretical methods. Empirical fitted potentials have the weakness of relying on the validity of the fitted potential terms, even when the interparticle spacings are different from those in the systems used for parametrization. In addition, a potential parametrized to reproduce accurately one experimental property may well give a poor description of other properties. Having established the functional dependence of E on the interparticle distances, we can proceed to minimize E with respect to some or all of the structural variables in a static simulation. Considerable care must be taken in this step, and the particular method chosen may depend upon the size of the minimization problem. Dynamic simulation methods employ either a Monte Carlo or a molecular-dynamics approach (Berry et al., 1980, pp. 846–51). In the Monte Carlo approach, a given number of particles N is confined at a fixed volume V (often a cubic box) at a temperature T. The particles interact by a potential V_{ij} and periodic boundary conditions are used to simulate an infinite system. An initial configuration for the particles is chosen, and they are then moved either sequentially or at random. If a move lowers the total energy of the system, it is accepted, and the resulting configuration is allowed to contribute to the average energy and other thermodynamic quantities. However, a particle move that raises the energy is only accepted with a probability proportional to its Boltzmann weight. After a sufficient number of configurations have been sampled, the average value of the energy stabilizes at the appropriate value. Fluctuations about this average provide information on specific heat and elastic constants, but no detailed information on particle motion is obtained. In molecular-dynamics simulation, Newton's second law of motion is solved:

$$m_i\ddot{r}_i = -\frac{\partial}{\partial r_i}\sum_{i>j}\sum V_{ij} \tag{3.49}$$

by numerical integration, starting from a fixed configuration of particles within a set of periodic boundary conditions. If the integrations are carried out with a sufficiently small time step, the total energy E is conserved as the system evolves in time to reach an equilibrium condition. The advantage of the molecular-dynamics approach is that one can study properties such as self-diffusion coefficients and correlation functions. The first molecular-dynamics calculations were done for a microcanonical (constant N, E, V) ensemble, but procedures have since been developed to perform calculations at constant temperature and/or pressure and to allow changes in the shape of the periodic cell.

Water has been the subject of many simulations, some relying upon quantum-chemical potentials and others upon empirical potentials. The first simulations were of the properties of bulk liquid water, with attention focused upon the structural features present in the x-ray radial distribution functions. Contemporary simulations also yield accurate values for structural properties such as density and thermodynamic properties such as heat of vaporization and specific heat at constant pressure. Although present empirical potentials provide a good description of water monomers and dimers, the description is by no means exact. Since the pair potential models used must in some way mimic the many-body forces existing in bulk liquid water, they do not provide exact results for oligomers with different mixes of two-body and many-body forces. Although most such simulations solve purely classical equations of motion, it has been shown that quantum-mechanical effects significantly influence some fundamental observables, such as the atom–atom radial distribution functions, leading to a general smoothing of the structure appearing in the classical simulation (Kuharski and Rossky, 1984).

Classical simulations have also been applied to various phases of ice (Tse et al., 1984), resulting in good descriptions of the vibrational frequency spectra of several forms of proton-ordered ice. Studies have also recently appeared on the dynamics of melting of ice using molecular-dynamics techniques (Weber and Stillinger, 1983). A topic of substantial interest in clay mineralogy is the modification of water properties between clay mineral surfaces. Several recent studies have focused upon liquid water enclosed by hydrophobic surfaces (Mulla et al., 1984; Lee et al., 1984). The general observation is that optimization of hydrogen-bonding interactions tends to prevent the water dipoles from aligning either with, or against, the surface normal. There have also been numerous studies by molecular dynamics of the structure and dynamics of dilute aqueous solutions of electrolytes (Chandrasekhar et al., 1984; Heinzinger, 1985; Bopp, 1987). Such studies have accurately reproduced radial distribution functions, heats of solution, and changes in self-diffusion coefficients. A general conclusion of these studies is that cations have fairly well-defined coordination shells, with coordination numbers and cation–oxygen distances much like those in solids, while anion coordination polyhedra are considerably less well defined. The structures and energetics of ions in solution are also found to be similar to those of gas-phase ion–molecule clusters, which have recently been extensively studied experimentally (Castleman and Keesee, 1986).

It is important to note that simulation techniques are also used routinely within organic chemistry and biochemistry, where they are generally known as effective-force-field or molecular-mechanics approaches (Allinger, 1976; Burkert and Allinger, 1982). It is now common to optimize the geometries of very large biomolecules using such techniques (see issues of the *Journal of Computer Assisted Molecular Design*), and such methods have been extended to siloxanes (Timofeeva *et al.*, 1984; Abraham and Grant, 1988) and zeolites (Mabilia et al., 1987). Usually, force-field parameters are obtained from *ab initio* SCF calculations on small model molecules.

3.14. Combined local-density-functional molecular dynamics approach

An important new development within solid-state theory is the combination of self-consistent band structure, structure determination, and molecular dynamics within the local-density approximation as developed by Car and Parrinello (1985). Our discussion follows that of Srivastava and Weaire (1987).

The basic theory for crystal-structure determination involves choosing input atomic coordinates, iterating the LDA equations to electronic charge self-consistency, calculating the forces on the atoms, adjusting the coordinates appropriately, reiterating to self-consistency in the electronic charge distribution, and continuing to follow this procedure until the equilibrium geometry is obtained. Thus, one must do two distinct types of iterative calculations, one of the electron distribution and one involving the adjustment of nuclear coordinates. Along the way, much superfluous information on electronic structures at nonequilibrium geometries is generated. It would be desirable to simplify this procedure, performing only one interative step on electron and nuclear coordinates simultaneously.

In the Car and Parrinello (1985) scheme, ion dynamics is combined with a fictitious classical electron dynamics, with nuclei assigned real masses and the electron wave functions arbitrary fictitious masses. One starts the molecular-dynamics simulation at high temperature and "cools" progressively to zero temperature to find the ground state of both electrons and ions simultaneously. Although this approach at first seems strange and unphysical, it has yielded excellent results for amorphous Si (Car and Parrinello, 1988) and recently for SiO_2 (Allan and Teter, 1987) and S clusters (Hohl et al., 1988) and will probably play an important role in the future development of the field.

3.15. Relationships between localized and delocalized approaches

3.15.1. Orbital and band energies

For many problems in solid-state science, one can usefully employ either localized cluster approaches or delocalized band-structure approaches. Comparison of results between the two different approaches is sometimes straightforward, for example, in comparing equilibrium bond distances from cluster calculations on $Si(OH)_4$ or band calculations on polymorphs of SiO_2 (although analysis of the reasons for discrepancies may be very difficult). Comparison of energy spectra obtained by the different approaches can, however, be difficult.

The qualitative relationship between molecular-orbital and electron band energy levels has been discussed by a number of authors (Gerstein, 1973; Albright et al., 1985; Hoffman, 1986) based on a tight-binding or LCAO approach. In general, the energies of crystal or band orbitals are functions of the wave vector or crystal momentum *k* of the electron, leading to characteristic plots of orbital eigenvalues versus *k*, such as that shown in Fig. 3.1 for GaAs, labeled with respect to symmetry directions in *k* (reciprocal) space (Wang and Klein, 1981). Such structure in *E* versus *k* is directly observable in angle-resolved photoemission spectroscopy

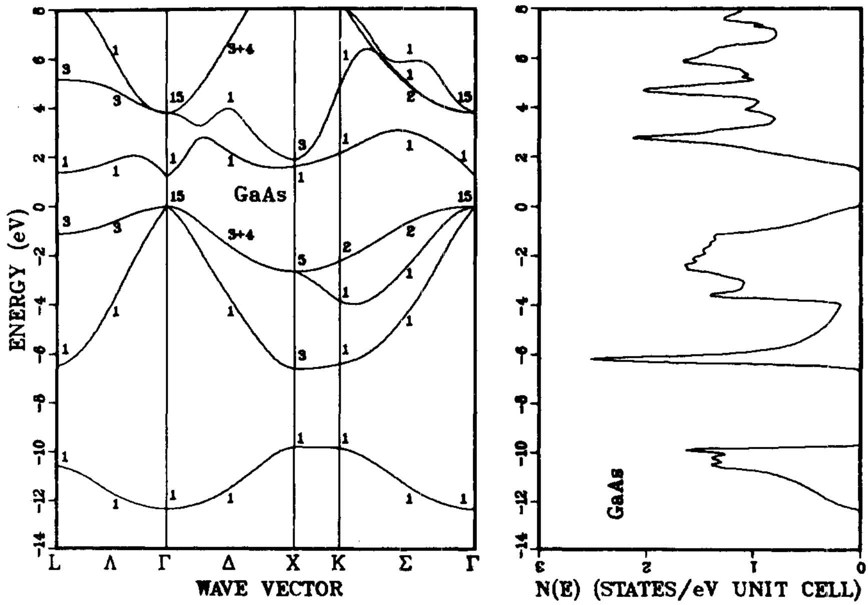

Fig. 3.1. Self-consistent energy bands and density of states calculated for GaAs (after Wang and Klein, 1981, reproduced with the publisher's permission).

(Himpsel, 1983), as shown in Fig. 3.2. However, such angle-resolved photoemission results are not yet commonly available for minerals. It is more common to construct from the E versus k diagram a density of states (DOS), in terms of number of states per (eV unit cell), as shown in Fig. 3.1, by taking $[\partial\varepsilon(k)/\partial k]^{-1}$ integrated over all directions. Such DOS plots can be qualitatively compared with photoemission spectra, as shown in Fig. 3.3 for GaAs. One can also decompose the DOS into partial DOS (PDOS) corresponding to partial orbital character on the atoms and estimate photoemission spectra intensities more accurately from the PDOS and atomic-orbital cross sections. We will later illustrate this approach for SiO_2 and other materials. The calculated DOS for GaAs in Fig. 3.3 can be characterized in terms of energies at particular points in k space, positions of DOS maxima, and widths of various parts of the DOS.

The difficulties of quantitatively relating orbital eigenvalues of a finite cluster model to the DOS of an infinite solid have not often been discussed explicitly, although Cartling (1975) has examined the question for Si. In general, it has been assumed that the energies of the cluster molecular orbitals correspond to positions of peaks in the DOS. Many cluster calculations apparently give good values for the separations of DOS peaks, but they invariably underestimate band widths; that is, the separation of highest- and lowest-energy molecular orbitals within a part of the valence region is less than the width of that portion of the DOS, measured between two points at which the DOS drops to zero. Of course,

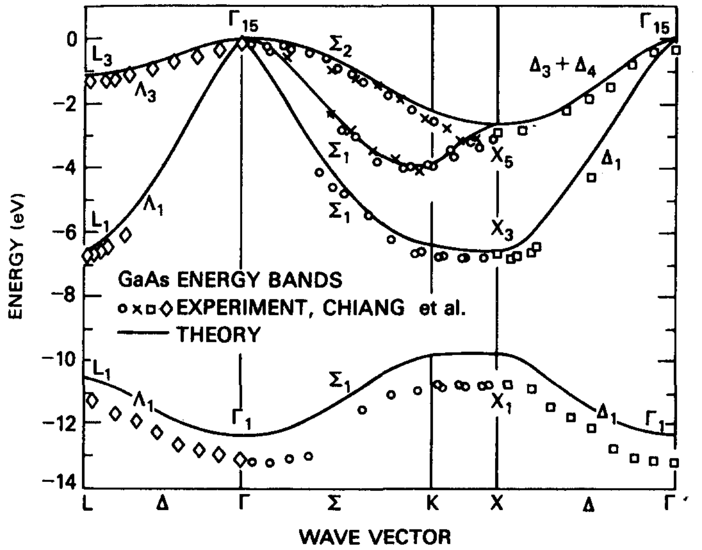

Fig. 3.2. Comparison of theoretical valence-band energies (solid lines; cf. Fig. 3.1) with experimental angle-resolved photoemission measurements (after Wang and Klein, 1981; reproduced with the publisher's permission).

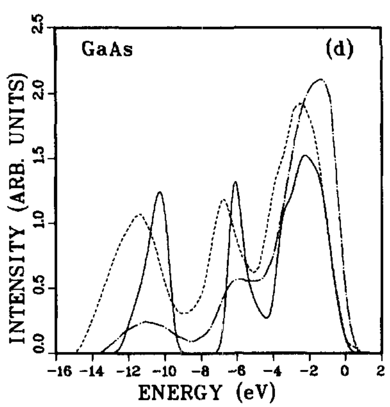

Fig. 3.3. Comparison of calculated density of states (solid line) with experimental x-ray (dashed lines) and ultraviolet (chain-dotted lines) photoemission measurements for GaAs (after Wang and Klein, 1981; reproduced with the publisher's permission).

such comparisons must be made cautiously, since neither the orbital energies from a molecular-orbital calculation nor the DOS from a band calculation are real observables. They are only approximations to ionization energies and will differ from them due to relaxation and correlation, which are very different (at least formally) in the molecular-orbital and band approaches. It is sometimes argued that, if the $E(k)$ versus k plot is flat, a localized or molecular-orbital approach will be (more) appropriate. Although this is in general true, the $E(k)$ versus k dependence varies with the size of the crystalline fragment contained within the unit cell, and molecular-orbital cluster calculations almost invariably include less than a unit cell of atoms.

3.15.2. Incorporation of external atoms of the solid into cluster calculations

Molecular clusters used to model solids are generally charged and do not have the correct stoichiometry. For example, the simplest model for four-coordinate Si in oxides is SiO_4, which, using formal charges for all atoms, has a charge of 4− (i.e., SiO_4^{4-}). We can approximate the effect of the atoms external to the SiO_4 groups in a number of ways. The simplest is to enclose the SiO_4^{4-} ion in a shell of uniformly distributed positive charge, often called a *Watson sphere*. Such a procedure has also been used to study unbound anionic states of free molecules (Tossell and Davenport, 1984; Chou and Jordan, 1987). If the electron density in all the molecular orbitals lies inside the radius of this sphere, then all the eigenvalues are shifted by about the same amount, and the spectrum of relative eigenvalues is little affected by the choice of Watson sphere radius. A slightly more complicated procedure is to surround the cluster by an array of point charges (with either formal or calculated values) at the appropriate lattice positions that will give the correct Madelung potential at each atom of the cluster. In principle, this is a better approach, but in practice it seems to give much the same results as does the Watson sphere. Both methods give reasonable relative eigenvalues and orbital-to-orbital excitation energies, and the Madelung potential method can also give reasonable absolute eigenvalues. Accurate absolute energies with respect to the vacuum are of value in interpreting spectra (such as XANES; see Section 2.2.3) but are difficult to obtain. Neither approach is adequate for calculating the effect of external atoms on the geometry or cohesive properties of the cluster, since there is no unambiguous way to change the Watson sphere radius or the ion positions, and since only the attractive electrostatic component of the cluster–ion interaction is represented when using the point-charge array.

One can also use "saturator" atoms or pseudoatoms. For example, SiO_4^{4-} could be protonated to give $Si(OH)_4$. This approach works well for geometries if the electronic structure of the resulting group is not too greatly perturbed. However, structural ambiguity is produced by the need to choose angles involving the saturators (e.g., Si–O–H angles) and the results [e.g., equilibrium (Si–O) distances] are somewhat dependent upon choice of angle. If straight angles are assumed, T_d symmetry is retained for the $Si(OH)_4$, and calculations on it are little more difficult than those for SiO_4^{4-}. However, full geometric optimization of $Si(OH)_4$ yields a structure of S_4 symmetry (Gibbs, 1982; Hess et al., 1988), with bent Si–O–H angles, and the computational problem is much more difficult.

One could also attempt to develop saturator "pseudoatoms" that differ from H in having different bond distances to the cluster atoms (Kenton and Ribarsky, 1981), or in the characteristics of the expansion basis set. The difficulty is in determining how such pseudoatoms should be parametrized. Although reasonable schemes have been developed for cluster models of elemental Si (Redondo et al., 1981), it is not clear how these can be generalized to other solids. Another approach used for slightly larger clusters, with atoms that are equivalent in the solid but inequivalent in the chosen cluster (e.g., central and peripheral metal atoms) is an "embedding" procedure (Ellis et al., 1979). In this approach, the potentials of exterior cluster atoms are required to be identical to those of equivalent internal atoms, thus building up the correct potential from the inside outwards. Not only does this procedure eliminate cluster termination effects on electronic structure, it gives equilibrium bond distances that are in good agreement with experiment; for example, that in FeO is too long by only three percent (Press and Ellis, 1987).

The development of the best method for constructing cluster models for solids has concerned many researchers. Gilbert (1972) and Adams (1962) independently developed a Hartree–Fock theory of localized orbitals, but this method has never been applied in an *ab initio* form. Heine (1980) discusses, in detail, several local approaches to solid electronic structure, and Sauer (1989) discusses pseudoatom approaches within a Hartree–Fock framework.

It is clear that both localized and delocalized approaches will be of value in mineralogy and geochemistry for the forseeable future. In addition to their direct capabilities in describing the structures of minerals, such approaches encourage transfer of ideas and techniques into mineralogy from different areas. Localized-cluster-type approaches emphasize and exploit the connections between gas-phase inorganic and physical chemistry and mineralogy, while the delocalized band methods build a connection between mineralogy and the physics of simpler crystalline solids.

3.16. Concluding remarks on different theoretical approaches

In this book, the main focus is on the application of quantum-mechanical methods to elucidate the geometric and electronic structures of minerals, so that detailed discussion of the relative merits of the different approaches is not appropriate. Nonetheless, it is important for the reader to appreciate some of the major controversies that have arisen between theoreticians in the field.

First and foremost is the disagreement over whether delocalized (e.g., band-theoretical) or localized (e.g., MO cluster) approaches are preferable. Our position is that both approaches are essentially computer experiments that can incorporate some, but not all, of the basic physics of the problem, and that success in any particular case depends not only upon the methodology but on the nature of the property and the material studied. Some properties of some materials (e.g., lattice parameters of close-packed solids) might be accurately described even by a fairly low-level band approach, while other properties (e.g., spectral excitations at transition-metal centers in minerals) might be more efficiently studied with localized methods. An interesting scientific question related to this controversy is the speed of convergence of cluster results to band results with increasing size of the cluster. Unfortunately, it appears that such a question can only be addressed theoretically, since, experimentally, small metal clusters generally have geometries much different from simple truncations of the bulk solid (e.g., Raghavachari, 1986).

Another area of controversy has been the choice of Hartree–Fock (or Hartree–Fock plus CI) methods as against density-functional methods. For example, Goodgame and Goddard (1982, 1985), Bernholc and Holzwarth (1983), and Delley et al. (1983) have debated the use of Hartree–Fock versus density-functional theory to describe the very complex and subtle bonding in Cr_2 and Mo_2. It appears that both Hartree–Fock–CI and density-functional approaches, if employed carefully and at the highest levels possible, can describe the bonding in these molecules well but not exactly. The question of whether density-functional theory in some way incorporates electron correlation (which is actually defined with respect to the Hartree–Fock formalism) has also been much debated. Bursten et al. (1981) have provided evidence that the potential averaging in the MS-$X\alpha$ method actually mimics some effects of correlation for transition-metal compounds, and Cook and Karplus (1987) have noted that the density-functional energy does not suffer from the incorrect mixture of covalent and ionic terms in the molecular-orbital wave function as much as does the Hartree–Fock energy for diatomics. More general comparisons of Hartree–Fock and density-functional theory have not yet been convincingly made.

The terminology employed in the rest of this book is essentially defined in the previous text and in Appendix C. In addition, it should be noted that Hartree–Fock-based methods with no integral approximations will be described in this book as *ab initio,* in conformity with standard quantum-chemical usage. We shall not use this term for density-functional calculations (even when they clearly give better results than competing *ab initio* Hartree–Fock methods) but shall refer to them as "first principles." We will generally use the term *nonempirical* for methods that are based upon model potentials and/or model charge distributions, but which do not incorporate experimental data, such as the MS-$X\alpha$ method or the potential-induced breathing method.

Computer codes based on the various methods differ substantially in availability and ease of use. Gaussian-orbital *ab initio* SCF programs such as the GAUSSIAN series described by Hehre et al. (1986) and the GAMESS series (Schmidt et al., 1987), data for which are described by Hinchliffe (1988), are the most easily obtainable and are "user-friendly." An *ab initio* SCF band-theory program, CRYSTAL 88 (Dovesi et al., 1988), is also available All these can be obtained through the Quantum Chemistry Program Exchange at Indiana University, although the most recent version of GAUSSIAN should be obtained directly from the company founded to distribute it. Multiple-scattering $X\alpha$ codes are also available from QCPE, and some band-structure programs (e.g., LMTO) are available from the Computer Physics Communications Program Library in Belfast. More sophisticated band-structure programs and analytic orbital-basis LDA programs (such as DVM $X\alpha$) must generally be obtained from their developers or other users.

It is important to keep in mind that each such piece of software is the product of hundreds (or more) person-years of work and should be treated as a valuable resource. Even the most user-friendly programs can be unintentionally misused to produce erroneous or misleading results, vindicating the ancient computer science axiom: garbage in = garbage out. On the other hand, few creators of such complicated software have the time to acquaint themselves with the most recent and interesting developments within geochemistry and materials science. Some of the most interesting applications of such software have thus been made by basically experimental scientists who have identified and solved computationally critical problems within their areas of interest.

Notes

1. A functional is an expression whose value depends on the values of a function [in this case $\rho(r)$] rather than on a set of independent variables.

2. In principle, the Kohn–Sham orbitals obtained as solutions to Eq. (3.39) are for noninteracting particles, not the real electrons, but in practice this difference is often ignored.

4

APPLICATION OF QUANTUM-MECHANICAL METHODS TO SIMPLE INORGANIC "MOLECULES" OF RELEVANCE TO MINERALOGY, AND TO OXIDE MINERALS

As noted in the introduction to this text, much can be learned through the application of both quantum-mechanical calculations and experimental techniques to simple molecules that contain bonds of the type found in the important groups of minerals. One reason for this approach is that calculations at a higher level of quantum-mechanical rigor can be applied to such simple systems. This approach will be illustrated with reference to the SiO, SiO_2, Si_2O_2, Si_3O_3, and SiF_4 molecules.

Attention will then be turned to the major oxide minerals MgO, Al_2O_3, and SiO_2 and the binary transition-metal oxides of Ti, Mn, and Fe, with some brief discussion of the series of transition-metal monoxides (MnO, FeO, CoO, NiO) and complex oxides ($FeCr_2O_4$, $FeTiO_3$, etc.), and of the problem of the calculation of Mössbauer parameters in iron oxides (and other compounds).

4.1. The inorganic molecules SiO, SiO_2, Si_2O_2, and Si_3O_3

Although silicon monoxide, SiO, is not an important component of minerals, it is an important chemical constituent in interstellar and circumstellar space and an important starting material for the gas-phase synthesis of silicates from components of the nebula (Day and Donn, 1978). The structure, energetics, and spectral properties of SiO have been calculated by a number of different methods. The Si–O bond distance calculated using *ab initio* Hartree–Fock–Roothaan SCF methods at the 6-31G* basis-set level is 1.487 Å (Snyder and Raghavachari, 1984), slightly smaller than the experimental value of 1.5097 Å (Field et al., 1976). A near Hartree–Fock limit basis set and limited configuration-interaction calculation has given the slightly better value of 1.496 Å (Langhoff and Arnold, 1979). This study also gave a bond dissociation energy of 8.10 eV, compared to an experimental value of 8.26 ± 0.13 eV (Hildenbrand, 1972), and a bond-stretching frequency of 1248 cm^{-1}, compared to an experimental value of 1242 cm^{-1} (Anderson and Ogden, 1969). Even more highly correlated calculations give a bond distance of 1.515 Å and a stretching frequency of 1242 cm^{-1} (Werner et al., 1982).

The 6-31G* basis-set Hartree–Fock–Roothaan calculation also gives an almost exactly correct bond-stretching frequency after the standard correction factor describing correlation effects is applied (Hehre et al., 1986). Energies and intensities for transitions to low-lying excited states were also obtained from CI calculations and were in good agreement with experiment. Valence-region uv photoelectron spectra have also been obtained for SiO and compared with values calculated using *ab initio* Hartree–Fock–Roothaan SCF methods and MS-SCF-$X\alpha$ transition-state methods, as shown in Table 4.1 (Colburn et al., 1978).

Studies of triatomic SiO_2 using *ab initio* Hartree–Fock–Roothaan SCF calculations near the Hartree–Fock limit (Pacansky and Hermann, 1978) gave an equilibrium $D_{\infty h}$ geometry and yielded a Si–O bond distance of 1.488 Å (compared to 1.494 Å in SiO for calculations using the same basis set). This near constancy in Si–O bond distance with decrease in formal bond order is unexpected. It is contrary to the increase in C–O bond length observed between CO and CO_2 (1.13 versus 1.16 Å). Similarly, the calculated Si–O bond stretching force constant is as large in SiO_2 as in SiO, contrary to the trend for CO and CO_2. The experimental bond energy of each Si–O bond in SiO_2 is about 6.5 eV, compared to a Si–O bond energy of 8.3 eV in SiO, so that SiO_2 is bound with respect to SiO and the ground-state (^3P) oxygen atom by about 4.7 eV.

Since the estimated energy of the Si–O bond is 4.7 eV (Huheey, 1983), it would be expected that 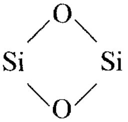 (with four Si–O bonds) might be bound with respect to two SiO (two Si≡O). Indeed, accurate quantum-mechanical calculations indicate that 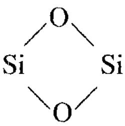 (D_{2h} symmetry) is about 1.9 eV more stable than two SiO, in very good agreement with the gas-phase dimerization data (Snyder and Raghavachari, 1984). The vibrational frequencies calculated after standard correction for correlation effects are also in reasonable agreement with the experimental data. The calculated minimum energy structure is of D_{2h} symmetry, with a Si–O bond length of 1.683 Å and a O–Si–O angle of 85.7°. A very similar distance (1.670 Å) and O–Si–O angle (87.1°) were obtained for $H_4Si_2O_6$ (which has edge-sharing 4-coordinate Si polyhedra) by O'Keeffe and Gibbs (1984) using identical theoretical methods. This suggests that the

Table 4.1. Comparison of orbital ionization potentials (in eV) for SiO observed experimentally from uv photoelectron spectroscopy with those calculated by the MS-SCF-$X\alpha$ method, *ab initio* Hartree–Fock–Roothaan method, incorporating the ΔSCF approach (HFR ΔSCF), and with perturbation theory (HFR + PT)

Molecular orbital	Experimental data	Calculated ionization potentials			
		MS-SCF-$X\alpha$[a]	HFR[a]	HFR ΔSCF[a]	HFR + PT[b]
7σ	11.6	10.1	12.0	10.7	11.4
2π	12.2	13.8	13.0	10.3	12.3
6σ	14.8	14.9	16.6	15.4	15.3

[a] Colburn et al. (1978).

[b] Chong and Takahata (1977).

Si–O bond distance is determined largely by the oxygen coordination number and the number and type of polyhedral contacts.

It is well known that CO_2 is most stable in its molecular form, while SiO_2 is stable as a condensed phase. A similar difference exists for the dimerization of CO and SiO—the first step toward formation of a solid. The lowest-energy state of the CO dimer is a triplet state (two unpaired spins) with a linear geometry O=C=C=O, and this is unstable with respect to two C≡O molecules by about 2.8 eV (Raine et al., 1983). The analogous O=Si=Si=O dimer of Si–O is calculated to be unstable by 4.8 eV with respect to two Si≡O molecules (Snyder and Raghavachari, 1984). The important qualitative differences between CO and SiO that affect their dimerization are: (1) charge separation is greater in SiO than in CO [as for the Pacansky and Hermann (1978) discussion of CO_2 and SiO_2], so that approach of Si and O stabilizes $(SiO)_2$ more than approach of C and O stabilizes $(CO)_2$; (2) the C–C π bond is much stronger than the Si–Si π bond (Kutzelnigg, 1984), so that a Si=Si configuration has relatively low stability, and (3) all π bonds formed by Si are weaker than the corresponding bonds formed by C so that the decrease in bond strength with decrease in bond order is greater for C–O than for Si–O bonds (Table 4.2). Using simple bond-strength arguments and Table 4.2, one would predict the D_{2h} form of $(CO)_2$ (four C–O bonds) to be unstable with respect to two C≡O by 1.6 eV and the corresponding D_{2h} dimer of Si≡O to be stable by 5.8 eV. The lesser stability of $(SiO)_2$ obtained in the *ab initio* calculations (and shown by experiment) probably arises from the presence of the strained four-membered ring. Calculated and experimental structural properties of SiO and Si_2O_2 are summarized in Table 4.3.

Snyder and Raghavachari (1984) have suggested that $(SiO)_2$ with the D_{2h} geometry may model solid amorphous SiO. The existence and structure of solid SiO is a subject of considerable debate. X-ray diffraction (Yasaitis and Kaplow, 1972) yields a Si–O distance of 1.64 Å and an O–Si–O angle of 96.7°, in reasonable agreement with those calculated for

Table 4.2. Experimental carbon–oxygen and silicon–oxygen bond energies (in eV)

C–O	3.7	Si–O	4.7
C=O	8.3	Si=O	6.5
C≡O	11.1	Si≡O	8.3

Source: From Kutzelnigg, 1984.

$(SiO)_2$. Recent x-ray spectroscopic studies (Costa Lima and Senemaud, 1976; Bianconi and Bauer, 1980) also indicate that SiO does not contain any Si in four coordination with oxygen. Whether the x-ray emission and absorption results are consistent with two-coordinate Si is not yet clear.

The same approach may, of course, be extended to higher oligomers, such as the Si_3O_3 molecule, but the computations become rapidly more

Table 4.3. Experimental properties of SiO and Si_2O_2 compared to those calculated by Snyder and Raghavachari (1984) using *ab initio* Hartree–Fock–Roothaan SCF calculations

Si–O molecule

HFR calculation	Bond length R(Si–O) (Å)	Vibrational frequency ν (cm^{-1})
Basis set		
STO-3G	1.475	1349
6-31G*	1.487	1407 (scaled to 1252)
Experimental value	1.51	1242

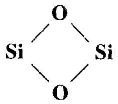

molecule

HFR calculation	Bond lengths R(Si–O) (Å)	Bond lengths R(Si–Si) (Å)	Bond angle (∢O–Si–O) (deg)	ΔE_{dimer} (kcal/mol)
Basis set				
STO-3G	1.684	2.530	82.6	
6-31G*	1.683	2.469	85.7	−59.8 (HF), −38.9 (MP4)
Experimental value	—	—	—	−44.6 ± 3.0

Vibrational frequency	$\nu_{B_{2u}}$	$\nu_{B_{3u}}$	$\nu_{B_{1u}}$
Scaled 6-31G* basis	789	758	247
Experimental value	804	766	252

time consuming due to the larger number of electrons and of geometric degrees of freedom. Calculations using the *ab initio* Hartree–Fock–Roothaan method with the STO-3G basis set (Tossell, unpublished results) on the D_{3h} structure of Si_3O_3 yield a Si–O bond distance of 1.636 Å and Si–O–Si angle of 141°. Si_3O_3 is calculated to be stable with respect to D_{2h} symmetry Si_2O_2 and SiO by 82 kcal/mol. Although the geometry of Si_3O_3 calculated using the STO-3G basis set is expected, by comparison with Si_2O_2, to be in reasonably good agreement both with results from larger basis-set calculations and with experiment, the condensation exothermicities appear to be exaggerated by basis-set errors and by neglect of correlation effects. For example, in the reaction $SiO + SiO \rightarrow Si_2O_2$ the calculated exothermicity is 78 kcal/mol using a STO-3G basis set, 50 kcal/mol using a 6-31G* + diffuse, *s,p* basis, and 39 kcal/mol after fourth-order Moller–Plesset correlation corrections (Snyder and Raghavachari, 1984). Nonetheless, the STO-3G basis-set results certainly suggest stability for a Si_3O_3 species with planar D_{3h} geometry.

Although the Si_2O_2 species seems strange in terms of solid silicate structures due to its long Si–O distance (1.68 Å), small Si–O–Si angle (97.4°), and short Si–Si distance (2.53 Å), the geometry of Si_3O_3 calculated using the STO-3G basis set seems much more understandable, with its Si–O distance of 1.64 Å, Si–O–Si angle of 141°, and Si–Si distance of 3.09 Å. Its Si–O skeleton is very much like that calculated for $H_3Si_3O_3$ at both the STO-3G basis-set (Chakoumakos et al., 1981) and 6-31G* basis-set (O'Keeffe and Gibbs, 1984) level. O'Keeffe and Gibbs (1984) have argued that their calculated frequency of 650 cm^{-1} for the A_1' vibrational mode of $H_3Si_3O_3$, which primarily involves oxygen motion, supports the assignment of a 600 cm^{-1} feature in the Raman spectrum of amorphous SiO_2 to a three-Si-ring structure, as suggested by Galeener (1982a,b). Their calculated frequency is also consistent with the observed value for benitoite of 564 cm^{-1} (Griffith, 1969). Similarly, a peak in the Raman spectrum of Si_3O_3 (Khanna et al., 1981) has been assigned to an A_1' vibration and may be the analog of that observed in amorphous SiO_2. It appears, therefore, that the condensation of SiO monomers leads to structures similar to those observed in amorphous SiO_2. It is indeed striking how similar the Si–O skeletons seem to be for two-coordinate and four-coordinate oxides. This similarity indicates that addition of O (e.g., in the reaction: $Si_3O_3 + 3O \rightarrow Si_3O_6$) does not greatly disturb the Si–O bonding. For Si_3O_3, the lowest-energy unoccupied orbitals are predominantly Si $p\pi$ (i.e., *p* orbitals perpendicular to the Si_3O_3 ring) and have the right symmetry to accept electrons from the π^* orbitals of O_2.

Rings containing three silicate tetrahedra are observed in cyclosilicates (e.g., benitoite). The relative prevalence of three-, four-, and higher-membered rings has been discussed by Chakoumakos et al. (1981), and we will return to this topic in Chapter 5.

4.2. The SiF_4 molecule

Although SiF_4 does not occur as a mineral, it represents an isoelectronic model for SiO_4^{4-} and has many properties similar to those of silicates. Because, unlike SiO_4, it is a stable gas-phase molecule, it can be readily studied by many spectroscopic techniques, and because it has high symmetry and contains relatively few electrons, it can be treated with a fairly high level of quantum-mechanical rigor. We shall, therefore, explore a number of aspects of the geometric and electronic structure of SiF_4, starting with its geometry and stability, proceeding to its photoelectron spectrum and x-ray emission and absorption spectra, and concluding with a discussion of the ^{29}Si NMR chemical shift in SiF_4.

4.2.1. *Geometric structure of SiF_4*

The dependence of calculated Si–F bond distance on the basis set used in *ab initio* Hartree–Fock–Roothaan SCF calculations has been studied systematically, giving the results shown in Table 4.4. The near Hartree–Fock limit basis of Tossell and Lazzeretti (1986) also gives a Si–F bond energy of 109 kcal/bond mol, compared with an experimental value of about 142 kcal/bond mol (Kutzelnigg, 1984), and the force constant for symmetric stretching is calculated to be 7.654 mdyn/Å, compared with an experimental value of 7.15 mdyn/Å (Heicklen and Knight, 1964). Calculations using the AM1 method (the newest version of MINDO) also give struc-

Table 4.4. Experimental properties of SiF_4 compared to those calculated by Hess et al. (1986) using *ab initio* Hartree–Fock–Roothaan SCF calculations

HFR calculation	Bond length R(Si–F) (Å)
Basis set	
STO-3G	1.585
6-31G	1.625
6-31G*	1.557
TZ + TD (triple ζ plus triple Si *3d*)	1.54
Experimental value	1.552

	Vibrational frequencies (cm^{-1})			
HFR calculation	E	T_2	A_1	T_2
Basis set				
STO-3G	263	370	761	1,099
6-31G	233	356	757	1,037
6-31G*	274	406	849	1,108
Experimental value	267	390	807	1,044

tures and bond energies for SiF_4 in good agreement with experiment (Dewar and Jie, 1987).

4.2.2. Electronic structure of SiF_4—electron spectroscopy

Valuable information on the electronic structure of this molecule is contained in its photoelectron spectrum (Bassett and Lloyd, 1969; Hall et al., 1972). Qualitative molecular-orbital theory suggests that the four F 2*s* orbitals will generate a_1 and t_2 symmetry molecular orbitals, as will the σ symmetry F 2*p* orbitals. The F 2*p* orbital of π symmetry with respect to the Si–F bond will generate t_1, t_2, and *e* molecular orbitals. Si 3*s* orbitals can contribute to the molecular orbitals of a_1 symmetry, and Si 3*d* orbitals to those of *e* and t_2 symmetry. Initial disagreement as to the assignment of peaks in the photoelectron spectrum arose from the use of a He I uv source with insufficient energy to excite the a_1 symmetry Si–F bonding molecular orbital, and from the use of the semiempirical CNDO molecular-orbital calculations that give exaggerated Si 3*d* participations and exaggerated stability for the *e* molecular orbital. It is now well established, on the basis of experimental and theoretical studies, that the order of orbitals in terms of increasing ionization potentials is $1t_1 < 5t_2 < 1e < 4t_2 < 5a_1 < 3t_2 < 4a_1$, where the numbering system includes both core and valence orbitals. Experimental ionization potentials from Perry and Jolly (1974a) are compared with a number of different calculated values in Fig. 4.1. The ionization spectrum of $SiCl_4$ is quite similar to that of SiF_4, merely showing slightly larger spacings. For example, the t_1 orbital to a_1 bonding orbital spacing is 6.0 eV in $SiCl_4$ versus 5.0 eV in SiF_4. As we shall see in Chapter 5, the SiO_4^{4-} anion (e.g., in Li_4SiO_4) has a very similar photoelectron spectrum.

It is apparent from the results shown in Fig. 4.1 that all of the methods give the right sequence of orbital ionization potentials. However, only the *ab initio* Hartree–Fock–Roothaan SCF many-body perturbation theory results of Fantoni et al. (1986) are in good quantitative agreement with experiment. For $SiCl_4$, both MS-SCF-$X\alpha$ calculations using overlapping spheres (Zhu et al., 1983) and DVM-$X\alpha$ calculations (Andersen et al., 1979) give results in reasonable quantitative agreement with experiment, but no studies by Hartree–Fock–Roothaan ΔSCF or many-body perturbation theory techniques have yet appeared for this molecule.

Information on the electronic structure of the molecule is contained in the energies, intensities, and widths (or the vibrational structure) of the photoelectron peaks. Early studies suggested that the 1*e* orbital is more stable than the $5a_1$ orbital due to Si 3*d* π bonding with the F 2*p*. It is now clear that the strength of such Si 3*d* bonding is modest. Attempts to deduce the amount of stabilization of the predominantly F 2*p* orbitals ($1t_1$, $5t_2$, and 1*e*) from the experimental ionization energies of SiF_4 and HF compounds lead to an average stabilization of 0.9 eV compared to pure F

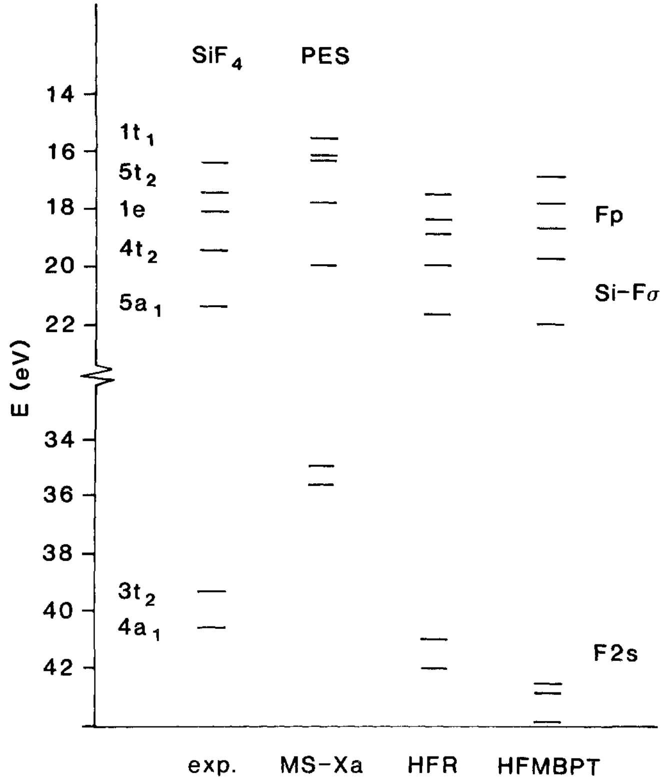

Fig. 4.1. Ionization potentials for SiF_4 derived experimentally (exp.) from x-ray photoelectron spectroscopy (after Perry and Jolly, 1974a) and compared with values calculated using MS-SCF-$X\alpha$ (MS-$X\alpha$; DeAlti et al., 1978), Hartree–Fock Roothaan (HFR; Tossell and Lazzeretti, 1986) and Hartree–Fock many-body perturbation theory (HFMBPT; Fantoni et al., 1986) (after Tossell, 1987).

$2p$ orbitals (Jolly, 1983). It is, however, unclear whether this stabilization should be attributed to Si $3d$ or Si $3p$ admixture, which is substantial for the $5t_2$ orbital. This question can also be studied theoretically by performing calculations with and without d functions on the Si. However, such a procedure yields ambiguous results since: (1) the calculations even with d functions do not show exact agreement with experiment, and the effects of including d functions may be small compared to other errors still present; (2) the self-consistency procedure causes most of the orbital energies to change, even if participation of Si $3d$ atomic orbitals in the molecular orbitals is forbidden by symmetry; and (3) any decomposition of molecular electron density between nuclear centers is nonunique, although certain decompositions are more theoretically justified than others. Given these caveats, available MS-SCF-$X\alpha$ studies of SiF_4 (DeAlti et al., 1978) indicate that the $5t_2$ and $1e$ orbitals are stabilized by 0.27 and 0.15 eV, respectively, upon the addition of Si $3d$ functions. MS-SCF-$X\alpha$ calculations are particularly suited to the elucidation of such differences since, for each angular momentum, they utilize an infinitely flexible basis set. Thus, a MS-SCF-$X\alpha$ calculation using $\ell = 0$ and 1 functions on Si has an effectively complete Si *s,p* basis (although the potential is, of course, only a spherically symmetric model potential within the Si sphere).

Information on orbital composition can also be obtained by analysis of the relative intensities of the photoelectron peaks, particularly when more than one radiation source is available. For the case of x-ray excitation, in which the electron is excited to high energies in the continuum, we can ignore possible structure in the low-energy continuum and express the photoionization cross section for a molecular orbital as a sum of contributions from its component atomic orbitals. Schofield (1976) calculated x-ray photoelectron spectroscopy cross sections for various atomic orbitals, while Leckey (1976) obtained cross sections through analysis of experimental data. Orbital compositions and intensities calculated from Schofield's (1976) atomic cross sections are compared with experiment in Table 4.5. When uv photons are used, this simple summation of atomic-orbital contributions is not adequate, and multiple-scattering effects must be included. Such calculations have been done by two slightly different methods, producing significantly different total photoionization cross sections and decompositions over different symmetry channels in the continuum. Results for ionization of the $1t_1$ electrons from Yates et al. (1985) and Gofman et al. (1986) are compared in Fig. 4.2. Yates et al. (1985)

Table 4.5. Compositions of molecular orbitals of SiF_4 from semiempirical molecular orbital (CNDO) calculations and MS-SCF-$X\alpha$ calculations, together with comparison of calculated x-ray photoelectron transition intensities with experimental values

Molecular orbital	Calculated atomic-orbital composition[a]		Intensities[b,c,d]	
	CNDO method	*MS-SCF-Xα method*	*Calculation*	*Experiment*
$1t_1$	100% F 2*p*	100% F 2*p*	0.28	0.11
$3t_2$	97% F 2*p*, 3% Si 3*p*	96% F 2*p*, 4% Si 3*p*	0.27	0.13
$1e$	100% F 2*p*	98% F 2*p*, 2% Si 3*d*	0.18	0.09
$2t_2$	86% F 2*p*, 2% F 2*s*, 12% Si 3*p*	85% F 2*p*, 14% Si 3*p*	0.25	0.17
$2a_1$	75% F 2*p*, 5% F 2*s*, 20% Si 2*s*	71% F 2*p*, 14% Si 3*p*, 22% Si 3*s*	0.11	0.12
$1t_2$	91% F 2*s*, 9% Si 3*p*	94% F 2*s*, 6% Si 3*p*	1.00	1.00
$1a_1$	86% F 2*s*, 14% Si 3*s*	88% F 2*s*, 9% Si 3*s*	0.32	0.60

[a] Tossell, unpublished results.

[b] Jonas et al., (1972).

[c] Using MS-SCF-$X\alpha$ compositions and atomic-orbital cross sections from Schofield (1976).

[d] Perry and Jolly (1974[a]).

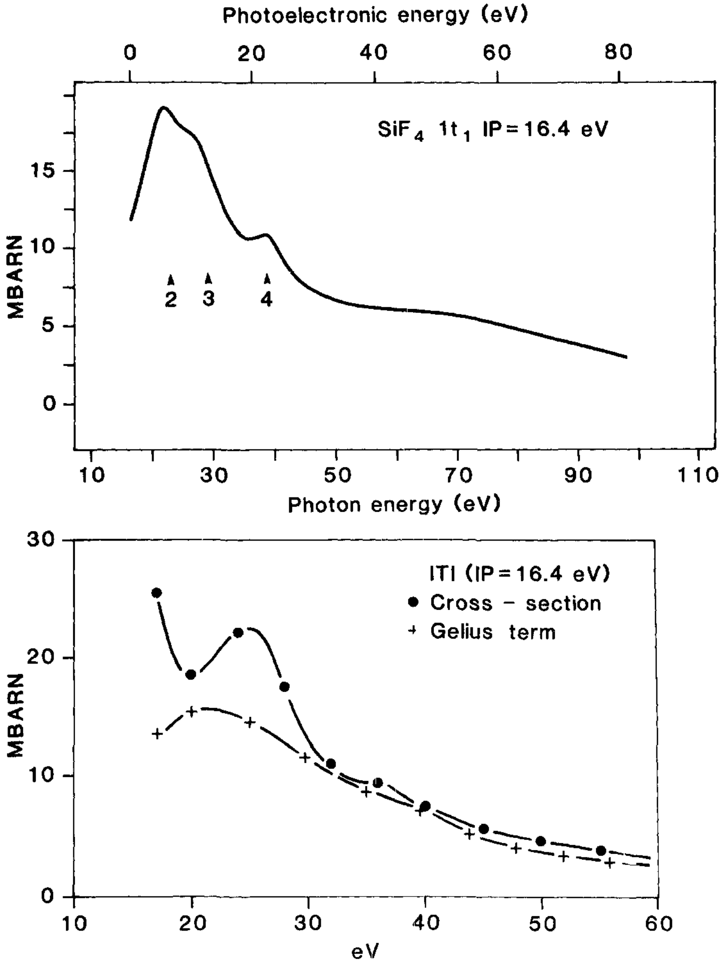

Fig. 4.2. Calculated cross sections for $1t_1$ orbital ionization from: (a) Yates et al. (1985), and (b) Gofman et al. (1986).

assign the lowest-energy cross-section peak to the t_2 channel (qualitatively speaking, a t_2 "orbital" embedded in the continuum), while Gofman et al. (1986) assign it to the *e* channel. The experimental data in this energy range are sparse, and neither calculation seems to provide an accurate description.

Additional information on orbital type and composition is available from "(*e*,2*e*)" or electron momentum spectroscopy (Moore et al., 1982; see Appendix B) performed on SiF_4 by Fantoni et al. (1986). Electron momentum distributions measured at various binding energies have been compared with those from *ab initio* Hartree–Fock–Roothaan SCF calculations using a double-ζ wave function with a single Si 3*d* polarization function for SiF_4 and are shown in Fig. 4.3. In most cases, agreement is good, and the comparison confirms the identification of the 21 eV ionization as the $5a_1$ Si–F σ bonding orbital. Agreement between calculation and experiment is actually poorest for the $1t_1$ orbital, essentially pure F 2*p* in character, which has a much lower momentum than calculated. Such discrepancies for diffuse orbitals at, or near, the lowest binding energies are often seen in (*e*,2*e*) spectra (Bagawan et al., 1988) and arise from correlation effects.

High-resolution uv photoelectron spectroscopy also allows the observation of vibrational structure in the ionizations of those electrons that are of strong bonding or antibonding character, and whose ejection produces a substantial change in bond distance. For SiF_4, ionization of $5t_2$ electrons produces a peak, the fine structure of which has been interpreted in terms of excitation of vibrations of both A_1 and T_2 symmetry, with the vibrational energies observed for the cation being about 10% less than those for the neutral molecule (Lloyd and Roberts, 1975).

One can also obtain information on charge distribution and bonding character from the Auger electron spectrum. As discussed in Chapter 2, the Auger spectrum results from the ejection of electrons accompanying de-excitation of a core hole. For example, when a Si 1*s* hole is created (e.g., by photon impact) a Si 2*p* electron can drop into the hole, and the energy released can either be emitted as an x-ray or utilized to eject a second Si 2*p* electron, identified as a Si(*KLL*) Auger electron. Experimental Si(*KLL*) Auger energies and those obtained from MS-SCF-$X\alpha$ calculations (Hartmann and Szargan, 1979) are in good agreement for SiF_4. For the Si(*LVV*) Auger of SiF_4 (involving holes in the Si 2*p* orbital and two valence orbitals), the situation is more complicated (Rye and Houston, 1983), with the results showing localization of the valence-orbital hole states that cannot be accommodated within a T_d symmetry model.

4.2.3. Electronic structure of SiF_4 — x-ray-absorption spectra

Although x-ray emission spectra are available for some gaseous molecules, such as SF_6 (Taniguchi and Henke, 1976), they are not yet available for SiF_4. Calculations suggest that the x-ray emission spectra of SiF_4 should be qualitatively similar to those of MO_4^{n-} anions such as SO_4^{2-} (discussed in Taniguchi and Henke, 1976) or SiO_4^{4-}, to be discussed in Chapter 5. X-ray absorption spectra are, however, available for SiF_4 in the region of the Si 2*p* ionization limit (e.g., Friedrich et al., 1980, and references therein). Angle-resolved Si 2*p* photoelectron spectra have also been obtained for SiF_4 (Keller et al., 1983). The Si 2*p* XANES, previously discussed in Chapter 2, is shown again in Fig. 4.4. Direct measurement of the Si 2*p* ionization potential using hard x rays yields a value of 111.65 eV (Perry and Jolly, 1974b), establishing that two of the SiF_4 XANES features lie below the ionization threshold and correspond to bound

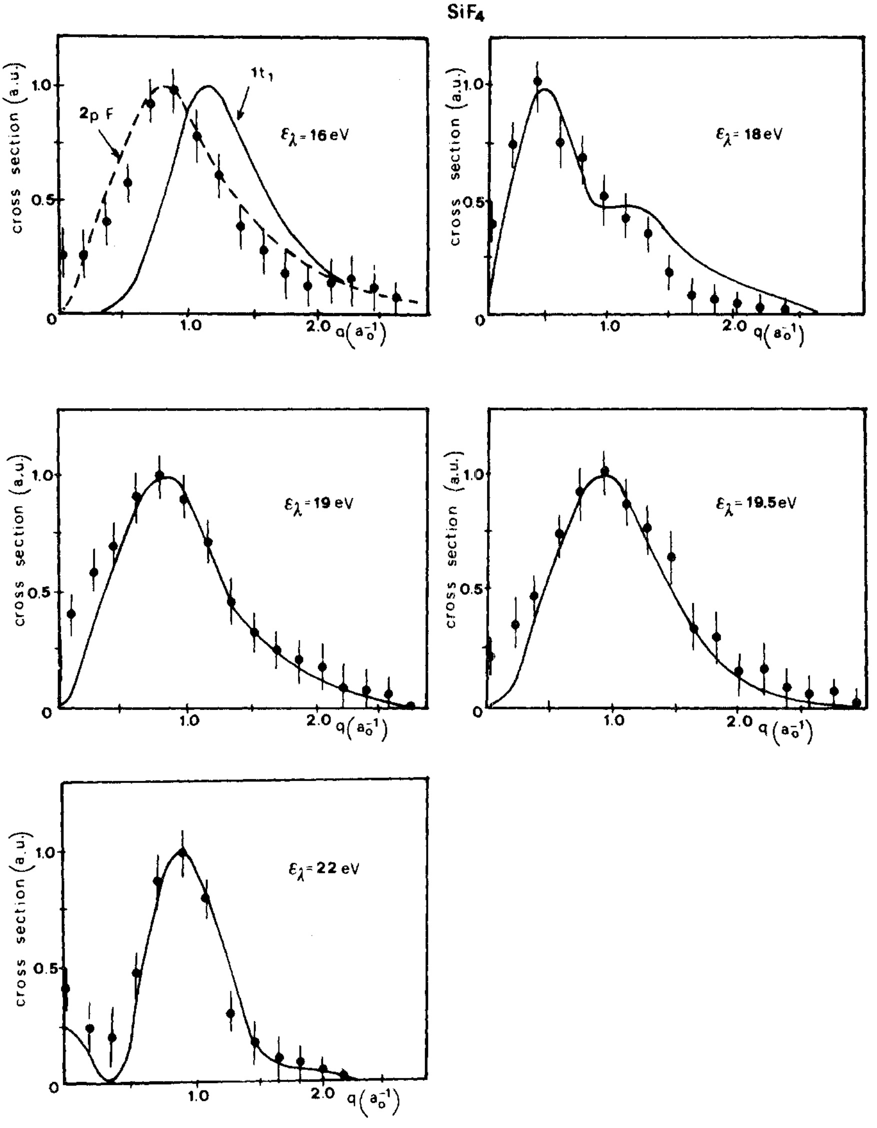

Fig. 4.3. Measured momentum distributions (dots) of the outer valence band of SiF_4 obtained from electron momentum spectroscopy and compared with values obtained using *ab intitio* Hartree–Fock–Roothaan (SCF) calculations (solid line) (after Fantoni et al., 1986; reproduced with the publisher's permission).

states, and two lie above corresponding to scattering resonances. Hartree–Fock calculations using the equivalent ionic-core virtual-orbital model and treating SiF_4 with a core hole as PF_4^+ (Friedrich et al., 1980), and MS-SCF-$X\alpha$ calculations (Tossell and Davenport, 1984), give the same assignments and energies for the bound-state peaks (Table 4.6) with

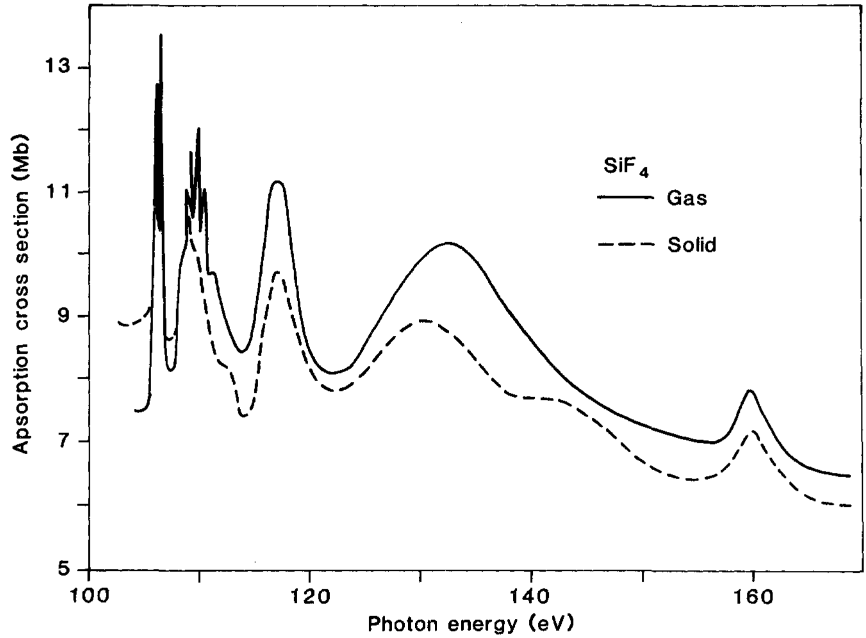

Fig. 4.4. The Si $2p$,$2s$ x-ray absorption (XANES) spectra of gaseous (molecular) and solid SiF_4 (after Bianconi, 1981; reproduced with the publisher's permission).

the deepest peak arising from an a_1 symmetry σ^* orbital and the next peak having a contribution from the t_2 symmetry σ^* orbital. The peaks lying above threshold have been assigned using the continuum version of the MS-SCF-$X\alpha$ method by Pavlychev et al. (1982), Tossell (1987), and Bancroft et al. (1986). According to the first two studies, the first continuum peak corresponds to continuum states of e symmetry, while the second corresponds to t_2 symmetry states. However, Bancroft et al. (1986) assign

Table 4.6. Experimental term energies of a_1 and t_2 bound states in Si $L_{2,3}$ XANES spectra of SiF_4 compared with energies calculated using the MS-SCF-$X\alpha$ method and *ab initio* Hartree–Fock–Roothaan SCF calculations. Oscillator strengths are given in parentheses for MS-SCF-$X\alpha$ calculations

	Calculated values			**Experimental**[b] **values**
	MS-SCF-$X\alpha$ method[a]		**HFR method**[b]	
a_1	4.7 (0.00304), 2.1 (0.00190)		4.4, 2.1	5.5
t_2	2.8 (0.00097)		2.6	2.7
	Continuum	Bound state		
e	~ −7.7	−6.0 (.0824)	—	−5.5
t_2	~ −20.0	—	—	−18.1

[a] Tossell and Davenport (1984).

[b] Friedrich et al. (1980).

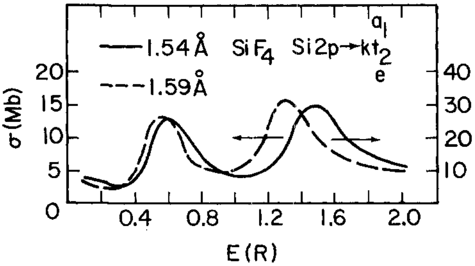

Fig. 4.5. Si $2p \rightarrow$ continuum x-ray absorption cross sections (σ in megabarns, Mb) calculated by the MS-SCF-$X\alpha$ method for SiF_4 at Si–F distances of 1.54 and 1.59 Å; electron energies (E) in rydbergs (after Tossell, 1987).

both these features to the t_2 channel. In the Si $2p$ XANES of SiO_2 and other silicates, the second peak is qualitatively the same as that for SiF_4. The separation of the continuum peaks, corresponding to the energy difference of e and t_2 channels, may be qualitatively interpreted as an Si $3d$ orbital "crystal-field" splitting, mainly due to the large Si $3d$ orbital radius (Pavlychev et al., 1982). Continuum MS-SCF-$X\alpha$ calculations on SiF_4 as a function of Si–F distance [R(Si–F] indeed show that the t_2 resonance is substantially lowered as R(Si–F) is increased and that the $t_2 - e$ separation varies approximately as R^{-5} (see Fig. 4.5, from Tossell, 1987). Si $1s$ XANES have also recently been reported for SiF_4 (Bodeur et al., 1986), but the term energies and splittings seem inconsistent both with the Si $2p$ XANES and with calculations suggesting an erroneous value for the Si $1s$ IP. Recently, further experimental and theoretical studies on the $Si(CH_3)_xF_{4-x}$, $x = 0$–4, series (Bozek et al., 1990) have confirmed the existence of peaks in both the e and t_2 channels above the Si $2p$ edge.

4.2.4. Electronic structure of SiF_4 — ^{29}Si NMR spectra

The e and t_2 resonances occurring in the XANES of SiF_4 are very high-energy features that probably have little effect upon the uv absorption or other properties dependent upon excited orbital energetics, such as the ^{29}Si NMR shifts. Within the context of quantum-mechanical perturbation theory, we can calculate the NMR shielding as the sum of a diamagnetic term (σ^d) dependent only upon the ground-state electron density and a paramagnetic term (σ^p) arising from transitions to excited states induced by the magnetic field (Tossell, 1984a). Direct calculations using the coupled version of Hartree–Fock perturbation theory (Lipscomb, 1966) have been performed for SiH_4 (Lazzeretti and Zanasi, 1980) and for SiF_4 (Tossell and Lazzeretti, 1986). Such calculations indicate that the diamagnetic contribution to the shift may be readily obtained from fairly crude SCF molecular-orbital calculations or even from an atom superposition model, while accurate determination of the paramagnetic term requires an extremely accurate wave function (in the above studies, the Si atom was the origin of the vector potential for the magnetic field in each case). It is found, however, that the dominant contribution to the average σ^p, representing 50% or more of the total, arises from mixing of the electrons in the occupied $t_2\sigma$ orbital with those in the empty $t_2\sigma^*$ orbital. Energies for such orbitals are available from photoelectron and x-ray absorption spectroscopies, providing an opportunity for interpreting σ^p in terms of other spectral properties. The coupled Hartree–Fock calculations also reproduce semiquantitatively the change in ^{29}Si chemical shift from SiF_4 to SiO_4^{4-}, and from SiF_4 to SiF_6^{2-}, as shown in Fig. 4.6. It thus appears that at least major trends (if not details) of ^{29}Si chemical shift variation can be understood through coupled Hartree–Fock perturbation theory calculations on small molecular cluster models. Recently, Fleischer et al. (1987) have obtained a more accurate value for the ^{29}Si NMR shielding of SiF_4 using a modified coupled Hartree–Fock method with individual choices of origin for individual localized molecular orbitals (the IGLO method). Their results indicate that conventional coupled Hartree–Fock calculations like those of Tossell and Lazzeretti (1986) probably exaggerate the increase in total σ with coordination number. Both conventional and IGLO results indicate that σ changes very slowly with Si–F distance in SiF_4.

It is thus apparent that ground-state structural and energetic properties of $(SiO)_n$ and SiF_4 can be calculated quite accurately using Hartree–

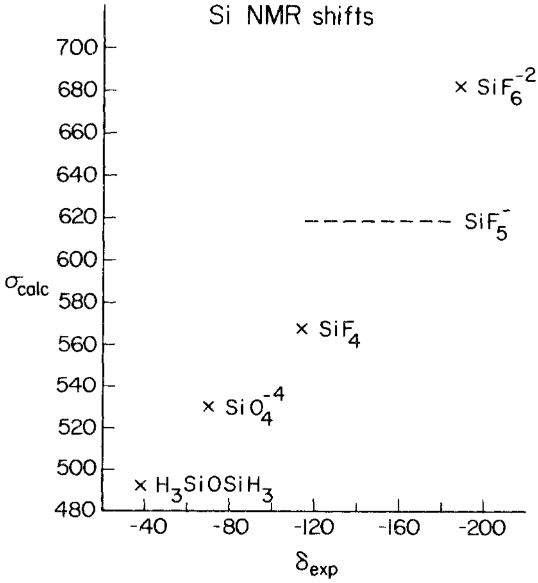

Fig. 4.6. Comparison of calculated ^{29}Si NMR shielding constants (σ_{calc}) and experimental ^{29}Si chemical shifts (δ_{exp}) for SiF_4 and other silicon compounds (after Tossell and Lazzeretti, 1986; see text for discussion).

Fock theory with many-body perturbation corrections for correlation. Much progress has also been made in the calculation of spectral properties, although it remains difficult to calculate intensities in photoemission and x-ray absorption spectra.

4.3. Major oxide minerals

A very large number of theoretical studies have been performed on MgO and Al_2O_3. Only some of the early studies and some of the most recent will be described here, in order to give some idea of the extent of progress over the past two decades. Important advances have recently been made in the application of ionic models to such materials as well as in band-theory studies and embedded-cluster studies. After reviewing the early work, contemporary studies of structure, stability, phase relations, and dynamic properties will be described, followed by recent studies of spectral properties and characteristics of the electron-density distribution for each of these materials. Attention is then turned to SiO_2, the silica polymorphs, and various compounds and clusters that may be used to model tetrahedrally coordinated Si in silica and the silicates.

4.3.1. MgO (periclase)

In the mid-1970s, accurate band-theoretical and cluster methods were first applied to MgO, with a Hartree–Fock approach being used by Pantelides et al. (1974), Hartree–Fock–Slater density-functional band and cluster approaches used by Walch and Ellis (1973), and the MS-SCF-$X\alpha$ cluster method by Tossell (1975a). These calculations represented a considerable methodological advance over the earlier calculations of Cohen et al. (1967) (employing the empirical pseudopotential method), in that they involve no parameters fitted to experiment. Comparison was made with experimental optical properties obtained by absorption or reflectance measurements, with x-ray emission spectra, and with x-ray absorption and electron-energy-loss spectra (EELS). The available photoelectron spectra were of rather poor resolution, partly due to limitations in photon sources and partly due to problems of surface preparation and contamination. Generally, spectral interpretations were made on the basis of ground-state orbital energies, although it was recognized that effects of relaxation for the various charge states (e.g., core ion states in x-ray absorption spectra) could be of importance. Such comparisons also suffered from the well-known overestimation of band gaps calculated by Hartree–Fock methods and their underestimation when calculated using density-functional theory. For example, the results of Pantelides et al. (1974), before correlation corrections, give a band gap of 18.3 eV compared to an experimental value of 7.8 eV. The width of the upper O $2p$-like valence band calculated by Pantelides et al. (1974) was more than 7 eV after incorporation of correlation, in apparent agreement with an experimental value of about 6.5 eV from Kowalczyk et al. (1977). By contrast, non-self-consistent Hartree–Fock–Slater density-functional calculations by Walch and Ellis (1973) using both a MgO_6^{10-} cluster and a band model gave band gaps around 7–8 eV for the band approach and 10–14 eV for the cluster (depending upon starting electron configuration and choice of statistical exchange parameter, α). The calculated O 2*p* bandwidth was smaller for both band and cluster results, about 2.5 eV for the band calculation and about 5 eV for the cluster, contrary to the naive expectation that bandwidths should always be larger than the spread of eigenvalues (molecular-orbital energy levels) obtained for the cluster.

It was, therefore, clear in 1974 that electronic-structure methods were not sufficiently advanced to reproduce experimental data accurately for even a simple ionic oxide such as MgO. The emphasis at the time was on the determination of the effects of different approximations upon the calculated results. Comparison was usually made between one calculation and another rather than between calculation and experiment. The theoretical papers reported the quantities arising directly from the calculations, such as orbital eigenvalues and atomic-orbital charge decompositions, and spectral properties were interpreted primarily in terms of orbital energies. No attempt was made to evaluate equilibrium structural or energetic properties.

In fact, comparison of experimental and theoretical photoelectron spectra was somewhat ambiguous. In the experimental photoelectron spectrum, one can distinguish both an overall bandwidth (i.e., the energy separation between the points at which the spectral intensity decreases to background levels) and, in most cases, a set of peaks in the intensity versus energy spectrum. It is generally easier to determine accurate values for peak energies than for bandwidths, although the peak energies and overall appearance of the spectrum will, of course, vary with the energy resolution. High-resolution x-ray photoelectron studies of MgO show a two-peak O 2*p* spectrum with a peak separation of about 2.5 eV (Kowalczyk et al., 1977) and an O 2*p* bandwidth of 6.5 eV (see Fig. 4.7). None of the existing calculations accurately reproduced this, with the band calculations giving too large a peak separation, and the cluster calculations giving too small a bandwidth.

A more detailed analysis of the chemical bonding in MgO may be obtained by a study of the full series of x-ray emission spectra, as shown by Nicholls and Urch (1976; see Fig. 2.9). The relative energies of features in the Mg $K\beta$, Mg $L_{2,3}$, and O $K\alpha$ spectra may be obtained using a MgO_6^{10-} cluster model. Essentially, the upper valence region is divided into a low-binding-energy, almost entirely O 2*p* region, and a higher-binding-energy region with some Mg *s* and *p* character mixed into the O 2*p* band. However, there has been no satisfactory explanation, as yet, of the relative intensities of these spectral peaks. No direct intensity calcula-

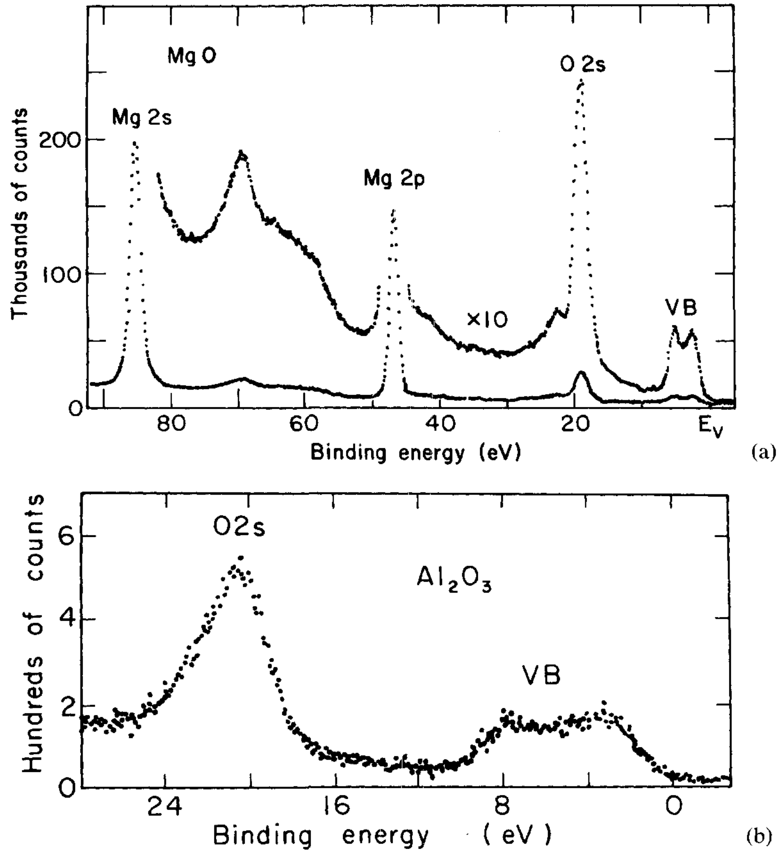

Fig. 4.7. X-ray photoelectron spectra for (a) MgO and (b) Al_2O_3 (after Kowalczyk et al., 1977; reproduced with the publisher's permission).

tions have been done either within a cluster or a band model formalism, and semiquantitative assessments of intensity based on orbital electron distribution seem inconsistent with the spectra.

The nature of the unoccupied states in MgO may be addressed through uv absorption, x-ray absorption, or electron-energy-loss spectroscopy. Comparison of Mg *K*, Mg *L*, and O *K*α x-ray absorption spectra (Fomichev et al., 1969) establishes that the lowest-energy unoccupied orbitals, giving a prominent peak in the Mg *L* x-ray absorption spectra, are predominantly of Mg 3*s* character, consistent with an "ionic" interpretation. Recent EELS studies of Mg (as well as Al and Si) *K* edges in minerals (Tafto and Zhu, 1982) have also established a unique signature for octahedral Mg, presumably involving transitions into states with Mg 3*p* character. Calculation of oxygen EELS spectra of MgO (Weng and Rez, 1989) using multiple-scattering methods reproduce the spectra semiquantitatively.

The accuracy of theoretical studies of MgO began to improve substantially in the late 1970s and early 1980s particularly because of interest in its high-pressure behavior, a topic further discussed in Chapter 7. The self-consistent Korringa–Kohn–Rostoker band calculations of Liberman (1978) established for both *B*1 (NaCl structure-type) and *B*2 (CsCl structure-type) phases that the band gap actually increases with applied pressure to above 1 Mbar and only approaches zero (metallization) under pressures on the order of 50 Mbar. The calculated pressure versus volume curves for the *B*1 phase are also in reasonable agreement with experiment. This result for the band gap was supported by the later augmented-plane-wave calculations of Bukowinski (1980), establishing that experimental reports of MgO metallization at mantle pressures were erroneous. Modified electron-gas studies by Cohen and Gordon (1976) gave a reasonably accurate lattice constant and compressibility for MgO and predicted a *B*1→*B*2 transition pressure of 256 GPa. Self-consistent KKR calculations were reported by Yamashita and Asano (1983a), which yielded accurate lattice constants, cohesive energies, and bulk moduli for MgO, using any of a number of different exchange-correlation potentials. The equation of state was also in good agreement with experiment. More recently, self-consistent (APW) methods (Bukowinski, 1985), *ab initio* pseudopotential methods (Chang and Cohen, 1984), potential-induced-breathing ionic model methods (Mehl et al., 1986), full potential linear augmented-plane-wave methods (Mehl et al., 1988), and *ab initio* Hartree–Fock methods (Causa et al., 1986a; Pisani et al., 1988) have been used to calculate the *B*1→*B*2 transition pressure for MgO. Although all methods give transition pressures above 200 GPa, consistent with the lack of an experimentally observed transition at pressures up to 120 GPa, the calculated values differ by a factor of five. In addition, the pseudopotential results apparently underestimate the O 2*p* valence-band width (although no densities of states were given to compare with experiment) and certainly underestimate the band gap, as is observed in other density-functional calculations. Early Hartree–Fock band-structure calculations on MgO (Causa et al., 1986a) yielded a *B*1→*B*2 phase transition pressure of 220 GPa, but exponent optimization increased this value to 770 GPa (Pisani et al., 1988). The equilibrium parameters at ambient pressure for the *B*1 phase were also in good agreement with experiment.

Modified electron-gas procedures also yield quite accurate results for equilibrium and dynamic properties of MgO, if the effect of the Madelung potential upon the oxide ion charge density is properly incorporated, as in the potential-induced breathing model (Mehl et al., 1986, and references therein). As described previously, this approach yields less information than that from a band calculation (e.g., no spectral quantities are obtained), but it is extremely rapid computationally and can readily be extended to low-symmetry situations, so as to evaluate properties such as shear moduli in addition to the bulk moduli readily obtained from the band calculations. The calculated $B1 \rightarrow B2$ transition pressure using the PIB form of this model is also 251 GPa, in good agreement with other estimates. MgO has also been used as a test case for two other forms of the shell-stabilized MEG method: one in which the charge on the stabilizing Watson sphere is reduced below 2.0 (to ~ 1.7) to reflect the actual charge within the Watson sphere (Jackson and Gordon, 1988a), and one in which the Watson sphere radius is varied to obtain the lowest total energy (Wolf and Bukowinski, 1988), called a variationally stabilized MEG method. Differences between the results of these methods and the PIB results are at the 1% level for the 1 atmosphere density but can be significantly larger for the bulk modulus and the $B1 \rightarrow B2$ phase-transition pressure. It is not yet clear whether either of these procedures will lead to systematically improved results for other oxides.

It is now clear that accurate band-theoretical and MEG results for MgO are converging toward the experimental values, but even for this simple material some important properties (e.g., the $B1 \rightarrow B2$ transition pressure) are very sensitive to details of the method. Nonetheless, all accurate methods agree that the transition pressure is above the range of pressures encountered in the Earth's mantle.

There has also been a great deal of interest in assessing the nature of the bonding in MgO. The basic question is whether MgO can be considered, in some sense, an "ionic" material. There are a number of ways in which such a question can be answered, all of which focus upon one or more properties of the material and consider how accurately they can be described using various limiting models. An old criterion is to utilize a semiempirical pair potential of ionic form (i.e., point-charge Coulomb interaction plus short-range repulsion) and evaluate the lattice energy. Another approach is to construct charge densities by superposition of limiting-case component atomic or ionic charge densities and calculate properties for these limiting cases. The general observation is that many properties vary little with the assumed input charge densities. A third approach is to calculate accurately some fundamental observable, such as the electron density, and then examine the match between it and simple model quantities. There is also the question of how much refinement a model can undergo without losing its essential character. For example, a charge-density model for MgO in which the component anion charge densities vary with their site potentials could reasonably be described as ionic, whereas a model in which the valence electron density is distributed among shells, some situated along bond directions, might be reasonably described as partly covalent.

We shall consider, in detail, studies of MgO lattice properties using the potential-induced breathing model and three complementary band-theoretical studies of electron distribution. Early studies using the modified electron-gas method (Cohen and Gordon, 1976) gave reasonably good agreement with experiment for equilibrium static lattice properties and bulk modulus, and predicted a $B1 \rightarrow B2$ transition pressure of 256 GPa. However, in the early studies, the effect of lattice potential on the O^{2-} charge density was not determined in a self-consistent way. When the lattice potential was incorporated self-consistently by Mulhausen and Gordon (1981), agreement with experiment was somewhat improved. Further improvement occurred when the effect of lattice potential on oxygen self-energy was correctly incorporated (Hemley et al., 1985). Allowance for relaxation of the O^{2-} ion density as a function of lattice Madelung potential for both the high-symmetry lattice and for the distorted lattice arising from shear motion, allowed an accurate calculation of both the bulk modulus and the elastic modulus tensor, including the failure to satisfy the Cauchy relation, $C_{12} = C_{44}$ (Mehl et al., 1986). The latter observation is very important, since departures from the Cauchy relation have traditionally been considered indicative of covalent (or at least of "three-body") forces. The calculations thus established that an ionic-model approach to pair potentials could, in fact, explain this failure with semiquantitative accuracy.

Three studies using band-theory approaches that address the question of bonding character and charge distribution in MgO are those of Bukowinski (1980), Causa et al. (1986a), and Redinger and Schwarz (1981). Bukowinski (1980) and Redinger and Schwarz (1981) performed augmented-plane-wave calculations and analyzed the charge distribution both by radial charge-density plots within the atomic spheres, and by integrations of total charges within the spheres. Redinger and Schwarz (1981) also compared the APW charge distributions with those obtained through superposition of free spherical atoms or Watson sphere stabilized ions. The general conclusion was that MgO is very close to the "ionic limit," with only a small valence charge density within the Mg sphere associated with the "tails" of the O $2p$ functions, and with ~ 7 valence electrons within the sphere and ~ 1 valence electron in the intersphere region. However, it was noted that such a distribution of charge could almost equally well be obtained by a superposition of free atoms in which charge would be accumulated on the oxygen through charge overlap, or by a superposition of free ions in which charge is accumulated on the oxygen through charge transfer. Comparison of the difference density for superimposed atomic and ionic models compared to the APW density do show, however, that the discrepancies are considerably smaller for the ionic-model limit. In fact, a properly Watson-stabilized O^{2-} ion density reproduces the APW results almost exactly. Both workers note that the effect of lattice stabilization on the anion electron density is quite significant. The Hartree–Fock study of Causa et al. (1986a) discusses the electron distribution both in terms of Mulliken populations and in terms of electron-density distributions. The Mulliken charges indicate almost complete charge transfer, and the electron-density maps at Mg and O are consistent with a Watson-stabilized ion model. Causa et al. (1986b) and Podloucky and Redinger (1984) have also considered the electron momentum distributions in MgO as obtained by the technique of Compton scattering. The general result is that the Compton scattering data are reasonably consistent with an ionic model, but that both ionic models and band calculations, whether APW or Hartree–Fock, underestimate the density of slow electrons. Such an underestimation appears to be a correlation effect, which can only be eliminated using very high-level calculations of the type performed for small molecules like H_2O.

The use of electron densities or interaction energies from accurate *ab initio* calculations to generate pair potentials for simulations is a powerful approach. A version of this approach was developed for MgO by Boyer (1983). He fitted O^{2-} electron densities from an APW band calculation on MgO to a Slater-orbital basis set and used the resulting electron density to calculate pair potentials within a MEG scheme. These potentials were then very efficiently used within a quasiharmonic approximation (see Chapter 3) to calculate the normal-mode vibrational frequencies as a function of volume, the vibrational free energy and pressure, and the thermal expansion, obtaining results in reasonable agreement with experiment. This approach also allows calculation of the temperature at which the isothermal bulk modulus will go to zero (when the vibrational pressure exceeds the static pressure for all values of lattice constant). This critical temperature is, in many cases, very close to the melting point and, therefore, provides a way to estimate the melting point without considering the free energy of the melt (which would have to be treated by a statistical-mechanical technique such as molecular dynamics).

4.3.2. Al_2O_3 (corundum)

In contrast to the extensive theoretical studies described above for MgO, there has been relatively little theoretical research on Al_2O_3. This is primarily due to the much larger and less symmetric unit cell (two Al_2O_3 units) for this corundum structure material. Another factor may be that Al_2O_3 is not expected to be quite so well described by a model involving spherical ions, partly because of a smaller electronegativity difference between the ions than that in MgO, and partly because of the low symmetry at the Al and O sites. This neglect is unfortunate, since Al_2O_3 is an important ceramic material and ruby ($Cr{:}Al_2O_3$; corundum containing Cr as an impurity) provides the calibration material for many high-pressure studies.

The first theoretical studies on Al_2O_3 were of electronic structure and spectra. Photoelectron studies on Al_2O_3 (Balzarotti and Bianconi, 1976; Gignac et al., 1985) show a two-peak O 2*p* valence band with a peak separation of 4–4.7 eV and an overall width of about 8.5 eV (Fig. 4.7). Cluster calculations using the MS-SCF-$X\alpha$ method (Tossell, 1975a), and the semi-empirical molecular-orbital EHMO (Ciraci and Batra, 1983) and CNDO

(Balzarotti et al., 1984) methods, all give orbital energies for AlO_6^{9-} clusters in qualitative agreement with the experimental photoelectron density of states. The EHMO band calculations of Ciraci and Batra (1983) also give a density of states in reasonable agreement with the photoelectron results, for both the O 2*p* upper valence band and the O 2*s* lower valence band. No significant difference is seen in the photoelectron spectra of the various crystalline and amorphous forms of Al_2O_3. Comparison can also be made with x-ray emission spectra obtained in the Al *K*β, Al *L*, and O *K*α regions (see Tossell, 1975a). Similarly, the empty states can be probed by x-ray absorption (Balzarotti et al., 1984) and by electron-energy-loss spectroscopy (Gignac et al., 1985). Comparison of energies from photoelectron spectra with energies and intensities in x-ray emission spectra allows identification of the higher-binding-energy feature in the upper valence band as having substantial Al *s* character (the $6a_{1g}$ orbital within an AlO_6^{9-} cluster model).

Comparison of the various x-ray emission and x-ray absorption spectra of Al_2O_3 on a common energy scale and employing selection rules appropriate to the AlO_6^{9-} octahedral cluster yields assignments for the features shown in Table 4.7 (from Tossell, 1975a). The general conclusion is that the states with Al *s* character lie lowest in energy, followed by the Al *p* and Al *d* states. A surface state was found to lie more than 4 eV below the valence-band minimum. EHMO calculations on the α-Al_2O_3(0001) surface indicate the presence of surface states involving Al *s* orbitals and Al *p* orbitals perpendicular to the surface. However, the energies of these orbitals seem to be strongly dependent upon geometry and atomic charge. Surface studies are discussed in detail in Chapter 7.

Table 4.7. Comparison of relative molecular-orbital energies (ΔE in eV) in Al_2O_3 obtained from x-ray emission and absorption spectra and from calculations using the MS-SCF-$X\alpha$ method on an AlO_6^{9-} cluster (after Tossell, 1975[a])

Molecular-orbital assignment	Experimental ΔE	Calculated ΔE
Al Kβ x-ray emission spectrum		
$4t_{1u}$	−15.6	−15.1
$5t_{1u}$	−2.2	−3.1
$6t_{1u}$	0	0
Al *L* x-ray emission and absorption spectra		
$2t_{2g}$	12.7	+11.4
$7a_{1g}$	10.1	+7.5
$2e_g$	0	0
$1t_{2g}$, $6a_{1g}$	−3.5	−2.7
$5a_{1g}$, $1e_g$	−16.0	−16.1
O *K*α x-ray emission spectra		
$1t_{1g}$-$1t_{2u}$	0	0
$1t_{2g}$-$5t_{1u}$	−4.1	−3.1

There have been many studies of the equilibrium geometry and energy of Al_2O_3 using semiempirical ionic models, and some incorporating shell model distortion of the oxygen anions. Early studies using the modified electron-gas model without a self-consistent O^{2-} electron density (Tossell, 1980) yielded reasonable agreement with experiment, but revealed systematic errors in the Al–Al distances, which were much too long. Recent MEG calculations incorporating potential-induced breathing (Cohen et al., 1987; Cohen, 1987) give better agreement with experiment. The c:a axial ratio and the internal O and Al coordinates calculated for the Al_2O_3 crystal still show substantial errors (attributed by Cohen, 1987, to deficiencies in the kinetic-energy expression) giving Al–Al distances that are too long. Nonetheless, the calculated equation of state and elastic constants are in quite good agreement with experiment (see Table 4.8). The results also indicate high-pressure lattice instabilities that are certainly of interest to experimentalists using ruby as a high-pressure calibrant. Further studies using the PIB method (with a number of different forms for the input ion charge densities and the details of the exchange-correlation energy functional) confirm that a Rh_2O_3(II) structure for Al_2O_3 should become most stable thermodynamically somewhere between 6 and 62 GPa (Cynn et al., 1990). Al_2O_3 is currently being studied experimentally at high pressure to determine whether the predicted phase transitions actually occur. *Ab initio* Hartree–Fock band calculations have recently been reported for Al_2O_3 (Causa et al., 1987) at the equilibrium geometry with a STO-3G basis set. The calculated density of states has a two-peak structure and approximately the width seen in the photoelectron spectra. The Al and O Mulliken charges from this minimum-basis-set calculation are similar to those obtained in an x-ray diffraction study (Lewis et al., 1982).

Table 4.8. Elastic constants (in GPa) and their pressure derivatives at zero pressure for corundum (from Cohen, 1987), calculated using the potential-induced breathing model and compared with experimental (expt.) values[a]

	Elastic constants		**$\delta/\delta P$ of elastic constants**	
	PIB static	**Expt.**	**PIB static**	**Expt.**
C_{11}	540	498	5.78	6.17
C_{12}	157	163	3.44	3.28
C_{13}	130	177	3.56	3.65
C_{14}	−48	−23	0.18	0.13
C_{33}	455	502	4.36	5.00
C_{44}	157	147	1.62	2.24
C_{66}	191	168	1.17	1.45
$K\ (=B_R)$	261	254	4.06	4.32
B_V	264	255	4.11	4.28
G_V	176	166	1.24	1.64
G_R	163	161	1.50	—

[a] See Cohen (1987) for clarification of symbols and for sources of experimental data.

Charge-density difference maps from the band calculation (crystal minus superimposed free atoms) clearly show charge transfer, but the limited basis set precludes detailed comparison with experiment.

Another feature of the charge distribution in Al_2O_3 that has been much studied is the electric field gradient (EFG) at Al, which can be obtained from the Al nuclear quadrupole coupling constant (NQCC) derived from NQR or NMR spectroscopy. This property has traditionally been calculated within an ionic model, using both monopole and higher-order terms, and sometimes incorporating distortion of the ions due to their mutual overlap. Within this approach the EFG at the Al site induces an enhanced EFG at the Al nucleus through "antishielding," distortion of the core *p* orbitals resulting from the valence-region EFG. This model has recently been tested by Nagel (1985c) using an MS-SCF-$X\alpha$ cluster method, modified to avoid the muffin-tin averaging of the charge distribution. He found that the local contribution to the NQCC of Al was about 80% of the total, while the lattice sum contribution was only about 20%. The local contribution arose mainly from charge transfer from O to the Al 3*s*, 3*p*, and 3*d* orbitals rather than from distortion of the Al 2*p* core. The overall NQCC calculated was in good agreement with experiment. As noted by Nagel (1985c), previous ionic-model studies had also obtained good agreement, but the earlier studies utilized adjustable or inaccurately known antishielding parameters. The difference densities obtained from this MS-SCF-$X\alpha$ study, as well as those from the Hartree–Fock band calculation and experiment, show almost spherical ions with no (or weak) charge accumulations along the Al–O bonds. By contrast to the results for the EFG at Al in the AlO_6^{9-} cluster, the MS-SCF-$X\alpha$ calculation of the oxygen EFG from an Al_4O cluster calculation seems to be qualitatively incorrect, both in comparison to experiment and to the Hartree–Fock band calculations. This illustrates the principle that metal-centered oxygen-rich clusters seem to give much better representations of bulk solids than the reverse oxygen-centered clusters, at least for ordinary choices of boundary conditions. Lewis et al. (1982) attempted to evaluate the EFG at Al directly from their x-ray-determined charge density, but concluded that only the qualitative symmetry and sign of the EFG could be determined, not accurate numerical values. In general, the valence electron density and the nuclear EFGs were found to be loosely coupled, so that one property was not well constrained by the other. The density difference maps were also found to depend significantly on the details of the x-ray refinement.

The electronic structure of $Cr^{3+}:Al_2O_3$ has also been studied by a number of workers using density-functional theory. Attention has been focused on the so-called *R* peak and *U* band, corresponding roughly to the single-electron transitions: $t_{2g\uparrow} \rightarrow t_{2g\downarrow}$ (spin flip) and $t_{2g} \rightarrow e_g$ (crystal field), respectively. Experimental and calculated energies for these transitions are given in Table 4.9. Shangda et al. (1987) showed that the calculated

Table 4.9. Optical absorption transition-state calculation for ruby, Cr:Al_2O_3 *(energies in eV)*

	Peak *R*	**Band *U***
Transition	spin flip $t_{2g\uparrow} \rightarrow t_{2g\downarrow}$	crystal field $t_{2g} \rightarrow e_g$
Experimental data	1.79	2.26
Parameter fitting	1.83	2.12
DV-$X\alpha$ calc. on isolated CrO_6	1.63	2.27
Embedded cluster $Cr\bar{O}_6$	2.29	2.70
Embedded cluster $(Cr\overline{AlO}_6)$	2.17	2.74

Source: From Shangda et al., 1987.

spectrum for Cr^{3+} in an unrelaxed Al_2O_3 oxygen environment exhibits a trigonal splitting much larger than that observed experimentally. Requiring octahedral symmetry for the nearest-neighbor oxygens (their $Cr\bar{O}_6$ cluster, where the bar signifies an O modified by their embedding procedure), and embedding the cluster in the potential for undistorted Al_2O_3, gave a qualitatively correct spectrum, but the excitation energies were in worse agreement with experiment than for an isolated CrO_6^{9-} cluster. Larger clusters were considered, for example, $Cr\overline{AlO}_6$ in which the nearest-neighbor Al and the six oxygens are allowed to relax and all their electrons treated explicitly, with this cluster embedded in the Al_2O_3 lattice potential. This model is in only marginally better agreement with experiment. No studies of $Cr^{3+}:Al_2O_3$ spectra as a function of applied pressure or Cr–O distance have been published. Earlier unpublished MS-SCF-$X\alpha$ studies by Tossell yielded the surprising result that the spin-flip transition $t_{2g\uparrow} \rightarrow t_{2g\downarrow}$ producing the sharp *R* peak actually decreases in energy as the Cr–O distance decreases. Clearly, a study of this property using a method avoiding the model potential assumptions of MS-SCF-$X\alpha$ would be desirable.

4.3.3. SiO_2 [silica polymorphs; also $Si(OH)_4$, SiO_4^{-4}, $(SiH_3)_2O$, and $(OH)_3SiOSi(OH)_3$]

The same methods described for the SiF_4 molecule in the earlier part of this chapter may also be applied to $Si(OH)_4$, a model for tetrahedrally coordinated Si in silica and the silicates. Hess et al. (1986, 1987) have calculated the geometry and vibrational frequencies of this molecule in both its D_{2d} and its equilibrium S_4 symmetry geometries. A tabulation of earlier SCF results for $Si(OH)_4$ is given in Sauer (1989), and the previous results of Sauer (1983) have been presented in Table 3.2. The equilibrium Si–O bond distance of 1.629 Å calculated using a Hartree–Fock–Roothaan method with 6-31G** basis set (and found for both D_{2d} and S_4 symmetries) is close to the average value for orthosilicates; the calculated vibrational frequencies for D_{2d} symmetry $Si(OH)_4$ are between those observed in aqueous silicate solutions, presumably containing $SiO_2(OH)_2^{2-}$, and those observed in orthosilicate glasses (e.g., $CaMgSiO_4$) as shown in Table 4.10. Of course, $Si(OH)_4$ is only a simple model for the silicate species occurring in condensed phases, and so we can expect it to reproduce at best only the average properties of such species. Nonetheless, agreement between calculation and experiment for the $Si(OH)_4$ species, although slightly poorer than that for SiF_4 (Hess et al., 1986), is good enough to suggest that the basic features of the Si–O bonding are being correctly reproduced. The $Si(OH)_4$ results also indicate that, in contrast to the usual assumption of rigidity for the $SiO_4{}^{4-}$ tetrahedral group, the O–Si–O angles are, in fact, readily deformable within the range of about 103–116°, consistent with experimentally observed values in olivines. Further, the torsional angles (angles of the H–O–Si versus the O–Si–O planes) and O–Si–O angles are strongly coupled (Hess et al., 1988).

These results for $Si(OH)_4$ are consistent with the observation that average bond distances in solids can be reproduced quite well using molecular cluster models and *ab initio* Hartree–Fock techniques, at least for three- to six-coordinate central metal atoms from the first through third rows of the Periodic Table. Gibbs et al. (1987) have shown excellent agreement between calculated equilibrium bond distances in tetrahedral molecules and average experimental bond distances for tetrahedrally coordinated metal atoms. For the third-row elements, the addition of flexible *d* polarization functions was required to match experiment closely (in

Table 4.10. The Si–O bond lengths [R(Si–O)] and vibrational frequencies calculated[a] using Hartree–Fock–Roothaan (SCF) molecular-orbital methods with different basis sets and compared with experimental[b] properties of $Si(OH)_4$ in D_{2d} symmetry

Basis set	***R*(Si–O) (Å)**
STO-3G	1.655
6-31G	1.662
6-31G*	1.629
Experimental value (average)	1.635 (Si–O in monosilicates)
	Vibrational frequency (cm^{-1}) A_1 **Symmetric stretch**
STO-3G	770
6-31G	604
6-31G*	816
Experimental value	854

[a] From Hess, McMillan, and O'Keeffe (1986).

[b] From Piriou and McMillan (1983).

agreement with studies by other researchers on related gas-phase molecules). However, for central atoms from the second row, relatively modest basis sets give reasonable absolute average values and properly reproduced trends as a function of both central atom identity and coordination number.

Another structural parameter of great importance in silicate mineralogy is the Si–O–Si bond angle, which has a typical value around 140–150° but shows a range of observed values from about 120° to 180°. For the simplest possible molecular model, disiloxane $(SiH_3)_2O$, *ab initio* Hartree–Fock–Roothaan (SCF) calculations with an STO-3G basis set give a minimum-energy Si–O–Si angle as noted in Chapter 3 (Table 3.2) but only at the double ζ plus polarization basis-set level are both the Si–O distance and Si–O–Si angle reproduced correctly, as shown in Table 4.11. Indeed, disiloxane appears to be a very flexible molecule with a very small barrier to linearity. The calculated equilibrium Si–O–Si angle is even sensitive to the detailed values chosen for the O 3*d* and Si 3*d* Gaussian orbital exponents (Grigoras and Lane, 1987). Only when SCF-CI calculations are done can quantitative accuracy in the Si–O–Si angle and the barrier to linearity be obtained (Koput, 1990). However, even for more strongly bent molecules, inclusion of *d* polarization functions on the oxygen has generally been found necessary to obtain accurate bond angles (Hehre et al., 1986). A molecular species that is probably more relevant to mineralogy, although involving more demanding computation, is $(OH)_3SiOSi(OH)_3$. This molecule has a deeper energy minimum as a function of Si–O–Si angle and low-level calculations such as *ab initio* Hartree–Fock–Roothaan calculations with an STO-3G basis set fortunately give reasonable equilibrium Si–O–Si angles, as also shown in Table 4.11. Full optimization at the 6-31G* basis-set level also gives accurate bond distances and angles. Note that no unpolarized split-valence basis-set results have been reported for $(OH)_3SiOSi(OH)_3$ because such studies on $(SiH_3)_2O$ gave poor results. Similar methods have been applied to a num-

Table 4.11. Hartree–Fock–Roothaan SCF molecular-orbital calculations of Si–O–Si angles (in degrees) for $(SiH_3)_2O$ and $(OH)_3SiOSi(OH)_3$

Basis set	$(SiH_3)_2O$[a]	$(OH)_3SiOSi(OH)_3$
STO-3G	128 [*R*(Si–O) = 1.63 Å]	137 [*R*(Si–O) fixed at 1.62 Å][b]
DZ	180	—
DZ + Si *d*	180	—
DZ + O *d*	145	—
DZ + Si, O *d*	154 (143)	139 [*R*(Si–O) = 1.615, 1.623 Å, opt.][c]
Experimental value	144 (α-quartz)	

[a] Ernst et al. (1981) and references therein; see also Sauer (1989).

[b] Gibbs (1982).

[c] O'Keeffe and McMillan (1986).

ber of molecules containing *T*–O–*T* linkages (where *T* is a tetrahedrally coordinated metal atom), and they show minimum energy angles, and variations of energy with angle, consistent with the average values and the ranges of bridging angles observed in solids (Geisinger et al., 1985).

It is worth noting here that *ab initio* cluster calculations can also be used to evaluate the compressibility or bulk modulus of the SiO_2 polymorphs. *Ab initio* Hartree–Fock–Roothaan calculations on $H_6Si_2O_7$ by Newton et al. (1980) using a STO-3G basis set yielded a value of 3.97×10^{10} Pa for the bulk modulus of α-quartz, in fortuitous agreement with the experimental value estimated as 3.93×10^{10} Pa. Using a 6-31G* basis set (*d* functions on both Si and O), O'Keeffe and McMillan (1986) obtained a value of 5.1×10^{10} Pa, consistent with the usual overestimation of force constants at this level of calculation. Calculations on structure and compressibility for α-quartz using Hartree–Fock band theory at the STO-3G basis-set level (Dovesi et al., 1987) give results much like those from the STO-3G cluster calculations and will be discussed in more detail in Chapter 7.

As discussed in Chapter 2, accurate x-ray diffraction studies give information on electron-density distributions in solids. Such studies for coesite (Geisinger et al., 1987) show that the difference density, or difference of total electron density and the sum of the superimposed free spherical atom electron densities, shows bond-charge accumulations in reasonable agreement with calculated electron-density distributions for $Si_4O_4H_8$ (Fig. 4.8). However, rather than being directly along the Si–O internuclear vectors, the bond-charge peaks are displaced into the interior of the Si–O–Si angle (i.e., the bonds are "bent"). Such bent bond character is shown in the calculations for any value of the Si–O–Si angle (i.e., the bond-charge distribution is reasonably independent of the angle chosen). At present, the valence electron-density distribution is primarily useful for testing the adequacy of theoretical models and giving some qualitative idea of bond character. For example, Hartree–Fock band calculations on α-quartz using an STO-3G basis set (Dovesi et al., 1987) show essentially no bond-charge accumulation, in disagreement with the 6-31G* basis-set cluster calculation results of Gibbs (1982). This result probably arises from insufficient basis-set flexibility in the band calculations. More quantitative interpretation of bond character from such electron-density maps awaits a fuller understanding of the relationship of difference densities to other properties, as will be discussed in Chapter 7.

Further information on the electronic structure of SiO_2 and other silicates may be obtained from various spectroscopic studies. An excellent review of the various spectra and their interpretation can be found in Griscom (1977). We will consider, in turn, the photoelectron, x-ray emission, x-ray absorption, uv absorption, Auger, NMR, and NQR spectra of SiO_2, primarily in the quartz polymorph. A discussion of the spectra of other polymorphs of SiO_2 and their differences compared to quartz will be presented in Chapter 7.

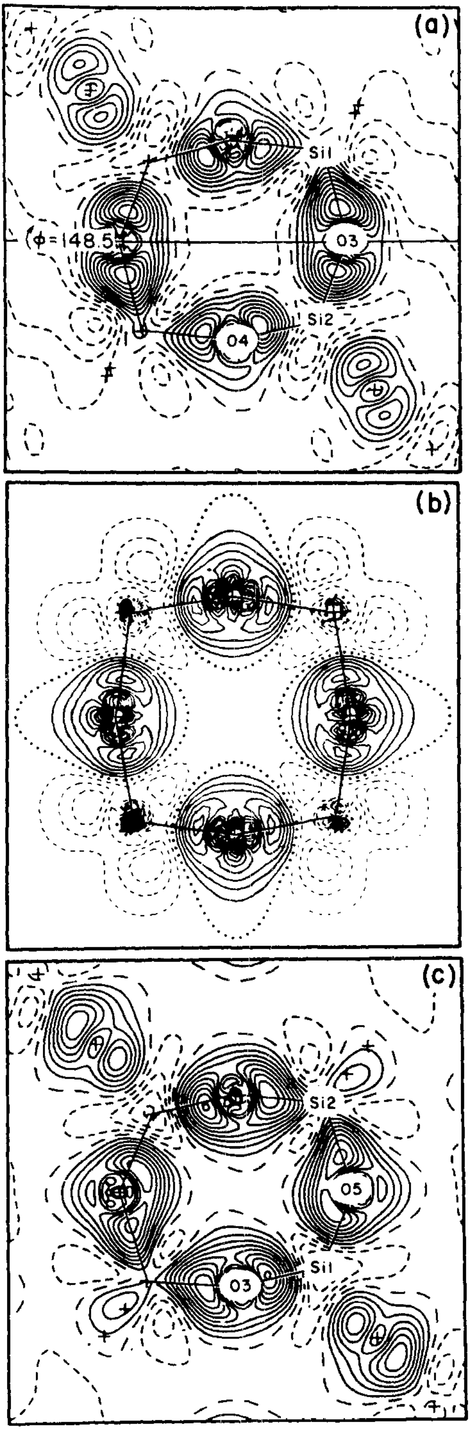

Fig. 4.8. Total deformation electron densities ($\Delta\rho$) in 4-membered silicate rings: (a) experimental $\Delta\rho$ in O(3)–O(4) ring of coesite; (b) theoretical $\Delta\rho$ for $H_8Si_4O_4$, calculated using Hartree–Fock–Roothaan method with a 6-31G* basis set; and (c) experimental $\Delta\rho$ in O(3)–O(5) ring of coesite (after Geisinger et al., 1987; reproduced with the publisher's permission).

In photoelectron spectroscopy, the energies required to create various ion states starting from the neutral material are determined (see Section 2.2.1). Both the energies and the intensities of the peaks in the photoelectron spectrum may yield information on the electronic structure of the material. As described in Chapter 2, different relative intensities are obtained from different excitation sources. As noted earlier in this chapter for SiF_4, calculations at the Hartree–Fock plus MBPT level can accurately reproduce ionization energies in the upper valence region, but inner-valence ionization spectra are still difficult to calculate accurately. Inspection of the x-ray and ultraviolet photoelectron spectra of amorphous SiO_2 [Fig. 4.9, adapted from DiStefano and Eastman (1971) by Griscom (1977)] shows their similarity to that of gaseous SiF_4.

The SiO_2 spectrum may be interpreted using either a cluster model (e.g., SiO_4^{4-}) or a band-theoretical model for a SiO_2 polymorph. The bond character of the states generating the photoelectron spectrum features may be determined from energy, symmetry, atomic function composition, or charge density within the calculation. Within a cluster model, it is generally easy to account for relaxation, and incorporation of correlation corrections, though more difficult, is still feasible. Consideration of such effects in an *ab initio* way in a band-theoretical calculation is more difficult since, if the hole produced by photoemission is localized, it will disrupt the translational periodicity of the lattice. Recently, supercell approaches, that is, consideration of a material with a larger unit cell and periodic

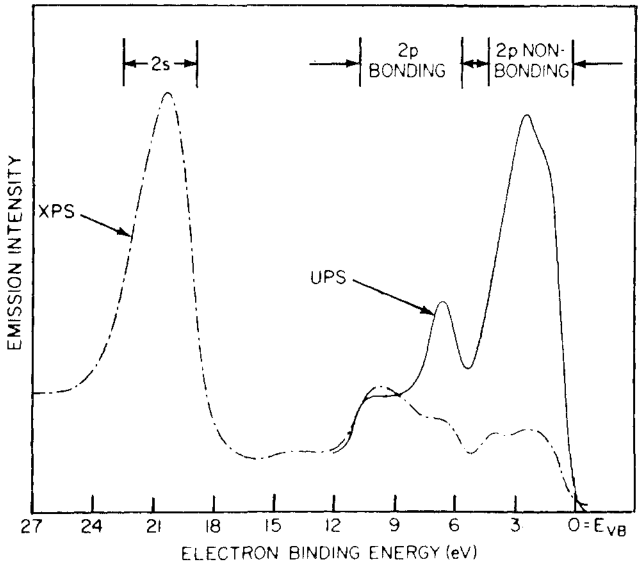

Fig. 4.9. X-ray photoelectron (XPS) and ultraviolet photoelectron (UPS) spectra of amorphous SiO_2 [from Griscom (1977) modified from DiStefano and Eastman (1971); reproduced with the publisher's permission].

holes, have become feasible for some materials. On the other hand, cluster calculations obviously cannot incorporate all of the interactions present in the solid. In favorable circumstances, they can reproduce the main features in the density of states, but cannot properly give the breadth of the features.

For simplicity, we will qualitatively interpret the photoelectron spectrum of SiO_2 using the MS-SCF-$X\alpha$ cluster calculation on SiO_4^{4-} (shown in Fig. 4.10) as our interpretive model (Tossell et al., 1973b). The feature with the lowest binding energy (~2 eV in Fig. 4.9) is then identified with the $1t_1$ orbital, which is essentially O $2p$ nonbonding, and the feature at ~4 eV is identified with $1e$ and $5t_2$ orbitals, which are weakly Si p,d–O $2p$ π bonding. At higher binding energies lie the $4t_2$ orbital (~7 eV), with Si $3p$–O $2p$ σ bonding character, and the $5a_1$ orbital (~10 eV), with Si $3s$–O $2p$ σ bonding character. In the inner-valence region are the $3t_2$ and $4a_1$ orbitals (~22 eV), which are both predominantly O $2s$ in character but with some Si $3p$ or $3s$ contribution, respectively. Assessment of the orbital type for the various peaks from band calculations (Chelikowsky and Schluter, 1977) is similar; the lowest-binding-energy peak is O $2p$ non-

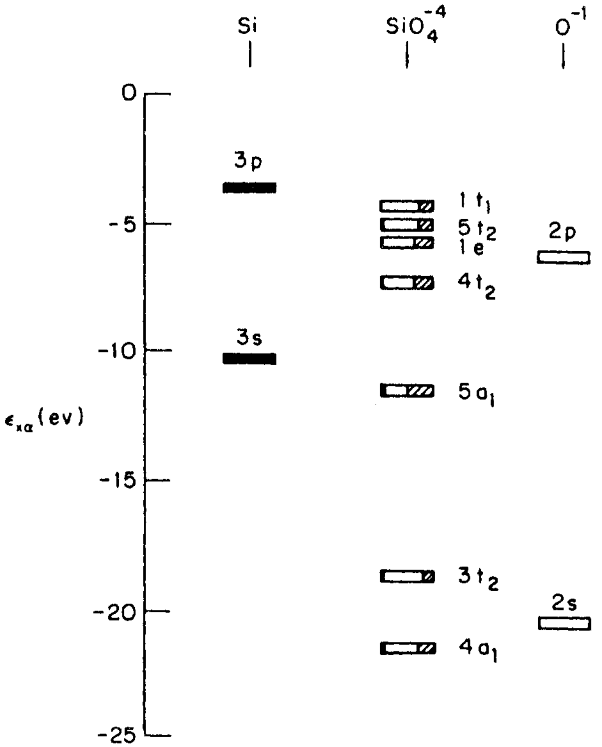

Fig. 4.10. Molecular-orbital diagram for the SiO_4^{4-} cluster from MS-SCF-$X\alpha$ calculation (after Tossell et al., 1973b; reproduced with the publisher's permission).

bonding; the density of states maximum corresponding to the $4t_2$ orbital is Si $3p$, O $2p$ bonding; the peak corresponding to the $5a_1$ is Si $3s$–O $2p$ σ bonding; and the DOS maximum corresponding to the $3t_2$ and $4a_1$ orbitals is predominantly O $2s$ in character. Calculated and experimental energies are shown in Table 4.12. There are relatively minor differences between different band calculations for a given polymorph, and modest but measurable differences between the photoelectron spectra of α-quartz and the various other SiO_2 polymorphs. In the $5a_1$ region, both the α-quartz photoelectron spectrum and the quartz band calculations show a two-peak structure arising from mixing of Si $3s$–O $2p$ and Si $3p$–O $2p$ like states away from the center of the Brillouin zone. Discrepancies between calculation and experiment are actually largest in the O $2s$ region for both cluster and band calculations, and localization of the photoelectron hole may increase the magnitude of relaxation and correlation effects in this region, as observed in SiF_4.

In addition to the reasonable agreement of experimental and calculated photoelectron energies, the overall intensity distribution is given reasonably well by cluster and band calculations. DVM-$X\alpha$ cluster calculations (Sasaki and Adachi, 1980a,b) on SiO_4^{4-} reproduce the overall valence-region x-ray photoelectron spectrum intensities observed in Li_4SiO_4 (which are similar to those in SiO_2), although relative intensities in the upper valence region are not particularly good. The band-structure calculations of Chelikowsky and Schluter (1977) give a density of states that matches relative intensities in the photoelectron spectrum of the upper valence region fairly well, as shown in Fig. 4.11. Nucho and Madhukar (1980) have shown that the weighting of their parametrized version of the DOS by atomic-orbital photoelectron cross sections causes only slight modifications in photoelectron intensities. Similar densities of states are found in the Hartree–Fock band calculations of Dovesi et al. (1987).

The overall conclusion from these studies should be that, although the basic features of the photoelectron energies and intensities of SiO_2 can be explained by either molecular-cluster or band calculations, the quality of agreement with experiment is clearly inferior to that for SiF_4. While this may well be due to deficiencies in the methods so far applied to SiO_2, it

Table 4.12. Features in the electronic density of states for SiO_2. The energies are in eV and the valence-band maximum is referenced to zero

Feature	Experimental value	Theoretical value (LDA pseudopotential)
Nonbonding oxygen $2p$	-2.5	-2.5
Bonding oxygen $2p$–silicon $3p$	-6.5	-7.0
Oxygen $2p$–silicon $3s$	-10.0	-12.0
Oxygen $2s$	-20.5	-25.5

Source: From Chelikowsky and Schluter, 1977.

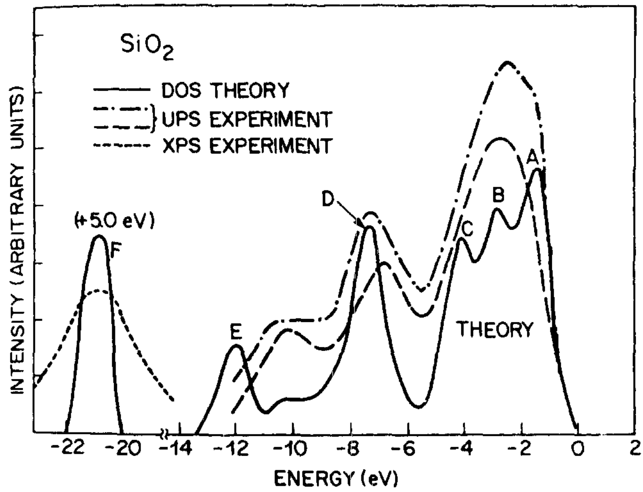

Fig. 4.11. Theoretical density of states of α-quartz from *ab initio* LDA pseudopotential calculations compared to experimental x-ray and uv photoelectron spectra (after Chelikowsky and Schluter, 1977; reproduced with the publisher's permission).

may also involve some difference in the physics of the photoionization process in solids versus molecules.

Additional information on electronic structure may be obtained from the x-ray emission spectra of the SiO_2 polymorphs. As explained in Chapter 2, x-ray emission spectra obey rather strict selection rules, and their intensities can therefore give information on the symmetry (atomic or molecular) of the valence states involved in the transition. In order to draw a correspondence between the various x-ray emission spectra and the photoelectron spectrum, the binding energies of core orbitals must be measured. In Fig. 4.12 (Fischer et al., 1977), the x-ray photoelectron and x-ray emission spectra of α-quartz are aligned on a common energy scale. All three x-ray emission spectra may be readily interpreted within the SiO_4^{4-} cluster model. Indeed, the Si x-ray emission spectra of silicates are all similar to those of SiO_2, no matter what their degree of polymerization. Some differences in detail exist between the spectra of α-quartz and other well-studied silicates, such as olivine, and such differences will be discussed later.

The O *K*α x-ray emission spectrum shows transitions from the O 1*s* core into valence-band states with significant O 2*p* character. The maximum in the O *K*α x-ray emission spectrum can be identified with the $1t_1$ O 2*p* nonbonding orbital, while three additional features at higher binding energy can be identified with the ($1e$,$5t_2$), $4t_2$, and $5a_1$ orbitals. The $4t_2$ and $5a_1$ orbitals are expected to have significant Si contributions, which is consistent with their high intensity in the Si x-ray emission spectral series, thus reducing their O *K*α intensities. Nonetheless, there has been no

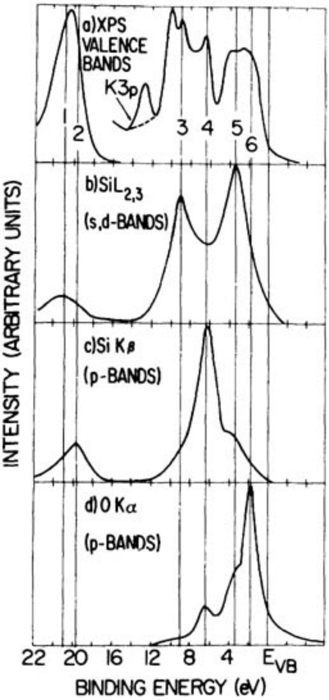

Fig. 4.12. Comparison of the x-ray photoelectron spectrum of α-quartz with the x-ray emission spectra (after Fischer et al., 1977; reproduced with the publisher's permission).

accurate calculation of O *K*α intensities incorporating localization or relaxation effects. The band calculations of the O *K*α x-ray emission spectra of SiO_2 give qualitatively correct results but significantly underestimate the intensity variation between the different peaks. It is important in obtaining a complete representation of the x-ray emission spectra to include at least the complete SiO_4 cluster. Previous studies using Si_2O were unable to reproduce the complete valence region, giving essentially a two-feature spectrum from the O 2*p* nonbonding and the Si 3*s*,*p*–O 2*p* bonding orbitals, rather than the four features found in the experimental O *K*α of SiO_2 (Gilbert et al., 1973). The Si *K*β spectrum arises through transitions from the valence-band states with Si *p* character to the Si 1*s* core. The main Si *K*β peak arises from the $4t_2$ orbital, with significant Si 3*p*–O 2*p* bonding character, while its low-binding-energy shoulder comes from the $5t_2$ orbital. An additional peak at higher binding energy comes from the $3t_2$ orbital, of predominantly O 2*s* character with some Si 3*p* admixture. Interpretation of the Si *L* x-ray emission spectrum is somewhat less certain. A two-peak structure is observed at low binding energy, consistent with contributions from the $(1e,5t_2)$ and $5a_1$ orbital sets. A small blip that may occur between them can be associated with the $4t_2$ orbital. The $4a_1$ orbital gives a Si *L* feature at considerably higher binding energy. Calculated and experimental x-ray emission energies based on these assignments are given in Table 4.13.

Table 4.13(a). Si Kβ and $L_{2,3}$ spectral results for quartz from experimental data and SiO_4^{4-} ground-state eigenvalue differences (calculated by the MS-SCF-$X\alpha$ method); energies in eV (from Tossell, 1975b). Also shown are energy separations from x-ray photoelectron spectra

	Assignment	Expt. Δ*E*	Calc. Δ*E*	Δ*E* from XPS
Si *K*β	$3t_2 \rightarrow$ Si 1*s*	−13.7	−11.3	−13.7
	$4t_2 \rightarrow$ Si 1*s*	0	0	0
	$5t_2 \rightarrow$ Si 1*s*	2.9	2.2	2.8
Si $L_{2,3}$	$4a_1 \rightarrow$ Si 2*p*	−13.0	−10.1	not resolved
	$5a_1 \rightarrow$ Si 2*p*	0	0	0
	$4t_2 \rightarrow$ Si 2*p*	3.3	4.2	≈3.0
	$1e,5t_2 \rightarrow$ Si 2*p*	5.5	5.7, 6.4	≈5.8

Table 4.13(b). O *K*α spectral results for quartz from experimental data and SiO_4^{4-} ground-state eigenvalue differences calculated by the MS-SCF-$X\alpha$ method; energies in eV (from Tossell, 1975b). Also shown are energy separations from x-ray photoelectron spectra

Assignment	Expt. Δ*E*	Calc. Δ*E*	Δ*E* from XPS
$4t_2 \rightarrow$ O 1*s*	0	0	0
$1e,5t_2 \rightarrow$ O 1*s*	3.0	1.6, 2.2	2.8
$1t_1 \rightarrow$ O 1*s*	4.8	2.7	4.8

Although the Si *L* peak energetics are easily explained with this model, the high intensity of the lowest-binding-energy peak, presumably from the ($1e,5t_2$) orbital set, is difficult to reconcile with the small percentage contribution of Si 3*d* character in these orbitals. Local-density calculations performed on the isoelectronic anions PO_4^{3-} and ClO_4^- by Tossell (1980c) and by Dietz (1983) have established that relative intensities in good agreement with experiment can be obtained if the transition moments are accurately calculated using a flexible representation of the central atom 3*d* function, accounting for the effect of the core hole on the valence orbitals using the transition-state method and including the so-called "cross transitions" involving the oxygen components of the valence orbitals, as shown in Table 4.14. Thus, the high intensity of the low-binding-energy Si *L* peak in SiO_4^{4-} does arise, at least partly, from Si 3*d* participation, but a small percentage Si 3*d* participation has a disproportionate effect on the intensity. Another interesting result of these calculations is the appreciable intensity from the $4t_2$ and $3t_2$ orbitals, which have no Si 3*s* and negligible Si 3*d* character. Contributions from these orbitals should be apparent at high resolution in the Si *L* x-ray emission spectrum.

Information on electronic structure is also present in the x-ray absorption spectrum, as has been previously discussed for SiF_4. Based on results for the SiF_4 molecule as an isoelectronic analog, and upon the SiO_4^{4-} molecular-orbital diagram, we expect to find features below the core ion-

Table 4.14. Variation of relative Cl x-ray emission spectra intensities from different calculations on ClO_4^-. Intensities are given relative to that for the $5a_1 \rightarrow$ Cl $2p$ transition

		Localized Cl $2p$ hole		
Orbital	**Pop. ratio x ($\Delta E/\Delta E_{2a_1}$)**	**Ground state**	**XES transition state**	**Delocalized Cl $2p$ hole XES transition state**
$1e$	0.15	0.91	1.25	1.68
$4t_2$	0.31	2.29	2.58	2.60
$5a_1$	1.0	1.0	1.0	1.0
$4a_1$	2.36	1.98	2.50	2.57

Source: From Tossell, 1980a.

ization potential corresponding to excitation to unoccupied a_1 and t_2 orbitals, and two resonances in the continuum, corresponding to e and t_2 symmetries. Qualitatively, exactly such spectra are observed for SiO_2 and silicates as well as for other tetrahedral oxyanions such as PO_4^{3-}, SO_4^{2-}, and ClO_4^- (Bianconi, 1988).

In Fig. 4.13 (from Griscom, 1977), the x-ray emission and absorption spectra of SiO_2 are shown on a common scale. All the above features appear in the Si L x-ray absorption spectrum, which by symmetry should sample a_1, e, and t_2 unoccupied states. In previous work (Tossell, 1975b), the lowest-energy Si L x-ray absorption peak was assigned to the t_2 orbital and the more intense peak about 2 eV higher to the a_1, on the basis of the ground-state eigenvalue spectrum of SiO_4^{4-}. This ignored the effect of core-hole creation, which is found to lower the a_1 significantly with respect to the t_2 (as shown in Tossell and Davenport, 1984; compare their Fig. 1 and Table 1). It now appears more probable that the lowest-energy Si L x-ray absorption peak arises from excitation to the a_1 orbital in SiF_4. Features appear in the Si $K\beta$ x-ray absorption spectrum from the t_2 orbitals, and there is an additional peak in the position expected for the e resonance. Although such a feature may arise from the reduction of symmetry at the real crystallographic Si site, it may also be due to intrachannel coupling in the continuum, as previously discussed for SiF_4. Thus, although such features may contain information on site distortion, one must consider other possible contributions to their intensity, such as interchannel coupling and magnetic quadrupole transitions. For the O $K\alpha$ x-ray absorption spectrum, the interpretation is less straightforward. A major peak is observed about at the position of the bound t_2 orbital observed in the Si L x-ray absorption spectrum, and a t_2 continuum peak appears about 30 eV above the O $1s$ ionization potential. However, the spectrum is broad, and it is not clear whether the SiO_4^{4-} unit is of sufficient size to describe the delocalized states involved in the continuum resonances. Multiple-scattering calculations by Stizza et al. (1987) on a Si_2O_7 cluster show a substantial effect of the Si–O–Si angle variation on

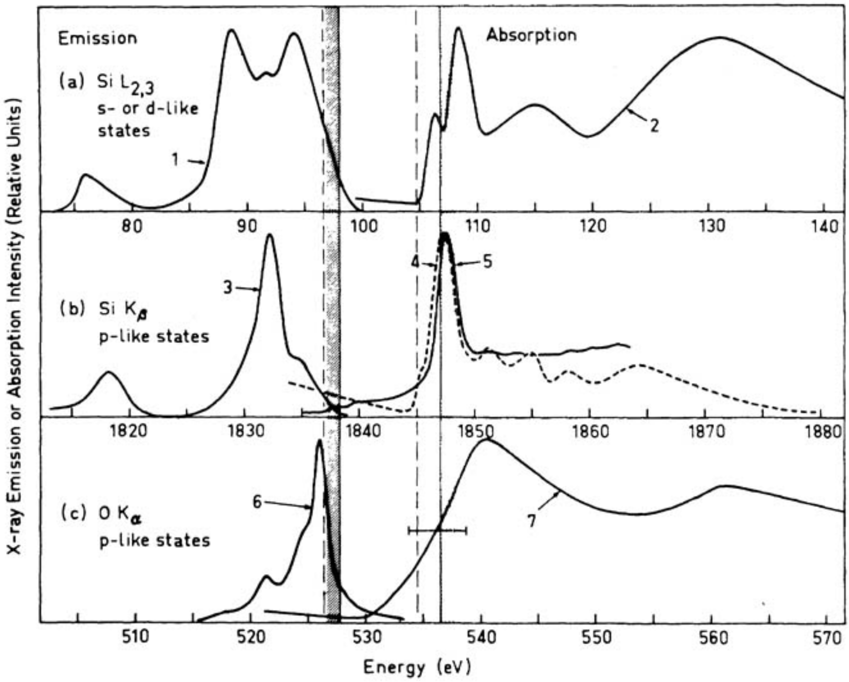

Fig. 4.13. X-ray emission and absorption spectra of SiO_2. Dashed curve in (b) is for α-quartz; other curves are for amorphous SiO_2. Vertical lines indicate the conduction-band and valence-band edges. Numbers refer to original data sources — see Griscom (1977) for further details (after Griscom, 1977; reproduced with the publisher's permission).

the peak about 25 eV above the O 1*s* ionization potential, suggesting that the x-ray absorption spectrum can give some information on the Si–O–Si angle.

Some additional information on electronic structure is available through the Auger spectra of SiO_2 (Ramaker et al., 1979). Through the use of experimental values for valence-orbital binding energies, calculated valence-orbital compositions, and fitted values for relaxation energies (which cause the Auger energy to differ from the difference of orbital binding energies by a systematic amount), the various Auger spectra can be calculated. Both energies and intensities are reasonably well reproduced. The Si *LVV* Auger spectrum of SiO_2 shown in Fig. 4.14 is actually somewhat simpler than that of SiF_4 (Rye and Houston, 1983), which apparently shows two different values of relaxation energy corresponding to two different types of hole localization.

The experimental uv spectra of SiO_2, as shown in Fig. 4.15, have been known accurately for some time (Philipp, 1971). Little difference is seen between the spectra of crystalline quartz and fused quartz. In fact, the same features are seen in the uv spectra of Na_2O:CaO:SiO_2 glass (Ellis et

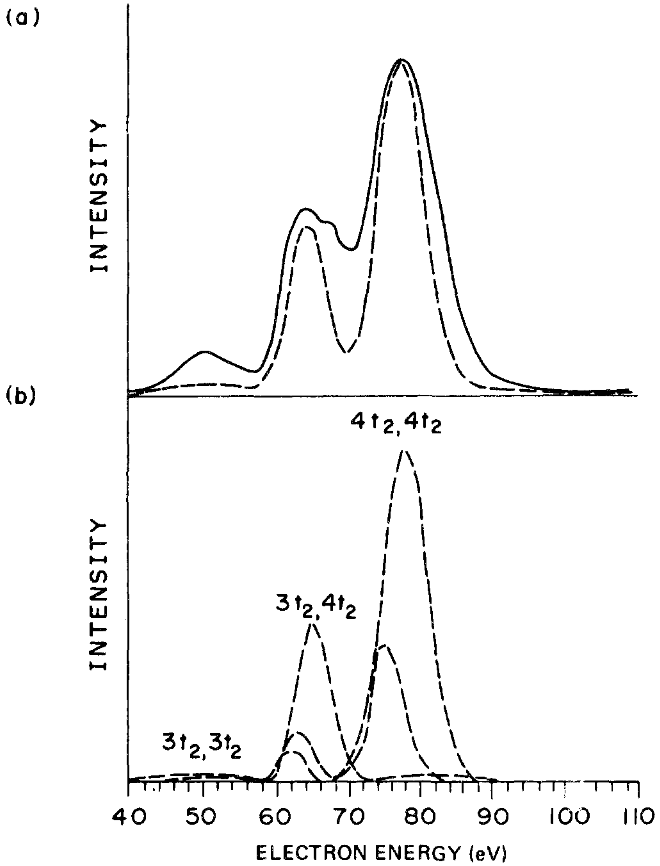

Fig. 4.14. Auger electron spectra of SiO_2. (a) Comparison of experimental (solid line) Si *LVV* Auger spectrum with that calculated (dashed line); (b) major Auger transitions arising from individual molecular orbitals (after Ramaker et al., 1979; reproduced with the publisher's permission).

al., 1979). A large number of different assignments have been given for the quartz uv spectrum, as discussed in detail by Griscom (1977). The most recent semiempirical band-theoretical studies (Laughlin, 1980) indicate that all four uv peaks (at 10.2, 11.7, 14.3, and 17.2 eV) should be interpreted as "excitons" (i.e., localized excitations) from maxima in the upper-valence-region density of states to a single final state lying below the vacuum threshold, but this is still a point of debate. The idea of a single final state for the uv transitions has been favored by many workers (see Nithianandam and Schnatterly, 1988, and discussion in Griscom, 1977). Within the SiO_4^{4-} cluster model, calculated excitation energies from occupied valence orbitals to the t_2 symmetry empty orbital are consistent with experimental uv spectral energies, as shown in Table 4.15.

^{29}Si and ^{19}O NMR spectroscopies have recently been employed to study the local geometric and electronic structure in SiO_2 and other sili-

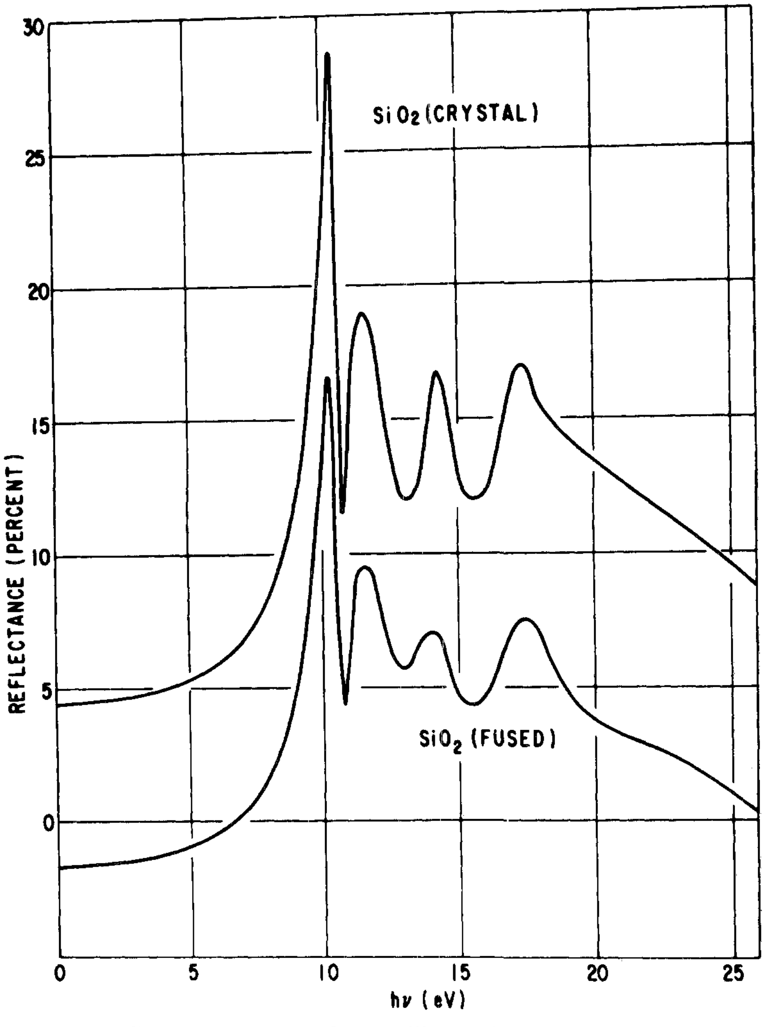

Fig. 4.15. uv reflectance spectra of crystalline and fused quartz. Reflectivity values for fused quartz have been reduced by 5% to separate spectra (after Philipp, 1971; reproduced with the publisher's permission).

Table 4.15. uv spectral results for SiO_2, showing assigned molecular-orbital transition, energy separation (ΔE) from ultraviolet (uv) and x-ray emission spectra, and calculated energy separation; energies in eV

MO transition	Experimental uv ΔE	ΔE from XES	Calculated ΔE
$1t_1 \rightarrow 6t_2$	10.2	9.8	10.2
$5t_2$, $1e \rightarrow 6t_2$	11.7	11.8	11.1, 11.5
$4t_2 \rightarrow 6t_2$	14.3	14.0	13.3
$5a_1 \rightarrow 6t_2$	17.2	17.3	17.5

Source: From Tossell, 1975b.

cates. Direct *ab initio* calculations of the NMR shielding requires Hartree–Fock perturbation theory, preferably in its self-consistent or coupled form (CHFPT; Lipscomb, 1986; Ditchfield, 1974) and very large basis sets. Although CNDO level theories have been applied in the past (Wolff and Radeglia, 1980) and continue to be applied to the present (Malkin et al., 1988), such methods require extensive parametrization, and the physics of the phenomena is therefore obscured. *Ab initio* calculations for the simplest model of SiO_2 having correct first and second coordination shells about the central atom [e.g., $Si(OSiH_3)_4$] have not yet been done. However, coupled Hartree–Fock calculations are feasible for SiF_4, SiO_4^{4-}, $(SiH_3)_2O$, H_3SiOTH_3, where $T = Al$ or P, and $(H_2Si)_nO_n$, where $n = 2$–4, and such model system calculations allow us to study a number of important trends in the Si and O NMR shielding (σ^{Si} and σ^{O}) and the electric-field gradient at oxygen (q^{O}) as a function of nearest-neighbor identity, degree of polymerization, ring size, Si–O distance, and Si–O–Si angle.

NMR shielding calculations on isoelectronic SiF_4 and SiO_4^{4-} (Tossell and Lazzeretti, 1986) give a difference in σ^{Si} consistent with the experimental data for gaseous SiF_4 and the SiO_4^{4-} anion within orthosilicates. The lower value of σ^{Si} in SiO_4^{4-} (calculated difference ~43 ppm, versus experimental difference ~40) can be attributed to the larger amount of Si character in the Si–O t_2 symmetry bonding orbital and the consequently larger magnitude for σ^{p}. Recent calculations on $Si(OH)_4$, at its optimum S_4 geometry, give a σ^{Si} value that differs from that for SiO_4^{4-} by only a few ppm; so $Si(OH)_4$ and SiO_4^{4-} seem to be models of equivalent accuracy for describing the Si NMR shieldings of orthosilicates (Tossell, 1991). Analysis of changes in σ^{Si} with $\sphericalangle$Si–O–H in $Si(OH)_4$ also allows a connection to be made between the orbital energy approach to shielding trends developed by Tossell (1984) and the Si–O bond-polarization model recently developed by Sternberg (1988). The calculated absolute Si shielding of 556 ppm in SiF_4 is in reasonable agreement with the accurate experimental value of 482 ± 10 ppm (Jameson and Jameson, 1988), although distributed origin CHFPT methods like that of Fleischer et al. (1987) give more accurate absolute values (e.g., 488 ppm for SiF_4).

Increases in σ^{Si} with increased coordination number for F (Tossell and Lazzeretti, 1986) and O (Tossell, 1989) can also be accurately obtained from CHFPT calculations on molecular clusters such as SiO_3^{2-}, SiO_4^{4-}, and SiO_5^{6-}. For example, the calculated increase in σ^{Si} between SiO_4^{4-} and SiO_5^{6-} is 77 ppm, while the experimental difference between unpolymerized SiO_4^{4-} and a species identified as SiO_5^{6-} at high pressure in silicate glasses is about 75 ppm (Stebbins and McMillan, 1989). This increase in shielding with coordination number can be understood in terms of a slight increase in the diamagnetic shielding with increased coordination number and a substantial decrease in the magnitude of σ^{p} due to decreased Si–O mixing in the σ-bonding orbitals.

Analysis of the effect of polymerization of the SiO_4^{4-} groups is more difficult, since the only computationally feasible models are H_3SiO^- or H_3SiOH versus $H_3SiOSiH_3$. $H_3SiOSiH_3$ is indeed calculated to be shielded by ~19 ppm with respect to H_3SiO^- (Tossell and Lazzeretti, 1988a), which is near to the typical difference between orthosilicates and sorosilicates (Magi et al., 1984). Calculations for $(SiH_3)_2O$ at a series of Si–O–Si angles (holding the Si–O distance constant) also reproduce the experimentally observed decrease in σ^{Si} as the Si–O–Si angle decreases (Engelhardt and Radeglia, 1984), as shown in Fig. 4.16. A simple orbital interpretation of the decrease in σ^{Si} as the Si–O–Si angle decreases is that the Si–O σ-bonding orbital is destabilized as the angle narrows, so that its separation from the unoccupied orbitals decreases. The consequence is that the magnitude of the σ^p contribution from this orbital increases, thus reducing σ overall. This interpretation focuses upon the dominant changes in σ^p and attributes them mainly to changes in orbital energy differences, as in the original qualitative interpretation of Tossell (1984a) for the σ^{Si} difference between orthosilicates and tektosilicates. In that work, excitation energies from occupied to unoccupied states were obtained from experimental spectral data rather than from calculations.

NMR shieldings at the oxygen can also be obtained for mineral systems and are calculated to show the same angular trends as for silicon (Tossell and Lazzeretti, 1988a). However, ^{17}O is a quadrupolar nuclide (i.e., with a nonzero quadrupole moment), and its nuclear quadrupole coupling constant is thus an easier to measure quantity and, probably, one of more interest. When few data on the ^{17}O NMR of silicates existed, Janes and Oldfield (1986) noted that different bonding models for silicates predicted different dependence of q^O upon Si–O–Si angle. In particular,

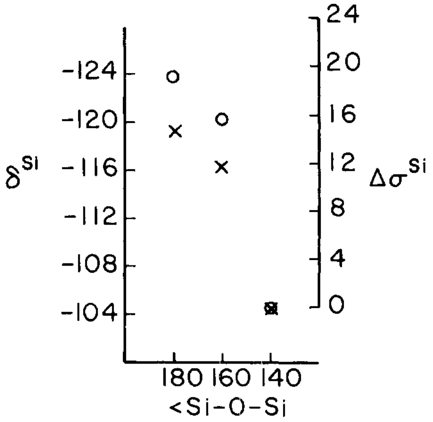

Fig. 4.16. Experimental chemical shift δ^{Si} and calculated change in NMR shielding $\Delta\sigma^{Si}$ as a function of Si–O–Si angle (∢Si–O–Si); experimental correlation shown as crosses, trend in calculated values shown as circles and referenced to experimental value at ∢Si–O–Si = 140°. (after Tossell and Lazzeretti, 1988a; reproduced with the publisher's permission).

for a σ-bonding-only model, q^O should decrease as the Si–O–Si angle decreases, while for a π overlap model, it should increase. However, for Si–O–Si angles from 180° to 120° in $(SiH_3)_2O$, in calculations with *d* polarization functions on both Si and O, and for similar calculations on $(H_2Si)_nO_n$, with energy-optimized Si–O–Si angles (Tossell and Lazzeretti, 1988a; Tossell, 1990b), it is clear that q^O invariably decreases as the Si–O–Si angle decreases (Fig. 4.17), in clear disagreement with the π overlap model as developed by Janes and Oldfield (1986) but qualitatively consistent with their constant overlap model. The value of the nuclear quadrupole coupling constant at the oxygen calculated for an Si–O distance = 1.607 Å and Si–O–Si angle = 144° by Tossell and Lazzeretti (1988a) is about 5.3 MHz, in good agreement with the value obtained for amorphous SiO_2 by Geissberger and Bray (1983). Given the calculated dependence of q^O on Si–O–Si angle, one could determine the distribution of Si–O–Si angles from the distribution of oxygen NQCC values.

The question of the dependence of σ^{Si} or other quantities upon Si–O–Si angle is a very important one, since this angle is such a significant local structural parameter in both crystalline and amorphous SiO_2. A number of different correlations of σ^{Si} and Si–O–Si angle have appeared (Coombs et al., 1985; Pettifer et al., 1988, being some of the most recent). For example, different assumptions for the relationship between σ^{Si} and Si–O–Si angle lead to different interpretations of the Si–O–Si angle distribution in amorphous SiO_2, as shown in Fig. 4.18 (from Pettifer et al., 1988). In all cases, however, we believe that both bond distance and angle must be considered in evaluating σ^{Si}. We therefore feel that the best calculated dependence of σ^{Si} on Si–O–Si angle is that obtained for the $(H_2Si)_nO_n$, where $n = 2$–4, series, with results shown in Table 4.16.

The overall conclusion from our discussion of crystalline SiO_2 is that

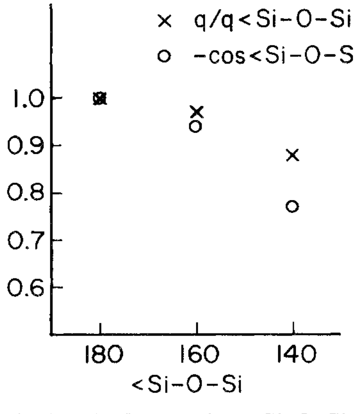

Fig. 4.17. Ratio of calculated q^O at a given Si–O–Si angle (∢Si–O–Si) to q^O at ∢Si–O–Si = 180 versus ∢Si–O–Si compared with cos(∢Si–O–Si) (after Tossell and Lazzeretti, 1988a; reproduced with the publisher's permission).

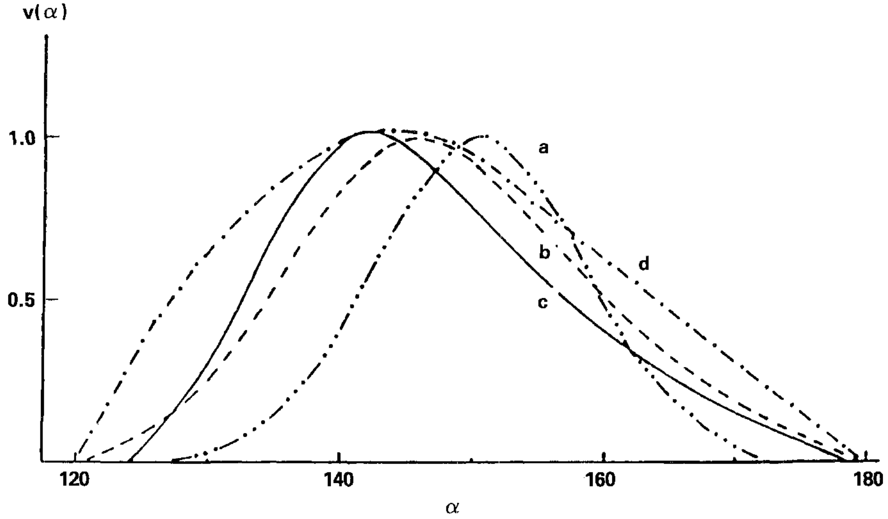

Fig. 4.18. Si–O–Si bond angle ($\sphericalangle$Si–O–Si; here labeled α) distributions deduced for SiO_2 glass using various models for δ^{Si} versus $\sphericalangle$Si–O–Si. (a) Linear model, (b) point-charge model, (c) secant model, and (d) x-ray result (after Pettifer et al., 1988; reproduced with the publisher's permission).

the average structural parameters (i.e., Si–O distances and Si–O–Si angles) can now be calculated with errors of a few hundredths of an angstrom and a few degrees, respectively. No systematic attempts have been made to calculate differences in structural parameters between different structure types at the *ab initio* level for the tetrahedrally coordinated polymorphs, although some such studies have been performed using modified electron-gas methods and, for polymorphs with other Si coordination numbers, using band-theoretical methods. Further discussion of these calculations will be presented in Chapter 7. Those spectral properties involving the occupied orbitals of SiO_2 (e.g., photoelectron and x-ray emission spectra) can be considered reasonably well understood, although calculated energies and (particularly) intensities are still not particularly accurate. Properties involving empty orbitals (e.g., x-ray absorption and

Table 4.16. Calculated ^{29}Si NMR shielding constants for $H_2Si(OH)_2$ and the oligomers $(H_2Si)_nO_n$, n = 2–4

	σ^{Si} (ppm)
$H_2Si(OH)_2$	469
$H_4Si_2O_2$ ($\sphericalangle$Si–O–Si = 90°)	472
$H_6Si_3O_3$ ($\sphericalangle$Si–O–Si = 133°)	526
$H_6Si_4O_4$ ($\sphericalangle$Si–O–Si = 160°)	541

Source: From Tossell, 1990b.

uv spectra) are not yet well understood; in particular, assignments are still in doubt in many cases. NMR properties seem to be well understood in principle, but calculations on model systems of adequate size remain a daunting task.

4.4. Transition-metal oxides

The transition-metal oxides are a particularly important group of compounds in terms of their interest to mineralogists, geochemists, and materials scientists.

The partially filled *d*-shell responsible for the distinctive properties (particularly optical and magnetic properties) of these phases also makes them an interesting and challenging group for which to develop electronic-structure models. We begin by considering the titanium oxides and the manganese oxides, using them to compare crystal-field, molecular-orbital, and band-structure approaches. The iron oxides are then considered in detail before some general comments are made on molecular-orbital and band-theory models for transition-metal oxides as a whole, and a brief discussion of some complex oxides containing transition metals is given.

4.4.1. Titanium oxides

Titanium is commonly found in nature as the TiO_2 polymorph rutile, containing the Ti^{4+} cation in octahedral coordination. Although rutile is tetragonal, the distortion of the coordination polyhedra is small (two Ti–O distances are 1.988 Å, four are 1.944 Å; Grant, 1959). The Ti^{4+} cation in octahedral coordination is the most common naturally occurring form (also found in more complex oxides and silicates), although the Ti^{3+} species does also occur, sometimes in fourfold coordination.

The Ti^{3+} ion, with its single *d* electron, offers the simplest example that can be treated using crystal- (or ligand-) field theory. It may be recalled that in an octahedral environment the *d* orbitals of Ti are split by the crystal field of surrounding O^{2-} ions into t_{2g} and e_g sets (Fig. 4.19) and the single *d* electron in the ground state occupies one of the t_{2g} levels, the energy separating t_{2g} and e_g sets being Δ, the crystal-field splitting parameter. An energy-level diagram of the type shown in Fig. 4.20 can be constructed to show the variation of orbital energies with Δ, the applied crystal (or ligand) field. Only one transition is expected when the *d* electron goes from a t_{2g} orbital (the ground state) to an e_g orbital. Such a transition is observed in the solution species $Ti(H_2O)_6^{3+}$, in which Ti^{3+} ions are in sixfold coordination, which exhibits a violet color due to absorption of light at 500 nm resulting from this transition. Recent HF-CI studies on $Ti(OH)_2)_6^{3+}$ (Tachikawa et al., 1990) have established that there is a slight D_{3d} symmetry distortion in the equilibrium geometry and that

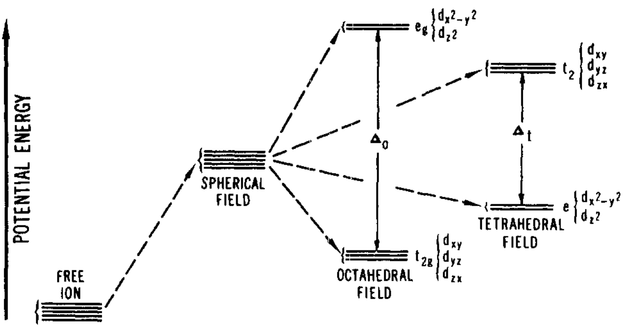

Fig. 4.19. Energy levels of the five *d* orbitals of a transition-metal ion in different environments (after Bloss, 1971; reproduced with the publisher's permission).

the shoulder observed near 570 nm probably arises from a Jahn–Teller distortion in the excited E_g' symmetry state.

Molecular-orbital cluster calculations have been performed on Ti^{3+} and Ti^{4+} in regular octahedral coordination with oxygen (Loeffler et al., 1974; Tossell et al., 1974). Calculations using the MS-SCF-$X\alpha$ method on the TiO_6^{8-} cluster yield the energy-level diagram shown in Fig. 4.21, which shows both the molecular orbitals labeled according to the irreducible representations of the O_h symmetry group and the energy levels of

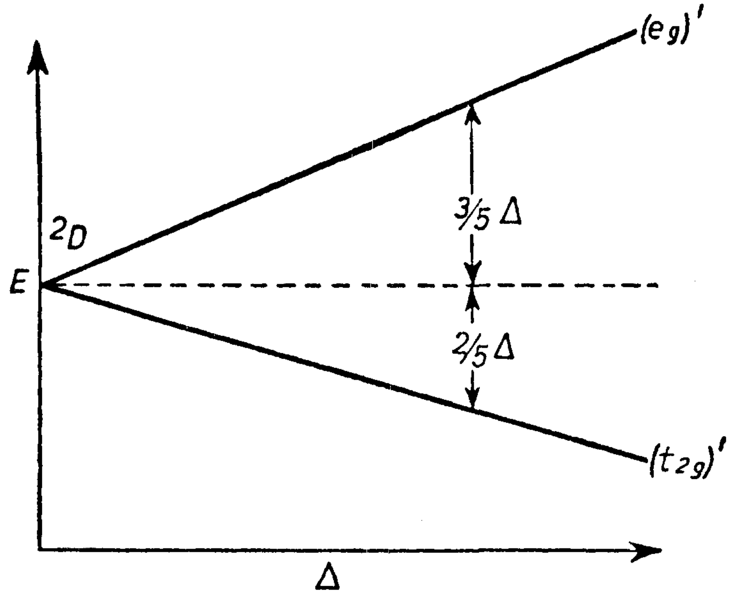

Fig. 4.20. Crystal-field-theory energy-level diagram for a d^1 ion (after Orgel, 1966; reproduced with the publisher's permission).

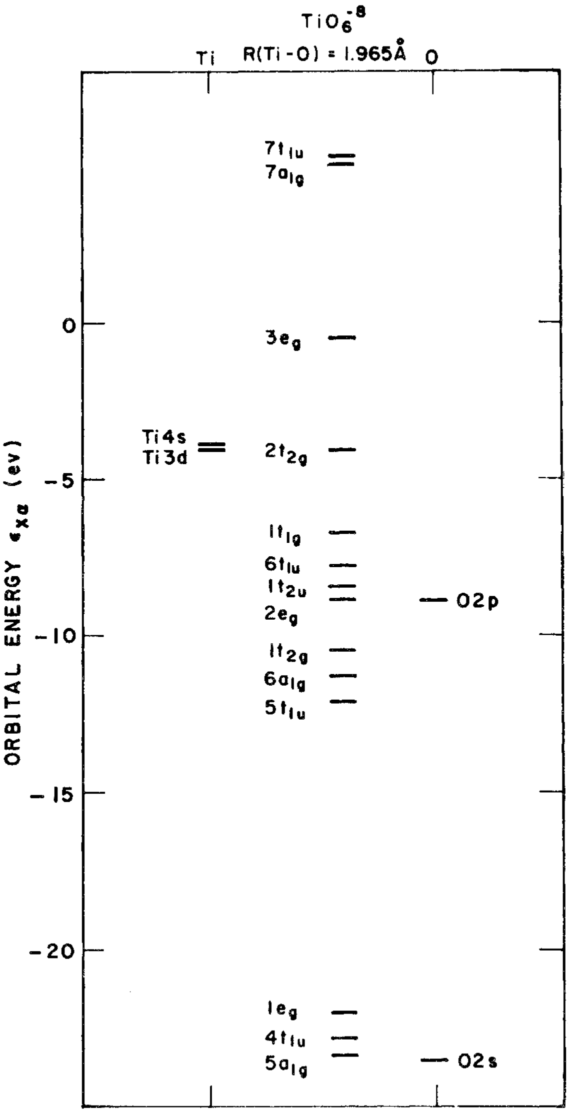

Fig. 4.21. Molecular-orbital diagram for a TiO_6^{8-} cluster (Ti–O distance = 1.965 Å) calculated using the MS-SCF-$X\alpha$ method; the highest occupied orbital is the $1t_{1g}$ (after Tossell et al., 1974; reproduced with the publisher's permission).

the free atoms. In this and other transition-metal oxide octahedral clusters, the molecular orbitals fall into five sets distinguishable by their energies and by the spatial distribution of electron density. The orbitals with eigenvalues around −22 eV ($5a_{1g}$, $4t_{1u}$, $1e_g$) are essentially O 2*s* nonbonding orbitals with a slight metal orbital admixture. The main bonding orbitals of the system ($5t_{1u}$, $6a_{1g}$, $1t_{2g}$, and $2e_g$) possess appreciable metal and oxygen character. The $1t_{2u}$, $6t_{1u}$, and $1t_{1g}$ orbitals are all primarily O $2p$ nonbonding orbitals with relatively little metal character. The $1t_{1g}$ is the highest-energy filled orbital. The two lowest-energy empty orbitals are the $2t_{2g}$ and $3e_g$ "crystal-field" orbitals, which have both Ti $3d$ and O $2p$ character. The empty orbitals that form the "conduction-band" levels ($7a_{1g}$ and $7t_{1u}$) are diffuse Ti–O antibonding orbitals.

The results of the calculations on the TiO_6^{8-} cluster were compared by Tossell et al. (1974) with the experimentally determined x-ray and uv photoelectron, optical absorption, and uv reflectivity, and x-ray emission and absorption spectra of rutile. The experimental and calculated values are shown in Tables 4.17, 4.18, and 4.19, and, in all cases, the agreement between calculation and experiment is relatively good. In the case of the photoelectron spectra (Table 4.17), uncertainties in the absolute values of photoelectron binding energies due to charging and reference-level effects were avoided by setting the energy of the $1t_{1g}$ orbital equal to that of the lowest-binding-energy photoelectron peak, and adjusting other orbital energies accordingly. The optical absorption spectrum shows an absorption edge at 3.03 eV (Cronemeyer, 1952) that arises from a ligand → metal charge-transfer transition, specifically the $1t_{1g} \rightarrow 2t_{2g}$ transition from an O $2p$ nonbonding orbital → Ti $3d$ type orbital according to the calculations (Fig. 4.21, Table 4.18). The uv reflectivity spectra (Table 4.18) and the x-ray emission and absorption spectra (Table 4.19) provide a great deal of information on the relative energies of the five main sets of molecular orbitals shown in Fig. 4.21. Assignments of all features are shown in the tables and are discussed in more detail by Tossell et al. (1974).

The MS-SCF-$X\alpha$ calculation for the TiO_6^{9-} cluster, corresponding to Ti^{3+} ions octahedrally coordinated to O^{2-}, yielded molecular-orbital en-

Table 4.17. Experimental and calculated uv and x-ray photoelectron spectra of rutile (*energies in eV*)

Experimental peak label	Experimental relative E[a]	Calculated relative E	MO assignment
uv photoelectron spectrum			
	0	0	$1t_{1g}$
O $2p$	−2.2	−1.5	$6t_{1u},1t_{2u},2e_g$
O $2s$[b]	−4.8	−4.6	$1t_{2g},6a_{1g},5t_{1u}$
X-ray photoelectron spectrum			
O $2p$	~5 eV wide	5.4 eV wide	$1t_{1g}$ — $5t_{1u}$
O $2s$	~ −16 eV[c]	13.9 eV[c]	$1e_g,4t_{1u},5a_{1g}$

[a] Experimental uv data from Derbenwick (1970); experimental x-ray data from Hüfner and Wertheim (1973).

[b] As shown by Fischer (1972), this labeling is definitely erroneous.

[c] Relative E taken with respect to center of O $2p$ peak (experimental) or to center of valence region (calculated).

Source: After Tossell et al., 1974.

Table 4.18. Experimental and calculated optical spectra of rutile (*energies in eV*)

Observed feature	Experimental ΔE	Calculated ΔE	MO assignment[a]
Optical absorption			
Absorption edge	3.03*	3.2	$1t_{1g} \rightarrow 2t_{2g}$ (O $2p$ nb $\rightarrow$ Ti $3d$)
uv reflectivity			
Peak A	~4.7**	4.2, 4.8	$(6t_{1u},1t_{2u}) \rightarrow 2t_{2g}$ (O $2p$ *nb* $\rightarrow$ *Ti* $3d$)
Peak C	~8.8	8.4	$5t_{1u} \rightarrow 2t_{2g}$ (Ti–O b $\rightarrow$ Ti $3d$)
Peak D	10.7		O^{2-} $2p \rightarrow 3s$
Peak E	14.0	13.3	$(6t_{1u},1t_{2u}) \rightarrow (7a_{1g},7t_{1u})$ (O $2p$ nb $\rightarrow$ Ti–O ab)
Peak F	17.4	18.5	$(1e_g,4t_{1u},5a_{1g}) \rightarrow 2t_{2g}$ (O $2s$ nb $\rightarrow$ Ti $3d$)

[a] b, nb, and ab refer to bonding, nonbonding, and antibonding orbitals, respectively.

[b] Cronemeyer (1952).

[c] Cardona and Harbeke (1965).

Source: After Tossell et al., 1974.

ergy levels very similar to those described above for TiO_6^{8-} (Loeffler et al., 1974). The single $3d$ electron of Ti^{3+} occupies a $2t_{2g}$ level, producing a crystal-field transition to the $3e_g$ level at energies around 2.4 eV in oxide environments (Burns and Huggins, 1973). The lowest-energy, fully allowed oxygen → Ti^{3+} transitions are calculated to occur at 5.1 eV ($6t_{1u} \rightarrow 2t_{2g}$) and 5.7 eV ($1t_{2u} \rightarrow 2t_{2g}$) and to lead to intense absorption well into the ultraviolet region of the spectrum.

Band-structure models and calculations of various types have been applied to the oxides of titanium. The qualitative one-electron model for rutile proposed by Goodenough (1971), as shown in Fig. 4.22, clearly relates in a simple way to the molecular-orbital diagram of Fig. 4.21. Now the overlap between s and p orbitals on Ti^{4+} and O^{2-} is shown as giving rise to filled and empty bonding and antibonding bands. The empty d orbitals of Ti^{4+} are shown here as split, not just into t_{2g} and e_g levels, but also by an axial field resulting from the distortion of the octahedral site. As in the perfect octahedron, the orbitals not proximal to the oxygen ligands (a_{1g},b_{2g},b_{3g}) are shown as remaining nonbonding, whereas those proximal to the ligands (a_{1g},b_{1g}) are involved in a bonding–antibonding interaction. Recent quantitative band-structure calculations include those of Schwarz (1987) on TiO_2 with the rutile structure, employing a self-consistent augmented-spherical-wave method (Williams et al., 1979). Results from this calculation are shown in Fig. 4.23, where information obtained on the total density of states is compared with the site-projected partial density of states for Ti $3d$ and for oxygen s and p. The separation between

Table 4.19. Experimental and calculated x-ray emission and absorption spectra of rutile (*energies in eV*)

Experimental peak label	Experimental relative E^a	Calculated relative E	MO assignment
Ti$K\beta$ emission			
$K\beta^1$	~ -16	-15.8	$3t_{1u} \rightarrow$ Ti $1s - (1t_{2g} \rightarrow 7t_{1u})$
$K\beta_1$	0	0	$3t_{1u} \rightarrow$ Ti $1s$
$K\beta''$	15.2	17.1	$4t_{1u} \rightarrow$ Ti $1s$
$K\beta_5$	30.4, 29.7 31.4	27.8	$5t_{1u} \rightarrow$ Ti $1s$
$K\beta_5'$		32.1	$6t_{1u} \rightarrow$ Ti $1s$
TiL emission			
F	0	0	$1t_{1g} \rightarrow$ Ti $2p_{3/2}$
A	-4.2	-2.1	$2e_g \rightarrow$ Ti $2p_{3/2}$
		-3.8	$1t_{2g} \rightarrow$ Ti $2p_{3/2}$
G		-4.6	$6a_{1g} \rightarrow$ Ti $2p_{3/2}$
C	-18.8	-15.3	$1e_g \rightarrow$ Ti $2p_{3/2}$
D	-21.3	-16.7	$5a_{1g} \rightarrow$ Ti $2p_{3/2}$
O $K\alpha$			
Main peak	0	0	$(1t_{1g}, 6t_{1u}, 1t_{2u}, 2e_g) \rightarrow$ O $1s$
Low-energy shoulder	-2.6 -2.7	-3.4	$(1t_{2g}, 6a_{1g}, 5t_{1u}) \rightarrow$ O $1s$
Ti K, Ti L, O K absorption^b			
b	3.1	2.6	Core hole $\rightarrow 2t_{2g}$
c	5.2	6.2	Core hole $\rightarrow 3e_g$
d	11.5	12.5	Core hole $\rightarrow 7a_{1g}, 7t_{1u}$
e	18.9		

[a] See Tossell et al. (1974) for original data sources. E values calculated relative to $1t_{1g}$ (ground-state energy differences).

Source: After Tossell et al., 1974.

groups of energy levels and their makeup in terms of metal and oxygen contributions can be gauged from this diagram and is clearly in general agreement with that obtained from the MS-SCF-$X\alpha$ cluster calculation (Fig. 4.21).

4.4.2. *Manganese oxides*

Manganese most commonly occurs in nature as various oxide and hydrated oxide minerals, ranging from simple binary compounds such as manganosite (MnO), partridgite (Mn_2O_3) and pyrolusite (MnO_2), containing manganese in the Mn^{2+}, Mn^{3+}, and Mn^{4+} oxidation states, respectively, to complex mixed-valence oxides such as birnessite $(Ca,Na)(Mn^{2+},Mn^{4+})_7O_{14}\cdot 3H_2O$ and todorokite $(Na,Ca,K,Ba,Mn^{2+})_2Mn_5O_{12}\cdot 3H_2O$ (see Burns and Burns, 1979). In the crystal structures of the

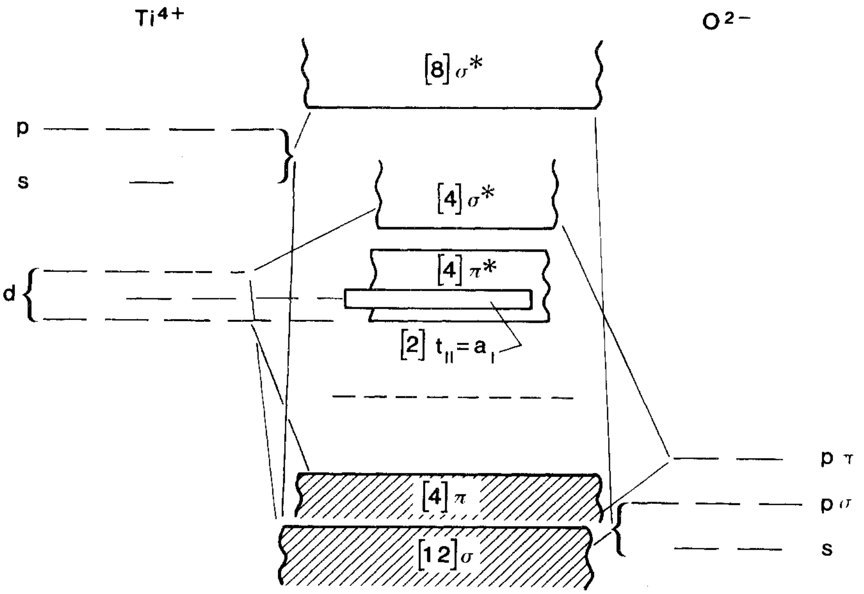

Fig. 4.22. Qualitative one-electron band model for the bonding in TiO_2 (modified figure after Goodenough, 1971).

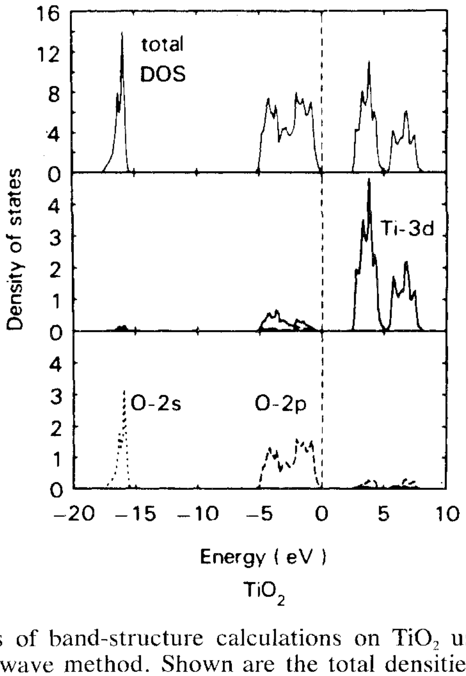

Fig. 4.23. Results of band-structure calculations on TiO_2 using the SCF augmented-spherical-wave method. Shown are the total densities of states and the site-projected partial densities of states for Ti 3*d*, O 2*s*, and O 2*p* (normalized to one atom) (after Schwarz, 1987; reproduced with the publisher's permission).

manganese oxides, manganese cations are octahedrally coordinated to oxygen anions; the resulting MnO_6 polyhedra are linked by either edge or corner sharing to form infinite-chain, sheet, or three-dimensional units. The simple binary oxides, in fact, have the rocksalt (MnO), rutile (MnO_2), or the *C* rare-earth sesquioxide (Mn_2O_3) structure.

If we consider the octahedrally coordinated Mn^{2+} ion (as in MnO), the crystal-field model has the five *d* orbitals of Mn split by the crystal (or ligand) field of the surrounding oxygens into the lower-energy t_{2g} set and higher-energy e_g set (Fig. 4.19). For ions with more than one *d* electron (cf. Ti^{3+} discussed previously), there are more than two ways of arranging the electrons in the *d* orbitals leading to different configurations and Russell–Saunders states. The relative energies of different arrangements of the electrons in the *d* orbitals of the free ion and in an octahedral crystal (ligand) field of increasing strength are as already shown in Fig. 2.19, an energy-level diagram calculated using the formalisms of crystal-field theory. Such diagrams have commonly been used to assign peaks in an absorption spectrum (such as in Fig. 4.24) to transitions between the $^6A_{1g}$ ground state and the excited states shown in the energy-level diagram. The intensities of observed transitions are governed by the selection rules (notably the spin multiplicity and Laporte selection rules; see Burns, 1970), which greatly reduce the intensities of "forbidden" transitions.

The cluster molecular-orbital approach has also been successfully applied to studies of the electronic structures of manganese oxide minerals and related compounds, notably in the work of Sherman (1984) using the MS-SCF-$X\alpha$ method. Calculations were performed on the clusters

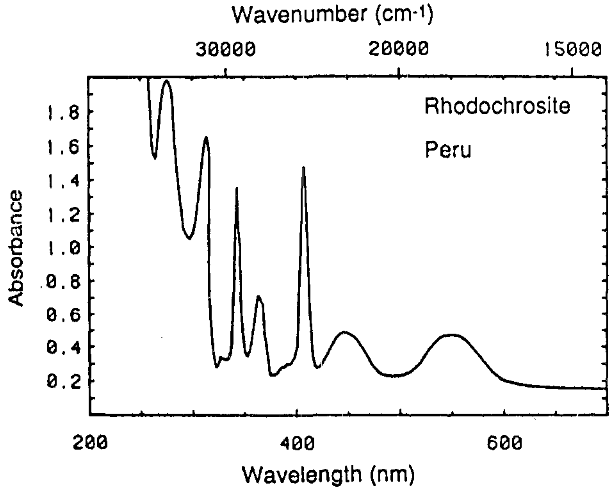

Fig. 4.24. Optical absorption spectrum of Mn^{2+} in octahedral coordination to oxygen in rhodochrosite, showing the numerous spin-forbidden peaks (after Rossman, 1988; reproduced with the publisher's permission).

MnO_6^{10-}, MnO_6^{9-}, and MnO_6^{8-}, corresponding to Mn^{2+}, Mn^{3+}, and Mn^{4+} in regular octahedral (O_h) coordination to oxygen. The calculated molecular-orbital energy-level diagrams for the clusters are shown in Fig. 4.25. Since the manganese oxides have ground states with total spins $S \neq 0$, an unrestricted MS-SCF-$X\alpha$ calculation, in which the spin-up (α) and spin-down (β) electrons occupy different orbitals, must be performed. It is notable that the spin splittings are quite large for the crystal-field-type ($2t_{2g}$,$3e_g$) orbitals. The energy levels shown in Fig. 4.25 are those of the valence, crystal-field, and low-energy conduction-band molecular orbitals derived from the manganese 3*d*, 4*s*, 4*p*, and oxygen 2*p* atomic orbitals. The core molecular orbitals are not shown and are essentially the manganese 1*s*, 2*s*, 2*p*, 3*s*, and 3*p* and oxygen 1*s* atomic orbitals that occur at much lower energy, are localized on Mn or O, and are not involved in bonding.

The valence-band orbitals include nonbonding oxygen orbitals such as the $1t_{1g}$, $6t_{1u}$, $1t_{2u}$, and $5t_{1u}$ and those orbitals with appreciable metal and oxygen character ($2e_g$, $6a_{1g}$, $1t_{2g}$). The atomic compositions of the latter are given in Table 4.20 along with the compositions of the crystal-field

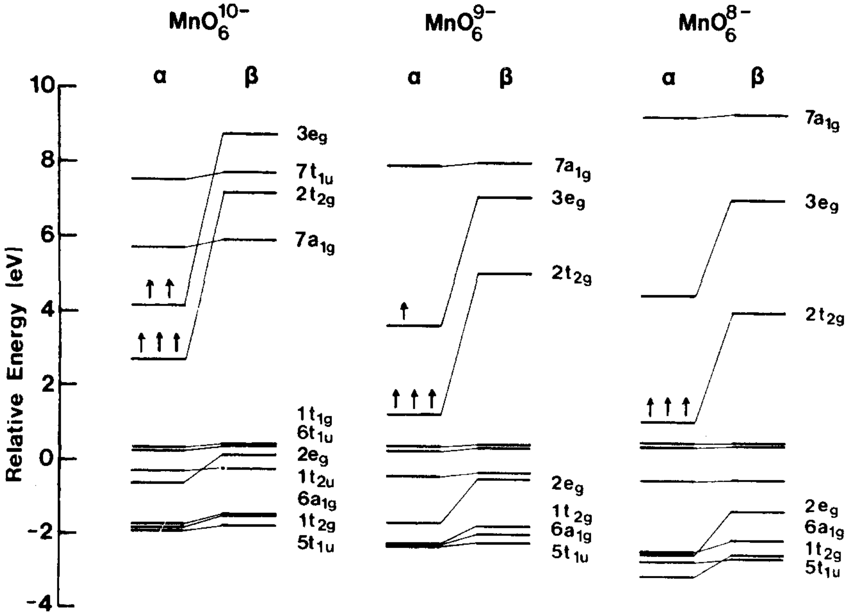

Fig. 4.25. Molecular-orbital diagrams for the MnO_6^{10-}, MnO_6^{9-}, and MnO_6^{8-} clusters (O_h symmetry) obtained using the MS-SCF-$X\alpha$ method. Orbital energies have been scaled relative to the nonbonding $1t_{1g}$, $1t_{2u}$, and $6t_{1u}$ orbital energies. The numbers of electrons in the highest occupied molecular orbitals are shown by the arrow symbols, and the α and β symbols refer to spin-up and spin-down orbitals, respectively (after Sherman, 1984; reproduced with the publisher's permission).

Table 4.20. Molecular-orbital compositions in three MnO_6 clusters for crystal-field-type and bonding orbitals shown in terms of percentage Mn, percentage O, and percentage intersphere contributions

	MnO_6^{10-}			MnO_6^{9-}			MnO_6^{8-}		
	% Mn	% O	% Int	% Mn	% O	% Int	% Mn	% O	% Int
$3e_{g\downarrow}$	80	13	6	80	18	1	71	27	2
$3e_{g\uparrow}$	73	25	1	56	39	4	52	43	4
$2t_{2\downarrow}$	56	21	23	84	8	8	82	10	8
$2t_{2\downarrow}$	86	8	6	73	18	8	67	22	10
$2e_{g\downarrow}$	7	90	2	17	64	17	26	59	13
$2e_{g\uparrow}$	24	75	1	43	43	13	46	43	10
$1t_{2g\downarrow}$	2	73	24	5	57	36	10	56	33
$1t_{2g\uparrow}$	7	69	23	21	46	32	27	43	29
$6a_{1g\downarrow}$	8	76	16	8	57	34	8	62	30
$6a_{1g\uparrow}$	10	75	15	10	57	33	8	61	29

Source: After Sherman, 1984.

orbitals. The most important bonding orbitals are the σ-bonding $2e_g$ and π-bonding $1t_{2g}$, composed of manganese $3d$ and oxygen $2p$ atomic orbitals. With increasing oxidation state of the manganese atom, these orbitals become more bonding in character, inasmuch as they donate more electron density to the Mn atom and become more stable. The $2t_{2g}$ and $3e_g$ orbitals correspond to the one-electron crystal-field states. Whereas in the purely ionic bonding description of crystal-field theory, these are the Mn $3d$ atomic orbitals that have lost their degeneracy by electrostatic interaction with the surrounding oxygen anions, in the molecular-orbital description they are the antibonding equivalents of the $1t_{2g}$ and $2e_g$ bonding orbitals. As the metal atom character of the bonding $1t_{2g}$ and $2e_g$ orbitals increases, the ligand character of the antibonding $2t_{2g}$ and $3e_g$ orbitals increases accordingly. Thus, as the $1t_{2g}$ and $2e_g$ orbitals become more bonding in character, the $2t_g$ and $3e_g$ crystal-field orbitals become more antibonding. Despite this, the average energy of the crystal-field orbitals (relative to the O $2p$ nonbonding orbitals) decreases with increasing oxidation state of the manganese atom. Since these orbitals are dominantly manganese in character, their increasing stability is a consequence of the increasing electronegativity of the manganese atom. As anticipated, the crystal-field splitting increases with the formal oxidation state of the manganese cation, partly because of increased electrostatic interaction between the cation and the oxygen anions, but more importantly because of an increased degree of e_g σ bonding relative to t_{2g} π bonding in the clusters. The $7a_{1g}$ and $7t_{1u}$ orbitals in Fig. 4.25 are the lowest-energy orbitals of conduction-band character and are the antibonding equivalents of the $6a_{1g}$ and other bonding orbitals. In a very localized (ionic) description they would be the manganese $4s$ and $4p$ atomic orbitals, whereas the MS-

SCF-$X\alpha$ calculations show them to be extensively delocalized over the oxygen, interatomic, and extramolecular regions.

As with the MS-SCF-$X\alpha$ calculations on titanium oxides, the calculated orbital energies for the MnO$_6$ clusters can be verified by comparison with experimental x-ray emission, x-ray photoelectron, and optical spectra for manganese oxides (Sherman, 1984). For example, the Mn $K\beta$ and Mn $L\alpha$ x-ray emission spectra, involving electron transitions from higher-energy (including valence region) orbitals to holes in the Mn 1*s* and Mn 2*p* levels, have been studied by Koster and Mendel (1970), Tsutsumi et al. (1976), and Wood and Urch (1976). The transition energies measured by these authors are shown in comparison with the calculated energies obtained using the transition state procedure in Table 4.21 (after Sherman, 1984). The situation with regard to optical spectra is somewhat more complex, since it may be recalled that, whereas the spectroscopic transitions are between multielectron wave functions (spectroscopic states), the results of molecular-orbital calculations employ a one-electron formalism. As a consequence of interelectronic repulsion, a given electronic configuration over several one-electron orbitals can generate several multielectronic states. Thus, for example, the ground-state configuration of Mn^{4+} in MnO$_6^{8-}$ is $(2t_{2g\uparrow})^3$, which gives the multielectronic state $^4A_{2g}$. However, the excited-state configuration $(t_{2g\uparrow})^2(e_g)^1$ yields the two states $^4T_{2g}$ and $^4T_{1g}$, so that the energy of the one-electron transition $2t_{2g} \rightarrow 3e_g$ corresponds to a weighted average of the energies of the spectroscopic transitions $^4A_{2g} \rightarrow {}^4T_{2g}$ and $^4A_{2g} \rightarrow {}^4T_{1g}$. In some cases, however, an electronic transition between two one-electron orbitals does correspond to a unique transition between two multielectronic spectroscopic states. Comparison between the energies calculated for one-electron transitions using the MS-SCF-$X\alpha$ method and the experimentally observed spectral transitions

Table 4.21. Experimental [E(expt.)] K and L x-ray emission spectral energies for MnO and MnO$_2$ compared with energies calculated [E(calc.)] using the MS-SCF-$X\alpha$ method

		MnO		**MnO$_2$**		
XES band	**Transition**	***E*(expt.)**	***E*(calc.)**	***E*(expt.)**	***E*(calc.)**	**Reference**
$K\beta_1$	Mn $3p \rightarrow 1s$	6491.8	6495.1	6490.0	6495.1	*a,b*
$K\beta''$	O $2s \rightarrow 1s$	~6521.0	6520.0	6521.0	6528.5	*a*
$K\beta_5$	$5t_{1u} \rightarrow 1s$	6533.2	6532.8	6534.7	6541.0	*a,b,c*
$K\beta'''$	$7t_{1u} \rightarrow 1s$	~6549.8	6549.5	6549.8		*a*
$L\alpha$	$2t_{2g} \rightarrow 2p$	643.	643.1	643.	643.3	*c*

[a] Koster and Mendel (1970).

[b] Tsutsumi et al. (1976).

[c] Wood and Urch (1976).

Source: After Sherman, 1984.

for oxygen → metal charge-transfer (CT), crystal-field (CF), and valence-band (VB) or conduction-band (CB) transitions are shown in Table 4.22.

The molecular-orbital cluster calculations described in the preceding text have been used to consider more general problems concerning the crystal chemistry of manganese oxides (Sherman, 1984). For example, in spite of radius ratio considerations, Mn^{4+} is found to be considerably more stable in octahedral than in tetrahedral coordination. Although crystal-field theory predicts a very large octahedral site preference energy for Mn^{4+} (2.79 eV; Burns, 1970), the molecular-orbital approach offers a more complete picture. Comparison of calculations for MnO_6^{8-} and a tetrahedral MnO_4^{4-} cluster show the occupied Mn^{4+} crystal-field orbitals to be less stable in the tetrahedral cluster, whereas the bonding molecular orbitals in the MnO_6^{8-} cluster are more stable than the analogous orbitals in MnO_4^{4-} by about 1 eV. In another application, the distribution of charge between the different regions was used to estimate the covalence of bonding, which was shown to increase as the formal oxidation state of the manganese atom increases. The covalent nature of bonding in the MnO_6^{8-} cluster explains the low solubilities of Mn^{4+} oxides in solutions where strong complexing agents are absent; conversely, the ionic nature

Table 4.22. Optical spectral (one-electron) transition energies (*E*) calculated for manganese oxides using the MS-SCF-$X\alpha$ method, compared with experimentally observed transitions assigned to charge transfer, crystal field, valence band → conduction band and crystal field → conduction band transitions

One-electron transition	*E*(calc.)[a]	Corresponding spectral transitions[b]
$(MnO_6)^{8-}$		
$1t_{2u}(\downarrow) \rightarrow 2t_{2g}(\downarrow)$	5.17	$O^{2-} \rightarrow Mn$, CT
$6t_{1u}(\downarrow) \rightarrow 2t_{2g}(\downarrow)$	4.32	$O^{2-} \rightarrow Mn$, CT (ca. 4.3)
$2t_{2g}(\uparrow) \rightarrow 3e_g(\uparrow)$	3.33	$^4A_2 \rightarrow {}^4T_2$ (2.64), $^4T_1$
$2t_{2g}(\uparrow) \rightarrow 2t_{2g}(\uparrow)$	2.95	$^4A_2 \rightarrow {}^2E, {}^2T_1, {}^2T_2$
$(MnO_6)^{9-}$		
$1t_{2u}(\downarrow) \rightarrow 2t_{2g}(\downarrow)$	6.27	$O^{2-} \rightarrow Mn$, CT
$6t_{1u}(\downarrow) \rightarrow 2t_{2g}(\downarrow)$	5.55	$O^{2-} \rightarrow Mn$, CT
$6t_{1u}(\uparrow) \rightarrow 3e_g(\uparrow)$	4.65	$O^{2-} \rightarrow Mn$, CT (4.09, 4.2, 4.5)
$2t_{2g}(\uparrow) \rightarrow 3e_g(\uparrow)$	2.42	$^5E \rightarrow {}^5T_2$ (2.25–2.73)
$2t_{2g}(\uparrow) \rightarrow 2t_{2g}(\downarrow)$	3.42	
$(MnO_6)^{10-}$		
$6t_{1u}(\downarrow) \rightarrow 2t_{2g}(\downarrow)$	7.00	$O^{2-} \rightarrow Mn$, CT (7.2, 6.9)
$1t_{1g}(\uparrow) \rightarrow 7t_{1u}(\uparrow)$	5.80	VB → CB (5.7)
$2t_{2g}(\uparrow) \rightarrow 7t_{1u}(\uparrow)$	5.17	CF → CB (5.4?)

[a] Energies in eV.

[b] Observed spectral features given in parentheses.

Source: After Sherman, 1984; see this reference for sources of experimental data.

of bonding in the MnO_6^{10-} cluster is in agreement with the higher solubility of Mn^{2+} in aqueous solutions and the ability of Mn^{2+} to act as an exchangeable cation in complex oxides. An explanation was also offered for the relative instability of Mn^{3+} cations (Sherman, 1984).

Certain manganese oxides have also been the focus of band-structure calculations, notably MnO (see Yamashita and Asano, 1983b; Terakura et al., 1984a,b), and these aspects will be further discussed in the following.

4.4.3. Iron oxides (and hydroxides)

Iron is the most important naturally occurring transition element because it is the most abundant in the Earth, and therefore occurs in a wide range of minerals and geochemical systems. The most important oxidation states of iron in minerals are the Fe^{3+} and Fe^{2+} states, and these are most commonly found in essentially (albeit often distorted) octahedral sixfold coordination and tetrahedral fourfold coordination to oxygen in a wide range of oxides and silicates. The bonding of iron to oxygen in such systems has been studied using a wide range of experimental methods and calculational approaches, both because of its geochemical importance and because of the applicability of so many techniques, some of which (notably Mössbauer spectroscopy) are particularly well suited to the study of iron. Like many of the other transition-metal oxides, the iron oxides are of interest to materials scientists because of their properties. They also have a special importance in geophysics because they are, by far, the dominant contributors to the magnetic properties of rocks.

In the crystal-field-theory approach, Fe^{3+} with its d^5 configuration can be described in octahedral coordination by the energy-level diagram already shown in Fig. 2.19. Such diagrams have been widely used in the interpretation of optical absorption spectra, such as the spectrum of andradite garnet also already shown in Fig. 2.18, and which contains Fe^{3+} in octahedral coordination. In order of increasing energy, the peaks here can be assigned as ${}^6A_{1g}$ to ${}^4T_{1g}$, ${}^4T_{2g}$, ${}^4E_g$ + ${}^4A_{1g}$, ${}^4T_{2g}$, ${}^4E_g$ transitions.

Cluster molecular-orbital methods were first applied to iron oxides by Tossell et al. (1973a, 1974) and by Vaughan et al. (1974) using the MS-SCF-$X\alpha$ method to calculate the electronic structures of the FeO_6^{9-}, FeO_6^{10-}, and FeO_4^{6-} octahedral and tetrahedral clusters. Further calculations using the same method for tetrahedrally coordinated Fe^{3+} (an FeO_4^{5-} cluster) were done by Tossell (1978a) and by Tang Kai et al. (1980), who used them to interpret Mössbauer isomer shifts of Fe^{3+}, as further discussed later in this chapter. Maruthe and Trautwein (1983) used simple extended Hückel molecular-orbital calculations on FeO_6^{9-} clusters to interpret isomer shifts, quadrupole splittings, and magnetic hyprfine splittings in the Mössbauer spectra of Fe^{3+} in oxides. More recently, the MS-SCF-$X\alpha$ method has again been applied to the octahedral FeO_6^{9-}

cluster, tetrahedral FeO_4^{5-} cluster, and to a trigonally distorted FeO_6^{9-} cluster (Sherman, 1985a).

The FeO_6^{9-} cluster (Tossell et al., 1973a, 1974; Sherman, 1985a) provides a model for hematite (Fe_2O_3) and for octahedrally coordinated Fe^{3+} in a variety of other oxides, including spinel oxides, and in silicates. The calculated molecular-orbital diagram in its spin-unrestricted form is shown in Fig. 4.26(a) (after Sherman, 1985a). The order of the molecular-orbital energy levels is the same as in the earlier studies, but there are slight differences in energy separation and orbital compositions compared with Tossell et al. (1973, 1974). The orbitals grouped together in Fig. 4.26(a) as in O $2p$ include nonbonding orbitals ($1t_{1g}$, $1t_{2u}$, and $6t_{1u}$), and the Fe–O bonding orbitals of which the most important is the $3e_g$ orbital, which corresponds to the Fe $3d$–O $2p$ σ-bonding interaction. Of next importance is the $1t_{2g}$ orbital, which corresponds to the Fe $3d$–O $2p$ π-bonding interaction. The orbitals labeled $2t_{2g}$ and $4e_g$ are the antibonding versions of the $1t_{2g}$ and $3e_g$ bonding molecular orbitals. If the Fe–O bond were purely ionic, they would be the iron $3d$ atomic orbitals, but since there is significant covalency they have a significant oxygen $2p$ component. At an energy approximately 10 eV above the $2t_{2g}$ and $4e_g$ orbitals are the $7t_{1u}$ and $7a_{1g}$ orbitals, which correspond to Fe $4p$ and Fe $4s$ atomic orbitals, although the calculations show them to be highly delocalized in nature.

Tossell et al. (1973a, 1974) compared the results of their calculations with data from x-ray emission and x-ray photoelectron spectroscopic studies, demonstrating reasonably good correlation between calculated and experimental energies. Sherman (1985a) concentrated on the calculation of electronic ("optical") absorption spectra including the crystal- (or ligand-) field transitions and the ligand-to-metal charge-transfer transitions. The problem of using calculated "one-electron" orbital energies to interpret transitions involving multielectronic states was actually addressed in this work by using the multiplet theory of Slater (1968, 1974). A full account of this approach is given by Sherman (1985a), who, as well as presenting the results of MS-SCF-$X\alpha$ calculations on the tetrahedral FeO_4^{5-} and FeO_6^{9-} trigonally distorted clusters, also used these in the calculation of "optical" spectra. The molecular-orbital energy-level diagram for the trigonally distorted (C_{3V}) cluster is shown in Fig. 4.26(b) and is a closer approximation to the coordination polyhedron of Fe^{3+} in Fe_2O_3 (hematite). Compared to the octahedral FeO_6^{9-} cluster, the descent in symmetry to C_{3V} causes splitting of the triply degenerate orbitals into combinations of twofold-degenerate e and singly degenerate a_1 or a_2 orbitals. Although the makeup of the molecular orbitals in terms of atomic-orbital character is fairly similar to that in the octahedral cluster, the width of the O $2p$ nonbonding orbital set (~2 eV) is much greater because the shortening of certain oxygen–oxygen distances and lengthening of others causes either increased or decreased repulsive O–O interaction.

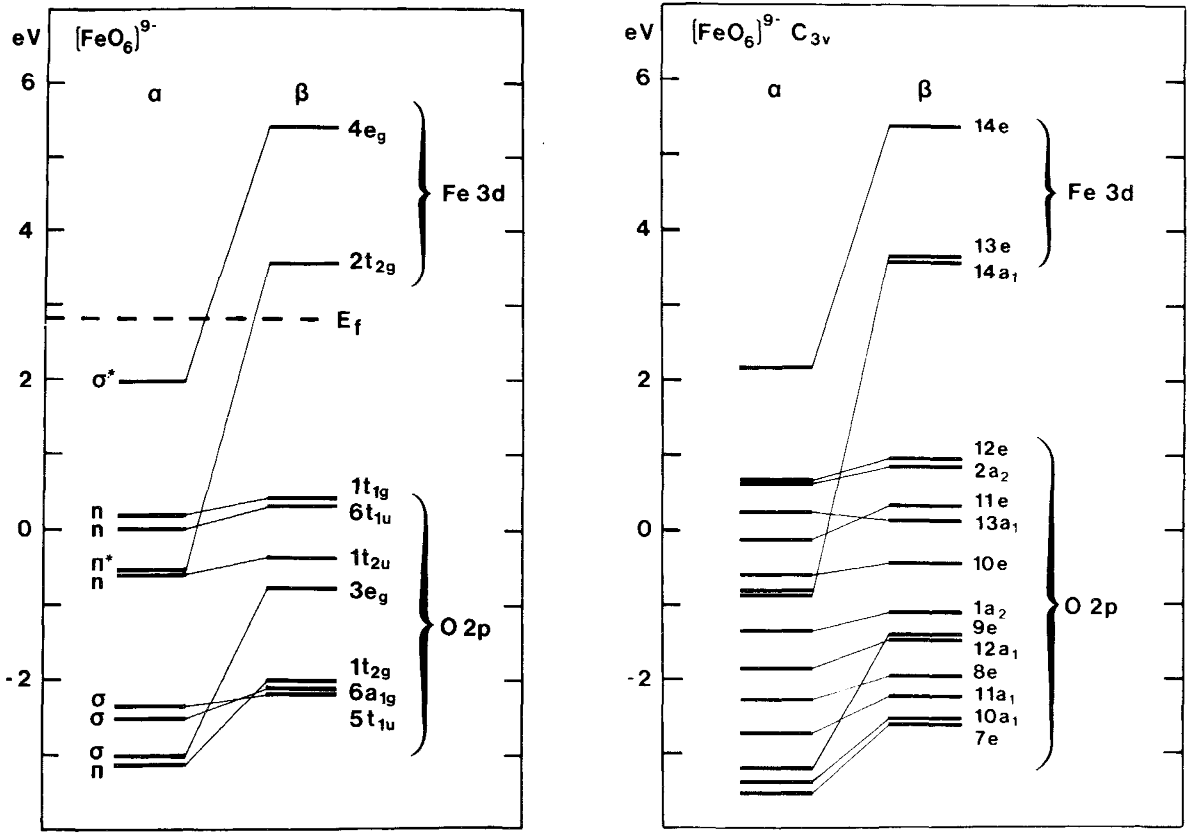

Fig. 4.26. Molecular-orbital energy-level diagrams for the $(FeO_6)^{9-}$ cluster calculated using the MS-SCF-$X\alpha$ method: (a) in regular octahedral (O_h) symmetry; (b) in the distorted octahedral (C_{3v}) symmetry. The symbols α and β refer to spin-up and spin-down electron orbitals, respectively; E_F is the Fermi level below which all the orbitals are occupied; σ and *n* refer to σ bonding (or σ* antibonding, etc.) and nonbonding molecular orbitals (after Sherman 1985a; reproduced with the publisher's permission).

Sherman (1985a) also uses the results of these calculations to discuss the covalency of the Fe^{3+}–O bond and the magnetism in iron oxides. The problems arising in any attempt at a quantitative estimation of covalency are addressed in Chapter 7; the point made by Sherman is that, whereas the Fe^{3+}–O bond has significant covalency as measured by the donation of charge from O^{2-} to Fe^{3+}, the extent of this covalence is much the same in the three clusters studied. However, it is highly spin dependent, and the spin polarization of the Fe–O covalency differs appreciably among the different clusters, a feature that can be used to predict the main features of the magnetic structures of Fe^{3+}-containing oxides. For example, in the $(FeO_6)^{9-}$ cluster, the α-spin e_g and t_{2g} antibonding orbitals are occupied and cancel much of the α-spin t_{2g} and e_g Fe–O bonding interaction. At the same time, the β-spin antibonding orbitals are unoccupied. Hence, most of the charge donated to the Fe^{3+} by the O^{2-} anions is of β-spin character. The spin-dependent covalency leaves the oxygen atoms with a net α-spin excess, and they will favor donating α-spin electron charge to any other Fe^{3+} ions to which they are bonded. This can be done only if the antibonding orbitals localized on these Fe^{3+} ions are occupied by β-spin electrons (i.e., if these Fe^{3+} ions are antiferromagnetically coupled to the first Fe^{3+} center).

The FeO_6^{10-} octahedral cluster (Tossell et al., 1974) has the electronic structure shown by the molecular-orbital energy-level diagram in Fig. 4.27. In this case, the crystal-field-type $2t_{2g}$ and $3e_g$ orbitals are at, or above, the O $2p$ nonbonding orbitals ($1t_{1g}$, $6t_{1u}$, $1t_{2u}$) but, whereas the $2t_{2g\uparrow}$-$3e_{g\uparrow}$ energy separation is somewhat smaller in the octahedral Fe^{2+} cluster than in the Fe^{3+} case, the spin splitting is somewhat larger. The $6a_{1g}$, $5t_{1u}$, $1t_{2g}$, and $2e_g$ are the Fe^{2+}–O bonding orbitals of the system. As in many other studies employing MS-SCF-$X\alpha$ calculations, comparisons were made with optical and x-ray emission spectroscopic data to aid in spectral interpretation and to establish the validity of the calculations. For example, in Table 4.23 are shown experimental data for Fe $K\beta$ x-ray emission spectra of FeO and Fe_2O_3 (hematite) in comparison with energies of spectral features calculated by MS-SCF-$X\alpha$ methods by Tossell et al. (1974).

Hematite and the other binary iron oxides have been the subject of numerous experimental and theoretical studies, particularly of their complex magnetic and electrical properties as well as of electronic structure. Notable among more recent investigations have been those centered on "photoemission" studies (i.e., uv and x-ray photoelectron spectra obtained using "tunable" synchrotron radiation) of electronic structure (e.g., Fujimori et al., 1986; Lad and Henrich, 1989). Fujimori et al. (1986) studied α-Fe_2O_3 (hematite) using XPS, Auger, and uv photoemission and compared their results with a calculation on an FeO_6^{9} cluster using the methods of configuration interaction. As shown by the example in Fig.

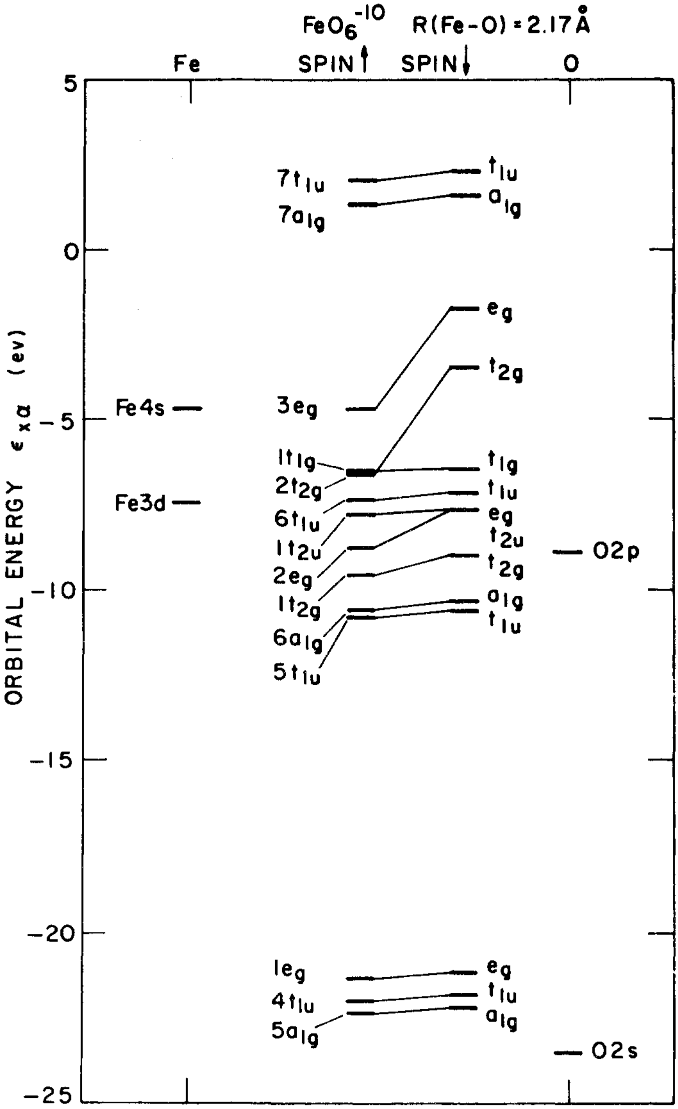

Fig. 4.27. Molecular-orbital energy-level diagram for the $(FeO_6)^{10-}$ cluster calculated using the MS-SCF-$X\alpha$ method. The highest-energy occupied orbital is the $2t_{2g\downarrow}$ containing one electron. Also shown are the energies of Fe and O atomic orbitals. Spin-up (↑) and spin-down (↓) molecular orbitals are shown in this spin-unrestricted calculation on a regular octahedral (O_h) cluster at an iron–oxygen distance of 2.17 Å (after Tossell et al., 1974; reproduced with the publisher's permission).

Table 4.23. Comparison of experimental Fe $K\beta$ x-ray emission spectra for FeO and α-Fe_2O_3 with energies (in eV) calculated using MS-SCF-$X\alpha$ methods[a]

	FeO		Fe_2O_3		
XES peak	**Experimental relative energy**	**Calculated relative energy**	**Experimental relative energy**	**Calculated relative energy**	**Assignment**
$K\beta'$	−13.4	−11.3	−14.3	−13.4	$3t_{1u} \rightarrow$ Fe 1s $(1t_{2g}\downarrow \rightarrow 7t_{1u}\downarrow)$
$K\beta_{1,3}$	0	0	0	0	$3t_{1u} \rightarrow$ Fe 1s
$K\beta''$	33.0	32.8	34.2	34.6	$4t_{1u} \rightarrow$ Fe 1s
$K\beta_5$	47.4	44.0	48.1	45.5	$5t_{1u} \rightarrow$ Fe 1s
$K\beta_5'$		47.4		49.5	$6t_{1u} \rightarrow$ Fe 1s
$K\beta'''$		56.8	61.7	60.9	$7t_{1u} \rightarrow$ Fe 1s

[a] See Tossell et al. (1974) for sources of experimental data.

4.28, this calculation successfully reproduces the features in the valence-band x-ray photoelectron spectrum of Fe_2O_3 that arise from Fe 3d-derived emission, specifically from multiplet structure involving mixed d^4, d^5L, and d^6L^2 configurations (where L is a ligand hole). In Fig. 4.28 are shown both the final-state multiplet lines giving rise to the spectrum and the components giving rise to them. In effect, the XPS of Fe_2O_3 in the valence region is not only derived from the ejection of d electrons, and hence a simple d^4 multiplet, but also involves oxygen (ligand) to 3d charge-transfer screening of the 3d holes. Lad and Henrich (1989) undertook even more detailed photoemission studies of the valence-band electronic structure of α-Fe_2O_3 (and also Fe_xO and Fe_3O_4) by using cleaved single crystals. They also found good agreement between experiment and the CI calculations on the FeO_6^{9-} cluster of Fujimori et al. (1986). The application of band theory to understanding of the transition-metal monoxides is further discussed later. Wüstite ($Fe_{1-x}O$) has also been the subject of numerous studies because of its defect structure (e.g., the work of Chou et al., 1986, using the DV-Xα method).

The differences between Fe–O and Fe–OH bonding in hydroxyl-bearing iron oxides and silicates have also been investigated using MS-SCF-$X\alpha$ calculations and x-ray photoelectron spectroscopy (Sherman, 1985b; Welsh and Sherwood, 1989). The molecular-orbital energy-level diagram for the trans-$[FeO_4(OH)_2]^{7-}$ cluster (Sherman, 1985b) is shown in Fig. 4.29. In this cluster, which has C_{2h} symmetry, the calculated molecular-orbital energy levels should be compared with those of the FeO_6^{9-} cluster in Fig. 4.26(a). As for the latter cluster, the molecular orbitals can be grouped into sets in relation to their atomic-orbital character, with the dominantly Fe 3d (crystal-field-type) orbitals being at the top of the "valence band." Now, however, as shown in Fig. 4.29, the orbitals below these in energy fall into four groups: O 2p nonbonding orbitals, Fe–O

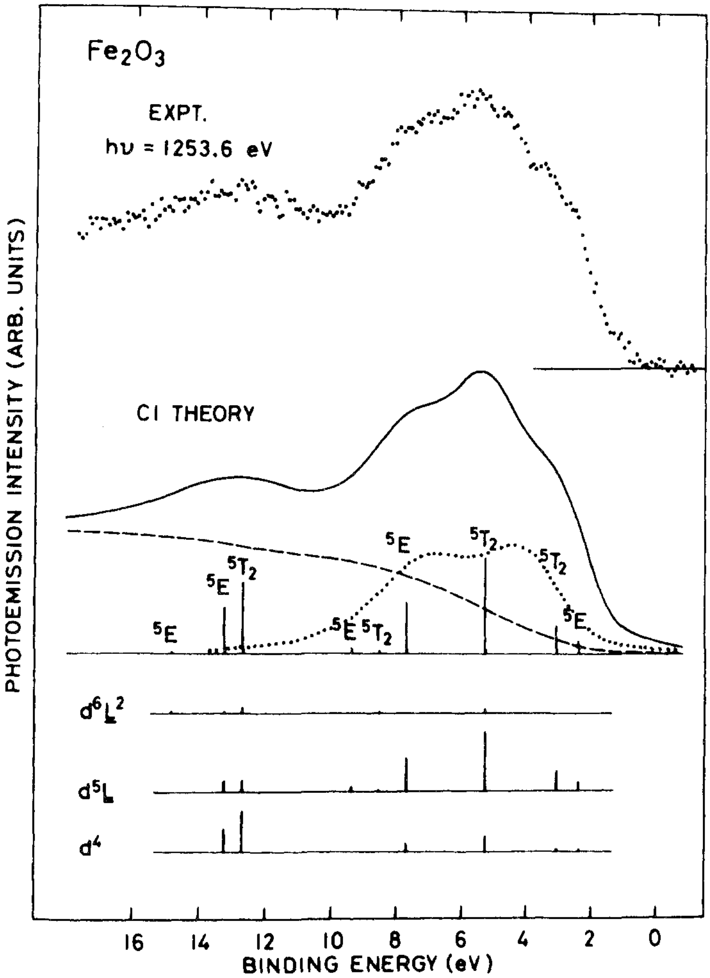

Fig. 4.28. The experimental valence-band x-ray photoelectron ("photoemission") spectrum of α-FeO_3 compared with a calculated spectrum based on a configuration-interaction calculation on an FeO_6^{9-} cluster. The dotted and dashed curves represent O 2*p* emission and integral background, respectively. The bottom panel shows a decomposition into configuration components for each final-state line (after Fujimori et al., 1986; reproduced with the publisher's permission).

bonding orbitals, Fe–OH bonding orbitals, and O–H bonding orbitals (with increasing binding energy). Study of the charge distribution in the different regions of the cluster (i.e., in Fe, O, H atomic regions, intersphere and outer sphere regions) shows that the Fe^{3+}–OH^- bond is more "ionic" than the Fe^{3+}–O^{2} bond; it also has a smaller spin polarization, and this explains why the magnetic coupling via superexchange interaction between OH-bridged Fe^{3+} cations is much weaker than that between

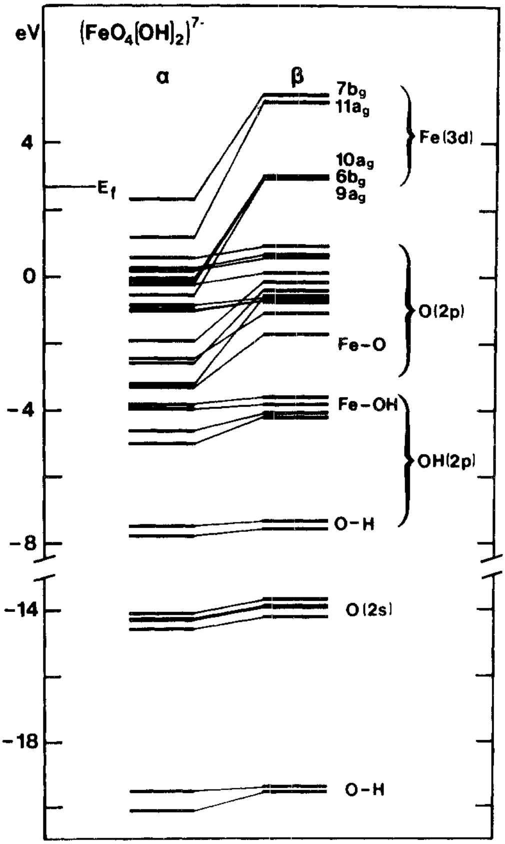

Fig. 4.29. Molecular-orbital energy-level diagram for the trans-$[FeO_4(OH)_2]^{7-}$ cluster calculated using the MS-SCF-$X\alpha$ method. The symbols α and β refer to the spin-up and spin-down electron orbitals, respectively, and E_F is the Fermi level below which all the orbitals are occupied (after Sherman 1985b; reproduced with the publisher's permission).

O-bridged Fe^{3+} cations (Sherman, 1985b). The MS-SCF-$X\alpha$ calculations on a C_{2V} symmetry $FeO_6H_3^{3-}$ cluster (Welsh and Sherwood, 1989) showed good agreement with the valence-band x-ray photoelectron spectrum and show that FeOOH and Fe_2O_3 can clearly be distinguished by XPS in the valence-band region.

4.4.4. *Complex oxides*

Many of the mineralogically important transition-metal oxide phases contain more than one cation species, or more than one type of coordination site for the cations. Commonly, the cations are in more than one oxidation state. Examples include ilmenite ($FeTiO_3$) and the family of minerals with the spinel-type crystal structure, including magnetite (Fe_3O_4), chromite

($FeCr_2O_4$), and ulvöspinel (Fe_2TiO_4). In addition to their mineralogical importance, such phases have proved of interest in materials science because of the diversity of their properties. One other complex oxide family of interest to mineralogists has proved of very great importance to materials scientists; the perovskites ($CaTiO_3$ and numerous other ABO_3 phases) have become the focus of intense research since the discovery of high-temperature superconductivity in certain perovskite-type phases. The perovskite family is also of particular interest in mineralogy because of the proposed importance of perovskite-structure high-pressure phases at depth in the Earth, as further discussed in Chapter 7.

Attempts have been made to model the electronic structures of complex oxides by combining the results of molecular-orbital cluster calculations on relevant polyhedra, or by using various band-structure methods. Vaughan and Tossell (1978) used the results of MS-SCF-$X\alpha$ calculations of the type described above to discuss the electronic structures of ilmenite, magnetite, chromite, and ulvöspinel. Energy-level diagrams from the calculations (as in Fig. 4.27) were used to construct schematic "one-electron" MO/band-theory energy-level diagrams, as shown in Figs. 4.30 and 4.32. In Fig. 4.30, such an energy-level diagram is shown for ilmenite ($FeTiO_3$) alongside the model for the isostructural hematite (Fe_2O_3). Although these are relatively simplistic models, they have the advantage of clarifying the major features of the electronic structures of these phases and the relationship between electronic structure and mineral properties. For example, the lower resistivity of hematite correlates with the smaller separation between occupied and unoccupied levels in this phase than in ilmenite, and the spectral reflectance curves of these minerals in the visible region (Fig. 4.31) show features that can be correlated with electronic transitions [labeled (a), (b), and (c) in both Figs. 4.30 and 4.31] giving higher values of k and hence of $R(\%)$ (see Section 2.3.2). These and other properties are discussed in more detail by Vaughan and Tossell (1978). The same approach was used by these authors to discuss the electronic structures of the spinel-structured oxides chromite, ulvöspinel, and magnetite, as illustrated in Fig. 4.32. Again, a wide range of properties were discussed using these models. Tossell (1978a) also presented a one-electron energy-level diagram for Fe_3O_4 based on such calculations.

An extension of the molecular-orbital cluster calculation approach relevant to the complex oxides, and to silicates containing transition metals of more than one element or oxidation state, is the study of clusters composed of two (or more) linked polyhedra. Sherman (1987a,b) has applied this approach to the study of metal–metal charge-transfer processes by performing MS-SCF-$X\alpha$ calculations on pairs of edge-sharing octahedral clusters containing adjacent Fe^{2+} and Fe^{3+} or Fe^{2+} and Ti^{4+} cations. Thus, the $(FeTiO_{10})^{14-}$ cluster shown in Fig. 4.33(a) was used to model Fe^{2+}–Ti^{4+} charge transfer of the kind occurring in ilmenite and in ulvöspinel. The molecular-orbital calculation yields an energy-level diagram

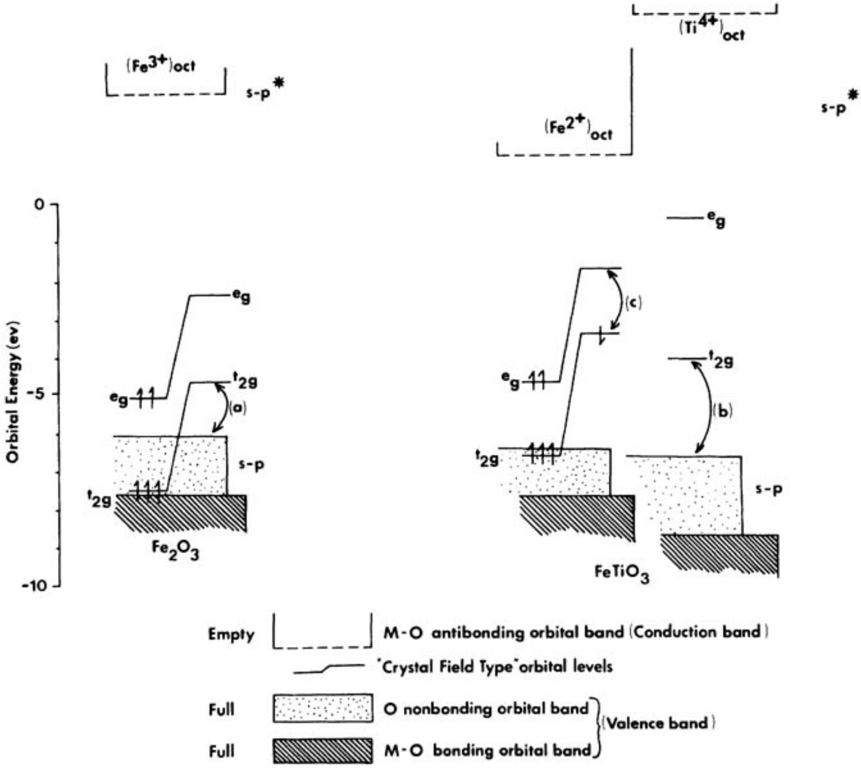

Fig. 4.30. Molecular-orbital/band models to illustrate the electronic structures of hematite and ilmenite and based on MS-SCF-$X\alpha$ calculations on FeO_6^{9-}, FeO_6^{10-}, and TiO_6^{8-} clusters. The double arrows labeled (a), (b), (c) refer to electronic transitions giving rise to optical properties (after Vaughan and Tossell, 1978).

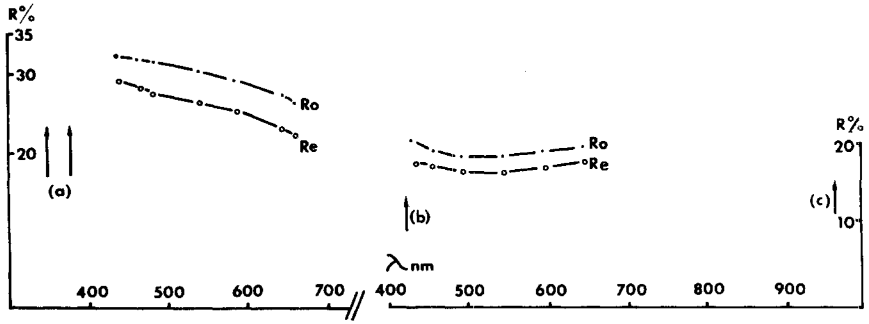

Fig. 4.31. Spectral reflectance data in the visible light range (~400–700 nm) for hematite (left) and ilmenite (right). Data are shown for both the ordinary (R_o) and extraordinary (R_e) vibration directions in plane-polarized light. The arrows (labeled to correspond with Fig. 4.30) indicate energies of calculated major electronic transitions (after Vaughan and Tossell, 1978).

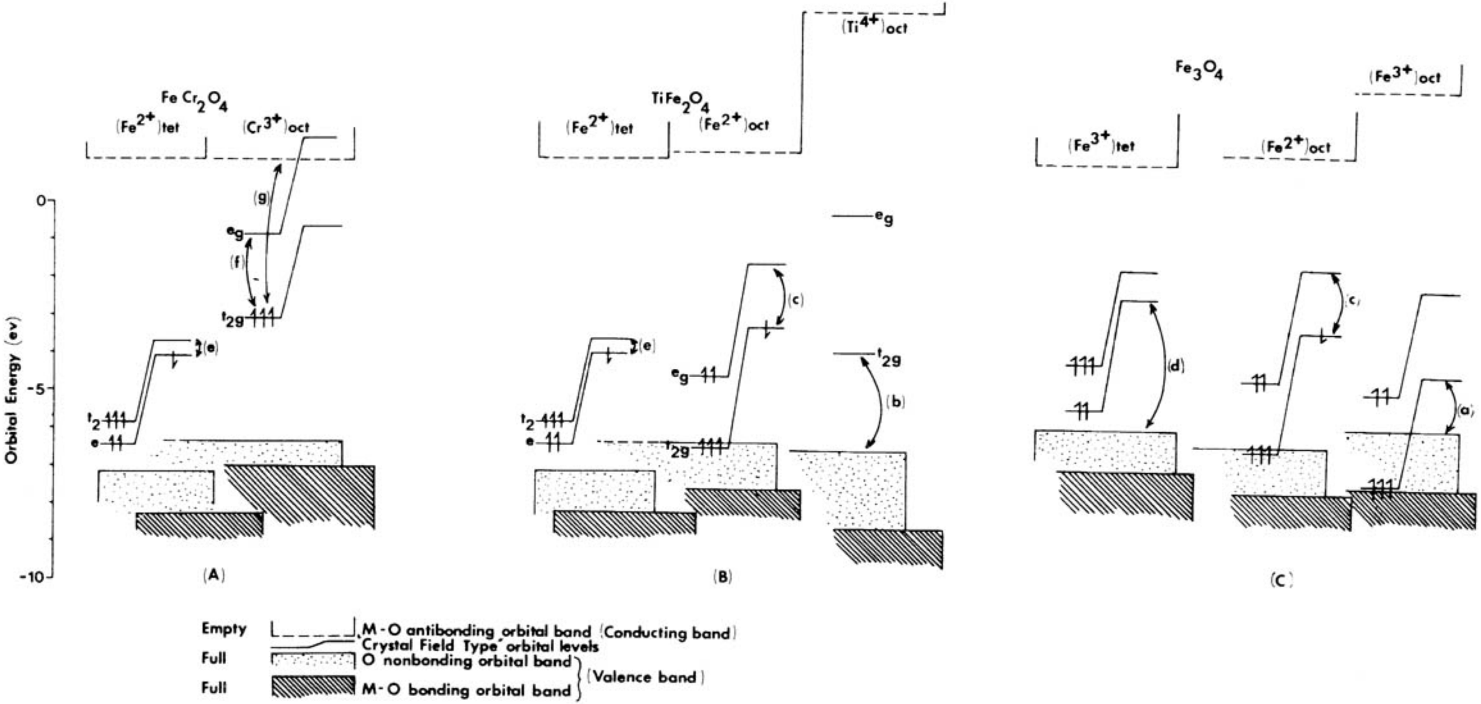

Fig. 4.32. Molecular-orbital/band models to illustrate the electronic structures of chromite, ulvöspinel, and magnetite and based on MS-SCF-$X\alpha$ calculations on FeO_6^{9-}, FeO_6^{10-}, TiO_6^{8-}, FeO_4^{6-}, FeO_4^{5-}, and CrO_6^{9-} clusters. The double arrows labeled (a) through (g) refer to electronic transitions giving rise to optical properties (after Vaughan and Tossell, 1978).

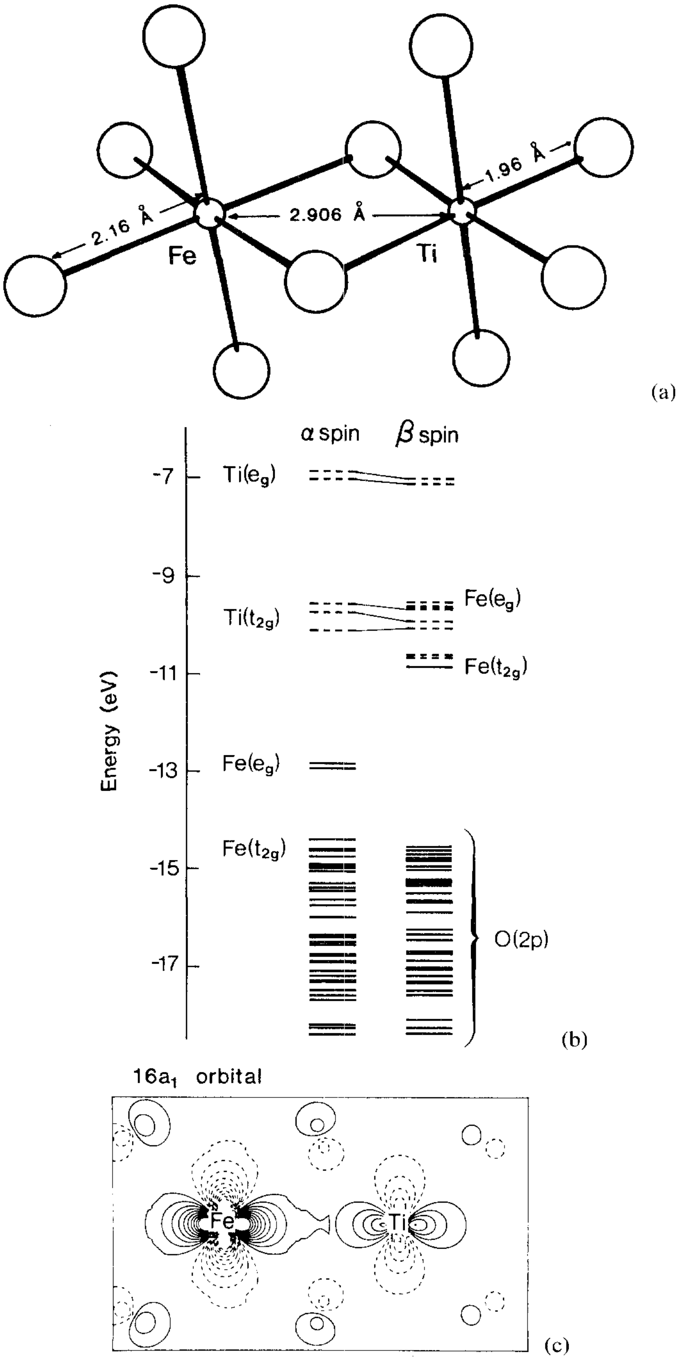

Fig. 4.33. Molecular-orbital calculations on the $(FeTiO_{10})^{14-}$ cluster using the MS-SCF-$X\alpha$ method: (a) geometry of the $(FeTiO_{10})^{14-}$ cluster; (b) molecular-orbital energy-level diagram for the cluster; α and β spin are spin-up and spin-down electron orbitals; energy levels indicated by dashed lines are unoccupied; (c) calculated wave-function contours for the $16a_1$ orbitals of the cluster; the $16a_1$ orbital corresponds to the d_{xy} Fe(t_{2g}) orbital and is clearly Fe–Ti bonding in character (after Sherman, 1987b; reproduced with the publisher's permission).

shown in Fig. 4.33(b) and the lowest-energy Fe^{2+}–Ti^{4+} electron transfer according to this calculation takes place from a filled, dominantly Fe(t_{2g}) orbital to an empty Ti(t_{2g}) orbital. The energy of this transition is calculated to be 18,040 cm^{-1}, in reasonable agreement with experiment (ulvöspinel: 18,150 cm^{-1}; ilmenite: 20,200 cm^{-1}; see Sherman, 1987b). It is interesting to note that such calculations show that both Fe^{2+}–Ti^{4+} and Fe^{2+}–Fe^{3+} charge transfer are associated with weak chemical bonding between the metals across the shared edge [e.g., by overlap of Fe(t_{2g}) and Ti(t_{2g}) orbitals, as shown in Fig. 4.33(c)].

4.4.5. *Band theory and the transition-metal monoxides*

Although the series of oxide phases, MnO, FeO, CoO, and NiO are relatively unimportant as mineral species, they occupy a special place in solid-state physics because of the problems they pose in understanding their electronic structures. All have the simple rocksalt-type crystal structure, but, despite having fully occupied oxygen *p* states, empty metal *s* states, and *partially occupied* metal *d* states, they are all antiferromagnetically ordered and electrically *insulating*. It is the apparent incompatibility of this insulating behavior with the partial occupation of the *d* shell, expected in terms of the independent-electron model to give these materials metallic conductivity, that has proved so puzzling. The longstanding explanation is that their behavior arises from electron–electron correlations not encompassed within the independent-electron model, concepts first put forward by Mott and later associated with the term *Mott insulator* (Mott, 1974). This view was challenged by Wilson (1970) on the basis of non-self-consistent band calculations that were not considered convincing and, more recently, by Terakura et al. (1984a,b). The latter workers performed more accurate calculations using the local-spin-density formalism, and the augmented-spherical-wave method (Williams et al., 1979); calculations that were fully self-consistent. The results of these calculations suggest that the oxides have a band gap at the Fermi energy and are therefore *band* (or *Bloch*) insulators rather than Mott insulators. The qualitative picture arising from the calculations of Terakura et al. (1984a) is illustrated in Fig. 4.34. It differs from the widely held (Mott-insulator) model in terms of the energy position of the empty *d* states.

The interpretation of spectral properties in oxides such as NiO, in particular the valence-band photoemission spectra and inverse photoemission data (McKay and Henrich, 1984) has proved controversial. However, recent calculations using a supercell approach have given results for NiO in good agreement with such spectroscopic data (Norman and Freeman, 1986). These calculations reconcile the band picture of Terakura et al. (1984a,b) and the experimental studies that have indicated large values (~ 8 eV) for the intra-atomic Coulomb integral (Hufner et al., 1984; McKay and Henrich, 1984; Sawatzky and Allen, 1984).

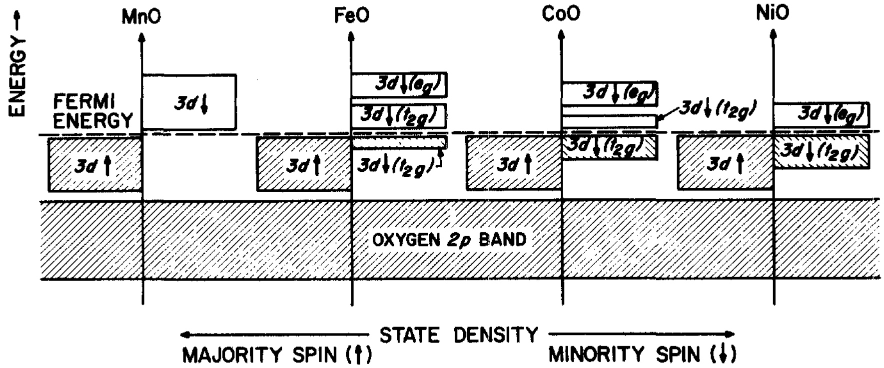

Fig. 4.34. Band picture of the transition-metal monoxides. The qualitative difference between this picture and the Mott insulator is the energy position of the empty *d* states (after Terakura et al., 1984a; reproduced with the publisher's permission).

Band-structure calculations (using a self-consistent KKR method; see section 3.11) have yielded accurate equilibrium lattice parameters for the oxides MnO, FeO, CoO, and NiO (Yamashita and Asano, 1983b). As shown in Table 4.24, the calculations were performed for nonmagnetic, ferromagnetic, and antiferromagnetic states, and the effect of magnetic ordering on the lattice constants was shown to be quite significant. The same authors also calculated the lattice energies and total energies, showing the antiferromagnetic states to be the most stable, in agreement with experiment. It therefore appears that, since these materials are highly symmetric (cubic) structures, and can be viewed simplistically as "tightly packed," calculational methods of the type used by Yamashita and Asano

Table 4.24. The equilibrium lattice constant (a_L) of CaO and some transition-metal monoxides. The experimental values are given in the second column. The theoretical values of a_L in the nonmagnetic state are given in the third column. The theoretical values of a_L are also calculated for the ferromagnetic and antiferromagnetic states

		a_L(calc.) (Å)		
	a_L(expt.) (Å)	**Nonmag. state**	**Ferromag. state**	**Antiferromag. state**
CaO	4.81	4.820		
TiO	4.24	4.374		
VO	4.08	4.222		
MnO	4.446	4.121	4.419	4.436
FeO	4.34	4.141	4.304	4.288
CoO	4.27	4.112	4.238	4.216
NiO	4.17	4.174	4.17	4.183

Source: after Yamashita and Asano, 1983b.

(1983b) or, indeed, by Terakura et al. (1984b), and that use spherically averaged atomic potentials, can nevertheless give accurate structural properties.

4.5. Calculation of Mössbauer parameters in iron oxides (and other iron compounds)

Although the Mössbauer isomer shift (δ) and the electric-field gradient at the nucleus both depend only upon the ground-state electron distribution, they are still difficult to calculate accurately. This is because they depend upon properties at the nucleus, where relativistic effects are important, the effects of core-orbital polarization cannot be neglected, standard Gaussian basis sets are problematic because they do not satisfy theoretically necessary "cusp conditions", and many other basis sets may have inadequate flexibility. Another difficulty in any comparison of calculation and experiment is that the nuclear parameters that relate the "observable" electron density to the measured spectral properties are not well constrained. For example, Duff (1974) has noted that the proportionality factor (α) for ^{57}Fe in the expression $\delta_i - \delta_j = \alpha[\rho_i(o) - \rho(o)]$, where $\rho(o)$ is the electron density at the nucleus and δ the isomer shift, has quoted values from -0.11 to $-0.62a_0^3$ mm sec^{-1}. Given such uncertainty in nuclear parameters, observed changes in Mössbauer isomer shifts can be explained by a wide range of theoretical results.

There have, however, been some important advances in the direct calculation of isomer shifts and quadrupole splittings within the past decade or so, particularly for Fe, Zn, and Sb. Nieuwpoort et al. (1978) carried out *ab initio* Hartree–Fock–Roothaan calculations on FeF_6^{4-}, FeF_6^{3-}, $Fe(CN)_6^{4-}$, and $Fe(CN)_6^{3-}$ with large Gaussian bases, for example $(14s11p6d) \rightarrow [9s7p4d]$ on Fe, obtaining $-0.30a_0^3$ mm s^{-1} for the calibration constant α. They also established that, although their Gaussian bases give a $\rho(o)$ considerably different from Hartree–Fock results for Fe^{2+} and Fe^{3+} free ions, the *difference* of $\rho(o)$ [which may be symbolized as $\Delta\rho(o)$] for the two charge states is given very accurately. It was also found that inclusion of the crystal Madelung potentials for the FeF_6^{n-} cases gives little change in $\rho(o)$ and essentially no change in $\Delta\rho(o)$ for FeF_6^{4-} versus FeF_6^{3-}. Important contributions to $\Delta\rho(o)$ occur in both the Fe core orbitals ($1s$, $2s$, $3s$) and in the outermost two a_{1g} symmetry valence molecular orbitals. Neglect of changes in core-orbital contributions to $\rho(o)$ would lead to an α value several times larger. These results suggest that all-electron *ab initio* Hartree–Fock–Roothaan SCF calculations with moderate bases would probably give $\rho(o)$ values that correlate very well with observed isomer shifts, although there is still uncertainty about the relationship between Hartree–Fock and more accurate relativistic, so-called Dirac–Hartree–Fock (DHF) values for $\Delta\rho(o)$.

Ab initio Hartree–Fock–Roothaan SCF calculations have also been used to calculate the nuclear quadrupole moment (*eQ*) of $^{57}Fe^{m}$, using calculated values of *eq* and the measured quadrupole splittings for $FeBr_2$ and $FeCl_2$ in certain matrices (Duff et al., 1981). Unfortunately, details of the Gaussian basis set used in these calculations were not given. One interesting aspect of the calculations is the importance of the effect of the Fe 3*p* orbitals on the electric-field gradient (*eq*), which shows a larger difference between $FeCl_2$ and $FeBr_2$ than does the larger-magnitude Fe 3*d* contribution. One should note, however, that later DVM-$X\alpha$ calculations on $FeCl_2$ and $FeBr_2$ (Ellis et al., 1983) found *eq* to have a sign *opposite* to that found by Duff et al. (1981), and to be strongly dependent on the assumed Fe–anion bond distance. Recent *ab initio* HFR SCF studies on $Fe(CO)_n$ (Sawaryn et al., 1986) suggest the even more optimistic conclusion that minimum basis sets (e.g., [4*s*2*p*1*d*] for Fe), and calculation of $\rho(o)$ from Mulliken populations and DHF atomic orbital values of $\rho(o)$, give good correlations between experimental isomer shifts and calculated $\rho(o)$ values (although with a considerably smaller magnitude of α). Calculated EFG values are also in good agreement with experiment for the whole $Fe(CO)_n$ series. It thus appears that even small-basis-set *ab initio* studies may be useful in evaluating both the electron density at the nucleus and the EFG for transition-metal compounds.

Mössbauer parameter calculations using density-functional methods have been somewhat less successful. In MS-SCF-$X\alpha$ studies, it has been found that $\rho(o)$ is strongly dependent upon the choice of Fe sphere radius. If ratios of Fe and anion (X) sphere radii are kept constant, then MS-SCF-$X\alpha$ calculation of $\rho(o)$ as a function of Fe–X distance for a given polyhedron (e.g., FeO_4^{6-}) gives results that correlate well with experimental isomer shifts (Tang Kai et al., 1980). Presumably, such studies could be extended to other Fe–O (and Fe–S) polyhedra, evaluating $\rho(o)$ as a function of bond distance or applied pressure. However, the dependence of the results on the choice of sphere radii makes the quantitative comparison of different bonding environments (e.g., four- versus six-coordinate Fe) a difficult matter, although normal choices of radii give reasonable semiquantitative trends in $\rho(o)$ for different materials with only moderate scatter (Guenzburger et al., 1977). MS-SCF-$X\alpha$ wave functions have also been used to calculate electric-field gradients using the extended sphere charge partitioning schemes of Case and Karplus (1976) or Nagel (1985a). Even for very complicated systems, such as iron (II) porphine (Sontum et al., 1983) and Fe_2O_3 (Nagel, 1985b), the results are in reasonable agreement with experiment, but the variation in calculated quantities with the choice of MS-SCF-$X\alpha$ sphere radii does render these results somewhat ambiguous. Guenzberger et al. (1984) have used the DVM-$X\alpha$ method to calculate electric-field gradients and isomer shifts in the $Fe(CO)_n$ series, obtaining results that are qualitatively correct although, sometimes, considerably in error quantitatively. It therefore appears that either Hartree–Fock–Roothaan or density-functional molecular cluster methods with reasonably flexible core–valence basis sets should provide good isomer shift and electric-field-gradient values for molecules, and probably also for molecular cluster models of solids. Of course, for a solid the electric-field gradient may be influenced by the ions outside the molecular cluster, but for many cases such effects will be small. For example, Nagel (1985b) found the external contribution to *eq* to be very small compared to the local FeO_6^{9-} cluster contribution in Fe_2O_3.

Reasonable results have also been obtained for ^{67}Zn Mössbauer isomer shifts in zinc chalcogenides from LMTO band calculations (Svane and Antoncik, 1986) and for Sb compounds (Ravenak et al., 1983) using the DVM-$X\alpha$ method. The overall conclusion must be that the time is ripe for the systematic calculation of Fe isomer shift and electric-field-gradient values in Fe–O, Fe–S, and other polyhedra using *ab initio* Hartree–Fock–Roothaan or DVM-$X\alpha$ methods.

5

APPLICATIONS TO SILICATE, CARBONATE, AND BORATE MINERALS AND RELATED SPECIES

5.1. Introduction

The most abundant materials making up the crust of the Earth (i.e., the "rock-forming minerals") can be regarded as dominated by oxyanion units; notably, the units that can be formally represented by SiO_4^{4-} and AlO_4^{5-} clusters of the silicate minerals, and the CO_3^{2-} unit of the carbonates. Less common, but geochemically interesting, oxyanion units include, for example, BO_3^{3-}, BeO_4^{6-}, and PO_4^{3-}.

In this chapter, applications of quantum-mechanical calculations and experimental techniques to such materials are considered. First, the silicates are discussed, commencing with the large amount of work undertaken on the olivines, before considering such work as has so far been done on the other silicate minerals and related materials. Second, the most important of the nonsilicate rock-forming mineral groups, the carbonates, are discussed. Finally, although of less petrological importance but interesting geochemically and in terms of contrast with the other groups, the borates and related species are considered. In each case, geometric aspects of structure and the problems of calculating structural properties are considered before going on to consider electronic structures and the factors controlling stabilities and a wider range of physical properties. In all of these materials, there is considerable interest in the bonding in the oxyanion unit and how this is affected by, and controls, the interaction with counterions or the polymeric units. The building up of the minerals by such interactions exerts the dominant control over their crystal chemistries and properties and thus forms a central theme of this chapter.

5.2. Silicates

The silicate minerals are, of course, characterized by the presence of the tetrahedral SiO_4 cluster unit and the crystal chemistry and classification of silicates dominated by the structures built up by the linking together (polymerization) of these units. In the "simplest" of the silicates, the island silicates such as the olivine minerals (dominated by the forsterite (Mg_2SiO_4)–fayalite (Fe_2SiO_4) solid solution series), the SiO_4 units are isolated by counterions such as Mg^{2+}, Fe^{2+}, Ca^{2+}. The most highly polymerized phases, the framework silicates, in which all oxygens of a tetrahedral unit are shared, include silica itself (see Chapter 4 for a full discussion of SiO_2) and the feldspars ($KAlSi_3O_8$–$CaAl_2Si_2O_8$), in which both SiO_4 and AlO_4 tetrahedra are important. Silicates of intermediate polymerization range from those with pairs of linked tetrahedra (Si_2O_7 units), to various single-chain [$(SiO_3)_n$] structures, as in the pyroxenes, and double-chain structures [$(Si_4O_{11})_n$], as in the amphiboles, to the sheets of linked tetrahedra characteristic of layer silicates, such as micas and clay minerals. The formation of structures containing rings of linked tetrahedra (with typically 3, 4, or 6 members) commonly leads to more complex phases with other oxyanion units present, for example, BO_3 in tourmaline $NaMg_3(Al,Fe)_6(OH)_4(BO_3)_3[Si_6O_{18}]$.

The extensive crystal chemical, geochemical, and mineralogical literature on the silicates has been reviewed in the classic texts of Deer, Howie, and Zussman (1966, 1978, 1982, 1986) and in volumes of the *Reviews in Mineralogy* series of the Mineralogical Society of America.

5.2.1. Olivines: Geometric structures

Magnesium olivines (Mg_2SiO_4) were among the first minerals to be studied quantum mechanically, due both to the simplicity of their chemical makeup as "salts" of SiO_4^{4-} and Mg^{2+} ions, and to the considerable complexity of their precise structures, that is, the distortions from idealized symmetry of their polyhedral units. Only when high-accuracy crystal structure refinements were obtained could the great complexity of structural distortions in olivines be appreciated (Birle et al., 1968). To explain the geometric distortions qualitatively, a number of theories could be evoked at that time. Some of these were theories current within solid-state and inorganic chemistry, such as the *d-pπ* bonding (Cruickshank, 1961) and valence-shell electron-pair repulsion (VSEPR) theories (Gillespie, 1960), first applied to silicates by Brown and Gibbs (1970). The central concept of *d-pπ* bonding theory, the structural importance of overlap of unoccupied central atom 3*d* orbitals and ligand 2*p* orbitals (e.g., Si 3*d*–O 2*p* interactions in silicates), has since been significantly modified to de-emphasize the directional π-bonding aspects and emphasize the greater penetration of *d* polarization functions into the atomic core for the third-row atoms, Si–Cl (Cruickshank, 1985). The central concept of VSEPR, the structural importance of maximizing the separation of valence electron pairs, has since been much used, and its quantum-mechanical basis has been elucidated (Bader et al., 1988).

Unfortunately, all of the phenomenological theories, even when apparently contradictory in terms of the electronic structures of the bonds they described, could be construed to explain experiments. An important advance occurred when the importance of Bartell's work on distortions in the lengths of P–O and S–O bonds using extended Hückel molecular-orbital theory (Bartell et al., 1970) was realized and this semiempirical method then applied to silicates (Louisnathan and Gibbs, 1972a,b). In the extended Hückel method, equilibrium bond distances cannot be calculated directly, but shorter, stronger bonds are expected to be associated with larger overlap populations (often symbolized by *n*). For various molecules, extended Hückel wave functions can be calculated, assuming either experimental bond distances and angles, or requiring all bond distances of a given type (e.g., Si–O) to be equal and utilizing experimental angles. If the extended Hückel results for the given cluster correctly describe the energetics determining the bond lengths, a correlation of increasing *n* with decreasing experimental bond distances should be found. Such correlations were found, and are shown for P–O and Si–O bonds in Figs. 5.1 and 5.2, respectively. The most convincing results of this type utilized constant distances and *sp*-only basis sets, avoiding the bias due to the different bond distances and the uncertainties regarding *d*-orbital size and involvement in bonding. However, all such EHMO calculations, no matter what their details, gave good correlations of *n* against observed bond length. Such calculations were later extended to many other *M*–O bonds, and direct calculation of minimum energy angles for silicic acid molecules with unequal bond lengths showed that short Si–O bonds lead to large equilibrium O–Si–O angles (Fig. 5.3). However, there was some

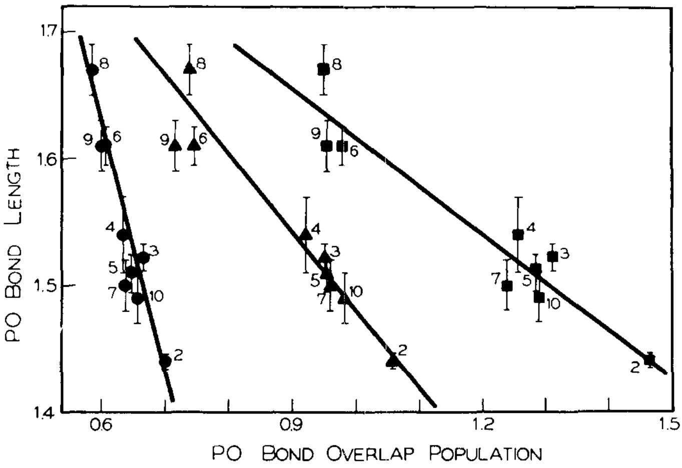

Fig. 5.1. Experimental P–O bond length versus bond overlap population calculated using extended Hückel molecular-orbital theory. See Bartell et al. (1970) for further details (after Bartell et al., 1970; reproduced with the publisher's permission).

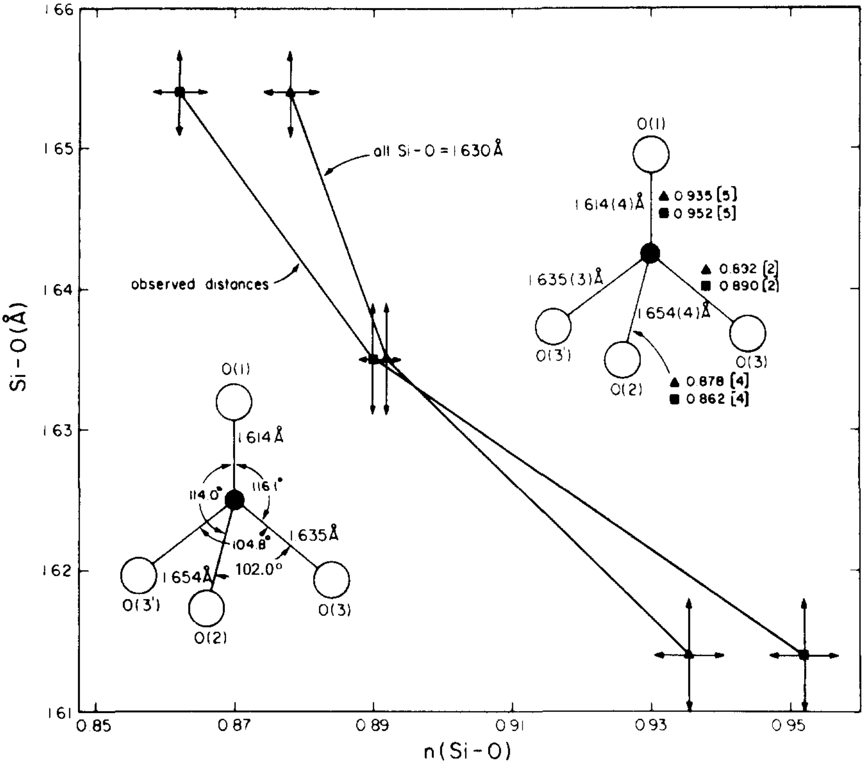

Fig. 5.2. Bond overlap populations, *n*(Si–O), calculated using extended Hückel molecular-orbital theory for the $(SiO_4)^{4-}$ tetrahedron of forsterite and plotted against Si–O bond distance (Å). Inset tetrahedron at left shows dimensions observed for SiO_4 cluster and one at the right shows overlap populations with maximum range of *n*(Si–O) in square brackets for the estimated standard deviations in the bond length (after Louisnathan and Gibbs, 1972b; reproduced with the publisher's permission).

skepticism about these results; first, because the EHMO method is approximate, non-self-consistent, and not designed to handle ionic systems; second, because of the indirectness of the geometric prediction, and, third, because of the neglect of atoms outside the $SiO_4{}^{4-}$ or $Si(OH)_4$ cluster. An alternative approach (Baur, 1971) attributed the distortions to ionic effects, due either to mismatch of the dimensions of edge-sharing polyhedra, distortions due to deviations from electrostatic neutrality related to Pauling's second rule, or to shared-edge shortenings related to the operation of Pauling's third rule (see Section 7.1.3). Such shared-edge effects were described by Tossell and Gibbs (1976) using semiempirical SCF molecular-orbital methods for a $SiMgO_8H_{10}$ cluster, a SiO_4 unit sharing an edge with a MgO_6 unit. They found that the shared O–O edge was indeed shortened, with a calculated O–Si–O angle of 103°, in fortuitously

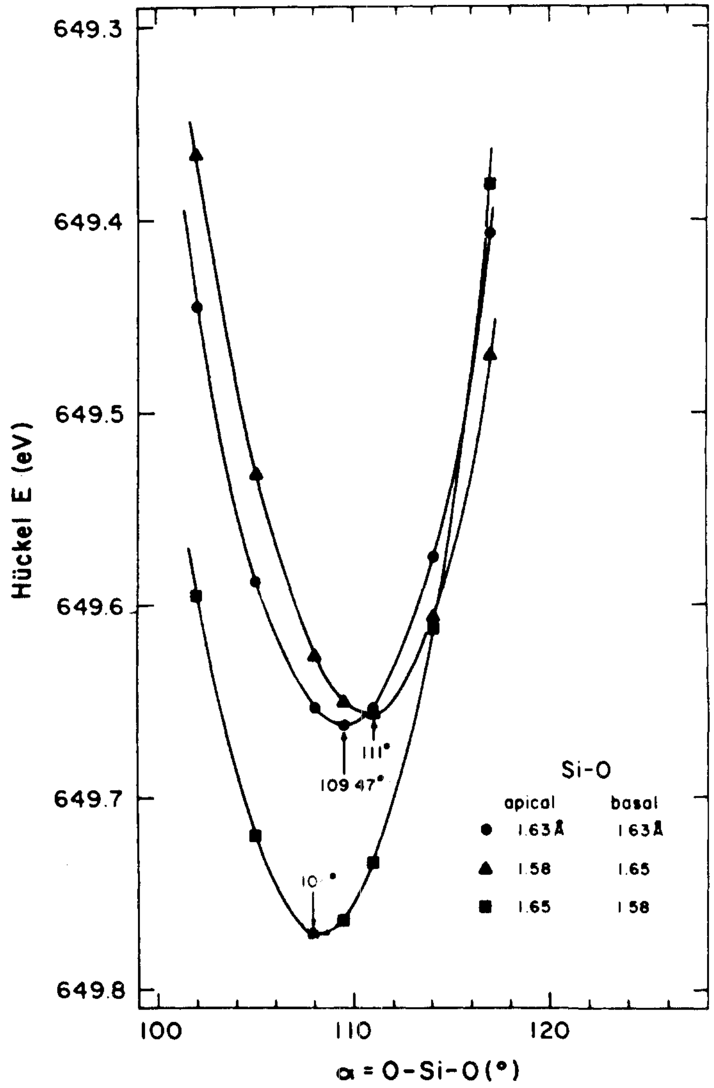

Fig. 5.3. Plot of total Hückel energy of a silicate ion (C_{3v} symmetry) as a function of α = O(apical)–Si–O(basal) angle for the three cases indicated in the figure (after Louisnathan and Gibbs, 1972a).

good agreement with the experimental angle in olivine (Table 5.1). Later studies by McLarnan et al. (1979) extended this work by applying the method to large clusters [$(SiO_3(OH)Mg_3(OH)_{10})^{7-}$] and to some fluoride and sulfide olivine structures. Although the resulting equilibrium shared-edge angles for the Mg_2SiO_4 case were similar, the analysis was somewhat more complex. Tossell and Gibbs (1976) focused upon bond overlap populations as a measure of bond energy and identified a negative Si–Mg

Table 5.1. Energy and charge distribution as a function of O_{br}–Si–O_{br} angle in $SiMgO_8H_{10}$

O_{br}–Si–O_{br} angle	E(Hartree)	Si–Mg distance (Å)	n(Si–Mg)[a]	$n(O_{br}–O_{br})$
109.95	−1074.963	2.59	−0.259	−0.009
105.0	−1074.969	2.67	−0.225	−0.011
99.5	−1074.967	2.77	−0.196	−0.015
90.0	−1074.932	2.93	−0.161	−0.024

[a] n is the bond overlap population, as defined in Mulliken (1955).

Source: From Tossell and Gibbs, 1976.

overlap population with an antibonding interaction that leads to shared-edge shortening or Si–Mg avoidance across the shared edge. McLarnan et al. (1979) used an energy decomposition scheme for their semiempirical molecular-orbital (CNDO/2) calculations and found that many energy terms changed significantly as a function of angle, resulting in a complex balance of forces. All these studies suffered from the limitations of approximate molecular-orbital methods (which were clearly inadequate for quantitative bond-distance prediction) and from the use of highly constrained models with many geometric variables held constant.

It is now possible to calculate directly some of the basic structural properties of olivine. For example, the calculated Si–O bond distance in a fully geometrically optimized $Si(OH)_4$ molecule (of S_4 symmetry) obtained from *ab initio* SCF Hartree–Fock–Roothaan calculations at the 6-31G** basis-set level is 1.629 Å, very close to the average value of 1.635 Å in olivine and in other monosilicates (Hess et al., 1986; see Fig. 5.4). Minimum-basis-set (STO-3G) calculations on $Mg(OH)_2(OH_2)_4$ (Gibbs, 1982) give a Mg–O distance of 1.91 Å, somewhat smaller than the average Mg–O distance of 2.103 Å in fayalite. Since the calculated equilibrium distance of 1.77 Å for diatomic MgO obtained using the same method is much closer to the experimental value of 1.75 Å, it appears that $Mg(OH)_2(OH_2)_4$ is not an adequate model for six-coordinate Mg in an oxide environment. On the other hand, a MgO_6 model with fewer H saturators would be negatively charged, and we would thus expect the calculated bond distance to be too large.

No *ab initio* SCF calculations have yet been performed on the geometries of distorted SiO_4 environments in olivines. *Ab initio* SCF calculations on SiO_4^{4-} with the olivine geometry (Tossell, unpublished results) do not give larger bond overlap populations for the shorter Si–O distances; so this result must be considered an artifact of the non-self-consistent EHMO calculations.

There have been a number of atomistic simulations, most of which have focused upon unit-cell parameters and fractional coordinates in olivines or upon elastic properties. Many such simulations are reviewed by

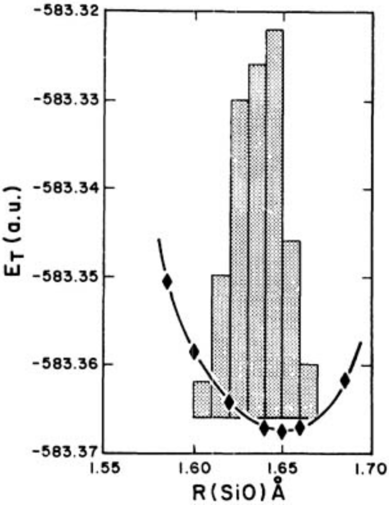

Fig. 5.4. The total energy of $Si(OH)_4$ as a function of Si–O distance [*R*(SiO) (Å)]. The histogram superimposed on the plot is a frequency distribution of the experimental Si–O bond lengths in monosilicates, with average value 1.635 Å (from Gibbs, 1982).

Price and Parker (1984), who found that simulations with full ionic charges could satisfactorily reproduce either the structure or the elastic properties of olivines but not both. They presented a simulation with fractional charges and a semiempirical Morse potential[1] for the Si–O bond and found that both structural and elastic properties could be adequately modeled (see Chapter 7 for further discussion). Their calculated Si–O distances, shown in Table 5.2, are in quite good agreement with experiment. The atomic charges used in this simulation are also in reasonable agreement with the effective charges inferred from x-ray diffraction studies (Fujino et al., 1981).

It is apparent from this description that both ionic and covalent forces are probably important in determining the detailed geometries of olivines. The balance of forces determining the structures seems complex, and it is not clear whether the observed distortions can be attributed to any single qualitative factor.

5.2.2. Olivines: Electronic structures

As noted by Tossell (1977a), the electronic structure of Mg_2SiO_4 can be partly described in terms of the same SiO_4^{4-} anion cluster used to interpret the photoelectron and x-ray emission spectra of SiO_2 (see Chapter 4). Moreover, there are clear indications that quantitatively the SiO_4^{4-} cluster model gives a better description for Mg_2SiO_4 than for SiO_2. Tossell (1977a) noted that the experimental energies for the Si 3*s*–O 2*p* bonding

Table 5.2. Observed Si–O and Mg–O bond lengths in forsterite and ringwoodite (units of Å) compared with those derived from atomistic simulation

		Calculated length	
Bond	**Observed length**	***P4*[a]**	***P5*[a]**
Forsterite			
Si–O(1) (1)	1.614	1.608	1.615
O(2) (1)	1.651	1.645	1.655
O(3) (2)	1.635	1.634	1.640
Mg(1)–O(1) (2)	2.096	2.079	2.047
O(2) (2)	2.068	2.087	2.062
O(3) (2)	2.130	2.135	2.117
Mg(2)–O(1) (1)	2.156	2.214	2.243
O(2) (1)	2.049	2.065	2.023
O(3) (2)	2.067	2.105	2.043
O(3) (2)	2.213	2.239	2.263
Ringwoodite			
Si–O (8)	1.655	1.660	1.671
Mg–O (16)	2.070	2.064	2.040

[a] *P4* and *P5* are different potentials used in the calculations.

Source: After Price and Parker, 1984.

orbitals of SiO_2 show them to be more stable than those calculated for SiO_4^{4-}. Comparison of the experimental Si *L* x-ray emission spectra of quartz and olivine (Fig. 5.5; from Kuroda and Iguchi, 1971) shows the $5a_1$ Si $3s$–O $2p$ bonding orbital producing peak C to be less stable in olivine than in quartz by about 1.4 eV and the $4t_2$ Si $3p$–O $2p$ producing peak B to be less stable by 1.8 eV. A comparison of quartz and olivine experimental energies with theoretically calculated energies in Table 5.3 shows this clearly. Neither small changes in Si–O distance, nor distortions from tetrahedral symmetry occurring in olivine, change the calculated orbital energies by more than a few tenths of an electron volt. Later experimental studies by Dikov et al. (1976, 1977, 1986) confirmed the differences between olivine and quartz spectra, giving stabilizations of the Si $3p$–O $2p$ and Si $3s$–O $2p$ b orbitals of 1.1 and 2.0 eV, respectively, in quartz compared to olivine. DVM-$X\alpha$ calculations (see Section 3.9) by Dikov et al. (1986) on SiO_4^{4-} and $Si_2O_7^{6-}$ also show a significant stabilization of a $Si_2O_7^{6-}$ orbital ($6a_2''$ in their notation), which is strongly bonding across the bridging oxygen (described as $[3s,3p(Si_1)–2p\sigma(O_{br})–3s,3p(Si_2)]$. Such stabilization of bonding orbitals involving bridging oxygen is probably responsible for the differences between olivine and quartz. Additional support for this interpretation comes from a comparison of orbital energies along the anion series (TO_4^{n-}) ClO_4^-, SO_4^{2-}, PO_4^{3-}, SiO_4^{4-} (Fig. 5.6; from Tossell, 1977a) obtained from Li_nTO_4 spectra, which show both the anom-

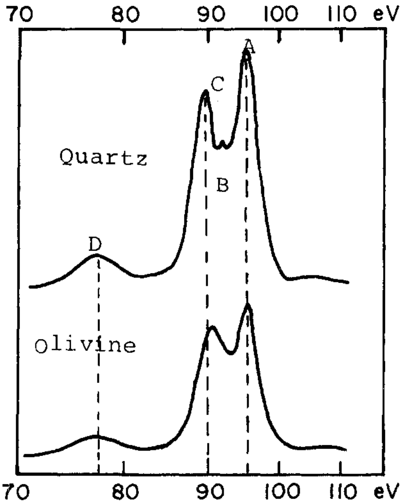

Fig. 5.5. The Si L x-ray emission spectra of quartz and olivine (after Kuroda and Iguchi, 1971).

alous character of SiO_2 versus Li_4SiO_4 and the continuity of SiO_4^{4-} orbital energies with the trends shown by the other tetrahedral oxyanions.

A more complete view of the electronic structure of Mg_2SiO_4 may be obtained by comparing its photoelectron spectra with Si, Mg, and O x-ray emission spectra (Al-Kadier et al., 1984). The only feature not seen in our previous analysis of the electronic structure of SiO_2 is the position of the Mg 3*p*–O 2*p* bonding orbitals. From the data of Urch (1985) shown in Fig. 5.7, we see that the Mg *p* character, as shown in the Mg $K\beta$ x-ray emission spectrum, occurs both in the predominantly O 2*s* orbital set and

Table 5.3. Comparison of experimental quartz and olivine relative molecular-orbital energies (in eV) with MS-SCF-$X\alpha$ results for silicon–oxygen bond lengths, R(Si–O) = 1.609 and 1.634 Å

Molecular orbital	$4a_1$	$3t_2$	$5a_1$	$4t_2$	$1e,5t_2$	$1t_1$
Experimental energies						
SiO_2: XPS data	−20.8	−18.4	−7.8	−4.8	−1.9	0
Olivine: XPS and XES data	−20.2	—	−6.4	−3.0	−1.1	0
Difference (SiO_2 versus olivine)	−0.6	—	−1.4	−1.8	−0.8	0
Calculated energies						
MS-SCF-$X\alpha$ calculation R(Si–O) = 1.609 Å	−17.4	−14.5	−7.4	−3.2	−1.2	0
MS-SCF-$X\alpha$ calculation R(Si–O) = 1.634 Å	−17.2	−14.4	−7.3	−3.1	−1.2	0
Difference (1.609 versus 1.634 Å)	−0.2	−0.1	−0.1	−0.1	−0.1	0

Source: From Tossell, 1977.

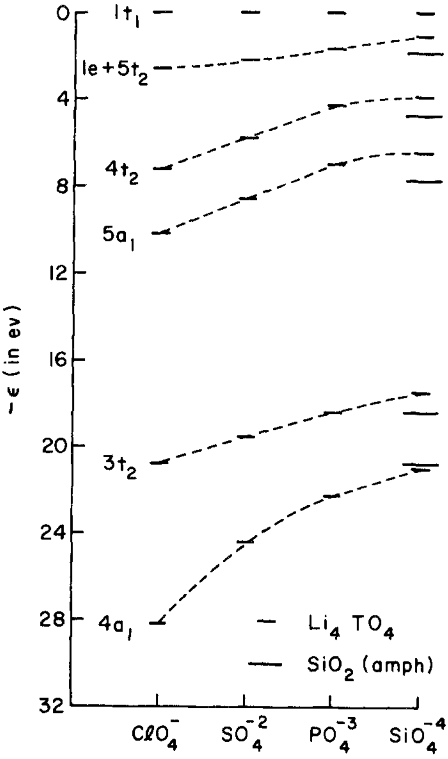

Fig. 5.6. Energies (relative to the $1t_1$ molecular orbital) of the valence orbitals of third-row tetrahedral oxyanions derived from x-ray photoelectron spectra (after Tossell, 1977a; reproduced with the publisher's permission).

in the O $2p$ nonbonding (with respect to Si) orbitals near the top of the valence region.

Additional evidence for the effect of polymerization appears in the x-ray photoelectron spectral intensities of silicates. DVM-$X\alpha$ calculations on the energies and intensities of spectra by Sasaki and Adachi (1980a,b) satisfactorily reproduce relative intensities in the upper-valence-band region for SO_4^{2-} [Fig. 5.8(a)] but seriously underestimate the intensity of the $5a_1$ orbital feature of SiO_2 using a SiO_4^{4-} cluster model [Fig. 5.8(b)]. This error may be a result of the influence of polymerization in SiO_2, although the calculated spectrum is also somewhat different from that observed for olivine in Fig. 5.7.

Information on unoccupied orbital electronic structure is available from the XANES of silicates. Although few data are available for olivines, studies of the anion series ClO_4^-, SO_4^{2-}, PO_4^{3-}, as described in Bianconi (1988), indicate them to have structures similar to SiF_4, with a_1 and t_2 absorptions below threshold, and e and t_2 resonances in the continuum (Tossell et al., 1985a; Tossell, 1987). Si $L_{2,3}$ XANES for Mg_2SiO_4 are

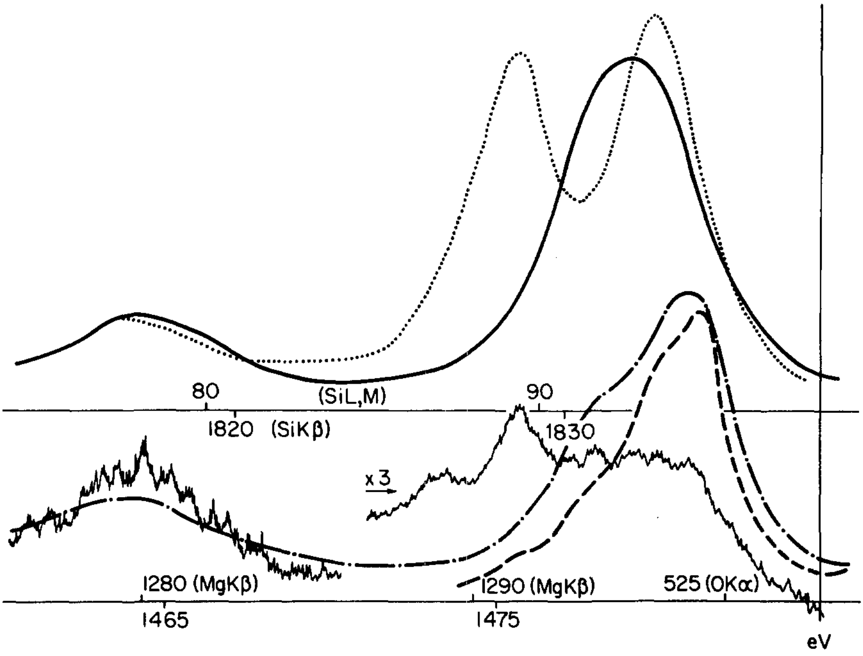

Fig. 5.7. X-ray emission (Si *K*β,——; $L_{2,3}M$,···; Mg *K*β,–·–; O *K*α,– –) and x-ray photoelectron spectra for forsterite (Mg_2SiO_4). The x-ray photoelectron energy is shown on the lowest scale — the other scales are for the x-ray spectra, as indicated (after Urch, 1985; reproduced with the publisher's permission).

similar to those for quartz, but the XANES of Fe and Ni olivines show additional features on the low-energy side of the a_1 and t_2 bound-state peaks, presumably due to excitation to predominantly metal 3*d* empty orbitals (Iguchi, 1974).

There have also been investigations of the electron density distribution in olivines (Fujino et al., 1981), which show positive difference densities ($\Delta\rho$) along the Si–O bond that are larger for the shorter Si–O bonds [Fig. 5.9(a)]. *Ab initio* Hartree–Fock–Roothaan SCF calculations on monosilicic acid [$Si(OH)_4$, Gibbs, 1982] show qualitatively similar $\Delta\rho$ maps [Fig. 5.9(b)]. Quantitative reproduction of experimental $\Delta\rho$ plots may require even larger basis sets, thermal motion corrections, and perhaps also consideration of correlation effects. Information on the charge distribution surrounding oxygen in Mg_2SiO_4 may also be obtained using the measured e^2qQ/h value from ^{17}O NMR studies (Schramm and Oldfield, 1984; Oldfield and Kirkpatrick, 1985). The three inequivalent oxygens in Mg_2SiO_4 have e^2qQ/h values of 2.35, 2.35, and 2.70 MHz, typical of nonbridging oxygens. The calculated value of e^2qQ/h for isolated tetrahedral SiO_4^{4-} with an Si–O distance = 1.634 Å (Tossell and Lazzeretti, 1987a) is about 2.9 MHz when the proper Hartree–Fock value of $eQ = 2.233 \times 10^{-2}$

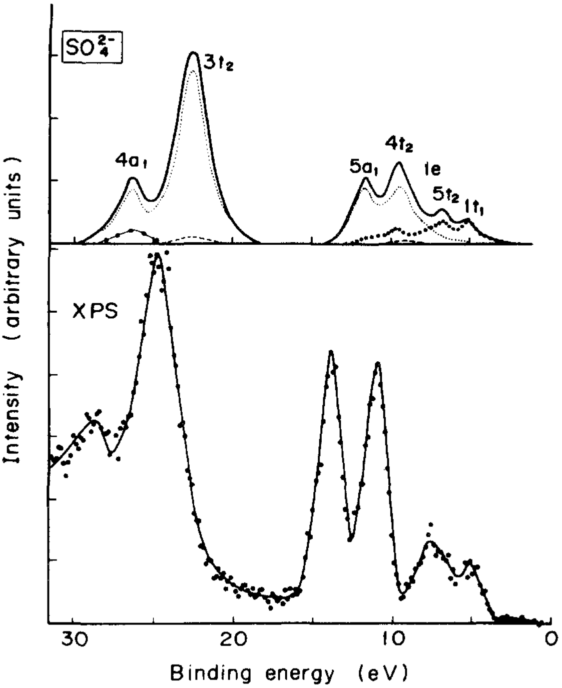
SO_4^{2-}
3t₂
4a₁
4t₂
5a₁
1e
5t₂
1t₁
XPS
Intensity (arbitrary units)
30
20
10
0
Binding energy (eV)

(a)

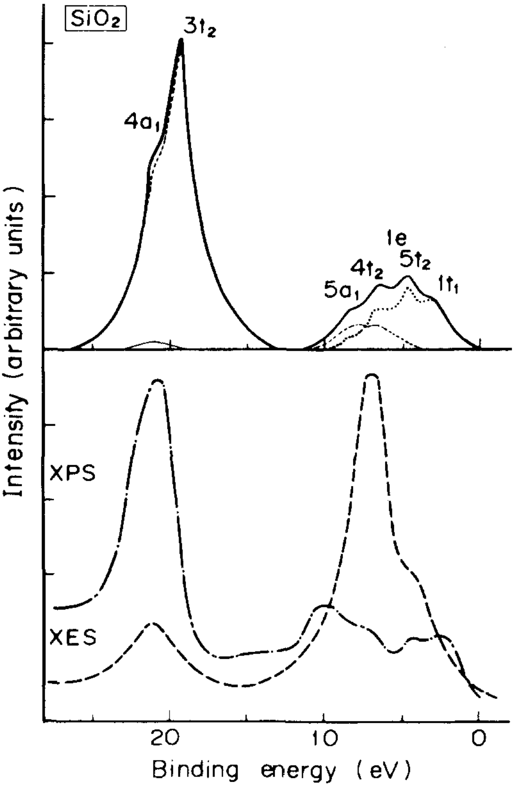
SiO_2
3t₂
4a₁
1e
4t₂
5t₂
5a₁
1t₁
XPS
XES
Intensity (arbitrary units)
20
10
0
Binding energy (eV)

(b)

barns is used (see Tossell and Lazzeretti, 1988a), in semiquantitative agreement with experiment. NQCC values for bridging oxygen are considerably larger, for example, 5.8 MHz in cristobalite (Oldfield and Kirkpatrick, 1985) and about 5.2 MHz in amorphous SiO_2 (Geissberger and Bray, 1983). The calculated value for oxygen in $(SiH_3)_2O$ with an Si–O distance of 1.607 Å and Si–O–Si angle of 144° is about 5.3 MHz (Tossell and Lazzeretti, 1988a).

The response of the silicate group in olivine to magnetic fields has recently been studied experimentally using ^{29}Si and ^{17}O NMR, and computationally using Hartree–Fock perturbation theory. Computed NMR shieldings for SiF_4 and SiO_4^{4-} clusters compare well with experimental data for the gas-phase SiF_4 molecule and SiO_4^{4-} in olivines, while the Si shieldings of H_3SiO^- and $H_3SiOSiH_3$ reproduce reasonably well the effect of silicate polymerization (Table 5.4). Anisotropies in the shielding tensor have been accurately reproduced for phosphates, such as HPO_4^{2-} and PO_3F^{2-} (Tossell and Lazzeretti, 1987b), but preliminary calculations indicate that silicate NMR anisotropies such as those measured in olivine (Weiden and Rager, 1985) may be more difficult to evaluate accurately and may depend upon second-nearest (or more) neighbor atom identities and positions as well as on the geometry of the first coordination sphere.

The electronic polarizability of Mg_2SiO_4 has been evaluated from refractive index and volume data by Lasaga and Cygan (1982) as 6.35 Å^3. Assuming ~0.087 Å^3 for the polarizability of Mg^{2+}, the polarizability of SiO_4^{4-} (for sodium *D* light) should be ~6.2 Å^3. Coupled Hartree–Fock calculations (unpublished) by Tossell, using the same basis sets as in Tossell and Lazzeretti (1987a), give a static polarizability of 5.7 Å^3.

5.2.3. *Element distributions and solid solutions in olivines*

The distribution of divalent cations over the inequivalent *M*1 and *M*2 sites in olivines has long been of interest. Alberti and Vezzalini (1978) modeled ordering in olivine structures using observed structures and considering only the electrostatic energy. They calculated energies for various charge distributions in *M*1 and *M*2 sites and obtained results in agreement with experiment. Bish and Burnham (1984) modeled eight ordered and antiordered olivine pairs using an optimum-distance least-squares procedure (Dollase, 1980) to determine the structure, and evaluated energies from

Fig. 5.8. (a) Calculated x-ray photoelectron spectum for the SO_4^{2-} cluster (upper curve), together with the experimental spectrum (below) for Li_2SO_4. In the calculated spectrum: O 2*s*,···; O 2*p*, (•••); S 3*s*–·–; S 3*p*, ——. (b) Calculated x-ray photoelectron spectrum for the SiO_4^{4-} cluster (upper curve), together with the experimental x-ray photoelectron spectrum and x-ray emission spectrum of amorphous SiO_2. In the calculated spectrum: O 2*s*, ——; O 2*p*, ···; Si 3*s*, --- (after Sasaki and Adachi, 1980b; reproduced with the publisher's permission).

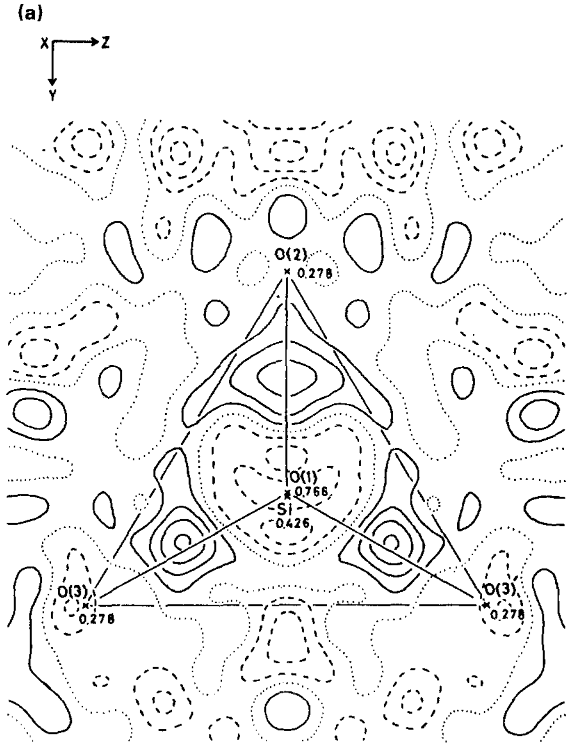

Fig. 5.9. Electron density distributions in olivines: (a) Experimental difference density map of part of the forsterite structure showing the residual peaks around Si. Contours are at intervals of 0.1 electrons Å^{-3}, negative contours being broken and zero contours dotted. Numbers in decimal fractions of the *a* length indicate the heights of the atoms. The tetrahedron formed by oxygen atoms around Si is shown (after Fujino et al., 1981; reproduced with the publisher's permission). (b) A comparison of a theoretical difference density map (i) of the O–Si–O group in the monosilicic acid molecule [$Si(OH)_4$] with an experimental map (ii) of the same group in the monosilicate mineral andalusite (Al_2SiO_5). Contours are at intervals of 0.07 electrons Å^{-3} in (ii). The region around the nucleus of each atom in the theoretical map represents the core region, where the data are not expected to be accurate (after Gibbs, 1982; reproduced with the publisher's permission).

electrostatic plus repulsion contributions, with repulsive parameters obtained from empirical fits to crystal structure data. Site preferences were correctly predicted qualitatively in all cases (Table 5.5), although no crystal-field stabilization energy (CFSE) or covalency effects were included. Ottonello (1987) used a similar procedure, but with significantly different parametrization in both the distance-least-squares and lattice energy calculations, to model the enthalpies and free energies of both end members and intermediate compositions in a number of olivine solid solution series, obtaining reasonable agreement with experiment for both phase

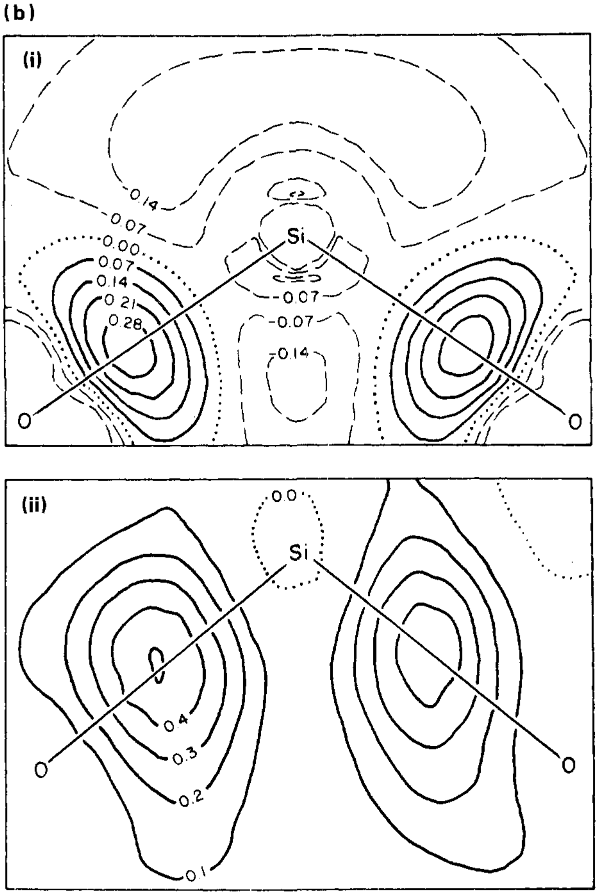

Fig. 5.9. Continued

Table 5.4. Calculated NMR shieldings (σ^{Si}, σ^{O}, and q^{O}) for linear $(SiH_3)_2O$, $SiH_3OAlH_3^+$, SiH_3OH, SiH_3OMg^+, and PH_3OAlH_3 units obtained from Hartree–Fock perturbation theory (*sp*; O 3*d*, *T* 3*d* basis)

				SiH₃OH			
	$(SiH_3)_2O$	**$SiH_3OAlH_3^-$**	**PH_3OAlH_3**	**134°**	**115°**	**SiH_3O^-**	**SiH_3OMg^+**
σ^{Si}	515.5	525.9	—	443.8	438.5	454.0	451.4
σ^{O}	418.5	389.8	400.9	339.6	—	328.7	363.7
$\lvert q^{O}\rvert$	1.290	0.9945	1.534	1.116	1.208	0.792	1.218
$e^2qQ/\hbar$	6.77	5.22	8.05	5.86	6.34	4.16	6.39
$(e^2qQ/\hbar)/6.77$	1	0.77(0.63)[a]	1.19(1.13)[a]	—	—	—	—

[a] Experimental values from Table III of Timken et al. (1986).

Source: After Tossell and Lazzeretti, 1988a.

Table 5.5. Structure energy differences (ΔU) between optimum distance models of ordered and antiordered olivines, $M1$-$M2$-SiO_4 (kcal/mol). Positive values indicate the cation distribution shown (ordered) has the lower energy; negative values indicate the opposite (antiordered) distribution has the lower energy

$M1$	$M2$	ΔU, Coulomb only parameters	ΔU, Coulomb plus repulsive parameters	Observations
Fe	Mg	−5.0	−0.1	Fe usually in $M1$—very slight ordering; some CFSE[a] from Fe^{2+}
Co	Mg	−2.7	+0.1	Co in $M1$—partial ordering; CFSE from Co^{2+}
Ni	Mg	+4.3	+2.3	Ni in $M1$—strong ordering; CFSE from Ni^{2+}
Fe	Mn	+1.3	+6.8	Fe in $M1$—partial ordering; some CSFE from Fe^{2+}
Mg	Mn	+11.1	+11.0	Mg in $M1$—nearly complete ordering
Mg	Ca	+11.0	+17.1	Mg in $M1$—complete ordering
Mn	Ca	+16.7	+6.6	Mn in $M1$—nearly complete ordering
Fe	Ca	−6.7	+10.5	Fe in $M1$—strong ordering; some CFSE from Fe^{2+}

[a] CFSE, crystal-field stabilization energy (see section 1.2).

Source: After Bish and Burnham, 1984.

boundaries and site occupancies as functions of composition (Fig. 5.10a,b). Further developments within this approach will require *ab initio* potentials for the transition-metal–oxygen interactions and incorporation of crystal-field effects and covalency corrections, but it is clear that the empirical potentials reproduce most of the structural and energetic properties.

5.2.4. Structure and stability of silicates of intermediate polymerization

Direct quantum-mechanical study of the stabilities of silicates of intermediate polymerization is currently impossible because of the immense complexity and variety of structures. However, some principles have emerged as a result of quantum-mechanical calculations on cluster units (Tossell and Gibbs, 1978; Newton and Gibbs, 1980; Meagher et al., 1979; Meagher, 1980). The basic conclusions are that not only the Si–O–Si angles ($\sphericalangle$Si–O–Si), but the O–O–O bridging angles [$\sphericalangle(O\text{–}O\text{–}O)_{br}$] are restricted to about 125–180°, regardless of the presence of counterions. A contour plot of energy as a function of $\sphericalangle$Si–O–Si and $\sphericalangle(O\text{–}O\text{–}O)_{br}$ gives a partial explanation for the presence of only certain structure types (Fig. 5.11). Unfortunately, the systems studied in the chain silicate work were so large that it was necessary to employ an approximate molecular orbital

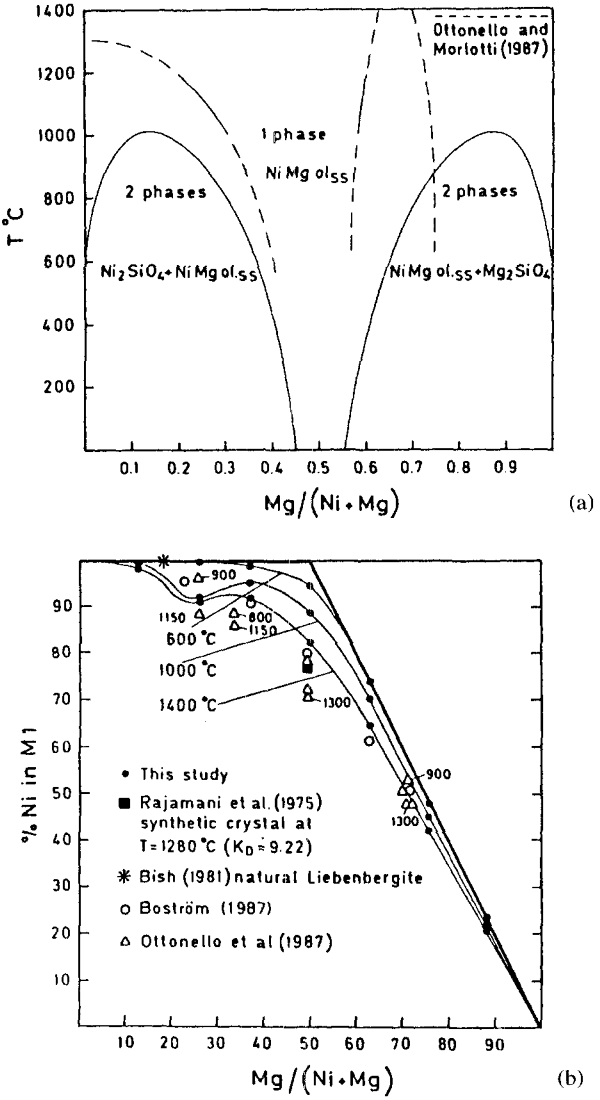

Fig. 5.10. Calculations of the properties of olivine solid solutions (see Ottonello, 1987, for full details and data sources): (a) Calculated phase field boundaries in the system $(Mn,Mg)_2SiO_4$; full circles are calculated boundaries, dashed curves are extrapolated, dotted lines are experimental solubility gap. (b) Plot of site occupancy versus molar composition along the binary join $(Ni,Mg)_2SiO_4$.

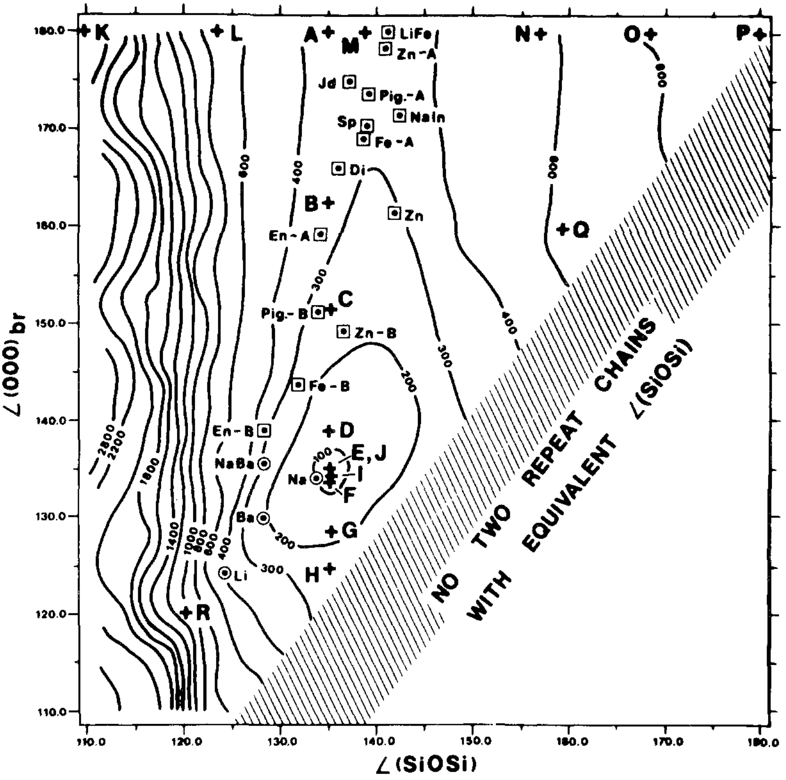

Fig. 5.11. A contour total-energy map for two-repeat chains over a range of ∢(Si–O–Si) and ∢(O–O–O)$_{\text{br}}$. Observed structures indicated by letters have energy values near valley in middle of diagram (from Meagher, 1980).

method, CNDO (see Section 3.7 and Appendix C). A similar problem was encountered in studies of the relative stability of silicate rings by Chakoumakos et al. (1981). Although the bond distances and angles calculated using *ab initio* Hartree–Fock–Roothaan SCF methods (at the minimum-basis-set, STO-3G level) for a four-membered ring [modeled by $(H_2SiO)_4$] were in reasonable agreement with experimental electron diffraction studies on the molecule, the calculated equilibrium geometry was different from that observed, corresponding to a different type of distortion of the Si_4O_4 unit from planarity. Similarly, the stability of the three-membered ring $(H_2SiO)_3$ was overestimated due to the tendency of the STO-3G basis set to underestimate the Si–O–Si angles, giving undue stability to the Si–O–Si angle of 130° calculated for $(H_2SiO)_3$. CNDO calculations (which give larger Si–O–Si angles) gave the four-membered ring as more stable than the three-membered ring, but showed continuously decreasing energy per Si as the ring size expanded rather than higher stability for the six-membered rings, which are more numerous in silicates. Later studies of $(H_2SiO)_3$ using 6-31G* (*d* functions on Si only) basis sets (O'Keeffe and Gibbs, 1984) yielded a somewhat larger Si–O–Si angle (136.7°) and a reversal in the calculated stabilities of D_{3h} and C_{3v} geometries with the D_{3h} structure now more stable. Kudo and Nagase (1985) obtained similar results at the 3-21G level while Tossell (1990b) using 3-21G** bases (polarization functions on all atoms; Si 3*d*, O 3*d*, H 2*p*) obtained a Si–O distance of 1.630 Å and Si–O–Si angle of 133.4°, and a rigorously planar D_{3h} geometry. The geometry of $[(CH_3)_2SiO]_3$ was found to involve an Si–O distance of 1.635 Å and Si–O–Si angle of 131.6° from electron diffraction (Oberhammer et al., 1973). Kudo and Nagase (1985) established that oligomerization in the $(H_2SiO)_n$ series is exothermic, for $n = 2$–4; that is, for the reactions:

$$3(H_2SiO)_2 \rightarrow 2(H_2SiO)_3$$

and

$$4(H_2SiO)_3 \rightarrow 3(H_2SiO)_4$$

the calculated ΔE values at the 3-21G basis-set level are -162.3 and -74.2 kcal/mol.

Atomistic simulations have also been performed on pyroxenes and pyroxenoids by Catlow et al. (1982) and predict the stable Mg end member to have the diopside structure and the stable Ca end member the wollastonite structure, as observed. However, only pair potentials were employed in this study, and Post and Burnham (1986) have found that diopside structures are poorly described within such a model. It would clearly be of interest to repeat the simulations using the three-body silicate potentials, which have yielded accurate Si–O–Si angles in quartz (Catlow et al., 1985).

Separate from the question of preferred structure type is the question of existence. Why are there so many topologically and compositionally possible silicates that do not exist? Dent Glasser (1979) suggests that for stability the Lewis acid strength of the cation and the Lewis base strength of the silicate anion must be matched, where the Lewis acid strength is simply the atomic valence divided by the average coordination number. The Lewis base strength for bonding to the cation is the atomic valence divided by coordination number, less the base strength expended in bonding to Si, so that silicate anions with different degrees of polymerization have different base strength. Thus, cations with high acid strength typically form depolymerized silicates, while those with low acid strengths are found in more highly polymerized silicates. Jensen (1980) has noted that the less electronegative of isovalent cations tends to partition into more polymerized silicates. Ramberg (1952) has noted that the more electronegative Fe^{2+} ion partitions into olivines while the more electropositive Mg^{2+} partitions into pyroxenes.

5.2.5. Electronic structures of silicates other than olivines and SiO_2

The electronic structures of silicate minerals of polymerization intermediate between nesosilicates and tektosilicates have been studied to a lesser extent than have SiO_2 or the olivines. The complexity of their crystal structures makes calculation difficult, and their diversity in terms of local chemical environment makes phenomenological assignment of their spectra difficult. Nonetheless, some recent comparative studies have given valuable electronic structure information on such materials.

For example, band calculations have been performed, and x-ray photoelectron spectra have been determined of crystals and glasses along the $(Na_2O)_x\cdot(SiO_2)_{1-x}$ series (Ching et al., 1983). These studies complement earlier work on the Si $K\beta$ spectra (Sakka and Matusita, 1976; de Jong et al., 1981) and the O 1*s* x-ray photoelectron spectra (Bruckner et al., 1980) of this series of materials. Si NMR data have also been studied for this series (Stebbins, 1987; Selvaray et al., 1985). As x increases along this series, the silica framework gradually depolymerizes, producing species with nonbridging oxygens and lower polymerization, as well as modifying the Si–O distances and Si–O–Si angles (Soules, 1979). The band calculations on crystalline Na_2SiO_3 using a non-self-consistent, valence-only LCAO method (Ching et al., 1983) show distinct differences in the partial densities of states for bridging and nonbridging oxygens (Fig. 5.12). The nonbridging oxygen levels are, in all cases, less tightly bound than the bridging oxygen levels. This effect occurs in the O 2*s* nonbonding levels and the O 2*p* nonbonding levels (and presumably in the O 1*s* cores as well, according to experiment; Bruckner et al., 1980). The Si 3*p*–O 2*p* bonding levels also differ in energy in the same way. These calculated trends appear clearly in the experimental x-ray photoelectron spectra (Fig. 5.13), with the splitting of O 2*s* nonbonding and O 2*p* nonbonding, and the destabilization of Si–O 2*p* bonding orbitals readily observable. The destabilization of the Si 3*p*–O 2*p* orbitals is also evident from the Si $K\beta$ spectrum, where low resolution shows a shift of a broad peak to higher energy while x increases (Sakka and Matusita, 1976), and higher-resolution spectra show the appearance of a high-energy shoulder (de Jong et al., 1981). These spectra are shown in Fig. 5.14. The O 1*s* x-ray photoelectron spectrum, as shown in Fig. 5.15 (Jen and Kalinowski, 1989), has an asymmetric peak that can be decomposed into a peak associated with nonbridging oxygen at lower energy, and a bridging oxygen peak at higher binding energy, with an energy separation of about 2 eV.

Glasses along the $(Na_2O)_x(SiO_2)_{1-x}$ series have also been studied by ^{29}Si NMR (Stebbins, 1987; Selvaray et al., 1985). Stebbins (1987) demonstrated, for sodium silicate glasses, the existence of polymerized species not dictated by the stoichiometry (e.g., in $Na_2Si_2O_5$ composition glass), which in crystalline form contains entirely Q^3 species.[2] He found

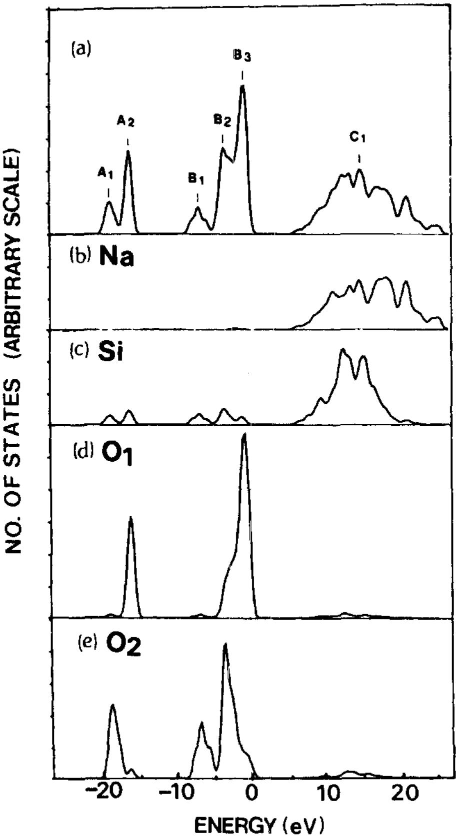

Fig. 5.12. Calculated density of states and partial density of states for Na_2SiO_3: (a) total DOS in arbitrary units; (b)–(e) PDOS for each type of atom, as indicated and normalized to the number of states per atom [O(1), nonbridging oxygens; O(2), bridging oxygens] (after Ching et al., 1983; reproduced with the publisher's permission).

Q^2, Q^3, and Q^4 species all present, with Q^3 predominant (Fig. 5.16). Studies of glasses with $Li_2Si_2O_5$ composition also yielded Q^2, Q^3, and Q^4 species by curve fitting and, based upon ^{29}Si chemical shift distributions, the Si–O–Si angles were interpreted as narrowing as the polymerization decreased (Fig. 5.17). This would be consistent with the expected effect of increased coordination of the bridging oxygens to Na. Studies of the optical absorption spectra of Cu^{2+} as a probe ion in Na_2O–SiO_2 glasses (Hosono et al., 1979) also indicate changing electronic structure with composition. For Na_2O mole percent above 55, the optical (ligand-field) absorption was interpreted as arising from an orthosilicate microscopic environment for the Cu^{2+} ion.

For silicates such as $MgSiO_3$, differences in electronic structure with respect to SiO_2 are more elusive. Si $K\beta$ spectra (Dodd and Glenn, 1969;

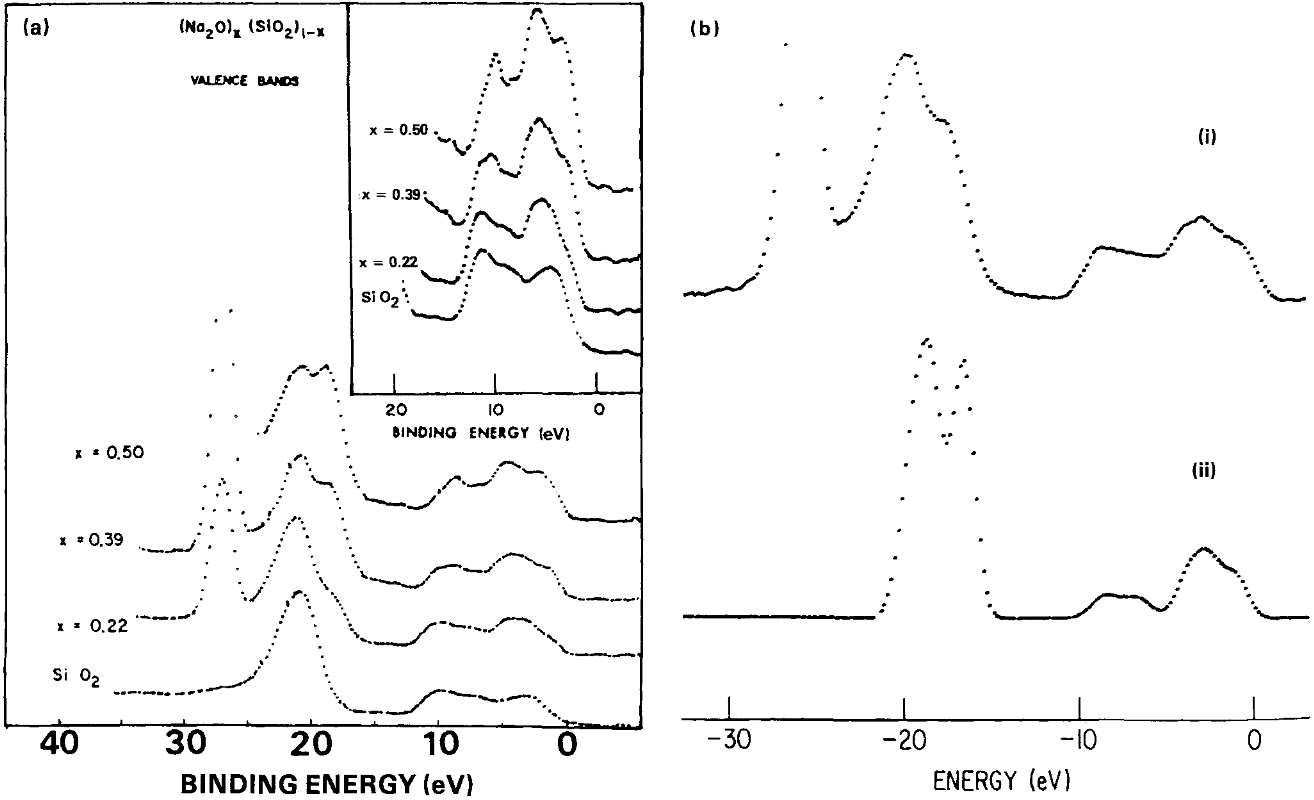

Fig. 5.13. (a) X-ray photoelectron spectra of $(Na_2O)_x(SiO_2)_{1-x}$. The inset shows an enlargement of the valence region (after Ching et al. 1983). (b) X-ray photoelectron spectrum of $Na_2Si_2O_5$ (i) compared with (ii) a density of states calculation (after Ching et al., 1983).

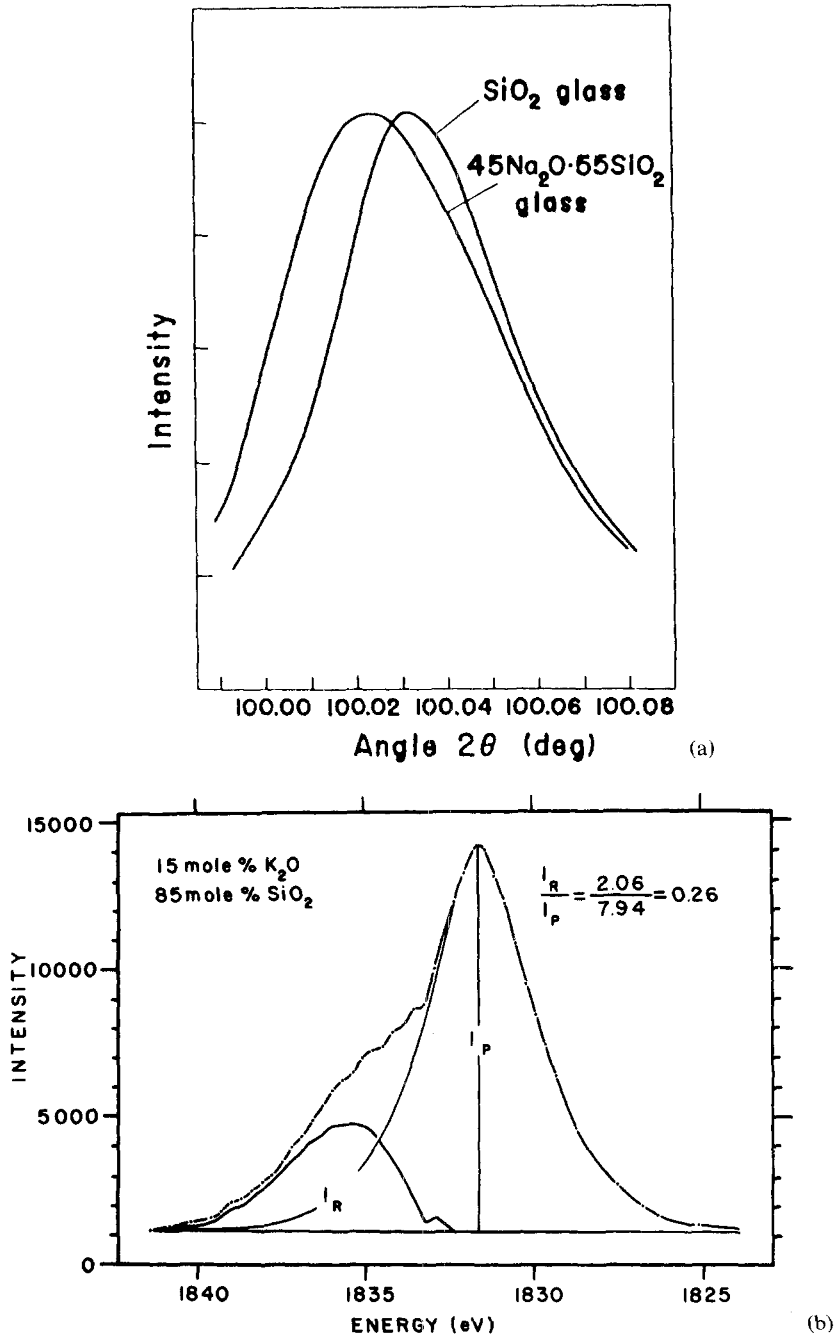

Fig. 5.14. X-ray emission spectra of silicate glasses: (a) Si $K\beta$ spectra of SiO_2 and 45 Na_2O–55 SiO_2 glasses (after Sakka and Matusita, 1976; reproduced with the publisher's permission). (b) Si $K\beta$ spectrum of 15 K_2O–85 SiO_2 glass and the decomposition of this spectrum into two peaks (I_p and I_r), which represent the "ideal" Si $K\beta$ spectrum and the deviation of this spectrum due to potassium ions, respectively (after de Jong et al., 1981; reproduced with the publisher's permission).

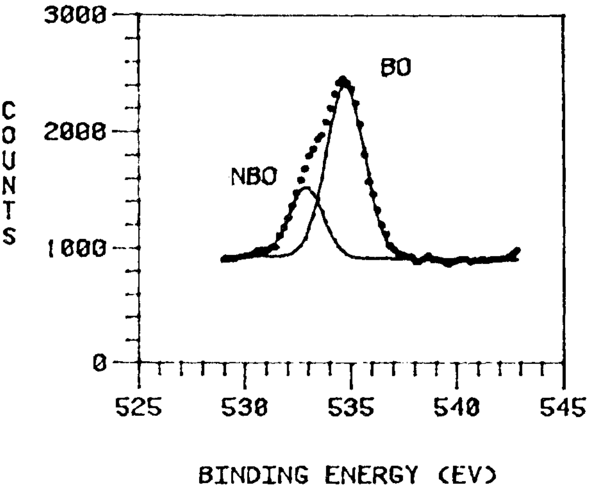

Fig. 5.15. The x-ray photoelectron oxygen 1*s* spectrum of a sodium silicate glass (30 Na_2O–70 SiO_2), showing contributions from bridging oxygens (BO) and nonbridging oxygens (NBO) (after Jen and Kalinowski, 1989; reproduced with the publisher's permission).

de Jong et al., 1981) for enstatite and for $MgO–SiO_2$ glasses are very similar to those for quartz. Si *L* x-ray emission spectra also apparently show little difference (Dikov et al., 1977). Mg $K\beta$ and $L_{2,3}$, x-ray emission spectra (Brytov et al., 1984) are somewhat more informative, clearly distinguishing between enstatite and periclase, but not between enstatite and forsterite. More information can be obtained by focusing upon properties of the oxygen. For example, Yin et al. (1971) obtained O 1*s* x-ray photoelectron spectra for enstatite, which could be deconvoluted into peaks for bridging and nonbridging oxygen, although the difference is in the opposite sense to that found in the $(Na_2O)_x(SiO_2)_{1-x}$ series. Tossell (1973), using semiempirical molecular-orbital calculations, was able to reproduce this difference in O 1*s* binding energies. More recently, ^{17}O NMR studies (Timken et al., 1987) have distinguished between bridging and nonbridging oxygens in alkaline earth metasilicates and have found symmetric changes in the NQCC values for nonbridging oxygens as a function of the identity of the alkaline earth counter ion (Table 5.6). NQCC values are systematically smaller for nonbridging (O_{nb}) than for bridging (O_{br}) oxygens, and decrease as the alkaline earth element becomes heavier. *Ab initio* calculations by Tossell and Lazzeretti (1987a; 1988a) indeed give smaller ^{17}O NQCC values in SiO_4^{4-} than in $(SiH_3)_2O$ by an amount similar to that observed (Table 5.4), but calculations of the effect of nearby counterions on the NQCC are yet to be performed. Analysis of the spectra is also difficult, since chemical shielding anisotropies affect magic-angle spinning and static spectra differently, reducing the accuracy of the static results.

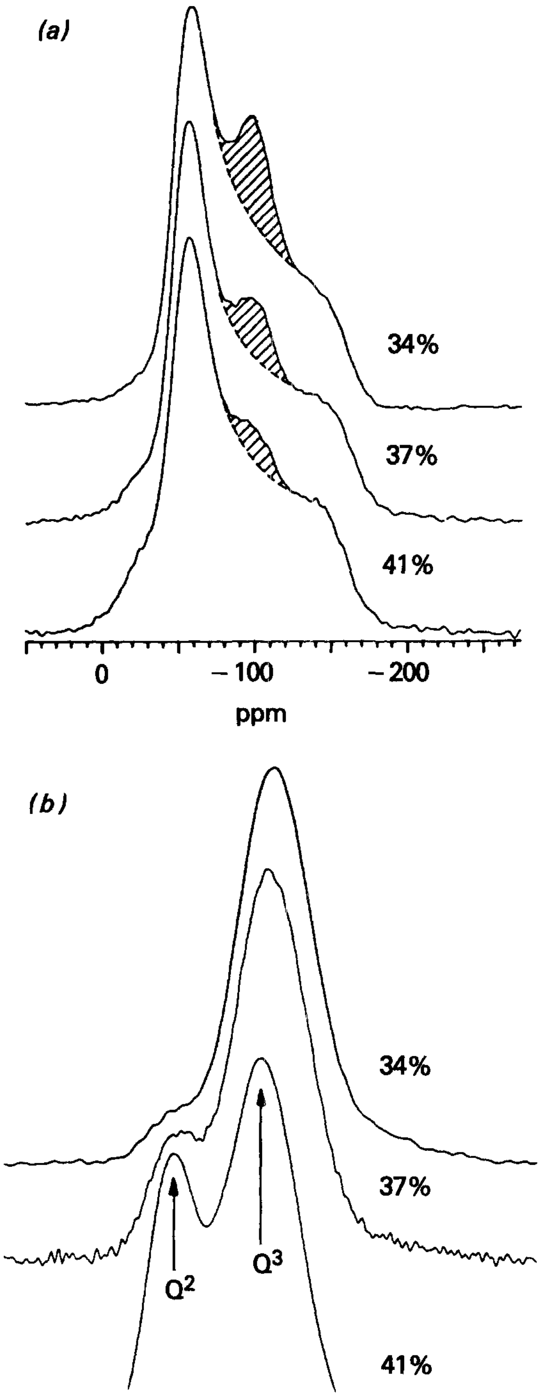

Fig. 5.16. ^{29}Si NMR spectra of sodium silicate glasses (Na_2O–SiO_2) with mol % Na_2O composition as shown: (a) spectra recorded without sample spinning; (b) spectra recorded with magic-angle spinning (MAS) of samples. Samples studied were enriched to 57% ^{29}Si. Cross-hatching shows the areas of Q^4 peaks (after Stebbins, 1987; reproduced with the publisher's permission).

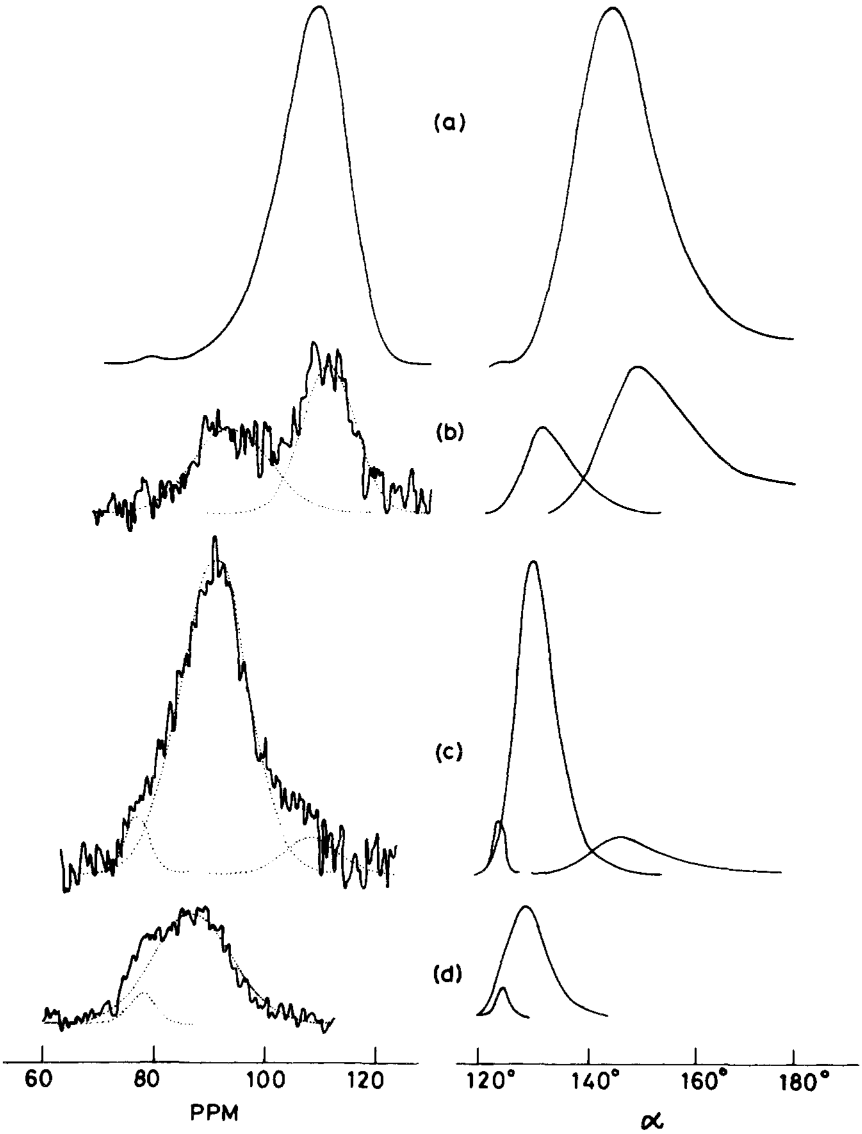

Fig. 5.17. ^{29}Si MAS NMR spectra of lithium silicate glasses and their decomposition to Gaussian components both in terms of the chemical shift (δ in ppm, with Gaussians shown as dotted lines on left-hand side above) and in terms of Si–O–Si bond angle (α) distribution (right-hand side above). Samples studied were: (a) vitreous silica; (b) 15 Li_2O–85 SiO_2 glass; (c) 33.3 Li_2O–66.7 SiO_2 glass; (d) 40 Li_2O–60 SiO_2 glass (after Selvaray et al., 1985; reproduced with the publisher's permission).

Table 5.6. Oxygen-17 (both bridging, O_{br}, and nonbridging, O_{nb}) nuclear quadrupole coupling constants, asymmetry parameters (η), and isotropic chemical shifts (δ_i) for the alkaline earth metasilicates[a]

System	Oxygen type	e^2qQ/h (MHz)	η	δ_i
$MgSiO_3$	O_{nb}	(3.2)	(0.0)	(60)
	O_{nb}	(3.2)	(0.0)	(42)
	O_{br}	(5.1)	(0.3)	(62)
$CaMgSi_2O_6$	O_{nb}	2.7(2.9)	0.0(0.0)	84(86)
	O_{nb}	2.7(3.0)	0.1(0.1)	63(64)
	O_{br}	4.4(4.5)	0.3(0.2)	69(71)
α-$CaSiO_3$	O_{nb}	2.1	0.1	94
	O_{nb}	2.3	0.1	91
	O_{br}	3.8	0.2	75
α-$SrSiO_3$	O_{nb}	2.1	0.1	108
	O_{nb}	2.2	0.1	105
	O_{br}	4.1	0.4	80
$BaSiO_3$	O_{nb}	2.1	0.1	169
	O_{nb}	1.6	0.1	159
	O_{br}	3.7	0.4	87

[a] All parameters are derived from spectral simulations of 67.8 MHz (11.7 T) ^{17}O NMR spectra, except for the values derived from the static spectra of diopside and clinoenstatite, which were obtained at 48.8 MHz (8.45 T). Values in parentheses indicate that the sample was static. All other values are taken from MAS NMR spectra. Errors are typically ± 0.2 MHz e^2qQ/h, $\pm$ 0.1 (η), and ± 2 (δ_i).

Source: Taken from Tinkin et al., 1987.

More general studies of the electronic structures of silicate minerals have been performed by Dikov et al. (1976, 1977, 1986). From Si $L_{2,3}$ spectra (see Fig. 5.18), they were able to divide silicates into two categories: (type I) those showing "two-humped" Si $L_{2,3}$ x-ray emission spectra, similar to SiO_2, although actually showing three humps in the complete valence region, corresponding to $4a_1$ (O 2*s*), $5a_1$ (Si 3*s*–O 2*p*) and $1e$, $5t_2$ (Si π– O 2*p*) orbitals, respectively (labeled C, B, and A in Fig. 5.19); (type II) those showing "three-humped" Si $L_{2,3}$, x-ray emission spectra (with the additional features B′ and A′ in Fig. 5.18). Type I spectra are found in silicates that are fully condensed (e.g., SiO_2), and those that are isolated (e.g., Mg_2SiO_4). In both cases, there are no other strongly covalently bonded atoms present. For such minerals the B peak, corresponding to very weakly bonding orbitals, is essentially fixed in position while the A peak, corresponding to Si 3*s*–O 2*p* σ bonding, is about 1.4 eV more stable in SiO_2 than in olivine (as previously discussed). In minerals of spectral type II, there are other tetrahedral oxyanions (e.g., BeO_4^{6-}, BO_4^{5-}, or $Al(OH)_6^{3-}$ groups) linked to SiO_4^{4-} by more than one oxygen. Covalent bonding to these oxyanions perturbs the oxygens of the SiO_4^{4-} tetrahedron, and mixes other metal orbital character into them, giving a

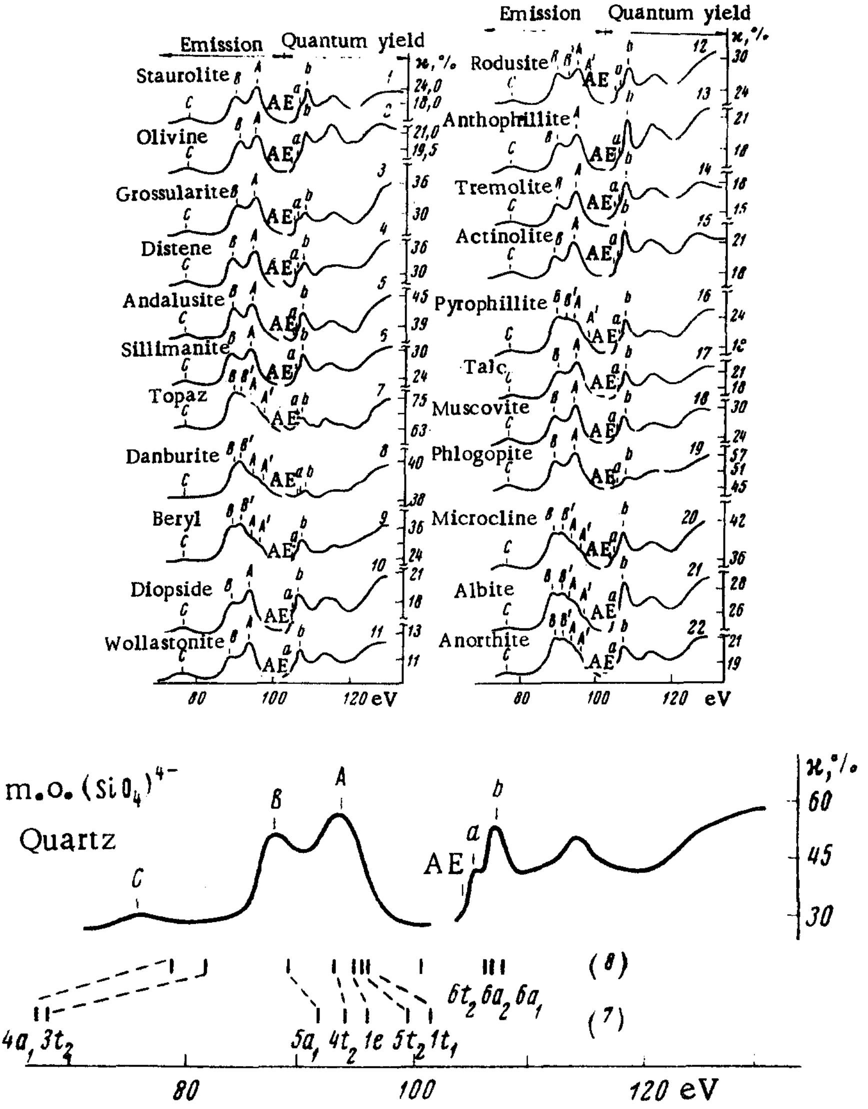

Fig. 5.18. The Si $L_{2,3}$ x-ray emission spectra of various silicates, as shown, and of quartz. In terms of structural silicate groups: (1–7) are island silicates, (8–9) ring silicates, (10–11) single-chain silicates, (12–15) double-chain silicates, (16–19) sheet silicates, (20–22) framework silicates (after Dikov et al., 1976; reproduced with the publisher's permission).

more complex spectrum. Semiempirical MO calculations (Dikov et al., 1977) indicate that the widths of the Si–O $2p$ σ bonding and the Si π–O $2p$ (weakly) bonding regions are both changed by substitution of some Si by Be, B, Al, or P, but no quantitative interpretation of the resulting Si $L_{2,3}$, x-ray emission spectra has been provided. Earlier theoretical studies of the Si $K\beta$ x-ray emission spectrum by Tossell (1973) satisfactorily reproduced the change in Si $K\beta$ peak position when Al is substituted for Si, using an average of orbital eigenvalues weighted by the Si $3p$ atomic orbital contribution in the $Si_2O_7^{2-}$ and the $AlSiO_7^{3-}$ clusters. In the Si $L_{2,3}$ x-ray absorption spectra of Dikov et al. (1977), there are also changes with mineral identity, although their categorization is not so clear. It appears that in aluminium-containing minerals, such as andalusite, the low-energy Si $L_{2,3}$ x-ray emission peaks (corresponding to Si $3p$–O $2p$ σ^* orbitals), are intensified while the corresponding peaks in boron-containing minerals, such as danburite, are reduced in intensity.

It is surprising that no significant differences in Si $K\beta$ x-ray emission spectra are observed between olivines and pyrosilicates, since the P $K\beta$ spectra of pyrophosphates (Mazalov et al., 1979) clearly show extra features around the P $3s$–O $2p$ σ position arising from symmetry lowering.

The effects of polymerization upon Si $2p$ and O $1s$ binding energies has been controversial. Early studies (Yin et al., 1971; Huntress and Wilson, 1972) indicated distinguishable O $1s$ binding energies for different minerals, but later studies by Adams et al. (1972) found no differences outside experimental error. Later, more comprehensive studies by Clarke and Rizkalla (1976) and Wagner et al. (1982) showed more systematic behavior. In the work of Wagner et al. (1982), the Si $2p$ and O $1s$ binding energy was stated to decrease by about 0.5–0.6 eV in each depolymerization step, from SiO_2 to layer to chain to dimer structure, but inspection of the actual data shows considerable scatter. It seems clear that the Auger parameter, as discussed below, correlates better with structure. This is somewhat surprising since the x-ray photoelectron spectra of phosphates (although admittedly for a small sample) show systematic changes in P $2p$ (Fluck and Weber, 1975) and O $1s$ binding energies (Gresch et al., 1979) with structure type.

General studies of the absorption spectra of silicate minerals have also been performed (Nitsan and Shankland, 1976). The results indicate that the band-gap transition in Mg silicates involves charge transfer from O $2p$ nonbonding states to the M–O σ^* states associated with the weakest bond, for example, Mg–O in Mg_2SiO_4 (Fig. 5.19). The band gap increases with average M–O bond strength, being larger in Mg_2SiO_4 than in MgO, and consequently also with degree of silicate condensation or mole fraction SiO_2 in MgO–SiO_2 systems (Fig. 5.20). When transition metals are present, they invariably lead to a lowering of the band gap compared to

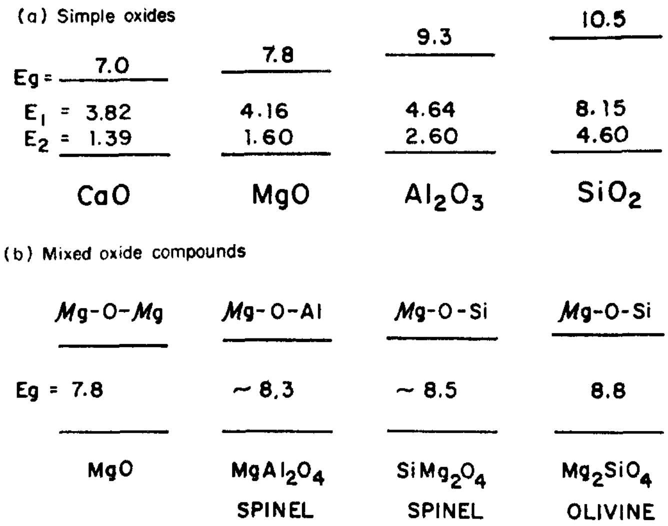

Fig. 5.19. Band gaps (E_g) in (a) simple oxides and (b) mixed oxides. E_1 is the bond strength of the corresponding diatomic molecule; E_2 is the strength of a single bond in the corresponding oxide. All values are in eV. For sources of data see Nitsan and Shankland, 1976 (after Nitsan and Shankland, 1976; reproduced with the publisher's permission).

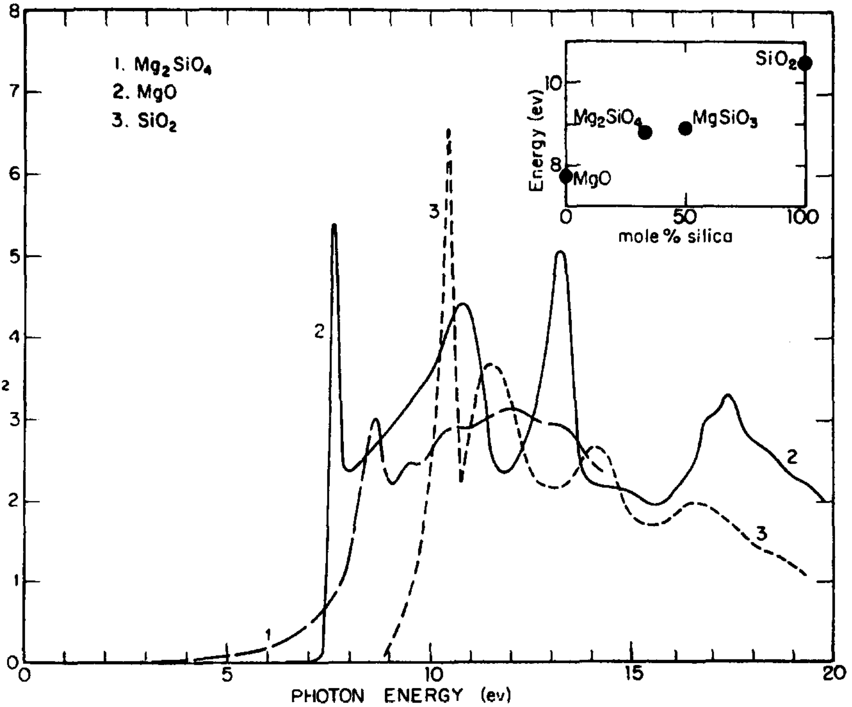

Fig. 5.20. UV absorption spectra of forsterite, MgO and SiO_2, with dependence of the band gap energy on composition in the system MgO – SiO_2 also shown as an inset. For sources of data see Nitsan and Shankland (1975) (after Nitsan and Shankland, 1976; reproduced with the publisher's permission).

the Mg-only system. A systematic correlation of the energy gap (E_g) with $(n_0^2 - 1)^{-1}$, where n_0 is the refractive index at 2.1 eV, was also observed (Fig. 5.21). Studies of the Si Auger parameter A [where $A = E_b(1s) + E_{KLL} - h\nu$] across a broad series of silicates have also established that increasing polymerization leads to decreasing Auger parameter and that A correlates with $(n_0^2 - 1)$ (Fig. 5.22; West and Castle, 1982). The Auger parameter (A) can also be written as $A = A_0 + E_{pol}$, where A_0 is the Auger parameter for free Si^{4+} and E_{pol} is the polarization energy of the lattice, dominated by the contribution from the oxygens. Clearly, the Auger results indicate that bridging oxygens give less polarization stabilization than nonbridging oxygens. As described by Duffy and Ingram (1976), the optical basicity also decreases with increasing polymerization, since bridging oxygens are less polarizable than nonbridging oxygens. Recall that Wagner et al. (1982) have also established systematic changes in Si 2p and O 1s binding energies as the polymerization changes, with variations of the order of 0.5 eV as Q^n changes by one unit. The general conclusion of these studies is that change in degree of polymerization significantly influences the environments of metal atoms in silicates, since

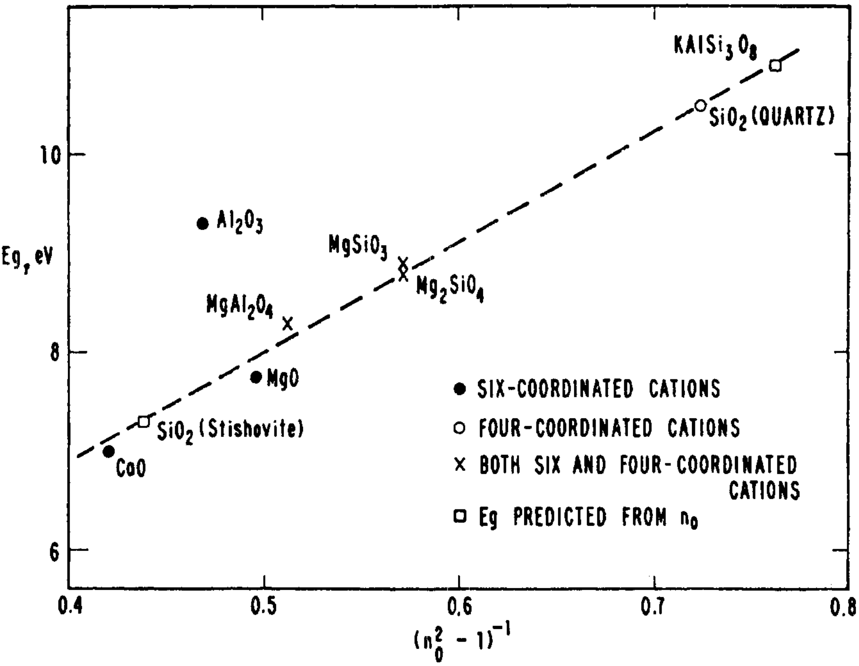

Fig. 5.21. Relationship between the (lowest) energy of the band gap (E_g) and $(n_0^2 - 1)^{-1}$, where n_0 is the refractive index (at 2.1 eV), for several oxides and silicates. For sources of data see Nitsan and Shankland (1975) (after Nitsan and Shankland, 1976; reproduced with the publisher's permission).

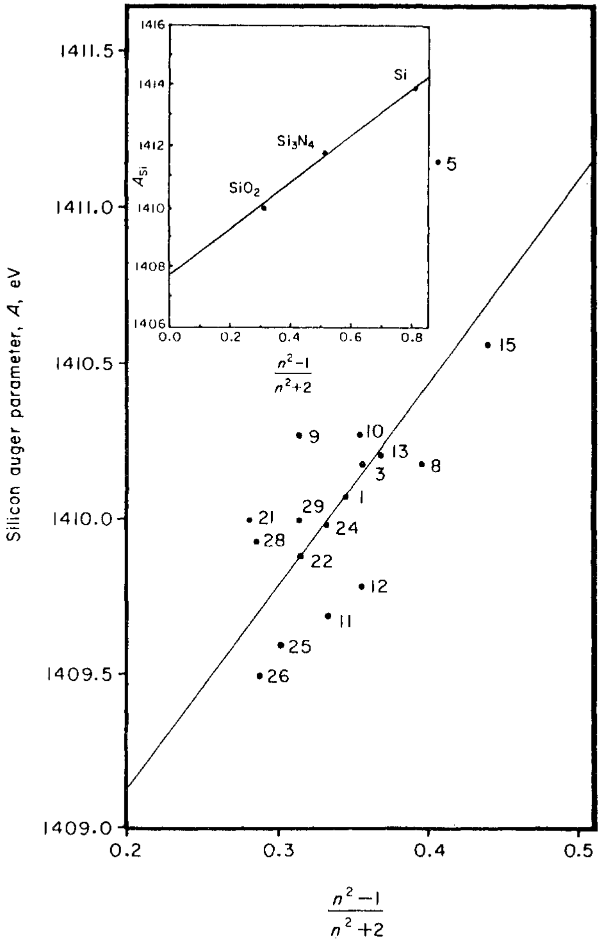

Fig. 5.22. Correlation of the Si Auger parameter with refractive index (n) for various silicates; the inset shows the whole Auger parameter range for Si (after West and Castle, 1982; reproduced with the publisher's permission).

nonbridging oxygens are more basic and more polarizable than bridging oxygens.

Crystal-field stabilization energies, obtained from optical absorption (*d-d*) spectra of the metal ion, have been quite successful in interpreting many aspects of trace-metal partitioning in silicates. There are, however, some cases in which such considerations alone seem insufficient to explain the results. For example, in pyroxenes Fe^{2+} partitions into *M*2 sites at the expense of Mg^{2+}, even though the *M*1 and *M*2 site crystal-field stabilization energies are very similar. An important distinction between the *M*1 and *M*2 sites is the presence of bridging oxygens at *M*2. An increased covalency of the bridging oxygen at the site has been invoked in order to explain the Fe^{2+} partitioning (Burnham et al., 1971; O'Nions and Smith, 1973). Electrostatic plus repulsion energy calculations on orthopyroxenes using empirical metal–oxygen potentials (Ohashi and Burnham, 1972) and modified electron-gas potentials (Tossell, 1980b) give estimated *M*1-*M*2 site energy differences of 5–8 kcal/mol, compared to an experimental free-energy difference less than 4 kcal/mol (Virgo and Hafner, 1969). Such calculations ignore crystal-field effects (calculated to be <1 kcal/mol by Burns, 1970) and the influence of the different electronic character of bridging and nonbridging oxygens. X-ray diffraction studies by Sasaki et al. (1982) indicate that the *M*2 sites in orthopyroxenes, composed partly of bridging oxygens, are more covalent than the *M*1 sites.

In fact, there is considerable general evidence from studies of transition-metal optical absorption (*d-d*) spectra, transition-metal EPR spectra, and main-group metal uv absorption ($s \rightarrow p$) spectra that the bonding character of an anion such as O^{2-} or Cl^{-} is strongly influenced by the numbers and identities of the major cations within the phase. In general, the more highly charged, more highly polarizing cations such as Si^{4+} reduce the basicity of the oxygens to which they are bound and decrease the covalency of the *M*–O interaction. A hard acidic cation such as Mg^{2+} would thus prefer a more basic site with no bridging oxygens. A weakly basic site also favors large *M*–*X* distances and coordination numbers. For example, M^{2+} transition-metal ions are four-coordinated in alkali chloride melts, but when the basicity of the Cl^{-} is reduced by the presence of polarizing cations like Al^{3+} in $AlCl_3$ melts, the coordination changes to octahedral (Angell and Gruen, 1967).

This basicity concept (further discussed in Chapter 8) may be quantified by study of the spectra of probe ions such as Pb^{2+}, leading to values of "optical basicity." These optical basicities can be correlated with polarizabilities, either macroscopic optical polarizabilities or the molecular-level polarizabilities, which influence the Auger parameter.

5.3. Carbonates

The carbonate minerals, characterized by the presence of the $CO_3{}^{2-}$ anion unit, are dominated petrologically by calcite ($CaCO_3$) and the isostructural phases magnesite ($MgCO_3$) and dolomite [$CaMg(CO_3)_2$]. The calcite structure is illustrated in Fig. 5.23, and in this phase, as in all the mineral carbonates, the CO_3 groups are linked by the intermediate (Ca^{2+}) cations (counterions). The mineral carbonates have been reviewed by Reeder (1983).

In the carbonate minerals, the $CO_3{}^{2-}$ group can be regarded as quite well isolated from the counterions, as evidenced by the independence of its properties [such as bond distance (Zemann, 1981), vibrational frequencies, and photoemission spectra] on the nature of the counterions. Thus,

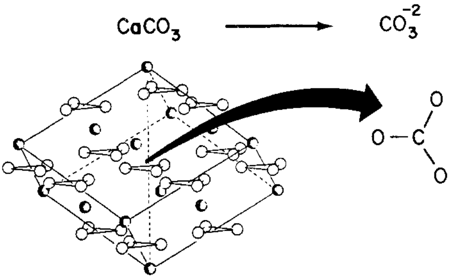

Fig. 5.23. The CO_3^{2-} cluster taken from the structure of calcite, $CaCO_3$.

most calculations of carbonate properties have focused upon the isolated CO_3^{2-} ion (Fig. 5.23), although the influence of stabilizing charge arrays has sometimes been considered. The effect of the counterions on most of the properties appears to be smaller than the expected errors in the quantum-mechanical calculations, so that identifying the sources of discrepancy with certainty is difficult.

5.3.1. Carbonates: Geometric structures

Calculations of the equilibrium carbon–oxygen distance in $CaCO_3$ have been done at a number of different levels, starting with a modified electron-gas approach (not shell stabilized; Tossell, 1985a) and proceeding through various SCF-MO calculations, with the simplest minimum basis set incorporating some effects of counterions (Julg and Letoquart, 1978). The small-basis-set calculations give C–O distances a few hundredths of an angstrom larger than experiment, and larger basis sets (Radom, 1976) converge closer to the experimental values (Table 5.7). The trend is that expected, the more flexible basis sets giving shorter calculated distances. However, split-valence basis-set plus polarization 6-31G* calculations on both the CO and CO_2 molecules give bond distances shorter than experiment (by 0.014 and 0.019 Å, respectively), while similar calculations give a bond distance at just about the experimental average for CO_3^{2-} (Table 5.7). For the CO molecule, correlation increases the calculated bond distance by about 0.02 Å (Hehre et al., 1986). We estimate that the effect of the surrounding lattice is to increase R(C–O) by about 0.02 Å. This is in the same direction, but considerably larger than the 0.005 Å effect calculated by Julg and Letoquart (1978) using a point-charge array to simulate the counterions. By comparison for the NO_3^- cluster, the calculated distances tend to be about 0.02 Å lower compared to the experimental range in nitrates than for CO_3^{2-} (Radom, 1976), indicating that the effect of the lattice is even smaller. The calculated symmetric stretching frequency for CO_3^{2-} shows the same level of agreement with experiment, with the split-valence plus polarization SCF calculation value for isolated CO_3^{2-} being larger than experiment by about 5% (Table 5.7). Since correlation generally reduces such stretching force constants by about 10%,

Table 5.7. Calculated and experimental C–O distances (in Å) and A_1 vibrational frequencies (ν_{A1} in cm^{-1}) in carbonates

	C–O distance (Å)	$\nu_{A1}(cm^{-1})$
Calculated values		
Modified electron-gas method	1.34	
Free CO_3^{2-} cluster, Hartree–Fock–Roothaan Calculations		
Minimum-basis SCF	1.327, 1.330	1105
Split-valence basis SCF	1.316	1046
Split-valence and polarization SCF	1.288	1138
CO_3^{2-} in charge array, Hartree–Fock–Roothaan Calculations		
Minimum-basis SCF	1.332	1064
Experimental values[a]		
$CaCO_3$	1.283	1082
All carbonates	1.27–1.31	1076–1099

[a] See Julg and Letoquart (1978).

a correlated calculation on free CO_3^{2-} would probably underestimate the symmetric stretching frequency. The other vibrational frequencies are obtained with equivalent accuracy for CO_3^{2-} and, for comparison, NO_3^- (Table 5.8, after Konovalov and Solomonik, 1983). The polarizability derivative for the A_1' symmetric stretching mode in CO_3^{2-} was calculated to be 1.07 Å^2 per bond by Tossell and Lazzeretti (1988b) by coupled Hartree–Fock perturbation theory using a [4*s*3*p*2*d*] basis on each atom. The experimental value obtained from the Raman intensity by Chantry and Plane (1960) was 1.04 Å^2 per bond. The calculated dipole derivatives of Konovalov and Solomonik (1983) also give ir intensities in good agreement with experiment (Table 5.8).

Recently Hotokka and Pyykkö (1989) have calculated geometries and vibrational spectra at the 6-31G* basis-set level for BO_3^{3-}, CO_3^{2-}, and

Table 5.8. Calculated (calc.) and experimental (expt.) vibrational frequencies ν (in cm^{-1}) and dipole derivatives, $\partial\mu/\partial Q$ (in debye per Å) for NO_3^- and CO_3^{2-}

	NO_3^-		CO_3^{2-}	
	Calc.	Expt.	Calc.	Expt.
$\nu_1(A_1')$	1087	1048–1062	1046	1076–1099
$\nu_2(A_2'')$	849	838–852	926	852–879
$\nu_3(E')$	1388	1372–1426	1493	1429–1504
$\nu_4(E')$	700	712–736	692	704–735
$\partial\mu/\partial Q_2$	2.90	0.47–0.51	4.09	—
$\partial\mu/\partial Q_3$	3.83	3.3–4.1	4.30	—
$\partial\mu/\partial Q_4$	0.05	—	0.28	—

Source: From Konovalov and Solomonik, 1983.

NO_3^-. Although calculated values were in reasonable agreement with experiment, there was a clear tendency to predict bond distances that were too large and stretching frequencies that were too small for the highly charged BO_3^{3-}, while the NO_3^- calculations gave bond distances too short and stretching frequencies too large, typical of 6-31G* calculations on neutral molecules.

There has been little attempt to go beyond calculations on the CO_3^{2-} cluster and to model the full carbonate structure, although such work has been quite successfully undertaken for nitrates. Tossell (1985a) has performed a modified electron-gas calculation on $MgCO_3$ using R(C–O) = 1.27 Å as a constant value and varying the Mg^{2+}–CO_3^{2-} distance. The Mg^{2+}–CO_3^{2-} interaction was calculated using both free CO_3^{2-} and charge-stabilized CO_3^{2-} wave functions, and the calculated Mg–C distance was found to be 3.1 Å for the stabilized ion and 3.3 Å for the free ion, compared to the 2.95 Å experimental value. This indicates that such an MEG approach to the structures of $MgCO_3$ and other saltlike crystals is feasible. Previous atomistic simulations of carbonates focused upon determination of the CO_3^{2-} charge distribution (e.g., Ladd, 1980), which, as we have seen, is a rather arbitrary concept.

5.3.2. Carbonates: Electronic structures and properties

The electronic structure of CO_3^{2-} may be determined from a study of its x-ray and ultraviolet photoelectron spectra, x-ray emission, and x-ray absorption spectra. Early studies of the x-ray photoelectron spectra of carbonates (Connor et al., 1972; Calabrese and Hayes, 1975) indicated the basic structure shown in Fig. 5.24, in which the spectrum is divided into O $2s$ nonbonding (IV), C–O bonding (III and II), and O $2p$ nonbonding (I) levels. Structure was apparent within the C–O bonding region, corresponding to separable C $2s$–O $2p$ and C $2p$–O $2p$ bonding regions, III and II. An MS-SCF-$X\alpha$ orbital energy diagram is shown in Fig. 5.25, and experimental relative orbital energies are compared with those from *ab initio* Hartree–Fock–Roothaan calculations (Connor et al., 1972) and MS-SCF-$X\alpha$ calculations (Tossell, 1976b) in Table 5.9. Later, uv photoelectron spectroscopy studies (Connor et al., 1978) were able to resolve two components in the O $2p$ nonbonding region (Fig. 5.26).

Further information is available from the carbon and oxygen x-ray emission spectra, which can be obtained in angle-resolved form for CO_3^{2-}, perpendicular to and inclined to the CO_3^{2-} planes. This allows orbitals with σ and π character with respect to the C–O bond to be separately identified. The only occupied orbitals of π type are the $1a_2''$ and $1e''$, which produce the π features in the oxygen and carbon x-ray emission spectra. By aligning the experimental x-ray emission and uv photoelectron spectra using core-electron binding energies, we can show that the orbitals at the top of the valence region ($4e'$, $1e''$, $1a_2''$) that yield the

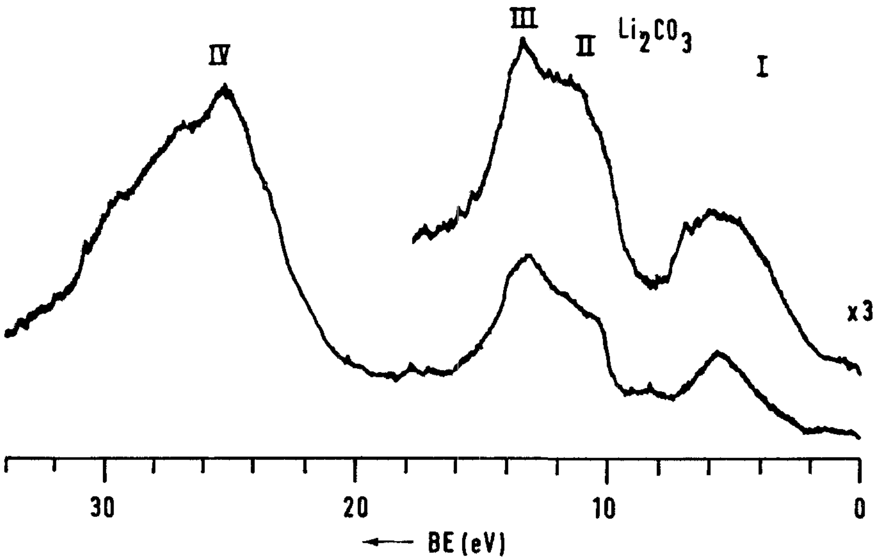

Fig. 5.24. The x-ray photoelectron spectrum of Li_2CO_3 (after Connor et al., 1972).

lowest-energy uv photoelectron peak and the main oxygen x-ray emission peak, are predominantly O 2*p* in character. The next orbitals ($3e'$, $1a_2''$) have C 2*p*–O 2*p* bonding character and generate the second photoelectron peak (at about − 10 eV binding energy), the second oxygen x-ray emission peak, and the carbon x-ray emission peak. The angle resolution allows us to distinguish between π-type ($1a_2''$) and σ-type ($3e'$) C 2*p*–O 2*p* bonding orbitals. The next orbital, $4a_1'$, is of C 2*s*–O 2*p* bonding character and gives the photoelectron spectrum shoulder at around − 12 eV and a weak shoulder in the oxygen x-ray emission spectrum. It is symmetry forbidden in the carbon x-ray emission spectrum. The $3a_1'$ and $2e'$ orbitals are mostly O 2*s* in character, with some C 2*s* ($3a_1'$) and C 2*p* ($2e'$) admixture. In x-ray photoelectron spectra, they produce a broad feature with some structure. Compositions of the molecular orbitals are given in Table 5.10 based upon the MS-SCF-*X*α calculations, and in Table 5.11 based upon the *ab initio* Hartree–Fock–Roothaan SCF calculations. Although the decomposition schemes used are quite different, the results are comparable. From the atomic-orbital characters of the molecular orbitals, we can obtain some qualitative understanding of the relative spectral intensities. However, as we have seen for SiO_4^{4-}, present calculations cannot quantitatively reproduce x-ray photoelectron intensities using an atomic-orbital analysis, and there have been no direct calculations of uv photoelectron or x-ray emission spectra for CO_3^{2} . Without such calculations, discrepancies remain; for example, although the $4e'$, $1e''$, and $1a_2'$ orbitals are all almost 100% O 2*p* in character, the uv photoelectron and oxygen

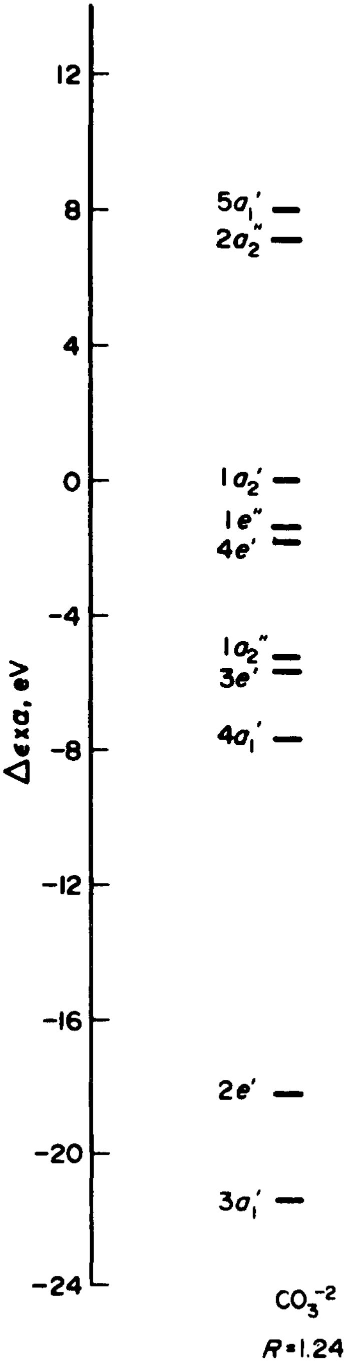

Fig. 5.25. Molecular-orbital energy-level diagram for the CO_3^{2-} cluster obtained using the MS-SCF-$X\alpha$ method (after Tossell, 1976; reproduced with the publisher's permission).

Table 5.9. Electronic structure of the CO_3^{2-} cluster: comparison of experimental ionization potentials (in eV) for valence-region molecular orbitals with those derived from multiple-scattering $X\alpha$ calculations and from Hartree–Fock–Roothaan calculations (in eV)

MO	Experimental	MS-SCF-$X\alpha$[a]	HFR[b]
$1a_2'$		0	
$1e''$	0		0
$4e''$		−1.6	
$3e'$ $1a_2''$	−6.0	−5.5	−6.0
$4a_1'$	−7.7	−7.6	−8.0
$2e'$	−19.8	−18.2	−23.3
$3a_1'$	−24.1	−21.4	−27.7

[a] After Tossell (1976b). [b] After Connor et al. (1972).

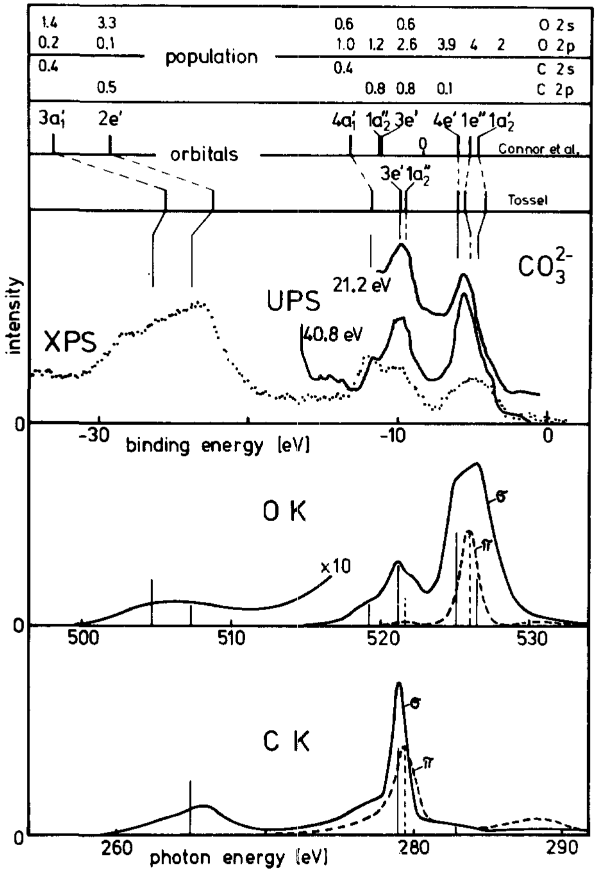

Fig. 5.26. X-ray photoelectron, uv photoelectron, and angle-resolved carbon *K* and oxygen *K* x-ray emission spectra for carbonates, shown along with molecular-orbital assignments and atomic-orbital populations derived from the calculations of Connor et al. (1972) and orbital assignments derived from the calculations of Tossell (1976b) (after Tegeler et al., 1980; reproduced with the publisher's permission).

Table 5.10. Electronic structure of the CO_3^{2-} cluster: distribution of valence electron density between regions of the cluster as defined by a multiple scattering $X\alpha$ calculation [electron density values are percentages; R(C–O) = 1.240 Å][a]

	Cluster regions			
Molecular orbitals	Carbon atomic	Oxygen atomic	Interatomic	Extramolecular
O $2p$ nonbonding				
$1a_2'$	0	79	18	3
$1e''$	1	72	24	3
$4e'$	3	70	24	3
C–O $2p$ bonding				
$1a_2''$	16	45	37	2
$3e'$	17	66	13	4
$4a_1'$	16	66	14	4
O $2s$ nonbonding				
$2e'$	14	76	9	1
$3a_1'$	23	64	12	1

[a] After Tossell (1976b).

x-ray emission peaks they generate are significantly different in shape. Similarly, the calculated ionization potentials are based upon either a Koopmans' theorem or on a transition-state approach and do not correct for many-body effects, which are important for quantitative matching with spectra (Cederbaum et al., 1977). This is particularly important for the O 2*s* region, which does not show the clear two-peak structure expected on the basis of the SCF calculations in the x-ray photoelectron

Table 5.11. Electronic structure of the CO_3^{2-} cluster: molecular-orbital compositions in terms of atomic-orbital components based on *ab initio* Hartree–Fock–Roothaan SCF calculations[a]

		Atomic components (per cent)			
		Carbon orbitals		Oxygen orbitals	
Molecular orbital	Energy (eV)	$2s$	$2p$	$2s$	$2p$
$1a_2'$	3.7	—	—	—	100
$1e''$	3.1	—	—	—	100
$4e'$	2.3	—	3	—	97
$3e'$	−2.8	—	20	15	64
$1a_2''$	−2.9	—	40	—	60
$4a_1'$	−4.9	19	—	30	51
$2e'$	−20.2	—	13	83	3
$3a_1'$	−24.6	19	—	70	10

[a] After Connor et al. (1972).

spectra. Such "inner-valence" spectra typically show a "severe breakdown" of the one-electron ionization model (Nakatsuji, 1983).

The XANES of carbonates have been studied by Madix et al. (1988), who observed a transition at 290 eV to an orbital they identified as $\pi^*_{C\text{-}O}$, corresponding to the $2a_2''$ orbital in Fig. 5.25, about 1 eV above the C 1*s* ionization potential (Fig. 5.27; Tegeler et al., 1980). The carbon x-ray emission spectrum and XANES calculated for $C(OH)_3^+$ by Tossell (1986) are compared with experimental values in Table 5.12 and show reasonable agreement. Note that the previously calculated C 1*s* ionization potential of Tossell (1986) was too high by almost 20 eV (306.4 versus 288.8 eV), leading to the erroneous conclusion that the C $1s \rightarrow 2a_2''$ XANES peak lay *below* the C 1*s* ionization threshold. As observed in numerous other cases, the core → σ^* resonance (C $1s \rightarrow 4e'$ in this case) is sensitive to nearest-neighbor distance and is thus a measure of *R*(C–O).

Based on the carbon and oxygen x-ray emission and XANES energies in Figs. 5.26 and 5.27, we would estimate a $1e'' \rightarrow 2a_2''$ uv excitation energy of about 7 eV (~533 for the O $1s \rightarrow 2a''$ XANES, less ~526 for the O $1s \rightarrow 1e''$ x-ray emission). Studies of carbonate in solution give an absorption that goes off scale at about 6 eV, with a distinguishable shoulder at 5.7 eV (Muller et al., 1967), consistent with expectations from the x-ray spectra.

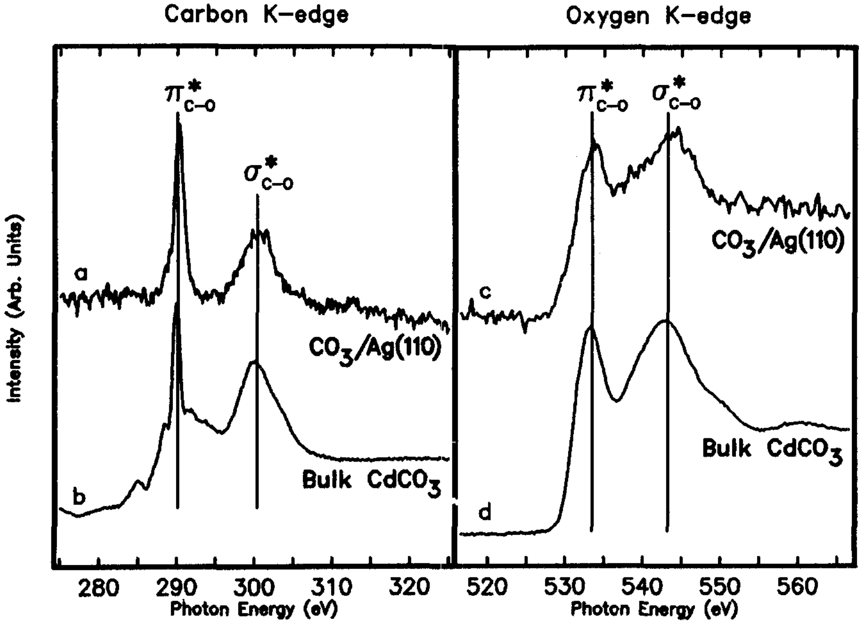

Fig. 5.27. Surface carbonate compared to bulk $CdCO_3$ C1*s* XANES, with $\pi_{C\text{-}O}^*$ and $\sigma_{C\text{-}O}^*$ orbital features identified (from Madix et al., 1988).

Table 5.12. Comparison of calculated and experimental carbon *K* x-ray emission and XANES energies for the carbonate ion

Transition	Calculated value [for $C(OH)_3^+$ cluster][a]	Experimental value
$C1s \rightarrow 1a_2''$	289.7	279.0[b]
$C1s \rightarrow 2a_2''$	297.5	290[c]
$C1s \rightarrow 3e'$	306.8	300[c]

[a] Tossell (1986).

[b] Tegeler et al. (1980).

[c] Madix et al. (1988).

The electron distribution on the carbonate ion in dolomite has been determined experimentally by Effenberger et al. (1983) and has been calculated using *ab initio* Hartree–Fock–Roothaan theory by Tossell (1985a). Calculated and experimental difference densities (see Section 2.1.1) are compared in Fig. 5.28. There is an accumulation of charge in the bond region compared to free spherical atoms. It is also informative to compare the molecular density to that of superimposed free component ions, as shown in Fig. 5.28. Clearly, there is charge buildup both in the bond region and near to the carbon and a reduction in the charge external to the carbon.

A new area of theoretical study is that of the "second-order response properties" of CO_3^{2-} such as the dipole polarizability or the ^{13}C or ^{17}O NMR shielding. Earlier studies of the NMR properties of anions in the series NO_3^-, CO_3^{2-}, and BO_3^{3-} (Tossell and Lazzeretti, 1988c) showed increased shielding of oxygen, along with a lowering of the oxygen NQCC value. At the same time, the anisotropy in the shielding of the trigonal atom decreases (Table 5.13). That calculated for CO_3^{3-} is in fair agreement with the experimental value of Lauterbur (1958). Recent, more accurate calculations on CO_3^{2-} (Tossell and Lazzeretti, 1988b) show substantial distance dependence for both the ^{13}C NMR shielding (Table 5.14) and the electric-dipole polarizability (Table 5.15). The polarizabilities and refractive indices calculated using the most flexible CO_3^{2-} basis set feasible (Table 5.16) are in reasonable agreement with experimental values for $CaCO_3$ from Lo (1973) and Kinase et al. (1979). Only for the magnetic susceptiblity (Pauling, 1979) are the calculated values in poor agreement with experiment, indicating that this property (which scales as the expec-

⟶

Fig. 5.28. Electron-density distributions in the carbonate ion: (a) electron density in CO_3^{2-} minus the sum of the superimposed spherical free atom densities in the CO_3 plane; (b) electron density in CO_3^{2-} minus the sum of the superimposed spherical free ion densities along the C–O internuclear axis (after Tossell, 1985a; reproduced with the publisher's permission).

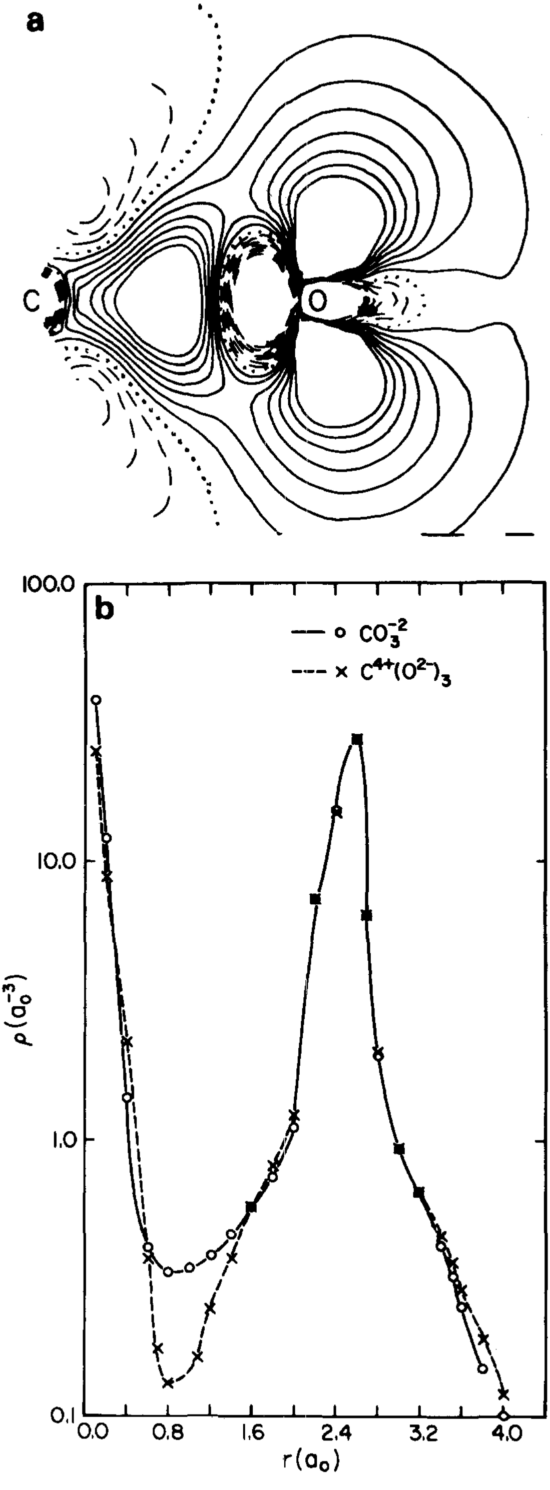
a
C
O
b
— o CO_3^{-2}
--- × $C^{4+}(O^{2-})_3$
100.0
10.0
1.0
0.1
$\rho(a_0^{-3})$
0.0
0.8
1.6
2.4
3.2
4.0
$r(a_0)$

Table 5.13. Calculated NMR properties of trigonal oxyanions (experimental values of $\Delta\sigma^T$ in parentheses)

	$\lvert q^o \rvert$(a.u.)	σ^o_{av}	$\lvert q^T \rvert$	σ^T_{av}	$\Delta\sigma^{T\,a}$
NO_3^-	2.220	−19.3	0.696	−99.6	372.2(210)^b
CO_3^{2-}	1.336	182.1	0.615	80.2	124.3(75)^b
BO_3^{3-}	0.684	239.1	0.360	141.3	33.6

[a] $\Delta\sigma = \sigma_\parallel - \langle\sigma_\perp\rangle$, directions with respect to C_3 axis.

[b] Experimental values.

Source: From Tossell and Lazzeretti, 1988c.

Table 5.14. Calculated ^{13}C NMR shielding components: average diamagnetic (σ^d_{av}) and paramagnetic (σ^p_{av}) components, overall average (σ_{av}), and shielding anisotropy ($\sigma_\parallel - \sigma_\perp$) as a function of carbon–oxygen distance, *R*(C–O), for CO_3^{2-}

R(C–O) (Å)	σ^d_{av}	σ^p_{av}	σ_{av}	$\sigma_\parallel - \sigma_\perp$
1.24	450.1	−386.0	64.0	101.3
1.265	446.1	−390.6	55.5	105.1
1.29	442.3	−396.1	46.2	110.1
1.315	438.8	−402.7	36.0	116.1

Source: After Tossell and Lazzeretti, 1988b.

Table 5.15. Calculated electric-dipole polarizability, α, of CO_3^{2-} in sodium *D* light as a function of carbon–oxygen distance, *R*(C–O). Components of α(*D*) are given ∥ and ⊥ to the C_3 axis. Δ is the difference of ⊥ and ∥ components

	α(*D*) (Å³)			
R(C–O) (Å)	∥	⊥	Δ	average
1.24	2.457	3.655	1.198	3.256
1.265	2.490	3.753	1.263	3.332
1.29	2.521	3.856	1.335	3.411
1.315	2.552	3.963	1.411	3.493

Source: From Tossell and Lazzeretti, 1988b.

Table 5.16. Calculated electric-dipole polarizability for CO_3^{2-} and refractive index *n* of calcite in sodium *D* light, for carbon–oxygen distance = 1.29 Å

	α(*D*) (Å³)				*n*(*D*)			
	∥	⊥	av	Δ	∥	⊥	av	Δ
Calculated value	3.215	4.632	4.165	1.414	1.429	1.632	1.564	0.203
Experimental value	3.185	4.204	3.865	1.019	1.486	1.658	1.601	0.172

See Table 5.15 for explanation of symbols.

Source: From Tossell and Lazzeretti, 1988b.

tation value of r^2) may be significantly perturbed by the presence of counter ions.

In Table 5.17 we show a decomposition of the isotropic polarizability, α_{av}, the average paramagnetic contribution to the C NMR shielding, $\sigma_{av}{}^{p}$, and the average paramagnetic susceptibility, $\chi_{av}{}^{p}$, over the valence molecular orbitals of $CO_3{}^{2-}$. The qualitative bond type of the molecular orbitals in the second column of Table 5.17 are in accord with numerous calculations and x-ray emission studies on $CO_3{}^{2-}$. For α and χ, the largest contributions come from the O 2*p* nonbonding-type orbitals ($1a_2'$, $1e''$, and $4e'$), while for σ^{pC} the C 2*p*, O 2*p* bonding orbital in the CO_3 plane ($3a'$) gives the dominant contribution. The core contribution (O 1*s*, C 2*s*, and O 2*s*) is negligible for α but for χ is 25% of the total.

Before leaving the carbonates, we should note that carbon in four coordination with oxygen is observed in inorganic compounds and has been studied quantum mechanically. Tossell (1976b) calculated a molecular-orbital diagram for $CO_4{}^{4-}$ for a range of distances; the results showed valence orbital energies for the occupied orbitals to be much like those in $CO_3{}^{2-}$, suggesting that the $CO_4{}^{4-}$ polyhedral anion is not intrinsically unstable. Calculations on $C(OH)_4$ using modified electron-gas and *ab initio* SCF Hartree–Fock–Roothaan (STO-3G basis-set) methods (Tossell, 1981; Gupta et al., 1981) yielded equilibrium C–O distances of 1.42 Å, compared to an experimental value of 1.40 Å in $C(OCH_3)_4$. The calculated symmetric stretching frequencies were 1170 and 961 cm^{-1}. Recent SCF Hartree–Fock–Roothaan 6-31G* basis-set calculations on $C(OH)_4$ by Hess et al. (1988) yielded C–O distances of 1.38 Å and a symmetric stretching frequency of 969 cm^{-1}. The optimized symmetry of $C(OH)_4$ [and the other $T(OH)_4$ molecules considered] was S_4.

As noted much earlier, the stable crystalline form of CO_2 is molecular in nature, not a framework structure like quartz. Instability in a postulated quartz-type structure for CO_2 may arise from repulsions of oxygens on adjacent CO_4 groups. For a C–O distance of 1.40 Å and a C–O–C angle of ~120°, this O–O distance is only 2.42 Å, much shorter than typical O–O distances in solids.

Table 5.17. Decomposition of α, σ^{pC}, and χ^{p} over valence MOs for $CO_3{}^{2-}$

MO	Type	$-\varepsilon_i$ (eV)	α_{av} (Å^3)	$-\sigma_{av}^{pC}$ (ppm)	χ_{av}^{p} (ppm emu)
$1a_2'$	O 2*p* nb	−2.1	0.429	23.0	20.65
$1e''$	″	−1.8	1.441	37.5	29.41
$4e'$	″	−0.3	1.171	83.5	26.45
$1a_2''$	C 2*p*, O 2*p* b	3.6	0.360	38.9	5.66
$3e'$	″	4.4	0.524	165.6	15.99
$4a_1'$	C 2*s*, O 2*p* b	6.8	0.174	4.5	4.29
Cores			0.060	46.0	33.8

5.4. Borates

Boric oxide, B_2O_3, is a material of less mineralogical interest than SiO_2, since it represents a relatively minor component in a few mineral systems. The structure of B_2O_3 (at low pressure) is composed of BO_3^{3-} clusters, as shown in Fig. 5.29. The BO_3^{3-} unit, as already noted, is an important constituent of some of the more unusual and complex silicates. B_2O_3 and the related borates are also of much interest in structural chemistry, since they have a potential range of structure types even greater than those observed in SiO_2. Borosilicate glasses (e.g., "Pyrex") are also of considerable technological importance.

As noted by Geisinger et al. (1985), the calculated optimum bridging angle at oxygen is considerably smaller for the B–O–Si (125°) than for the Si–O–Si (144°) or Si–O–Al (139°) linkages, and the barrier to linearity is larger by a factor of two or more. This explains the limited miscibility and intermediate compound formation in systems like Na_2O–B_2O_3—SiO_2, compared to the analog system containing Al_2O_3 rather than B_2O_3. Unfortunately, there is relatively little experimental information on the molecular structures of the compounds in the former system, and essentially no theoretical studies have been done of their properties.

In general, borates are structurally complex, since the boron atoms can be in 3 and/or 4 coordination and oligomer, ring, and chain polymers are all found (Christ and Clark, 1977; Wells, 1975). We shall not attempt to describe fully the complexity of these structures but will concentrate on the fundamental polyhedral units. The molecular geometric and electronic structures of these materials can be studied using many of the site-specific spectroscopies previously discussed. The bulk properties of the materials also change, of course, depending upon the molecular structure.

5.4.1. *B_2O_3 and the borates: Geometric structures*

Crystalline B_2O_3 has two different forms, a low-pressure structure containing only BO_3 triangular units with bond lengths of 1.34—1.40 Å (Gurr et al., 1970), and a high-pressure form with rather asymmetric BO_4 units (three long bonds of 1.506–1.512 Å, and one short bond of 1.373 Å) (Prewitt and Shannon, 1968). Our understanding of the structure of B_2O_3 glass

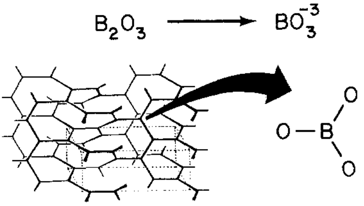

Fig. 5.29. The BO_3^{3-} cluster taken from the structure of B_2O_3.

is described in the book edited by Pye et al. (1978). B_2O_3 glass is believed, on the basis of NMR (Jellison et al., 1977) and Raman (Konijnendijk and Stevels, 1976) spectroscopies and x-ray diffraction studies (Mozzi and Warren, 1970), to consist of boroxol (B_3O_6) rings and linked BO_3 triangles (Fig. 5.30). The strongest evidence for such a distribution of species comes from the NMR studies of Jellison et al. (1977), showing two distinct oxygen sites, with significantly different nuclear quadrupole coupling constants and asymmetry parameters. Recent calculations of electric-field gradients at bridging oxygens as a function of B–O–B angle (Tossell and Lazzeretti, 1988c) support the existence of distinct populations with angles of 120°, as expected in boroxol rings, and about 130°, as expected for non-ring-bridging groups. This is in substantial opposition to the results of molecular-dynamics simulations of B_2O_3, which give no boroxol groups and B–O–B angles in the range of 150–160° (Soules, 1980; Amini et al., 1981). This suggests, as in the Si–O case, that molecular-dynamics simulations without covalency corrections, or angle-dependent terms in the potential, fail to satisfactorily reproduce bridging-angle variations.

The structural properties of B–O bonds have been calculated by *ab initio* SCF Hartree–Fock–Roothaan theory applied to molecular clusters, such as the BO_3^{3-} cluster in Fig. 5.29, the minimal-basis-set (STO-3G) calculations of Gupta and Tossell (1981) and Gupta et al. (1981) yielded B–O bond lengths for $B(OH)_3$ and $B(OH)_4^-$ within 0.03 Å of the average experimental values. Modified electron-gas ionic model calculations based on B^{3+} and OH^- ions (Tossell, 1981) also gave reasonably accurate B–O bond distances. These early studies established that fairly crude methods could give reasonable absolute values and trends in bond distance for oxy and hydroxy anions of boron, so long as the cluster charge was made close to neutral by saturating with hydrogens. More recent

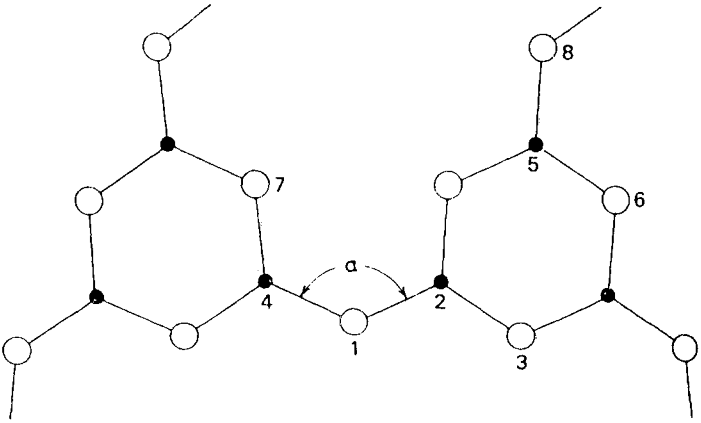

Fig. 5.30. Two boroxol (B_3O_6) rings linked by a shared oxygen atom (filled circles, boron atoms; open circles, oxygen atoms).

MNDO calculations (Uchida et al., 1985) have also given accurate equilibrium geometries for monomers. Large-basis-set *ab initio* SCF Hartree–Fock–Roothaan calculations (Fjeldberg et al., 1980; Zang et al., 1985) give slightly shorter B–O distances, in even better agreement with experiment, provided that O 3*d* polarization functions are included. Calculated geometries for three- and four-coordinate B–O polyhedra and for dimers formed from such polyhedra are shown in Table 5.18. It is interesting to note that the BO_3 unit is often slightly distorted from planarity (Zobetz, 1982), but that all calculations to date have assumed a planar geometry.

The boroxol ring, $B_3O_6^{3-}$, and its protonated form, $H_3B_3O_6$, have also been studied by *ab initio* Hartree–Fock–Roothaan SCF methods (Gupta and Tossell, 1983; Zang et al., 1985; Tossell, 1990b; Tossell and Lazzeretti, 1990) and the semiempirical MNDO method (Uchida et al., 1985). All the $H_3B_3O_6$ calculations give the bonds to nonbridging oxygens as somewhat shorter than those to bridging oxygens (O_{br}), and the B–O_{br}–B angles as within 2–3° of 120° (Table 5.19). This is qualitatively in accord with experiment, although the difference in B–O bond distances changes with basis set and the experimental data are, in some cases, better described by unprotonated $B_3O_6^{3-}$.

For a $(OH)_2BOB(OH)_2$ model, the calculated B–O_{br}–B angles are

Table 5.18. Calculated and experimental geometries in borate polyhedra. Bond lengths and bond angles for the borate clusters shown calculated using *ab initio* SCF Hartree–Fock–Roothaan methods with various basis sets, and the modified electron-gas and modified neglect of differential overlap method, and compared with experimental values (see text for data sources)

Bond lengths [*R*(B–O) in Å]

	Ab initio SCF-HFR					Experimental values	
Cluster	STO-3G basis	4-31G basis	6-31G* basis	MEG method	MNDO method	Average	Range
BO_3^{3-}	1.419	1.435	—			1.37	1.34–1.40
$B(OH)_3$	1.364	1.364	1.358	1.37	1.371	1.361	1.353 1.365
$B(OH)_4^-$	1.48	—	1.474	1.53	~1.47[a]	1.478	

Bond angles (∢B–O_{br}–B in degrees)

	Ab initio SCF-HFR			Experimental values	
Cluster	STO-3G basis	4-31G basis	6-31G* basis	Average	Range
$[(OH)_2B]_2O$	130	180	131.3	134	128–153
$(OH)_3B$–O–$B(OH)_2^-$	123				118–128
$H(OH)_3B$–O–$B(OH)_3H$	123			119	

[a] $B(OH)_4$ value not reported but tetrahedral B bond distances in larger cluster have value given.

Table 5.19. Calculated and experimental geometries of protonated boroxol rings $B_3O_6H_3$. Bond lengths involving bridging oxygens [$R(\text{B–O})_{\text{br}}$] and nonbridging oxygens [$R(\text{B–O})_{\text{nbr}}$], and B–O–B angles involving bridging oxygens ($\sphericalangle\text{B–O}_{\text{br}}\text{–B}$) calculated using *ab initio* SCF Hartree–Fock–Roothaan methods with different basis sets, the Modified Neglect of Differential Overlap method, and compared with experimental values (see text for data sources)

	Calculated values *Ab initio* SCF-HFR					
	STO-3G[a]	6-31G[a]	3-21G*[c]	MNDO method[d]	Average experimental value	v-B_2O_3
$R(\text{B–O})_{\text{br}}$ (Å)	1.374	1.390	1.371	1.389	1.401	1.36
$R(\text{B–O})_{\text{nbr}}$ (Å)	1.289	1.351	1.351	1.354	1.322	
$\sphericalangle\text{B–O}_{\text{br}}\text{–B}$ (deg)	121	123.8	119.9	120	122.7	121

[a] Gupta and Tossell (1983).

[b] Zang et al. (1985).

[c] Tossell (1990a).

[d] Uchida et al. (1985).

larger than in $B_3O_6^{3-}$ (on the order of 132°) and inclusion of 3*d* polarization functions on the bridging oxygen seems necessary to obtain accurate results. An interesting feature of the geometry of $(OH)_2BOB(OH)_2$ is that its lowest-energy form has a nonplanar C_2 geometry with a nonzero dihedral angle between the two BO_3 groups. *Ab initio* SCF Hartree–Fock–Roothaan calculations with large basis sets give dihedral angles of about 60° (Zang et al., 1985), while MNDO semiempirical molecular-orbital calculations (Uchida et al., 1985) give a value of around 30°. In either case, the barrier to bending for the planar structure is very low, around 5 kcal/mol. Of course, without such twisting, the structure of B_2O_3 would be planar like that of graphite. The question of why the borate groups twist instead of adopting a planar π-system geometry is an intriguing one. Accurate theoretical studies on H_2BOBH_2 by Fjeldberg et al. (1980) have established a strong interdependence of the B–O–B angle and the dihedral angle. It is presumably this strong dependence that accounts for the variability in B^{III}–O–B^{III} angles in metaborates noted by Wells (1975). In the planar C_{2v} geometry, one O 2*p* lone pair is involved in π bonding with the $-BH_2$ group, while the other is nonbonding. In the twisted structure, the bonding is more complex, indicating that other properties than the energy may vary strongly with dihedral angle. For example, Tossell and Lazzeretti (1988c) observed substantial changes in the oxygen electric-field gradient (EFG) in twisted geometries. MNDO studies of large clusters in which boroxol rings are connected by bridging oxygens confirm the twisting, while giving B–O_{br} bond lengths somewhat shorter and $\text{B–O}_{\text{br}}\text{–B}$ angles somewhat larger than those in $(OH)_2BOB(OH)_2$.

Calculations have also been performed on other borate dimers, such as two linked BO_4 units (B^{IV}–O–B^{IV}) or one BO_3 unit linked to a BO_4 unit

(B^{III}–O–B^{IV}) using *ab initio* SCF Hartree–Fock–Roothaan methods (Zang et al., 1985) and on larger molecular clusters using semiempirical molecular-orbital (MNDO) methods (Uchida et al., 1985, 1986). The *ab initio* results, even at the STO-3G basis-set level, give accurate bond lengths and reproduce the experimentally observed reduction in B–O_{br}–B angles when one or more B^{IV} units is present in the linkage. The calculated potential energy curve for B–O_{br}–B angle variation in the B^{III}–O–B^{IV} case (as in $H_5B_2O_6^-$) matches well against a histogram of observed B^{III}–O–B^{IV} angles. MNDO calculations on two boroxol rings bridged through oxygen give almost the same B–O_{br}–B angle as in $(HO)_2BOB(OH)_2$, but the exocyclic bond R(B–O_{br}) is shortened so that the bridging bond between the rings is substantially shorter (by 0.03 Å) than the bond within the boroxol ring. MNDO calculations on larger clusters also give good agreement between optimized structures and experimental geometries; for example, the $H_8B_9O_{18}^-$ model for pentaborate structures (Fig. 5.31) matches well against the structure of $K_2B_4O_7 \cdot 4H_2O$ (Table 5.20).

Accurate calculations have also been performed on gas-phase B_2O_3 species, establishing clearly that the equilibrium geometry is planar and V shaped with symmetry C_{2v} (Sellers et al., 1981; Barone et al., 1981) and that the bipyramidal D_{3h} structure is of much higher energy (Snyder and Wasserman, 1980). An interesting feature of the calculated geometry is the very small barrier to linearity of ~2.4 kcal/mole for the B–O_{br}–B angle. This contrasts with H_2BOBH_2, for which the barrier to linearity for the B–O–B angle is much larger. This difference may be associated with the π-orbital conjugation possible in linear B_2O_3 (Sellers et al., 1981).

The discrete B_2O_3 molecule is of interest since it is the principal component of boric oxide vapor and has been presumed to be the dominant species in B_2O_3 melts above about 800K. Although the bipyramidal species lies around 200 kcal/mole above the experimental energy of the vapor species, as shown by Snyder and Wasserman (1980), the calculated energy of the C_{2v} structure is lower by about 140 kcal/mol for a (roughly) comparable basis set, suggesting that its energy is compatible with that of B_2O_3 vapor. Theoretical studies have also been performed on the gas-phase $LiBO_2$ molecule, which is predicted to have a linear $C_{\infty h}$ geometry with a B–O bond length of about 1.22 Å (Nguyen, 1986). The calculated ir spectra are also in reasonable agreement with experiment, although there is some indication that the structure may be the less symmetric C_s when held in a matrix.

Frequencies for the symmetric stretching vibrations of $B(OH)_3$ and $B(OH)_4^-$ have also been calculated (Gupta and Tossell, 1981), with good agreement between calculation and experiment. The minimum bases used in the *ab initio* Hartree–Fock–Roothaan calculations gave B–O distances that were slightly too long and force constants smaller than their Hartree–Fock limit values (recall that, as discussed in Chapter 3, Hartree–Fock results typically underestimate bond distance by 1–2% and overestimate stretching vibrational frequencies by about 10%). Much more accurate

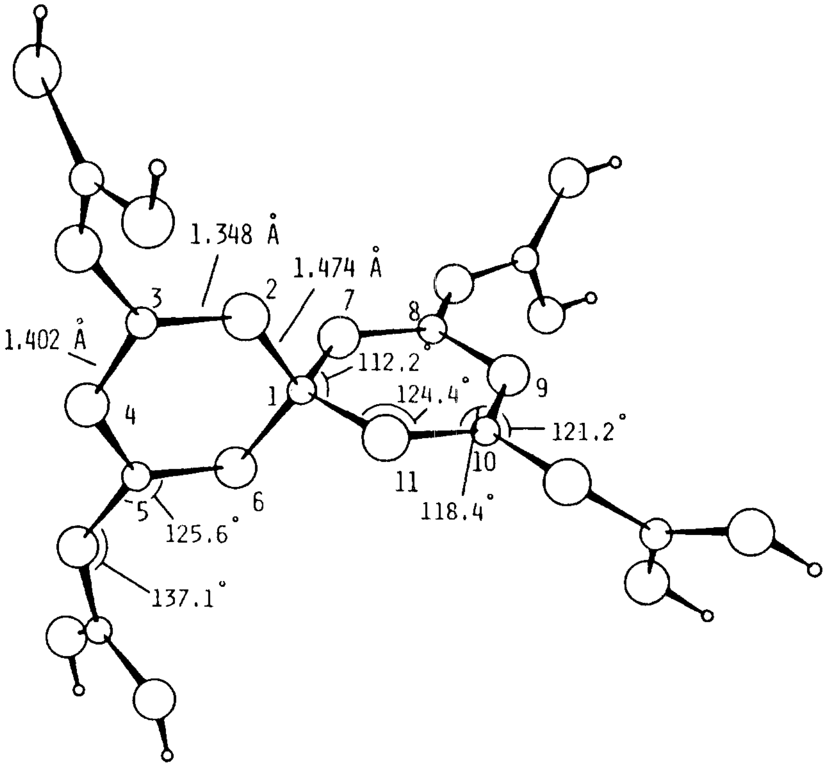

Fig. 5.31. The $H_8B_9O_{18}^-$ cluster, a model for the pentaborate structures.

calculations employing double-ζ plus polarization basis sets and full geometry optimizations have recently been performed on $H_4BO_4^-$ (Hess et al, 1988), yielding calculated vibrational frequencies in reasonably good agreement with the experimental values of Edwards et al. (1955). Results are shown in Table 5.21. For gas-phase B_2O_3, the two calculated transitions of highest intensity are also in reasonable agreement energetically

Table 5.20. Comparison of experimentally determined bond lengths with those calculated using the modified neglect of differential overlap method for the pentaborate structure (see text for data sources)

		Bond length (Å)	
Cluster	Bond[a]	Calculated	Experimental
Pentaborate structure	B1–O2	1.474	1.478
	O2–B3	1.348	1.349
	B3–O4	1.402	1.373

[a] See Fig. 5.31 for labeling of atoms.

Table 5.21. Comparison of calculated vibrational frequencies and those observed in aqueous solution for the $H_4BO_4^-$ ion

Assignment, T_d	Species, T_d	Observed, T_d (assumed)	Species, S_4	Calc., S_4
ν_1	A_1	754	A	775
ν_2	E	379	$A + B$	420, 430
ν_3	F_2	947	$B + E$	940, 1086
ν_4	F_2	533	$B + E$	515, 569

with the two bands most definitively assigned to B_2O_3 in the experimental spectrum.

5.4.2. *B_2O_3 and the borates: Spectra and electronic structures*

In addition to the geometric structures, many other properties of borates have been studied. The valence-region photoemission spectrum and the boron *Kα* x-ray emission spectra of solid B_2O_3 have been studied by Joyner and Hercules (1980) and the oxygen *Kα* x-ray emission spectra by Hayashi (1968) (Fig. 5.32). The valence region consists of features with binding energies of 6.9, 10.7, 14.4, and 26.4 eV, corresponding respec-

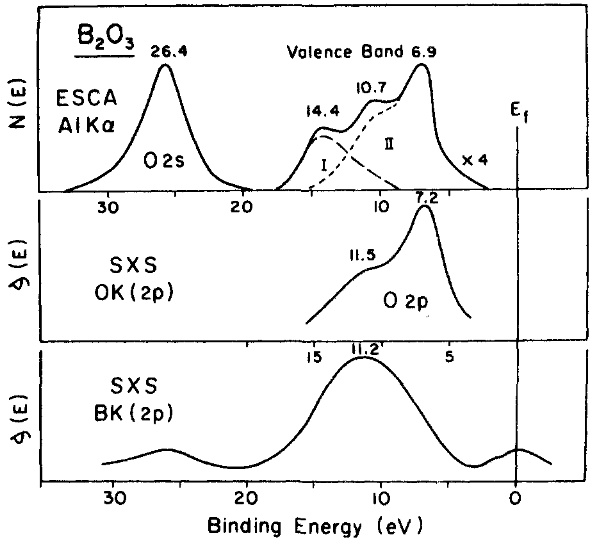

Fig. 5.32. X-ray photoelectron and x-ray emission spectra for B_2O_3. The O 2*s* and valence-band x-ray photoelectron (ESCA) spectra (obtained using Al *Kα* radiation) are shown aligned with the oxygen *K* and boron *K* x-ray emission spectra ("soft x-ray spectra," SXS). Peak I in the ESCA spectrum is B 2*s*; peak II is O 2*p*. Spectra were aligned using 1*s* core-level binding energies (after Joyner and Hercules, 1980; reproduced with the publisher's permission).

tively to O 2*p* nonbonding, B 2*p*–O 2*p* bonding, B 2*s*–O 2*p* bonding, and O 2*s*–type orbitals (Gupta and Tossell, 1981). This assignment is supported by the correspondence of x-ray photoelectron and x-ray emission features and by calculations on the BO_3^{2-} and $B(OH)_3$ groups, the energy-level diagram for the latter of which is shown in Fig. 5.33. The B 2*s*–O 2*p* bonding feature does not appear in the oxygen $K\alpha$ spectrum, in the same way that the analogous feature is remarkably weak in SiO_2. There was a suggestion in Gupta and Tossell (1981) that their BO_3^{2-} calculation underestimated the stability of the B 2*s*–O 2*p* bonding orbital, presumably because of cluster-size effects. However, neither the effect of cluster size upon theoretical energies nor the effect of degree of polymerization upon experimental binding energies has been systematically investigated for either solids or gas-phase molecules. Based on relative spectral intensities in the x-ray photoelectron and various x-ray emission spectra, a qualitative valence-band structure (shown in Fig. 5.34) has been constructed by

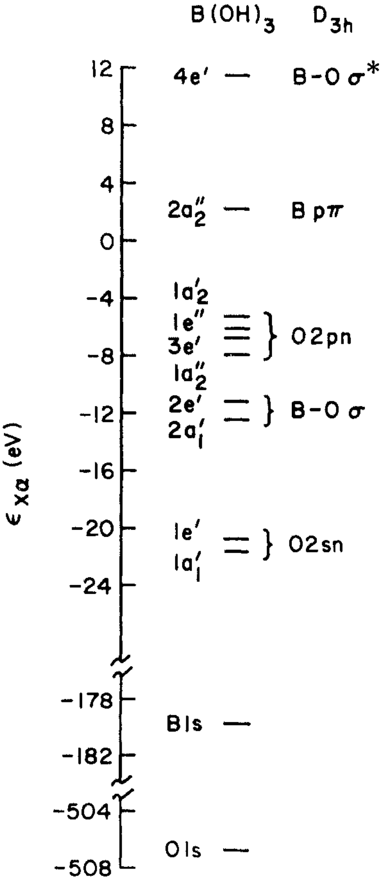

Fig. 5.33. Molecular-orbital energy-level diagram for $B(OH)_3$ in D_{3h} symmetry (ground state) with a B–O distance of 1.361 Å, calculated using the MS-SCF-$X\alpha$ method (after Tossell, 1986; reproduced with the publisher's permission).

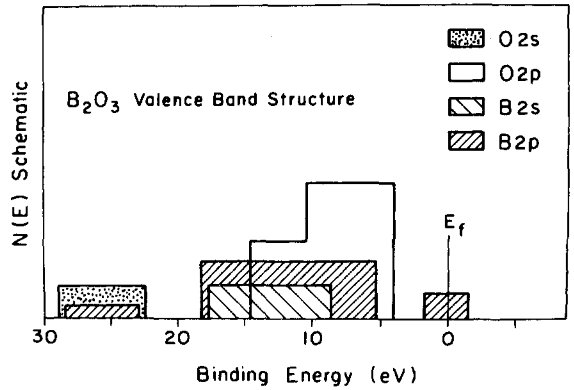

Fig. 5.34. Schematic valence-band structure of B_2O_3 (band limits and shapes are not intended to be accurate) (after Joyner and Hercules, 1980; reproduced with the publisher's permission).

Joyner and Hercules (1980) that is consistent with the $B(OH)_3$ calculation of Gupta and Tossell (1981).

The boron Auger electron spectrum of B_2O_3 shows peaks that can be assigned as KL_1L_1 and $KL_{2,3}L_{2,3}$, with energies and widths consistent with those seen in the x-ray photoelectron spectrum, but it also shows several additional features associated with solid-state processes. The resolution of the Auger spectrum is insufficient to resolve contributions from individual molecular orbitals.

X-ray absorption spectra have also been calculated by Tossell (1986) for three- and four-coordinate boron using the continuum MS-$X\alpha$ method. For the D_{3h} symmetry BO_3 unit, the lowest-energy empty orbitals that yield XANES features are of a_2'' symmetry and B–O $p\pi^*$ type, and e' symmetry and B–O σ^* type, with the π^* orbitals lower in energy. The a_2'' orbital lies below threshold, and its energy is rather insensitive to the B–O distance, while the e' orbital is actually a shape resonance in the continuum, and its energy varies strongly with the B–O distance. The calculated spectra of $B(OH)_3$ and BF_3 are in reasonable agreement with experiment (Table 5.22). For $B(OH)_4^-$ the lowest x-ray absorption peak is just at threshold. The spectrum of $B(OH)_3$ and BF_3 are qualitatively similar, but the a_2'' and e' lie at higher relative energy versus threshold for $B(OH)_3$. The variation of the e' orbital energy with distance is about 24 eV/Å, similar to that observed for other σ^* resonances (Sette et al., 1984), while the a_2'' orbital changes at about half this rate. It is important to note that the properties of solid borates, such as $B(OH)_3$, are mimicked well by those of gas-phase molecules such as $B(OCH_3)_3$, which have similar widths in their valence-region photoelectron spectra (Kroner et al., 1973). The electron transmission spectrum (ETS; see Appendix B) of $B(OCH_3)_3$

(Tossell, 1986) also shows a feature attributable to an a_2'' orbital resonance.

Information is also directly available about the electron distribution in the B–O bond from x-ray diffraction studies (Gajhede et al., 1986; Kirfel et al., 1983) and, indirectly, from studies of the gradient of the electric field at B and O (Snyder et al., 1976; Gajhede, 1985; Tossell and Lazzeretti, 1988a; Tossell, 1990b). For solid lithium metaborate, $LiBO_2$, with chains of BO_3 triangles, x-ray studies yield deformation densities that do not change with B–O distance as expected. Rather, the shortest and longest B–O bonds (with distances of 1.325 and 1.407 Å) have significant positive difference density (~0.6 e Å^{-3}), while the intermediate bond (1.392 Å) shows very little deformation density along the B–O bond. What deformation density exists is cylindrical about the bond (e.g., of σ symmetry), while the deformation densities for the other B–O bonds are elongated and π-like. These results were interpreted in terms of strongly bonded $LiBO_2$ units that were more weakly coupled by an empty B sp^2 hybrid on one unit and an oxygen lone pair on an adjacent one. However, calculations by Zang et al. (1985) on $H_4B_2O_5$ indicate that a $\Delta\rho$ peak exists for B–O_{br} but is off the bond axis, interior to B–O_{br}–B angles. Thus the $\Delta\rho$ peak is merely displaced rather than being missing (Fig. 5.35).

Table 5.22. Term energies (in eV) of empty $4e'$ (B–O σ^*) and $2a_2''$ (B $p\pi$) orbitals in BF_3 and $B(OH)_3$ (experimental values in parentheses)

Orbitals	BF_3	$B(OH)_3$
$4e'$	−1.8 (−2.3)	−5.1 (−4.1)
$2a_2''$	8.4 (7.2)	4.0 (4.2)

The deformation density of $B(OH)_3$ is less dramatic, showing the expected positive deformation densities along the B–O and O–H bonds and the O $2p$ lone pairs. Although calculations such as those of Gupta and Tossell (1981) give a reasonable qualitative description of the $\Delta\rho$ map, the more sophisticated calculations of Gajhede et al. (1986), utilizing d polarization functions, are in better agreement with experiment and show higher charge density in the bond region and less charge around the oxygens. Studies by the above authors show that such basis-set expansion is more important than configuration interaction in determining deformation densities that are in agreement with experiment (Fig. 5.36).

As noted in Chapter 2, deformation densities suffer from ambiguities in definition of reference state and are not (even in theory) directly related to other bond properties. Inspection of the total molecular density or its derivative may ultimately prove more valuable (Bader et al., 1979; Bader, 1985). A start has been made in this endeavor by Swope and Downs (1988), who found features in the Laplacian of the density for B–O bonds

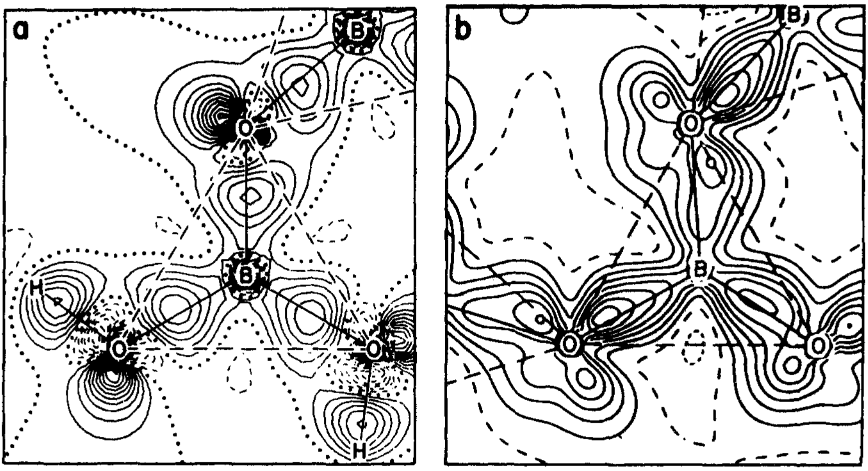

Fig. 5.35. Electron-density distributions in borates — deformation density maps for corner-sharing BO_3 planar triangular units: (a) calculated density map for planar $H_4B_2O_5$; (b) experimental density map for $LiBO_2$ (contour interval 0.1 electrons Å^{-3}; dashed contour is zero; negative contours are dotted) (after Zang et al., 1985; reproduced with the publisher's permission).

indicative of shared interactions. A comparative theoretical study of a number of boron-containing rings shows shared interactions between B and O in boroxine ($H_3B_3O_3$) (Boyd et al., 1984).

Studies of the electric-field gradient at the B atom in borates (Snyder et al., 1976; Gajhede, 1985; Tossell and Lazzeretti, 1988c) all yield results for $B(OH)_3$ in reasonable agreement with experiment, but uncertainty remains concerning the proper value of eQ to use for ^{11}B, and substantial changes are observed depending on basis-set size and correlation. In general, larger basis sets give larger EFGs, and correlation decreases the EFG. The ^{17}O EFGs in $(H_2B)_2O$ and $H_3B_3O_6$ were also calculated by Tossell and Lazzeretti (1988c), and it was confirmed that oxygens in boroxyl rings with B–O–B angles of 120° and those outside such rings with B–O–B angles of around 132° should indeed give the distinctive NQCC values of 4.7 and 5.8 MHz observed experimentally (Jellison et al., 1977) (Table 5.23). However, in the H_2BOBH_2 calculations, the ^{17}O NQCC was found to depend strongly upon the dihedral angle between the $-BH_2$ planes. In the isolated molecule, the minimum-energy dihedral angle is 61°, but its energy is only 6 kcal/mole below that of the untwisted geometry (Zang et al., 1985). Soppe et al. (1988) have suggested that $(BH_2)_2O$ groups with dihedral angles not equal to zero could explain the Raman spectra of vitreous B_2O_3. Tossell (1990b) found that for a B–O–B angle of 132°, a good fit of calculated and experimental oxygen NQCC values occurred only for a dihedral angle of zero and that no $(BH_2)_2O$ model could reproduce the intense Raman peak observed at 800 cm^{-1} and usually attributed to

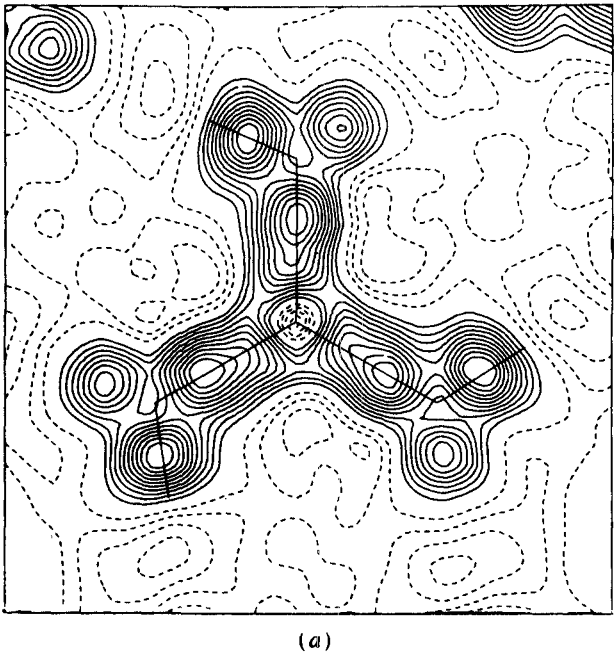

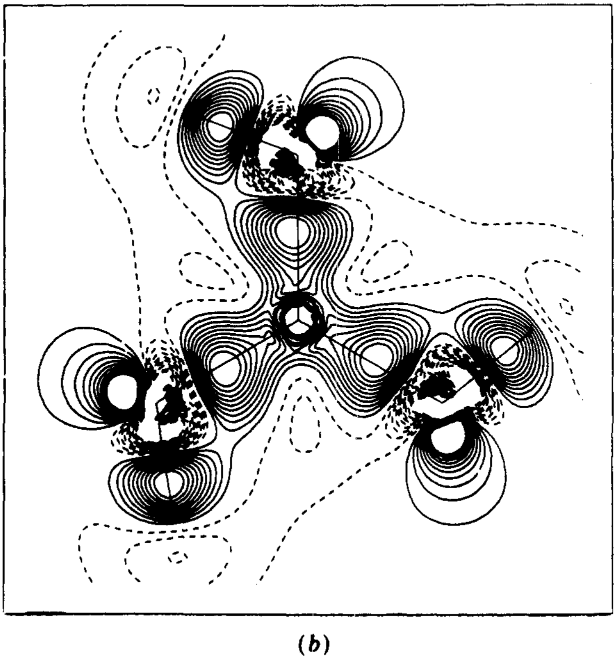

Fig. 5.36. Electron-density distributions in borates — deformation density maps calculated for $B(OH)_3$: (a) static model map calculated from pseudoatom model; (b) theoretical deformation density map from *ab initio* Hartree–Fock configuration-interaction calculation (after Gajhede et al., 1986; reproduced with the publisher's permission).

Table 5.23. Calculated properties at O in H_2BOBH_2 (planar C_{2v}; B 3*d*, O 3*d*, H 2*p* basis) as a function of B–O–B angle ($\sphericalangle$B–O–B) (experimental values in parentheses)

$\sphericalangle$B–O–B (deg)	**120**	**132**	**144**
$\lvert q^O \rvert$ (a.u.)	0.957	1.158	1.291
$e^2q^OQ^O/\hbar$[a]	5.02 (4.69)	6.07 (5.75)	6.77
η^O	0.54 (0.58)	0.58 (0.4)	0.36
σ^O (ppm)	76.8	86.8	104.6

[a] Assuming $eQ^O = 2.233 \times 10^{-26}$ cm^2.

boroxol rings. By contrast, direct calculation at the Hartree–Fock 3-21G* basis-set level of the ir and Raman spectra of $H_3B_3O_3$, the simplest possible boroxol ring model, give an A_1' symmetry oxygen symmetric breathing mode with an energy that matched well against experiment (Tossell and Lazzeretti, 1990).

The NMR properties of B in three and four coordination with oxygen have also been studied (Tossell, 1986; Tossell and Lazzeretti, 1988c). For three-coordinate and four-coordinate B, the B 2*p*–O 2*p* σ-bonding orbitals make the dominant contribution to the paramagnetic shielding, σ^p. Large-basis-set calculations on BO_3^{3-} indicate that it has a less anisotropic shielding tensor at the B atom than do isoelectronic CO_3^{2-} and NO_3^-, and a more shielded oxygen. BO_3^{3-} also has a smaller polarizability anistropy than do CO_3^{2-} or NO_3^-, consistent with a smaller separation of π^* and σ^* unoccupied orbitals (Lo, 1973). Four-coordinate boron is predicted to have a 38 ppm higher ^{11}B shielding than three coordinate, a difference in the right direction but considerably larger than the experimental value of 17 ppm (as discussed for Si, conventional coupled Hartree–Fock calculations overestimate coordination number effects). Of course, the main difference in NMR spectra between three- and four-coordinate boron is the large NQCC value in the three-coordinate case, compared to values near zero for four coordination (exactly zero for a perfect tetrahedron). Thus three- and four-coordinate boron can easily be distinguished by NMR both in glasses and by wide-line NMR in crystalline solids (e.g., Cuthbert and Petch, 1963). More recently MAS-NMR has revealed changes in ^{11}B shielding with second-nearest-neighbor effects (Turner et al., 1986).

Limited information is available on the uv–visible spectral properties of B_2O_3 and related materials, both as pure materials and with transition-metal impurities. The lowest-energy fundamental absorption in B_2O_3 is at about 8.6 eV (Izumitani and Hirota, 1985), close to the value of 8.4 eV calculated by Tossell for $B(OH)_3$ (Tossell, 1986). To assess the environment encountered by metal ion impurities, crystal-field (*d-d*) transitions, uv absorption spectral transitions (e.g., $6s \rightarrow 6p$ in Pb^{2+}), or ESR spectra of odd electron species can be studied. For example, Lin and Angell

(1984) found Ni^{2+} to coexist in tetrahedral and octahedral coordination in potassium borate glass. Interesting interpretations can be made by studying impurity "probe ion" properties as a function of composition in alkali borate glasses, since above 17 mol % M_2O, the BO_3 groups are partially converted to BO_4 groups, which have substantially different effects upon the probe metals. As explained by Kawazoe et al. (1978a,b) and discussed in more general terms by Duffy and Ingram (1971, 1976) the oxygen attached to three-coordinate boron has a relatively low basicity, presumably due to B–O π bonding, which renders the O $2p$ orbital less susceptible to attack by acids. As discussed earlier, basicity in solids may be related to spectral quantities called *optical basicities*. It is apparent from changes in Pb^{2+} probe ion s→p energies and from Cu^{2+}–oxygen covalencies deduced from ESR, that BO_3 groups provide less covalent (or less "basic") environments than do BO_4 groups. Thus, addition of alkali oxide to B_2O_3 (e.g., in $(Na_2O)_x(B_2O_3)_{1-x}$, which converts B^{III} to B^{IV} starting at about $x = 0.17$ (Griscom, 1978), increases the basicity of the glass. Presumably the basicity of oxygen coordinated in B^{IV} species is greater because there are no low-energy empty orbitals to bond covalently with the oxygen lone pairs to reduce their availability.

Notes

1. That is, a potential of the form $V = D_e\,[1 - \exp(-\beta\rho]^2$, where $\rho = R - R_e$ is the departure from equilibrium, D_e the dissociation energy, and β a parameter.

2. Q notation specifies the number of oxygens of the SiO_4^{4-} unit bridging to other Si (or Al) atoms (e.g., a Q^3 silicate has three bridging and one nonbridging oxygen per silicate tetrahedron).

6

APPLICATION OF BONDING MODELS TO SULFIDE MINERALS

6.1. Introduction

The sulfide minerals are a group of materials dominated by binary and ternary compounds of sulfur with iron, cobalt, nickel, copper, zinc, and lead. Other members of this group of naturally occurring crystalline materials incorporate a variety of cations (e.g., Mn^{2+}, Mo^{4+}, Ag^{+}, Hg^{2+}, Cr^{3+}, Sn^{4+}, Pt^{4+}) and several other anions (Se^{2-}, Te^{2-}, As^{2-}, Sb^{2-}). The sulfides are not only the most important group of ore minerals, constituting the raw materials for most of the world's supplies of nonferrous metals, but also are substances that exhibit a fascinating diversity in structural chemistry and in electrical, magnetic, and other physical properties (Ribbe, 1974; Vaughan and Craig, 1978). The sulfide minerals range in properties from materials that are diamagnetic insulators, forming virtually colorless crystals when pure (e.g., ZnS), to diamagnetic semiconductors (e.g., PbS), to semiconductors or metallic conductors exhibiting various forms of ordered magnetism (e.g., $CuFeS_2$, Fe_7S_8, CoS_2), and to metals exhibiting weak temperature-independent Pauli paramagnetism (e.g., Ni_3S_4, Co_9S_8). The diversity of sulfide properties indicates that the valence electrons in these materials can range from extensively delocalized as in metals, to localized on the atoms as in insulators. This has presented problems for those attempting to develop bonding models and has also led to certain misconceptions regarding the kinds of models that may be appropriate.

Earlier attempts to develop qualitative bonding models for sulfide minerals have been reviewed by Vaughan and Craig (1978) and include applications of valence-bond theory (Pauling, 1970) and ligand-field theory (Nickel, 1968, 1970), zone theory (Freuh, 1954), and qualitative molecular-orbital/band models (Burns and Vaughan, 1970; Vaughan et al., 1971; Prewitt and Rajamani, 1974). At about the same time, band-structure calculations on some of the binary sulfides of importance in materials science were being performed by physicists, and certain of the data of mineralogical interest have been reviewed by Marfunin (1979). The mid-1970s saw the first successful attempts to perform MO calculations on metal–sulfide mineral systems, and a substantial number of systems have since been studied (many having been reviewed by Vaughan and Tossell, 1983).

In this chapter, the application of bonding models to an understanding of the sulfide minerals will be discussed. A diversity of approaches will be illustrated by considering certain of the major sulfide mineral groups as examples. The subdivision of the sulfide minerals into groups is based largely on crystal structure and follows the system proposed by Vaughan and Craig (1978). It is presented in a summarized form in Table 6.1, to enable the reader to place the examples discussed below into the context of the rest of the sulfide minerals. The emphasis in this chapter is more on electronic structure and the interpretation of spectra and properties rather than on geometric structure. Indeed, far fewer studies have been performed on the sulfides with the aim of understanding geometric structural variations, partly because of the difficulties of undertaking calculations at a high level of quantum-mechanical rigor. The opportunity is also taken, in this chapter, to illustrate the relationships between qualitative and quantitative molecular-orbital and band-model approaches when applied to a group of materials with diverse properties.

6.2. Sphalerite, würtzite, and related phases [ZnS, CdS, HgS, (Zn,Fe)S]

Sphalerite (β-ZnS) has a cubic crystal structure in which both Zn and S occur in regular tetrahedral coordination. Pure sphalerite is a diamagnetic semiconductor with a large band gap (~3.6 eV; Shuey, 1975). On the basis of the observed structure and properties, the simple MO energy-level diagram shown in Fig. 6.1 can be proposed to describe the bonding in a "ZnS_4" cluster molecular unit. Overlaps between outermost *s* and *p*

Table 6.1. Structural classification of the sulfide minerals

Major subdivision and group	Structure type	Examples
Disulfide group (all containing dianion units in the structure)	Pyrite-type (cubic)	Pyrite (FeS_2), cattierite (CoS_2), vaesite (NiS_2), etc.
	Marcasite-type (orthorhombic)	Marcasite (FeS_2) Ferroselite ($FeSe_2$), etc.
	Arsenopyrite-type (orthorhombic)	Arsenopyrite (FeAsS), gudmundite (FeSbS), safflorite ($CoAs_2$)
	Loellingite-type (orthorhombic)	loellingite ($FeAs_2$), $FeSb_2$, etc.
Galena group	NaCl-type (cubic)	Galena (PbS), clausthalite (PbSe), altaite (PbTe), alabandite (α-MnS)

Table 6.1. Continued

Major subdivision and group	Structure type	Examples
Sphalerite group	Sphalerite (zinc-blende)-type (cubic)	Sphalerite (β-ZnS) hawleyite (CdS), etc.
	Derivative of sphalerite-type	Chalcopyrite ($CuFeS_2$), stannite (Cu_2FeSnS_4), talnakhite ($Cu_9Fe_8S_{16}$), etc.
Würtzite group	Würtzite-type (hexagonal)	Würtzite (α-ZnS), greenockite (CdS), etc.
	Derivatives of würtzite-type	Cubanite ($CuFe_2S_3$), enargite (Cu_3AsS_4), etc.
Niccolite group	NiAs-type (hexagonal)	Niccolite (NiAs), breithauptite (NiSb), etc.
	Derivatives of NiAs-type	Troilite (FeS), monoclinic pyrrhotite (Fe_7S_8), etc.
Thiospinel group	Spinel-type (cubic)	Linnaeite (Co_3S_4), polydymite (Ni_3S_4), greigite (Fe_3S_4) violarite ($FeNi_2S_4$), etc.
Layer sulfides group (various layer structures)	Molybdenite-type (hexagonal)	Molybdenite (MoS_2), tungstenite (WS_2)
	Covellite-type (hexagonal)	Covellite (CuS), idaite ($\sim Cu_3FeS_4$)
	$Cd(OH)_2$-type (hexagonal)	Berndtite (SnS_2), melonite ($NiTe_{2-x}$)
	Tetragonal PbO-type	Mackinawite $(Fe,Co,Ni,Cu)_{1+x}S$
Metal-excess group (various unusual structures adopted by metal-rich sulfides)	Pentlandite-type (cubic)	Pentlandite [$(Ni,Fe)_9S_8$], cobalt pentlandite (Co_9S_8)
	Chalcocite-type (monoclinic)	Chalcocite (Cu_2S), acanthite (Ag_2S)
	Argentite-type (cubic)	Argentite (Ag_2S), crookesite (Cu_2Se)
	Digenite-type	Digenite (Cu_9S_5), bornite (Cu_5FeS_4)
Chain structure group (various structures containing chains of atoms)	Stibnite-type (orthorhombic)	Stibnite (Sb_2S_3), bismuthinite (Bi_2S_3), etc.
	Cinnabar-type (hexagonal)	Cinnabar (HgS)
Sulfosalt group(s) (complex minerals of formula $A_mT_nX_p$, where A = Ag,Cu,Pb; T = As,Sb,Bi; X = S)	A range of complex structures with TS_3 pyramidal groups present (T = As, Sb, or Bi)	Pyrargyrite (Ag_3SbS_3) tetrahedrite [$(Cu,Fe)_{12}Sb_4S_{13}$], boulangerite ($Pb_5Sb_4S_{11}$)

Source: After Vaughan and Craig, 1978.

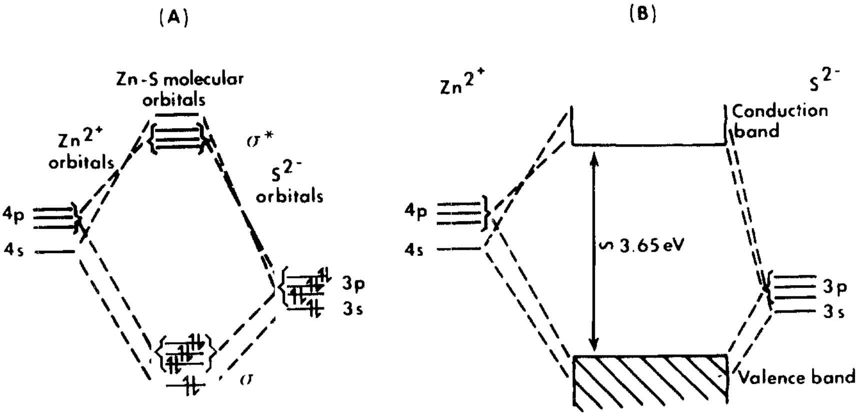

Fig. 6.1. The electronic structure of ZnS: (a) simplistic qualitative one-electron MO energy-level diagram for a ZnS_4 (tetrahedral) cluster; (b) simplistic one-electron band model for ZnS.

atomic orbitals on zinc and sulfur are regarded as resulting in the more stabilized σ-bonding molecular orbitals of the cluster and corresponding destabilized σ*-antibonding molecular orbitals, the former being completely filled with electrons and the latter empty. Overlap between molecular orbitals on adjacent "ZnS_4" clusters in a sphalerite crystal will lead to broadening of the MO energy levels into bands, as shown by the simple one-electron MO/band model shown in Fig. 6.1.

The structure of the valence band in ZnS has been investigated using x-ray photoelectron and x-ray emission spectroscopy (Ley et al., 1974; Sugiura et al., 1974; Domashevskaya et al., 1976). As outlined in Chapter 2, combinations of these two spectroscopic methods aids in the assignment of features in the spectra. Thus, in Fig. 6.2, we can suggest that peak I in the XPS and XES arises from the same orbitals. Since this is the S $K\beta$ main peak in the XES, we can assign it in both spectra to orbitals that are dominantly sulfur $3p$ in character. Using similar arguments, peaks II, III, and IV may be assigned to orbitals with zinc and sulfur s and p and some zinc $3d$ character (II), to dominantly zinc $3d$ orbitals, and to orbitals of dominantly sulfur s character (IV).

Quantum-mechanical calculations on sphalerite have been performed using a variety of band-structure methods (see the following) and using the MS-SCF-$X\alpha$ cluster method (Tossell, 1977c). The latter involved a ZnS_4^{6-} cluster, and the results in the form of MO energy levels labeled according to the irreducible representations of the T_d symmetry group are also shown in Fig. 6.2. Results are given here for both the *ground-state* (GS) electronic configuration and using the *transition-state* (TS) procedure, which incorporates electronic relaxation effects occurring during ionization (see Section 3.10). As seen in Fig. 6.2, the latter show quite

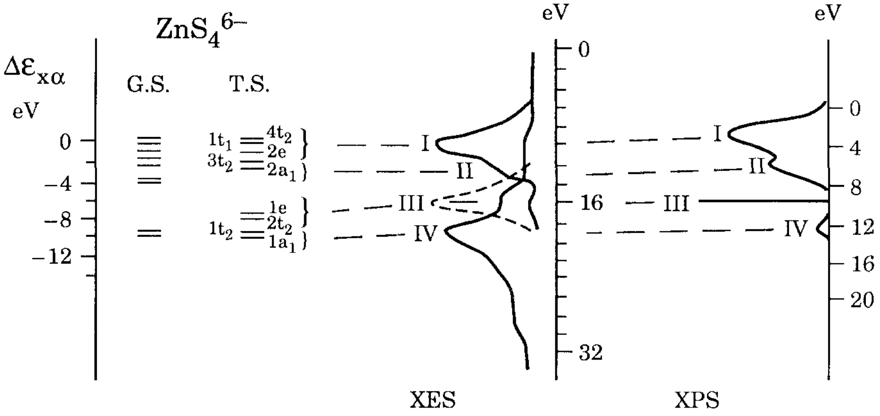

Fig. 6.2. Valence-region x-ray photoelectron and x-ray emission spectra for ZnS (after Ley et al., 1974; Sugiura et al., 1974; Domashevskaya et al., 1976) compared to MS-SCF-$X\alpha$ cluster calculation results, both for the ground state and transition state (after Tossell, 1977c).

good agreement with the XPS and XES results. Of course, as well as providing information on the order and relative separation of the MO energy levels, the MS-SCF-$X\alpha$ calculations also provide information on the composition of particular molecular orbitals in terms of the contribution of atomic orbitals of metal or sulfur. Thus, the $4t_2$, $1t_2$, and $2e$ molecular orbitals are dominantly sulfur $3p$ in character and nonbonding, whereas the $3t_2$ and $2a_1$ orbitals are the main metal–sulfur bonding orbitals. The $1e$ and $2t_2$ orbitals are the dominantly metal $3d$ ("crystal-field")-type orbitals in this system, and the $1t_2$, $1a_1$ orbitals are sulfur $3s$ nonbonding in character. In Fig. 6.3, the results of the MS-SCF-$X\alpha$ calculation on a single ZnS_4^{6-} cluster are compared with the results of a (non-self-consistent) band-structure calculation on sphalerite using the Korringa–Kohn–Rostoker method (Eckelt, 1967). Here a conventional energy band-structure diagram is shown, with data also simplified to a one-dimensional representation indicating the band limits. The band model also shows that the top of the valence band of ZnS is composed of essentially sulfur $3p$ nonbonding orbitals and that the zinc $3d$ levels are buried ~7 eV beneath the top of the valence band.

In fact, because of its importance in solid-state science, a large variety of band-structure approaches have been used to calculate the electronic structure of sphalerite. These have included self-consistent and semiempirical orthogonalized-plane-wave (OPW) (Stukel et al., 1969), empirical-pseudopotential (Cohen and Bergstresser, 1966), tight-binding (Pantelides and Harrison, 1975), APW (Rössler and Lietz, 1966), and modified OPW (Farberovich et al., 1980), as well as KKR (Eckelt, 1967) methods. In a recent and extremely detailed study using a density-functional approach (specifically a method termed the self-consistent potential variation

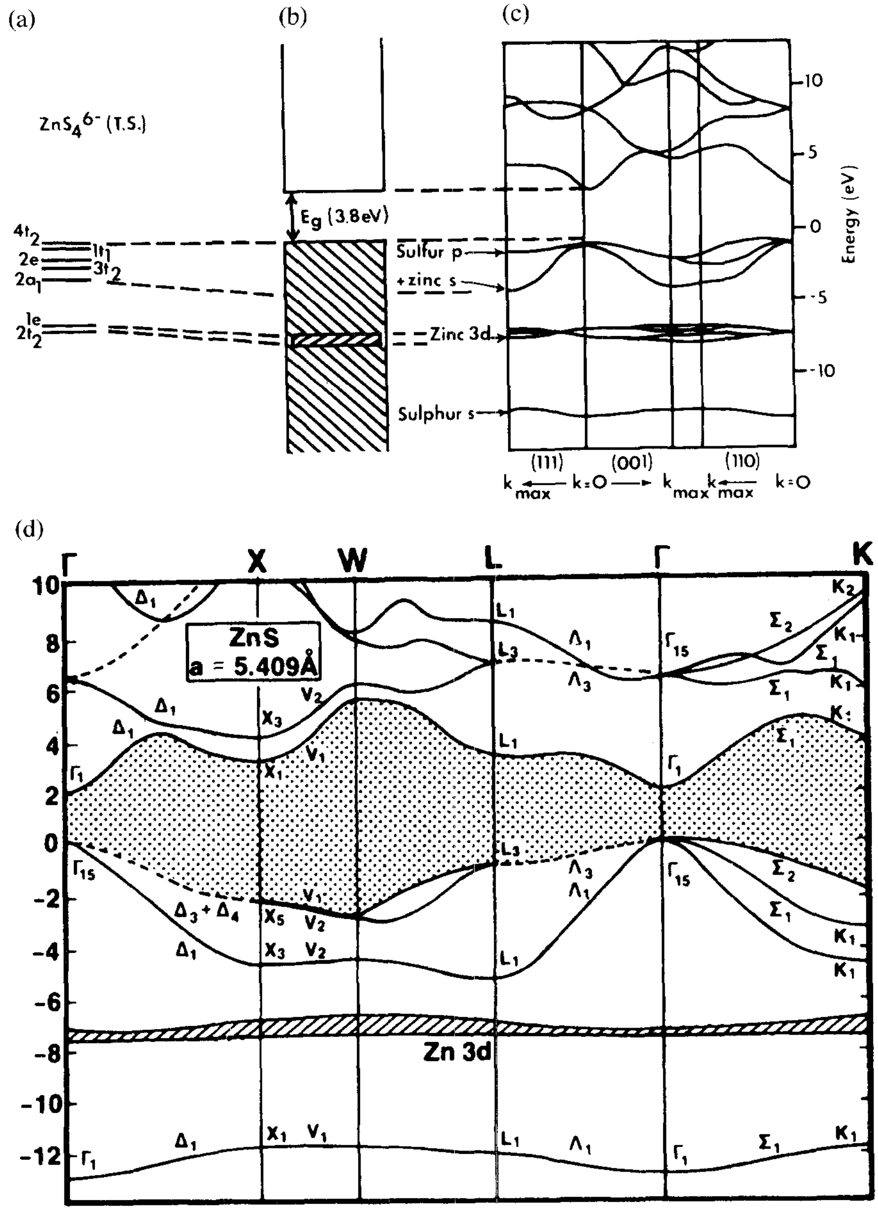

Fig. 6.3. Comparison of results obtained from (a) a cluster calculation on a ZnS_4^{6-} tetrahedron using the MS-SCF-$X\alpha$ method (transition state) with the results of an earlier band-structure calculation employing (c) the Korringa–Kohn–Rostoker method via (b) a simplistic one-dimensional representation derived from the band-structure calculation (after Vaughan and Tossell, 1983). Below this is shown (d) a self-consistent local-density band structure of sphalerite calculated by Bernard and Zunger (1987), in which dashed lines show doubly degenerate bands and the shaded area is the fundamental band-gap region. The origin of the coordinate system is on the anion site. Also shown on the next page, (e) is a plot of charge-density contours for the valence band of ZnS (logarithmically spaced in units of e/a.u.^{3}). Solid circles represent core regions (after Bernard and Zunger, 1987; reproduced with the publisher's permission).

(e)

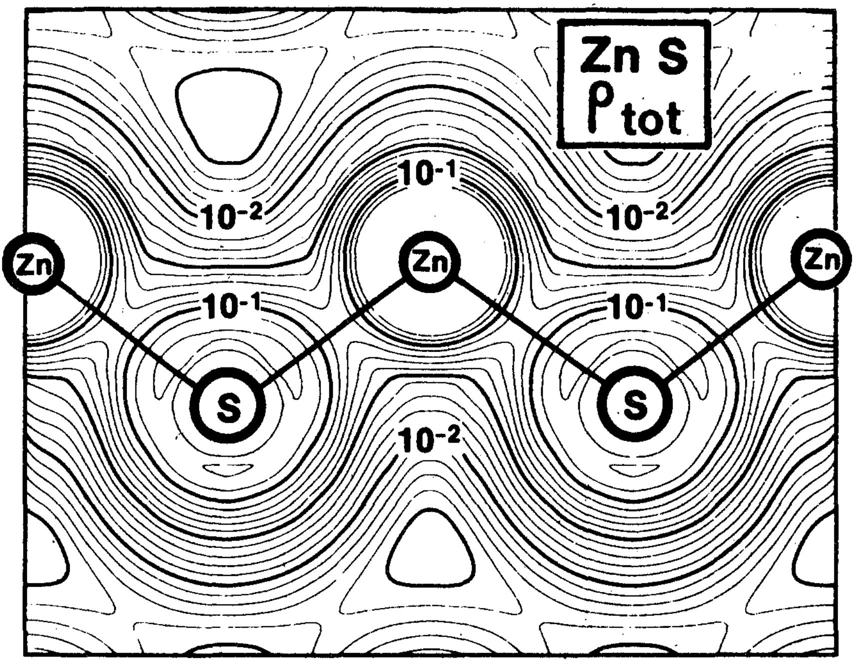

Fig. 6.3. Continued

mixed basis), Bernard and Zunger (1987) calculated the electronic structures of ZnS along with the sphalerite-type ZnSe and ZnTe and various ordered intermediate ZnS–ZnSe–ZnTe compounds. The calculated band structure of sphalerite is shown in Fig. 6.3(d) and the charge density contours for the valence band in Fig. 6.3(e). These calculations do show significant differences compared to the older OPW and KKR calculations and are more similar to the results of the self-consistent OPW calculation of Stukel et al. (1969). As commonly found with a local-density model, interband transition energies are underestimated when compared with experiment.

Isostructural with sphalerite are the phases hawleyite (CdS) and metacinnabar (HgS), providing an interesting series of compounds for comparative study. Thus, for example, the results of MS-SCF-$X\alpha$ calculations on appropriate clusters are presented and discussed by Tossell and Vaughan (1981). As shown in Fig. 6.4, the overall structure of the valence region is similar. In each case a group of S $3p$ nonbonding orbitals occurs at the top of the valence region, then the main metal–sulfur bonding orbitals of the system, then the dominantly metal $3d$ orbitals and the S $3s$ nonbonding orbitals. Although the order of molecular orbitals with increasing binding energy is the same in each case, there are some marked variations in the relative stabilities of different groups of orbitals between

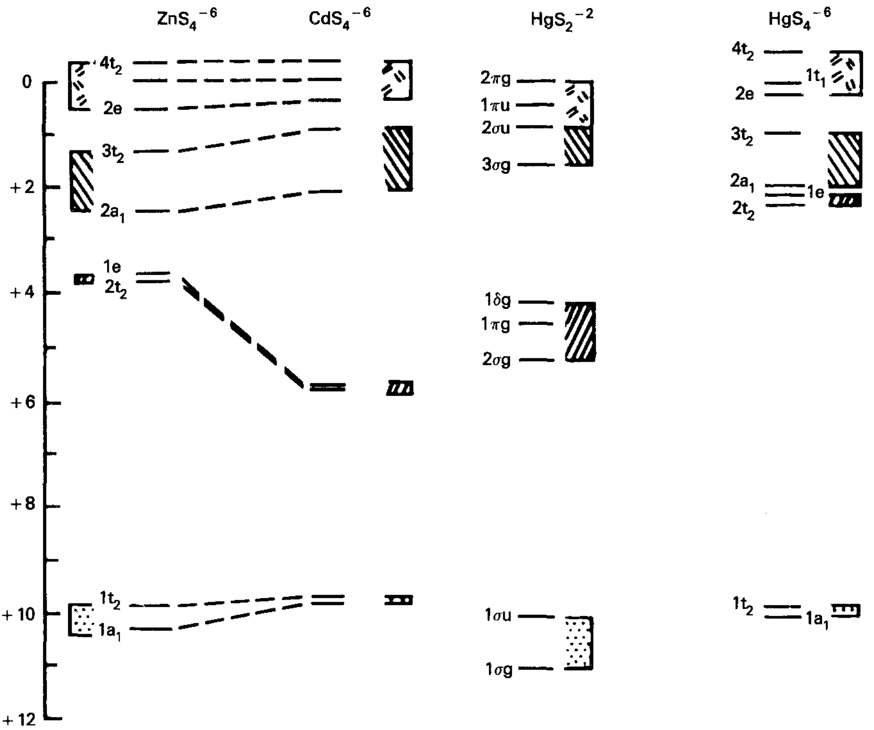

Fig. 6.4. Energy-level diagrams derived from MS-SCF-$X\alpha$ calculations on tetrahedral ZnS_4^{6-}, CdS_4^{6-}, and HgS_4^{6-} clusters and the linear HgS_2^{2-} cluster (after Tossell and Vaughan, 1981). Makeup of particular molecular orbitals in terms of atomic-orbital character is shown by the boxes in the diagram.

the compounds, for example, the trend towards decreasing stabilization of the main metal–sulfur bonding orbitals in the series ZnS–CdS–HgS. The marked fluctuations in the energies of the metal *d* orbitals are due partly to relativistic effects (incorporated in the calculations in an approximate way for Hg 5*d* states). In Fig. 6.4 results are also shown for a calculation on a HgS_2^{2-} cluster considered by Tossell and Vaughan (1981) as the basic unit occurring in the mineral cinnabar (HgS). Again, band-structure calculations have been performed on CdS (hawleyite) using a variety of methods (e.g., Zunger and Freeman, 1978; Farberovich et al., 1980). Several authors have pointed out the importance of including metal *d* states in the calculations in order to obtain results in reasonable agreement with experimental data (e.g., Farberovich et al., 1980).

Many natural sphalerites contain substantial amounts of Fe^{2+} substituting for Zn^{2+} in the tetrahedral sites, and this system provides the opportunity to study a sulfide with increasing amounts of this transition metal. Detailed studies of the electrical and magnetic properties of iron-containing zinc sulfide by Keys et al. (1968) showed that a sphalerite with

12.4 at. % iron exhibits typical semiconductor behavior with the forbidden energy gap reduced to 0.49 eV. Magnetic susceptibility measurements showed paramagnetic behavior at lower iron concentrations and suggested antiferromagnetic coupling at higher iron concentrations. The latter suggestion, however, is not supported by the Mössbauer spectra of iron in sphalerite. Gerard et al. (1972) observed a single peak for iron concentrations <1 at. % and a superimposed quadrupole doublet for higher concentrations (<31 at. %). They interpret the single peak as due to iron atoms without other iron impurity atoms as nearest neighbors, and the doublet as the effect of one or more other iron atoms as nearest neighbors.

The most obvious effect of iron substitution in sphalerite is on the optical properties: Pure sphalerite is transparent and virtually colorless; with increasing iron content the color ranges from pale yellow to dark brown, and some specimens appear black and opaque in hand specimen. Thus, whereas pure sphalerite has an absorption edge in the ultraviolet (~3400 Å; 29,400 cm^{-1}), Low and Weger (1960) observed an absorption band in the infrared (at ~30,000 Å; 3500 cm^{-1}) attributed to the spin-allowed transition between the *e* and t_2 levels of the 3*d* orbitals ($^5E \rightarrow {}^5T_2$) and hence a measure of the crystal-field splitting (Δ). Marfunin et al. (1968) reported the spectrum shown in Fig. 6.5 for iron-bearing sphalerite and obtained a value of 3500 cm^{-1} for Δ. Data for the visible and near-ultraviolet regions are also shown in Fig. 6.5, and these spectral features have been variously attributed to spin-forbidden *d-d* transitions and to Fe-S charge transfer.

An MS-SCF-$X\alpha$ calculation on an FeS_4^{6-} tetrahedral cluster (Vaughan et al., 1974) can be used to model the nature of the iron–sulfur bonding in this system and can be compared with the optical absorption spectra. The results of the calculation are shown in Fig. 6.6; they illustrate the importance of spin polarization due to the four unpaired 3*d* electrons on the Fe^{2+} cation. This splits the MO energy levels into spin-up and spin-down

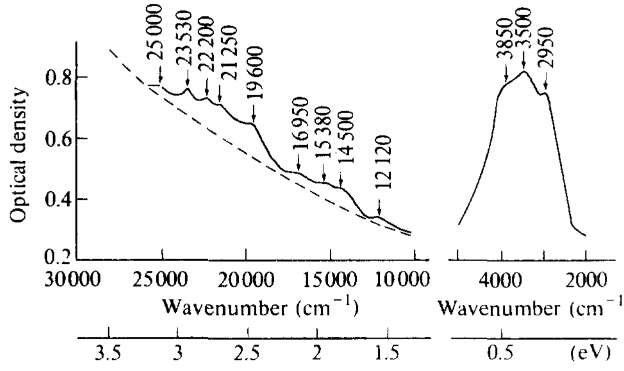

Fig. 6.5. The electronic (optical) absorption spectrum of iron-bearing sphalerite (after Vaughan and Craig, 1978; based on data of Marfunin et al., 1968).

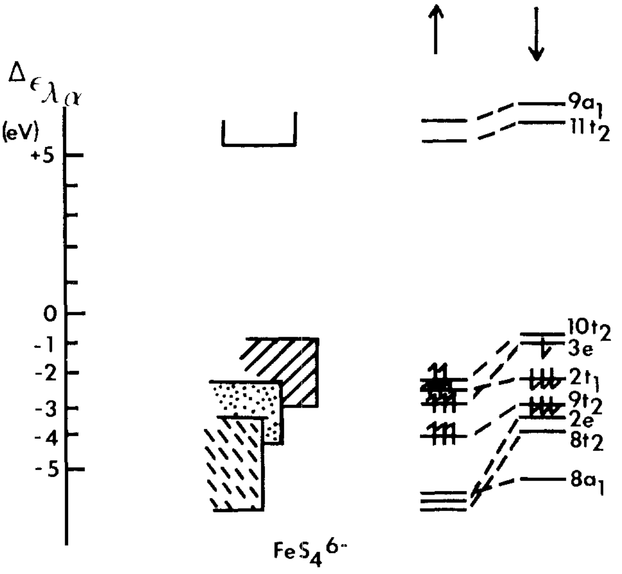

Fig. 6.6. Energy-level diagram to illustrate the electronic structure of iron-bearing sphalerite and based on MS-SCF-$X\alpha$ cluster calculations on the FeS_4^{6-} tetrahedron (after Vaughan et al., 1974). Discrete MO energy levels (spin up, ↑, and spin down, ↓) are shown on the right; on the left is a simplistic band model based on this, with filled (or partly filled) bands shown shaded (lines: crystal-field-type band; dots: sulfur nonbonding band; dashes: metal–sulfur bonding band).

groups, and, in some cases, the calculated energy difference between a spin-up and its equivalent spin-down MO is as much as ~2 eV. The calculations provide information on the composition and character of particular molecular orbitals, as shown schematically in Fig. 6.6. Comparison of the observed peak energies from the optical absorption spectra with those from the calculation (utilizing the transition-state procedure) show generally good agreement, as seen from Table 6.2. The energies of the spin-forbidden spin-flip *d*→*d* transitions and of the ligand → metal charge-transfer transitions are particularly well reproduced by the calculations; that of the spin-allowed *d*→*d* transition is not so well reproduced, and none of the experimentally observed fine structure associated with this transition is reproduced. However, this fine structure has been attributed by several authors to Jahn–Teller distortion of the Fe^{2+} sites in sphalerite (Marfunin et al., 1968; Ham and Slack, 1971), although this is not supported by the Mössbauer data (Gerard et al., 1972). However, any effects resulting from distortion of the tetrahedral FeS_4 cluster would not, of course, be predicted by the calculation on a perfect tetrahedron. The good overall agreement between calculation and experiment shown in Table 6.2 both establishes the validity of the calculation and clarifies interpretation of the spectra.

Other impurity ions found in sphalerite and hawleyite include Ni^{2+},

Table 6.2. Experimental and calculated optical spectra for the FeS_4^{6-} unit. Transition energies, ΔE, are all in cm^{-1}

Type of transition	Assignment	Calc. ΔE (TS)	Experimental ΔE
Spin-allowed *d*-*d*	$3e_{\downarrow} \rightarrow 10t_{2\downarrow}$	2194	3850, 3500, 2950 3700, 2850
Spin-forbidden	$10t_{2\uparrow} \rightarrow 3e_{\downarrow}$	13,149	12,120, 13,000
Spin-flip (very weak)	$10t_{2\uparrow} \rightarrow 10t_{2\downarrow}$	14,279	14,500
	$3e_{\uparrow} \rightarrow 3e_{\downarrow}$	17,586	16,950
	$3e_{\uparrow} \rightarrow 10t_{2\downarrow}$	18,586	19,600
Ligand–metal charge transfer	$2t_{1\downarrow} \rightarrow 3e_{\downarrow}$	14,279	14,500
	$2t_{1\downarrow} \rightarrow 10t_{2\downarrow}$	13,100	
	$9t_{2\downarrow} \rightarrow 3e_{\downarrow}$	17,586	16,950
	$9t_{2\downarrow} \rightarrow 10t_2$	19,764	19,600

Source: After Vaughan et al., 1974, who provide details of the experimental data.

Co^{2+}, Mn^{2+}, and Cu^{+} and the optical absorption spectra resulting have been studied by various authors (e.g., Platonov and Marfunin, 1968). Again, calculations using cluster models have been successfully employed to interpret and predict these spectra (e.g., Mueller and Scherz, 1980, and Weider and Scherz, 1985, used a CNDO method to model ZnS:Cu, CdS:Cu, ZnS:Ni, and CdS:Ni). One other interesting experimental observation, recently supported by calculations using the MS-SCF-$X\alpha$ method (Lie et al., 1988), is of tetrahedrally coordinated Fe^{+} as a product of the decay of ^{57}Co as a dilute impurity in ZnS.

6.3. Galena (PbS) and the isostructural selenide and telluride minerals (PbSe, PbTe)

The sulfides of the galena group have the familiar rocksalt (NaCl) structure (Table 6.1) with metals and anions in regular octahedral coordination. Galena is a diamagnetic semiconductor, the electrical properties of which have been reviewed by Dalven (1969). The forbidden energy gap at 300 K is ~0.41 eV. For the isostructural PbSe (clausthalite) and PbTe (altaite), values of 0.27 and 0.31 eV, respectively, have been reported for the energy gaps (Zemel et al., 1965). The conduction mechanisms and carrier concentrations in all of these compounds are very sensitive to precise stoichiometry and to the presence of minor impurities. The electronic properties of the lead monochalcogenides have been extensively studied because of the technological applications of these compounds.

The valence-region x-ray photoelectron spectra of the lead chalcogenides have been reported by McFeely et al. (1973); as Fig. 6.7(a) shows, there is a remarkable similarity between the sulfide, selenide, and telluride. Band-structure calculations (e.g., Tung and Cohen, 1969; Rabii and

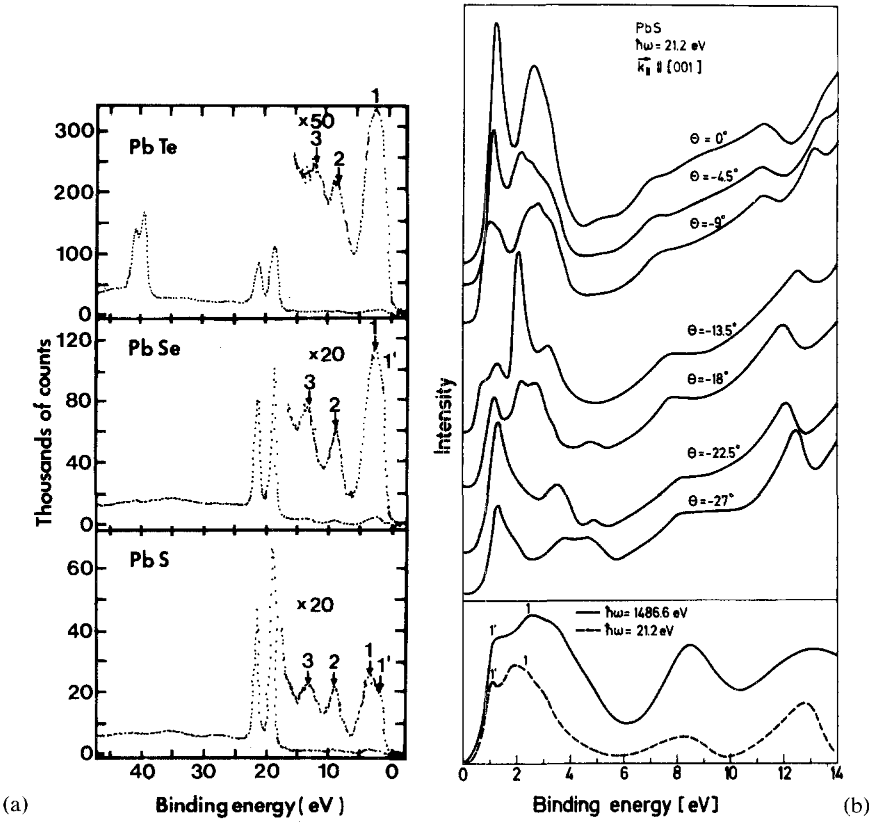

Fig. 6.7. (a) Valence-band x-ray photoelectron spectra of PbTe (altaite), PbSe (clausthalite), and PbS (galena) (after McFeely et al., 1973; reproduced with the publisher's permission). (b) Angle-resolved uv photoemission spectra of PbS along with the x-ray and uv photoelectron spectra. The diagram gives data on the incident photon energy ($\eta\omega$) and angle of measured photoemission (θ) relative to the normal ($\theta = 0°$) to the (100) surface (after Grandke et al., 1978; reproduced with the publisher's permission).

Lasseter, 1974) and MO calculations using the MS-SCF-$X\alpha$ method (Hemstreet, 1975) have been undertaken on these compounds, which aid in the interpretation of the spectra. It is also possible, therefore, to compare the results of band-structure and MS-SCF-$X\alpha$ calculations and their agreement with the experimental data, as illustrated in Fig. 6.8. Hence, in examining the spectra alongside the calculations, we can see that the peaks labeled 1 and 1′ at the top of the valence band are essentially sulfur (or Se or Te) p orbital in character (and therefore nonbonding molecular orbitals). Below these lie the main bonding orbitals of the system, which are chiefly lead 6s/sulfur (Se,Te) p in character. Peak 3 represents sulfur 3s orbitals that are not involved in bonding, and the intense double peak below this (at ~20 eV binding energy) arises from the lead 5d orbitals.

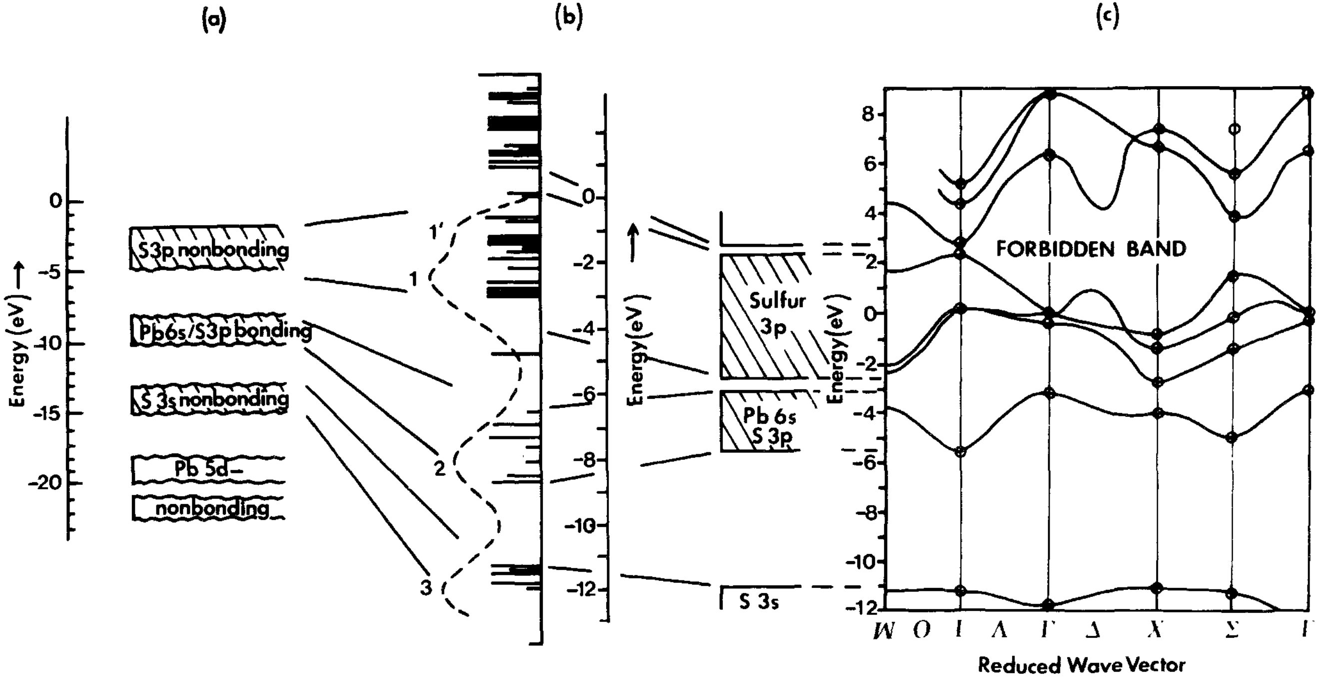

Fig. 6.8. Electronic structure models for galena (PbS): (a) simplistic band-structure representation based on spectroscopic data; (b) molecular-orbital energy levels calculated for $SPb_6S_{12}Pb_8$ cluster using the MS-SCF-$X\alpha$ method (after Hemstreet, 1975) and with features from the x-ray photoelectron spectrum (labeled as in Fig. 6.7) superimposed; (c) band-structure model for PbS calculated using the orthogonalized-plane-wave method (after Tung and Cohen, 1969); (d) information on the band structure of PbS obtained from uv photoemission measurements ($\hbar\omega$ is the incident photon energy). In these plots of peak position (in terms of binding energy) versus momentum component ($\mathbf{k}_{\parallel}$), crosses represent well-defined peaks and open symbols weak peaks or shoulders (after Grandke et al., 1978).

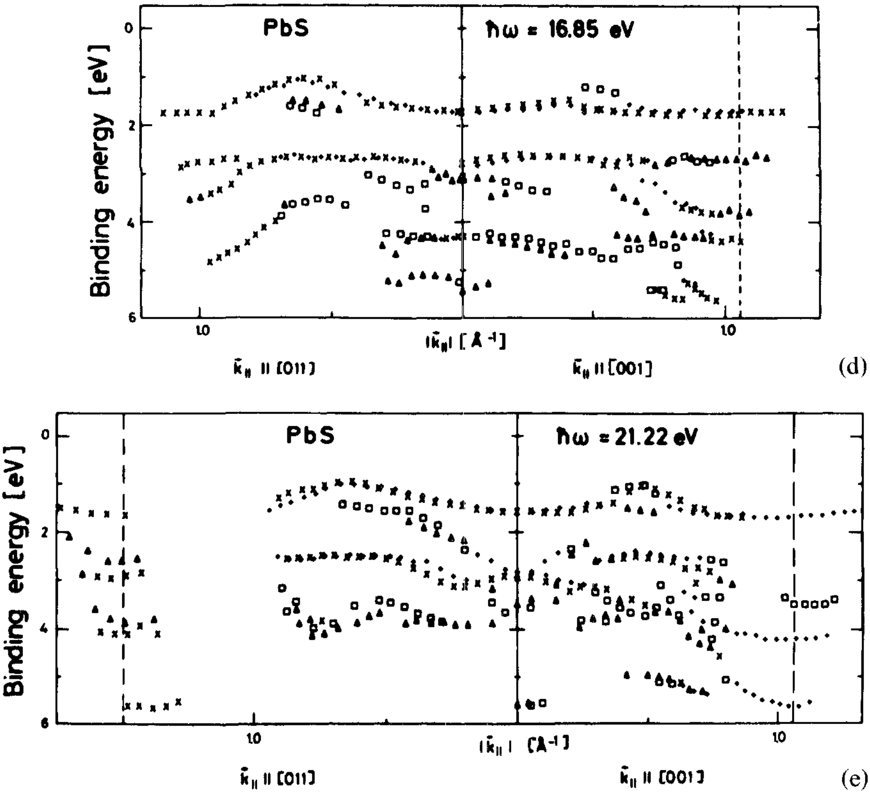

Fig. 6.8. Continued

A much more detailed "dissection" of the valence-band electronic structure of these compounds is possible using angle-resolved photoemission studies of single crystals. In a classic example of this approach, Grandke et al. (1978) used angle-resolved uv photoemission measurements of PbS, PbSe, and PbTe to study electronic structure. The spectra obtained for PbS are shown in Fig. 6.7(b). Here are shown the spectra obtained from a (100) surface of PbS and representing different angles (θ) relative to the normal to this surface and, hence, an electron wave vector (**k**) parallel to the [001] direction. Also shown, for comparison, are the x-ray and uv photoelectron spectra of the type already discussed for polycrystalline material. Because of the relationship of binding energy (E) and sin θ with the wave-vector component parallel to the surface ($\mathbf{k}_{\parallel}$), whereby $\mathbf{k}_{\parallel} = \sqrt{2E}\sin\theta$, a direct formulation of the energy band structure showing peaks in binding energy versus momentum component can be acquired from the spectra, as shown in Fig. 6.8(d). Comparison of the experimental data with band-structure calculations shows best agreement with augmented-plane-wave (Rabii and Lasseter, 1974) methods. Similar studies have also been undertaken on PbSe and PbTe (Hinkel et al., 1989).

The optical properties of galena, PbSe, and PbTe have been studied in considerable detail, as reviewed by Schoolar and Dixon (1965); numerous subsequent studies have refined these data. Schoolar and Dixon (1965) performed specular reflectance measurements and transmittance measurements on a thin film of galena, as shown in Fig. 6.9. Galena is translucent at long wavelengths (<3225 cm^{-1}, <0.4 eV) but is opaque beyond the fundamental absorption edge. Specular reflectance measurements on the lead chalcogenides were performed over a longer energy range by Cardona and Greenaway (1964), as also shown in Fig. 6.9. The electronic structure models shown in Fig. 6.8 can again be applied in initial attempts

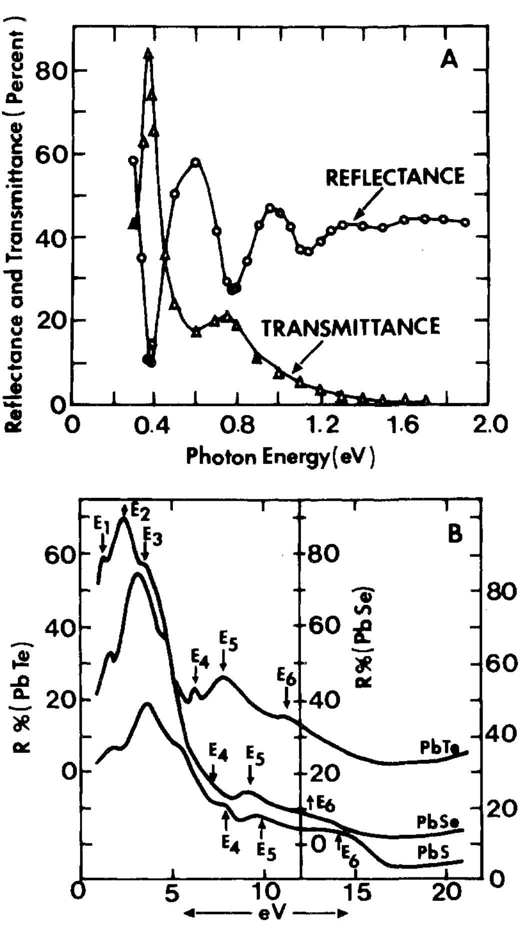

Fig. 6.9. Electronic (optical) absorption and reflectance data for galena (PbS) and the isostructural PbSe and PbTe: (a) reflectance and transmittance data for a thin film (0.37 μm thick) of galena on an NaCl substrate (after Schoolar and Dixon, 1965); (b) reflectance spectra of PbS, PbSe, and PbTe (after Cardona and Greenaway, 1964). See text for explanation of labeling.

to interpret these data. Hence, peaks E_1, E_2, E_3 arise from transitions into the conduction band from sulfur (Se,Te) *p*-type nonbonding molecular orbitals at the top of the valence band, and E_4, E_5, E_6 from lead 6*s*/sulfur (Se,Te) *s* nonbonding orbitals. Schoolar and Dixon (1965) attribute the rise in reflectance at energies >15 eV to transitions into the conduction band from the 5*d* band, which is filled with electrons and, as shown by the x-ray photoelectron spectra, "buried" beneath the valence band. A more detailed assignment of peaks in the reflectance spectra is possible by comparison with detailed band-structure calculations (Bass and Parada, 1970). The magnitude of spin-orbit splitting is very high for compounds of the heavy elements; thus, interband transitions are the transitions between spin-orbit sublevels, and a peak in the reflectance spectrum usually arises from a superposition of two or three transitions close to each other in energy.

6.4. Pyrite (FeS_2), pyrrhotite ($Fe_{1-x}S$), and related phases (CoS_2, NiS_2, CuS_2, ZnS_2; CoS, NiS)

Pyrite (FeS_2), the most abundant natural sulfide, has a crystal structure in which octahedrally coordinated iron atoms are at the corners and face centers of a cubic unit cell and dumbell-shaped disulfide groups at the cube center and midpoints of the edges. Pyrite is a diamagnetic semiconductor with an energy gap of 0.9 eV (Bither et al., 1968). These magnetic and electrical properties, along with the Mössbauer parameters for iron in pyrite (see Vaughan and Craig, 1978) are consistent with low-spin Fe^{2+} in the octahedral sites.

Simple qualitative MO energy-level diagrams to illustrate iron–sulfur bonding in pyrite were first published by Bither et al. (1968) and by Burns and Vaughan (1970), and a modified version is shown in Fig. 6.10(a) (although see also Fig. 8.25). Overlap between orbitals on adjacent "FeS_6 clusters" leads to broadening of the energy levels to give bands as shown in the qualitative "one-electron" energy-band diagram of Fig. 6.10(b) (after Goodenough, 1972). Here, conduction results from promotion of an electron from the filled t_{2g} levels (shown as localized on the cation) into the antibonding band formed by overlap of e_g orbitals via sulfur intermediaries (a $\sigma^* e_g^*$band).

The valence-region uv photoelectron spectrum of pyrite shows an intense peak at low binding energy arising from the six spin-paired electrons in the t_{2g} levels (Fig. 6.11). Less pronounced features arise from the other valence-band electrons. The photoelectron spectrum can be aligned with x-ray emission spectra using more deeply buried core orbitals and, as shown from Fig. 6.11, provide further experimental data on the composition of the valence region. Thus, the Fe $K\beta$ spectrum shows the contribution from orbitals that are predominantly Fe 4*p* in character, the S $K\beta$

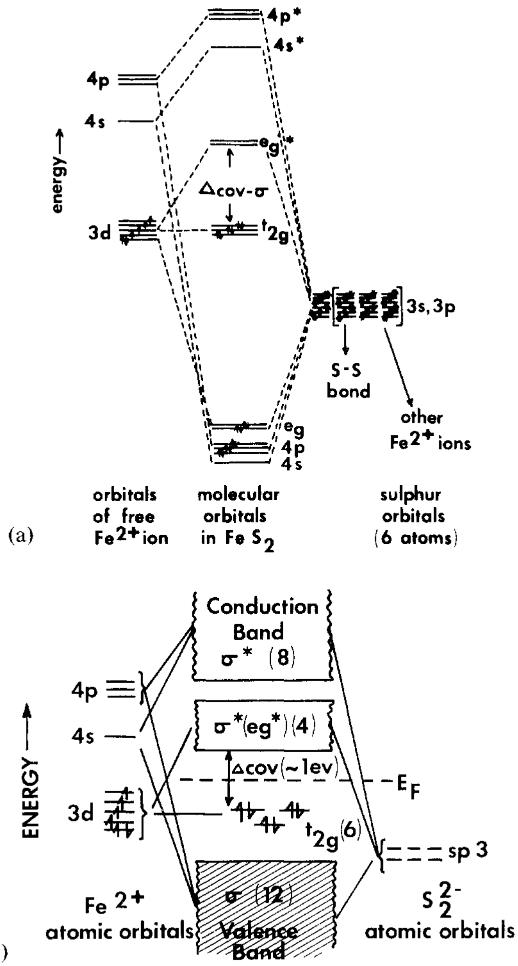

Fig. 6.10. Electronic structure of pyrite: (a) molecular-orbital energy-level diagram (modified after Burns and Vaughan, 1970); (b) schematic "one-electron" energy-band diagram. Numbers in brackets refer to the number of electron states per molecule available. E_F is the Fermi level; hatched bands are filled with electrons (modified after Bither et al., 1968; Goodenough, 1972).

spectrum shows the S 3*p* contribution, and the S *L* spectrum arises from orbitals with S 3*s* character. Interpretation of these spectroscopic data are facilitated by comparison with the results of calculations.

Pyrite has been the subject of a number of molecular-orbital and band-structure calculations. Thus, MS-SCF-$X\alpha$ calculations on an FeS_6^{10-} cluster have been performed by Li et al. (1974), Tossell (1977b), Harris

(1982), and Braga et al. (1988), and the data of Tossell (1977) are shown in Fig. 6.12 [and also in Fig. 6.17(a)] and compared against the spectroscopic data in Fig. 6.11. The calculation places the filled $2t_{2g}$ levels 2.7 eV above the top of the main valence-band orbitals and shows them to be localized nonbonding orbitals of almost entirely Fe $3d$ character. The empty $3e_g$ orbitals have, by contrast, appreciable S $3p$ character as well as Fe $3d$ character. The $1t_{1g}$ and $3t_{1u}$, $2e_g$, and $1t_{2u}$ levels are largely nonbonding S $3p$ type, whereas the $2t_{1u}$, $1t_{2g}$, and $2a_{1g}$ orbitals are the main bonding orbitals of the system with substantial iron and sulfur character. About 10 eV below the sulfur nonbonding orbitals are a set of orbitals ($1a_{1g}$, $1t_{1u}$, and $1e_g$) that are essentially S $3s$ nonbonding orbitals.

Khan (1976) used a non-self-consistent LCAO tight-binding method to calculate the energy bands in FeS_2, Bullett (1982) used a partially self-consistent scheme, and Lauer et al. (1984) used a self-consistent LCAO tight-binding method to calculate the band structure, as well as MO cluster calculations to derive local properties (Mössbauer parameters). The band structure of pyrite has also been calculated by Folkerts et al. (1987) using a self-consistent augmented-spherical-wave method. The results of Lauer et al. (1984) are similar to those of Bullett (1982), and Fig. 6.13 shows the energy dispersion of the bands along some principal symmetry directions in the Brillouin zone of FeS_2. The bands can be roughly labeled as shown in Fig. 6.13, although all except the t_{2g} band contain significant admixtures from other orbitals. In particular, for example, the e_g band has contributions arising from sulfur p orbitals resulting in some antibonding character. There is much in common between the valence-band structure shown in Fig. 6.13 and that calculated using the MS-SCF-$X\alpha$ method (Fig.

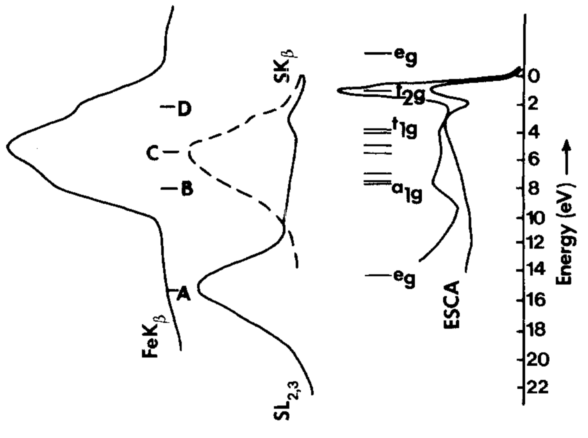

Fig. 6.11. The Fe $K\beta$, S $L_{2,3}$, and S $K\beta$ x-ray emission spectra of pyrite together with the uv photoelectron (ESCA) spectrum and energy levels from a MS-SCF-$X\alpha$ cluster calculation (based on Tossell, 1977b).

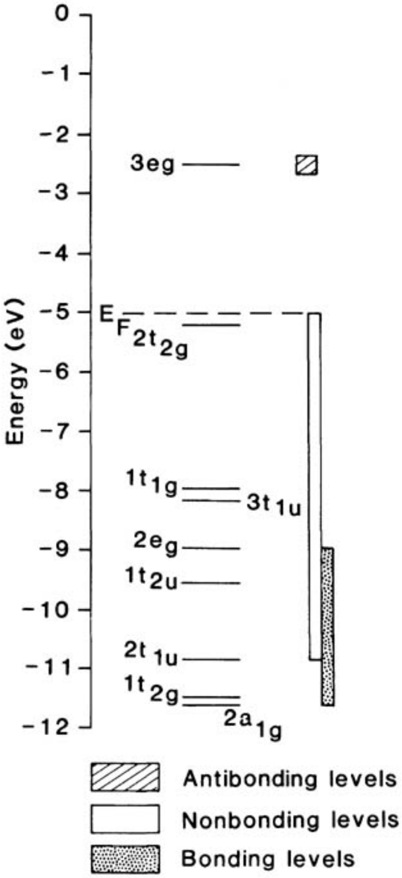

Fig. 6.12. Energy-level diagram for the octahedral FeS_6^{10-} cluster from an MS-SCF-$X\alpha$ calculation (after Tossell, 1977b).

6.12), although the former includes the effects of S–S bonding such as the splitting of the sulfur 3*s* band into bonding (S_2 $s\sigma$) and antibonding (S_2 $s\sigma^*$) states.

The pyrite-structure disulfides CoS_2 (cattierite)–NiS_2(vaesite)—CuS_2–ZnS_2 have also been extensively studied experimentally and using various calculational methods. Earlier work (reviewed by Vaughan and Craig, 1978) emphasized the importance of successive addition of *d* electrons across this series in describing the changes in electronic structure. As shown schematically in Fig. 6.14, whereas the e_g^* band is empty in pyrite, in CoS_2 it is one-quarter filled, as supported by the *n*-type metallic conductivity. The properties of NiS_2 (a semiconductor with a band gap of ~0.27 eV at 300 K) have been explained by spin splitting of the e_g^* band, whereas the *p*-type metallic conductivity of CuS_2 was originally explained by a three-quarters-filled e_g^* band. When the composition of ZnS_2 is reached, the *d* levels are completely filled with electrons, and the material is a diamagnetic semiconductor with a large band gap.

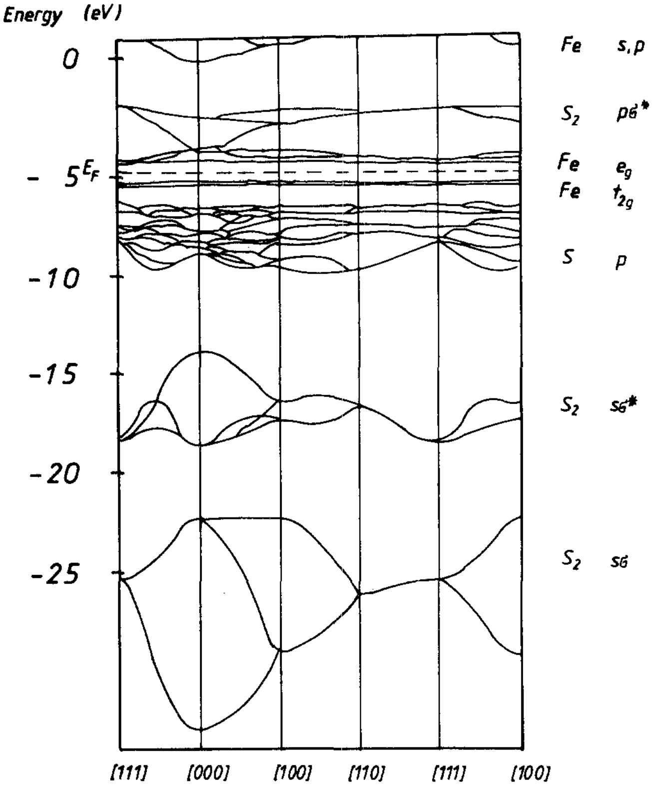

Fig. 6.13. Results of a band-structure calculation on pyrite showing dispersion of energy bands along some principal symmetry directions (after Lauer et al., 1984; reproduced with the publisher's permission).

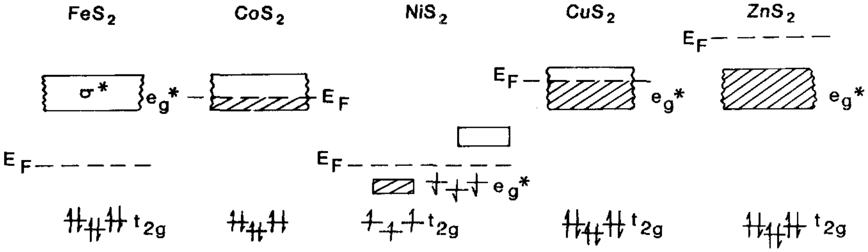

Fig. 6.14. A qualitative energy-level diagram illustrating the changing electronic structure with occupation of metal 3*d*-type orbitals along the series of pyrite-structure disulfides from FeS_2 to ZnS_2 (after Vaughan and Tossell, 1983).

Again, x-ray emission and absorption spectra (Sugiura et al., 1976; Matsukawa et al., 1978), numerous uv and x-ray photoelectron spectra (Li et al., 1974; Ohsawa et al., 1974; van der Heide et al., 1980; etc.), bremsstrahlung isochromat spectra (Folkerts et al., 1987; see Appendix B), and near-ir–visible–uv reflectance spectra (Bither et al., 1968; Schlegel and Wachter, 1976; Suga et al., 1983; Sato, 1984; etc.) have been reported for these compounds and the data compared with MO cluster (e.g., Vaughan and Tossell, 1983; Harris, 1982) and band-structure (Khan, 1976; Bullett, 1982; Lauer et al., 1984) calculations. Certain trends in valence-band structures are evident from the results of these calculations, the validity of which may be supported by comparison with experiment. Thus, as illustrated in Fig. 6.15, calculations on MS_6^{10-} clusters using the MS-SCF-$X\alpha$ method (Vaughan and Tossell, 1983; Harris, 1982) show a generalized trend towards decreasing stabilization of the metal–sulfur bonding orbitals across the series from FeS_2 to ZnS_2. The narrowing of the valence band resulting from this trend is also seen in the schematic diagram of band limits based on the calculations of Bullett (1982) and reproduced as Fig. 6.16. This diagram also shows the way in which the t_{2g} and e_g* bands (of essentially metal 3*d* character) drop down beneath the top of the valence band in moving across the series. Although this was not seen for CuS_2 in Fig. 6.15, this is because the oxidation state was assumed

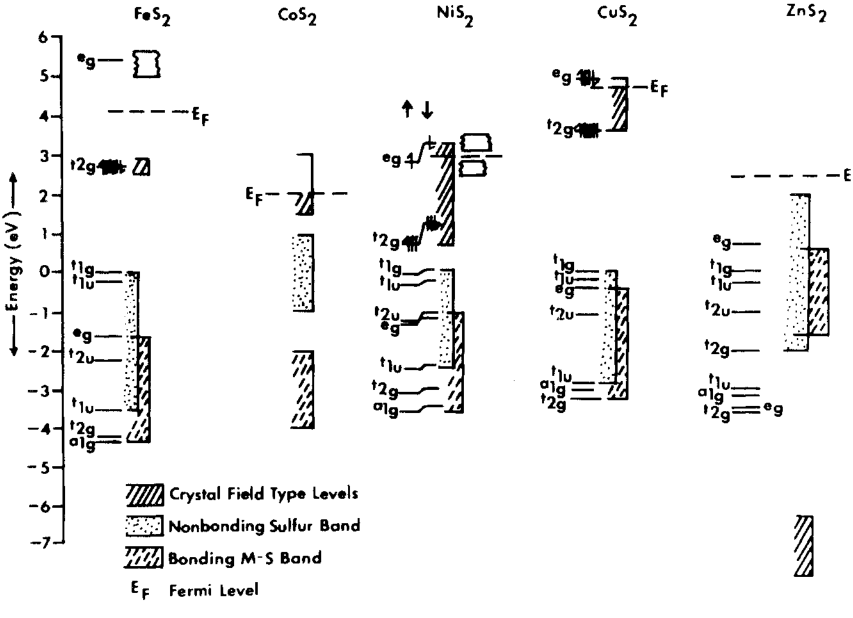

Fig. 6.15. The electronic structures of pyrite-type disulfides based on MS-SCF-$X\alpha$ calculations on MS_6^{10-} clusters (after Harris, 1982; Vaughan and Tossell, 1983).

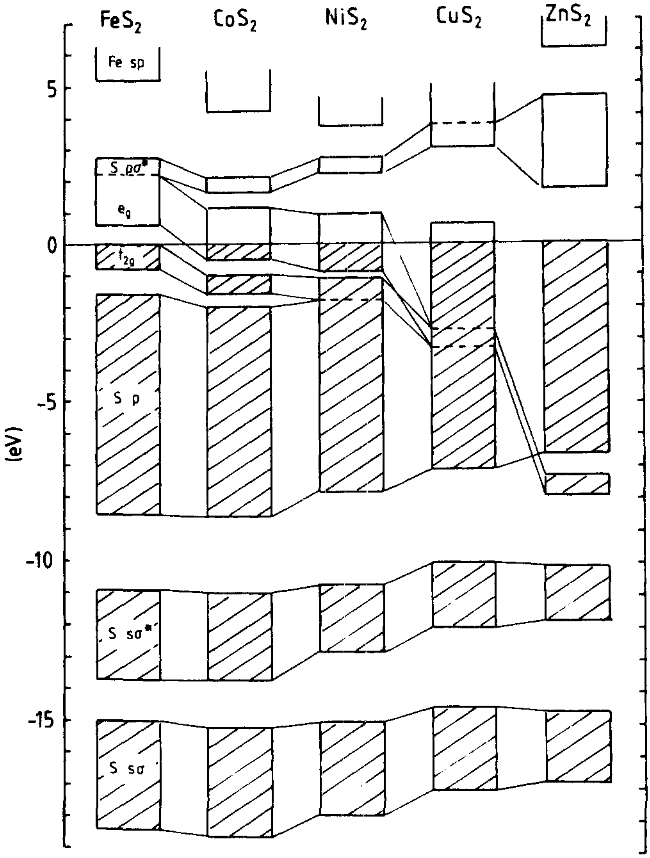

Fig. 6.16. Schematic diagram of band limits in the electronic structures of FeS_2, CoS_2, NiS_2, CuS_2, and ZnS_2 from the calculations of Bullett (1982). The zero level of energy is taken as the highest occupied state (after Bullett, 1982; reproduced with the publisher's permission).

to be Cu^{2+}; in fact, an appreciable body of spectroscopic evidence (e.g., Nakai et al., 1978) now shows the copper to be present in CuS_2 as Cu^+.

The monosulfides FeS, CoS, and NiS possess the nickel arsenide structure at elevated temperatures but undergo distortion, structural transformation, or breakdown on cooling (see Vaughan and Craig, 1978). In the case of FeS, troilite is a distorted form of the NiAs structure, but there is also an omission solid solution of the type $Fe_{1-x}S$, extending to approximately Fe_7S_8 to form the minerals known as the "pyrrhotites." Ordering of vacancies of the iron atom sites leads to a complex variety of superstructures, and very complex structural and phase relations, and electrical, magnetic, and related properties (aspects of which have been reviewed by Vaughan and Craig, 1978; Ward, 1970; Power and Fine, 1976; and Putnis and McConnell, 1980). FeS is an antiferromagnetic semiconductor with T_N ~588 K); the pyrrhotites are highly conducting and exhibit both antiferromagnetic and ferrimagnetic properties; CoS is reportedly metallic and antiferromagnetic (T_N ~350 K); NiS (in the high-temperature form) exhibits a transition from an antiferromagnetic semiconductor at low temperature to a paramagnetic metallic phase at close to room temperature (T_N ~263 K). These complex properties have resulted in a considerable number of studies; however, only the pyrrhotites are of much importance as minerals.

As with the disulfides, a variety of spectra have been studied of FeS, CoS, and NiS, for example, S $K\beta$ x-ray emission spectra (Suguira et al., 1974) and x-ray photoelectron spectra (Gopalakrishnan et al., 1979). Band-structure and cluster calculations have also been undertaken (e.g., the DV-$X\alpha$ cluster calculations of Freidman and Gubanov, 1983), as well as speculations on electronic structure based on observed properties (e.g., Goodenough, 1967; Wilson, 1972). Tossell (1977b) has performed MS-SCF-$X\alpha$ calculations on an FeS_6^{10-} cluster with Fe^{2+} in the high-spin state (quintet) as a model for NiAs-structure-type FeS phases. The result of this calculation is shown in Fig. 6.17(a) alongside the energy levels calculated for low-spin Fe^{2+} in octahedral coordination to sulfur. In the quintet state, the $2a_{1g}$, $2t_{1u}$, and $1t_{2g}$ orbitals are the main Fe–S bonding orbitals and are followed by a group of essentially S $3p$ nonbonding orbitals ($2e_g$, $1t_{2u}$, $3t_{1u}$, and $1t_{1g}$). Above these lie the $2t_{2g}$ and $3e_g$ antibonding crystal-field orbitals of Fe $3d$ and S $3p$ character. Calculated energies are in reasonable agreement with data available from x-ray emission and absorption spectra (Tossell, 1977b). An energy-band model for pyrrhotite presented by Sakkopoulos et al. (1984) and based on the MS-SCF-$X\alpha$ cluster calculations by Tossell (1977) is shown in Fig. 6.17(b). The model consists of a sulfur $3p$ valence band, 5.4 eV wide, separated by a 0.8 eV gap from the conduction band. The spin-pairing energy (2.3 eV) deduced from spectroscopic data puts the one-third-filled $t_{2g}\beta$ band in such a position that the 0.8 eV gap is almost bridged. The occupancy of the $t_{2g}\beta$ band determines the position of the highest occupied level (E_F) and leaves an empty strip about 0.2 eV wide, at the top of the valence band.

In troilite, the NiAs-type structure undergoes a distortion below T_α (140°C) that involves triangular clusters of iron atoms forming in the basal plane and some associated movement of sulfur atoms (Evans, 1970). Goodenough (1967) has discussed the distortion at T_α to form the troilite structure in terms of band models [see Fig. 6.17(c)]. At high temperature, the majority spin electrons in the t_{2g} orbitals parallel to the c direction (where cation–cation interaction can take place) form a filled band; the remaining t_{2g} and e_g electrons remain localized. The minority spin electrons in t_{2g} orbitals can form bands both perpendicular and parallel to c with the $e_g{}^*$ orbitals again remaining discrete. Only the $\Gamma_1{}^*(\beta)$ band shown in Fig. 6.17(c) contains electrons and is actually half-filled. Accord-

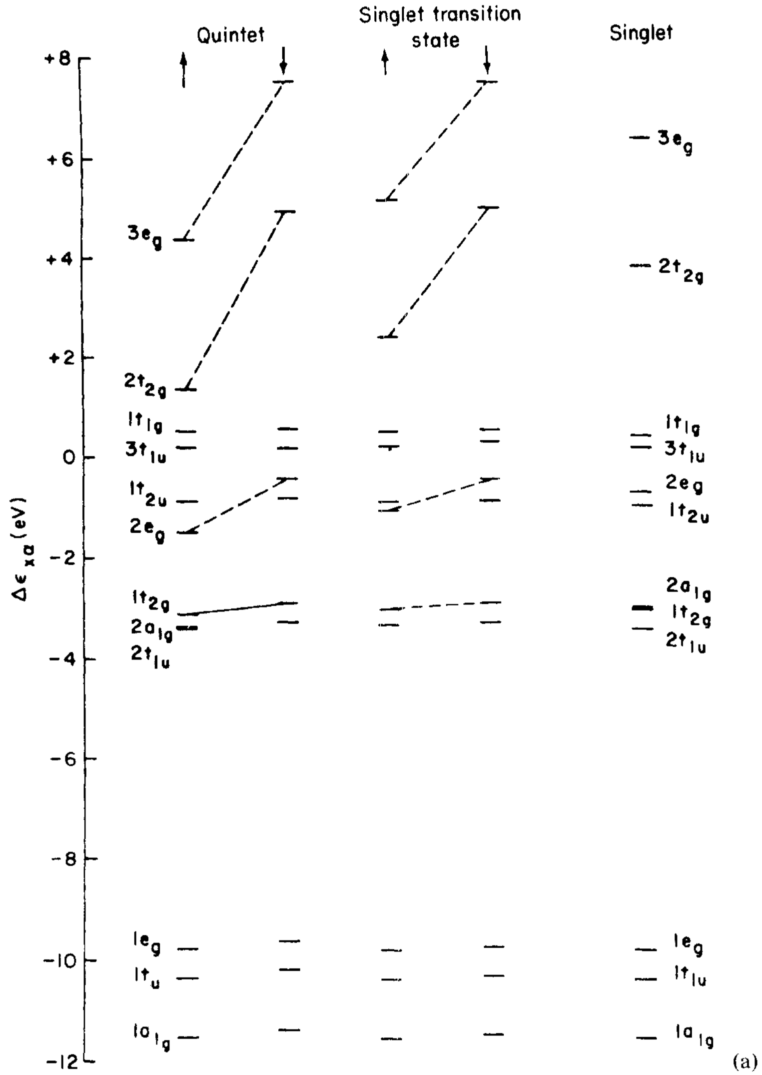

Fig. 6.17. Electronic structure models for FeS: (a) molecular-orbital energy levels for the FeS_6^{10-} octahedral cluster calculated using the MS-SCF-$X\alpha$ method, for low-spin Fe^{2+} (singlet, as in pyrite) and high-spin Fe^{2+} (quintet) states (after Tossell, 1977); (b) electron structure model for pyrrhotite based on calculated energy levels for the FeS_6^{10-} cluster (from Tossell, 1977) and sulfur $K\beta$ emission and K absorption spectra (Diagram after Sakkopoulos et al., 1984); (c) schematic energy-level diagram for the troilite form of FeS (after Goodenough, 1967).

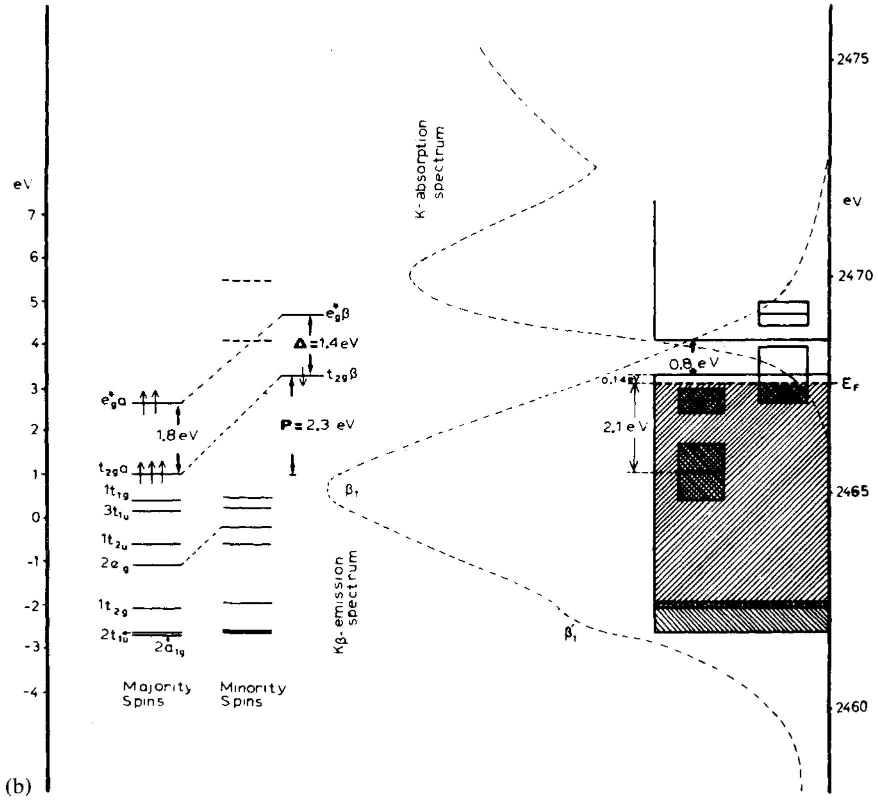

Fig. 6.17. Continued

ing to Goodenough (1967), this narrow band "invites a spontaneous distortion that will split the band in two," and this is what happens below T_α.

There are, in fact, two other known forms of FeS, both containing iron in tetrahedral coordination. One is the tetragonal layer structure sulfide mineral mackinawite (see Table 6.1), and the other is a cubic FeS with the sphalerite structure. In an interesting study of the electronic structures of both of these phases, Welz and Rosenberg (1987) used a self-consistent LMTO method. Both sulfides were calculated to be metallic with conduction bands of mainly *d* character. However, whereas the cubic sulfide is ferromagnetic at low temperature and the moment can be fairly well reproduced by the calculations, direct Fe–Fe interactions across edge-sharing FeS_4 tetrahedra are shown to be responsible for a reduced density of states at the Fermi level and the absence of magnetism in mackinawite, in accordance with Mössbauer data (Vaughan and Ridout, 1971).

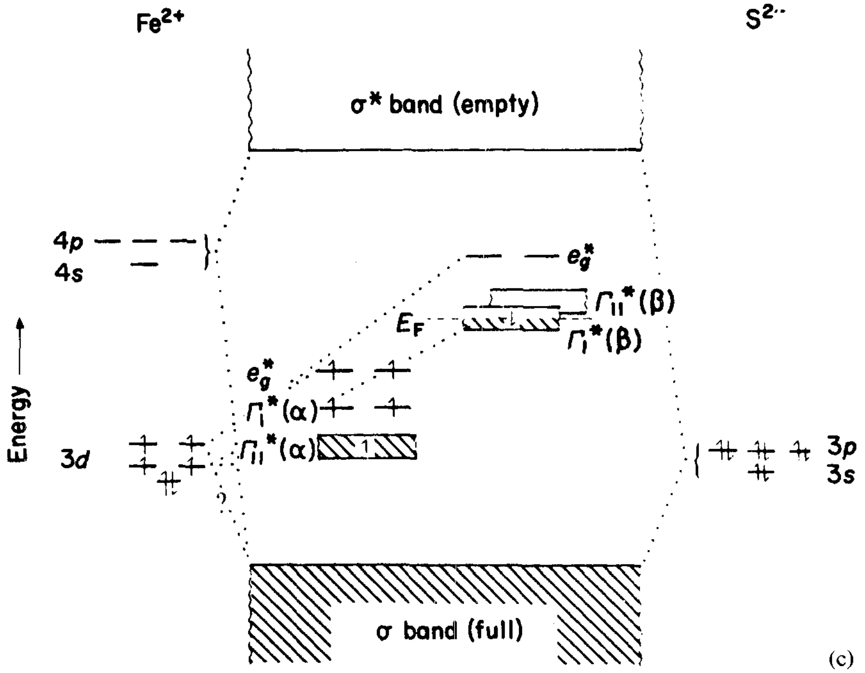

Fig. 6.17. Continued

6.5. Marcasite (FeS_2), arsenopyrite (FeAsS), loellingite ($FeAs_2$), and related minerals

The marcasite–arsenopyrite–loellingite series of minerals have crystal structures related to that of pyrite; all contain dianion groups and cations in octahedral coordination. However, whereas in pyrite the MX_6 octahedra share corners, in marcasite, arsenopyrite, and loellingite they share edges and form chains of linked octahedra parallel to the *c* axis (Fig. 6.18). Compared to marcasite, loellingite has an appreciably compressed *c* axis, and arsenopyrite contains metal atoms that are displaced along the *c* axis, so that short metal–metal distances alternate with longer ones. The pyrite, marcasite, arsenopyrite, and loellingite structures occur in other minerals and related compounds, examples of which are listed in Table 6.3. Much has been written in attempts to establish the structure-determining principles that relate to membership of these groups, and it is instructive to consider the different approaches employed.

Earlier workers emphasize the possible importance of interactions involving electrons in *d* orbitals on the metals. Thus, Hulliger and Mooser (1965) and Nickel (1968) applied a ligand-field model that centers on interaction of the t_{2g} orbitals across the shared octahedral edge. Magnetic

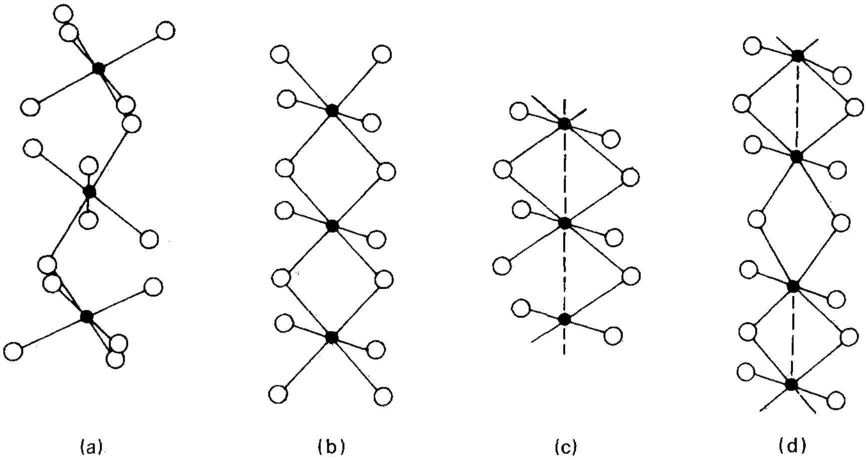

Fig. 6.18. The linking of MX_6 octahedra in the: (a) pyrite; (b) marcasite; (c) loellingite; and (d) arsenopyrite structures.

and Mössbauer data indicate that marcasite (and pyrite) contain low-spin Fe^{2+} (t_{2g}^6), and mutual repulsion between filled t_{2g} orbitals across the shared edge in marcasite was regarded as causing an elongation in this (*c*-axis) direction. In loellingite, for which magnetic data again indicate spin pairing of *d* electrons in the t_{2g} orbitals, it was suggested that the number of *d* electrons not involved in *M–X* bonding is reduced to four. The model

Table 6.3. Disulfide minerals and their structure types (ignoring minor structural distortions)

Pyrite-type structure	FeS_2 (pyrite) CoS_2 (cattierite) NiS_2 (vaesite) MnS_2 (hauerite) $CoSe_2$ (trogtalite) CoAsS (cobaltite) NiAsS (gersdorffite) NiSbS (ullmannite) $NiSe_2$ (penroseite) CoSbS, CuS_2, ZnS_2
Marcasite-type structure	FeS_2 (marcasite) $FeSe_2$ (ferroselite) $FeTe_2$ (frohbergite) $CoSe_2$ (hastite) $NiAs_2$ (rammelsbergite)
Arsenopyrite-type structure	FeAsS (arsenopyrite) FeSbS (gudmundite) $CoAs_2$ (safflorite)
Loellingite-type structure	$FeAs_2$ (loellingite), $FeSb_2$

proposed spin pairing of these electrons in two of the three t_{2g} orbitals, leaving the one across the shared edge empty, thus enabling a compression of the structure in this direction. The alternate long and short metal–metal distances along the *c*-axis direction in arsenopyrite, assumed to have 5 available *d* electrons, were attributed to spin pairing of 4 electrons in two t_{2g} orbitals and use of the additional electron in forming electron-pair metal–metal bonds. These authors pointed to a correlation between compounds that (largely on magnetic evidence) have 4 available *d* electrons ($FeAs_2$, $FeSb_2$) and 5 available *d* electrons (FeAsS, FeSbS, $CoAs_2$) and the occurrence of the loellingite and arsenopyrite structure types.

Goodenough (1972) criticized the ligand-field approach outlined above, attributing the observed distortions to metal–anion interactions, not metal–metal interactions, and proposing energy-band models of the type shown in Fig. 6.19 (for FeAsS or $CoAs_2$). Here, splitting of the metal 3*d* orbital energy levels by the ligand field in the arsenopyrite structure differs markedly from that in regular octahedral coordination and is such as to raise the energy of the t_{2g} orbital, which is parallel to the *c* axis. The other t_{2g}-type orbitals remain nonbonding and form a narrow filled band; the e_g-type empty antibonding orbitals form a conduction band. The unique t_{2g}-type orbital is split by a bonding interaction into a lower-energy filled band and higher-energy empty band. The important difference between this model and the ligand-field model is that the interaction (and hence the structural deformation) is attributed to metal–anion bonding not metal–metal bonding. Goodenough (1972) argues that the arsenopyrite structure represents an expansion, not a contraction, of alternate metal–metal separations along the *c* axis and that electron density is concentrated in the regions of *greater* separation.

Tossell, Vaughan, and Burdett (1981) and Tossell (1984c) suggested that the above models give inadequate attention to the influence of the dianion electron distribution upon structure types in these compounds, and used MO calculations on the dianion units along with qualitative perturbational MO arguments to provide another interpretation. Here, atten-

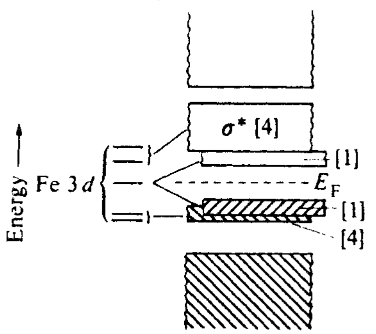

Fig. 6.19. Schematic one-electron energy-band diagram for arsenopyrite, FeAsS (or safflorite $CoAs_2$) (after Goodenough, 1972).

tion is focussed on the highest occupied MO of the electron donor and lowest unoccupied MO of the electron acceptor and their energies and overlaps. A molecular-orbital scheme for the S_2^{2-} ion, based on calculations using the MS-SCF-$X\alpha$ method, is shown in Fig. 6.20. In S_2^{2-}, 14 electrons are involved in filling the orbitals up to $1\pi_g^*$, which is antibonding in character. Mixing of this $1\pi_g^*$ orbital with metal d orbitals of σ symmetry with respect to M–S bonding generates two pairs of orbitals, one oriented in the xz plane and the other in the yz plane (where z is the internuclear axis direction). Each pair consists of an orbital stabilized compared to $1\pi_g^*$ and hence a metal–sulfur bonding orbital (π_b) together with a destabilized antibonding orbital (π^*) (see Fig. 6.20). In a disulfide such as FeS_2 with a 14-electron dianion, counting the electrons added to the orbitals shows that all of the π_b orbitals will be filled and all the π^* empty. If we consider $FeAs_2$, the evidence from Mössbauer isomer shifts (Vaughan and Craig, 1978) strongly suggests that the oxidation state of iron remains Fe^{2+} (not Fe^{4+}, as suggested in the ligand-field model arguments above) and hence the dianion is As_2^{2-}. Calculations show that the molecular-orbital scheme for this dianion is the same as for S_2^{2-} (Fig. 6.20), but there are only 12 valence electrons, so that only one component of the π_b orbital set would be filled (say π_{bx}). This should be reflected in a difference in the geometry of metal–anion coordination, and, indeed, whereas the metals are symmetrically disposed about the anion in the pyrite structure, in loellingite the metal–anion coordination is distorted so that the metal atoms lie almost in the same (say xz) plane (Fig. 6.20). This approach points to the electron occupancy in the dianion system as the structure-determining factor, and can be extended to explain the structures adopted by other disulfides, diarsenides, and sulfarsenides. In FeAsS, for example, the As end of the AsS group is effectively a "12-electron system," resulting in alternately greater or less distortion of the coordination of metals around the anion, and hence crystallization with the arsenopyrite-type structure.

Generally, accurate quantum-mechanical calculations on fragments large enough to model the whole of the structure for these minerals have not yet proved possible. However, Bullett (1982) did use a partially self-consistent band-structure calculation to model the marcasite as well as the pyrite structure form of FeS_2. The energy bands for marcasite are shown in Fig. 6.21; comparison with the electronic structure of pyrite calculated using the same method (also shown in Fig. 6.21) indicates the essential difference to be increased splitting of the t_{2g} orbitals in the less regular octahedral environment. Also predicted is some overlap of the lower t_{2g} band with the sulfur p valence bands and a slight decrease in the semiconducting indirect gap between filled t_{2g} and empty e_g bands. The question of structural deformation, however, was not considered. Burdett and McLarnan (1982) and Wijeyesekera and Hoffman (1983) have both discussed structure and bonding in a wide range of compounds with

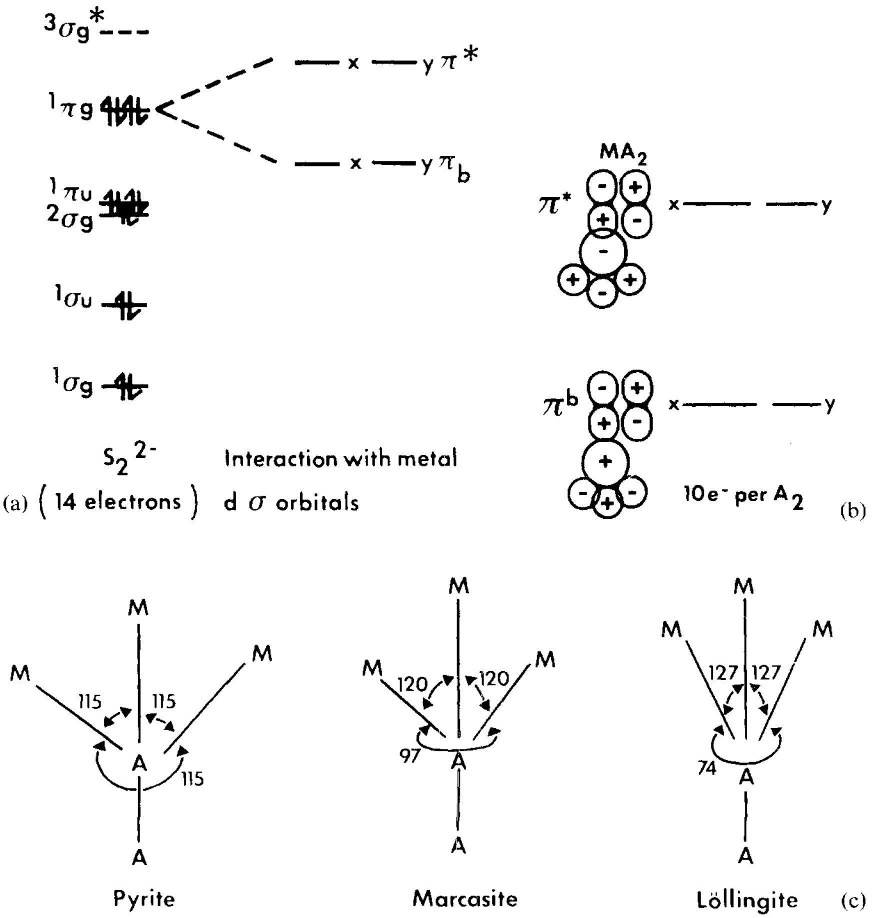

Fig. 6.20. Crystal chemical models for the disulfides (after Tossell et al., 1981): (a) molecular-orbital energy-level diagram for the S_2^{2-} dianion and splitting of the highest-energy orbital containing electrons on interaction with metal $d\sigma$ orbitals; (b) perturbed molecular orbitals formed by mixing of A_2 $1\pi_g$* and M $d\sigma$; (c) geometries of M atoms about A in pyrite, marcasite, and loellingite structures.

pyrite, marcasite, and loellingite, or with marcasite and arsenopyrite structures. Wijeyesekera and Hoffman (1983) used extended Hückel calculations on model systems such as the $[Fe(PH_2)_2H_2]_2$ chain in attempting to define the interactions causing distortions. Their calculations do not support the theory of Tossell et al. (1981) that one of the As_2 π_g* orbitals is involved in stronger Fe–As interaction than the other (Fig. 6.20) and that electron occupancy of the dianion is the structure-determining factor. It is argued that M–M and X–X interactions all work together to produce the observed effects. Burdett and McLarnan (1982) considered the stabilities of the pyrite, marcasite, and loellingite structures using structural

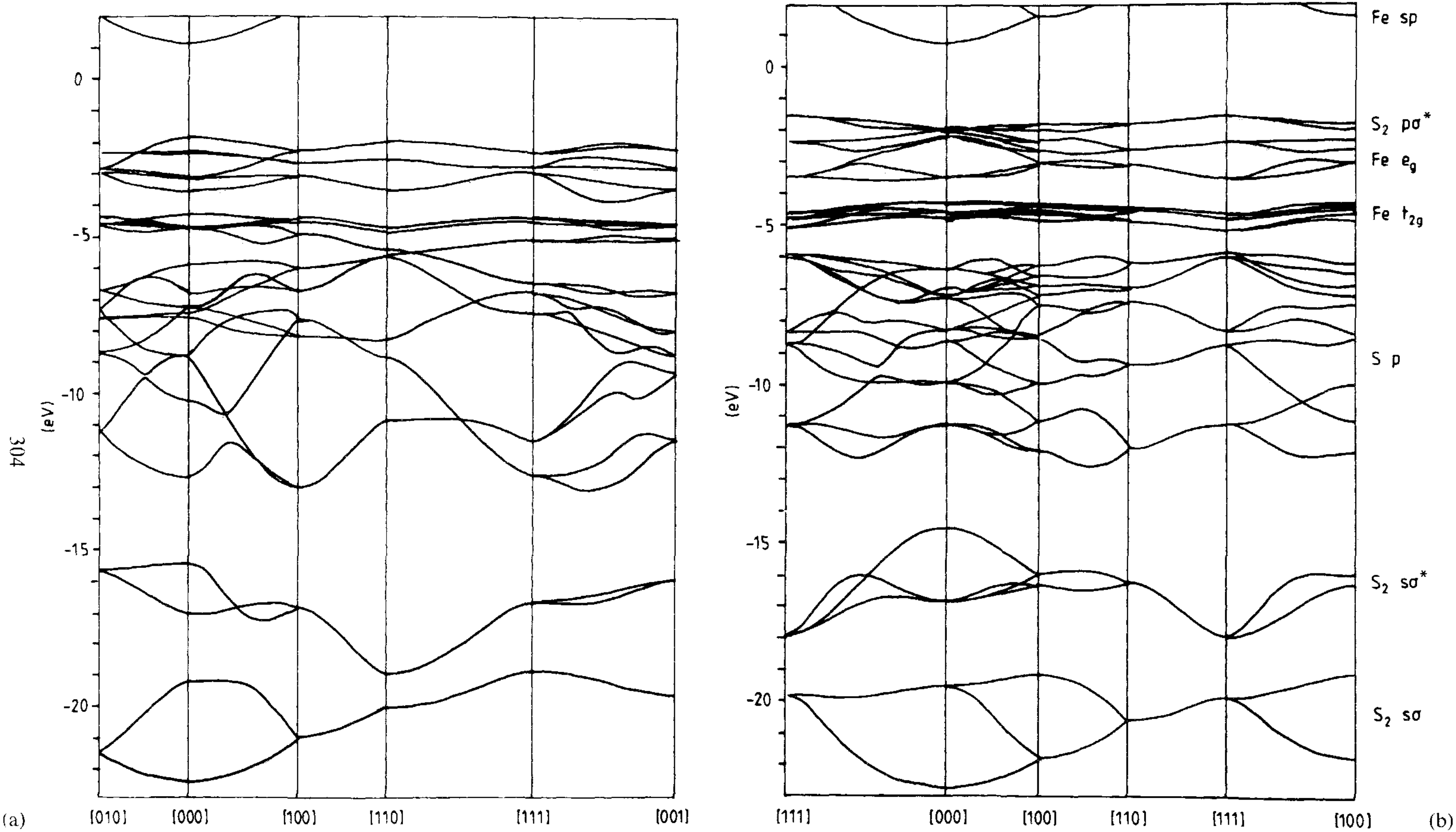

Fig. 6.21. Calculated dispersion of energy bands along some principal symmetry directions in: (a) marcasite and (b) pyrite forms of FeS_2 (from the band-structure calculations of Bullett, 1982; reproduced with the publisher's permission).

enumeration and extended Hückel band-structure calculations. Although the computations are approximate, they do show the pyrite structure to be the most stable for FeS_2, with marcasite appreciably less stable. The loellingite distortion was also predicted, but although the interpretation of Tossell et al. (1981) could not be directly addressed, the calculations suggested that *d* orbitals play a role in stabilizing the structures. On the other hand, Tossell (1984c) provided additional evidence in support of the interpretation of Tossell et al. (1981). This evidence included an examination of: (1) electron affinites of diatomic molecules (S_2, etc.); (2) bimetal cluster and band calculations; (3) new MS-SCF-$X\alpha$ cluster calculations on $FeAs_6$ and As_4 polyhedra; all of these suggest that the stable configuration of loellingite is $Fe^{2+}(As_2)^{2-}$. Further consideration of perturbational MO models indicated that both *M s* and *M d* orbital effects influence *M*–*X*–*X* angles, which may account for the observed variations in geometry with numbers of *d* electrons. However, the emphasis placed on *M*–*M* interactions in previous models is regarded as erroneous; interactions between X_2 units are likely to be much more significant.

6.6. Copper, copper–iron, and related sulfides (Cu_2S, CuS, $CuFeS_2$, Cu_5FeS_4, Ag_2S)

The copper, copper–iron, and the silver sulfides are more complex than the sulfides discussed previously, containing several cations or cation sites in their structures. Thus chalcopyrite ($CuFeS_2$), although having a fairly simple structure based on that of sphalerite, but with Cu and Fe alternately replacing Zn atoms, contains both Cu^+ and Fe^{3+} in regular tetrahedral coordination (as indicated by neutron diffraction and Mössbauer studies; see Vaughan and Craig, 1978). A family of more than thirty synthetic compounds with the chalcopyrite structure is known, and their properties have been studied because of potential applications as semiconductors. Miller et al. (1981) have reviewed the crystal structures, vibrational properties, and band structures of these materials.

A fairly complete series of x-ray emission and x-ray photoelectron spectra have been reported by Tossell et al. (1982) for $CuFeS_2$, as shown in Fig. 6.22. Features in the spectra were assigned using the results of MS-SCF-$X\alpha$ calculations on the clusters CuS_4^{7-} and FeS_4^{5-} (Fig. 6.23). The orbitals shown here comprise $1a_1$ and $1t_2$, which appear to be mainly S 3*s* in character; $2a_1$ and $3t_2$, which are mostly sulfur 3*p* with some metal *s* or *p*; the $1t_1$, which is nonbonding sulfur 3*p*; the $2t_2$ and $1e$, which are the bonding metal 3*d*–S 3*p* orbitals; and the $2e$ and $4t_2$, which are the antibonding metal 3*d*–S3*p* or "crystal-field" orbitals. In the FeS_4^{5-} cluster, the composition of the $1e$, $2t_2$, $2e$, and $4t_2$ orbitals is highly spin dependent with 70–80% Fe 3*d* character in the $1e_\uparrow$, $2t_{2\uparrow}$, $2e_\downarrow$, and $4t_{2\downarrow}$

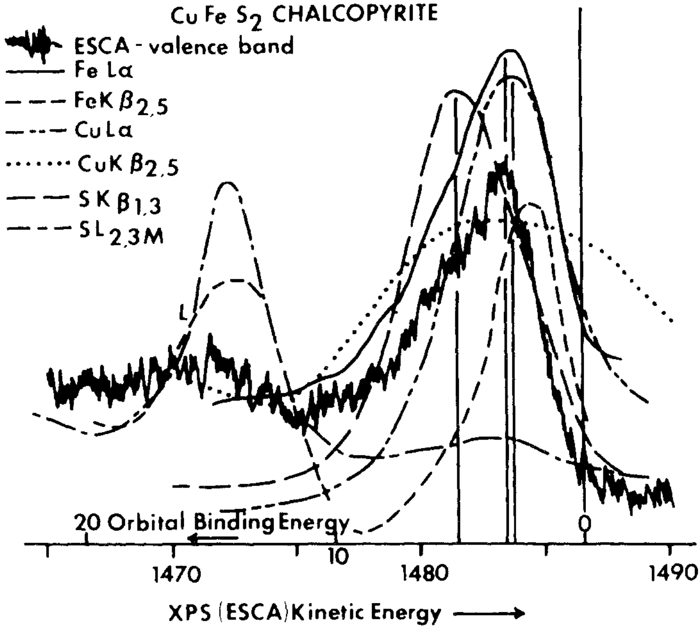

Fig. 6.22. Valence-region x-ray photoelectron and Fe $L\alpha$, Fe $K\beta_{2,5}$, Cu $L\alpha$, Cu $K\beta_{2,5}$, S $K\beta_{1,3}$, and S $L_{2,3}M$ X-ray emission spectra of chalcopyrite (after Tossell et al., 1982).

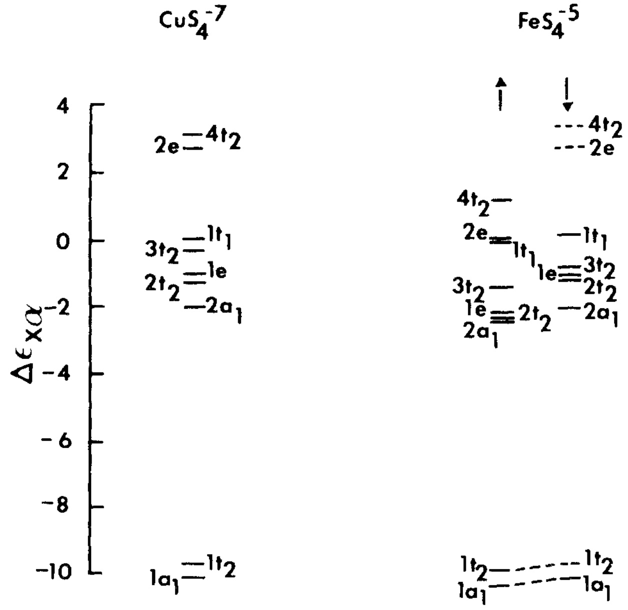

Fig. 6.23. Energy-level diagrams calculated for the tetrahedral CuS_4^{7-} and FeS_4^{5-} clusters using the MS-SCF-$X\alpha$ method. Occupied orbitals are shown as solid lines, and unoccupied orbitals as broken lines. Energies are in eV relative to the average energy of the $1t_1$ orbital. The M–S distances employed were, respectively, Cu–S = 2.302 Å and Fe–S = 2.258 Å (after Tossell et al., 1982).

orbitals and about 10–20% Fe 3*d* character in the $1e_{\downarrow}$, $2t_{2\downarrow}$, and $4t_{2\uparrow}$. The strong peak in the S $L_{2,3}$ spectrum at about 14 eV arises from the predominantly S 3*s* nonbonding $1a_1$ and $1t_2$ orbitals, and broad features at this energy in the Fe and Cu $K\beta_{2,5}$ spectra indicate some mixing of Fe 4*p* and Cu 4*p* into these orbitals. The main S $K\beta_{1,3}$ peak, at about 5 eV, is assigned to predominantly S 3*p*-type orbitals ($2a_1$, $2t_2$, $1e$, $3t_2$, and $1t_1$). The maximum in the Fe $L\alpha$ spectrum at ~3 eV can be assigned to $2e$ and $4t_2$ orbitals in the FeS_4^{5-} unit. The Cu $L\alpha$ spectrum also peaks at about 3 eV and is assigned to the $2e$ and $4t_2$ orbitals in the CuS_4^{7-} unit. The shoulder at low binding energy in this spectrum may represent a contribution from orbitals like the Cu 3*d* $4t_2$.

Comparison of the energies of measured and calculated orbital eigenvalues showed generally good correlation between experiment and calculation, although the calculations do overestimte the binding energies of the Fe 3*d* orbitals. Somewhat better agreement with experiment is found on comparison with a band-structure study of $CuFeS_2$ using the discrete variation (DV)-$X\alpha$ method (Hamajima et al., 1981), although even here the Fe 3*d*-type orbitals are calculated to be somewhat too stable. It is not apparent why the Cu^+ cluster results agree well with experiment while the Fe^{3+} cluster results are in poor agreement. The poor results may be due to perturbation of the FeS_4^{5-} cluster by neighboring atoms in the $CuFeS_2$, with the Fe 3*d* orbitals destabilized either through mixing with the Cu 3*d* orbitals or as a result of saturation of the S valences. The high-pressure properties of $CuFeS_2$ have also been interpreted using these models.

The binary copper sulfides are much more complex structurally than their formulas suggest. In chalcocite (Cu_2S), copper occurs in two kinds of triangular coordination (Evans, 1971), whereas in covellite (CuS) copper occurs in tetrahedral as well as triangular coordination in a mineral that also contains dianion groups. X-ray emission and x-ray photoelectron spectra are available for the valence region in Cu_2S and CuS (Narbutt, 1974; Nemnonov and Mikhailova, 1974; Domashevskaya et al., 1976; Nakai et al., 1978; Folmer and Jellinek, 1980), as illustrated in Fig. 6.24. Interpretation of these spectra has been facilitated by cluster calculations using the MS-SCF-$X\alpha$ method (Tossell, 1978b) and the calculations and/or spectra used to construct "one-electron" band model energy-level diagrams for Cu_2S and CuS (Vaughan and Tossell, 1980b; Tossell and Vaughan, 1981). Thus, in Fig. 6.25 is shown an energy-level diagram for Cu_2S constructed from spectroscopic data. The agreement between calculation and experiment is quite good, as shown by the data presented in Table 6.4. A CuS_3^{5-} cluster calculation was used in an analysis of the electronic structure of CuS, although initially, calculations were performed on the clusters CuS_3^{4} and CuS_4^{7-} on the assumption of formal oxidation states in covellite of Cu_{III}^{2+} $(Cu_{IV}^{+})_2S^{2-}(S_2^{2-})$. The results of these calculations are shown in Fig. 6.26. However, spectroscopic data

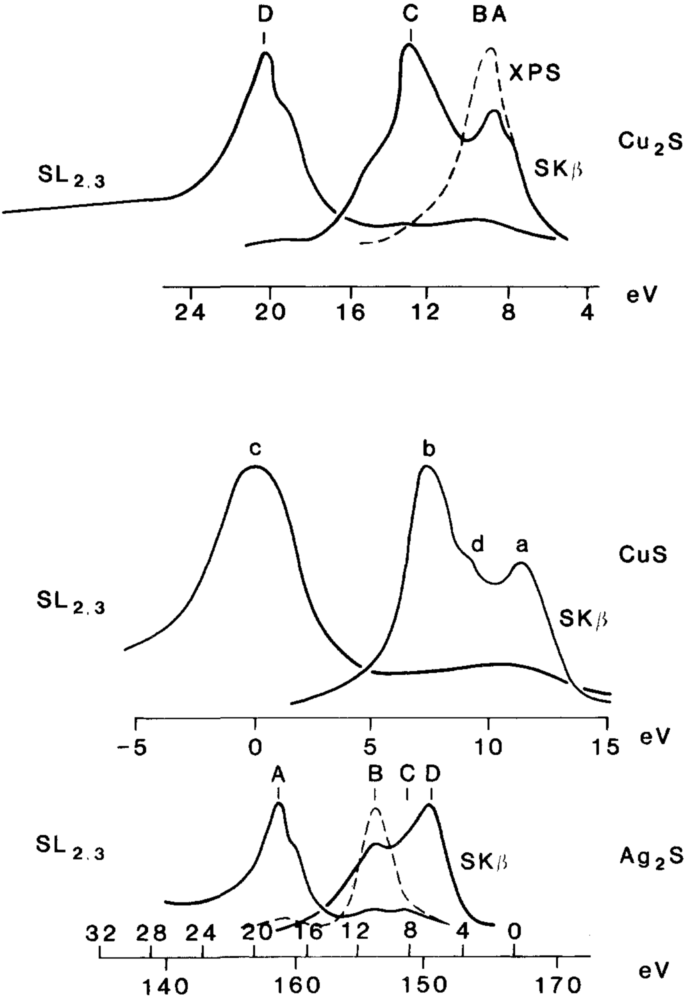

Fig. 6.24. Valence-region x-ray emission (and x-ray photoelectron) spectra for Cu_2S, CuS, and Ag_2S (see text for sources of data).

indicate that the oxidation state of copper in CuS is essentially Cu^+ (e.g., Folmer and Jellinek, 1980), and the metallic conductivity observed in CuS (Shuey, 1975) also indicates that the highest-energy orbitals containing electrons form a collective electron band. Further calculations indicated that, to form such a band, charge should flow from the $4t_2$ orbital on the tetrahedral Cu^+ to the $4e$ orbital on the triangular Cu^{2+}. The resulting change in electronic structure was then represented by performing a cluster calculation on $CuS_4^{6.5-}$ and using this along with the CuS_3^{5-} calculation as shown in Fig. 6.26. As shown by the composite "one-electron" band model energy-level diagram for covellite on the right of Fig. 6.26,

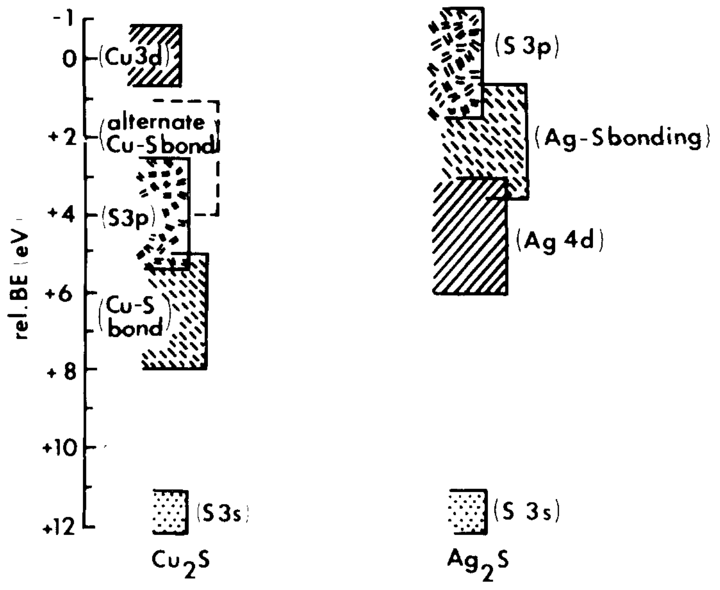

Fig. 6.25. Relative orbital binding energies for Cu_2S and Ag_2S (rel. BE in eV) obtained from spectra (from Vaughan and Tossell, 1983; see Tossell and Vaughan, 1981, for sources of data).

beneath an incompletely filled band of dominantly Cu 3*d* character lies a nonbonding sulfur band and the metal–sulfur bonding band.

Another important "metal-excess" sulfide with a complex structure is Ag_2S; as the mineral acanthite, half of the silver atoms occur in a twofold,

Table 6.4. Orbital binding energies from MS-SCF-$X\alpha$ calculations and x-ray photoelectron and x-ray emission spectra for copper and silver sulfides[a]

Peak	Relative binding energy (eV) Measured	 Calculated	Orbital assignment
CuS_3^{5-} calculations and Cu_2S XPS and XES			
A	+3.1, +2.5	−2.9	$4t_2$
B	+1.8, +1.3	−2.0	$2e$
C	0	0	$1t_1, 3t_2, 1e, 2t_2, 2a_1$
D(S 3*s*)	−8	−8.8	$1t_2, 1a_1$
AgS_2^{3-} and AgS_4^{7-} calculations and Ag_2S XPS and XES			
D	0	0–0.5,[b] 0–1.6[c]	S 3*p* (nonbonding)
C	1.9		Ag–S 3*p* (bonding)
B	4.4	7.7,[b], 3.9[c]	Ag 4*d*
A	11.6	10.1,[b] 10.3[c]	S 3*s*

[a] After Tossell and Vaughan (1981); see these authors for details of the sources of experimental data, etc.

[b] AgS_2^{3-}.

[c] AgS_4^{7-}.

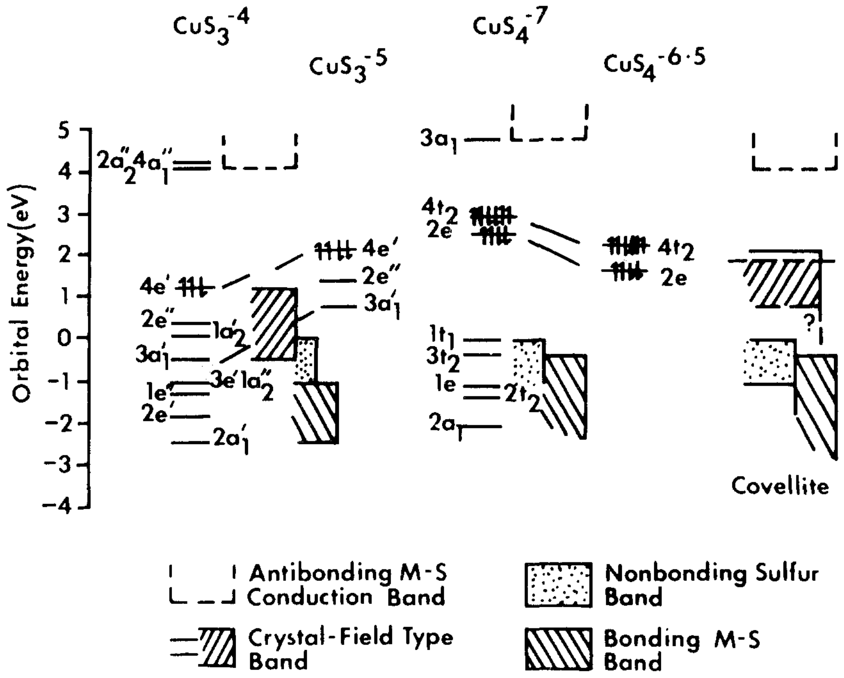

Fig. 6.26. An electronic structure model for covellite (CuS), based on calculations using the MS-SCF-$X\alpha$ method. Discrete energy levels are shown for the clusters CuS_3^{4-}, CuS_3^{5-}, CuS_4^{7-}, $CuS_4^{6.5-}$, and a composite "one-electron" band model energy-level diagram for the mineral.

nearly linear coordination and half in a distorted tetrahedral coordination. Again, as shown in Fig. 6.24, x-ray photoelectron and x-ray emission spectra are available for Ag_2S (Domashevskaya et al., 1976) and MS-SCF-$X\alpha$ calculations have been performed for AgS_2^{3-} and AgS_4^{7-} clusters (Tossell and Vaughan, 1981). Agreement between calculation and experiment is reasonably good (Table 6.4), although the calculations underestimate the width of the S 3*p* nonbonding and the Ag–S 3*p* bonding orbital region. The experimental spectra, however, show no evidence of the tightly bound Ag 4*d* orbitals predicted for two-coordinate Ag. It seems improbable, therefore, that the Ag_2S studied in the photoemission experiment had the acanthite structure. At high temperature (173°C), acanthite transforms to the cubic modification, argentite, in which Ag occurs partly in tetrahedral and partly in octahedral coordination, with no two-coordinate sites (Lowenhaupt and Smith, 1974). The material studied may be related to this structure.

The electronic structure of Ag_2S, shown alongside that of Cu_2S in Fig. 6.25, shows a remarkable inversion of the metal *d* and sulfur 3*p* levels between the two compounds. In Cu_2S, the Cu 3*d* orbitals are considerably less tightly bound than are the sulfur 3*p* nonbonding orbitals, while in

Ag_2S, the Ag 4*d* orbitals are more tightly bound than the sulfur 3*p*. As further discussed in later chapters, Tossell and Vaughan (1981) have studied the systematic variation in metal *d* and ligand *p* orbital binding energies in the sulfides and chlorides of Cu, Ag, Au, Zn, Cd, and Hg, and related this variation to the occurrence of particular oxidation states and coordinations for the metals, and to the occurrence of polyhedral distortions.

6.7. The thiospinels [Co_3S_4, $CuCo_2S_4$, $(Co,Ni)_3S_4$, Ni_3S_4, $FeNi_2S_4$, $FeCr_2S_4$]

The thiospinels are a group of sulfide minerals and of synthetic compounds having the spinel structure and, therefore, containing (chiefly transition-metal) cations in both tetrahedral and octahedral coordination. Although spectroscopic data for these materials are limited, they have been well characterized as regards their electrical and magnetic properties, as shown in Table 6.5. On the basis of these properties, bonding in the thiospinel minerals has been discussed in terms of qualitative MO and band-theory models (Goodenough, 1969; Vaughan et al., 1971). According to these models, transition-metal ions in the octahedral (*B*) sites of these AB_2S_4 compounds have bonding (σ_B) molecular orbitals and antibonding (σ_B^*) molecular orbitals formed by overlap of metal e_g, 4*s* and 4*p* orbitals with 3*s* and 3*p* orbitals of the sulfur ions. Filled t_{2g} orbitals probably remain essentially nonbonding. In the cations of the tetrahedral *A* sites, it is the *e* group of orbitals that remain nonbonding, whereas t_2, 4*s* and 4*p* orbitals form σ_A and σ_A^* molecular orbitals with sulfur. The σ_B and σ_A bonding molecular orbitals can then be considered part of the valence band, whereas the σ_B^* and σ_A antibonding orbitals containing antibonding e_g^* and t_2^* orbitals belong to the conduction band.

The increasing stability of the 3*d* electrons in progressing across the transition series leads to increased covalent mixing of metal and sulfur orbitals with rising atomic number, and lowering of the filled t_{2g} and *e* orbitals levels into the valence band. Also the energy levels of the σ_A^* and σ_B^* molecular orbitals may coalesce or separate depending on the types of cation in the *A* and *B* sites and the extent of metal–sulfur bonding in each site. If there is an energy gap between the σ_A^* and σ_B bands, the thiospinel has semiconducting properties; the electrons tend to be localized, and magnetic interactions occur through cation–sulfur–cation coupling, leading to ferro-, antiferro-, and ferrimagnetism. Alternatively, if the σ_A^* and σ_B^* bands coalesce, they become collective electron states, and the thiospinel has metallic properties including high electrical conductivity and temperature-independent Pauli paramagnetism.

Synthetic Co_3S_4, $NiCo_2S_4$, and $CoNi_2S_4$ all show metallic properties (Bouchard et al., 1965), and the qualitative energy-level diagram of Fig. 6.27 has been proposed for the 3*d* orbitals in linnaeite, Co_3S_4 (Good

Table 6.5. Electrical and magnetic properties[a] of thiospinel minerals

	Electrical properties			**Magnetic properties**		
Composition (mineral)	**Resistivity at 25°C (Ω cm)**	E_a **(eV)**	**Seebeck coefficient at 25°C (μV °C^{-1})**	**Susceptibility**	**Magnetic moment (μ_{eff})**	T_c **or** Θ
$CuCo_2S_4$ (carrollite)	4×10^{-4}	Metallic	$+12.7$	Pauli paramagnetic 3.8×10^{-4} emu g^{-1}	—	—
Co_3S_4 (linnaeite)	3×10^{-4}	Metallic	$+4.8$	Pauli paramagnetic		
$(Co,Ni)_3S_4$ (siegenite)	8×10^{-4} ($NiCo_2S_4$) 4×10^{-4} ($CoNi_2S_4$)	Metallic Metallic	-17.7 -1.8	Pauli paramagnetic		
Ni_3S_4 (polydmite)						
$FeNi_2S_4$ (violarite)		Metallic		Pauli paramagnetic 1.95×10^{-6} emu g^{-1}		
Fe_3S_4 (greigite)		Semiconducting		Ferrimagnetic		$T_c = 580$ K
$FeCr_2S_4$ (daubreelite)	20	0.038 ± 0.005	$+388$ $+80$	Ferrimagnetic at low temperature	$1.52\mu_B$ at 1.5 K	$T_c = 180$ K $\Theta = -290$ K
$FeIn_2S_4$ (indite)						$\Theta = -122$ K

[a] See Vaughan and Craig (1978) for original data sources.

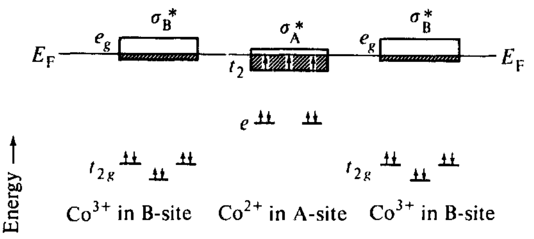

Fig. 6.27. Schematic energy level diagram for the 3*d* orbitals in Co_3S_4 (after Goodenough, 1969; Vaughan et al., 1971), E_F is the Fermi level.

enough, 1967, 1969). The high octahedral site preference energy of low-spin Co^{3+} and the stability of Co^{2+} in tetrahedral coordination has led to prediction of a formal cation distribution $Co^{2+}(Co^{3+})_2S_4$, although the assignment of formal valencies in such metallic compounds has very little meaning (Goodenough, 1969). The valence-band t_{2g} and e levels are completely filled, and the antibonding levels, capable of accommodating 14 electrons per Co_3S_4 formula unit, contain only three 3*d* electrons. The metallic properties indicate that the $\sigma_B{}^*$ and $\sigma_A{}^*$ band overlap, but the weak temperature-independent paramagnetism suggests that the σ^* band is narrow (Goodenough, 1969). Substitution of nickel for cobalt leads to the compositions $Co_{3-x}Ni_xS_4$ and an increase from 3 to $(3+x)$ electrons per molecule in the σ^* band. Similarly $CuCo_2S_4$ (carrollite), considered to be a normal spinel with low-spin Co^{3+} occupying octahedral *B* sites and Cu^{2+} in tetrahedral *A* sites, exhibits metallic properties. Thus, nickel substituting for cobalt in Co_3S_4, or copper substituting for cobalt, does not fundamentally alter the band structure but just leads to a raised Fermi level through introduction of more electrons into the antibonding levels. No compositions richer in copper than $CuCo_2S_4$ have been observed because of the instability of the Cu^{3+} oxidation state.

In contrast to this metallic group of thiospinels, greigite (Fe_3S_4) and a number of other minerals, including daubréelite ($FeCr_2S_4$), show evidence of having localized valence electrons and belonging to the group of thiospinels with semiconducting properties that exhibit ordered magnetism. As well as electrical and magnetic data, the low-temperature Mössbauer spectrum of greigite (Fig. 6.28) shows that it is magnetically ordered (probably ferrimagnetic to above room temperature) and is an inverse spinel containing high-spin Fe^{2+} and Fe^{3+} cations. It is therefore the sulfur analog of magnetite (Fe_3O_4). Daubréelite is also ferrimagnetic at low temperature (Table 6.5), and the Mössbauer spectrum shows that it contains high-spin Fe^{2+} in tetrahedral sites and is thus a normal spinel. A schematic energy-level diagram for the 3*d* orbitals in $FeCr_2S_4$ is shown in Fig. 6.29 (after Goodenough, 1967; Vaughan et al., 1971). Since the relative stability of the 3*d* orbitals increases with rising atomic number, they are shown as slightly more low lying in iron than in chromium. However, the

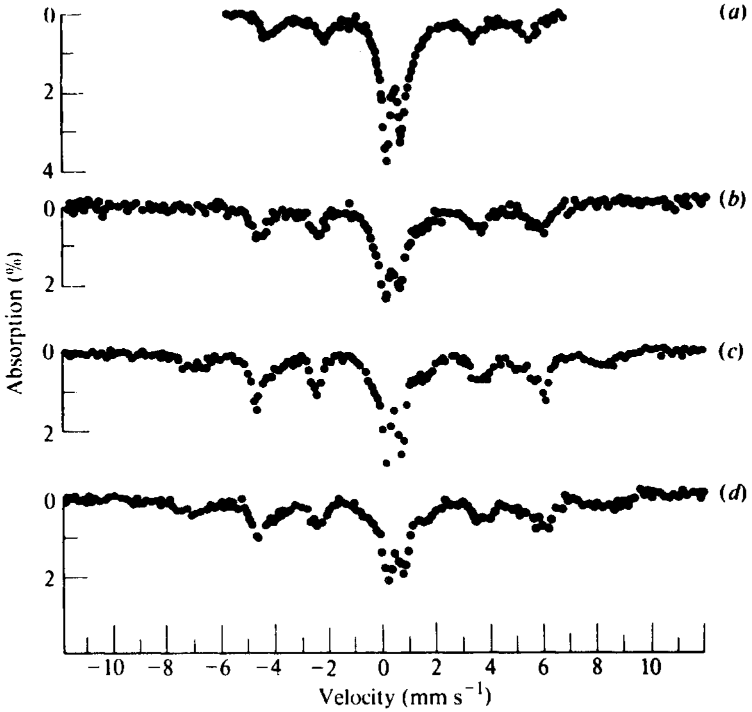

Fig. 6.28. Mössbauer spectra of greigite (Fe_3S_4): (a) at 300 K; (b) at 77 K; (c) at 4.2 K; (d) at 1.4 K (after Vaughan and Ridout, 1971; reproduced with the publisher's permission).

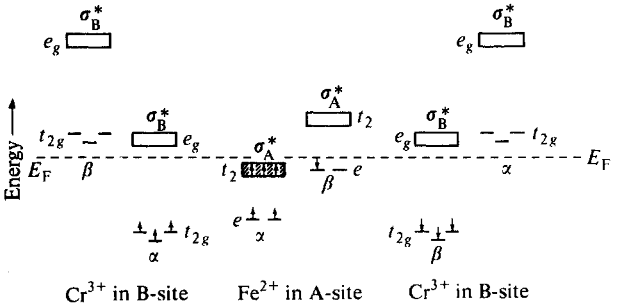

Fig. 6.29. Schematic energy-level diagram for the 3*d* orbitals in $FeCr_2S_4$ (after Vaughan et al., 1971). The diagram applies below the Curie temperature (T_C = 192 K). E_F is the Fermi level and α and β refer to spin-up and spin-down electrons.

t_{2g}-σ_B* separation in Cr^{3+} is greater than the e-σ_A* separation in Fe^{2+}, due to the increased metal–sulfur interaction in octahedral coordination. In the high-spin Fe^{2+}, the spin of the sixth electron is antiparallel (β) to the other five (α), occupying singly each of the 3*d* orbitals. The electrons in Cr^{3+} occupy each of the t_{2g} orbitals singly and have parallel spins above the Curie temperature (T_C = 192 K), antiparallel below. The energy gap between the σ_A* and σ_B* levels, although small in $FeCr_2S_4$ (Goodenough, 1969), is sufficient to make daubréelite a semiconductor.

In attempts to substantiate and to develop these qualitative models, calculations on the clusters CuS_4^{6-} (and CuS_4^{7-}), CoS_4^{6-}, CoS_6^{9-} (low-spin Co^{3+}), FeS_4^{5-}, FeS_6^{10-}, FeS_6^{9-} using the MS-SCF-$X\alpha$ method have been employed (Vaughan and Tossell, 1981). These have been used to construct one-electron MO models for the thiospinels Co_3S_4, $CuCo_2S_4$, and Fe_3S_4, as shown in Fig. 6.30. Only the highest-energy filled and lowest-energy empty orbitals are shown, the relative energies of these orbitals derived from calculations on the different clusters being estimated by taking the nonbonding sulfur 3*p*-type orbitals as the zero point on the energy scale.

The orbital energy diagrams shown in Fig. 6.30 for CoS_6^{9-} and CoS_4^{6-} indicate that the empty e_g orbitals of the octahedral cluster will be close in energy to the partially filled *e* orbitals of the tetrahedral cluster. Since the energy of the interaction between orbitals varies inversely with their energy difference, the octahedral site e_g and tetrahedral site *e* orbitals are

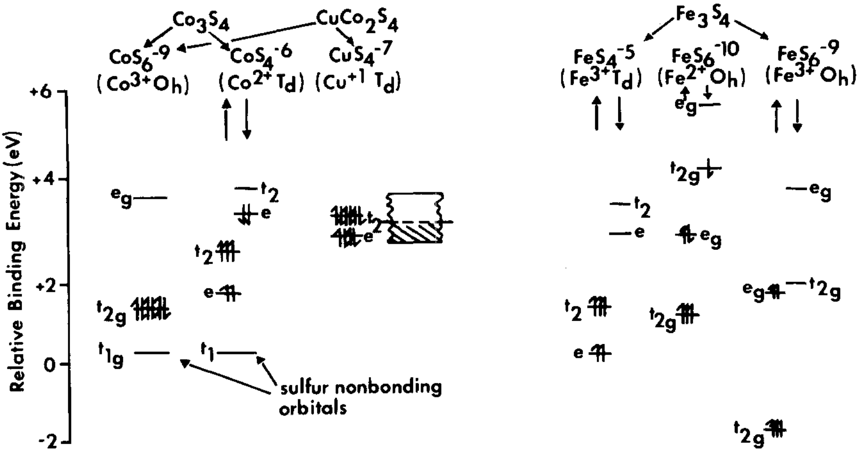

Fig. 6.30. Molecular-orbital energy-level diagram based on the results of MS-SCF-$X\alpha$ calculations on the clusters CoS_6^{9-}, CoS_4^{6-}, CuS_4^{7-}, FeS_4^{5-}, FeS_6^{10-}, and FeS_6^{9-} and used to model the electronic structures of the thiospinel minerals linnaeite (Co_3S_4), carrollite ($CuCo_2S_4$), and greigite (Fe_3S_4). For those systems containing unpaired electrons, the effects of spin splitting into spin-up (↑) and spin-down (↓) levels is also shown (after Vaughan and Tossell, 1981; reproduced with the publisher's permission).

expected to mix substantially. A band of energy levels would thus be formed with a width greater than the original e_g-e separation. This would lead to the observed metallic conductivity and Pauli paramagnetism, and the resulting band energy-level diagram is very similar to that proposed above on qualitative grounds (after Goodenough, 1969; Vaughan et al., 1971). In extending to $CuCo_2S_4$, overlap can again be envisaged between empty e_g orbitals on octahedral-site cobalt atoms and e and t_2 orbitals of the tetrahedral-site copper. Although the normally assumed oxidation state of copper is Cu^{2+}, other calculations and spectroscopic data (Tossell, 1978b; Nakai et al., 1978) suggest that the oxidation state of copper approaches Cu^+; hence the CuS_4^{7-} shown in Fig. 6.30. Again, the model proposed on the basis of calculations is very similar to that proposed on qualitative grounds.

The model for greigite (Fe_3S_4) based on the FeS_4^{5-}, FeS_6^{10-}, and FeS_6^{9-} clusters (Fig. 6.30) shows the very considerable effect of spin splitting into spin-up (↑) and spin-down (↓) molecular orbitals. The resulting large energy separations would prevent mixing between octahedral-site and tetrahedral-site orbitals; electrons would remain localized, resulting in the observed properties of this material. The magnetic properties and Mössbauer parameters of greigite have also been discussed on the basis of MS-SCF-$X\alpha$ calculations by Braga et al. (1988).

The electronic structure models of thiospinels form a basis for understanding a range of properties including solid solution limits, cell parameter variations, reflectance, microhardness, and relative stabilities. Further support for these models has been provided by ^{57}Fe Mössbauer studies of violarites (Vaughan and Craig, 1985) and by EXAFS spectroscopy studies of carrollite, daubréelite, and the violarites (Charnock et al., 1990).

6.8. Other (including complex) sulfides [MoS_2, Co_9S_8, $(Ni,Fe)_9S_8$, $Cu_{12}Sb_4S_{13}$, etc.]

Although examples of minerals from most of the major groups of sulfides (Table 6.1) have been discussed in the preceding sections of this chapter, there are a number of phases particularly worth considering that do not fit into any of the above categories. These are the layer sulfide molybdenite (MoS_2), the metal-excess sulfides of the pentlandite family [Co_9S_8, $(Ni,Fe)_9S_8$], and an example of a sulfosalt[1] family in the form of the tetrahedrite–tennantite minerals [$\sim Cu_3(Sb,As)_4S_{13}$].

Molybdenite has a structure in which the metal atoms are surrounded by six sulfurs at the vertices of a trigonal prism. The prisms are linked by their edges into a continuous layer, within which the centers of half of the prisms are occupied by cations. Layers are held together by van der Waals bonds, and different stacking sequences result in several molybdenite polytypes; two-layer (hexagonal) molybdenite-2*H* is most common in nature, but a three-layer (rhombohedral) molybdenite-3*R* also occurs. The interesting electrical properties of MoS_2 have led to its detailed study. A simple "one-electron" band model of the type shown in Fig. 6.31 (after Wilson and Yoffe, 1969) can be proposed on the basis of ligand-field arguments from the known electrical and magnetic properties of MoS_2. Here, the d_{yz} and d_{xz} orbitals are shown as involved in σ bonding and form part of the σ (valence band). The $d_{x^2-y^2}$ and d_{xy} orbitals mix somewhat with neighboring metal p_x and p_y states and form a *d*/*p* nonbonding band above and separate from a nonbonding band based on d_z^2, which overlaps very little with near-neighbor metals and forms a distinct narrow band. In MoS_2, sufficient electrons are available to fill the σ and d_z^2 bands only. This model has been used to interpret the electronic absorption spectrum of MoS_2 (Wilson and Yoffe, 1969), as shown in Fig. 6.31. The lowest-energy transition (*E* in Fig. 6.31) is associated with an absorption edge in the infrared (~0.2 eV) and assigned to excitation of electrons from the "d_z^2 band" into the empty "nonbonding *d*/*p* band." This transition across the "*d* band gap" is regarded as determining the important electrical properties of MoS_2 and related group VI semiconductors.

Many band-structure calculations have been performed on MoS_2; much of the earlier work has been reviewed by Calais (1977). A more recent study using self-consistent augmented-spherical-wave calculations was undertaken by Coehoorn et al. (1987). MO cluster calculations using the MS-SCF-$X\alpha$ method have also been undertaken by de Groot and Haas (1975) and by Harris (1982). In Fig. 6.32 are shown the energy levels for the MoS_6^{8-} cluster calculated by de Groot and Haas (1975), along with the x-ray photoelectron spectrum of MoS_2 from Wertheim et al. (1973).

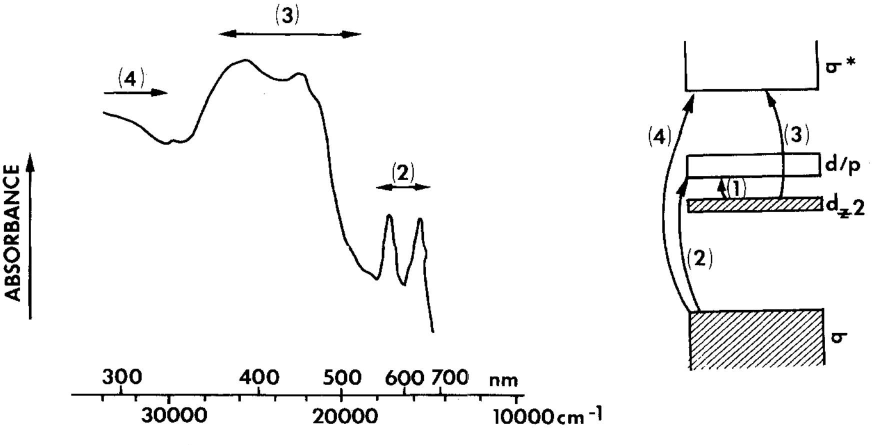

Fig. 6.31. The electronic (optical) absorption spectrum of MoS_2 (2*H* polytype) and a schematic band model interpretation (after Wilson and Yoffe, 1969; reproduced with the publisher's permission).

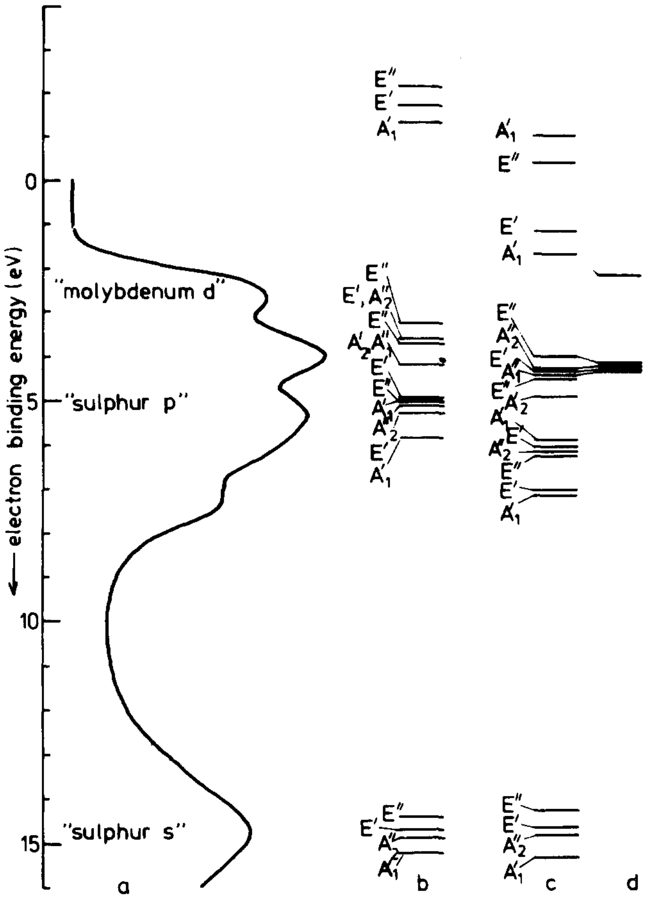

Fig. 6.32. Calculated energy levels for an MoS$_6^{8-}$ cluster as a model for MoS$_2$ obtained using the MS-SCF-$X\alpha$ method. Alongside (a) the x-ray photoelectron spectrum of MoS$_2$ are shown (b) the results of a non-self-consistent calculation on a MoS$_6$ cluster, (c) a self-consistent calculation for a MoS$_6^{8-}$ cluster, and (d) a self-consistent calculation for a MoS$_6^{8-}$ cluster including relaxation effects for the five highest energy orbitals (after de Groot and Hass, 1975; reproduced with the publisher's permission).

The calculation shows an electronic structure broadly the same as proposed in the previous material on qualitative grounds. Above the sulfur *s* band are a group of levels largely of sulfur *p* character but with some molybdenum character in the states of symmetry A_1', $E,'$ and E''. The highest occupied level is of symmetry A'_1, and this has mainly molybdenum d_z^2 character. The lowest unoccupied levels (E',E'') are of molybdenum *d* with some sulfur character. Agreement between calculation and the XPS data is reasonable, particularly when relaxation effects are incorporated.

Because large oriented single-crystal surfaces of molybdenite are readily prepared, x-ray emission spectra can be studied as a function of angular dependence and using polarized x rays (Haycock et al., 1978; Yarmoshenko et al., 1983; Simunek and Wiech, 1984). Such studies indicate that sulfur $3p$ and Mo $4d$ character are extensively mixed in the valence-band region (Haycock et al., 1978). The polarized x-ray emission spectra (S $K\beta_1$ and Mo $L\beta_2$) obtained from a single crystal of $MoS_2(2H)$ as a function of angle of incidence (θ) are shown in Fig. 6.33 (after Yarmonshenko et al., 1983). Again, detailed analysis of these spectra is used to suggest mixing of sulfur $3p$ and Mo $4d$ states, and specifically of S $3p_x$ and $3p_y$ orbitals with Mo $4d$. Angular dependence of the Mo $L\beta_2$ spectrum indicates (Fig. 6.33) that the Mo $4d_z^2$ orbital is among the least tightly bound.

The minerals pentlandite [$(Ni,Fe)_9S_8$] and cobalt pentlandite (Co_9S_8) form a solid solution series and are interesting examples of metal-excess sulfides. In the pentlandite structure (Fig. 6.34) of the Co_9S_8 end member, Co_8S_6 clusters are formed from concentric Co_8 cubes and S_6 octahedra. The resulting cube cluster of tetrahedrally coordinated cations (shown in Fig. 6.34) has very short metal–metal distances (Co–Co = 2.505 Å; Rajamani and Prewitt, 1975). The unit cell contains 36 metal atoms and 32 sulfur atoms; 32 of the cations occupy the tetrahedral sites of the cube

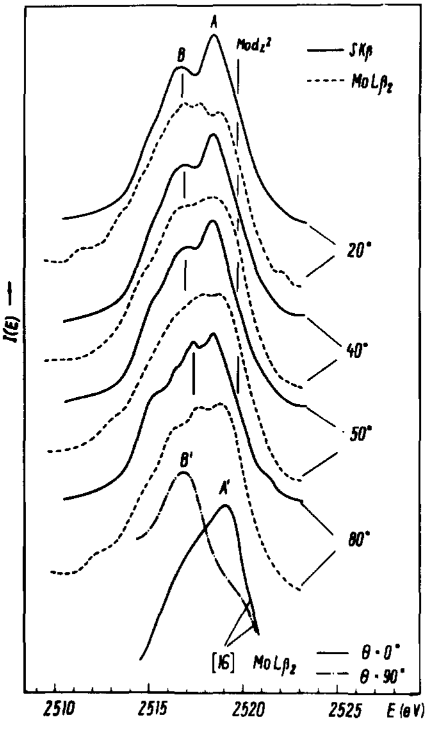

Fig. 6.33. Polarized x-ray emission spectra (S $K\beta_1$ and Mo $L\beta_2$) obtained from a single crystal of MoS_2 ($2H$ polytype) as a function of angle of incidence θ (= 20–80°) (after Yarmoshenko et al., 1983; reproduced with the publisher's permission).

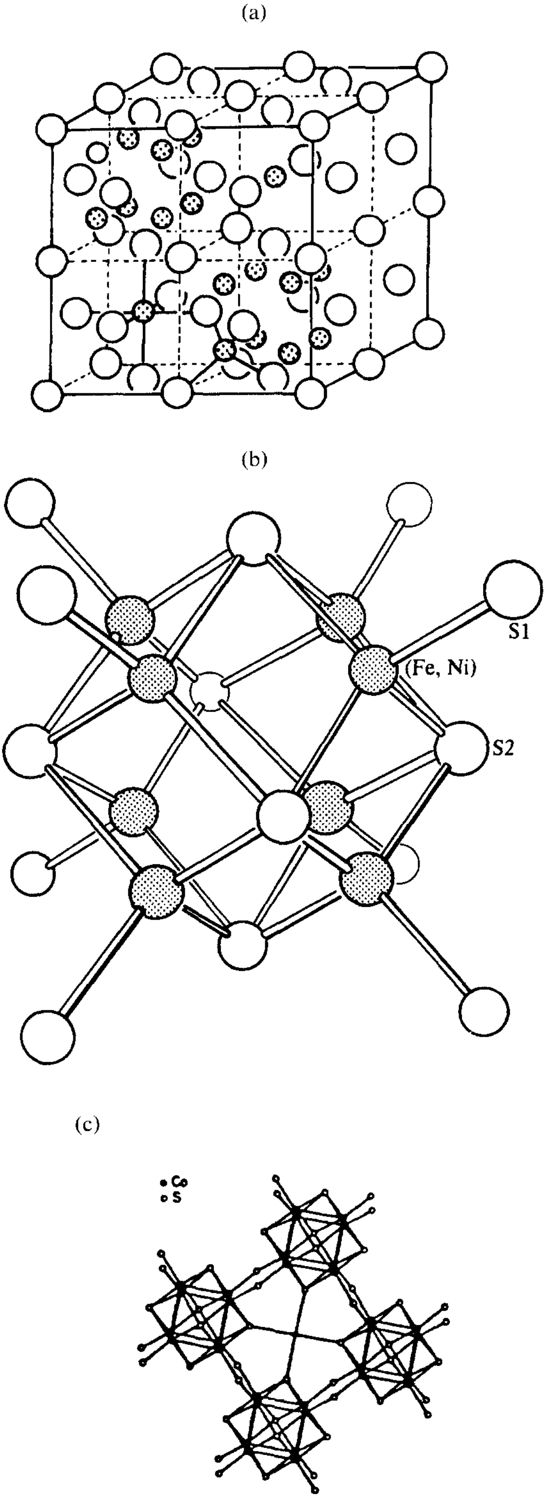
(a)
(b)
S1
(Fe, Ni)
S2
(c)
Co
S

clusters, and the remaining 4 occur in octahedral sites between the clusters (Fig. 6.34). X-ray studies suggest that the octahedral-site cobalt occurs as low-spin Co^{2+} and ^{57}Fe Mössbauer spectra of $(Ni,Fe)_9S_8$ show the tetrahedral-site iron atoms to have delocalized valence electrons (Vaughan and Ridout, 1971), in accordance with the observed metallic conductivity and Pauli paramagnetism of both Co_9S_8 and $(Ni,Fe)_9S_8$.

Qualitative MO/band models have been suggested to describe the bonding in Co_9S_8 (Vaughan and Burns, 1971; Rajamani and Prewitt, 1975). Here, tetrahedral-site cobalt atoms are considered to form mixed sp^3 and sd^3 hybrids, so that cobalt $4s$ and $4p$ and t_2 orbitals are involved with sulfur $3s$ and $3p$ orbitals in the formation of filled σ bonding and σ^* antibonding bands. Four of the cobalt $3d$ electrons per atom fill the e orbitals, and the three remaining electrons in the $t_2{}^*$ orbitals are considered to interact with the three near-neighbor cobalt atoms to form metal–metal bonds. The resulting σ and σ^* metal–metal bonding and antibonding orbitals are shown in Fig. 6.35. As also illustrated in Fig. 6.35, the filled e orbitals of tetrahedral cobalt and t_{2g} orbitals of octahedral cobalt may remain localized and essentially nonbonding orbitals. However, the magnetic and electrical properties suggest overlap of σ^* bands formed by the t_2 orbitals of tetrahedral-site metals and the e_g orbitals of octahedral site metals to give a single, broad, partly filled d band. For a composition of $Fe_{4.5}Ni_{4.5}S_8$, the metal–sulfur bonding may be considered in much the same way. The confining of pentlandite compositions to the general range between Co_9S_8 and $Fe_{4.5}Ni_{4.5}S_8$ suggest a need to retain the overall d electron configuration; the formation of metal–metal bonds in the cube clusters could impose this limitation (Vaughan, 1971). However, it has also been suggested that pentlandite may be a "Hume–Rothery" or "electron" compound like many alloys (Rosenquist, 1954) and be stable at a particular electron-to-atom ratio. Indeed, the numbers of d electrons in the unit cells of pentlandites of widely varying composition are remarkably uniform, even in argentopentlandites that contain a substantial quantity of silver. Pentlandite compositions falling some way from the Co_9S_8–$Fe_{4.5}Ni_{4.5}S_8$ join in composition need not cause change in the d electron population of the cube cluster, as nickel could be ordered into octahedral sites creating vacancies in tetrahedral sites, and excess iron could enter unoccupied tetrahedral sites (Rajamani and Prewitt, 1973). Thus, the structural formula for pentlandite could be $(Fe,Ni,Co)^{VI}$ $(Fe,Ni,Co,\square)_8{}^{IV}S_8$, where $\square$ represents tetrahedral vacancies in nickel-rich compositions or excess cations in iron-rich compositions.

Although quantitative data on electronic structures are not yet avail-

←

Fig. 6.34. The crystal structure of pentlandite [$(Ni,Fe)_9S_8$ and Co_9S_8] showing: (a) the cubic unit cell of the structure; (b) the cube cluster of tetrahedrally coordinated [(Fe,Ni) or Co] cations; (c) the octahedrally coordinated [(Fe,Ni) or Co] cation site.

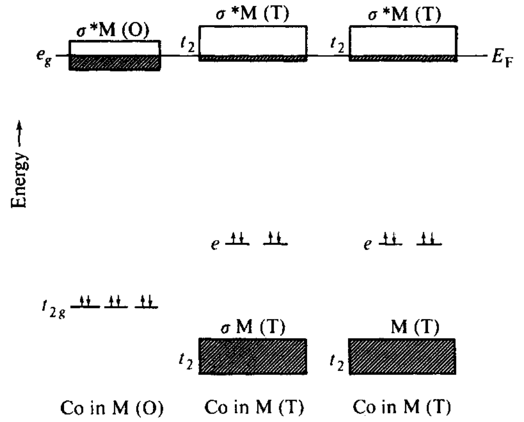

Fig. 6.35. Schematic energy-level diagram for the 3*d* orbitals in Co_9S_8 showing a conduction band formed through metal–metal interactions between tetrahedral-site cobalt atoms [σ^* *M*(*T*)] and metal–sulfur–metal interactions to octahedral-site cobalt atoms [σ^* *M*(*O*)] (after Prewitt and Rajamani, 1974; reproduced with the publisher's permission).

able for the pentlandites, they are clearly among the most interesting of sulfides. The successful synthesis of the cluster $[Co_8S_6(SPh)_8]^{4-}$ (Christou et al., 1985), containing the same Co_8S_6 unit as in pentlandite, should prompt further work on these compounds.

Another interesting family, in this case of sulfosalt minerals, is that of the tetrahedrites. Natural tetrahedrites are described approximately by the formula $A_{10}B_2C_4D_{13}$, where A = Cu,Ag; B = Cu,Fe,Zn,Hg,Cd,Pb; C = Sb,As,Bi,Te; D = S,Se, and are all stoichiometric. The tetrahedrite structure is complex (Fig. 6.36), involving half of the $(A + B)$-type atoms in tetrahedral and half in trigonal sites; the C-type atoms occupy the equivalent of a tetrahedral site in sphalerite, but are bonded to only three sulfur atoms; twelve D-type atoms are 4-coordinate, and the other single atom is 6-coordinate. The complex substitutions in the tetrahedrite-group minerals have been investigated using a variety of experimental approaches, most recently by EXAFS spectroscopy (Charnock et al., 1989a). These studies have shown, for example, that silver goes into trigonal sites and iron mainly occupies tetrahedral sites. Cadmium, as expected, occurs in tetrahedral sites in the structure. Combined EXAFS and ^{57}Fe Mössbauer studies (Charnock et al., 1989b) show that the $Fe^{2+}:Fe^{3+}$ ratio plays a part in maintaining charge balance when these complex substitutions occur. Synthetic samples in the Cu–Sb–S system, which are not necessarily stoichiometric, have compositions bounded by the line $Cu_{14}Sb_4S_{13}$–$Cu_{12}Sb_{4.67}S_{13}$ (Johnson and Jeanloz, 1983). As previously discussed for the pentlandites, the concepts associated with "Hume–Roth-

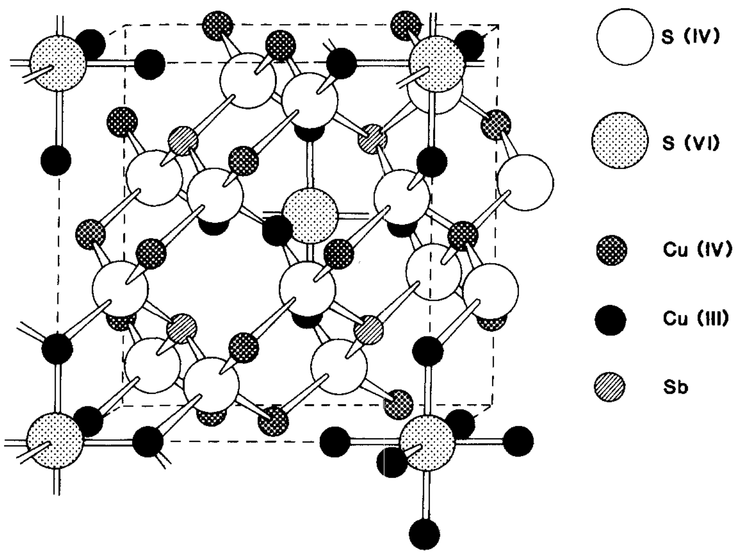

Fig. 6.36. A half-unit cell of the tetrahedrite ($Cu_{12}Sb_4Sb_{13}$) structure (after Charnock et al., 1989a; reproduced with the publisher's permission).

ery" compounds have also been applied to the tetrahedrites. Johnson and Jeanloz (1983) applied a simple Brillouin zone model to show that tetrahedrite should be stable with greater than 204 and up to 208 valence electrons per unit cell (filling the fifty-second Brillouin zone), and be most stable with 208 valence electrons. This model correctly predicts the observed compositional limits of natural and synthetic tetrahedrites as well as measured variations in resistivity. It represents the revival of an approach used by Freuh (1954) to discuss the stoichiometry of minerals in the Cu–Fe–S system.

In spite of their complexity, Bullett and Dawson (1986) and Bullett (1987) have used an LCAO tight-binding method (see Bullett, 1980, and Section 3.11) to calculate the band structure of Cu–Sb–S system tetrahedrites. Calculations on $Cu_{12}Sb_4S_{13}$ (see Fig. 6.37) confirm its intrinsic electron-deficient character. After doubly occupying 116 valence states per unit cell, one more than the available 115 pairs of valence electrons, a gap of 1.2 eV occurs in the energy distribution of electron states [Fig. 6.37(a)]. Hence, natural tetrahedrites can contain Zn atoms up to $Cu_{10}Zn_2Sb_4S_{13}$, and, at this composition, the compound behaves as a diamagnetic semiconductor. In the copper-rich phase of tetrahedrite, $Cu_{14}Sb_4S_{13}$, the almost exactly two additional Cu ions per formula unit are accommodated by displacing two of the tetrahedrally coordinated Cu atoms into a third kind of interstitial Cu site, adjacent to the base of the SbS_3 pyramids. The copper atoms in this interstitial site are mobile and diffuse easily through the structure, giving Cu-rich tetrahedrites solid electrolyte properties.

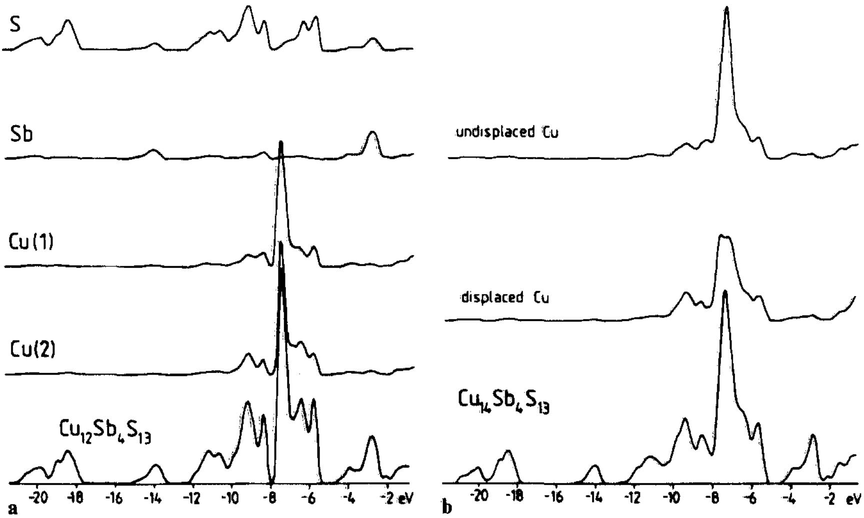

Fig. 6.37. The calculated density of states in the two tetrahedrites $Cu_{12}Sb_4S_{13}$ and $Cu_{14}Sb_4S_{13}$ and its local site projections for S, Sb, and various types of Cu atom. In the copper-rich phase the copper contribution from undisplaced and displaced (interstitial) Cu sites are compared (after Bullett, 1987; reproduced with the publisher's permission).

Calculations on copper-rich tetrahedrite ($Cu_{14}Sb_4S_{13}$) show a filled valence band with an energy gap of 0.9 eV between highest filled and lowest empty states.

6.9. Concluding remarks

The sulfide minerals are a complex group of materials as regards their electronic structures, and many challenging problems remain in attempting to understand their properties and crystal chemistry. As noted in the introduction to this chapter, few studies aimed at clarifying structural relationships and involving high-level quantum-mechanical calculations have, as yet, been undertaken on sulfide systems. However, Bartelmehs et al. (1990) have recently undertaken *ab initio* Hartree–Fock–Roothaan SCF calculations on hydrosulfide molecules ($H_{6-m}X^{m+}S_3$, $H_{8-m}X^{m-}S_4$, and $H_{12-m}X^{m+}S_6$, where X is one or more of Li, Be, B, C, Na, Mg, Al, Si, P, K, Ga, Ge, As, and Sn). These calculations yielded minimum-energy bond lengths [$R_t(X\text{–}S)$] that reproduce those observed in chemically similar sulfide crystals. A linear regression analysis of these bond lengths demonstrated that R_t (X–S) can be estimated by using the equation $R = 1.83(p)^{-0.21}$, where $p = s/r$, s is the Pauling bond strength, and r is the row number of the X cation in the Periodic Table. This equation for sulfides is similar to that found for oxides by Gibbs et al. (1987) using the same approach [for oxides, $R = 1.39(p)^{-0.22}$]. Using electron-density maps calculated for the hydrosulfide molecules, Bartelmehs et al. (1990) were also able to show that bonded radii for both the X cations and the S anion increase with $R_t(X\text{–S})$ (as, again, is the case for oxide systems). The bonded radius of the S anion is smaller (1.16 Å) when bonded to more electronegative atoms like 4-coordinate As, and larger (1.67 Å) when bonded to less electronegative atoms like 4-coordinate Li. However, the bonded radius of S is smaller than the crystal radius of Shannon (1981), which is 1.70 Å, and the ionic radius of Pauling (1960), which is 1.84 Å, in every case considered by Bartelmehs et al. (1990).

The question of the similarities and differences between the metal–oxygen bond and the metal–sulfur bond is fundamental in geochemistry, and relates to the "lithophile" versus "chalcophile" nature of particular elements. A full discussion is presented in Chapter 8.

Note

1. Sulfosalts are minerals with a general formula $A_mT_nX_p$ in which commonly A = Ag,Cu,Pb; T = As,Sb,Bi; X = S. They contain TS_3 pyramidal groups in the structure.

7

APPLICATIONS IN MINERAL PHYSICS AND CHEMISTRY

In this book we have concentrated up to this point on the experimental and theoretical methods involved in determining the electronic structure of minerals and related materials, and on the applications of these methods to major groups of compounds such as the oxides, silicates, carbonates, borates, and sulfides. It is now appropriate to turn to more general applications in the study of minerals.

Three major areas are addressed in this chapter. The first concerns the general field of crystal chemistry and the extent to which calculations can be used (alongside appropriate experiments) to approach such questions as the ionic versus covalent nature of a particular bond, the understanding and prediction of crystal structure of a material of a particular composition at room temperature and pressure (or other conditions, and hence key elements of the phase relations), and the rules and principles governing the crystal structures of solids. The second concerns the behavior of minerals and related materials at high pressures, of interest because of applications to understanding the physics and chemistry of the Earth's interior. Theoretical studies of phases at high pressure are discussed with particular reference to attempts to understand the materials that are believed to comprise the core and mantle of the Earth. The third addresses examples of application in areas of direct industrial interest, that is, to mineral materials of importance in ion-exchange and absorption, and in catalysis.

These three major areas represent applications of the theoretical (and experimental) methods discussed in earlier chapters to problems of importance in mineral and crystal chemistry, in mineral physics and geophysics, and in industrial mineralogy and materials science. They are illustrative of the value of these methods, but are far from being a comprehensive account.

7.1. Structure, bonding, and stereochemistry

The fact that almost all minerals are crystalline solids, indeed, were among the first crystalline solids to be systematically studied by x-ray diffraction, has led to intimate links between mineralogy and crystal and structural chemistry. Because crystal structure depends upon bonding character ("electronic" structure), it should be possible accurately to predict the crystal (or "geometric" structure) adopted by a particular composition material using quantum-mechanical methods. The extent to which this is possible is discussed below, with reference to the example of the SiO_2 polymorphs. Before that, however, a very general question (some would say a "nonquestion" for reasons that will become apparent) is considered, namely the "covalency" versus "ionicity" of solids as evidenced by calculation and experiment. These general questions lead to a consideration of principles and rules governing crystal structures: their basis, formulation, and application. The rules formulated by Pauling (1929) and widely applied to "ionic" structures are reappraised and the applications of qualitative molecular-orbital theory to the understanding of structures considered.

7.1.1. Covalency and ionicity in solids from calculation and experiment

There has been considerable effort directed towards the assessment of the covalency or ionicity of various solids. The output of standard *ab initio* (SCF) Hartree–Fock–Roothaan calculations contains Mulliken (1955) charge distribution analysis parameters such as the atomic-orbital populations, net atomic charges, and bond overlap populations described earlier (Chapter 3), which are often used to discuss the relative covalency or ionicity of materials. Considerable caution is required in using such parameters, however, since net atomic charges and other such quantities are not quantum-mechanical observables; that is, they cannot even in principle be measured, and are highly basis-set dependent, as noted by Hehre et al. (1986; pp. 336–41). This is illustrated for molecules more relevant to mineralogy in Table 7.1, in which a number of properties of CO_2 and SiO_2 are shown calculated at various basis-set levels. It is clear

Table 7.1. Comparison of observable and nonobservable charge distribution parameters[a] in CO_2 and SiO_2 obtained from *ab initio* Hartree–Fock–Roothaan calculations using different basis sets (and experimental equilibrium bond lengths)

Molecule	**CO_2**			**SiO_2**		
Basis set	**STO-3G**	**3-21G**	**4-31G****	**STO-3G**	**3-21G**	**4-31G****
Q(O)	−0.233	−0.541	−0.470	−0.485	−0.753	−0.667
$n(M$–O)	0.463	0.500	0.632	0.304	0.417	0.523
midpoint ρ	0.466	0.497	0.539	0.205	0.197	0.236

[a] Where Q(O) is the net charge on oxygen, $n(M$–O) is the bond overlap population, and midpoint ρ is the electron density at the midpoint of the bond.

that the net oxygen charge, Q(O), depends strongly upon the choice of basis set, with split valence basis sets giving larger apparent charge separation than either minimal or polarized basis sets. Even more variability would be observed if we considered charge partitionings obtained by the methods of Löwdin or Roby (see Hehre et al., 1986, for details and references), which are probably sounder in principle than the Mulliken scheme but more complicated and not so widely used. Even more ambiguous results are obtained with very large basis sets, which have diffuse and polarization functions. Considerable basis-set dependence is also seen in Table 7.1 for another nonobservable, $n(M\text{–O})$, and for the observable electron density (ρ) at the midpoint of the bond. Analysis of the *absolute* covalency on the basis of Mulliken net charges or overlap populations is therefore very dubious, and apparent agreement between such calculated charges and charges obtained through analysis of experimental data such as electron density distributions is probably meaningless. Discussion of *relative* covalency may be more meaningful; for example, from the data in Table 7.1 we could conclude that CO_2 is *more covalent* than SiO_2 since it has lower Mulliken net charges and higher overlap populations. In addition, the observable electron density is higher near the bond midpoint in CO_2.

Neither molecular calculations nor Mulliken partitioning schemes are unique in encountering such difficulties in defining charge distribution. Band calculations can also be charge partitioned, giving results depending upon the partitioning scheme employed as well as upon the material and the computational method used. In general, nonobservables can give us only knowledge of relative charge-distribution properties, and these only when equivalent charge partitioning methods and closely related compounds are compared. Appropriate uses of such nonobservables will be considered in this book; their unfortunately common misuses will be ignored. More detailed analysis of charge-distribution parameters is, of course, possible. We might examine not just total atomic-orbital populations summed over all occupied molecular orbitals, but the mixing of atomic-orbital character in one or more sets of molecular or band orbitals. Here, again, the results depend upon the method of charge-distribution analysis. Generally, such approaches exaggerate the extent of covalency. A charge distribution that is either neutral or highly polar, summed over all orbitals, may still have some orbitals with substantial mixing of the contributions from different centers.

Can an absolute description of covalency versus ionicity be obtained from *observable* properties? First, bond type is generally defined in principle in terms of the total electron density, since the molecular energy is a unique functional of the electron density (Hohenberg and Kohn, 1964). From x-ray diffraction, total densities are available, but the problem is to determine which aspects of the data are most informative. We can inspect the topology of the total density in the way described by Bader and Nguyen-Dang (1981) and thereby develop an objective partitioning scheme, yielding charges in atomiclike regions. One can also partition the charge density based upon readily observable features in the charge density, such as minima along a bond (Sasaki et al., 1980), fit the experimental charge density to a model of multipoles centered on the nuclei, and sum the charges in the various multipoles (Stewart and Spackman, 1981), giving charges on "pseudoatoms." Numerical charges obtained using the different methods are very different, with the scheme of Sasaki et al. (1980) giving Si charges around 2+ in silicates, and that of Stewart and Spackman (1981) giving values around 1+. We note, with approval, the statement in Stewart and Spackman (1981):

> Because of the continuous variation of the electron distribution in molecules or crystals, the counting of electron charge is hopelessly dependent on the nature of the distribution function over which the integration is taken. Clearly, the charge of an atom in a molecule or crystal is not an observable; it is arbitrary.

However, just as for the case of CO_2 and SiO_2 discussed above, charge quantities may well have meaningful *relative* values even if their *absolute* values are not meaningful. Sasaki and co-workers have evaluated effective charges using a consistent approach for a wide range of different minerals and find trends that appear to be reasonable. For example, the *M*2 site in orthopyroxenes consistently shows lower charges for formally divalent ions like Co^{2+} than does the *M*1 site, consistent with a lower ionicity (Sasaki et al., 1982).

More complete information is, of course, present in maps of the total electron distribution, but, since such maps closely resemble those obtained by superimposing free atoms, it is customary to examine density difference or $\Delta\rho$ maps (see Section 2.1.1). Positive density differences (i.e., where the molecular or crystal electron density is larger than that from the separated atoms) have traditionally been considered evidence of covalency. Many studies on mineral systems have established that Si–O bonds show positive $\Delta\rho$ values, either along the bonds or internal to Si–O–Si bridging bonds. Studies on other oxides (e.g., BeO) generally show smaller deformation densities (Downs and Gibbs, 1987). High-level quantum-mechanical calculations on model molecules give $\Delta\rho$ maps for Si–O bonds that match semiquantitatively against experiment (Gibbs, 1982). However, there are significant problems with such an approach. First, many strong bonds show no density accumulation compared to superimposed spherical free atoms. Schwarz et al. (1985) have proposed that the proper atomic reference state is the oriented atoms, with a proper quadrupolar interaction of charge distributions. A similar point has been made by Hall (1986). Although this approach recovers positive $\Delta\rho$ values along the bond for most, if not all, materials, the $\Delta\rho$ values obtained may not relate well to other properties such as bond energies. Indeed, Spackman and Maslen (1986) have established that the superimposed spherical atom electron densities (which they call "promolecular") give a substantial fraction of the experimental molecular binding energy, except for some aberrant homonuclear diatomics like H_2. Thus H_2, rather than being the prototype chemical bond, is an exceptional case (Hirshfeld and Rzotkiewicz, 1974) in its dependence of molecular binding upon charge-density accumulation. If positive values of $\Delta\rho$ along the bond are not necessary for binding, it may well be that the magnitudes of $\Delta\rho$ will not in general correlate with chemical bonding energies. Indeed, six-coordinate Si shows higher $\Delta\rho$ peaks along the bond than does four-coordinate, although one would expect lower bond energies in the six-coordinate case. Thus, the difference density, although a good observable for testing the quality of calculations, may not lead to any fundamental understanding of bonding.

Effective atomic charges also appear in a number of simple expressions for other observables, such as dipole moments, electric-field gradients, NMR chemical shifts, and photoelectron binding energy shifts. Good correlations of such properties with effective charges are sometimes obtained for restricted classes of materials (Huheey, 1983). On occasion, a set of charges obtained by fit to one type of experimental data can be used to interpret some other type of data. However, there does not appear to be any way to determine effective charges that accurately describe a range of properties. More accurate and quantitative theoretical analysis of properties inevitably shows deficiencies in simple effective charge-based models. We will, therefore, not attempt to develop a new consistent set of effective atomic charges from either calculation or experimental data.

There have also been attempts to evaluate ionicity and covalency in terms of the fit of limiting models to particular pieces of experimental data. For example, Rosenberg et al. (1978) found that their Compton scattering results for SiO_2 fit better to a $Si^{4+}(O^{2-})_2$ than to a $Si^0O_2^0$ model. However, their final model, in which the O^{2-} wave functions are orthogonalized to the Si cores, actually has considerable electron density on the Si, as established by Fowler (1981) in his study of Si x-ray emission spectra. Thus, even diametrically opposed limiting models, if they properly satisfy orthonormality conditions, may not really be that much different. Slater (1965) has noted the fundamental similarity of charge distributions in solids obtained from ionic- or covalent-limit models. Nonetheless, an ionic-limit model for the Compton scattering profile of SiO_2 may be preferable primarily because the O 2*p* atomic orbitals of such a model are very diffuse and provide a better description of the very low-momentum region contributing to the Compton peak.

The effect of ionicity on methods for computer simulation of solids of the type described in Section 3.13 has been discussed by Catlow and Stoneham (1983). They correctly note the arbitrary nature of charge partitioning in solids and present a strong case for a potential model based upon interionic pair potentials. These potentials are shown to be capable of evaluating a range of crystalline properties, including some substantially different from those employed in their parametric construction. Nevertheless, such potentials often fail to provide accurate descriptions for silicates, borates, and certain other materials.

7.1.2. Calculation of geometric structures and their (phase) relations: The example of the SiO_2 polymorphs

There have been several recent studies of the crystal structures of the 4-coordinate polymorphs of SiO_2. Dovesi et al. (1987) calculated the electronic structure of quartz using a Hartree–Fock–Roothaan band method with an STO-3G basis set. They also minimized the energy with respect to the Si–O distance and Si–O–Si angle. Their results for Mulliken charges on Si and O are virtually identical to those obtained by Gibbs (1982) in Hartree–Fock–Roothaan MO calculations with an STO-3G basis set on the $[(OH)_3Si]_2O$ molecule. Their calculated Si–O distance of 1.605Å and Si-O-Si angle of 133° are slightly smaller than the experimental values. Gibbs (1982) obtained an Si–O distance of 1.60Å and Si–O–Si angle of 140° as the global minimum in $[(OH)_3Si]_2O$. The deformation density maps of Dovesi et al. (1987) showed no buildup of electron density in the Si–O bond.

Both equilibrium Si–O–Si angle and charge density are known to be sensitive to the presence of other atoms, the effect of substituents, and to basis-set effects. They may also, of course, be influenced by electrostatic effects from the other atoms of an extended lattice. The reason for the small differences between the $[(OH)_3Si]_2O$ and α-SiO_2 STO-3G results is not currently apparent.

Nada et al. (1990) have recently performed HFR band calculations on the α-quartz and stishovite polymorphs of SiO_2 using polarized split valence bases (up to 6-21G*, with both Si 3*d* and O 3*d* functions). They obtained lattice constants within a few percent of experiment and correctly predicted the α-quartz polymorph to be more stable than stishovite. The inclusion of 3*d* functions on Si substantially lowered the total energy (and, less significantly, the Mulliken charge distribution) in α-quartz but had relatively little effect in stishovite. Partial densities of states from this calculation also gave a reasonable representation of the x-ray emission spectra of α-quartz. This was a heroic computational study that nicely shows the potential of the HFR band method. Such calculations could probably be made less demanding through the use of valence-only basis sets (e.g., Silvi and Bernard, 1987) and will probably become much more common within mineralogy in the future.

Self-consistent LCAO results within the density-functional formalism have also recently been obtained for α-SiO_2 (Xu and Ching, (1988a,b).

Calculated lattice constants were only about 1% different from experiment, but the unit cell was constrained to have the experimental shape. The calculated bulk modulus for α-SiO_2 using this fixed-shape unit cell was too large, presumably because such a model forces a volume reduction to be associated with a reduction of Si–O distance while the real structure compacts almost entirely by reducing the Si–O–Si angle (see the discussion of SiO_2 glass, in Section 8.1.1). This LCAO approach also apparently gives no charge buildup along the Si–O bond (Xu and Ching, 1988a). However, studies on both α-SiO_2 (Gibbs, 1982) and coesite (Geisinger et al., 1987) have experimentally shown such buildup of charge, and the major features of the experimental maps have been reproduced by large-basis-set (6-31G*) SCF Hartree–Fock–Roothaan calculations on $[(OH)_3Si]_2O$ (Geisinger et al., 1987).

As described briefly in Chapter 3, a promising new method of electronic structure calculation utilizing combined molecular-dynamics and density-functional theory has recently been developed by Car and Parinello (1985). This approach has recently been applied to cristobalite, yielding equilibrium lattice constants within 1% of experiment (Allan and Teter, 1987), as shown in Table 7.2. New oxygen nonlocal pseudopotentials were also an important part of this study. Such a method is a substantial advance upon density-functional pseudopotential band theory, since it can be efficiently applied both to amorphous systems and to systems at finite temperature.

Progress has also been made in the simulation of the structures of 4-coordinate SiO_2 polymorphs both by using force fields fitted to experiment or to *ab initio* calculations, and by modified electron-gas calculations including the effect of oxygen polarization. Catlow et al. (1985) and Sanders et al. (1984) have established that O–Si–O angle-dependent terms in the energy are needed to give proper structures and compressibilities

Table 7.2. Experimental and calculated unit-cell parameters and atom positions for α-cristobalite, and their percent difference. The numbers in parentheses are the standard deviations of the last significant digit for the time-of-flight neutron powder diffraction data. The atom locations are given in units of the primitive translation lengths $a = b$ and c

Parameter	Experimental value (at 10 K)	Calculated value	Difference (%)
Si $x = y$	0.3047(2)	0.3030	−0.56
($z = 0$)			
O x	0.2381(2)	0.2380	−0.04
y	0.1109(2)	0.1112	+0.27
z	0.1826(1)	0.1825	0.05
a (Å)	4.9570(1)	4.959	+0.04
c (Å)	6.8903(2)	6.906	+0.23

Source: From Allen and Teter, 1987.

for SiO_2. Lasaga and Gibbs (1987) have obtained a force field with angle-dependent terms from calculations on $(H_3Si)_2O$ and $Si(OH)_4$ molecules. Jackson and Gordon (1988b) have added to the original modified electron-gas approach a polarizable oxygen atom described by a shell model, improving agreement with experiment for Si–O–Si angle in the 4-coordinate SiO_2 polymorphs.

Many of the above structural studies have investigated bulk modulus and variation of structure with pressure as well as the static structure at absolute zero temperature. O'Keeffe et al. (1980) and O'Keeffe and Gibbs (1985) have calculated the bulk modulus of quartz by extracting bending force constants from $(H_3Si)_2O$, first at the STO-3G and then at the 6-31G** basis-set level, in each case obtaining reasonable agreement with experiment. Lasaga and Gibbs (1987) have used the quantum-derived central-force-field potentials to evaluate the bulk modulus and the change in Si–O–Si angle with pressure, and Catlow et al. (1985) have obtained equivalently good results using empirical potentials.

There has been little study of the phase relations of SiO_2 polymorphs, except for that of Nada et al. (1990). The structures are so complicated and require geometrical optimization over so many degrees of freedom that most investigators have been content with studying a single polymorph. The only study besides Nada et al. (1990) has been on the relationship between stishovite, a high-pressure polymorph with Si in 6-fold coordination in a TiO_2 (rutile) structure, a hypothetical CaF_2 (fluorite) structure-type polymorph with 8-coordinate Si, and distorted fluorite structures. These high-coordination-number structures have smaller unit cells, higher symmetry, and longer bond distances but closer packing, so that fewer parameters need to be minimized, and shape constraints to potentials and covalent bonding contributions are less important.

Early rigid-ion modified electron-gas studies (Tossell, 1980b) predicted that the most stable form of SiO_2 at atmospheric pressure should be four-coordinate and gave a predicted rutile → fluorite structure transition pressure of 390 GPa, far above the maximum pressure in the Earth's mantle. Carlsson et al. (1984) calculated the equation of state of fluorite-structured SiO_2 using the augmented-spherical-wave method (see Appendix C) and concluded that the previous MEG results for structure and transition pressure are probably reliable. They also noted that the band gap of fluorite-type SiO_2 could actually increase with pressure up to about 100 GPa and would only vanish at a volume equal to about 40% of the atmospheric pressure value, corresponding to a pressure on the order of 1000 GPa. Later, augmented-plane-wave calculations (see Appendix C) gave very similar results to those of Carlsson et al. (1984), and stabilized rigid-ion MEG calculations gave results comparable to those of Tossell (Bukowinski and Wolf, 1985). As noted by Bukowinski and Wolf (1985), the density calculated for fluorite-type SiO_2 is no larger than that observed for stishovite (Fig. 7.1), suggesting that its stability versus that of

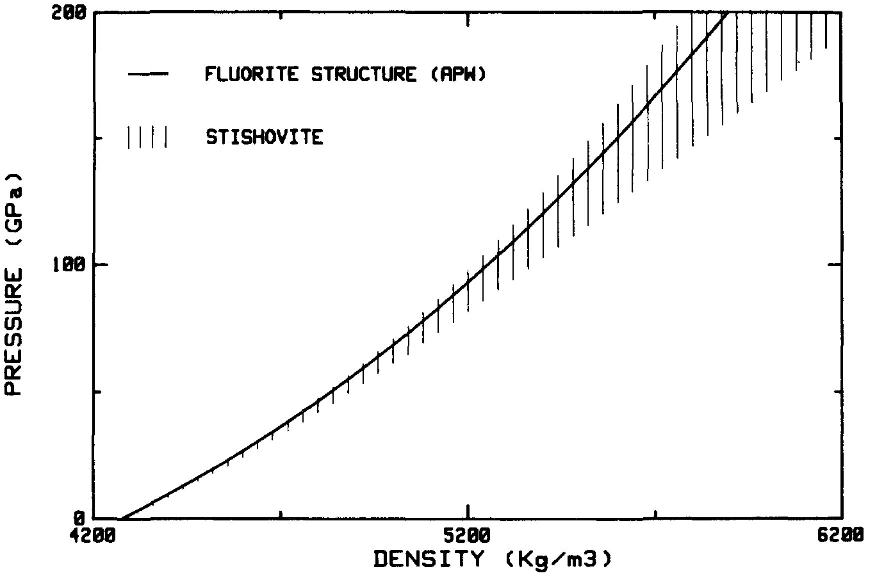

Fig. 7.1. Equation of state (EOS) of silica calculated using the modified electron-gas method by Bukowinski and Wolf (1985) and showing pressure–density relations for stishovite and fluorite-type SiO_2.

stishovite will not increase with pressure. They also used the MEG method to calculate the phonon spectrum, and from it estimated the Debye temperature and the entropy difference between fluorite–SiO_2 and stishovite, finding the entropic contribution to the free energy to be different by only about 0.1 eV per formula unit at 3000 K. It is thus clear that the fluorite-type SiO_2 should not be stable compared to stishovite within the pressure and temperature range of the Earth's mantle (see Fig. 7.12).

Recently, the FLAPW density-functional method has been used by Park et al. (1988) to investigate the structures and stabilities of rutile, fluorite, and distorted fluorite (space group $Pa\bar{3}$) structure SiO_2 at atmospheric and high pressure. They found that the rutile structure (i.e., stishovite) was the most stable of the three phases at atmospheric pressure, and that its structure, density, and bulk modulus were reasonably well described by the FLAPW calculations. The fluorite polymorph was found to be of highest enthalpy for all pressures, while the $Pa\bar{3}$ polymorph became the most stable above 60 GPa. This structure is quite unusual in having O–O distances of <2.4 Å. It was conjectured that other structures of even lower symmetry than the cubic $Pa\bar{3}$ might be even more stable. Evidence was also presented that the assemblage MgO (sodium chloride structure) + SiO_2 ($Pa\bar{3}$) would be denser than $MgSiO_3$ perovskite at pressures above 100 GPa, raising the possibility of high-pressure decomposition of perovskite to the mixed oxides. Calculations of mineral stability at high pressures in relation to the interior of the Earth are further discussed in Section 7.2.

7.1.3. Pauling's rules reinterpreted

The five rules governing the geometries of "ionic" crystals formulated by Linus Pauling in 1929 (Pauling, 1929) have since been widely used and taught by mineralogists, crystallographers, and solid-state chemists. They were intended to serve as generalizations to help in the solution of complex crystal structures using the experimental methods available at the time they were published. Although Pauling's Rules can be regarded as empirical generalizations, and their value lies in the extent to which they work for real structures, they have frequently been identified with the ionic model, and their success has been used as an argument to support the validity of the ionic model for many compounds.

The developments in quantum-mechanical methods and their applications to minerals and related substances that have formed the subject matter of this book lead to a reappraisal of Pauling's Rules. Calculations on molecular clusters (see in particular Chapters 3, 4, and 5; also Tossell and Gibbs, 1978; Gibbs et al., 1981) have clearly shown that many of the geometric predictions of Pauling's Rules are consequences not only of ionic forces but also of covalent effects. However, a limitation of the predictive power of calculations on molecular clusters or small fragments is the inability to assess the relative energies of structures formed by different ways of linking together such clusters. This problem has been addressed by Burdett and McLarnan (1984), who undertook band-structure calculations using the tight-binding approximation (in effect, molecular-orbital calculations applied not to clusters but to the crystal as a whole; see Appendix C) specifically to reappraise Pauling's Rules in their publication entitled "An orbital interpretation of Pauling's Rules." Their calculations were of the extended Hückel type (Hoffman, 1963; Hoffman and Lipscomb, 1962) and employed the standard tight-binding approach (e.g., Whangbo et al., 1978). The following discussion is based largely on their analysis.

Rule 1: Ionic radii and radius ratio. "A coordinated polyhedron of anions is formed about each cation, the cation–anion distance being determined by the radius sum and the coordination number of the cation by the radius ratio." (Pauling, 1929)

This rule centers on the much-used concept of ionic size, a concept that has been refined, or rather been better defined in recent years by the use of pseudopotential radii (Zunger and Cohen, 1978). Thus, the use of pseudopotential radii (r_l) to define atomic size more closely, and the identification of r_1^{-1} with electronegativity, has enabled the effectiveness of models based on hard-sphere atoms (or ions) to be explained in terms of modern ideas of electronic structure. In effect, the first rule is empirically valid and has predictive power not because it is valid to regard atoms in crystals as charged hard spheres of a particular radius, but because the qualitative concept of atomic size is still valid in the framework of modern electronic structure theories.

In rationalizing crystal structures and relationships involving structural families using the concepts of pseudopotential radii, progress has also been made using structure sorting procedures based on atomic properties (St. John and Bloch, 1974; Zunger and Cohen, 1978; Bloch and Schatteman, 1981; Burdett et al., 1981). Further discussion of this approach is given later in this section, after all five of Pauling's rules have been discussed.

Rule 2: Electrostatic valence sums. "In a stable coordination structure, the electric charge of each ion tends to compensate the strength of the electrostatic valence bonds reaching to it from the cations at the centers of the polyhedra of which it forms a corner; that is, for each anion

$$\zeta = \sum_i \frac{Z_i}{\nu_i} = \sum_i s_i$$

(Pauling, 1929) (where $-\zeta$ is the charge of an anion, i runs over all cations coordinated to that anion, Z and ν_i are the charge and coordination numbers, respectively, of cation i).

This rule requires that highly charged anions should be placed at sites of large positive potential (and hence high bond-strength sums). Because formal charge is not a quantity appearing in the molecular-orbital formalism, such calculations cannot be used to test the valence sum rule numerically (i.e., to predict departures of $\Sigma_i s_i$ from ζ), although they can be used to predict qualitatively if more highly charged anions should occupy sites with larger bond sums.

Burdett and McLarnan (1984) do this by considering the compound MgAlON, a wurtzite-derivative structure with two types of anion and cation species differing in charge. In such a structure, various ordered arrangements of anions and cations are possible, the one adopted being of space group $Pbc2_1$ and having half of the anions coordinated to three atoms of Mg and one of Al and the other half coordinated to 3Al and 1Mg (O'Keeffe et al., 1981). This arrangement produces a unit cell with $a = 2a_0$, $b = b_0$, and $c = c_0$ (where a_0, b_0, c_0 are the axes of the smallest orthohexagonal cell of hexagonal close packing) and is labeled a (2,1) unit cell. It is illustrated in Fig. 7.2, along with three other possible arrangements involving ordering of equal numbers of two cations over the metal sites and producing (1,1) unit cells [structures labeled W-$Pmn2_1(1,1)$;

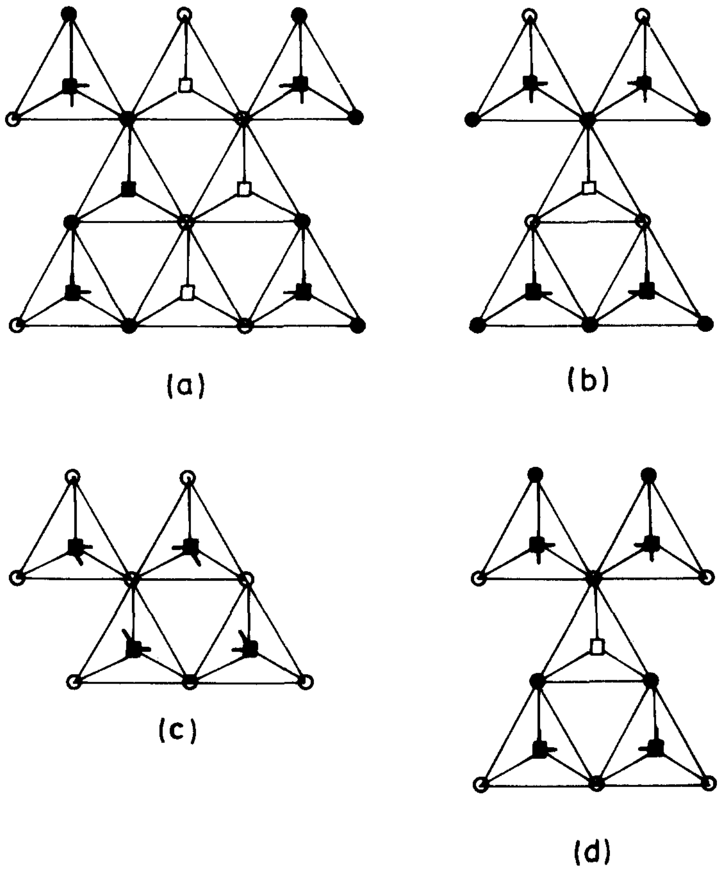

Fig. 7.2. Structures of the compound MgAlON with various arrangements of anion and cation: (a) (2,1) unit cell; $W\text{-}Pbc2_1(2,1)$; (b) (1,1) unit cell; $W\text{-}Pmn2_1(1,1)$; (c) (1,1) unit cell; $W\text{-}P3m(1,1)$; (d) (1,1) unit cell; $W\text{-}Pmc2_1(1,1)$. The anions are hexagonally close packed, and the cations fill tetrahedral holes. Filled squares = Al(0),N(⅜); empty squares = Mg(0),O(⅜); filled circles = Al(½),N(⅞); empty circles = Mg(½),O(⅞). Only the cation tetrahedra at Z = O are drawn (after Burdett and McLarnan, 1984; reproduced with the publisher's permission).

$W\text{-}P3m(1,1)$; $W\text{-}Pmc2_1(1,1)$, where the favored structure would be labeled $W\text{-}Pbc2_1(2,1)$].

Bond-strength sums for the sites with 3Mg + 1Al and 3Al + 1Mg, respectively, are 2.25 and 2.75 (from the solution of $\Sigma_i S_i$ given previously). These are the sites found in the structures labelled $W\text{-}Pbc2_1(2,1)$, $W\text{-}Pmn2_1(1,1)$, and $W\text{-}P3m(1,1)$. In the $W\text{-}Pmc2_1(1,1)$-type structure every anion is coordinated by 2Mg + 2Al, and the bond-strength sum is then 2.5. Calculations were performed in order to show that for the first three structures nitrogen atoms will occupy the sites of higher bond sum and that these structures all lie lower in energy than the *W-Pmc*2_1(1,1) type in which N and O atoms see the same bond sum. This was done by calculating the orbital wave function of a material in which O and N atoms are both replaced by hypothetical atoms intermediate in size and electronegativity, and determining the charge on each atom in the model crystal via a population analysis (Burdett, 1980). Results are shown in Table 7.3 and confirm that sites with small bond-strength sums (which should be occupied by O rather than N) are more electron-rich. Further calculations on the site charges and the energies of all four structures performed using values for actual O and N atoms are given in Table 7.4. The first four results are for the structures with O occupying the sites with lower bond-strength sum than N, as Pauling's Rule predicts; the last four have the positions of O and N reversed. The calculated energies confirm the prediction of Rule 2: The most stable arrangements (largest negative energies) are those where O occupies sites of lower bond strength than N; where the sites are of equal bond-strength sum [i.e., in the *W-Pmc*2_1(1,1) type] stability is less; least stable are the structures where N occupies sites of lower bond-strength sum than O.

Burdett and McLarnan (1984) went on to test the valence sum rule by assessing a further prediction implied in the rule, namely that anions of the same electronegativity should be found in sites of equal bond sum. This was confirmed by calculating that, when hypothetical anions with equal parameters midway between O and N are used, the most stable structure is the *W-Pmc*2_1(1,1) type, where all the sites are of equal bond-strength sum. Also investigated was the Zachariasen–Baur extension of the second rule (Baur, 1970), stating that oversaturated anions should

Table 7.3. Electronic charges in $MgAl(O,N)_2$ structures[a]

$\sum_i s_i$	**Structure**	q
2.75	*W-Pbc*2_1(2,1)	7.5238
2.75	*W-Pmn*2_1(1,1)	7.5223
2.75	*W-P*3*m*(1,1)	7.5213
2.5	*W-Pmc*2_1(1,1)	7.5919
2.5	*W-Pmc*2_1(1,1)	7.5932
2.25	*W-Pbc*2_1(2,1)	7.6643
2.25	*W-Pmn*2_1(1,1)	7.6653
2.25	*W-P*3*m*(1,1)	7.6653

[a] The number, q, of valence electrons on sites with different electrostatic bond strength sums in $MgAl(O,N)_2$. Four different structures with this composition are considered. In these calculations all anions were given identical parameters intermediate between those of O and N, so that variations in q reflect differences associated with the sites, not the nature of the anions.

Source: After Burdett and McLarnan, 1984.

Table 7.4. Bond sums, charges, and energies of MgAlON variants

	$\sum_i s_i$(vu)		q				
Structure[a]	**O**	**N**	**O**	**N**	**Al**	**Mg**	**Energy (eV)**
$W\text{-}Pbc2_1(2,1)$	2.25	2.75	7.7647	7.3654	0.8255	0.0444	−291.212
$W\text{-}Pmn2_1(1,1)$	2.25	2.75	7.7659	7.3627	0.8209	0.0505	−291.212
$W\text{-}P3m(1,1)$	2.25	2.75	7.7673	7.3586	0.8271	0.0470	−291.224
$W\text{-}Pmc2_1(1,1)$	2.5	2.5	7.7127	7.4349	0.8269	0.0255	−291.153
$W\text{-}Pmc2_1(1,1)^*$	2.5	2.5	7.7116	7.4383	0.8231	0.0270	−291.143
$W\text{-}Pbc2_1(2,1)^*$	2.75	2.25	7.6508	7.5302	0.6813	0.1377	−290.742
$W\text{-}Pmn2_1(1,1)^*$	2.75	2.25	7.6502	7.5310	0.6734	0.1453	−290.733
$W\text{-}P3m(1,1)^*$	2.75	2.25	7.6510	7.5289	0.6787	0.1414	−290.743

[a] Eight possible structures of MgAlON, the bond sums at the anion sites, the number of valence electrons associated with each atom, and the calculated energy per formula unit. Structures marked with an asterisk have the same cation arrangement as their unstarred counterparts, but have the positions of O and N reversed. The top three structures have the anion ordering expected from Pauling's second rule, the middle two have all anions in sites with the same bond sum, and the bottom three have an ordering opposite that expected. MgAlON is believed to be isostructural with α-LiSiON, which has the $W\text{-}Pbc2_1(2,1)$ structure.

Source: After Burdett and McLarnan, 1984.

form unusually short bonds. Using the calculations on the eight MgAlON structure types listed in Table 7.4, it was shown that bond-overlap populations of all crystallographically distinct Mg–O, Al–O, Mg–N, and Al–N bonds correlate inversely with bond-strength sum at the anion (i.e., with increasing anion saturation). Since bond-overlap populations are a measure of bond strength and correlate inversely with bond lengths, we see here a prediction by "molecular-orbital" methods of the bond-length variations observed by Baur, that is, that increasing bond-overlap population and hence decreasing bond length correlates with decreasing anion saturation (decreasing bond strength sum).

Rules 3 and 4: Sharing of polyhedral elements. "The presence of shared edges, and particularly of shared faces, in a coordinated structure decreases its stability; this effect is larger for cations with large valence and small coordination number, and is especially large in case the radius ratio approaches the lower limit of stability of the polyhedron.

"In a crystal containing different cations, those with large valence and small coordination number tend not to share polyhedron elements with each other." (Pauling, 1929)

These two rules can be discussed together, since Rule 4 is obviously a corollary of Rule 3; both rules deal with systems of linked polyhedra and, in Pauling's original formulation, the absence of shared elements is attributed to the destabilizing effects of cation–cation Coulombic repulsions. Although many examples of structures violating these rules are now known (e.g., β-BeO, $BeCl_2$, SiS_2, all of which contain edge-sharing tetrahedra), they are satisfied frequently enough to be useful in prediction.

Burdett and McLarnan (1984) examined these rules by comparing the observed wurtzite-type structure of α-BeO with alternative structures also having a hexagonal close-packed oxygen framework, but involving varying amounts of edge sharing among BeO_4 tetrahedra. Twenty-two such alternative structures are possible (hence a total of 23 structures), and for the composition BeO they all satisfy the electrostatic valence rule (Rule 2) exactly, so that from the standpoint of Pauling's Rules they should differ in energy only because they differ in the extent of edge sharing. Burdett and McLarnan (1984) evaluated the energies of these structures, both using their covalent band-structure calculations and using a pure point-charge Madelung sum, the simplest kind of ionic model. When the energies are plotted as a function of the number of shared edges (as shown in Fig. 7.3) for both the covalent band-structure model and purely electrostatic approach, a simpler linear relationship is observed. Hence both purely electrostatic and purely orbital models predict that counting shared edges is roughly equivalent to working out total energies.

In order to understand this variation in covalent bond-structure energy with edge sharing, Burdett and McLarnan (1984) examined the anion coordination in these 23 structures. They emphasize the importance of the anions (the atoms on which the majority of the electron density resides) and show, using extended Hückel molecular-orbital calculations on OBe_4^{6+} "molecules" for the five kinds of coordination polyhedra occurring in the structures (see Fig. 7.4) that energies calculated for such anion polyhedra (Table 7.5) approximate crystal energies when summed together. Having calculated the relative energies of these polyhedra, and shown how they appear to exercise the dominant influence on the total energies of the crystal, they develop the idea that increasing the number of shared edges increases the number of less stable anion coordination environments in a structure.

It is important to note that, although this analysis arrives at the same conclusion as does an ionic interpretation, the reasons are very different. In particular, the different anion coordination geometries do not differ in energy because of increased cation–cation repulsions at tighter Be–O–Be angles (as suggested by the original approach of Pauling, 1929). Rather, the energy differences are due almost entirely to the ability of the central oxygen atom to form stronger bonds when the Be atoms are tetrahedrally coordinated. This can be seen from the bond-overlap populations calculated for the five OBe_4 molecules (Table 7.5), where the Be–O overlap population increases for the more stable molecules. In contrast, the Be–Be overlap population correlates the wrong way and the less stable molecules have less total Be–Be repulsion, as measured by average bond-

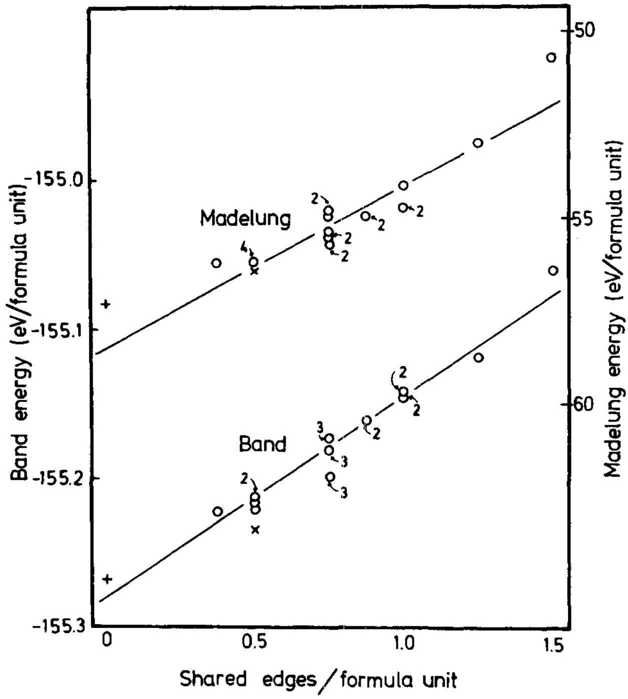

Fig. 7.3. The relationship between number of shared edges between cation tetrahedra and both the electrostatic Madelung energy and the one-electron covalent band-structure energy for 2 real observed and 21 hypothetical polymorphs of BeO. The structure types plotted are the wurtzite (α-BeO) type (+), the β-BeO type (X), and the 21 hypothetical dipolar tetrahedral structures with (1,1) or (2,1) unit cells. The small numbers by some of the points show how many points are represented by the single symbol (after Burdett and McLarnan, 1984; reproduced with the publisher's permission).

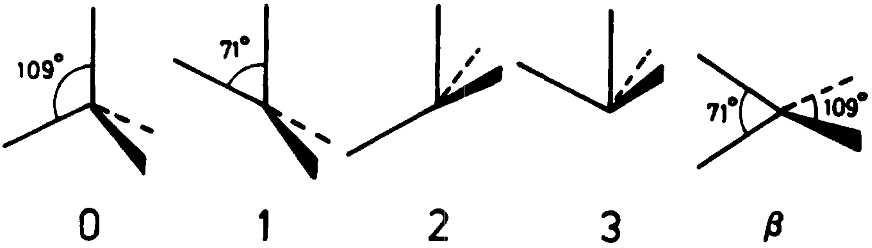

Fig. 7.4. The five different oxygen coordination environments found in the 23 structure types shown in Fig. 7.3. Conformation 0 is a regular tetrahedron. Conformations 1, 2, and 3 are derived from a tetrahedron by replacing tetrahedral angles $\theta = 109.47°$. with angles of $180° - \theta$ between 1, 2, and 3 pairs of bonds, respectively. Arrangement β, found only in β-BeO, has local symmetry *mm*2 (after Burdett and McLarnan, 1984; reproduced with the publisher's permission).

Table 7.5. Energies and overlap populations in OBe_4 molecular units[a]

"Molecule"	E (eV)	E' (eV)	Bond overlap populations	
			<Be–O>	<Be–Be>
0	0	0	0.0935	−0.0049
1	0.0255	0.0162	0.0905	−0.0039
2	0.0654	0.0469	0.0863	−0.0032
3	0.1221	0.0930	0.0803	−0.0028
4	0.0201	0.0117	0.0911	−0.0040

[a] The relative energies E of the 5 different OBe_4 "molecules" in Fig. 7.4. The energies E' for the same molecules are computed after dropping all direct ligand–ligand interactions. The average Be–O and Be–Be bond-overlap populations refer to the calculation including these interactions.

Source: After Burdett and McLarnan, 1984.

overlap populations. This result is not as surprising as it first appears; the Be atoms are very electron-poor, so that bringing them together enhances small bonding interactions between them. Further support for the importance of Be–O interactions rather than Be–Be interactions is given by data in column three of Table 7.5. This shows relative energies of the five OBe_4 "molecules" given by a calculation in which all overlap integrals and Hamiltonian elements between different Be atoms were set equal to zero (i.e., a calculation ignoring all ligand–ligand overlaps). Nevertheless the energy differences are proportional to, and nearly as large as, those obtained by the calculations including ligand–ligand overlaps.

Burdett and McLarnan (1984) also confirmed the relative dominance of Be–O interactions in stabilizing the structures by performing band-structure calculations on five of the possible BeO structures (i.e., on the infinite crystals rather than finite molecules). Bond-overlap populations obtained for the infinite crystals confirm the trends noted above for OBe_4 "molecules." The question remains as to why the results of the covalent band-structure calculations correlate so strongly with the results of Madelung calculations for the 23 possible BeO structures (Fig. 7.3). At the heart of this problem is an interesting correlation noted by Burdett and McLarnan (1984) between covalent energies of OBe_4^{6+} molecules of different geometries and the sum of the Be–Be distances ($\Sigma_{ij}\ 1/r_{ij}$). The authors note that the geochemical implications of this result are identical to the predictions of the valence-shell electron-pair repulsion model (see Chapter 5 and Burdett, 1980; Gillespie, 1972).

Rule 5: Parsimony. "The number of essentially different kinds of constituents in a crystal tends to be small." (Pauling, 1929)

This rule was regarded by Bragg (1930) as a corollary of Rule 1 (which limits variation in cation coordination number) and Rule 2 (which when combined with Rule 1 limits the number and type of cations around each anion). It is not clear that this rule can be elucidated using any particular electronic structure model, except to note that it is a consequence of the short-range nature of interatomic potentials. In fact, covalent forces in the extended Hückel approximation fall off much more rapidly than electrostatic forces (the former energies decrease at least as r^{-3} rather than the r^{-1} dependence of electrostatic energies). Burdett and McLarnan (1984) also use arguments based on perturbation theory to show that orbital interactions operating solely between nearest-neighbor atoms act to favor identically coordinated anions.

Perhaps the more important questions raised by Rule 5, as Burdett and McLarnan (1984) point out, concern the extent to which it really is borne out by observation. For example, Baur et al. (1983) have developed a numerical index for the degree of parsimony in a crystal structure and have shown that, using this measure, many crystal structures are "not parsimonious but lavish in their use of different local environments." Also, the dominance of short-range forces is by no means obvious when ordered structures with extremely large unit cells are observed (e.g., a *c* dimension of 1500 Å in some SiC polytypes; Shaffer, 1969). The explanation of such structures poses problems for electrostatic as well as covalent models.

In addition to the reinterpretation of Pauling's rules developed by Burdett and McLarnan (1984), there have been a number of other studies related to various aspects of these standard rules. Due to the substantial number of errors in classifying *AB* compounds in terms of ionic radius ratio (e.g., Phillips, 1970; Tossell, 1980b), there have been numerous attempts to create "structure maps" that have two atomic quantities as coordinates and that can provide a unique separation of the different structure types. Such atom quantities may be related primarily to size or energy or to some combination of the two. Some of the most important such approaches are those of Mooser and Pearson (1959), Phillips (1970), and Simons and Bloch (1973).

During the time that such structural maps have been evolving, our capacity to calculate structural parameters directly quantum mechanically has expanded so that we can now calculate structures, and even reasonable energies, for different polymorphs of simple *AB* compounds, as explained earlier. The relative stabilities of NaCl and CsCl polymorphs of the alkali halides have been systematically studied by Cohen and Gordon (1975) using the MEG method.

While radius ratio rules generally predict correct structure types for the alkali halides in only about 50% of the cases, the MEG calculations (not even shell stabilized) correctly predict the NaCl structure to be more stable for 15 of the 16 compounds studied. Calculated structural parameters were also in good agreement with experiment, and calculated pressures for the NaCl → CsCl transition were in fair agreement with the limited experimental data available. These results indicate that preferred coordination numbers and structural types in alkali halides can be accurately predicted by an ionic model—the failure of the radius ratio rules is a failure of the much more restrictive rigid-ion model. Subsequent calculations by Muhlhausen and Gordon (1981) using the shell-stabilized MEG method for LiF and NaF correctly predicted NaF to be more stable in the NaCl structure than in either CsCl or sphalerite. For LiF, however, the sphalerite structure was predicted to be slightly more stable, in disagreement with experiment. A number of possible sources of minor errors in cohesive energies were considered for LiF, but no single reason for the incorrect prediction could be isolated. For less ionic compounds a more general connection between phenomenological structure sorting approaches and direct quantum-mechanical calculations has recently been made by Chelikowsky and Burdett (1986). They used *ab initio* pseudopotentials and a Gaussian basis set to calculate total energy versus lattice parameter for the β-Sn, rocksalt, and zincblende structures of the III–V semiconductor GaAs, obtaining the zincblende structure correctly as that of lowest energy. They then added perturbing potentials of opposite sign to the cation and anion, to simulate the creation of successively II–VI and I–VII compounds, and saw the expected change in the relative energies of the different crystalline forms (Fig. 7.5), with the rocksalt structure becoming progressively more stable until it was the preferred polymorph for the simulated I–VII compound. Based on Mulliken population analysis from their band structures, they could define an ionicity that could be related to that from the dielectric theory of Phillips (1970). The experimental pressure for the zincblende-to-rocksalt transition was found to be reasonably well correlated with this calculated ionicity (Fig. 7.6), as it had been for the ionicities defined by Phillips (1970). These results indicate that variations in core potential produce changes in both charge distribution and structural stability that are in agreement with experiment. Thus, the relative atomic potentials, rather than sizes, should be seen as the determinants of structure.

Advances in understanding the electrostatic valence-bond sum rule (Rule 2) have developed from the extension of this rule by Baur (1970), leading to an understanding of bond-length distortions for non-charge-balanced anions, the generalization to a valence strength sum incorporating interatomic distances by Brown (1981), and the demonstration by Gibbs et al. (1987) that calculated bond lengths follow scaling laws like that developed by Brown (1981; see Fig. 7.7 from Gibbs et al., 1987).

►

Fig. 7.5. Calculated (using *ab initio* pseudopotentials and a Gaussian basis set) equations of state (expressed in terms of total energy versus cell size in atomic volume) for various binary compounds with the β-Sn, rocksalt, and zincblende structures: (a) a III–V compound, namely GaAs; (b) a prototypical II–VI compound; (c) a prototypical I–VII compound (after Chelikowsky and Burdett, 1986; reproduced with the publisher's permission).

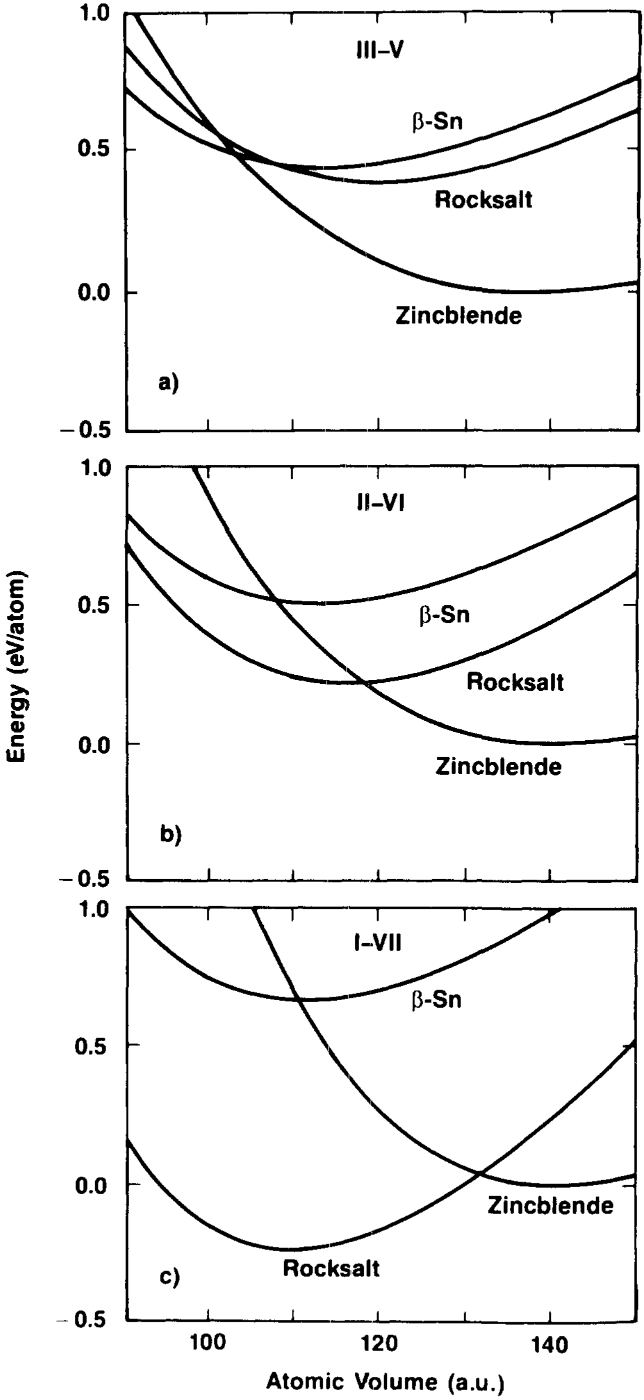
Energy (eV/atom)
1.0
0.5
0.0
−0.5
III–V
β-Sn
Rocksalt
Zincblende
a)
II–VI
β-Sn
Rocksalt
Zincblende
b)
I–VII
β-Sn
Zincblende
Rocksalt
c)
100
120
140
Atomic Volume (a.u.)

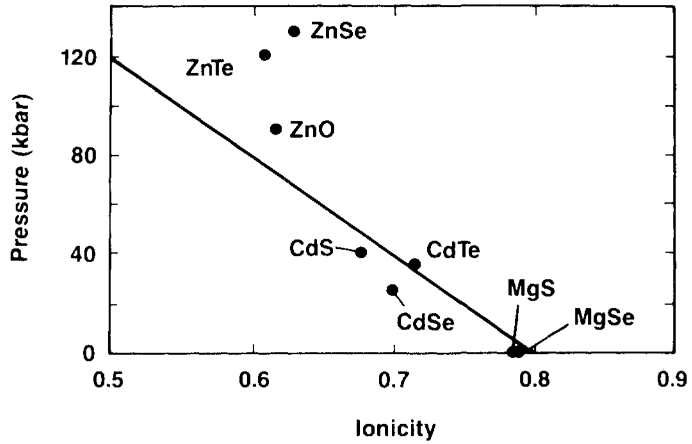

Fig. 7.6. Correlation between calculated ionicity and the transition pressure for the transformation from the 4-fold coordinated zincblende structure to the 6-fold coordinated rocksalt structure (after Chelikowsky and Burdett, 1986; reproduced with the publisher's permission).

Unfortunately, no quantum-mechanical basis for the existence of such scaling rules has yet been developed.

Effects arising from the sharing of polyhedral elements have also been studied more quantitatively, first using semiempirical approaches, as by Tossell and Gibbs (1976), and later using *ab initio* SCF Hartree–Fock–Roothaan theory (O'Keeffe and Gibbs, 1985). During this time, Si_2O_2 ring-containing molecules were first synthesized (Fink et al., 1984) and their properties studied theoretically (O'Keeffe and Gibbs, 1985; Kudo and Nagase, 1985). Both $(OH)_2Si$ 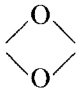 $Si(OH)_2$ and H_2Si 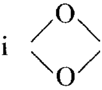 SiH_2 had calculated structures similar to those observed experimentally in tetramesitylcyclodisiloxane (Table 7.6), although the different substituents on Si clearly have some influence upon Si–Si distance since Si_2O_2 and tetramesitylcyclodisiloxane have appreciably different experimental values of this distance. Both calculated deformation density maps for $(OH)_2Si$ 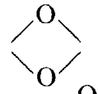 $Si(OH)_2$ (Fig. 7.8) and plots of localized molecular orbitals for H_2Si 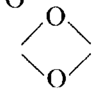 SiH_2 (Fig. 7.9) indicate the absence of Si–Si bonding in these molecules. Rather, the short, strong Si–O bond and the repulsion

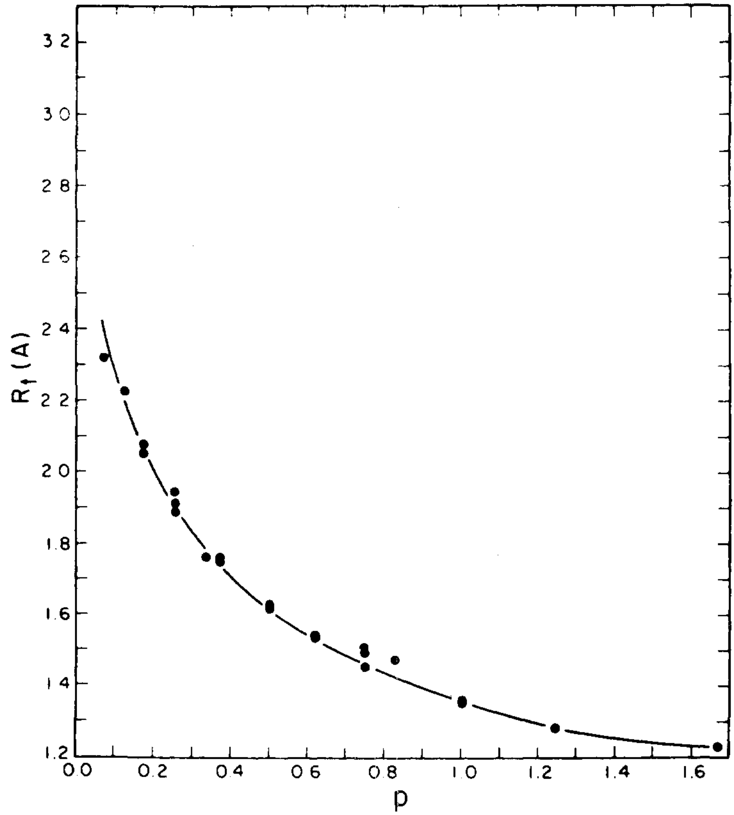

Fig. 7.7. A plot of theoretical X–O bond lengths (R_t in Å) for hydroxyacid molecules versus p, where p is the bond strength (s) divided by row number (r) for rows 1 and 2 in the Periodic Table. Bond strength (s) is cation charge divided by coordination number (from Gibbs et al., 1987).

Table 7.6. Observed and calculated dimensions (Å and degrees) of Si–O–Si–O rings

		Si–Si	O–O	∢Si–O–Si	Si–O
$H_4Si_2O_6$	6-31G*	2.420	2.303	92.7	1.670
	6-31G* (*)	2.375	2.320	91.3	1.660
	STO-3G	2.422	2.314	92.6	1.675
$H_4Si_4O_{10}$	STO-3G inner ring	2.419	2.316	92.5	1.674
	STO-3G outer ring	2.429	2.311	92.8	1.684, 1.669
Si_2O_2	6-31G*	2.469	2.249	94.3	1.683
tetramesityl-cyclodisiloxane		2.31	2.47	86	1.66, 1.72
silica-w		2.58	2.70	87	1.87

Source: After O'Keeffe and Gibbs, 1985.

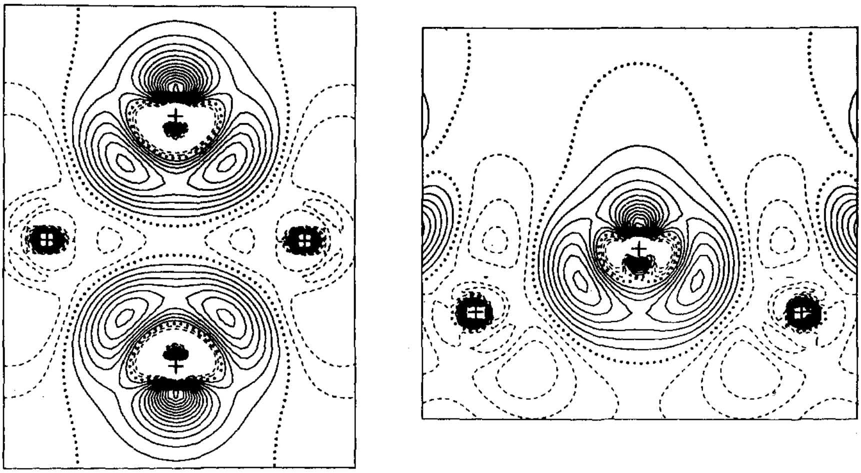

Fig. 7.8. Calculated (using *ab initio* SCF Hartree–Rock–Roothaan MO methods) deformation density maps for various Si_2O_2 ring-containing molecules: (a) $H_4Si_2O_6$ in the plane of the Si–O–Si–O ring; (b) $H_6Si_2O_7$ in the Si–O–Si plane. The contour interval is 0.05 $e\ Å^{-3}$, with negative contours dashed and the zero contour dotted (after O'Keeffe and Gibbs, 1985; reproduced with the publisher's permission).

of the oxygens force the Si atoms together. Study of larger clusters [e.g., $(OH)_2SiO_2SiO_2SiO_2Si(OH)_2$] yielded similar equilibrium geometries. Calculated geometries for the H_2Si 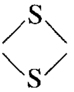 SiH_2 and $(HS)_2Si$  $Si(SH)_2$ molecules were also in good agreement with those observed in crystalline SiS_2 (Table 7.7). Comparison of calculated ring strain energies using prototype reactions:

$$2H_6Si_2O_7 \rightarrow H_4Si_2O_6 + 2H_4SiO_4$$

and

$$2H_6Si_2S \rightarrow H_4Si_2S_2 + 2SiH_4$$

indicates the oxide ring closing to be endothermic by 177 kJ mol^{-1}, while that for the sulfide is only 15 kJ mol^{-1} endothermic, consistent with the stability of an edge-sharing polymorph of SiS_2 and the instability of such structures for solid silicon oxides.

7.1.4. Qualitative molecular-orbital theory and its applications

It is certainly reasonable to believe that many of the qualitative structural questions important in mineralogy and in solid-state science in general will have fairly simple qualitative answers. While this may not always be

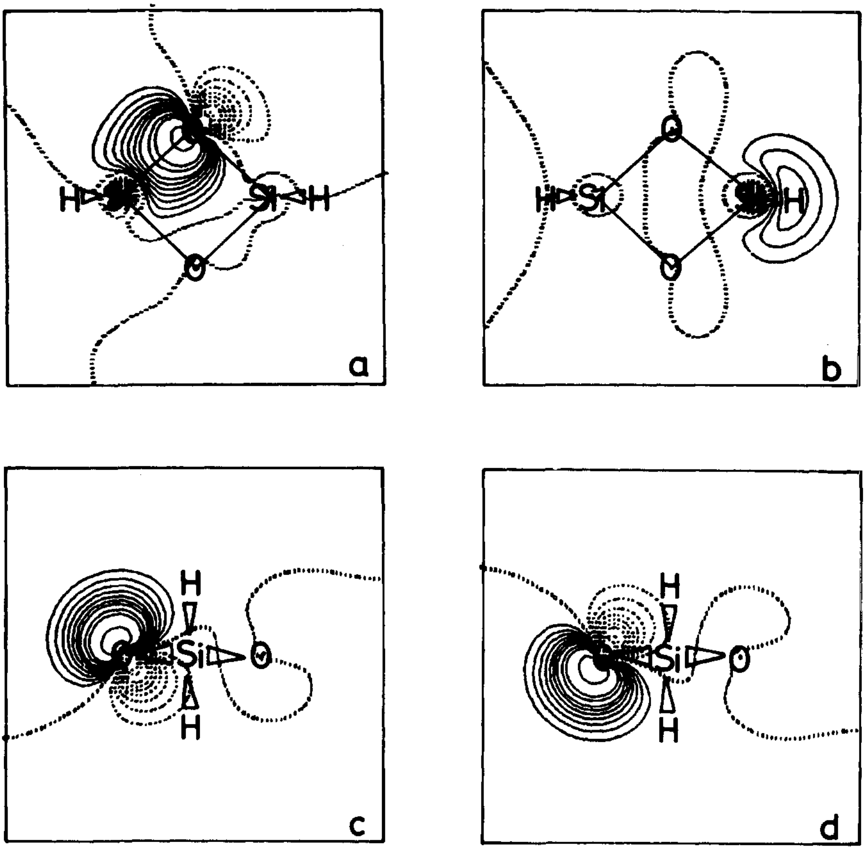

Fig. 7.9. Contour plots of the localized molecular orbitals in the $(H_2SiO)_2$ molecule for (a) the Si–O bond; (b) the Si–H bond; (c) and (d) the lone pair orbitals (after Kudo and Nagase, 1985; reproduced with the publisher's permission).

Table 7.7. Observed and calculated dimensions (Å and degrees) of Si–S–Si–S rings

		Si–Si	S–S	∢Si–S–Si	Si–S
$H_4Si_2S_2$	6-31G*	2.858	3.213	83.3	2.150
	STO-3G	2.861	3.141	84.7	2.124
$H_4Si_4S_6$	STO-3G, inner ring	2.882	3.124	85.4	2.125
	outer ring	2.869	3.134	85.0	2.123, 2.125
SiS_2		2.776	3.239	81.2	2.133

Source: After O'Keeffe and Gibbs, 1985.

true, an attempt to develop qualitative interpretations will often be worthwhile, both in its own right and as a complement to more quantitative approaches. A powerful method for developing such understanding is qualitative molecular-orbital theory, utilizing simple concepts of perturbation theory, symmetry, orbital overlap, and orbital electronegativity. In this section, we first present a brief discussion of the perturbation theory of orbital interactions, briefly discuss qualitative trends in orbital energies and compositions for some simple molecules, and then discuss MO interpretations of several structural trends observed in solid-state chemistry and mineralogy. Interested readers should consult Gimarc (1979), Burdett (1980), and Albright et al. (1985) for more extensive discussions of the applications of qualitative MO theory to molecules and solids. A briefer presentation can be found in Burdett (1979). Qualitative MO theory has already been used in the context of the interpretation of spectra and certain properties in Chapters 4 and 6 and our discussion of Pauling's Rules earlier in this chapter.

Qualitative perturbation theory. We may use a standard second-order perturbation energy expression to determine the small modification in the energy of an orbital m due to interaction with other orbitals n. The interaction matrix element may be approximated as: $H_{mn} = \frac{1}{2}KS_{mn}(H_{mm} + H_{nn})$, where H_{mm} is a diagonal matrix element and S_{mn} is the overlap integral. Such an approximation is an essential feature of the extended Hückel method, which is the basis for most qualitative MO schemes. The overlap integral may be simplified to: $S_{mn} = S_{mn}(r)F(\theta,d)$, where $S_{mn}(r)$ is a function of internuclear distance and orbital characteristics but not of angular variables; all of the dependence upon angular variables is contained in $F(\theta)$. Such a separation is the basis of the angular overlap method (see Burdett, 1980, Chap. 1). The angular term can be readily obtained from simple analytic formulae, so that the dependence of S_{mn} on simple angular variables can be readily calculated. For example, the overlap integral between a $p\sigma$ orbital on a central atom and σ-type orbitals on the exterior atoms of an AH_2 compound is given as: $S(r,\theta) = S_\sigma \cos\theta$, where θ is the angle between the axes of the orbitals. Using this approach, we can construct simple qualitative MO diagrams as a function of angular coordinates. Based upon the occupations of the molecular orbitals, we can then determine the structure that minimizes the sum of the orbital energies. This structure is then presumed to be the most stable.

Interpretation of angular geometries in molecules and minerals. A classic example of the application of qualitative MO theory is the interpretation of the angular geometry observed for H_2O. The qualitative MO orbital correlation diagram for an AH_2 molecule, adapted from Gimarc (1979), is shown in Fig. 7.10. Pictograms showing qualitative orbital compositions are shown alongside the orbitals. The core orbitals (e.g., O 1*s*

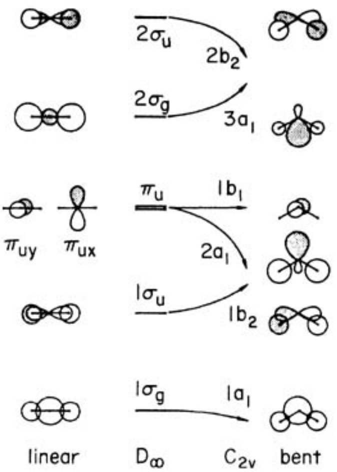

Fig. 7.10. A qualitative MO diagram for a linear and a bent AH_2 molecule. Shaded and unshaded orbital lobes are of opposite sign (adapted from Gimarc, 1979).

in H_2O) are not shown. For an H–A–H angle of 180° in $D_{\infty h}$ symmetry, the most stable valence MO is the $1\sigma_g$, which is a bonding combination of H $1s$ and A s orbitals, while the $1\sigma_u$ is the H $1s$–A p bonding combination, the $1\pi_u$ is a pure A p orbital, and the $2\sigma_u$ is the H $1s$–A p antibonding orbital. For H–A–H angles less than 180° in C_{2v} symmetry, the $1\sigma_g$ becomes the $1a_1$ and is somewhat stabilized by a bonding interaction between the H atoms. The $1\sigma_u$ becomes the $1b_2$, slightly destabilized by the reduced overlap of H $1s$ and A p orbitals. One component of the $1\pi_u$ orbital becomes the $1b_1$ in the C_{2v} geometry, remaining entirely A p in character and essesntially nonbonding. The other component, however, is of a_1 symmetry ($2a_1$) and can mix with the higher-energy a_1 orbital ($3a_1$), which correlates with the $2\sigma_g$ in $D_{\infty h}$ symmetry. The resulting stabilization of the $1a_1$ orbital by $2a_1$–$3a_1$ mixing may be understood to arise from a mixing of A s and H $1s$ character into the originally pure A p orbital. This gives bonding A–H and H–H interactions, thus lowering the energy. The extent to which the $2a_1$ orbital is stabilized by admixture of "$2\sigma_g$ character" may be approximated by perturbation theory (Gimarc, 1979, Chap. 1) as:

$$\Delta E = \frac{\beta^2}{\varepsilon_{2\sigma g} - \varepsilon_{1\pi u}}$$

where $\varepsilon_{2\sigma g}$ and $\varepsilon_{1\pi u}$ are orbital energies in the "unperturbed" (linear) geometry, $\beta = \int \psi_{2\sigma g} H' \psi_{1\pi u}\, dv$ and H' is the perturbation in the quantum-mechanical Hamiltonian. Burdett [1980, Eq. (4.2)] has shown that β is proportional to the product of the overlap of the central-atom p orbital with the outer-atom σ orbital and the coefficient of the outer atom σ orbital in the $2\sigma_g$ molecular orbital. Since changes in β are not easy to evaluate quantitatively, it is customary to focus upon changes in $\Delta\varepsilon = \varepsilon_{2\sigma g} - \varepsilon_{1\pi u}$ that are more easily assessed.

For systems with 4 valence electrons, the destabilization of the $1b_2$ orbital on bending favors a linear geometry. For systems with 5–8 valence electrons, the highest occupied molecular orbital in linear geometry, $1\pi_u$, is stabilized by bending and so such species are expected, and observed, to be bent (Gimarc, 1979, Chap. 3). Only if the $2a_1$ stabilization is very small will a linear geometry be observed. The extent of bending is expected to increase with ΔE, which is inversely dependent upon $\Delta\varepsilon = \varepsilon_{2\sigma g} - \varepsilon_{1\pi u}$. The eigenvalue of the purely A p $1\pi_u$ orbital will be determined mainly by the ionization potential of the A p orbital (or more qualitatively by the electronegativity of A), while that of the $2\sigma_g$ will depend both on the electronegativity of H and on the A–H distance. The observed H–A–H angle decreases from 104.5° in H_2O to 92.1° in H_2S (and remains almost the same for H_2Se and H_2Te). This change arises both from the reduced electronegativity or lowered valence ionization potential of the central A atom, which destabilizes the $1\pi_u$ orbital, and from the increased A–H bond distances, which stabilize the antibonding $2\sigma_g$ orbital. Barriers to linearity in AH_2 species are expected to change in a related way. Thus, an AH_2 species with A of low electronegativity and a long A–H bond will have both a small H–A–H angle and a large barrier to linearity.

The simple approach outlined above has been supported by accurate quantum-mechanical calculations for a number of AB_2 species with reasonably covalent bonding (Allen, 1972). Such studies show that total molecular energies exhibit the same trends as sums of valence-orbital eigenvalues, and that calculated eigenvalue changes with angle are in reasonable accord with qualitative molecular-orbital theory predictions. Even for highly polar molecules, such as Li_2O, for which MO eigenvalue trends give incorrect geometry predictions, a slight reformulation of the self-consistent-field equations gives orbitals whose eigenvalues do change with angle in a way consistent with experiment (Stenkamp and Davidson, 1973). This does not necessarily mean that the qualitative MO approach gives a complete picture of angular energetics—it may well ignore important changes in some energy components. Nonetheless, trends are predicted correctly so that the model provides at least a simple means for rationalizing and systematizing the data.

A similar approach has been applied to many other AB_2-type molecules in which an atom with valence p orbitals, or even a group of atoms, is bonded to a central atom A. For example, $H_3SiOSiH_3$ may be interpreted as an 8-valence electron AB_2 system with $A = O$ and $B = SiH_3$ (Tossell, 1984b). The $-SiH_3$ group interacts with O primarily by σ bonding and contributes one valence electron to the central atom. Thus, we would qualitatively expect the Si–O–Si angle to be bent, as observed. The SiH_3 σ orbital that interacts with the O p orbital is the $1a_2$ MO, which would be purely Si $3p$ in character for a planar SiH_3 group, and would acquire some Si $3s$ and H $1s$ character in a pyramidal geometry.

The approach described above clearly neglects a number of detailed changes occurring from molecule to molecule and from one geometry of a molecule to another. Nonetheless, this simple model is able to rationalize many trends in bond angles in gaseous molecules. Similarly, the following bond-angle trends observed in minerals can be rationalized:

1. For constant *B*, the *B*–*A*–*B* angle decreases as *A* becomes less electronegative.
2. For constant *A*, the B–A–B angle decreases as *B* becomes more electronegative.
3. For constant *A* and *B*, increasing *A*–*B* interatomic distance leads to decreasing *B*–*A*–*B* angle.
4. If B' is more electronegative than *B*, the angle B–A–B' is approximately equal to the angle B'–A–B'
5. Protonation of *A* causes the angle *B*–*A*–*B* to approach 130–140°.

An example of trend (1) is the decrease in bridging angle observed when *A* is changed from O (with an electronegativity value of 3.5) to S (with electronegativity of 2.4; Allred, 1961). Geisinger and Gibbs (1981) have shown that minimum-basis-set Hartree–Fock–Roothaan SCF calculations yield an Si–O–Si angle of ~125° and an Si–S–Si angle of ~100° for SiH_3OSiH_3 and SiH_3SSiH_3, and have noted that Si–O–Si angles in solids range from 120° to 180° (averaging about 145°), whereas Si–S–Si angles range only from 106° to 115° (averaging 110°). They also related the smaller angular range observed for Si–S–Si angles to the larger calculated value of the barrier to linearity. Decreasing the electronegativity of *A* destabilizes the $1\pi_u$ orbital, thus decreasing its separation from the $2\sigma_g$. The decreased separation leads to a greater stabilization of the $2a_1$ orbital upon bending, favoring a smaller bridging angle and giving a larger barrier to linearity. Similarly, Si–N–Si angles are systematically smaller than Si–O–Si angles because of the lower electronegativity of N compared to O.

Trend (2) is illustrated by the decrease in bridging angle from SiH_3OSiH_3 (144°) to CH_3OCH_3 (111°) (Tossell and Gibbs, 1978). The electronegativity of C is 2.50 and that of Si, 1.74, so that changing B from $-SiH_3$ to $-CH_3$ stabilizes the $2\sigma_g$ orbital, reducing its separation from the $1\pi_u$ and giving a stronger $2a_1$–$3a_1$ interaction and a smaller bridging angle. The lower observed values for Ge–O–Ge angles (average ~125°) compared to Si–O–Si angles may also be explained by the higher electronegativity of Ge compared to Si.

Trend (3) is seen in the reduction in Si–O–Si angle as the Si–O bridging bond lengthens (Newton and Gibbs, 1980). A lengthening of the *A*–*B* bond reduces the destabilization of the $2\sigma_g$ orbital, thus reducing $\Delta\varepsilon$.

Trend (4) has been observed in many calculations (see Gibbs, 1982), for example, Si–O–B angle = 126° and B–O–B angle = 133° from molecular-orbital calculations on $TH_3OT'H_3$ molecules. For such B–A–B' species, simple perturbation theory indicates that the lower-energy $2a_1$ orbital will be enhanced in the more electronegative of B and B' and the higher-energy $3a_1$ orbital enhanced in the less electronegative. For example, in a Si–O–B species, B σ character will be enhanced in the $2a_1$ orbital, giving a strong stabilization with decreasing angle, while Si σ character will be concentrated in the (empty) $3a_1$ orbital. Thus, the stabilizing interaction for the Si–O–B case will be much like that for B–O–B. Similarly, equilibrium Si–O–H angles are calculated to be 109° (Gibbs, 1982), much closer to the 100° H–O–H angle calculated in H_2O than to the 142° calculated for Si–O–Si in SiH_3OSiH_3 (Gibbs, 1982).

Trend (5) has also been observed in many cases (Gibbs, 1982) and may be interpreted by treating the $B\text{–}\underset{\substack{|\\ \mathrm{H}}}{A}\text{–}B^{+}$ species as one in which the B–A–B angle and B–A–H angle must accommodate each other to obtain the most favorable total energy. Since the B–A–H angles in isolated molecules are small (~100–120°) and have large barriers to linearity, they will tend to have values in $B\text{–}\underset{\substack{|\\ \mathrm{H}}}{A}\text{–}B^{+}$ species that are close to their equilibrium values in isolation if the B–A–B angle alone has a large value and a small barrier to linearity. Thus, the calculated decrease in equilibrium Al–O–Al angle from 150° to 140° when O is protonated arises from the requirement that the more rigid Al–O–H angle be 110°. However, when the B–O–B linkage is protonated, the angle expands from 133° to 137°, giving a B–O–H angle of 112°. In general, since calculated $B\text{–}\underset{\substack{|\\ \mathrm{H}}}{\mathrm{O}}\text{–}\mathrm{H}$ angles range only from 110° to 115°, the corresponding $B\text{–}\underset{\substack{|\\ \mathrm{H}}}{\mathrm{O}}\text{–}B$ angle in $B\text{–}\underset{\substack{|\\ \mathrm{H}}}{\mathrm{O}}\text{–}\mathrm{B}^{+}$ species will be 130–140°. The tendency for B–O–B angles to show less variability in the protonated case is evident from the results of Gibbs (1982). Since protonation (or interaction with other cations) is favorable when the bridging O is underbonded in the Pauling sense, we expect the protonated result to agree more accurately with experiment in such cases. For example, the average $\mathrm{Al}\text{–}\underset{\substack{|\\ \mathrm{H}}}{\mathrm{O}}\text{–}\mathrm{Al}$ angle observed is about 137°, in good agreement with that calculated for the saturated $\mathrm{Al}\text{–}\underset{\substack{|\\ \mathrm{H}}}{\mathrm{O}}\text{–}\mathrm{Al}^{+}$ species.

We have assumed up to this point that $B\text{–}\underset{\substack{|\\ \mathrm{H}}}{\mathrm{O}}\text{–}B^{+}$ systems are planar. However, such species, for example, $\mathrm{H_3Si}\text{–}\underset{\substack{|\\ \mathrm{H}}}{\mathrm{O}}\text{–}\mathrm{SiH_3}^{+}$, are analogues of eight-valence-electron AH_3 species whose predicted geometry is pyramidal (Gimarc, 1979). The degree of pyramidization is determined mainly by the $2a_1'$–$1a_2''$ separation, which decreases as the central A atom becomes less electronegative, or the exterior atom becomes more electronegative. For oxygen, the departure from planarity and the barrier to planarity are both small (H–O–H angle = 110°, barrier to planarity = 8 kJ/mol in H_3O^+), but these quantities are much larger for sulfur (H–S–H angle = 96.0°, barrier = 130 kJ/mol in H_3S^+; Dixon and Marynick, 1977). Therefore, three-coordinate O is nearly planar in H_3O^+ and in $(SiH_3)_3O^+$ (Tossell, 1984b), while S is distinctly pyramidal. Similar trends are observed in solids. For example, O in TiO_2 is three-coordinate and planar, while S in TiS_2 is three-coordinate but pyramidal with a Ti–S–Ti angle of 90°.

The above discussion has focused upon σ-bonding interactions, but π-bonding interactions may also be important, as described by Albright et al. (1985) and Burdett (1988) for Si–O–Si linkages. A linear Si–O–Si angle would be stabilized by interaction of the O $2p\pi$ orbitals with acceptor orbitals of π symmetry on the $-SiH_3$ group. This orbital is presumed in Albright et al. (1985) to be basically a Si–H σ^* orbital, in agreement with the conclusions of Tossell et al. (1985b) based on electron transmission spectral studies. The large value and flexibility of Si–O–Si angle would then arise from a balance of σ- and π-bonding effects. Such O $2p\pi$–Si–H σ^* interactions also stabilize planar three-coordinate oxygen. In TiO_2, acceptance of O $2p\pi$ electron density into empty Ti $3d$ orbitals also stabilizes a planar structure. Such π-bonding interactions occur as well for S compounds, but the relative strength of π bonds compared to σ bonds is considerably smaller for second-row atoms such as S, so that the pyramidal geometry stabilized by σ bonding prevails.

Structures of A_n anions and XA_n molecular anions. Tossell (1983) was able to rationalize a number of structural properties of polyatomic anions using qualitative MO theory in minerals, for example,

1. The frequency of occurrence of S_2^{2-} compared to O_2^{2-} in solids.
2. The large number of different polyanions observed for S and isoelectronic P^- (e.g., S_4^{2-} and P_4^{4-}).
3. The formation of O–O bonds as electron pairs are removed from oxyanions TO_n^{a-}.

The electron affinity of S_2 is higher than that of O_2 because the π bonding MO occupied in the anion is less strongly π antibonding in S_2 than in O_2. This enhanced stability in the π^* MO of S_2^{2-} requires less of the overall stability of a compound to arise through interaction with the counterions and explains why there are a greater number of S_2^{2-} than O_2^{2-} bearing compounds. The formation of polyanions involves, in general, a reduction in the number of π bonds and an increase in the number of σ

bonds. Since relative π to σ bond strengths are lower for second-row elements like S, polyanions such as S_4^{2-} are more favored than their oxygen analogs. Burdett (1980) has shown how addition of electrons to the 20-valence-electron structure P_4 leads to successive bond breaking. A similar approach explains the square planar structure of S_4^{2+} (a 22-electron system), the C_2 symmetry kinked chain structure of S_4^{2-} (a 26-electron system), and the square planar structure of As_4^{4-} in skutterudite (a 24-electron system). The formation of an O–O bond in CO_3^0 can be understood by treating the oxyanion as an O_3^{4-} group "stuffed" with a C^{4+}. The O_3^{4-} group would have 22 electrons (compared to a maximum of 18 allowed for a stable cyclic A_3 system), and two bonds would therefore break, giving a structure with two long and one short O–O distances, as observed. Such results support the idea that, if electron pairs are removed from ions such as CO_3^{2-} or SiO_4^{4-}, additional O–O bonds will form. Such oxidation of the ions could occur by coupled removal of cations and electrons (e.g., removal of Mg^{2+} and 2 electrons from CO_3^{2-} in $MgCO_3$).

It has been suggested that virtually all samples of MgO (and probably silicates as well) contain small amounts of H_2O and CO_2 (Freund, 1981). These impurities lead to formation of O^- species. The species CO_4^{4-} has also been postulated to occur on the surface of MgO exposed to CO_2. This species has recently been studied by *ab initio* SCF Hartree–Fock–Roothaan MO calculations, both in its anion form and as the protonated cluster $C(OH)_4$ (Gupta et al., 1981). Its calculated equilibrium bond distance is intermediate between those observed for B and N in tetrahedral coordination with oxygen, and there seems to be no intrinsic source of instability. Thus, such a species seems stable. However, the calculations indicate a charge on C in CO_4^{4-} very similar to that in CO_3^{2-}, arguing for the formulation $C^{4+}O_4^{8-}$ as first approximation to the electronic structure, rather than the $C^\circ(O_4^{4-})$ formulation suggested by Freund (1981). Perhaps such a species is better formulated as a chemisorption complex of a CO_2^{2-} anion (a bent, 18-valence-electron system) and an $O^- \ldots O^-$ species on the MgO surface. Such a CO_2^{2-} species might also be quite mobile within the MgO crystal structure.

Bond breaking and electron count. As we have observed for a number of different systems, the ordering of molecular orbitals is always bonding, below nonbonding, below antibonding, with respect to any given type of interaction. The same basic pattern pertains in the band structure of solids. Since the stability of a material depends upon the occupation of orbitals of various bonding energetics, we might expect to see common trends in the energetics of molecules and solids as a function of electron count. As described in Albright et al. (1985), plots of cohesive energies of molecules, main-group elements, and transition elements as a function of number of valence electrons show a characteristic plot, with stability maximized for intermediate numbers of electrons, in which bonding and nonbonding, but not antibonding, orbitals are occupied (Albright et al., 1985, p. 255). If additional electrons are added to a structure with all bonding and nonbonding orbitals occupied, the stability of the structure is reduced, and distortion accompanied by bond breaking often occurs, converting occupied antibonding orbitals to nonbonding orbitals. For example, the wurtzite structure is stable for eight electrons per atomic pair (e.g., ZnS) but addition of electrons (e.g., along the series β-GaSe→As→Se, Te→I_2→Xe with 9, 10, 12, 14, and 16 electrons, respectively) leads to systematic bond breaking, although a number of different patterns of bond breaking can arise (Burdett, 1979). A similar pattern of bond breaking upon successive electron addition can be seen starting with an 8-valence-electron NaCl structure. Two extra electrons per diatomic unit, as in As or black phosphorus, give a structure arising from bond breaking starting with rocksalt, as shown in Fig. 7.11 from Burdett and Lee (1983). Thus, given a simple structure, stable for a given electron count, we can often systematically explain its change as the electron count is increased.

We may visualize the depolymerization of silicate structures with increasing electron count in the same way, as shown in Table 7.8 (from Burdett, 1980). For the fully polymerized SiO_2 structure, with an average of 5.33 valence electrons per atom, the highest-energy occupied MOs are nonbonding O 2*p* and the lowest-energy empty MOs are Si–O antibonding. Increasing the number of valence electrons per atom without chang-

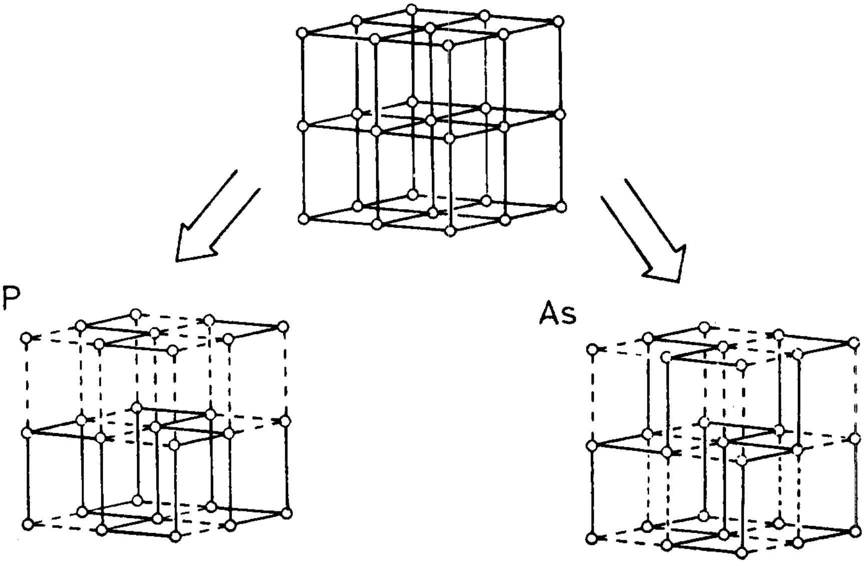

Fig. 7.11. Bond breaking in the rocksalt (NaCl) structure leading to the black phosphorous (P) and arsenic (As) structures (after Burdett and Lee, 1983; reproduced with the publisher's permission).

Table 7.8. Breakup of silicate structures with increasing electron count

System	Number of electrons per atom	Examples
SiO_2	5.33	Three-dimensional structures as in quartz (with isomorphous replacement by Al in feldspars and zeolites)
$(Si_2O_5)_n^{2n-}$	5.71	Double chains (e.g., gillespite, $BaFeSi_4O_{10}$) and sheets (e.g., micas)
$(Si_4O_{11})_n^{6n-}$	5.87	Double chains [e.g., amphiboles such as tremolite, $(OH)_2Ca_2Mg_5(Si_4O_{11})_2$]
$(SiO_3)_n^{2n-}$	6.00	Cyclic chains (i.e., rings), as in benitoite ($BaTiSi_3O_9$), and linear chains [e.g., pyroxenes such as diopside, $CaMg(SiO_3)_2$]
$(SiO_4)^{4-}$	6.4	Isolated tetrahedra as in orthosilicates (e.g., olivines M_2SiO_4, M mixture of Mg, Fe, Mn)

Source: From Burdett, 1980.

ing the structure would populate antibonding orbitals. The resulting compound can be stabilized by distortions in which bonds are broken and antibonding orbitals thus converted to nonbonding. The consequence is depolymerization, with specific numbers of valence electrons per atom giving specific types of silicate structures.

We can also see the descent in symmetry from NaCl to less connected structures, such as As, as a distortion induced by the presence of a half-filled band. A one-dimensional solid with a half-filled band is unstable with respesct to a geometric distortion lowering its symmetry, known as a Peierls distortion. For example, polyacetylene, a one-dimensional metal with a half-filled uppermost occupied band for a symmetric geometry (all C–C distances equal), lowers its energy by distorting to a structure with inequivalent C–C distances. Such a distortion is the solid-state analog of the Jahn–Teller distortions encountered in molecules (e.g., in cyclobutadiene, which distorts from square to rectangular). Distortions from a simple cubic structure in one to three dimensions can also be visualized as being of the Peierls type (Burdett and Lee, 1983). For the group V elements, with an s^2p^3 valence-electron configuration, by analogy with the one-dimensional case, we should expect a distortion away from simple cubic by the fission of alternative linkages along the x, y, and z directions. Such a distortion of the simple cubic structure to form the arsenic and black phosphorus structures is illustrated in Fig. 7.11. At high pressure, black phosphorus converts to the simple cubic arrangement, which is metallic as expected for a half-filled band. Such an approach also explains how the parent undistorted structure can be stabilized. For example, square cyclobutadiene can be stabilized by introducing substituents on the C that lift the degeneracy of the highest occupied molecular orbital

(HOMO). A similar approach can stabilize the rocksalt structure (the *AB* analog of the elemental simple cubic structure above). By introducing a large electronegativity difference between *A* and *B*, we generate a substantial HOMO–LUMO (lowest unoccupied molecular orbital) gap. Based on the relative positions of *A* and *B* *s* and *p* valence levels, a number of different sequences of structural energies can be expected. Only for the case in which both *s* and *p* orbitals of *A* lie below those of *B* will the rocksalt structure be favored.

Qualitative molecular-orbital analysis of computational results. Rather than employing purely qualitative, symmetry-based theory, we can also perform calculations on solids or clusters and then analyze them using qualitative MO arguments. We will consider two such studies: (1) an EHMO study of SiO_2 in β-quartz, stishovite, and hypothetical silica-w structures (Burdett and Caneva, 1985), and (2) an MS-SCF-$X\alpha$ study of electron-rich transition-metal compounds (Tossell and Vaughan, 1981).

Extended Hückel (EHMO) tight-binding band-structure calculations on β-quartz give a Si–O–Si angle fortuitously within about 1° of that observed. More interestingly, in the EHMO calculation one can easily "turn off" various covalent interactions by setting the corresponding overlap integrals equal to zero. Eliminating all Si–Si interactions and performing the calculation for the oxide ions alone (i.e., empty tetrahedra) gives very similar equilibrium values of Si–O–Si angle. These results indicate that Si–Si and even Si–O interactions have little influence upon the equilibrium angle, which is mainly determined by oxygen–oxygen repulsions. An EHMO cluster calculation on the $Si_2O_7{}^{6-}$ cluster constrained to adopt the geometry found within the crystal, and with only the u parameter of the β-quartz structure varied, gives much the same equilibrium Si–O–Si angle as the full band calculation, and similarly small effects for the Si–Si and Si–O interactions. For the stishovite structure, an EHMO band calculation also gives good agreement with experiment for the Si–O–Si angle, while calculations on discrete clusters with small numbers of Si atoms give smaller values of Si–O–Si angle due to a relative excess of O_{br}–O_{br} repulsive interactions in the discrete cluster. The calculated Si–O–Si angle for the edge-sharing silica-w structure is considerably smaller than for stishovite, and shows the same dependence on the number of Si atoms in the oligomer. For the stishovite and silica-w-type oligomers, the repulsions between terminal oxygens, overcounted in the finite oligomer clusters, have a strong influence upon the equilibrium angle. One conclusion of the work is that clusters used to model oxidic solids should have the same number of close O–O contacts as in the bulk solid, to avoid exaggerating the influence of such interactions.

Tossell and Vaughan (1981) used MS-SCF-$X\alpha$ calculations of orbital eigenvalues for clusters containing electron-rich transition metals such as Zn to rationalize preferred coordination numbers in the Cu family and Zn family solids. The metal valence *d* orbitals of heavy metals such as Pt, Au, and Hg are known to be raised in energy by relativistic effects. The energies of metal valence orbitals versus those of ligands were also known to be systematically raised by increase in coordination number, particularly in going from the two-coordination characteristic of gas-phase molecules like $ZnCl_2$, to the four-coordination observed in solids such as $ZnCl_2$. For compounds of d^{10} metals, the metal *d*-ligand *p* molecular orbitals of both bonding and antibonding type are completely filled. On the basis of simple overlap considerations, such completely filled bonding and antibonding orbital sets give an overall destabilization. This destabilization can be reduced by increasing the energy separation of the metal *d* and ligand *p* orbitals, thus reducing their covalent mixing. The 3*d* orbitals of Zn lie far below the 3*p* orbitals of S; so covalent destabilization is small for all coordination numbers. The 5*d* orbitals of Hg, on the other hand, are of much higher relative energy and thus can mix more strongly with S 3*p*. The destabilizing effect of such mixing can be reduced in structures adopting a lower Hg coordination number, which will both stabilize the Hg 5*d* orbital (moving it down in energy away from the S 3*p*) and reduce the number of covalent interactions. For Ag^+ compounds, the maximum Ag 4*d*–*L* *p* separation is achieved by raising the Ag 4*d* using high coordination numbers in the halides, which have high-stability ligand *p* orbitals, and by lowering the Ag 4*d* using low coordination numbers for the chalcogenides, where the valence *p* orbitals are less stable. By contrast to the case of d^{10} metals, compounds of d^9 metals such as Cu^{2+} are found to be stabilized by *M d*–*L p* bonding since the (partially unoccupied) HOMO is *M*–*L* antibonding. The coordination numbers and structural distortions characteristic for d^9 metal ions are found to be those leading to increased covalent mixing, for example, distorted octahedral coordination in Cu^{2+} halides, and planar three-coordination in Cu^{2+} sulfides. Thus, simple considerations of destabilization and stabilization depending upon the occupations of antibonding orbitals can rationalize at least some aspects of the structural chemistry of the Cu and Zn family metals.

7.2. Minerals at elevated pressures and the interior of the Earth

Seismological evidence has led to the realization that the Earth is a layered body, with the basic subdivisions into crust, mantle, and core being further refined to give an upper and lower mantle separated by a transition zone, and a liquid outer core and solid inner core. The different layers show fairly sharp contrasts in density and elastic properties, leading to speculation that changes in crystal structure (and possibly in electronic structure) as well as in overall composition are responsible for the layer-ing (Birch, 1952; Jeanloz and Thompson, 1983). Not surprisingly, high-pressure experimental studies have been employed to examine changes in crystal structures and physical properties of phases likely to occur in the mantle and core, with pressures equivalent to the deepest regions now being attainable (e.g., Manghnani and Akimoto, 1977; Akimoto and Manghnani, 1982; Schreyer, 1982; Sunagawa, 1984; Navrotsky, 1987; Manghnani and Syono, 1987). These references also show that a wide range of diffraction, spectroscopic, and related methods (see Chapter 2) have been applied, not only to phases synthesized at high pressures and quenched to ambient conditions, but also to materials studied *in situ* in diamond anvil cells and large volume assemblies such as multiple anvil systems.

In Fig. 7.12 are shown estimates based on geophysical (and other indirect) evidence of the variations of pressure, temperature, and density with depth in the Earth. Although samples of material derived from the upper mantle do appear at the Earth's surface, the nature of the other layers and origins of the discontinuities in density that separate them cannot be studied directly. The indirect evidence, including that from high-pressure laboratory studies, suggests that the discontinuity at 400 km depth, which separates the upper mantle from the transition zone, arises from the transformation of magnesium-rich olivine [$(Mg,Fe)_2SiO_4$] to a modified spinel (β) phase and then to a spinel structure. The discontinuity around 700–720 km is probably associated with the transformation of a spinel phase to an assemblage of oxides dominated by a $MgSiO_3$-rich per-

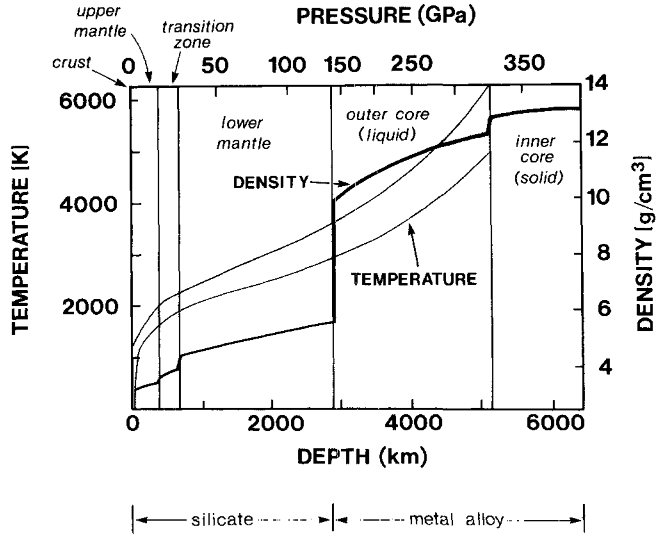

Fig. 7.12. Estimates of the variation of pressure, temperature, and density within the earth as a function of depth (Navrotsky, 1987).

ovskite structure phase. The iron likely to occur in the olivine and spinel phases may form a separate (Mg,Fe)O phase at this stage (a magnesiowüstite) since the solubility of $FeSiO_3$ in perovskite is rather low. Aluminum, with some iron and other elements, may also be present in the lower mantle as a garnet of composition in the region $Mg_4Si_4O_{12}$–$Mg_3Al_2Si_3O_{12}$. All of the geophysical and geochemical evidence points to the Earth's core being dominated by iron, probably alloyed with some nickel, but the density estimates indicate the presence of some lighter element, the identity of which is still debated. The most widely proposed candidate is S, although experimental evidence in support of O and H has been put forward in recent years and geochemical evidence has been put forward for the presence of K.

In addition to the contributions to understanding the Earth's interior from geophysical evidence and the geochemistry of solar system materials, and from very high-pressure experiments, an important contribution comes from attempts to calculate the effects of pressure on crystal and electronic structures of appropriate materials using quantum-mechanical methods. Some examples of this approach will now be considered, with reference to the phases thought likely to dominate the interior of the Earth.

7.2.1. *Olivine and Mg_2SiO_4 spinel*

The geometric and electronic structures of magnesium olivine have already been discussed in detail (see Section 5.2.2). Attempts to describe the structural and physical properties of both magnesium olivine and its spinel-structured polymorph (ringwoodite) and their response to increasing pressure have centered on atomistic simulations. Earlier work in this field was reviewed by Price and Parker (1984), who point out the limitations of fully ionic, rigid-ion models and introduce new model potentials that explicitly consider the contribution of covalency to the Si–O bond (via a Morse potential). Although the interatomic potential parameters developed for the fully ionic models reproduce the atomic coordinates and cell parameters reasonably well (e.g., Miyamoto et al., 1982), they give very poor agreement with elasticity and dielectric data, because such data depend on the second derivative of the potential. The partially ionic models employing potentials that utilize fractional or partial charges coupled with short-range repulsion terms satisfactorily reproduce both structural and elastic properties. Thus, the potentials *P*4 and *P*5 of Price and Parker (1984) not only reproduce the experimentally observed structural data for forsterite and ringwoodite well (see Table 5.2 in Chapter 5), but also the observed elasticity data for forsterite (see Table 7.9). Better fits are also achieved for the static dielectric constants (Table 7.10). *P*5 represents optimization of the potential, not only against structural data, but

Table 7.9. Observed and calculated elasticity constants for forsterite (units, Mbar)

	Observed	***P4***	***P5***
c_{11}	3.28–3.31	2.65	2.94
c_{22}	1.91–2.00	1.91	2.07
c_{33}	2.30–2.36	2.27	2.40
c_{44}	0.66–0.67	0.77	0.74
c_{55}	0.81–0.83	0.69	0.65
c_{66}	0.81–0.82	0.78	0.71
c_{12}	0.64–0.66	0.80	0.72
c_{13}	0.68–0.69	0.87	0.70
c_{23}	0.72–0.74	0.77	0.81

Source: After Price and Parker, 1984.

Table 7.10. Observed and calculated static dielectric constants for forsterite

	Observed	***P4***	***P5***
e_{11}	—	4.08	5.61
e_{22}	—	4.35	6.11
e_{33}	—	3.69	6.45
$e_{\text{isotropic}}$	5.5–6.6	4.04	6.06

Source: After Price and Parker, 1984.

also against the full elasticity data for forsterite. These overall potentials also give good agreement with the calculated bulk modulus (K_{Fo}) and individual cation polyhedral moduli (K_{SiO} and K_{MgO}) of forsterite and, so far as data are available, for ringwoodite (see Table 7.11). The calculated pressure derivatives of the elastic constants (dc_{ij}/dP) are also very similar to those measured by Brillouin scattering (Bassett et al., 1982; see Table 7.11).

7.2.2. $MgSiO_3$ and $CaSiO_3$ perovskite

Following the widespread acceptance of the view that silicate perovskites may be major components of the lower mantle (see Jeanloz and Thompson, 1983), there have been a number of attempts to calculate the structure, elastic properties, and equations of state of these materials (Wolf and Jeanloz, 1985; Wolf and Bukowinski, 1985, 1987; Matsui et al., 1987; Hemley et al., 1987). A great deal of interest has also been generated in the crystal chemistry of perovskite-structure phases because of their "high-temperature" superconducting properties.

Matsui et al. (1987) used an atomistic simulation approach to study the ilmenite and perovskite phases of $MgSiO_3$ and employed the WMIN computer program (Busing, 1981) to produce a potential model based on em-

Table 7.11. Predicted values of the elasticity data and its pressure dependence for forsterite and ringwoodite, using potentials *P*4 and *P*5

	Obs.	*P*4	*P*5		Obs.	*P*4	*P*5		Obs.	*P*4	*P*5
Forsterite											
K_{Fo}[a] (Mbar)	1.4	1.5	1.5	$K_{Si\text{-}O}$ (Mbar)	>5.5	9.0	6.8	$K_{Mg1\text{-}O}$ (Mbar)	1.2	1.6	1.7
				$K_{Mg2\text{-}O}$ (Mbar)	1.0	1.1	1.1				
$\frac{dc_{11}}{dP}$[b]	8.3–9.8	7.1	6.2	$\frac{dc_{22}}{dP}$	5.9–7.0	4.5	6.5	$\frac{dc_{33}}{dP}$	6.2–7.6	5.7	6.0
$\frac{dc_{44}}{dP}$	1.7–2.1	5.7	1.8	$\frac{dc_{55}}{dP}$	1.6–1.7	1.8	3.1	$\frac{dc_{66}}{dP}$	2.2–2.3	1.7	3.5
$\frac{dc_{12}}{dP}$	4.3–4.8	3.5	3.1	$\frac{dc_{13}}{dP}$	4.2–4.8	3.4	2.4	$\frac{dc_{23}}{dP}$	3.5–4.1	3.2	2.8
Ringwoodite[c]											
K_{Ri} (Mbar)	2.1	2.1	2.2	$K_{Si\text{-}O}$ (Mbar)	>2.5	6.1	6.5	$K_{Mg\text{-}O}$ (Mbar)	1.5	2.0	2.2
				$\frac{dK}{dP}$	4.0	4.2	3.6				
c_{11} (Mbar)	—	3.9	3.7	c_{44} (Mbar)	—	1.0	1.32	c_{12} (Mbar)	—	1.3	1.4
$\frac{dc_{11}}{dP}$	—	6.7	6.7	$\frac{dc_{44}}{dP}$	—	1.1	1.5	$\frac{dc_{12}}{dP}$	—	2.1	1.6

[a] Data from Hazen (1976).

[b] Data from Kumazawa and Anderson (1969) and Bassett et al. (1982.)

[c] Little observed data are available for ringwoodite. Observed values quoted come from Mizukami et al. (1975) for K_{Ri}, but other values refer to analogous Ni and Fe spinel silicates (e.g., Hazen and Finger, 1982).

pirical parametrization and energy minimization. The resulting model was applied to predict the elastic constants of the perovskite phase; reasonable agreement was obtained with data from volume-compression experiments. The model was then used to predict elastic constants of these two forms of $MgSiO_3$ at high pressure. In a later study, Matsui (1988) used the energy parameters from this model in a molecular-dynamics simulation of the structural and physical properties of $MgSiO_3$ perovskite. By contrast, Hemley et al. (1987) and Wolf and Bukowinski (1987) used parameter-free theoretical models based on quasiharmonic lattice dynamics[1] and the modified electron-gas theory.

Wolf and Bukowinski (1987), expanding on their earlier theoretical studies, obtained predictions of the stability and equations of state of $MgSiO_3$ and $CaSiO_3$ perovskite as a function of temperature and pressure. Their results were obtained by minimization of the free energy with respect to structural parameters. The static lattice energy component of the free energy was calculated by assuming pairwise additive central potentials derived from the MEG formulation (Gordon and Kim, 1972). Following the approach of Cohen and Gordon (1976), these authors chose to stabilize the O^{2-} ion wave functions by using a Watson sphere with a charge of 1+ and a radius of 2.66 atomic units. Nearest-neighbor cation–oxygen and up to third-shell oxygen–oxygen pair interactions were included. The thermal contribution to the free energy was calculated using quasiharmonic lattice dynamics. In accordance with observations, a cubic structure for $CaSiO_3$ and an orthorhombic structure for $MgSiO_3$ were predicted at zero pressure by the model. Calculated compressibility and thermal expansivity of $MgSiO_3$ were in good agreement with available data. Computer values of the equation of state for orthorhombic $MgSiO_3$ perovskite with some experimental data are shown in Fig. 7.13. Although the model predicts successive second-order phase transitions at elevated temperatures to a tetragonal and then a cubic structure, predictions of the pressure dependence of these high-temperature transitions (see Fig. 7.14) suggest that the orthorhombic phase would be stable throughout most of the lower mantle. For $CaSiO_3$, the model predicts that the cubic perovskite structure is stable to pressures of at least 70 GPa.

Hemley et al. (1987) used a very similar approach to that of Wolf and Bukowinski (1987), except that the MEG calculations involved shell-stabilized ion charge densities (SSMEG calculations). Again, the orthorhombic form of perovskite $MgSiO_3$ and a cubic perovskite $CaSiO_3$ were found to be stable at zero pressure, although the latter was predicted to be dynamically unstable at pressures above ~109 GPa. Again, predictions of compressibilities and the equations of state show good agreement with such experimental data as are available (Fig. 7.15 shows the extent of this agreement; cf. Fig. 7.13). In Table 7.12 are summarized the equation-of-state parameters calculated for $MgSiO_3$ and $CaSiO_3$ perovskites by Hemley et al. (1987).

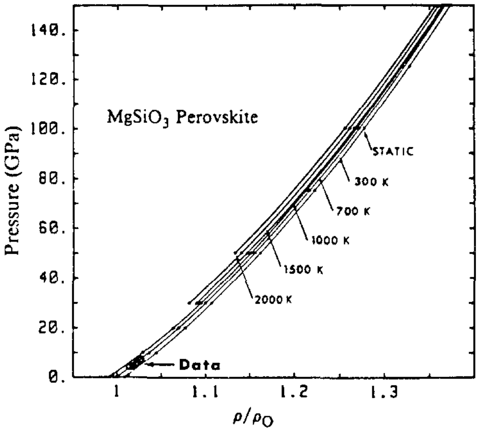

Fig. 7.13. Calculated equation of state for orthorhombic $MgSiO_3$ perovskite for the static lattice and at elevated temperatures (assuming regular octahedra). Experimental results (← data) also shown; see Wolf and Bukowinski (1987) for further details (reproduced from Wolf and Bukowinski, 1987, with the publisher's permission).

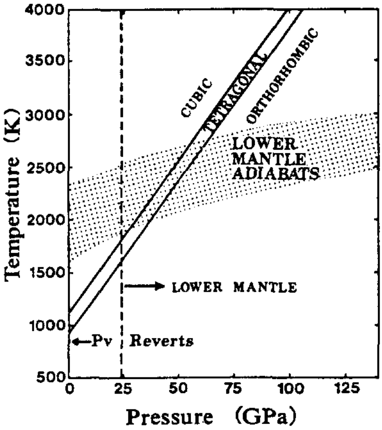

Fig. 7.14. Calculated stability fields for orthorhombic, tetragonal, and cubic $MgSiO_3$ perovskite polymorphs. Superimposed is a representative range of geotherm temperatures (stippled) and their adiabatic extrapolations to zero pressure (after Wolf and Bukowinski, 1987; reproduced with the publisher's permission).

7.2.3. Simple oxides, structural and electronic phase transitions

The simple oxides regarded as possible lower mantle components have proved amenable to a number of approaches involving quantum-mechanical calculations. For both MgO and CaO, the bonding, equations of state, and relative stabilities of the NaCl-type (*B*1) and the CsCl-type (*B*2) structures have been calculated using both modified electron-gas studies

(Cohen and Gordon, 1976; Tossell, 1980b; Muhlhausen and Gordon, 1981; Boyer, 1983) and first-principles band-structure calculations (Yamashita and Asano, 1970; Walch and Ellis, 1973; Liberman, 1978; Bukowinski, 1980, 1982; Yamashita and Asano, 1983a; Chang and Cohen, 1984). More detailed discussion of the electronic structure of MgO at room temperature and pressure is provided in Chapter 4. A good example of the more recent attempts to study the effects of high pressures on MgO and CaO is that of Bukowinski (1985). In this study, lattice properties were calculated using the band structure and charge density obtained from a self-consis-

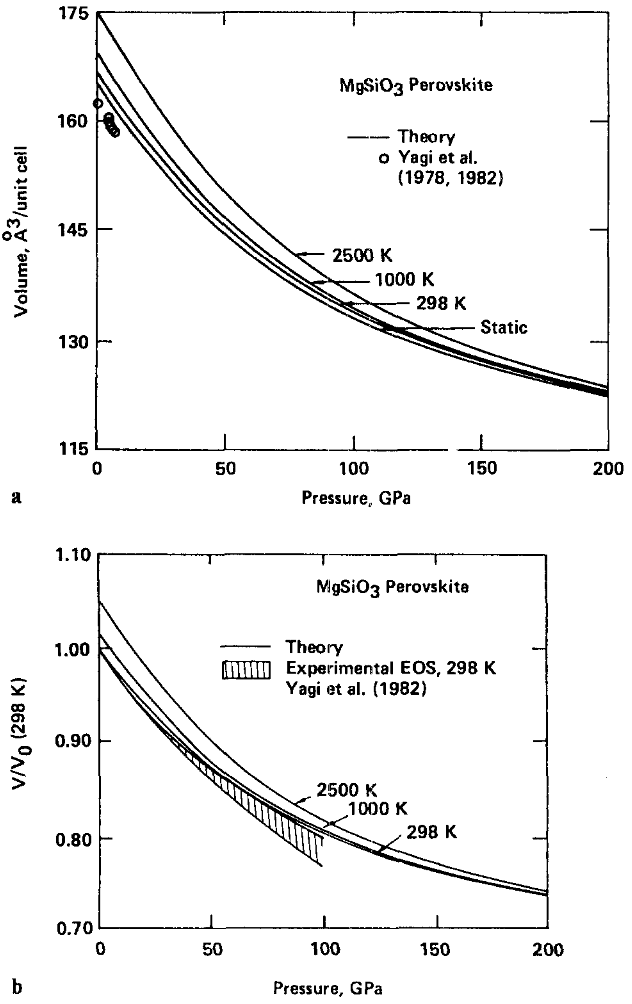

Fig. 7.15. Calculated and experimental equation-of-state data for $MgSiO_3$ perovskite (after Hemley et al., 1987; reproduced with the publisher's permission).

Table 7.12. Summary of equation-of-state parameters calculated for $MgSiO_3$ and $CaSiO_3$ perovskites[a]

	$MgSiO_3$	$CaSiO_3$
K_o(298 K) (GPa)	335(260 ± 20)[b]	347
K_o'(298 K)	0.2	5.3
$P_{ZP,o}$ (GPa)	2.77	2.40
$P_{TH,o}$(298 K) (GPa)	0.59	0.45
$\Theta_{H\infty}$ (K)	1340	1305
γ	1.44	1.25

[a] K_o and K_o' are the zero-pressure bulk modulus and its pressure derivative; $P_{ZP,o}$ and $P_{TH,o}$ are the zero-point and thermal pressures at zero pressure; $\Theta_{H\infty}$ is the harmonic Debye temperature; γ is the Grüneisen parameter.

[b] Experimental results in parentheses; Yagi et al. (1982).

tent augmented-plane-wave calculation. The Hedin–Lundquist exchange-correlation potential was used (Hedin and Lundquist, 1971), a "muffin-tin" approximation to the crystal potential in the self-consistent iterations, and equal-sized atomic spheres with radii equal to half the nearest-neighbor distance. The equations of state calculated for MgO and CaO in both *B*1 and *B*2 structural forms are shown in Fig. 7.16 and the equation of state parameters in Table 7.13. Agreement with available experimental data is generally good for the equations of state (Fig. 7.16), although the calculated values appear to overestimate the densities of the *B*2 phases. The pressures involved in the *B*1→*B*2 phase transformation for both MgO and CaO were calculated and compared with the results of other theoretical predictions and the limited available experimental data as shown in Table 7.14. For CaO, the transition is known from experiment to occur at ~60 GPa (Jeanloz et al., 1979; Mammone et al., 1981), and the predicted pressure from the APW calculations, although only half that determined experimentally, is much closer than predictions based on MEG calculations (Cohen and Gordon, 1976). Shock-wave experiments show no evidence of transformations in MgO up to 200 GPa (although they do not exclude a transformation involving a volume charge of less than 3%; Vassiliou and Ahrens, 1981). Predicted pressures for the *B*1→*B*2 transformation in MgO are all above this figure, ranging from 1050 GPa, based on *ab initio* pseudopotential calculations (Chang and Cohen, 1984), to 205 GPa, based on the APW calculations (see Table 7.14). The overestimation of densities of the *B*2 phases in the latter calculations suggest that a predicted pressure of 205 GPa should be a lower bounding value.

When the simple oxide involves a transition metal, other transformations than structure changes are possible at high pressures, in particular, changes in spin state. As early as 1960, Fyfe suggested that a pressure-induced high-spin→low-spin transition in Fe^{2+} might have important consequences for the interior of the Earth, and this theme was later devela.

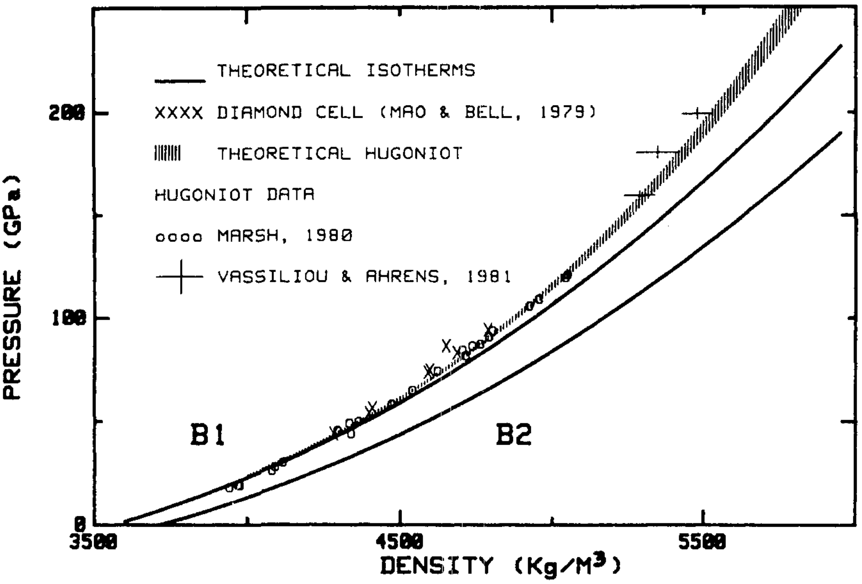

b.

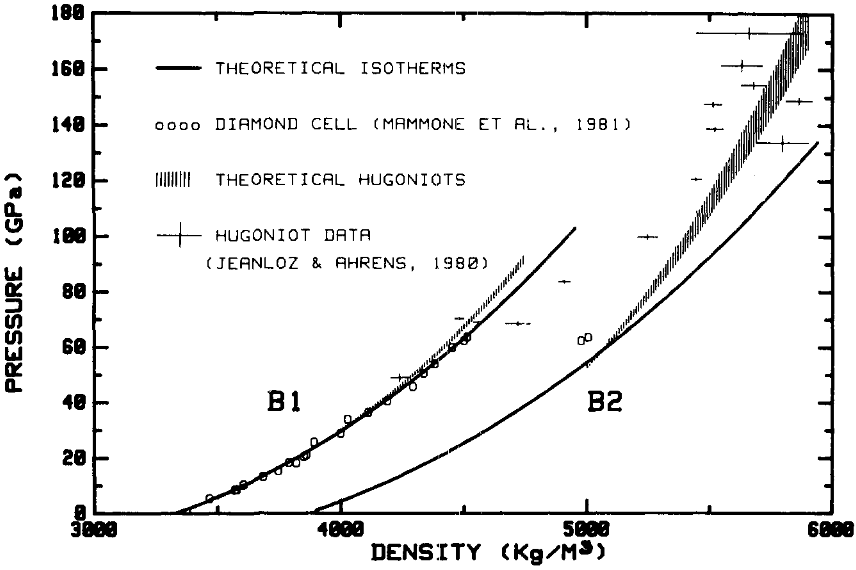

Fig. 7.16. Experimental and calculated equation of state for (a) MgO and (b) CaO taken from Bukowinski (1985). Both calculated isothermal compression data and Hugoniot data (with shading representing uncertainty due to possible errors in the Gruneisen parameter) are shown. See original text for details of sources of experimental data (after Bukowinski, 1985; reproduced with the publisher's permission).

Table 7.13. Equation-of-state parameters for MgO and CaO calculated by Bukowinski (1985) compared with experimental values from various sources (in parentheses)

	ρ_0 (kg/m^3)	K_0 (GPa)	K_0'	K_0K_0''	Θ (K)	γ
MgO(*B*1)	3559 ± 10	155 ± 5	4.16 ± 0.2	−4.6 ± 0.4	776	1.26
	(3583 ± 1)	(160 ± 0.2)	(4.13 ± 0.09)	(−10.1 ± 0.7)	(776)	(1.5)
		(155)				
MgO(*B*2)	3711 ± 10	156 ± 5	4.12 ± 0.2	−4.5 ± 0.4	698	1.18
CaO(*B*1)	3328 ± 10	109 ± 5	4.62 ± 0.2	−6.7 ± 1.0	638	1.40
	(3345 ± 1)	(111.25)	(4.85 ± 0.02)		(605)	(1.5)
CaO(*B*2)	3886 ± 10	123 ± 5	4.4 ± 0.2	−4.8 ± 0.5	600	1.48

oped by Burns (1970), Strens (1969, 1976), and Gaffney and Anderson (1973). These discussions were presented within the framework of crystal-field theory, and Ohnishi (1978) attempted to develop further application of this approach to prediction of such transitions for Mn, Fe, and Co ions in octahedral coordination to oxygen. Estimated pressures in the ranges 70–130 GPa for MnO, CaO, and Fe_2O_3 and 25–40 GPa for FeO were proposed for high-spin→low-spin transitions.

Tossell (1976a) used a molecular-orbital approach employing the MS-SCF-$X\alpha$ scattered wave cluster method to make predictions regarding the electronic structures of iron-bearing oxidic minerals at high pressure. The molecular-orbital energy levels (and their compositions) in the valence region were calculated for the square planar FeO_4^{6-} and octahedral FeO_6^{9-} and FeO_6^{10-} clusters at interatomic distances representative of appropriate minerals at atmospheric pressure (i.e., the square planar Fe^{2+} of gillespite, the octahedrally coordinated Fe^{3+} and Fe^{2+} of Fe_2O_3, FeO, and, to a first approximation, numerous silicate minerals). Subsequently, calculations were performed at reduced internuclear distances in order to simulate the effects of high pressures and their influence on spectral properties and spin states. The square planar FeO_4^{6-} cluster was studied be-

Table 7.14. Calculated and experimental *B*1-to-*B*2 transition pressures in MgO and CaO

	MgO	CaO
Experimental value	>200 GPa[a]	61 GPa[b]
APW calcs.	205[c]	32[c]
Pseudopotential calcs.	1050[d]	—
MEG calcs.	256–372[e]	121–162[e]

[a] Vassiliou and Ahrens (1981).

[b] Jeanloz et al. (1979); Mammone et al. (1981).

[c] Bukowinski (1985).

[d] Chang and Cohen (1984).

[e] Cohen and Gordon (1976).

cause the rare mineral gillespite ($BaFeSi_4O_{10}$) contains such a unit, and is one of the few examples where a high-spin→low-spin transition has been proposed on the basis of experimental evidence.

The order of the predominantly Fe $3d$ (crystal-field-type) orbitals in the $FeO_4{}^{6-}$ unit is calculated to be $x^2-y^2 > xy > xz,yz > z^2$ (with the ligands lying along x and y axes), in agreement with experiment. Studies at reduced internuclear distances (2.03 → 1.93 Å) show a calculated increase in the $d_{x^2-y^2} - d_{z^2}$ separation that is in close agreement with the crystal-field R^{-5} distance-dependence law, although the calculations suggest a high-spin→low-spin transition will not occur at Fe–O distances as small as 1.93 Å. For the $FeO_6{}^{9-}$ and $FeO_6{}^{10-}$ clusters at internuclear distances of 2.17, 2.06, and 1.95 Å, calculated trends in crystal-field energies are again in agreement with the R^{-5} law, as shown in Fig. 7.17, while O → Fe metal charge-transfer energies are found initially to increase as Fe–O distance is reduced, although they decrease at small distances for $FeO_6{}^{10-}$. A marked increase in covalency and width of the valence region is also observed. Although spin pairing in octahedral Fe^{2+} compounds is predicted to occur at mantle pressures on the basis of observed trends, uncertainties in such parameters as the molar volumes of high- and low-spin Fe^{2+} makes prediction of the pressures involved very difficult. The MO results do highlight the large changes predicted in bonding character of the iron oxides at high pressures compared with the small changes predicted in MgO using similar methods.

7.2.4. Iron (and Fe-rich alloys) at core pressures

Reviews of the experimental and theoretical work on the Earth's core have been published by Ringwood (1984) and, with special reference to the properties of iron at ultra-high pressures, by Anderson (1986). The earlier experimental work established that the body-centered cubic (α-Fe) phase undergoes a transition at room temperature and 13 GPa to a hexagonal close-packed structure (ε-Fe) that is not ferromagnetic, and that at high temperature a face-centered cubic form (γ-Fe) is stable. Although phase relations at moderate (<50 Gpa) pressures are reasonably well established, uncertainty remains regarding the form of iron stable at the megabar pressures encountered in the core.

The electronic structure of iron (α-Fe) has been the subject of numerous studies (see, for example, Moruzzi et al., 1977). As long ago as 1949, Elsasser and Isenberg suggested that at core pressures iron might undergo an electronic structure transition to a collapsed "$3d^8$ state" (from the approximate $3d^{7.0}4s^{1.0}$ configuration of the atoms of crystalline iron at standard conditions). A model to explain the inner-core–outer-core discontinuity in terms of such an electronic transition was constructed by Bukowinski and Knopoff (1976). However, band-structure calculations by Bukowinski (1976a) on α-Fe (chosen because it is probably closest in

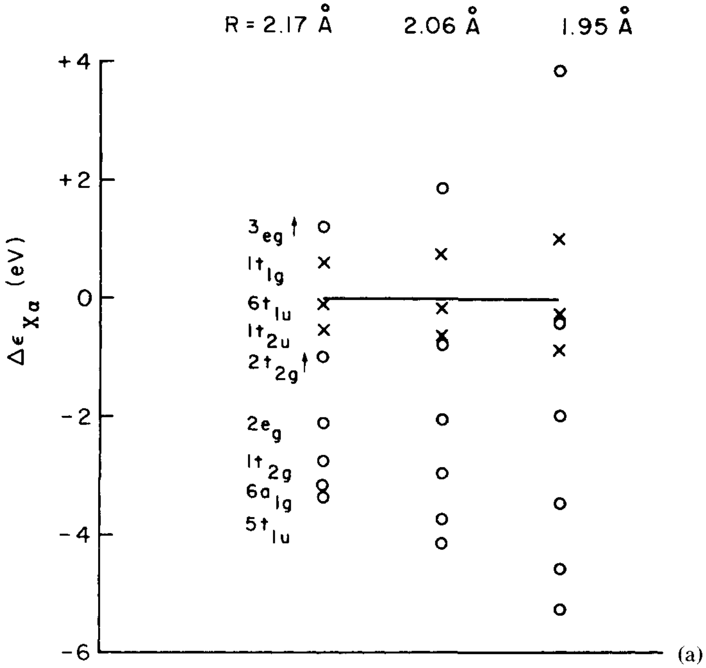
R = 2.17 Å
2.06 Å
1.95 Å
+4
+2
0
-2
-4
-6
Δε Xα (eV)
3eg ↑
1t1g
6t1u
1t2u
2t2g ↑
2eg
1t2g
6a1g
5t1u
(a)

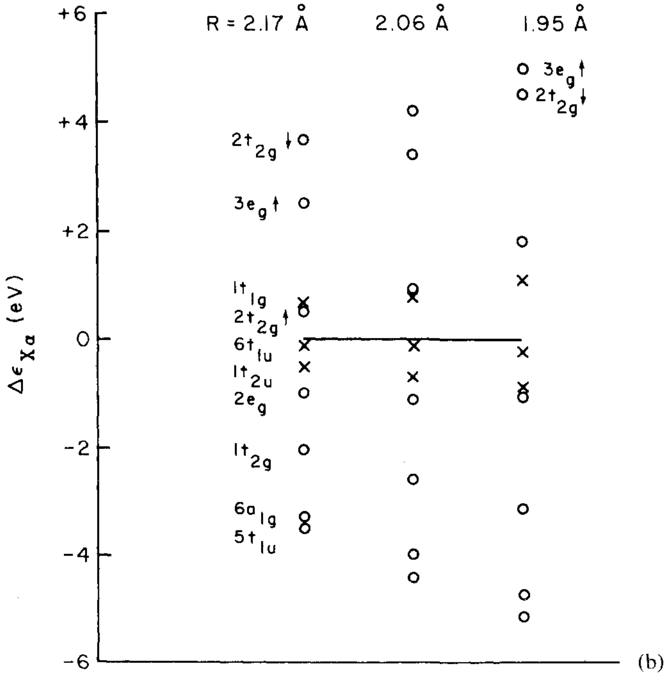
R = 2.17 Å
2.06 Å
1.95 Å
+6
+4
+2
0
-2
-4
-6
Δε Xα (eV)
3eg ↑
2t2g ↓
2t2g ↓
3eg ↑
1t1g
2t2g ↑
6t1u
1t2u
2eg
1t2g
6a1g
5t1u
(b)

structure to the high-density liquid iron in the outer core) were used to demonstrate that the electronic structure is very stable to at least twofold compression, and that the collapse to a "$3d^8$ state" does not occur until approximately fourfold compression. These calculations, in which the augmented-plane-wave method with the "muffin-tin" form of the potential was employed, clearly demonstrated the importance of quantum-mechanical investigations to an understanding of the core. They also suggest that there are not electronic transitions within the Earth's core.

More recently, Boness et al. (1986) calculated the band structure of both ε-Fe and γ-Fe using the linear muffin-tin-orbital method under conditions corresponding to pressures ranging from 4 to 980 GPa. The results were used to, in turn, calculate electronic thermodynamic quantities such as the electronic specific heat and the electronic Grüneisen parameter, useful quantities with which to constrain models of the Earth's core.

As regards other elements than iron that may occur in the core, electronic-structure calculations have again made an important contribution to current understanding. The suggestion that significant amounts of potassium occurs, at least in the outer core, has been proposed both to explain the relative depletion in potassium of the outer regions of the Earth (compared with values predicted from the study of meteorites), and to provide a radiogenic heat source to drive convection in the outer core. Although the differences in size and electronic structure between K and Fe would seem to preclude significant solid solution, K is very compressible and undergoes a transition from a body-centered-cubic to face-centered-cubic structure at 12 GPa and a further transformation at 19 GPa, the origin of which is uncertain. However, Bukowinski (1976b), again using the augmented-plane-wave method to perform band-structure calculations on potassium, predicted a series of pressure-induced phase changes brought about by the sequential filling of initially unoccupied *d*-like electronic states. In addition to the discontinuous density changes that accompany these phase transitions, the presence of the *d*-like bands is what makes potassium very compressible. Interestingly, the calculations predict that, at pressures as low as 50 GPa, the atomic radius of potassium becomes compatible with that of iron, and its electronic structure becomes like that of a typical transition metal. These changes could greatly enhance the miscibility of potassium in iron. Recently Boness and

Fig. 7.17. Molecular-orbital energy-level diagrams for the (a) FeO_6^{9-} and (b) FeO_6^{10-} clusters calculated using the MS-SCF-$X\alpha$ method by Tossell (1976a). The variation in MO energies is shown as Fe–O distance (R) is decreased to simulate the effects of increasing pressure. The horizontal line corresponds to a constant $1t_{1g}6t_{1u}1t_{2u}$ average energy. Crosses represent O $2p$ nonbonding orbitals; open circles represent other orbitals in FeO_6^{9-}. The highest occupied orbital is $3e_{g\uparrow}$ with two electrons; in FeO_6^{10-} it is $2t_{2g\downarrow}$ with one electron (after Tossell, 1976a; reproduced with the publisher's permission).

Brown (1990) have shown using LMTO band calculations similar changes in electronic structure and atomic radius for S at high pressure, and have used such changes to support the idea of Fe,S solid solution. A contrary viewpoint has been expressed for the K case by Sherman (1990) who found from MS-$X\alpha$ cluster calculations that in an Fe or Fe sulfide environment K is present as K^+ and shows little covalency in its bonding to S. This argues against K incorporation into an Fe or FeS core. Clearly, such questions cannot be entirely settled by quantum-mechanical calculation at present, given the necessary approximations in methods and in model systems.

7.3. Industrial mineral materials

Many minerals or their synthetic equivalents are of industrial importance, and the possibilities of greater understanding of their behavior and properties through application of the methods described in this book is a major stimulus to research. Two examples are chosen for discussion here: The first is the zeolites, a group of framework alumino-silicates (with interstitial Na^+, Ca^{2+}, and H_2O), characterized by very open frameworks with large interconnecting spaces or channels; the second is the transition-metal sulfide catalysts, materials already generally discussed in Chapter 6, but considered here specifically in relation to their catalytic properties.

7.3.1. Zeolites

Zeolites are an interesting class of materials for quantum-chemical study from a number of points of view. First, they are of substantial interest as ion exchangers, molecular sieves, and catalysts in industry, features depending upon their controllable porosity and Lewis acidity. Second, they have been studied by many spectroscopic methods, particularly by infrared and NMR spectroscopies, and synthetic efforts are constantly producing new zeolites (and related high-porosity materials) with new properties. Third, important aspects of their structure (e.g., Si, Al distributions, and the nature of their surficial hydroxyl-bearing sites) are not well understood (partly due to the similarity of Al and Si x-ray scattering factors and difficulty of crystallization). Fourth, they are very complicated structurally and thus strain the capabilities of *ab initio* calculational methods. *Ab initio* calculations on such materials typically require severe approximation in cluster size, basis-set size, and completeness of geometry optimization. Zeolites are also a fertile subject for simulations, both empirical atomistic crystalline simulations like those discussed in several previous chapters, and those based upon *ab initio* calculations on molecular units (molecular mechanics). They are also more studied by approximate MO methods than any other class of inorganic materials. It is also quite common in groups studying zeolites for experimentalists and theoreticians to collaborate closely and for calculations to be viewed as, at least in part, "computer experiments" on a par with traditional experimental techniques. Theoretical studies on zeolites have been recently reviewed by Suffritti and Gamba (1987).

A central problem in zeolite structure determinations is characterization of the Al, Si distribution. A central question is that of "Al avoidance" (Lowenstein, 1954), the infrequent occurrence of Al–O–Al linkages. This question has been treated using an MO approach by Hass et al. (1981). They obtained an energy difference of about 120 kcal/mol between the following two reactions:

$$(OH)_3SiOSi(OH)_3 + AlH_4^- \rightarrow (OH)_3SiOAl(OH)_3^- + SiH_4$$

$$(OH)_3SiOAl(OH)_3^- + AlH_4^- \rightarrow [(OH)_3AlOAl(OH)_3]^{2-} + SiH_4$$

with the AlOAl unit in the second reaction being less stable, in agreement with expectation. However, these calculations used minimal basis sets, performed only partial geometry optimization, and did not attempt to compensate for the differing total charges. It is certainly expected that the interaction of two anions to give a dianion in the second reaction would be unfavorable, but such charge effects would, of course, be at least partially compensated in the solid. Dempsey (1969) found that experimental Al,Si distributions could be correlated with electrostatic potentials at the various tetrahedral (T) sites, calculated with formal charges and observed atomic positions. Gibbs et al. (1977) showed that observed T–O distances in zeolites correlate with Mulliken overlap populations obtained using experimentally observed angles (and constant distances). Many recent calculations of the relative stability of Al in different T sites have appeared (Fripiat et al., 1985; O'Malley and Dwyer, 1988). The general method employed is an *ab initio* SCF Hartree–Fock–Roothaan calculation, generally using a minimum basis set, on polyhedral models of the various T sites, alternately occupied by Si or Al. The pentameric model used by Fripiat et al. (1985) for the T_2 site of ferrierite is shown in Fig. 7.18. Using experimental bond distances and angles for the atoms immediately adjacent to the T site, the total energy of the cluster is calculated. Total energies of Al- and Si-centered clusters will, of course, be quite different, but the quantity of interest is the relative value of the Al–Si energy difference for the various T sites. The smaller this difference, the more stable the Al relative to Si and the greater the preference of Al for the site. One can define, from the cluster energies, stabilization energies for Si and Al in the sites and Al for Si relative replacement energies. As shown in Fig. 7.19, calculated relative replacement energies for ferrierite confirm that the T_2 site is preferred by Al, with T_1 and T_3 being highly unfavorable and T_4 somewhat less favorable than T_2. Studies on Al and Si distributions in six-membered-ring hexameric clusters, of the type shown in Fig. 7.20, indicate that Al pairs are most stable when well sep-

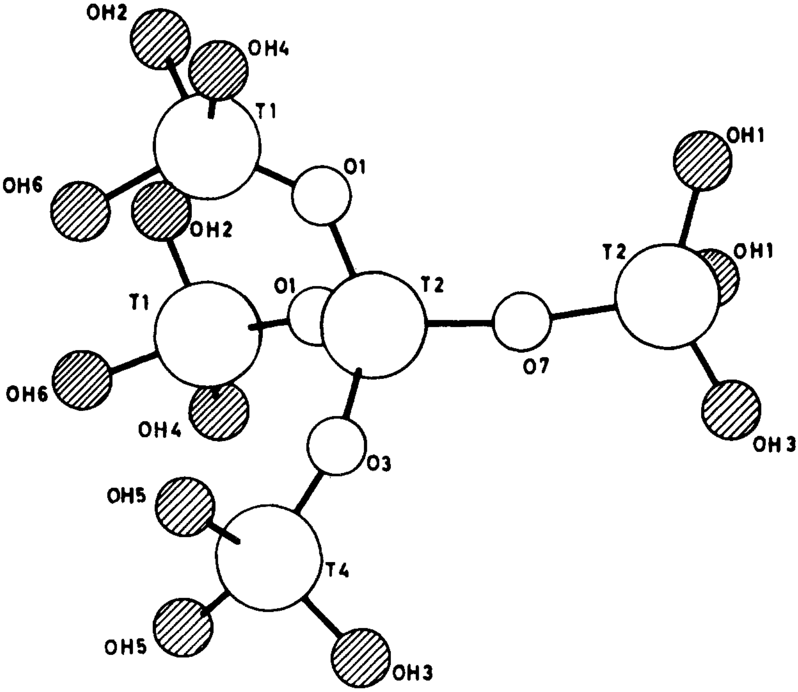

Fig. 7.18. The pentameric model cluster used for calculations centered on the T_2 site in zeolites (after Fripiat et al., 1985; reproduced with the publisher's permission).

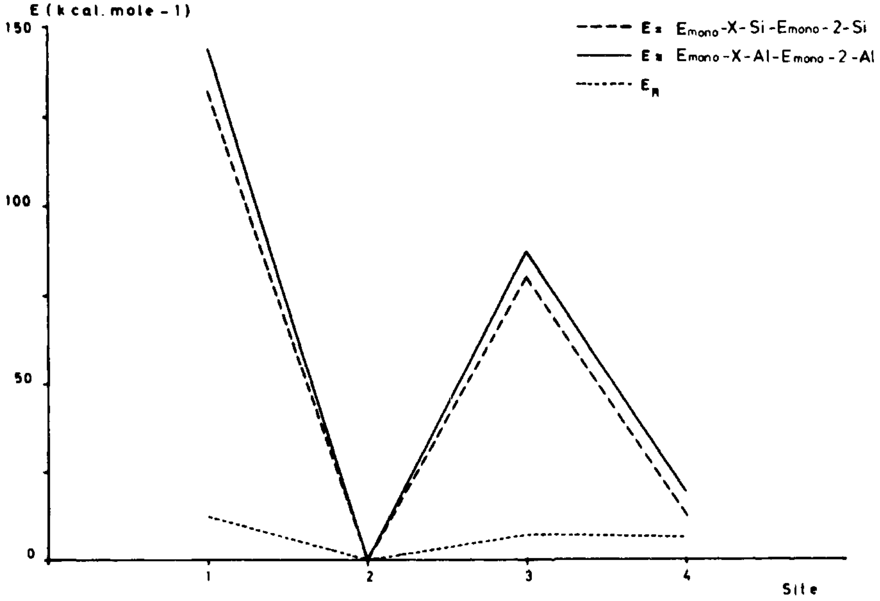

Fig. 7.19. Cluster energies calculated for the T_1, T_2, T_3, and T_4 sites in zeolites (after Fripiat et al., 1985; reproduced with the publisher's permission).

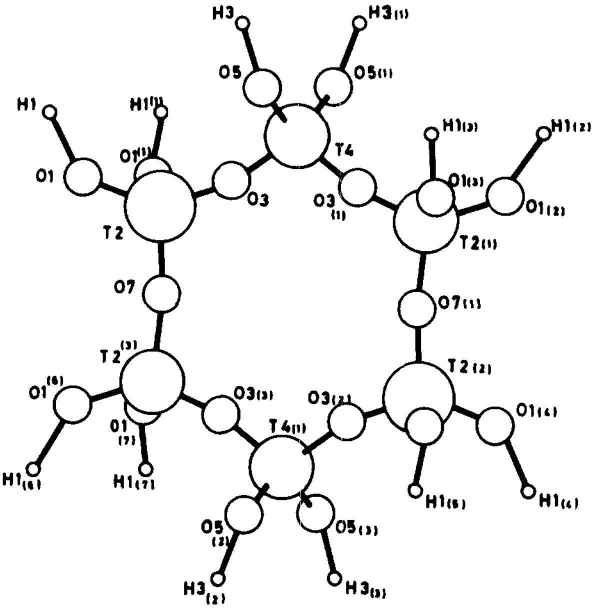

Fig. 7.20. The hexameric model cluster used in calculations on zeolites (after Fripiat et al., 1985; reproduced with the publisher's permission).

arated, and that adjacent Al atoms around the ring are destabilized by 50 kcal/mol, in agreement with the Al avoidance principle of Lowenstein (1954). This approach has been successful for many zeolites, although there have been disagreements over the interpretation of the site energy differences. In general, such differences depend upon both bond distance and bridging bond angle, with Al preferring sites with larger bond distances and smaller *T*–O–*T'* angles. As we have previously seen for $Si(OH)_4$, $Al(OH)_4^-$, $(H_3Si)_2O$, and $H_3SiOAlH_3^-$, *ab initio* SCF Hartree–Fock–Roothaan calculations using an STO-3G basis set give reasonably accurate bond distances and angles. For isoelectronic systems, correlation and basis-set energies are expected to be comparable; so relative energies should be reasonably accurate.

Sauer et al. (1980) have used more flexible basis sets to compare the interaction energies of the oxygens in $H_3SiOSiH_3$, $H_3SiOAlH_3^-$, and H_2O with cations and water. They found, in agreement with experiment, weaker binding of cations to $H_3SiOSiH_3$ than to H_2O. Mortier et al. (1984) studied deprotonation of terminal and bridging oxygens in aluminosilicate models and established that deprotonation of oxygens bridging between Si and Al was considerably less demanding energetically than deprotonation of O in terminal OH groups, so that protons attached to bridging oxygen were strongly acidic. Hobza et al. (1981) studied the interaction of $Si(OH)_4$ and $H_3SiOSiH_3$ groups with H_2O, establishing that $(H_3Si)_2O$ is H bonded less strongly than water itself, while $Si(OH)_4$ is H bonded more strongly, particularly when $Si(OH)_4$ is the proton donor to H_2O. Later calculations by Chakoumakos and Gibbs (1986) using larger basis sets and more complete geometry optimization confirmed this result, giving an even larger difference between proton donor and proton acceptor structures for $Si(OH)_4$. For the $Si(OH)_4$ as proton donor to H_2O, the lengthening of the O–H bond is accompanied by a contraction of the Si–O bond, stabilizing the system. This effect is much larger energetically for more flexible basis sets incorporating *d* polarization functions. This is consistent with many studies of the geometries of oxyanions of Si–Cl, which show that *d* polarization functions shorten and stabilize *T*–O bonds more than they do *T*–OH bonds. These results have been confirmed and extended by Ugliengo et al. (1990), who incorporated correlation corrections by many-body theory and calculated the normal modes of vibration to allow evaluation of zero-point vibrational energies. Although the calculated $SiH_3OH\cdots H_2O$ interaction energy was in the experimental range, the calculated equilibrium constant for the dissociation was in disagreement with experiment, a result attributed to inadequacies in the SiH_3OH molecular model for the silanol surface. The transition state for the $SiH_3OH\cdots H_2O$ reaction has also been studied at a high level (Lasaga and Gibbs, 1990; see Section 8.3.6 on surface studies).

So far, most MO studies of zeolite systems have employed H atoms as cluster saturators. An alternative approach utilizes a point-charge array (Vetrivel et al., 1988). However, it has been found that very large point-charge arrays are needed to reproduce the expected Madelung potentials at sites within the molecular cluster, and that the size, geometry, and assumed charge magnitudes on the point-charge array can significantly affect calculated properties such as –OH stretching frequencies.

Zeolites have also been recently studied using molecular mechanics simulation (Mabilia et al., 1987) with stretching and bending force constants and partial atomic charges taken from *ab initio* calculations. These calculations indicate that the sodalite cage structure is stabilized by replacement of Si by Al and by local concentration of Al for a given Si:Al ratio, but these results seem to be inconsistent with experiment.

7.3.2. *Transition-metal sulfide catalysts*

Catalytic hydrodesulfurization (HDS), the removal of sulfide in the form of H_2S from petroleum, is a critical step in the industrial refinement process and one of increasing importance as the cleaner world supplies of petroleum feedstocks dwindle and the poorer quality feedstocks have to be used. The removal of sulfur (and certain other impurities such as nitrogen in hydrodenitrogenation) is undertaken using transition-metal sulfide catalysts (Weisser and Landa, 1973). The most widely used materials are based on transition-metal disulfides with layer structures such as MoS_2 and WS_2 (and including mixed phases with combinations of Co, Ni, Mo, and W sulfides). The industrial catalysts are generally small porous sulfided crystallites bound to an Al_2O_3 or $SiO_2-Al_2O_3$ support.

Earlier work has been reviewed by Weisser and Landa (1973) and certain more recent studies reviewed by Chianelli (1983), who points to the primary catalytic effects being electronic in nature, related to the position occupied by the metal concerned in the periodic table, with first-row transition-metal sulfides being relatively inactive and second- and third-row transition metals (Ru and Os) showing maximum activity (by three orders of magnitude). A secondary effect appears to be geometric in origin; for example, MoS_2 catalysts seem to exhibit activity associated particularly with edges rather than basal planes.

Various theoretical studies have been undertaken to model the adsorption process and active sites of the catalysts, and, due to the complexity of the system, approximations and simplifications have often been severe. Both aromatic and nonaromatic organosulfur compounds are found in petroleum, but it is the aromatic species that are much less reactive. These are composed largely of thiophene, dibenzothiophene, and other thiophenic species. Thiophene, SC_4H_4, has a 5-membered planar ring structure and is the simplest aromatic in petroleum feedstock; hence, it has been much employed in calculational modeling. Under (HDS) catalytic conditions it yields mainly butane (C_4H_{10}), although yielding butadiene (C_4H_6) under low H_2 pressures. It is unknown whether desulfurization or hydrogenation of the thiophene ring occurs first, or if they occur simultaneously.

Earlier calculations employed extended Hückel theory and other approximate MO methods such as CNDO using just a proton to represent the electron-accepting (catalyst) surface for thiophene adsorption (Zdrazil and Sedlacek, 1977), or considering the adsorption of H_2O onto one and two molybdenum clusters. The latter approach (using EHMO theory) favored coordination to two metal centers (Vladov et al., 1983). The same method was subsequently applied to $MoS_3H_3^+$ clusters (Joffre et al., 1986) and led to a proposal favoring a perpendicular bound species (through the sulfur end and referred to as η^1) rather than a parallel bound species (through the five atoms of the ring and referred to as η^5).

A comprehensive study of periodic trends in the electronic structures of transition-metal sulfides using MS-SCF-$X\alpha$ calculations was undertaken by Harris (1982) and Harris and Chianelli (1984). This study employed MS_6^{n-} clusters (see Chapter 6) and led to a suggestion that the marked variations observed in catalytic activity (noted above) relate to filling of the highest occupied molecular orbital and the degree of covalency in the metal–sulfur bond. On the basis of these results, a model was proposed in which thiophenic molecules bind to the catalyst surface in a perpendicular (η^1) geometry at a sulfur vacancy. A weakening of the C–S bonds in the ring could result from backdonation of the metal electrons into a thiophenic π^* orbital (Harris and Chianelli, 1984).

In a detailed study of the nature of the active site and mechanism of desulfurization for the case of thiophene on MoS_2, Zonnevylle et al. (1988) used an extended Hückel band theory (tight-binding method) approach. They suggest that the η^5-bound sites, in which the thiophene ring lies parallel to the surface, are particularly advantageous in weakening of the S–C bond, whereas η^1 sites are less active. Also examined in this study were the effects of removal of surrounding surface sulfurs, which appears to increase the catalytic potential of the η^5 geometry, and possible surface reconstruction where Mo–Mo pairing is suggested. Study of the possible effects of poisoners and promoters led to suggestions that metals that replace a surface molybdenum atom tend to poison the catalyst (i.e., destroy its effectiveness in HDS applications), whereas those that "pseudointercalate" between the S–S layers can serve to promote catalytic HDS activity.

7.4. Concluding remarks

The material discussed in this chapter clearly illustrates the potential of quantum-mechanical methods (used in conjunction with appropriate experiments) in understanding and predicting the structures, stabilities, and physical and chemical properties of minerals and related solids. It is an approach that has important applications in fields as diverse as solid earth geophysics and industrial chemistry. It is important to re-emphasize the close links between materials science research and work in mineralogy and geochemistry, with minerals scientists generating knowledge of value to mineralogists (both now and in the future) and mineralogists capable of making significant contributions to the study of the wider range of materials.

Note

1. In the quasiharmonic approximation, the crystal potential is expanded as a power series in the displacement from the equilibrium lattice constant only through the displacement squared term.

8

APPLICATIONS TO GEOCHEMICAL PROBLEMS

In this, the last major chapter of the book, we turn our attention to the applications of modern electronic structure models and concepts to more general geochemical problems; namely, those described by Goldschmidt as being concerned with the "distribution of elements in the geochemical spheres and the laws governing the distribution of the elements" (see Preface).

The majority of minerals and rocks originally formed by crystallization from melts, and so the first section of this chapter is devoted to considering the nature of melts (and glasses), structure and bonding in melts, and the partitioning of elements (particularly transition elements) between the melt and crystallizing solid phases. The classic work of Bowen (1928) led to the recognition of particular sequences of crystallization and crystal–melt reaction relationships in the silicate melts from which major rock types form, as enshrined in the "Bowen Reaction Series." Attempts were also made to explain the incorporation of particular elements into particular mineral structures using simple crystal chemical arguments, notably as laid down in "Goldschmidt's Rules" (Goldschmidt, 1937). Such concepts are reappraised in the light of modern electronic structure theories.

The other major realm of formation of minerals and rocks, and the most important medium of transport and redistribution of the chemical elements at the Earth's surface, is the aqueous solution. The molecular and electronic structures of aqueous solutions, their behavior at elevated temperatures, formation and stabilities of complexes in solution, and the mechanisms of reactions in solution are all considered in the second section of this chapter.

The surfaces of minerals (or other crystalline solids) differ from the bulk material in terms of both crystal structure and electronic structure. A great variety of spectroscopic, diffraction, scanning, and other techniques are now available to study the nature of solid surfaces, and models are being developed to interpret and explain the experimental data. These approaches are discussed with reference to a few examples of oxide and sulfide minerals. Although relatively few studies have been undertaken specifically of the surfaces of minerals, many of the reaction phenomena that occur in natural systems take place at mineral surfaces, so that such surface studies represent an important area of future research.

In the final section, the overall geochemical distribution of the elements is considered in the light of electronic structure theories. Previous attempts to classify elements on the basis of their preferences for compound formation with oxygen or sulfur are reviewed.

8.1. The nature of melts, glasses, and crystal–melt equilibria

In the geochemical context, it is the *silicate* melt that is of overwhelming importance, and the understanding of melt structure forms the basis of understanding physical, chemical, and thermal properties of magmas and relevant liquid–crystal systems. Direct studies of silicate melts present obvious technical problems (pure SiO_2 melts at 1713°C), so that most experimental data have been obtained on the quenched equivalent of melts (glasses) on the assumption that the principal features of the structure of a melt are retained as the sample is quenched to a glass. Although numerous studies have provided general support for this assumption, it is known that a small ($\sim$1 kcal mol^{-1}) but significant heat effect is associated with the glass transition (Navrotsky et al., 1980). This effect is insufficient to account for a reconstructive transformation, but does show that small differences exist between melts and their glasses.

The simplest chemical compound relevant to the structure of magmatic liquids is SiO_2; indeed, the silica content of most magmas exceeds 40 wt %. The first topic discussed in the following section is, therefore, that concerned with structure and bonding in silica glass. Subsequently, the roles of aluminum in silicate melts, of alkali or alkaline earth metals, of transition metals illustrated by the specific example of iron, and of volatile species, are briefly considered. Over the years, it has become customary to divide the metal cations in silicate melts into network-forming cations that occur in tetrahedral coordination within the polymeric units that make up the melt, and network modifiers that connect such units together (Bottinga and Weill, 1972), and the same approach is adopted here. The subject of the structure of silicate melts has been reviewed by Mysen et al. (1982) and Mysen (1983).

8.1.1. Silica glass and melt

Silica glass or vitreous SiO_2 (abbreviated as v-SiO_2) is a material of considerable mineralogical and technological importance. In many respects, it differs little from crystalline silica polymorphs such as quartz. For example, the enthalpy of melting of quartz is very low, and the uv absorption spectra of quartz and quartz glass are very similar (Phillip, 1971). X-ray studies (Mozzi and Warren, 1969; DaSilva et al., 1974; Coombs et al., 1985) indicate that the Si coordination number, average Si–O distance,

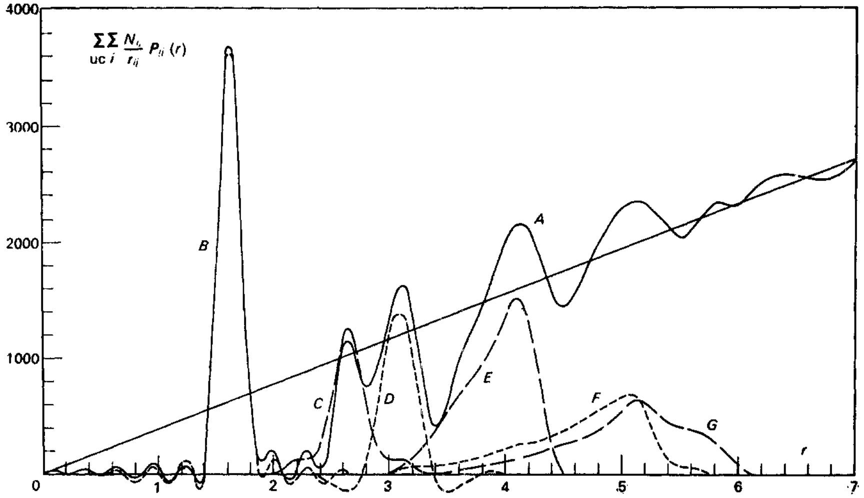

Fig. 8.1. The pair function distribution curves for SiO_2; *A* is the measured curve. The computed contributions are given by: *B*, Si–O; *C*, O–O; *D*, Si–Si; *E*, Si–second O; *F*, O–second O; *G*, Si–second Si (from Mozzi and Warren, 1969).

and O–Si–O angle in v-SiO_2 are very similar to those in quartz, but that there is a broad range of Si–O–Si angles (Fig. 8.1). In contrast to many semiconductor materials, v-SiO_2 shows only modest band broadening compared to quartz, as seen by ultraviolet photoelectron spectroscopy (DiStefano and Eastman, 1971; Fischer et al., 1977) and x-ray emission spectroscopy (Wiech and Kurmaev, 1985; Fig. 8.2).

However, v-SiO_2 does appear to have many more "defects," where the term *defect* signifies an unusual local or midrange bonding arrangement, than does quartz. For example, molecular-dynamics simulation studies (Garofalini, 1984a) indicate coordination numbers of 3 or 5 for some Si atoms and 3 for some O atoms although most Si atoms continue to be 4 coordinate and most O atoms 2 coordinate, as in earlier molecular dynamics studies (Woodcock et al., 1976; Mitra et al., 1981). Raman spec-

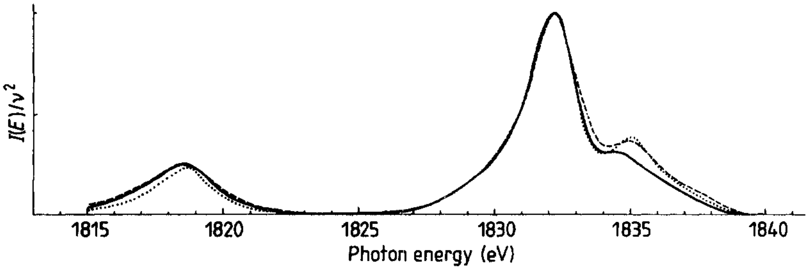

Fig. 8.2. Silicon *K* x-ray emission spectra of α-quartz (solid line), β-tridymite (dotted curve), and v–SiO_2 ("suprasil"; dashed curve) (after Wiech and Kurmaev, 1985; reproduced with the publisher's permission).

troscopy (Galeener, 1982a,b) and NMR studies (Brinker et al., 1988) indicate the presence of Si_3O_9 ring structures, which are not found in the SiO_2 polymorphs and are quite uncommon in other silicate structures. Studies of both quartz and v-SiO_2 at high pressure and low temperature have indicated near constancy of Si–O distances (Levien et al., 1980) but considerable variability of average values and distributions of Si–O–Si angles. Such angular distributions have been studied using ^{29}Si NMR (Dupree and Pettifer, 1984; Devine et al., 1987) and Raman spectroscopy (Hemley et al., 1986). Data on Si–O–Si angles are important in understanding the unusual physical properties of v-SiO_2, such as its increase in compressibility with pressure (Grimsditch, 1984) up to about 20 kbar (2 GPa) and its compaction by static high pressure on shock loading (Sakka and MacKenzie, 1969). Changes in Raman spectra, shown in Fig. 8.3, have been interpreted in terms of reduction in the average Si–O–Si angle and a narrowing in its distribution, along with an increased prominence of Si_3O_9 ring structures, at least up to 30 GPa, where the distinctive Si_3O_9 Raman signature begins to disappear. Studies using ^{29}Si NMR (Dupree and Pettifer, 1984; Devine et al., 1987) indicate a shift of Si–O–Si angle to smaller values in densified SiO_2, based on the relationship between Si NMR shift and Si–O–Si angle observed for crystalline SiO_2 polymorphs (Fig. 8.4). Studies of the correlation between Raman and ^{29}Si NMR spectra for v-SiO_2 prepared by sol–gel methods and heat treated (Brinker et al., 1988) are also consistent with the presence of Si_3O_9 rings with Si–O–Si angles around 137°, producing both Raman "defect" bands (labeled "D_2") and distinctive ^{29}Si NMR peaks. Brinker et al. (1988) have estimated a 20 mol % concentration for such species on silica surfaces. Molecular-dynamics simulations (Garofalini, 1983) and molecular models for the fracture of silica glass (Michalske and Bunker, 1984) have suggested even smaller Si–O–Si angles (on the order of 110°) associated with Si_2O_6 groups. Theoretical studies on the $H_4Si_2O_6$ molecule, with a shared-edge Si_2O_6 configuration, have yielded an equilibrium angle of ~91°, but with a ring strain energy of almost 200 kcal/mol (O'Keeffe and Gibbs, 1985). Calculations by Tossell and Lazzeretti (1987a) and Tossell (1990b) indicate that such shared-edge Si_2O_6 species should be substantially deshielded compared to conventional Q^4 species.

Recent preliminary XANES studies at the oxygen *K* edge (Stizza et al., 1987) are also consistent with a narrowing of Si–O–Si angle at high pressure. Experimental XANES and multiple-scattering calculations on a $Si_2O_7^{6-}$ cluster give a feature about 30 eV above the oxygen 1*s* edge that shifts in position with pressure and/or with Si–O–Si angle (Fig. 8.5). A

Fig. 8.3. Raman spectra of SiO_2 glass as a function of pressure. Above 8 GPa the spectra weaken, and no peaks are detectable above ~ 40 GPa (after Hemley et al., 1986; reproduced with the publisher's permission).

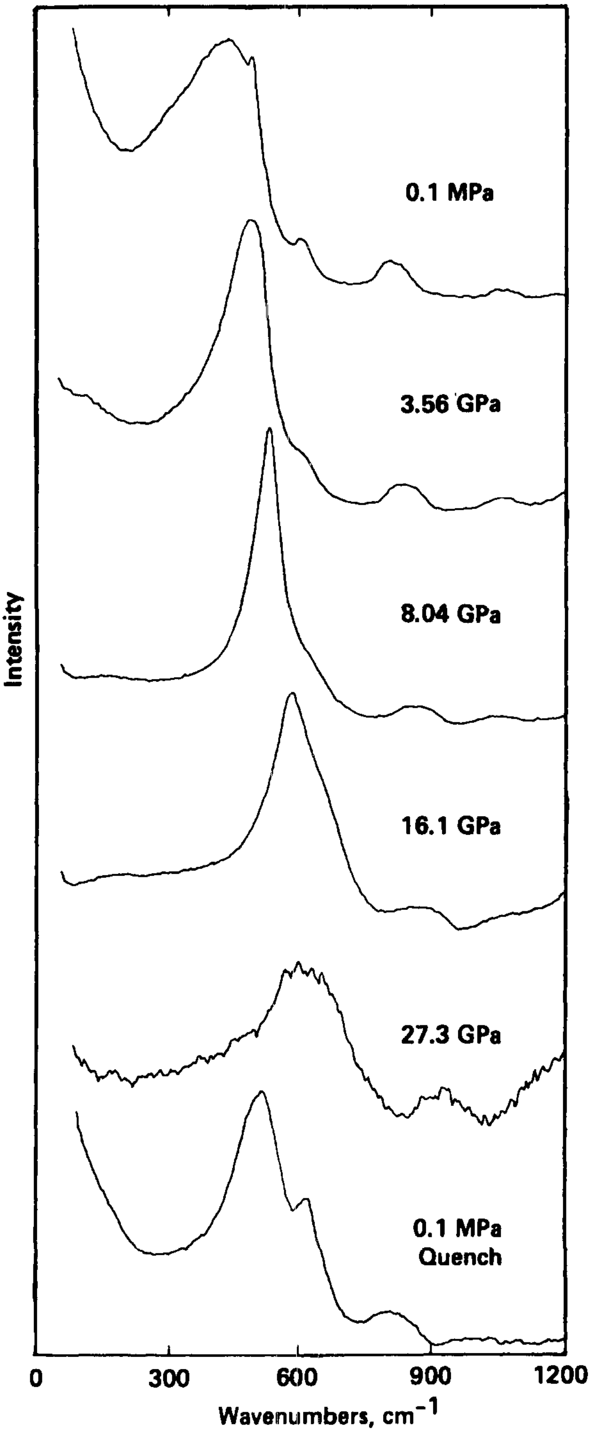
0.1 MPa
3.56 GPa
8.04 GPa
16.1 GPa
27.3 GPa
0.1 MPa
Quench
Intensity
0
300
600
900
1200
Wavenumbers, cm^{-1}

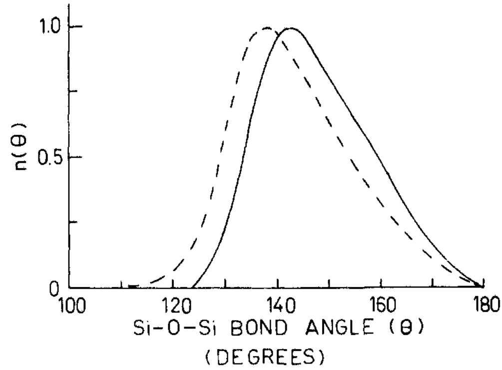

Fig. 8.4. The Si–O–Si bond angle distribution in undensified (solid line) and densified (dashed line) amorphous SiO_2 ("suprasil I") derived from NMR line shapes, where $n(\theta)$ is the relative number of bridging oxygens with bond angle θ (after Devine et al., 1987; reproduced with the publisher's permission).

similar feature, 30 eV above threshold, appears in the Si *L* XANES (Bianconi, 1979). Analysis of Si–O–Si angles is important for surface species because atomistic models (Michalske and Bunker, 1984), and comparison with properties of siloxanes (Brinker et al., 1988) indicate that reduced values of Si–O–Si angle can significantly accelerate nucleophilic attack by H_2O at the siloxane bond, via the mechanism shown in Fig. 8.6. ^{17}O NMR has been applied to v-SiO_2 only at atmospheric pressure, yielding an ^{17}O NQCC of 5.17 MHz and 0.2 (Geissberger and Bray, 1983). According to the calculations of Tossell and Lazzeretti (1988a), this is consistent with an average Si–O–Si angle of around 140°. From the calculated variations of NQCC and η with Si–O–Si angle shown in Figs. 8.7 and 8.8, the measured standard deviations correspond to an angular range of 120–180°.

Although the bulk of detailed work has been undertaken on v-SiO_2, *in situ* x-ray studies of molten silicates at high temperature have confirmed that Si is coordinated to four oxygens in the molten as well as the glassy state (Waseda and Toguri, 1977, 1978) and yielded information on Si–O bond lengths and some angular information (see Table 8.1).

8.1.2. Glasses and melts of more complex compositions

It is generally accepted that aluminum is tetrahedrally coordinated in aluminosilicate glasses and melts, provided that cations such as alkali metals or alkaline earth metals are present in sufficient amounts to charge compensate the replacement of Si^{4+} by Al^{3+} [i.e., $Si^{4+} \rightarrow Al^{3+} + (1/n)M^{n+}$, where monovalent or divalent *M* ions occur in nonframework sites associated with the tetrahedral aluminosilicate framework]. Experimental data for aluminosilicate glasses derived from both low-angle x-ray-scattering experiments and EXAFS studies show that as aluminum is substituted for silicon, the average *T* (tetrahedrally coordinated ion) –O bond

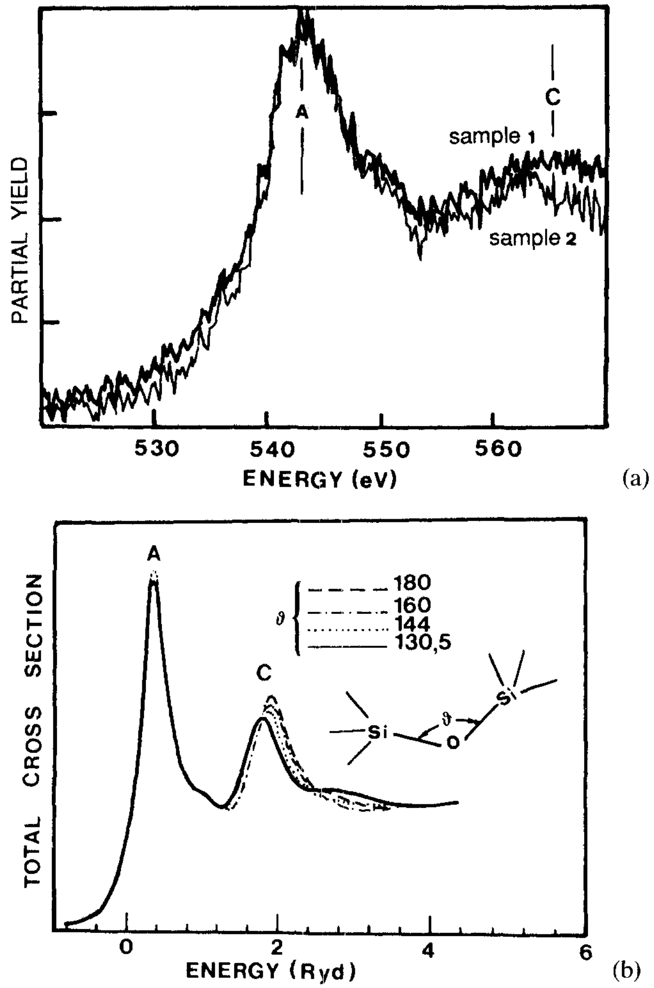

Fig. 8.5. (a) Experimental XANES of v–SiO_2 showing the oxygen 1*s* (*K*) edge in an untreated sample (1) and a sample (2) compressed to 20 kbar. (b) Calculated XANES for Si_2O_7 cluster with varying values of θ, the Si–O–Si angle.

length increases in the glass (from 1.62–1.63 Å in Al-free systems to 1.67 Å in $NaAlSiO_4$) and the average *T*–O–*T* angle decreases slightly. The experimental data are reviewed by Navrotsky et al. (1985), who also review the application of *ab initio* SCF molecular-orbital calculations undertaken on relevant cluster units to an understanding of the structure and properties of silicate and aluminosilicate glasses and melts of widely varying compositions. In Table 8.1 are shown experimental data on *T* distances and *T*–O–*T* angles, along with information on a larger range of cation–oxygen polyhedra, including coordination number and *M*–O bond lengths

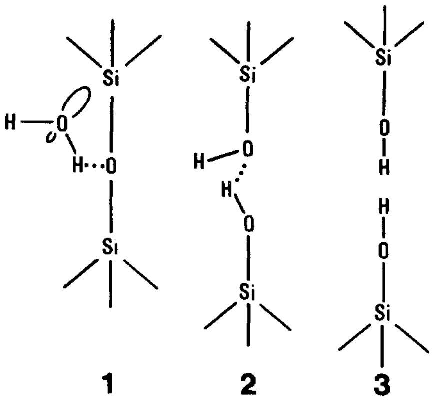

Fig. 8.6. Mechanism proposed for the breakage of the Si–O–Si bond, whereby a strained bond (at a slowly developing crack) adsorbs a water molecule (1), is cleaved by a dissociative reaction (2), and is converted to surface silanol groups (after Michalske and Bunker, 1984; reproduced with the publisher's permission).

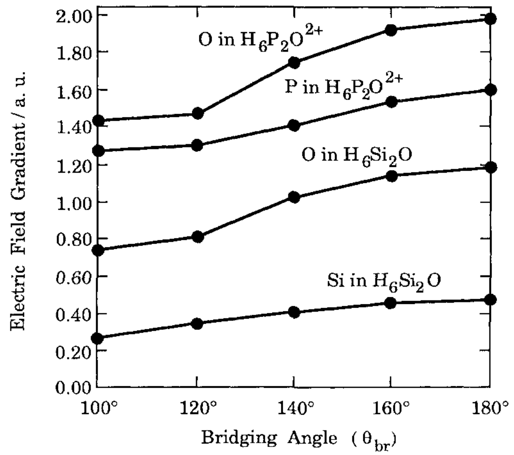

Fig. 8.7. Variation with θ_{br} of calculated EFGs at O, P, and Si in dimers (Tossell, unpublished results).

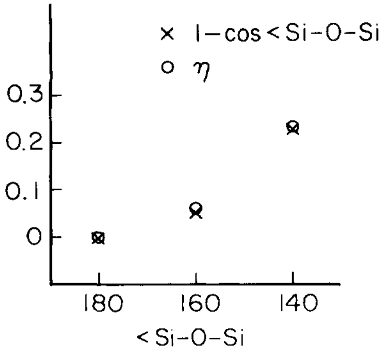

Fig. 8.8. Calculated anisotropy, η, and $1 - \cos\sphericalangle$Si–O–Si as a function of $\sphericalangle$Si–O–Si (from Tossell and Lazzeretti, 1988a).

Table 8.1. Crystal chemical data on glasses and melts: **(a)** tetrahedral cation–oxygen (*T*–O) distances and *T*–O–*T* angles ($\sphericalangle T\text{–O–}T$) in glassy and molten materials from x-ray data

Composition	Temp. (K)	*T*–O (Å)	$\sphericalangle$*T*–O–*T* (deg)
SiO_2	298	1.59	151
	298	1.62	146
	2053	1.62	140
$NaAlSi_3O_8$	298	1.63	146
$NaAlSi_2O_6$	298	1.64	145
$NaAlSiO_4$	298	1.67	143
$KAlSi_3O_8$	298	1.63	146
$CaAl_2Si_2O_8$	298	1.66	143
Fe_2SiO_4	1523–1673	1.62	—
Na_2SiO_3	1523–1673	1.62	167
K_2SiO_3	1523–1673	1.62	171
Na_2SiO_5	298	1.62	164
	1373–1873	1.62	162
K_2SiO_5	298	1.62	171
	1373–1873	1.62	171
$0.24CaO–0.76SiO_2$	1873–2053	1.63	162
$0.24MgO–0.76SiO_2$	1873–2053	1.63	151

(b) Cation–oxygen distances for various polyhedra from molecular-orbital calculations compared with experimental values in crystals, glasses, and melts

		M–O bond length (Å)			
Ion	**Coordination number**	**Calculated**	**Av. crystal**	**Glass (300 K)**	**Melt (>1473 K)**
Si^{4+}	4	1.65	1.62	1.62	1.62–1.63
Al^{3+}	4	1.72	1.75	1.72	
				1.76, 1.81	
	6	1.79	1.89		
Mg^{2+}	4	1.83	1.84		
	4.3–5.1			2.14	2.16
	4.1			2.08	
	6	1.91	2.08		
Na^{+}	4	2.02	2.35		
	4.1–6.1			2.36	2.36
	5			2.3	
	6	2.07	2.38		
Ca^{2+}	6		2.36		
	5.4–6.8			2.43	
	7		2.43		
Fe^{2+}	4		1.99		
	3.9–4.2				2.02–2.05
	6			2.07	
	6		2.13		

Source: After Navrotsky et al., 1985, who provide information on original data sources.

derived from experiment (on crystals, glasses, and melts) and from molecular-orbital calculations. It can be seen that the calculated and experimental tetrahedral atom–oxygen bond lengths are in good agreement, and that the observed Si–O and Al–O bond lengths remain relatively constant in crystalline, glassy, and molten materials. As already noted in earlier chapters, the flexibility of Si–O–Si, Si–O–Al, and Al–O–Al angles evidenced from calculations is in accord with easier glass formation in silicates and aluminosilicates compared with, for example, borates, sulfides, oxysulfides, or oxynitrides.

The presence of cations such as alkali or alkaline earth metals in the silicate melt results in the formation of nonbridging oxygen atoms, bonded to both the tetrahedrally coordinated cations and the network modifiers. The Si–O and Al–O bonds, the strongest in silicates and aluminosilicates, are perturbed by these other cations, increasing perturbation and weakening of the framework occurring with increasing ability of the other atom to compete with Si or Al in bonding to oxygen (i.e., with increasing cation field strength). The perturbation of T–O–T groups is evidenced by T–O bond lengthening observed in crystalline aluminosilicates and predicted by MO calculations and increases in the series Ca, Mg and K, Na, Li. This perturbation can be correlated with thermochemical mixing properties of glasses in the systems SiO_2–$M^{n+}{}_{(1/n)}AlO_2$ and SiO_2–$M^{n+}O_{n/2}$ (where M = Li, K, Na, Rb, Cs and Mg, Ca, Sr, Ba, Pb), with tendencies toward immiscibility in these systems. Systematic trends in vibrational spectra and in physical properties, including viscosity, can also be correlated.

As for v-SiO_2, the more complex glasses have been extensively studied by vibrational spectroscopy (see, for example, McMillan, 1984a,b) and high-resolution NMR (e.g., Murdoch et al., 1985; Ohtani et al., 1985). Important advances have also taken place in the use of high-temperature, high-resolution NMR studies of molten silicates. For example, Stebbins et al. (1985) studied ^{23}Na, ^{27}Al, and ^{29}Si in liquids in the system $Na_2O/Al_2O_3/SiO_2$ at temperatures up to about 1300°C. Typical spectra are illustrated in Fig. 8.9 and were studied to determine chemical shifts, linewidths, and line shapes. As indicated in Fig. 8.10, the ^{29}Si chemical shifts are systematically less negative in the melts than the corresponding glasses and crystals, and correlate with degree of polymerization (Q^n, where n is the number of other AlO_4 or SiO_4 units bound to a given SiO_4 tetrahedron). Also shown in Fig. 8.10 are the ^{23}Na chemical shifts, which correlate well with the ratio of number of oxygen to number of sodium atoms. High-temperature NMR techniques have also been used to study diffusion in alkali silicate melts (Liu et al., 1988), where line shape, spin–lattice, and spin–spin relaxation times yield useful information, such as the fact that exchange of oxygens between bridging and nonbridging sites takes place at the microsecond to nanosecond time scale at liquidus temperatures, making the lifetimes of silicate "molecules" very short.

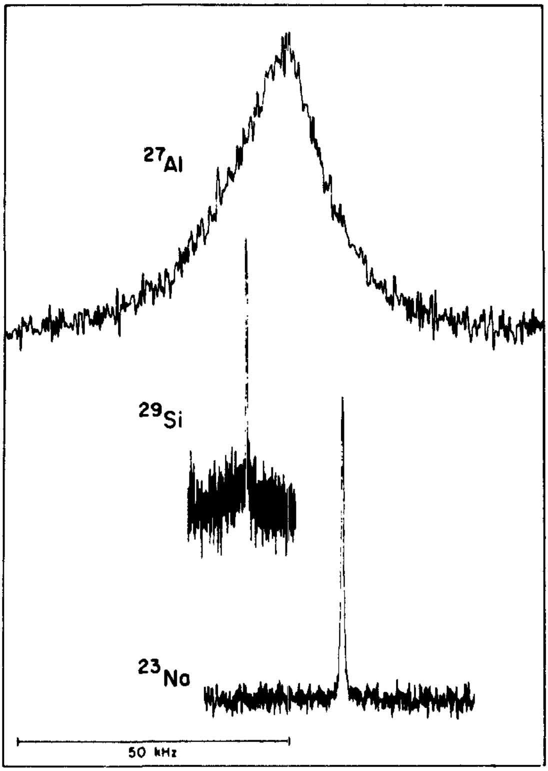

Fig. 8.9. Typical NMR spectra for molten silicates. Data are from Stebbins et al. (1985) and are for $NaAlSi_2O_6$ at ~ 1300°C. Relative location of the spectra is arbitrary, but they all have the same frequency scale (after Stebbins et al., 1985; reproduced with the publisher's permission).

Iron is probably the only major element in magmatic rocks that can occur in several oxidation states under the conditions relevant to igneous processes in the Earth. The role of iron in glasses and melts has, therefore, been studied quite extensively, and particular use has been made of Mössbauer spectroscopy (e.g., Virgo and Mysen, 1985; Mysen and Virgo, 1985; Mysen et al., 1985). The applications of ^{57}Fe Mössbauer spectroscopy in studying a wide range of glass compositions have also been reviewed by Dyar (1985). Despite a considerable volume of work, the structural role of iron is not well understood. Ferric iron is widely recognized as occurring both as a network former and a network modifier, the latter role possibly being of more importance at higher (> 1 GPa) pressures (Mysen and Virgo, 1985). Ferrous iron has been regarded generally as a network modifier (Mysen et al., 1985), but recent work involving the direct study of Fe^{2+} in molten alkali silicates by x-ray absorption spectroscopy (EXAFS and XANES) has provided evidence for Fe^{2+} as a four-coordinated network former in melts of compositions ~ $Na_2FeSi_3O_8$ and

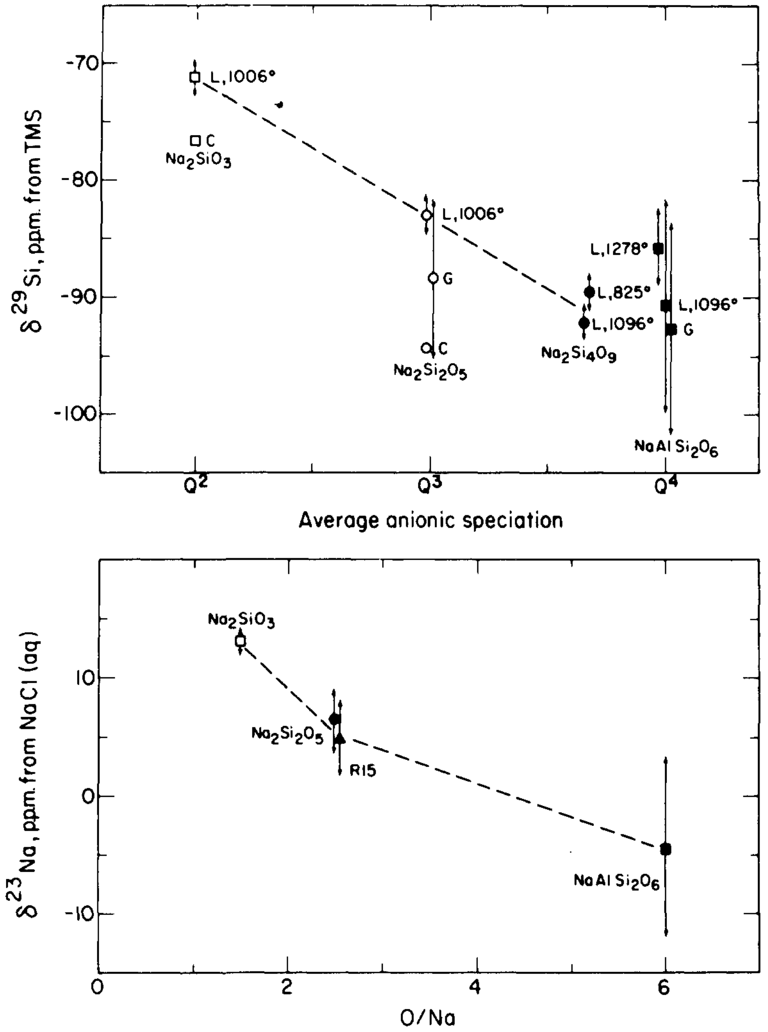

Fig. 8.10. Chemical shifts from NMR spectra of solid and molten silicates. L indicates liquid at temperature shown; G indicates glass; and C, crystalline solid. Arrows indicate linewidth (not errors) (after Stebbins et al., 1985; reproduced with the publisher's permission).

$K_2FeSi_3O_8$ (Waychunas et al., 1988). The EXAFS spectra of the melts along with certain model compounds and a quenched glass are shown in Fig. 8.11. There is no doubt that such direct studies of melts by x-ray absorption and related spectroscopic methods are the techniques of the future.

Volatile components, notably H_2O and CO_2, can dissolve in a molecular form in silicate melts even at 1 atm, and are well known to have a

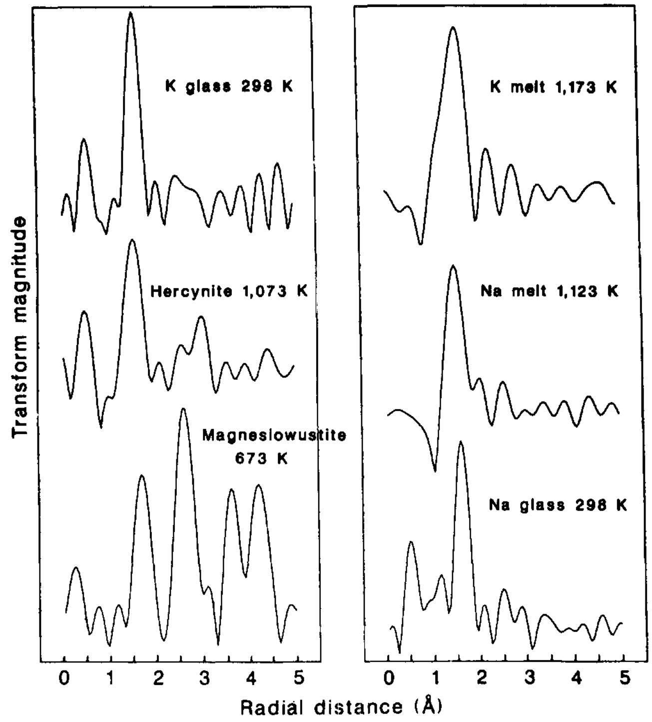

Fig. 8.11. EXAFS data for various alkali-metal–iron glasses and melts along with model compounds having mainly Fe^{2+} in tetrahedral (hercynite) and octahedral (magnesiowustite) coordination. Data are the Fourier transforms of the weighted EXAFS functions (after Waychunas et al., 1988).

radical effect on physical and chemical properties. Again, there is no detailed understanding of the changes in melt structure that result. Studies using vibrational spectroscopies suggest that H_2O forms OH complexes on dissolution, whereas CO_2 dissolves to form CO_3^{2-} complexes (Mysen et al., 1982; Mysen, 1983). It has been proposed that this extra oxygen is obtained by transforming two nonbridging oxygens in the melt to a bridging oxygen and CO_3^{2-}, thereby increasing the degree of polymerization and enhancing the activity of silicate components.

8.1.3. Crystal–melt equilibria

A fuller knowledge of the structure and bonding in silicate melts should enable detailed description and prediction of the chemical processes involved in magmatic crystallization and of the partitioning of elements between melt and crystals. A large body of experimental data is, in fact, available on this subject, but the only significant contributions so far made by application of bonding theories center on the simple ionic models or, for the transition metals, the application of crystal-field theory. The weaknesses inherent in many of the rules set up to explain trace-element distributions were critically appraised by Burns and Fyfe (1967a,b). It was also these authors (Burns and Fyfe, 1967a,b; Burns, 1970) who expounded the applications of crystal-field theory in this context.

Many aspects of crystal–melt partitioning for transition metals can be explained by assuming that metal sites in the melt typically give smaller crystal-field stabilization energies than do the available sites in crystals. For example, a certain proportion of metal sites in the melt might be tetrahedral, and such sites would be expected to give smaller CFSE values than octahedral sites in the crystal for virtually all transition-metal ions. Unfortunately, there has been very little study since the early 1970s of sites occupied by transition metals in silicate melts. The visible and Fe Mössbauer spectra of Fe^{2+} in quenched silicate glass showed essentially no evidence for tetrahedral Fe^{2+} (Boon and Fyfe, 1972), while earlier studies of Ni^{2+} spectra in glasses (Burns and Fyfe, 1964) had shown some tetrahedral Ni^{2+}, in spite of the larger octahedral site preference energy for Ni^{2+} (a d^8 system). It was suggested by Boon and Fyfe that the distribution of ions in the melt might be substantially different from that in the quenched glass. It has been observed for divalent transition-metal ion diffusion in AgCl that ions with low octahedral CFSE values have lower activation energies for diffusion (Batra et al., 1976), so that Fe^{2+} may diffuse from one site to another more readily than Ni^{2+} during the quenching process. To resolve this question, it would be desirable to do spectroscopy directly on the melt, using either optical absorption or some other techniques such as XANES, but such studies would be very difficult. Molecular-dynamics simulations of the melt structure would also be informative, if adequate potentials for describing the interaction of transition-metal ions with silicate units could be developed.

It is also important to note that first-principles calculations of phase diagrams such as those needed to evaluate solid–melt equilibria are just beginning. Several approaches utilizing first-principles interaction potentials within a statistical-mechanical approach appear to be promising for alloy systems such as Au–Cu (Ferreira et al., 1988) and Fe–Ni (Cheng and Ellis, 1989), but it is not clear whether such approaches can be extended to the more complicated silicate structures.

8.2. Solution species

8.2.1. Quantum-mechanical studies of water and aqueous (ionic) solutions

The free gas-phase H_2O molecule has been the subject of extremely accurate quantum-mechanical calculations of both its ground state, excited

Table 8.2. Comparison of experimental and calculated values for some properties of the water molecule

Property	Experimental value	Calculated value	
		Hartree–Fock	CI
Energy	−76.4376	−76.0666	−76.3736
Dipole moment	0.7296	0.7951	0.7588
Force on nucleus			
x component	0	0.0126	0.0002
y component	0	0.0125	0.0012
z component	0	0.0015	0.0029
Electric-field gradient at O, xx component	− 1.665	− 1.8508	− 1.7488
Electric-field gradient at H, xx component	0.4583	0.4702	0.4802

All values are given in atomic units. The experimental H_2O equilibrium geometry is used.

Source: From Davidson and Feller, 1984.

state and response properties. A comparison of calculated and experimental ground-state properties is given in Table 8.2 from Davidson and Feller (1984), and some response properties tabulated by Buckingham (1986) are presented in Table 8.3. These results indicate that sensitive ground-state properties such as electric-field gradients can still differ from experiment by 10% at the near-Hartree–Fock SCF level but that configuration interaction at feasible levels can usually eliminate half of this discrepancy. Response properties, such as polarizabilities, can show even larger deviations, which can again be significantly reduced by configuration-interaction methods. Small clusters of water molecules can also be treated accurately, and the results compare favorably with gas-phase experimental results (Amos, 1986). In the same way, reasonably accurate results can be obtained for simple cations or anions interacting with small numbers of H_2O molecules (Kollmann and Kuntz, 1972; Sano and Yamatera, 1982; Curtis et al., 1987). For cations, M^{n+}, the calculated M–O distances show the expected increase with increasing number of H_2O molecules and are in good agreement with crystal structure data for M cations

Table 8.3. Calculated and experimental dipole polarizabilities (in a.u.) for H_2O

	α_{xx}	α_{yy}	α_{zz}	$\bar{\alpha}$
Coupled Hartree–Fock calculation	9.11	7.50	8.42	8.25
Coupled Hartree–Fock plus CI calculation	9.84	9.02	9.33	9.40
Experimental value	10.01	9.26	9.62	9.64

Source: From John et al., 1980.

with the same coordination number. Some results are presented in Table 8.4. For those few cases in which *M*–O force constants or vibrational frequencies have been evaluated, agreement with experiment is as good as for comparable gas-phase molecules. In addition to the *M*–O stretching frequencies, many studies have examined changes in frequencies (Falk et al., 1986) or intensities (Hermansson et al., 1986) of the H_2O vibrations. Such calculations are at the quantum-chemical "state of the art," and simplifications must often be made in the basis set, symmetry of the species studied, assumptions about fixed bond distances, etc., which can cause discrepancies between different publications, but agreement with experiment is often quite good. For example, the subtle effect of Zn^{2+} versus Mg^{2+} coordination on H_2O vibrational intensities can be accurately predicted (Hermansson et al., 1986). In principle, such studies could be extended to the interactions of M^{n+} cations with other anionic species existing in mineral-forming solutions, such as Cl^-, H_2S, HS^-, and $CO_3{}^{2-}$ or to melt species such as $SiO_4{}^{4-}$. These species are more complicated and present greater computational demands. Polarizable species like $CO_3{}^{2-}$ are calculated to be appreciably distorted in M–CO_3 complexes (Tossell, 1985), but such distortions disappear in the more symmetric environments of crystals.

This raises a question often important in simulation studies: to what extent can a system such as $M^{n+}(H_2O)_m$ be described in terms of M^{n+}–H_2O and H_2O–H_2O pair interactions? Clearly, the most desirable situation for

Table 8.4. Calculated (Calc.) metal–water binding energies and bond lengths and hydration energies compared with experimental (Expt.) values

Metal (*M*)	Total energy (a.u.)		Hydration energy (kJ mol^{-1})		Metal–water distance (Å)	
	M^{2+}	$[M(H_2O)_6]^{2+}$	Calc.[a]	Expt.	Calc.	Expt.
Mg	−198.727	−654.600	1659	1997	2.07	
Ca	−657.4861	−1113.2116	1272	1668	2.40	2.40
Cr	−1041.4923	−1497.3156	1529	1925	2.13, 2.32	
Mn	−1147.8630	−1603.6791	1510	1920	2.19	2.20
Fe	−1260.2197	−1716.0611	1577	2008	2.14	2.12
Co	−1378.9569	−1834.8028	1588	2105	2.09	2.08
Ni	−1504.1535	−1960.0376	1689	2170	2.05	2.04
Cu	−1635.9457	−2091.8380	1710	2174	2.00, 2.12	1.94, 2.43
Zn	−1774.5536	−2230.4375	1688	2120	2.04	2.08
	M^{3+}	$[M(H_2O)_6]^{3+}$				
Cr	−1040.4239	−1496.8134	3015	4686	2.02	1.98
Fe	−1259.2999	−1259.2999	2767	5469	2.04	2.00

[a] Energy for the coordination of six water molecules; the total energy of water molecules, 6(−75.8735) a.u. was used in the calculation.

Table 8.5. Calculated Cl–O distances [R(Cl–O) in Å] and hydration energies (ΔE in kcal/mol) for Cl–$(H_2O)_n$ complexes

n	ΔE(two body)	R(Cl–O) (Å)	ΔE, MD (298 K)	ΔE_{HF}
1	11.9	3.30	10.9	11.9
2	23.3	3.31	21.1	22.9
3	34.3	3.34	30.7	32.7
4	46.7	3.37	39.4	
5	55.7	3.39		
6	69.2	3.42		

Source: From Kistenmacher et al., 1974.

modeling M^{n+} aqueous solutions would be one in which such a pairwise scheme yielded accurate geometries and energies for the larger species. For univalent cation–water interactions, pairwise additivity seems to be good enough to accurately predict properties of solutions (Clementi and Popkie, 1972) so long as the M^+–H_2O calculations used to generate potential parameters are of high quality. For Fe cations, however, departures from pairwise additivity are substantial so that a molecular-dynamics simulation based on Fe^{n+}–H_2O pair potentials predicts 8-coordination for Fe^{n+} in aqueous solutions, in disagreement with experimental results showing 6-coordination. Studies on $Fe(H_2O)_m$ show nonpairwise additive effects that, when properly incorporated, give more accurate descriptions of the aqueous solutions (Curtis et al., 1987). It is not yet apparent whether such failures of pairwise additivity can be accounted for in terms of ligand field effects, valence saturation, or other simple terms.

So far we have said little about anion solution. Studies of such species have been fewer, partly because of the smaller numbers and the more restricted charge on common anions, and their generally smaller contributions to heats of solvation. The quantum-mechanical calculations are also somewhat more difficult since diffuse functions are often required in the anion basis set, and since the stabilization often involves H bonding with significant perturbation of the H_2O molecule. Nonetheless, solvation of the common anions has been studied, and some properties from Kistenmacher et al. (1974) are tabulated in Table 8.5. In this study, the optimum geometries of Cl–O distances and angles were determined by static simulation using Cl^-–OH_2 pair potentials. For the smaller clusters, molecular dynamics was then used to evaluate hydration energies at 298 K to assess thermal effects, and direct Hartree–Fock calculations were performed on the $Cl^-(OH_2)_n$ clusters (at the Cl–O distance values obtained from the pair potential simulation) to assess many-body contributions to ΔE. From the limited data (essentially for $n \leq 4$), it appears that thermal and many-body effects are on the order of only 1–2 kcal/mol per H_2O molecule and that the overall trend in ΔE is reproduced fairly well at the pair-potential level. For $n>6$, ΔE increases by about 9 kcal/mol for each increase in n so that a number of different structures with large n have about the same stability per water molecule. Thus, one would expect a mixture of many different effective coordination numbers, and statistical-mechanical techniques such as molecular dynamics are necessary to assess the overall configuration and stability within the solution.

So far we have concentrated on species containing single metal cations, whereas the minerals deposited from solution involve arrays of closely interconnected cations. Although single metal centers can, of course, add to mineral surfaces, it may well be that oligomeric species with several metal ions are important in mineral deposition. Both oxidic species, like the metal alkoxides (Chisholm, 1985), and sulfidic species, like the metal polysulfides (Muller and Diemann, 1987), show oligomeric behavior with both M–O or M–S and M–M bonding being prominent. Calculations on such species are, however, very difficult.

8.2.2. Aqueous metal complexes, hydrothermal solutions, and hydrothermal ore deposits

It has long been recognized that major groups of metalliferous ore deposits have formed by precipitation from aqueous solutions at elevated temperatures, most commonly in the range of 25–400°C, although sometimes higher. These so-called hydrothermal solutions and the resulting hydrothermal ore deposits have been the focus of much research (see, for example, Barnes, 1979; Barnes and Ohmoto, 1990), from which it is clear that complex ions are responsible for the transport of metals in most of these solutions. The mode of origin of such deposits clearly depends on a range of interlinked geochemical and geological factors, but central to any understanding of the origin and nature of hydrothermal ore deposits is an understanding of certain aqueous metal complexes over a range of temperatures (and pressures).

The metals of importance in hydrothermal deposits include those of the first transition series, particularly Mn, Fe, Cu, Zn, along with certain members of later transition series such as Mo, Ag, Cd, Au, and Hg, and some nontransition metals including Sn, Pb, As, Sb, and Bi. The geologically most important ligands involved in complex formation include Cl^-, OH^-, and HS^-, in addition, of course, to H_2O. Other potential ligands, as noted by Barnes (1979), are organic acids, NH_3, F^-, S_x^{2-}, $S_2O_3^{2-}$, and HCO_3^-. The complex ions under consideration here are well-defined molecular entities with a specific geometry and coordination number. For example, over much of the range of hydrothermal ore-forming conditions, most complexes of the transition metals appear to be either octahedrally or tetrahedrally coordinated (Susak, 1981; Susak and Crerar, 1984). Such complexes are true molecules, in which the bonding is best described using molecular-orbital theory (in contrast to ion pairs, such as $NaCl^0$, held together primarily by Coulombic attraction; Pytkowicz, 1983). The application of modern electronic-structure theories to metal complexes can be pursued using spectroscopic techniques and MO calculations, and relatively little work has so far been done in this field, particularly under elevated temperature and pressure conditions. An overview has been provided by Crerar et al. (1985), on which the following discussion is partly based.

The aqueous behavior of the cations of interest in hydrothermal deposits can be divided on the basis of electronic configuration, following Giaquinta et al. (1983) as below.

1. Cations with the rare-gas configuration (e.g., Li^+, Na^+, K^+, Ca^{2+}, Mg^{2+}, Sc^{3+}, Ti^{4+}) exhibit interactions with ligands that are predominantly Coulombic or ionic. Here the stability of a complex increases with the ratio of charge to radius (Z/r) of the cation, and smaller anions are generally preferred. At room temperatures, such cations form fluoride species but do not combine with the heavier halogens, including chlorine. The halogens compete unfavorably with the water dipole in the first coordination shell, although at higher temperatures association does increase.
2. Cations with the noble-metal configuration (filled *d* shell) such as Zn^{2+}, Cd^{2+}, Hg^{2+}, Cu^+, Ag^+, Au^+, Sn^{2+}, and Pb^{2+} form more covalent complexes preferentially bonding with less electronegative ligands. Chloride complexes are more stable than fluoride, and HS^- is particularly preferred. The most stable complexes are formed with the most polarizable ligands, the established sequence being (Graddon, 1968):

   $$P > S >> N > O > F << Cl < Br < I$$

   The metals Cu, Ag most commonly occur as monovalent and Zn, Cd, Hg as divalent cations in natural hydrothermal systems, thus having the d^{10} configuration and forming highly stable chloride and bisulfide complexes (Barnes, 1979).
3. Cations of the transition metals having partly filled *d* shells (notably Ti^{3+}, V^{3+}, Cr^{3+}, Mn^{2+}, Mn^{3+}, Mn^{4+}, Fe^{2+}, Fe^{3+}, Co^{2+}, Ni^{2+}) exhibit a range of behavior, including a change from predominantly ionic to more covalent bonding with increasing electronegativities moving across each transition row ($d^1 \rightarrow d^9$), and a parallel increase in the electrostatic interaction, with anions or dipoles indicated by the general increase in ionic potential (Z/r) across each row. This increases the stability of complexes formed with a common ligand from left to right in each row. Such cations are also subject to ligand-field stabilization effects that may stabilize complexes formed with cations having configurations other than d^0, d^5, or d^{10}.

The overall behavior pattern outlined can be further examined using the hard–soft acid–base classification approach, by further consideration of ligand-field effects, and by considering relativistic effects that influence the behavior of the heavier cations.

As noted elsewhere in this text, and further discussed in Section 8.4, metal–ligand interactions may be broadly regarded as acid–base reactions with the metal acting as electron acceptor and the ligand as donor. Pearson (1963) divided metals and ligands into hard (small, highly charged, and only slightly polarizable) and soft (large, low charge, and highly polarizable), and examples of metals and ligands of geochemical importance being classified in this way are shown in Table 8.6. Pearson (1963) suggested that, in a competitive situation, soft acids bind preferentially with soft bases and hard acids with hard bases. The available data do show that the soft ligands HS^- and H_2S form relatively strong complexes with Hg, Au, Ag, Cu, and Sb; weaker complexes with Pb and Zn; very weak complexes with Fe and Sn; and probably do not form any complexes with W and Mo. On the other hand, the borderline base Cl^- forms relatively strong complexes with Fe, Sn, Pb, and Zn, and most transition metals. Experimental studies suggest that these trends are valid to at least 200°C, although Seward (1981) has pointed out that all metal–ligand interactions become harder at higher temperatures.

Ligand-field stabilization energy (LFSE) can exercise an important control on the stabilities of transition-metal complexes, particularly for

Table 8.6. Classification of geological metals and ligands[a]

Hard acids
H^+, Li^+, Na^+, K^+, Rb^+, Cs^+, Ca^{2+}, Mg^{2+}, Ba^{2+}, Ti^{4+}, Sn^{4+}, MoO^{3+}, WO^{4+}, Fe^{3+}, Al^{3+}, As^{3+}, CO_2

Borderline acids
Fe^{2+}, Co^{2+}, Ni^{2+}, Cu^{2+}, Zn^{2+}, Sn^{2+}, Pb^{2+}, Sb^{3+}, Bi^{3+}, SO_2

Soft acids
Cu^+, Ag^+, Au^+, Cd^{2+}, Hg^+, Hg^{2+}, M^0 (metal atoms and bulk metals)

Hard bases
NH_3, H_2O, OH^-, CO_3^{2-}, NO_3^-, PO_4^{3-}, SO_4^{2-}, F^-, Cl^-

Borderline bases
Br^-

Soft bases
CN^-, CO, H_2S, HS^-, I^-

Relative hardness of common metal ions and ligands[b]
$F^- > Cl^- > Br^- > I^-$
$Cu^+ > Ag^+ > Au^+$
$Zn^{2+} > Cd^{2+} > Hg^{2+}$
$Zn^{2+} > Pb^{2+}$
$H^+ > Li^+ > Na^+ > K^+ > Rb^+ > Cs^+$
$As^{3+} > Sb^{3+} = Bi^{3+}$

---

[a] According to relative hardness.

[b] Hardness decreases toward the right.

metals of the first transition series. The diagrams in Fig. 8.12 recall that LFSE, although zero for d^0, d^5, and d^{10} cations, rises to a maximum for the d^3 and d^8 cations, and this is reflected in the greater stability of molecules with high LFSE over the trends expected when this effect is not considered. The familiar double-hump trend shown in lattice energies in Fig. 8.12 is therefore picked up in the values of the enthalpy of hydration and in the stability constant for complex formation. As these figures show, coordination compounds of Ni^{2+} or V^{2+} can acquire roughly 200–

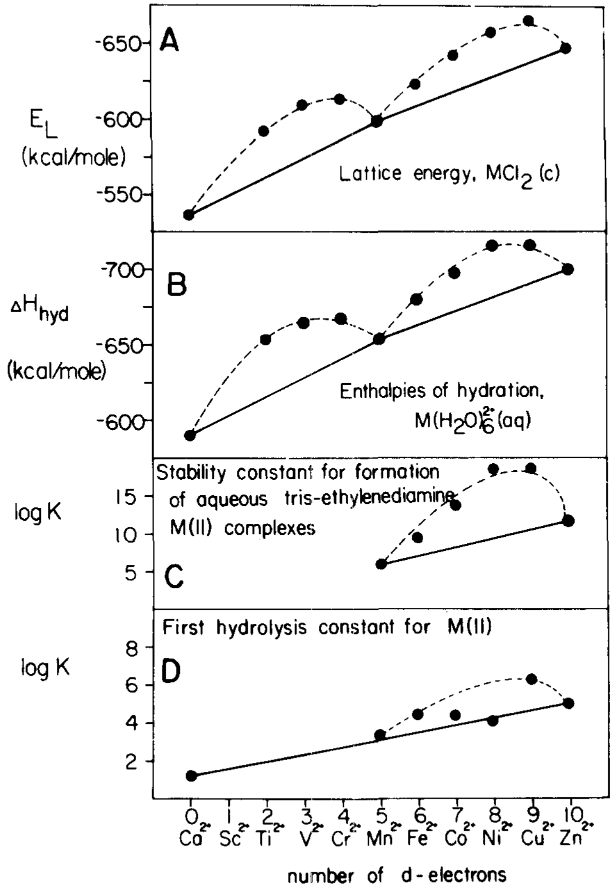

Fig. 8.12. Plot of various energy parameters against number of *d* electrons for the first row transition metals. (a) Lattice energy or heat of the reaction $M^{2+}(g)+2Cl^-(g)\rightarrow MCl_2(s)$. (b) Enthalpy of hydration, $M^{2+}(g)+6H_2O\rightarrow M(H_2O)_6^{2+}(aq)$. (c) Log equilibrium constant for the reaction $M(H_2O)_6^{2+}(aq)+\text{tren}\rightarrow M(\text{tren})(H_2O)_5^{2+}(aq)+H_2O$, where tren = trisethylenediamine. (d) Log equilibrium constant for the reaction $M(H_2O)_6^{2+}(aq)+OH^-\rightarrow M(H_2O)_5(OH)^+ + H_2O$. (After Crerar et al., 1985; reproduced with the publisher's permission.)

300 KJ/mol additional stability; the general rise from Ca to Zn and general increase in stability of complexes is due to the proportionality between bonding energy and Z^2/r_{cation} discussed previously.

An additional effect arises from the contraction of *s* and *p* orbitals of the heavier metals (Pt, Au, Pb, Bi, Hg, etc.). The velocity of electrons in these inner orbitals approaches the speed of light and, because of relativistic effects, they are drawn closer to the nucleus. This contraction of the *s* and *p* orbitals causes increased shielding of *d* and *f* orbitals and leads to a greater tendency towards covalent bonding (Pitzer, 1979; Pykko and Desclaux, 1979). In hydrothermal solutions, complex ions of the heavier transition metals should become increasingly covalent. For example, gold bisulfide complexes should be stronger than silver bisulfide complexes, and experimental evidence seems to support this observation (Wood, 1985). The apparent preference of bismuth for chloride and of antimony for bisulfide ligands (despite similar *Z*/*r* ratios and electronegativities) is probably due to relativistic effects.

Consideration of hard–soft acid–base theory, ligand-field, and relativistic effects provides insight into which complexes will be stable at 25°C and 1 atm and why. The effects of variations in temperature and pressure on complex stability are clearly very important, and this general subject has been discussed by Seward (1981). The most dramatic effect of temperature is its effect on the dielectric constant of water, which falls from 78.47 at 25°C to 12.87 at 350°C and vapor-saturated pressure (Helgeson and Kirkham, 1974). Since the Coulombic force is inversely proportional to the dielectric constant, all electrostatic interactions increase at elevated temperatures. Strong acids become weak and ionic salts form ion pairs at higher temperature, and complexes with intermediate or hard ligands (e.g., OH^- and Cl^-) become more stable. This is evidenced by increases in hydroxy complexing (Baes and Mesmer, 1981) and increased stability of chloro complexes (Barnes, 1979; Seward, 1981, 1984) with temperature. This, coupled with the anticipated increase in solubility products, helps to explain the higher solubilities of many metalliferous minerals in higher-temperature hydrothermal solutions. Another effect of increasing temperature, seen from experimental data, is a decrease in ligation numbers so that complexes of low to neutral charge (e.g., $FeCl_2^0$) predominate above ~300°C, and at very high temperature molecular aqueous species of feldspar stoichiometry such as $NaAlSi_3O_8^0$ may occur (Anderson and Burnham, 1983). There is also experimental evidence that tetrahedral complexes predominate over octahedral at higher temperatures (Susak and Crerar, 1984). Pressure effects are generally much less significant over the ranges relevant to fluids near the surface of the Earth; however, solubility does generally increase with pressure because of increased density of solvent, and pressure increases the dissociation of complexes to ionic species because of the general decrease in partial molal volume accompanying ion formation.

8.2.3. Theoretical studies on Zn chloride complexes in aqueous solution

Abundant data exist on the stabilities of complexes in aqueous solution with general stoichiometry $ZnCl_n$ at various temperatures and ionic strengths (Barnes, 1979). There are also substantial diffraction and spectral data bearing upon the composition of the first coordination sphere about Zn for many chloride to zinc composition ratios. Quantum-chemical methods have recently been used to calculate structures, stabilities, and spectra for both bare $ZnCl_n^{2-n}$ species and their hydrated analogs (Tossell, 1989, 1990a). Calculations have been performed for ground-state properties using *ab initio* Hatree–Fock–Roothaan SCF calculations with valence double-ζ basis sets (Barandiaran et al., 1986, and references therein) with added *p* and *d* polarization functions (designated SV* in Table 8.7). The actual probable speciations for the various complexes are given in Table 8.7, along with calculated and experimental structural data. Zn NMR shieldings have also been calculated using somewhat more flexible basis sets, and a relationship between Zn 4*p* orbital population and the paramagnetic contribution to the shielding has been found, consistent with earlier Hartree–Fock perturbation theory results by Nakatsuji et al. (1984). Calculated Zn NMR chemical shifts of $ZnCl_n(OH)_a^{2-n}$ species with respect to $Zn(OH_2)_6^{2+}$ as reference are compared with experimental data from Maciel et al. (1977) in Table 8.8. The calculations give the correct experimental order of NMR shieldings only for the real hydrated complexes [eg., compare $ZnCl_n$ and $ZnCl_2(OH_2)_4$], and correctly reproduce the difference between $ZnCl(OH_2)_5^+$, with long Zn–Cl and short Zn–O distances and very slight deshielding with respect to $Zn(OH)_2)_6^{2+}$, and $ZnCl_2(OH)_2)_4$, with shorter Zn–Cl and much longer Zn–O distances and a

Table 8.7. Probable identities and structures of hydrated $ZnCl_n^{2-n}$ species from calculations

	<Species>	*R*	Calc. (SV*)	Expt. (XRD)
Zn^{2+}	Actually $Zn(OH_2)_6^{2+}$	*R*(Zn–O)	2.09	2.08
$ZnCl^+$	Actually $ZnCl(OH_2)_5^+$	*R*(Zn–Cl)	2.29	2.24
		R(Zn–O)	2.13	2.07
$ZnCl_2$	Actually $ZnCl_2(OH)_4$	*R*(Zn–Cl)	2.21	
		R(Zn–O)	2.36	
$ZnCl_3^-$	Actually $ZnCl_3(OH_2)_2$	*R*(Zn–Cl)	2.23	
		R(Zn–O)	2.31	
$ZnCl_4^{2-}$	Actually $ZnCl_4^{2-}$	*R*(Zn–Cl)	2.31	2.30[b]

See text for further clarification of terminology.

[a] Paschina et al. (1983).

[b] Kruh and Standley (1962).

Source: After Tossell, 1990a.

Table 8.8. Comparison of calculated and experimental values of Zn NMR shieldings [with respect to $Zn(OH_2)_6^{2+}$] for $ZnCl_n^{2-n}$ and $ZnCl_n(OH_2)_a^{2-n}$

	$\Delta\sigma_{calc}$	$\Delta\sigma_{expt}$ (Maciel et al., 1977)
$ZnCl_4^{2-}$	−245	−253
$ZnCl_3^-$	−206	−119
$ZnCl_3(OH_2)_2^-$	−162	
R(Zn–Cl) = 2.23 Å		
R(Zn–O) = 2.31 Å		
$ZnCl_2$	−78	−295
$ZnCl_2(OH_2)_4$, D_{4h}	−250	
R(Zn–Cl) = 2.21 Å		
R(Zn–O) = 2.36 Å		
$ZnCl^+$	+267	−30
$ZnCl(OH_2)_5^+$	−91	
R(Zn–Cl) = 2.24 Å		
R(Zn–O) = 2.07 Å		

Source: From Tossell, 1990a.

very substantial deshielding. The comparison of calculation with experiment for the structural, NMR, and Raman data obtained for $ZnCl_4^{2-}$ confirms that it can be only weakly associated with water of hydration. By contrast, all of the species with lower ratios of Cl^- to Zn^{2+} have significant water involvement in the first coordination sphere, which strongly influences their structures and properties. For example, the calculated frequencies for the totally symmetric stretching vibration seen in the Raman spectrum is in agreement with experimental data from $ZnCl_2$ aqueous solutions only for $ZnCl_4^{2-}$ (after multiplication by the standard 0.9 factor appropriate to polarized split valence calculations; Hehre et al., 1986), as shown in Table 8.9 [see Irish, 1971, for a discussion of $ZnCl_2$(aq) Raman

Table 8.9. Calculated frequencies for Raman-active totally symmetric vibrations compared with experiment for $ZnCl_n^{2-n}$

	Calculated	Experimental[a]
$ZnCl^+$	502	—
$ZnCl_2$	380	361 (gas) 352 (Kr matrix) 305 [$ZnCl_2$(aq)]
$ZnCl_3$	326	286 [$ZnCl_2$(aq)]
$ZnCl_4^{-2}$	297	288 (M_2ZnCl_4) 275–282 [$ZnCl_2$(aq)]

[a] See Tossell (1990a) for experimental references.

spectra]. The large difference between values for "$ZnCl_2$" species in the gas phase and $ZnCl_2$ aqueous solutions makes clear the large effect of water coordination upon the Zn–Cl stretching frequencies. Calculated geometries, vibrational energies, and Zn NMR shieldings have also been presented for tetrahedral ZnX_4 species, including $Zn(SH)_4{}^{2-}$ (Tossell, 1990c). These calculations are a prelude to the study of the various hydrated $Zn(SH)_n$ complexes.

8.3. Mineral surfaces

Studies of the surfaces of solids have developed rapidly in recent decades, chiefly because of the technological importance of such studies in fields as diverse as semiconductor physics, chemical catalysis, and the corrosion of metals. Consequently, the literature of surface science is considerable. However, the number of publications dealing specifically with minerals is relatively small, although in certain cases the synthetic equivalents of minerals have been studied in detail because of their technological applications or general scientific interest. In this section, following a brief discussion of experimental techniques and mention of some key general references, four minerals are discussed as examples: periclase (MgO), rutile (TiO_2), sphalerite (ZnS), and bornite (Cu_5FeS_4). These relatively well studied compounds have been chosen to illustrate different aspects of surface properties and of the applications of surface studies.

Many of the experimental techniques developed for the analysis and characterization of surfaces are forms of spectroscopy, particularly electron spectroscopy. They include ultraviolet photoelectron spectroscopy, x-ray photoelectron spectroscopy, Auger electron spectroscopy, and electron-energy-loss spectroscopy. The surface sensitivity of these techniques derives from the very short mean-free paths that electrons with kinetic energies in the range of 10–1000 eV have when traveling in solids (e.g., about 3–5 Å for a 100 eV electron in most solids). Thus, only the first few monolayers beneath the surface are sampled. Other surface-sensitive spectroscopies include secondary-ion mass spectroscopy (SIMS), ion scattering spectroscopy (ISS), ion neutralization spectroscopy (INS), conversion electron Mössbauer spectroscopy, and soft-x-ray appearance fine-structure spectroscopy (SXAFS). The spectroscopic methods that make use of synchrotron radiation (EXAFS and XANES) also have applications to surface studies. Other techniques of importance in surface science include low-energy electron diffraction, reflection high-energy electron diffraction, and the scanning methods of scanning electron microscopy and the recently developed scanning tunneling microscope (STM). All of the above-mentioned techniques are very briefly described in Appendix B, where some key references are provided for each technique.

General references on surface characterization include Kane and Larrabee (1974), Ibach (1977), and Briggs and Seah (1980), the latter two references being concerned with electron spectroscopy. Auger spectroscopy in surface studies is discussed in detail by Weissman and Muller (1981) and by Grant (1982), and conversion electron Mössbauer spectroscopy by Jones et al. (1978). A general account of low-energy electron diffraction is provided by Mitchell (1973), and its application to determining the surface structure (geometry) of semiconductors (including MgO, ZnO, CdS, ZnS, TiO_2, and MoS_2) is given by Kahn (1983).

Articles dealing with the structure and chemistry of solid and crystal surfaces include Tabor (1981) and Forty (1983), who discusses metals and catalysts in particular. The surface of diamond is discussed by Pate (1986), metal oxides by Henrich (1985), transition-metal compounds by Langell and Bernasek (1979), and transition-metal oxides by Henrich (1983). Some of these articles deal with the electronic structures of the surfaces as well as the surface atom geometry; the volume edited by Rhodin and Ertl (1979) on the nature of the surface chemical bond and the review paper by Tsukada et al. (1983) on the electronic structure of oxide surfaces concentrate on this aspect. One of the few reviews directed specifically towards minerals is that of Berry (1985).

8.3.1. The surface of MgO (periclase)

Periclase (MgO) has the rocksalt structure, which is face-centered cubic with each Mg^{2+} cation surrounded by six O^{2-} anions in a regular octahedral arrangement, and each O^{2-} similarly coordinated to six cations at the corners of a regular octahedron. By far the most stable surface for oxides having the rocksalt structure is the (100), illustrated in Fig. 8.13

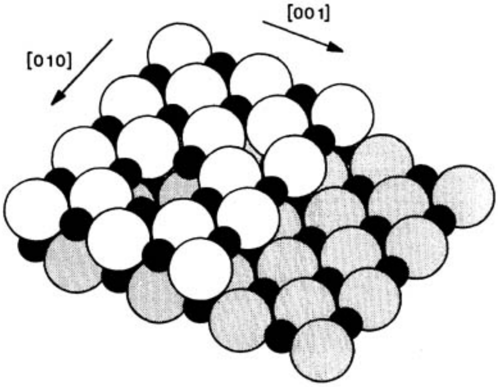

Fig. 8.13. A model of the (100) surface of the rocksalt structure of MgO. Large circles are oxygen anions, small circles are Mg cations. A (100) step to another (100) terrace is shown, as also is a missing anion point defect.

(after Henrich, 1983, 1987). This figure shows two (100) terraces separated by a (001) step of single atom height; an oxygen vacancy point defect is also shown on the upper terrace. The perfect (100) surface of MgO is characterized by a reduction of the ligand coordination of both Mg and O from six to five. The (100) surface of MgO has been studied using LEED by Welton-Cook and Berndt (1982), Urano et al. (1983), and Prutton et al. (1979), who also studied CaO, CoO, and NiO. These studies conclude that the (100) surface of MgO (and the other oxides) is very nearly a truncation of the bulk crystal structure, with any relaxation (inward or outward movement of cation or anion in the surface plane) or rumpling (alternate inward or outward movement) limited to a few percent of the bulk lattice constant or less. Atomistic simulation calculations of the relaxation and rumpling of MgO(100) agree with these results (Mackrodt, 1988), although recent *ab initio* Hartree–Fock–Roothaan SCF calculations by Causa et al. (1986c) indicate a surface geometry slightly changed from the truncated bulk material.

The electronic structure of the clean MgO(100) surface has been investigated experimentally by Henrich et al. (1980) and by Underhill and Gallon (1982) using electron-energy-loss spectroscopy. Both interionic transitions that excite electrons from the O 2*p* valence band into the normally empty Mg 3*s*, 3*p*, 3*d*, 4*s*, etc. levels, and intra-ionic transitions from the Mg 2*p* and Mg 2*s* core level to the same excited states have been observed. By varying the incident electron energy and hence the sampling depth, the spectra of fivefold-coordinated surface Mg^{2+} cations can be separated from those of bulk Mg^{2+} ions. The surface loss features are shifted to lower energy compared to those for the bulk. This is largely due to the strong localized electric fields at the surface of ionic materials, although some of the results for interionic transitions suggest a narrowing of the band gap on the (100) surface of MgO by 2 eV compared to bulk MgO.

The calculations undertaken by Tsukada et al. (1983) provide a theoretical framework for understanding the surface electronic structure of MgO. They performed DV-$X\alpha$ cluster calculations on $(MgO_6)^{10-}$ and $(MgO_5)^{8-}$ clusters, representative of the central cation and its nearest neighbors in the bulk solid and at the surface, respectively. The results of these calculations are shown in the energy level diagrams of Fig. 8.14; for the $(MgO_6)^{10-}$ cluster, the levels from $3e_g$ down to $1t_{2g}$ are occupied (valence levels) and are chiefly O 2*p* in character. The $6a_{1g}$ and $6t_{1u}$ levels (empty) come from the 3*s* and 3*p* states, respectively, of the Mg ion. If the size of cluster is increased, these two states broaden to form the conduction band. For the surface cluster, the occupied (valence) levels $4b_1$ to $1b_2$ are shifted to higher-energy positions compared to the $(MgO_6)^{10-}$ cluster, and the levels are more densely distributed in the upper part of the valence "band." The cation ("conduction-band") levels are more drastically affected, with a remarkable lowering of the $11a_1$ level. Tsukada

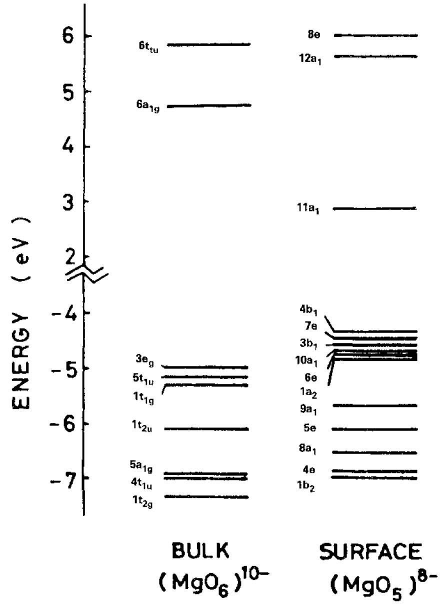

Fig. 8.14. Energy levels of the bulk $(MgO_6)^{10-}$ and surface $(MgO_5)^{8-}$ clusters calculated using the DV-$X\alpha$ method by Tsukada et al. (1983) (after Tsukada et al., 1983; reproduced with the publisher's permission).

et al. (1983) explain this in terms of distortion of the atomic orbitals due to the surface field, as illustrated in Fig. 8.15. Because of the field normal to the surface, the Mg 3*s* and 3*p* orbitals are admixed with each other to form the $3s+3p_z$-like $11a_1$ level and the $3s$-$3p_z$-like $12a_1$ levels. Since the potential decreases towards vacuum, the energy of the $11a_1$ level is considerably depressed and that of the $12a_1$ is raised. The energy of the $11a_1$ level is lowered by 1.9 eV compared to the lowest cation level $6a_{1g}$ in the

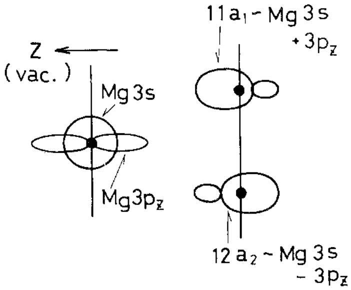

Fig. 8.15. Formation of the $11a_1$ and $12a_1$ state of the $(MgO_5)^{8-}$ cluster by the distortion of the atomic orbitals (after Tsukada et al., 1983; reproduced with the permission of the publishers).

bulk cluster. This narrowing of the band gap agrees remarkably well, quantitatively as well as qualitatively, with the experimental (EELS) data reported previously.

8.3.2. The surface of TiO_2 (rutile)

Rutile has a tetragonal lattice in which Ti^{4+} ions occur coordinated to O^{2-} ions in slightly distorted octahedral sites, one-half of the octahedral sites being empty. The most stable crystal face appears to be the (110), and in Fig. 8.16 is shown the (110) surface that results from breaking the smallest number of cation–anion bonds (after Henrich, 1983, 1987). Two kinds of Ti cation are present on this surface, one with five O^{2-} ligands and one with all six O^{2-} ions, as in the bulk material. The local environment of the five-coordinated cation is similar to that of the surface cation in MgO.

Only qualitative LEED measurements have been performed on rutile (Henrich and Kurtz, 1981), so that surface geometry is not known in great detail. More is known about the electronic structure of the rutile surface from experiments and calculations (Henrich, 1983, 1985; Henrich and Kurtz, 1981; Wolfram, 1981; Tsukada et al., 1983). Thus, Tsukada et al. (1983) performed DV-$X\alpha$ calculations for the cluster $(Ti_4O_{16})^{16-}$ representative of the (110) surface and containing two six-coordinated [Ti(1)] and two five-coordinated [Ti(2)] cations, as shown in Fig. 8.17. The calculated energy levels are shown in Fig. 8.18, their compositions being shown by Mulliken population distributions. The occupied groups of levels (labeled C′, C, D, E, F in Fig. 8.18) correspond to the dominantly oxygen valence band, while the empty levels (labeled A′, A, B) are mostly made up of Ti 3*d* orbitals. The orbitals for the group of lowest-energy unoccupied levels (A′) are strongly localized on the fivefold-coordinated [Ti(2)] cations. The highest-energy group of occupied levels (C′) arise dominantly from the 2*p*

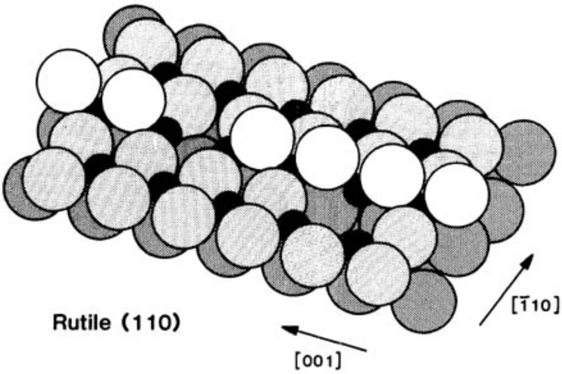

Fig. 8.16. Model of the (110) surface of rutile showing two kinds of anion vacancy point defects (after Henrich, 1983; reproduced with the publisher's permission).

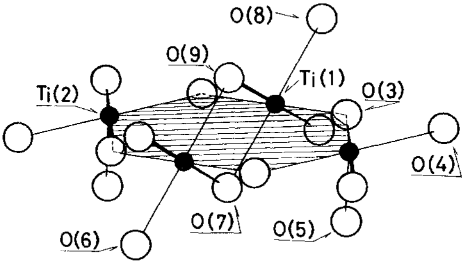

Fig. 8.17. Structure of a Ti_4O_{16} cluster as a model for the ideal (110) rutile surface. The shaded plane shows the (110) surface (after Tsukada et al., 1983; reproduced with the publisher's permission).

states of the oxygens [O(B) and O(9)] that protrude from the surface. DV-$X\alpha$ calculations were also performed on the cluster $(Ti_3O_{15})^{18-}$ representative of bulk TiO_2 (see Fig. 8.19). The densities of states calculated for the clusters representative of the bulk and of the surface are shown in Fig. 8.20, and show that the energy-level groups labeled A′ and C′ for the surface cluster are located within the energy gap of the bulk cluster. Thus, the level groups A′ and C′ are considered to be surface-state bands. An EELS peak was found at 2.4 eV for the ordered $TiO_2(110)$ surface by Chung et al. (1977); this can be assigned to the transition from the oxygen surface state (group C′) to the titanium surface state (group A′) of the ordered surface, which Tsukada et al. (1983) calculate at 2.8 eV.

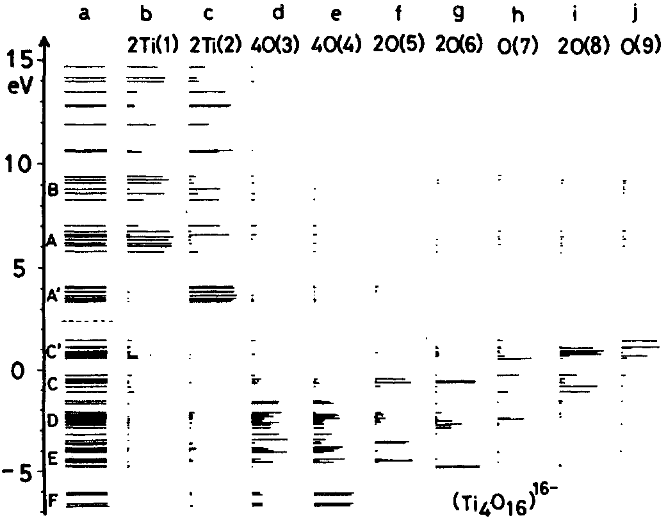

Fig. 8.18. Energy-level diagram (a) for the cluster $(Ti_4O_{16})^{16}$ obtained by DV-$X\alpha$ calculations along with Mulliken population distributions (b–j) of each cluster level (after Tsukada et al., 1983; reproduced with the publisher's permission).

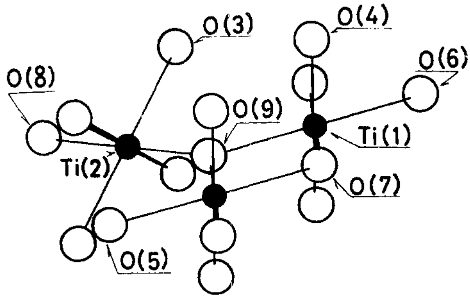

Fig. 8.19. Structure of the bulk Ti_3O_{15} cluster.

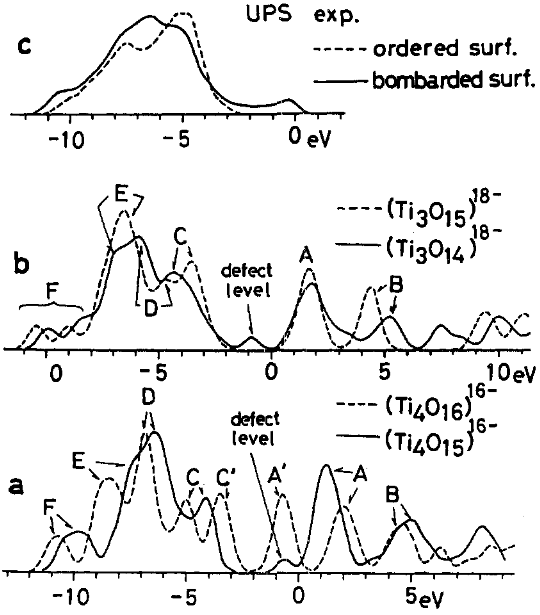

Fig. 8.20. (a) Densities of states of the surface clusters $(Ti_4O_{15})^{16-}$ (solid line) and $(Ti_4O_{16})^{16-}$ (dashed line) calculated by the DV-$X\alpha$ method. (b) Densities of states of the clusters $(Ti_3O_{14})^{18-}$ (solid line) and $(T_{13}O_{15})^{18-}$ (dashed line) representative of solid bulk TiO_2 calculated by the DV-$X\alpha$ method. (c) Ultraviolet photoelectron spectra for the ordered (dashed line) and bombarded (solid line) (110) surface of rutile (TiO_2) (after Tsukada et al., 1983; reproduced with the publisher's permission).

8.3.3. Oxide surface defects and the reactivity of surfaces

The most prevalent type of point defect that occurs at metal oxide surfaces is an oxygen vacancy (Henrich, 1983, 1985), and this is illustrated for MgO(100) and TiO_2(110) in Figs. 8.13 and 8.16. At such defects, there is a reduction of the ligand coordination of adjacent surface cations, generally from five to four. Removal of an oxygen anion also reduces the screening between cations adjacent to the defect, and, in order to maintain charge neutrality, the defect sites must be negatively charged. This results in large changes in surface electronic structure.

Point defects on TiO_2 surfaces produced by ion or electron bombardment have been studied experimentally; the negative charge on oxygen vacancy defect sites partially populates the 3*d* levels of surface Ti ions, and these Ti 3*d* electrons are observed in UPS spectra as a band of states lying in the bulk band-gap region (Henrich, 1979). At high defect densities, the defect band broadens and overlaps the bulk conduction band. Tsukada et al. (1983) have also performed DV-$X\alpha$ calculations on clusters containing a defect such as the $(Ti_4O_{15})^{16-}$ cluster formed by removing the central outermost oxygen [O(9)] in Fig. 8.17. The densities of states calculated for this cluster with an oxygen vacancy are shown in Fig. 8.20 and agree with the experimental data in showing that the vacancy states occur in the bulk band-gap region. Also shown in Fig. 8.20 is the UPS for the (110) surface of rutile (ordered) and the same surface bombarded with Ar^+ ions, so as to induce oxygen vacancies; a feature at low binding energy corresponding to the defect level in the calculations is clearly observable.

This defect level located near the conduction band is very important because of its high chemical activity. Experimentally, it has been established that the photocatalytic activity of the rutile surface increases greatly when reduced (oxygen deficient) compared to the clean surface (Mavroides et al., 1975). Defect sites on all oxide surfaces are usually very active for adsorption, whereas the nearly perfect surfaces of oxides where the cation is in its highest oxidation state are generally inert (Henrich, 1987).

8.3.4. The surface of ZnS (sphalerite)

Sphalerite (or "zincblende") has a lattice with zinc atoms at the corners and face centers of a unit cube and sulfur atoms at the centers of four out of the eight smaller cubes into which the large cube can be divided. Both zinc and sulfur are in regular tetrahedral coordination. The cleavage surface is the (110) surface, and this nonpolar face of ZnS (and other zincblende-structure binary compounds) is by far the best understood of all semiconductor surfaces (Kahn, 1983).

Detailed LEED studies of ZnS (and other zincblende-structure compounds, including ZnTe and CdTe) have established that the (110) surface is reconstructed by movement of the Zn atoms inward (towards the bulk solid) and of the S atoms outward. Displacements of the cation and anion in the uppermost layer by $<<0.5$ Å and in the second layer by 0.1 Å compared to the bulk are involved (Duke, 1983). Harrison (1976, 1980) has explained this in terms of an electronic structure model by conversion of half-occupied dangling-bond hybrid orbitals at both Zn and S on the unreconstructed surface to a combination of a fully occupied bond orbital on S and an unoccupied orbital on Zn for the reconstructed surface. The reconstruction stabilizes the orbital at S and converts it from sp^3 to s in type, while the Zn orbital is destabilized and converted from sp^3 to sp^2. An equivalent description within the delocalized molecular-orbital approach would relate the Zn site to a 6-valence-electron AB_3 species, expected to be planar as in BH_3, and the S site to an 8-valence-electron AB_3 species, expected to be pyramidal as in NH_3. The degree of distortion will depend upon the change in energy of the surface orbital upon distortion in the angle B–A–B. This will depend partly upon the difference in electronegativity of the A and B atoms, with a smaller electronegativity difference giving a larger degree of distortion from the unreconstructed geometry. Thus, ZnS suffers a larger reconstruction than ZnO.

8.3.5. The surface of Cu_5FeS_4 (bornite) and atmospheric tarnishing

Bornite is an ore mineral of copper with a crystal structure related to sphalerite (zincblende), although in bornite only three-quarters of the tetrahedral sites in the anion sublattice are filled. It is a mineral that exists as several polymorphic forms, but only the low-temperature form occurs naturally, and detailed analysis shows this form to have twelve different types of metal coordination, all of which can be considered tetrahedral or trigonal (Koto and Morimoto, 1975). Although studies have not been undertaken of surface reconstruction in materials as complex as bornite, the studies of sphalerite and related zincblende-structure semiconductors described above form a basis for discussion. As noted above, zincblende structure type and related species undergo surface reconstruction, the degree of distortion depending partly on the difference in electronegativity between cation(s) and anion. Since Cu and Fe are of similar electronegativity to Zn, we anticipate a substantial degree of reconstruction, with CuS_3 and FeS_3 groups on the surface of bornite being distorted towards a planar coordination.

Bornite is an interesting example of a relatively rapidly tarnishing sulfide mineral; freshly cleaned or polished surfaces have a "bronze" color that changes to purples and blues after a relatively short period of exposure to the atmosphere. Fresh and tarnished surfaces of bornite have been studied using x-ray photoelectron spectroscopy and Auger electron spectroscopy by Losch and Monhemius (1976), Buckley and Woods (1983), anf Vaughan et al. (1987), who also employed specular reflectance measurements and conversion electron Mössbauer spectroscopy. Specular reflectance as shown in Fig. 8.21 provides a method of monitoring, at least semiquantitatively, the development of surface alteration with time; different samples tarnish at different rates, and this appears to relate, in part, to precise Cu:Fe:S ratios and stoichiometry (Vaughan et al., 1987). Auger spectroscopy, when combined with argon ion bombardment to etch away surface layers, can be used to determine, semiquantitatively, concentrations of various species with depth below the surface (Fig. 8.22). Further information on surface species is provided by the XPS data, for example, the Fe 2*p* spectra for "clean" and tarnished surfaces shown in Fig. 8.23. The shift in position of the Fe $2p_{3/2}$ peak to slightly higher binding energy and appearance of a satellite peak in the spectrum of tarnished material is consistent with iron at the surface being present as Fe(III) oxide or hydrated oxide (Vaughan et al., 1987; Buckley and Woods, 1983). This was further substantiated by conversion electron Mössbauer spectroscopy (Vaughan et al., 1987), whereas the detailed XPS and AES work of Buckley and Woods (1983) led to the suggestion that beneath a surface layer of hydrated iron (Fe^{3+}) oxide is a layer enriched in copper sulfide ($\sim Cu_5S_4$). Further examination of the reflectance spectra confirm these suggestions (Vaughan et al., 1987).

Vaughan et al. (1987) propose that the rapid surface oxidation of bornite, and the products of this reaction, may result from the surface reconstruction that leads to Cu^+ and Fe^{3+} being in approximately trigonal planar coordination. Calculations using the multiple-scattering $X\alpha$ cluster method (MS-SCF-$X\alpha$) on Cu^+ in tetrahedral and triangular planar coordination with sulfur (on CuS_4^{7-} and CuS_3^{5-} clusters; see Tossell, 1978b;

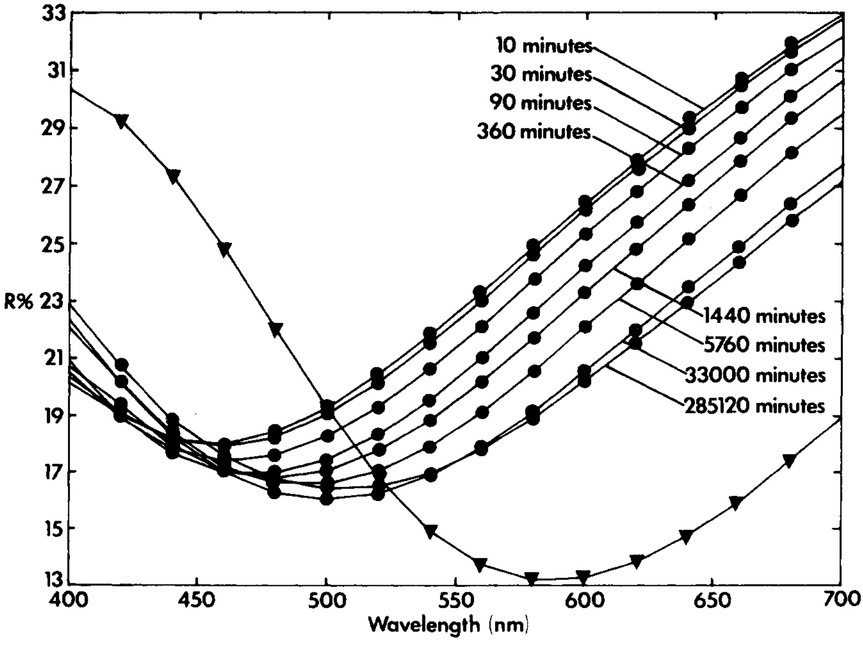

Fig. 8.21. Specular reflectance spectra of a natural sample of bornite (●) after exposure to oxidation in air for increasing lengths of time and of a second, heavily tarnished sample (▼) (after Vaughan et al., 1987).

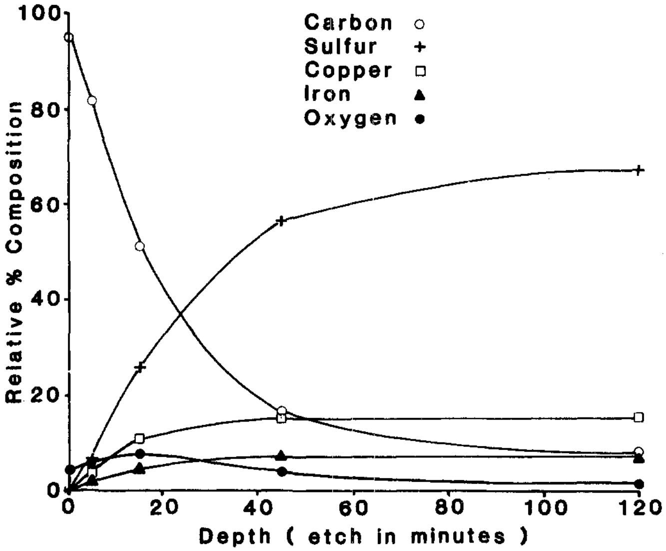

Fig. 8.22. Auger depth profile of tarnished bornite (after Vaughan et al., 1987).

Vaughan and Tossell, 1980b, and Chapter 6 of this book) show that Cu^+ is stable in triangular coordination; the bonding is considerably more covalent, with the lowest-binding-energy orbitals (of Cu 3*d*–S 3*p* bonding character) slightly stabilized relative to a tetrahedral environment. Although calculations have been performed on a cluster representing tetrahedrally coordinated Fe^{3+}, calculations have not been done on a planar triangular FeS_3^{3-} cluster. However, trigonal planar Fe^{3+} is apparently not found in sulfide minerals, suggesting its instability. Hence, whereas copper may be relatively stabilized in the reconstructed surface environment, Fe^{3+} may be destabilized and undergo reaction to form the hydrated oxide.

8.3.6. Concluding remarks on surface studies

The examples discussed in the previous material serve to illustrate the complexity of surface properties of minerals and related materials, the difficulties of adequate characterization, and the important role to be played by calculations of electronic structure.

The oxides containing cations in octahedral coordination, such as MgO and TiO_2, seem to suffer little or no reconstruction of the crystal structure at the surface, but there are major changes in electronic structure. These effects have important implications for surface reactivity, especially when oxygen vacancy defects are considered and particularly in transition-metal oxides. The example of TiO_2 was discussed above; more complex behavior is shown by species such as Ti_2O_3 and NiO (Henrich, 1987). The latter, like other transition metals, shows increasing *d*-orbital

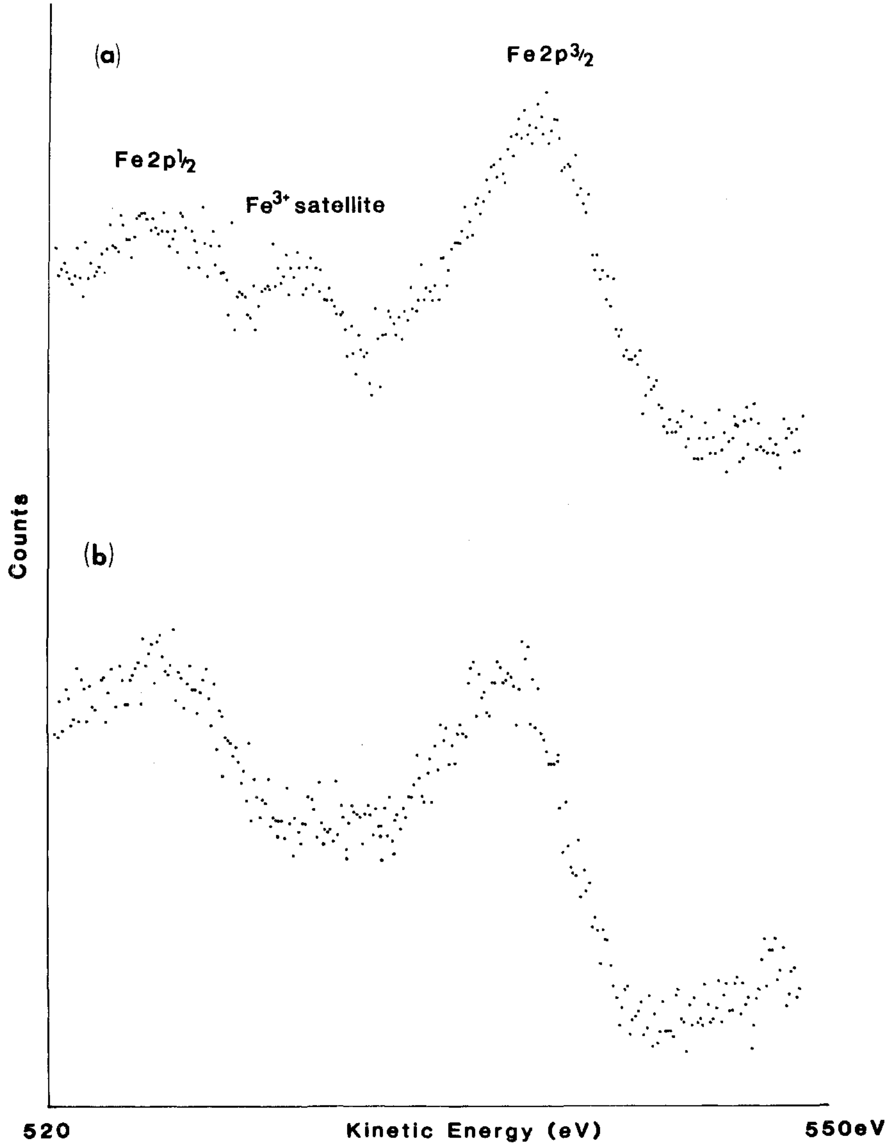

Fig. 8.23. Fe 2*p* x-ray photoelectron spectra of (a) tarnished bornite, and (b) bornite with the surface tarnish removed by argon ion etching (after Vaughan et al., 1987).

populations of cations adjacent to an oxygen vacancy defect. Such surface defects are the active sites for chemisorption, whereas the nearly perfect surfaces are relatively inert to most of the molecules that have been studied (e.g., H_2, O_2, H_2O, CO, SO_2).

Oxides and sulfides with tetrahedrally coordinated cations such as those with the zincblende structure may undergo substantial surface reconstruction. There are consequently also substantial changes in electronic structure. Much of the work undertaken on surface characterization of oxides and sulfides has been concerned with materials of importance in semiconductors and catalysts, but a certain amount of work has also been prompted by the importance of surface studies in mineral technology. Examples include studies of the surface properties of chalcopyrite (Buckley and Woods, 1984), galena (Tossell and Vaughan, 1987), or pyrite during extraction by flotation (Brion et al., 1980).

The whole field of surface studies of minerals and related materials is one that is ripe for expansion and development. New techniques that enable imaging of the atomic structures of surfaces in real space, such as scanning tunneling microscopy, are now starting to be applied to minerals (e.g., the work of Eggleston and Hochella, 1990, on sulfide surfaces; see Fig. 8.24). A start has also been made in theoretical investigations of surface reactivity, in particular the dissolution of quartz. *Ab initio* SCF calculations with correlation corrections have been performed by Lasaga and Gibbs (1990) on the absorption complex $H_3SiOH\cdots H_2O$ and on the transition state in the hydrolysis exchange reaction:

$$H_3SiOH + H_2O^* \rightarrow H_3SiO^*H + H_2O,$$

where the asterisk simply distinguishes the different oxygens. The transition state was fully optimized at a polarized split valence level with Moller–Plesset second-order correlation corrections, and the ΔH of activation was calculated to be ~15 kcal/mol, in reasonable agreement with experimental activation energies around 18 kcal/mol for quartz dissolution. Further calculations using larger bases and more complicated cluster models will be needed to confirm these results, but they certainly seem encouraging.

8.4. Geochemical distribution of the elements

The Earth is a highly differentiated body, with possibly only three elements (Fe, Ni, S, or perhaps O) comprising most of the core and only nine elements (O, Si, Al, Fe, Mg, Ca, Na, K, and Ti) making up more than 99% of the mantle and crust (on a water-free basis). Although the major part of this differentiation occurred during the early history of the Earth, continuing volcanism means that geochemical differentiation of the Earth is still operating, with the introduction into the crust of material

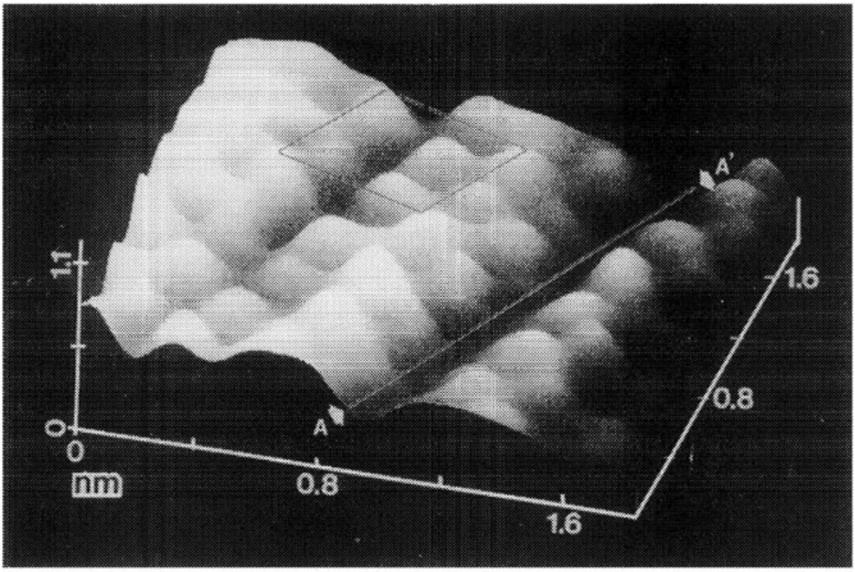

Fig. 8.24. A scanning tunneling microscope image of a pyrite growth surface taken under oil. The surface structure is arranged in "ranges" and "valleys" parallel to the line marked A-A′, which is parallel to a principal crystallographic axis. A 5.4 × 5.4 Å^2 surface cell, as expected for a termination of the bulk pyrite structure, is marked. However, the atomic arrangement does not correspond to a simple termination of the pyrite structure as discussed by Eggleston and Hochella (1990), from whose work this figure is reproduced (with the publisher's permission).

from the upper mantle. Convection in the mantle is regarded as the driving mechanism for bringing upper mantle material to the surface and causing the remelting of crustal material, which is subducted. At the surface, there are also the processes of transfer of material between the lithosphere, hydrosphere, and atmosphere. One of the major aims of geochemistry has been to explain the behavior of the elements during these processes.

8.4.1. The Goldschmidt classification: Ionic and orbital interpretations

Goldschmidt, in 1932, classified the elements into groups based initially on their distribution among the mineral phases in meteorites, as follows:

Siderophile elements, tending to occur as metals and alloys (e.g., Fe, Ni, Co, Pt);

Chalcophile elements, tending to occur as sulfides or other chalcogenides (e.g., Zn, Cd, As, Se);

Lithophile elements, tending to occur as oxides and silicates (e.g., Al, Na, K, Ca);

> *Atmophile elements,* tending to occur in the uncombined state (e.g., N, Ar);
>
> *Biophile elements,* tending to occur in biological systems.

Some elements fall into two or more categories of this very broad classification (e.g., nickel shows some siderophile and chalcophile characteristics), as shown in Table 8.10, which lists members of the above-mentioned groups.

Clearly the principles underlying the distribution of the elements as outlined by Goldschmidt, and the processes of differentiation involving solids, melts, solutions, and gases, are based on the nature of chemical bonding in the different geochemical systems. We shall consider by using selected examples: first, explanations for the Goldschmidt classification, and then for the behavior of elements during differentiation processes.

Goldschmidt's ideas were developed from the simple ionic model and the concepts of ionic radius and radius ratio as controlling factors governing crystal chemistry. Initially, attempts to account for deviation from the ionic model were made by employing electronegativity values (Ringwood, 1955; Ramberg, 1953), and Ahrens (1952, 1953) suggested using the electron affinity of a cation (measured by the nth ionization potential of the atom used to create a M^{n+} cation) as a measure of its polarizing power (i.e., its ability to cause departures from the ionic model when combined with highly polarizable anions). By comparing cations of similar charge and size, Ahrens (1965) showed that a general relationship exists between the differences in electron affinities of the cations and the differences in their chalcophilic and siderophilic tendencies (as well as differences in structures of their compounds predicted by the simple ionic model, and in certain of their properties). A more modern approach that is closely related to the work of Ahrens employs the hard–soft acid–base (HSAB) principle as discussed by Jensen (1980). As briefly noted earlier in this text, the terms *acid* and *base* here refer to the formulations of Lewis (1923) as translated into the idiom of quantum mechanics by Mulliken (see Mulliken and Pearson, 1969). This provides the definitions that:

> A base is a species that employs a doubly occupied orbital in initiating a reaction.
>
> An acid is a species that employs an empty orbital in initiating a reaction.

Here the term *orbital* may refer to a discrete molecular orbital or a band (or an atomic orbital in the case of atomic species). The donor orbital on the base is usually the highest occupied MO (or HOMO), and the acceptor orbital on the acid is usually the lowest unoccupied MO (or LUMO). Simple perturbational MO theory predicts that for two interacting orbitals of suitable symmetry and overlap, the smaller the difference in the orbital energies, the greater the mutual perturbation or interaction. The terms *soft* and *hard* relate to a range of properties, but essentially soft acids are

Table 8.10. Geochemical classification[a] of the elements, according to distribution between iron, sulfides, silicates, atmosphere, and organisms

	Sulfide, chalcophile				
Iron, siderophile	**In meteorites**	**Terrestrial**	**Silicate, lithophile**	**Gases, atmophile**	**Organisms, biophile**
Fe, Ni, Co	S, Se, (Te?)	S, Se, Te	O, (S), (P), (H)	H, N, C, O	C, H, O, N, P
P, (As), C	P, As, (Sb?)	As, Sb, Bi	Si, Ti, Zr, Hf, Th	Cl, Br, I	S, Cl, I, (B)
Ru, Rh, Pd	Cu, Ag, Zn, Cd	Ga, In, Tl	F, Cl, Br, I	He, Ne, A	(Ca, Mg, K, Na)
Os, Ir, Pt, Au	(Ti), V, Cr, Mn, Fe	(Ge), (Sn), Pb	(Sn)	Kr, X	(V, Mn, Fe, Cu)
Ge, Sn	(Ca)	Zn, Cd, Hg	B, Al, (Ga), Sc, Y		
Mo, (W)		Cu, Ag, (Au)	La, Ce, Pr, Nd, Sm		
(Nb), Ta		Ni, Pd, (Pt)	Eu, Gd, Tb, Dy		
(Se), (Te)		Co, (Rh, Ir)	Ho, Er, Tu, Yb, Lu		
		Fe, Rh, (OS)	Li, Na, K, Rb, Cs		
			Be, Mg, Ca, Sr, Ba		
			(Fe), V, Cr, Mn		
			((Ni)), ((Co)), Nb, Ta		
			W, U, ((C))		

[a] Elements shown in parentheses indicate elements that occur in small quantities within each group.

Source: After Goldschmidt, 1954.

characterized by low-lying acceptor orbitals and soft bases by high-lying donor orbitals; hard acids and bases have the opposite properties.

The concepts underlying the Goldschmidt classification can be explored in more detail with particular reference to lithophile versus chalcophile behavior and the nature of the metal–oxygen versus metal–sulfur bond.

8.4.2. Lithophile versus chalcophile behavior: The M–*O versus the* M–*S bond*

The electronic structures of specific oxide and sulfide minerals have already been discussed in Chapters 4 and 6.

The chalcophilic character of electron-rich transition metals, such as Fe through Cu and their congeners in the later transition series, is associated with a higher relative stability for the M–S bond. It is well known that crystal-field splittings of transition metals in octahedral sites in sulfides are systematically higher than those in oxides (Burns and Vaughan, 1970). This may be interpreted in terms of a greater t_{2g}-e_g orbital energy separation for an octahedral environment, produced by a stabilization of the t_{2g} crystal-field orbital through interaction with an empty orbital of π symmetry on S (with respect to the M–S bond), as shown in Fig. 8.25. A substantial part of the increased M–S bond energy arises from this stabilization of the metal t_{2g} orbital. Such interactions are well known within organometallic chemistry. For example, in $Cr(CO)_6$ the Cr–C bond is greatly strengthened by Cr $3d$–CO π^* interaction, that is, the occupied Cr $3d$ orbital interacting in bonding fashion with the empty CO π^* (Chornay et al., 1985; Lukehart, 1985), as shown qualitatively in Fig. 8.26. What is the nature of the orbital accepting electron density for a sulfur ligand bonded to a transition metal? The answer to this question is available from gas-phase spectroscopic studies and calculations.

Early theories stressed the importance of $3d$ orbitals in the bonding of Si–Cl (Cruickshank, 1961). However, as we have seen in our discussion of oxyanions, such essentially atomic orbitals seem to play the role of polarization functions, only slightly modifying most properties of most such materials (see also Cruickshank, 1985). Results using the gas-phase experimental technique of electron transmission spectroscopy indicate that the low-energy empty orbitals that can accept metal electron density in H_2S and related compounds are molecular orbitals of σ^* type with respect to the S–H bond (Giordan et al., 1986). Electron transmission spectroscopy is the conjugate to photoelectron spectroscopy, but, whereas the latter measures the energy required to remove an electron from an occupied orbital, ETS measures the energy of the anion state arising from electron capture into an unoccupied orbital. In practice, low-energy monochromatic electrons are passed through the sample and the creation of transient negative ions detected by fluctuations in the electron current.

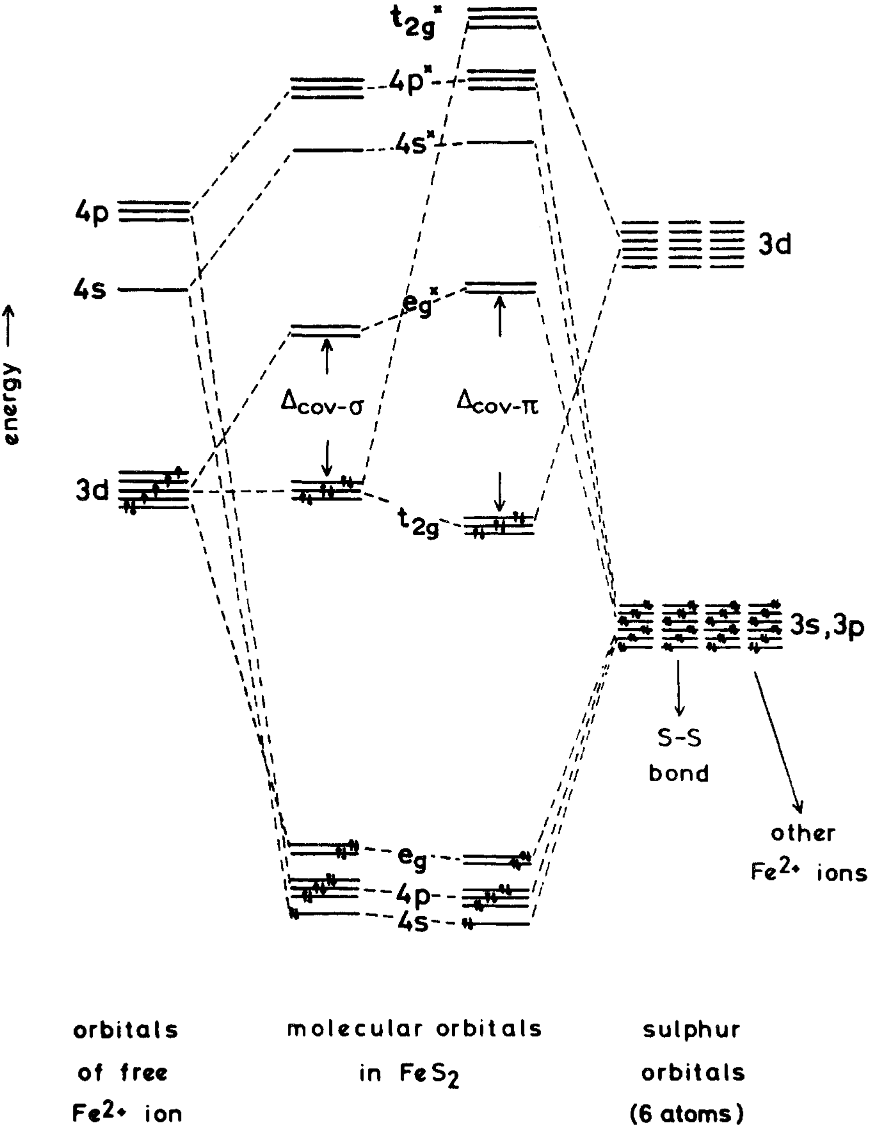

Fig. 8.25. A qualitative molecular-orbital energy-level diagram for pyrite, drawn to illustrate the possible interaction between $3d$ orbitals on iron and empty orbitals of π symmetry on sulfur (after Burns and Vaughan, 1970, reproduced with the permission of the publisher).

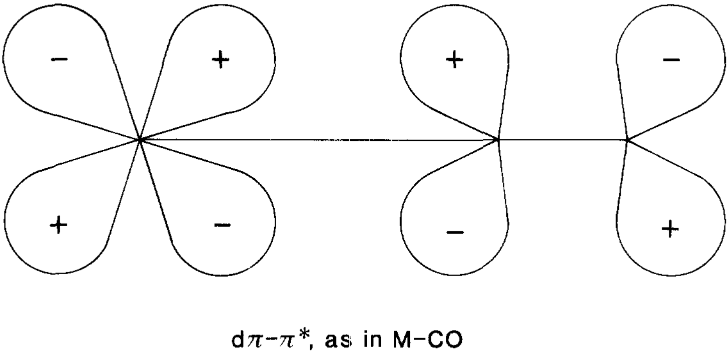

Fig. 8.26. $d\pi$-π^* bonding interaction in an *M*–CO system, such as occurs in $Cr(CO)_6$, where the occupied Cr 3*d* orbital interacts with the empty CO π^* orbital.

For H_2S a single transient anion is observed corresponding to occupation of the $3b_2$ orbital of H_2S with S–H σ^* character. Although the symmetry of this molecular orbital is such as to allow *d*-orbital participation, it can be described essentially as a S–H σ^* orbital. A contour plot of this orbital (Fig. 8.27) shows its S–H σ antibonding nature. No anions are observed corresponding to S 3*d* orbitals of other symmetry types, showing that the σ^* character of this orbital is its crucial element. Similar σ^* orbitals are observed at low energy in SiH_4 and PH_3, and in SiR_4, PR_3, and R_2S, where *R* is a hydrdocarbon group (Tossell et al., 1985b). By contrast, for compounds of the first-row elements (e.g., H_2O), the σ^* orbitals are much higher in energy and are so strongly mixed with diffuse outer (so-called Rydberg) orbitals of the same symmetry that they have essentially no electron acceptor capability (Schwarz, 1975; Robin, 1985). The reason for

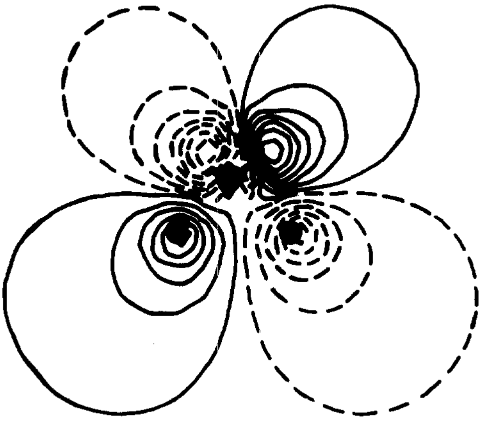

Fig. 8.27. A contour plot of the $3b_2$ ("valence") molecular orbital of the H_2S molecule (see Giordan et al., 1986, for further discussion).

this energy difference is not certain at present, but it apparently arises from the longer single bond distances in the compounds of the heavier elements leading to less destabilization of the σ* orbitals. As noted in our discussion of SiF_4, orbitals with substantial Si 3*d* character do indeed exist, but they are at much higher energy (in the continuum in XANES) and too high in energy to be seen in ETS.

Another factor in *M*–S bonding stability is the presence of S–S bonds. Calculations and fragmentary spectral studies indicate that the σ* orbitals of S–S bonds are even lower in energy than those of S–H bonds (i.e., σ* energies are lower in H_2S_2 than in H_2S). Thus disulfide ligands, and probably polysulfides in general, are better electron acceptors than sulfur itself. It is well known that transition metals form numerous compounds with polysulfides (Draganjac and Rauchfuss, 1985; Muller and Diemann, 1987). In many polysulfides (e.g., S_4^{2-}) there are also empty π* orbitals in addition to the empty σ* orbitals, and these may also accept electron density from the metal.

Investigations of analog compounds of O and S indicate that their relative σ and π bond strengths are very different (Kutzelnigg, 1984), with O forming stronger π bonds than σ bonds and S the reverse, as shown in Table 8.11. This explains why the stable form of elemental oxygen is O_2, a doubly bonded species, and that of sulfur is S_8, with all single (i.e., σ) bonds. Generally, polysulfides are formally close to single bonding, since they have all their π and almost all their π* orbitals filled. Such formally single-bonded structures may, however, be stabilized by the interaction of occupied S *p*π-type orbitals with S–H or S–S σ* orbitals of the appropriate symmetry (Aida and Nagata, 1986), that is, by σ-π mixing or hyperconjugation, as shown in Fig. 8.28. Thus, because S–S π bonds are weak, single-bonded structures are favored, and such structures will have long bonds, leading to low σ* orbital energies and the consequent favorability of σ-π interaction. Thus, the same type of orbital interaction that contributes to *M*–S bond stability also stabilizes S–S single-bonded species.

In addition to the difference in the energetics of their σ* acceptor orbitals, S and O differ as well in the nature of their occupied orbitals. The ionization potential (IP) of the S 3*p* orbital is less than that of the O 2*p* (10.4 eV versus 13.6 eV), and its electron affinity (EA) is larger (2.1 eV

Table 8.11. Calculated σ and π bond strengths in kcal/mol for different atom pairs

	C–C	N–N	O–O	Si–Si	P–P	S–S
σ	80	38	35	46	48	64
π	70	94	83	28	34	37

Source: From Kutzelnigg, 1984.

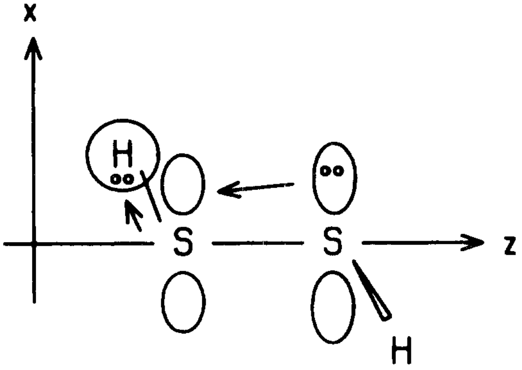

Fig. 8.28. Schematic representation of the change in electron density resulting from the interaction between the σ-type orbitals of a S–H bond and the *p* orbital corresponding to the lone pair of another S atom (after Aida and Nagata, 1986; reproduced with the publisher's permission).

versus 1.5 eV). The electronegativities, approximated as ½ (IP plus EA), are 6.22 for S and 7.54 for O (Pearson, 1988). Since the electronegativities of the transition-metal atoms are considerably smaller (e.g., 4.06 for Fe), the energy separation of *M* 3*d* and valence *p* orbitals will be considerably smaller for S than for O. For S_2 the IP value is lower than in S because the HOMO (highest-energy occupied MO) is π^*, destabilized with respect to the *p* orbital of the atom. The value of EA is also lower, since that same π^* is also the LUMO (lowest-energy unoccupied MO), and addition of electrons to it destabilizes the molecule. The approximate electronegativity of S_2 is about 5.5 eV, suggesting an even smaller metal $-S_2$ energy difference. Some important electron affinities for atoms and diatomic molecules are given in Table 8.12.

The higher energy of S 3*p* orbitals means that S will not form stable

Table 8.12. Electron affinities (EA) (in eV) for neutral atoms (*A*) and molecules (A_2) and electron configurations of neutral A_2 molecules

	EA(*A*)	EA(A_2)	Electron configuration of A_2
C	1.3	3.5	π^2
N	0 ± 0.2	−1.9	$\pi^4\pi^{*0}$
O	1.5	0.4	$\pi^4\pi^{*2}$
Si	1.2	2.2	π^2
P	0.8	0.2	$\pi^4\pi^{*0}$
S	2.1	1.7	$\pi^4\pi^{*2}$

Source: From Tossell, 1983.

compounds with transition-metal ions of high formal charge since partially empty orbitals on the metal would lie below occupied S 3*p* orbitals (Tossell and Vaughan, 1981). The reduced separation of *M* 3*d* and S or S_2 3*p*-derived levels also leads to increased covalent mixing in sulfides compared to oxides. Unfortunately, the quantification of covalency is difficult, as we have earlier discussed (see Section 7.1.1), and specific numerical quantities such as atomic charges or percent orbital character depend on rather arbitrary choices of the expansion basis sets used in the calculations.

Associated with the lower stability of the S 3*p* orbitals compared to O 2*p*, we have generally smaller HOMO–LUMO separations or smaller band gaps in sulfides than in oxides. The lesser π bonding strength of S also gives small π^*-π orbital energy separations, further reducing HOMO–LUMO gaps in many cases. This has two important effects upon sulfide geometric and electronic structure. First, HOMO–LUMO mixing, which stabilizes distortions from high symmetries, is more important in sulfides; for example, the H–S–H angle is smaller and has a higher barrier to linearity than does the H–O–H angle, because the $2a_1$ ligand *p* orbital (a degenerate HOMO for linear geometry) and the $3a_1$ ligand *p*–H σ^* orbital (the LUMO) interact more strongly for bent angles in the S than in the O compound (Tossell, 1984b). Analogously, three-coordinate S (e.g., in TiS_2) is much more distorted from planarity than is three-coordinate O (e.g., in TiO_2), again because of increased mixing upon geometric distortion of the HOMO and LUMO, which are of ligand *p* and ligand–*M* σ^* type, respectively. For the same reason, the S atoms in the (110) surface of ZnS are more distorted from tetrahedral geometry than are the surficial O atoms of ZnO (Vaughan et al., 1987). Thus, S will tend to occupy or produce distorted environments compared to oxygen. See Burdett (1988) for further discussion of this point.

A second difference is that, due to the closeness in energy of *M* 3*d* and S 3*p* orbitals, the electron configurations from a molecular-orbital point of view, or band fillings in a band picture, are often uncertain, even for stoichiometric compounds. For example, in CuS the photoelectron spectra show all Cu to be in the 1+ state (e.g., $3d^{10}$), with holes in the S 3*p* part of the valence band (Perry and Taylor, 1986). Our interpretation of the properties of $FeAs_2$ (Tossell, 1984c) indicates that its best model electron configuration is $Fe^{2+}(d^6)As_2{}^{2-}$, with the partially empty π^* orbital of the $As_2{}^{2-}$ unit interacting with another in a stabilizing manner to yield an incipient $As_4{}^{4-}$ anion, as in $CoAs_3$. Such holes in the ligand valence band are expected to be most important for transition elements near the extreme right of the transition series, and for the compounds containing diatomic anions.

The bonding characteristics we have described for S are also present in Se, Te, P, and As. We would therefore expect arsenides to show generally the same structural and electronic properties as sulfides, consistent with their observed chalcophilic nature.

8.4.3. *Geochemical coherence and geochemical differentiation*

In terms of the HSAB principle, for cations with similar charge control factors, the chalcopile and siderophile tendencies of a cation increase as its softness increases. Comparisons between cations of different charge and size are more difficult; generally the larger the charge and the smaller the size, the larger the electron affinity necessary to induce chalcophile behavior. Ahrens (1953) also lists pairs of cations with similar charges and sizes and gives the ratio of their electron affinities ϕ (the larger electron affinity always being used as the numerator). When $\phi \approx 1$ the cations have similar charge-control and orbital-control factors (see Table 8.13) and should be similar in their chemistry, exhibiting a high "geochemical coherence," and commonly being found together in rocks and minerals. When $\phi > 1$, the cations will show marked differences in their orbital control factors and low geochemical coherence.

Table 8.13. Ahrens' ϕ measure of geochemical coherence for various ion pairs[a]

Z	**Pairs**	I_n**(eV)**[b]	r**(Å)**[b]	ϕ	**Coherence**
1+	K Rb	4.34 4.18	1.33 1.47	1.04	High
1+	Tl Rb	6.11 4.18	1.47 1.47	1.45	Low
1+	Cu Na	7.72 5.14	0.95 0.97	1.50	Low
2+	Ni Mg	18.20 15.03	0.69 0.66	1.20	Moderate
2+	Ca Cd	11.9 16.9	0.99 0.97	1.42	Low
2+	Hg Sr	18.75 11.03	1.12 1.12	1.70	Low
3+	Ga Al	30.7 28.44	0.62 0.51	1.08	High
3+	In Sc	28.03 24.80	0.81 0.81	1.15	Moderate
4+	Ge Si	45.7 45.1	0.53 0.42	1.01	High
4+	Zr Hf	34.0 31.0	0.79 0.79	1.08	High
5+	Nb Ta	52.0 44.8	0.69 0.68	1.16	Moderate

[a] After Ahrens (1953).

[b] Ahrens' original data are used.

A similar approach may be used in discussing the substitution of cations in silicate structures (Jensen, 1980; Chapter 8). Thus, when an O^{2-} anion is placed in the field of an Si^{4+} cation, its electron cloud is tightened and its polarizability decreases. Also, as each of the oxygens of the SiO_4^{4-} anion is placed in the field of a second Si^{4+} cation, its polarizability further decreases, as does that of each of the remaining unshared oxygens of the tetrahedral anion. This leads to the prediction that the polarizability or softness of the oxygen donor atoms will decrease in the order:

$$O^{2} > \underset{\text{(isolated)}}{SiO_4^{4-}} > \underset{\text{(single chain)}}{SiO_3^{2-}} > \underset{\text{(double chain)}}{Si_4O_{11}^{6-}} > \underset{\text{(sheet)}}{Si_2O_5^{2-}}$$

If the substitution of Mg^{2+} and Fe^{2+} in silicates is considered, both have similar charge-control factors (ionic radii of 0.72 and 0.78 Å, respectively) but differ somewhat in their softness (second ionization potentials of 15 eV for Mg^{2+} and 16.2 eV for Fe^{2+}). Hence, although high geochemical coherence would be predicted, the softer Fe^{2+} cation would also be expected to show some preference for the softer silicate environments containing isolated tetrahedra, rather than the harder environments with chain and sheet silicate structures, and vice versa for the harder Mg^{2+} cation. In fact, the Mg-to-Fe ratio does increase on moving from left to right on the above scale, with the sheet silicate mineral talc being nearly pure magnesium silicate (see also Ramberg, 1952). Substitution of Al for Si in silicates increases the polarizability of the oxygen atoms (the Al^{3+} generating a smaller field) and so increases the Fe-to-Mg ratio over that observed in the pure silicate. The harder Ca^{2+} ion (second ionization potential of 11.9 eV) is preferentially concentrated into the harder chain and sheet silicates.

As discussed in Chapter 5, data from both Auger spectroscopy and optical studies confirm a decreasing polarizability and/or optical basicity for silicate units as the degree of polymerization increases, consistent with the above interpretation. Polarizabilities (or better still, polarizabilities per O atom) have not yet been calculated for silicate polymers, nor have interaction energies of cation pairs such as Mg versus Fe with oxygens of various type yet been studied.

9

THE FUTURE

In this final chapter, an attempt is made to provide an overview of the capabilities of quantum-mechanical methods at the present time, and to highlight the needs for future development and possible future applications of these methods, particularly in areas related to mineral structures, energetics, and spectroscopy. There is also a brief account of some new areas of application, specific directions for future research, and possible developments in the perception and use of quantum-mechanical approaches. The book ends with an epilog on the overall role of "theoretical geochemistry" in the earth and environmental sciences.

9.1. Capabilities of quantum-mechanical methods

The local structural characteristics of minerals such as Mg_2SiO_4, which contain only main-group elements, are reasonably well reproduced by *ab initio* Hartree–Fock–Roothaan (SCF) cluster calculations at the medium-basis-set level. Calculations incorporating configuration interaction will inevitably follow and probably lead to somewhat better agreement with experiment. The most pressing needs in this area of study are for the development of systematic procedures for cluster selection and embedding, for a greater understanding of the results at a qualitative level, and for more widespread efficient application of the quantum-chemical results currently available. In the last area, substantial progress has already been made by Lasaga and Gibbs (1987), Sanders et al. (1984), Tsuneyuki et al. (1988), and others, who have used *ab initio* calculations to generate theoretical force fields which can then be used in molecular-dynamics simulations. If the characteristics of the resultant force fields can be understood at a first-principles level, then it may be possible to understand details of the simulated structures at the same level. Unfortunately, as regards a greater qualitative understanding of the quantum-mechanical calculations, little progress has been made. Rather old qualitative theories describe some aspects of bond-angle variation (Tossell, 1986), but no general model to interpret variations in bond lengths has been developed within either chemistry or geochemistry beyond the model of additive atomic (Slater) or ionic (Shannon and Prewitt) radii. Indeed, global theories of bond-length variations within an *ab initio* framework seem to be nonexistent. Nonetheless, quantum-chemical studies have shown the presence of intriguing systematics in bond lengths (Gibbs et al., 1987), which had been already noted empirically. Furthermore, the application of density-functional theory has emphasized the importance of the *electron density* for understanding chemical bonding and has refined the meaning of much older chemical concepts such as *electronegativity.* A more general and more powerful theoretical basis for much of structural chemistry may result from investigations within these areas. Systematic studies of cluster selection and embedding are being pursued by Sauer (1989) and others, but no convincing general approach has yet been formulated.

There has also been great progress in the application of delocalized electron models to solids. Very accurate band-theoretical methods (such as the full-potential APW and the *ab initio* pseudopotential methods) can generate accurate crystal structures even for complex solids (although at considerable computer expense). These will certainly be applied to some of the simpler silicates and sulfides in the future. The geometric structures of solids can also be efficiently calculated within a combined molecular-dynamics–density-functional approach (Allan and Teter, 1987). If this approach fulfills its promise, it may well become the method of choice for the study of the structural properties of complex solids, both crystalline and amorphous. For more restricted classes of solids, other more approximate band-theoretical methods will be accurate enough, and much more efficient computationally. High-symmetry, close-packed solids can be modeled very well by methods that employ an atomic sphere approximation, as shown by the results of Williams and co-workers for transition-metal oxides (Terakura et al., 1984a,b). For reasonably "ionic" materials, self-consistent modified electron-gas models give accurate structures, and the potentials generated by their charge distributions may also give accurate densities of states and eigenvalue spectra. Such MEG methods will be very valuable for determining bulk moduli and other elastic properties for all those minerals in which such properties are dominated by local Mg–O and Al–O bonds. Simulation methods, increasingly based on quantum-mechanical potentials, will also be applicable to quite complex crystalline materials.

The quantum-mechanical description of minerals containing transition metals is at a less advanced stage. The accuracy of simple Hartree–Fock–Roothaan methods has not been fully determined for such systems. Local-density-functional methods have been successful for calculating the structural properties of high-symmetry materials, but excitation energies are still poorly reproduced. Local-density-functional cluster calculations have so far been restricted mostly to model potentials (e.g., muffin-tin potentials) so that their full power has not been utilized. We need to determine the accuracy and efficiency of Hartree–Fock–Roothaan (or Hartree–Fock plus configuration-interaction) and full-potential basis-set-type local-density-functional methods for calculating both structural and spectroscopic properties of such systems.

9.2. Future areas of application in structures and energetics

It is clear from our discussion of theoretical high-pressure studies in Chapter 7 that both molecular-orbital cluster and full-lattice calculations (involving band theory, ionic, and simulation methods) have already made considerable contributions to the understanding of high-pressure mineral phases. Thus, it is well established that such calculations have an important role in studies of the physics of the solid Earth. Many local structural properties of minerals have also been interpreted using cluster models, establishing their importance in structural mineralogy. Additional molecular-orbital cluster calculations will doubtless lead to understanding of the finer details of local geometry, both for crystalline materials and glasses.

We can anticipate further theoretical studies of high-pressure phases, particularly involving transition-metal oxides and silicates, and iron alloy systems. However, natural minerals have such complicated compositions and structures that very accurate calculation of their properties will be extremely difficult. For example, the calculation of compressibilities along the Mg_2SiO_4–Fe_2SiO_4 series would require truly heroic computation and, at present, unavoidable approximations would prevent the results from being definitive. Such a study would constitute only one piece of evidence useful for the determination of the composition of the mantle, although it would be no more ambiguous than most such evidence available on this topic.

Many fundamental questions concerning the geochemical distribution of the elements appear to be on the verge of being answered. We are gradually understanding differences in bond type (such as Fe–S as against Fe–O bonding, and Fe–O as against Mg–O bonding) so that we can "explain" why the element distributions occur as observed, and through computation determine quantitative energy differences and, thus, equilibrium and partition coefficients. A major stumbling block in this effort is finding theoretical methods that treat the different bond or structure types with equivalent accuracy, so that the choice of method does not introduce unacceptable artifacts. This is a particularly serious problem when comparing physically different phases, such as crystalline solids and melts. Cluster calculations may be adequate to give enthalpic properties for systems that are not disordered configurationally. However, for systems in which there is appreciable disorder in the possible local environments, molecular dynamics will be necessary, and free-energy differences will have to be evaluated. In modeling transition-metal-bearing minerals, we will be faced with the difficult task of extracting energy parameters from *ab initio* calculations on transition-metal systems for which terms simulating covalency and crystal-field effects will be important, particularly for low-symmetry metal environments. Another area of the science of the solid Earth where computer simulation of properties will prove valuable is in solid-state diffusion and reactivity, such studies leading to a better understanding of creep processes in minerals. Already, simulation methods have yielded valuable information on the relative energies of defects (Catlow, 1985).

9.3. Future applications in mineral spectroscopy

Many aspects of the electronic structures of minerals have been studied, but considerable gaps in knowledge remain. Studies of the photoelectron spectra of many such materials, particularly in the valence region, have been sparse, and for even the most common minerals there are virtually none of the variable-energy, angle-resolved photoelectron data now common for the inorganic solids. X-ray emission and x-ray absorption spectral data are also incomplete. Fortunately, some of the newer spectroscopic methods (e.g., ^{29}Si MAS-NMR) have attracted sufficient researchers that most mineral phases have been studied by numerous investigators, and the experimental results are being analyzed quantum mechanically as well as phenomenologically. For the more established techniques, such as visible–uv absorption. Mössbauer and ir–Raman spectroscopies, there are also fairly complete data. In the electronic absorption (crystal-field or *d-d*) spectra of minerals, detailed interpretations have often been made using a parametric crystal-field theory formalism, but, as we have seen, first-principles calculation of such spectral properties remains very difficult. In Mössbauer spectroscopy, some progress with regard to calculating overall trends in isomer shift has been made, and we can anticipate much progress in this area in the near future. There has also been considerable recent progress in the calculation of both the energies and the intensities of ir and Raman spectra [as described for $Si(OH)_4$ and CO_3^{2-} in Chapter 5]. Such calculations (employing cluster molecular-orbital methods) will serve to constrain the force fields needed to generate the theoretical phonon spectra of minerals. Direct band-structure calculations of phonon spectra are now also possible for simple materials, and applications to mineral systems will doubtless emerge. The "classical" optical properties of minerals such as refractive indices are also now being studied quantum mechanically (Tossell and Lazzeretti, 1988b).

We may confidently expect that the interpretation of mineral photoelectron data will move to a higher level, with more accurate correlated calculation of orbital ionization potentials and valence-region structure (including the so-called "satellite" structure, not found in a strictly independent-electron model) and with direct calculation of photoionization intensities, as described for SiF_4 in Chapter 4. Similarly, direct calculation of x-ray emission spectral intensities will be needed to resolve a number of unsolved problems. As we have mentioned, XANES theory is currently in turmoil, with considerable uncertainty about which spectral features are multiple scattering in character and which are single scattering (EXAFS-like) features. Considerable time may be needed to sort out this problem if important spectral features do turn out to be nonlocal, involving distant coordination shells. Local-density and Hartree–Fock–Roothaan with configuration-interaction methods will be used to study trends in visible and uv spectra at high pressure in transition-metal systems.

9.4. New areas of application

As in quantum chemistry, theoretical calculations within geochemistry will be particularly valuable for those systems that are hard to study experimentally, or for which atomistic-level information is unattainable. A number of areas are immediately suggested: aqueous geochemistry of metal-bearing hydrothermal fluids, properties of oxidic glasses, condensation processes in the solar nebula, and properties of mineral surfaces. Given the considerable resources required and the necessary expense of the most advanced quantum-mechanical methods, it may be expedient, and perhaps even desirable, to employ them primarily in those frontier areas rather than attempting quantum-mechanical studies of geochemical and solid-state systems "across the board." Calculation of the properties of hydrothermal fluids will first require quantum-mechanical calculation of ion–ion and ion–water interactions, followed by simulation using the potentials obtained. Oxidic glasses can be better understood by calculations on fragments of intermediate size (ring structures, etc.) as well as on unusual local fragments. Simulation of such structures using quantum-mechanical potentials will be of great value, although there may be cases where the molecular-dynamics–density-functional theory of the Car and Parinello (1985) type will be necessary. There has been rather little attention paid to the application of quantum-mechanical methods to understanding condensation processes in the solar nebula, although high-level theories have been used for many years to predict structures and spectra for gas-phase interstellar molecules (principally hydrocarbons). Previous successful studies of SiO polymerization indicate that such work should be possible. We can also expect to see those methods used for the study of small clusters, and now well established within chemistry and physics (Castleman, 1987), being applied to silicate clusters. There is also much scope for the application of quantum-mechanical methods to the study of mineral surfaces, a field that has so much in common with studies carried out by chemists on catalysis and adsorption, that strong cross-fertilization should occur.

9.5. Research directions

In writing this book, many relatively straightforward experimental and theoretical areas ripe for exploitation have been identified, as well as certain difficult but important problems that would require really heroic individual efforts or a well-coordinated program of team research. For example, it would be relatively easy to: (1) calculate transition-metal oxide and sulfide structural systematics using model-potential band methods; (2) calculate electron densities and electric-field gradients at iron nuclei using *ab initio* Hartree–Fock–Roothaan (SCF) or discrete-basis $X\alpha$ methods applied to molecular clusters; (3) systematically calculate the phonon spectra of magnesium silicates using modified electron-gas methods. On the other hand, it would be difficult to: (1) accurately evaluate the relative stabilities of all the different polymorphs of SiO_2; (2) evaluate speciation in aqueous solutions (e.g., structures, stabilities, and spectra of Cu sulfides); (3) evaluate local geometries at transition-metal sites in minerals and the influence of local structure on spectra and stabilities.

In general, the most difficult problems require the determination of local properties in complex materials and the relating of local properties to bulk properties. Problems of this type are becoming more important in quantum chemistry with its shift from chemical physics (concerned primarily with microscopic properties) towards physical chemistry (concerned more with macroscopic properties), a shift occurring as theoretical methods and computer capabilities improve.

There will be continuing change in the way that quantum-mechanical calculations are perceived within the sciences. Such calculations may be treated as "computer experiments," which, for a given price (in personnel, computer hardware and software, and computer time), yield values of a property with specified average errors. They, therefore, serve as a useful complement to existing spectral and structural methods. Given the increased availability of new-generation computer and quantum-chemical software and the increasing costs of research equipment, such "computer experiments" may soon be much cheaper, and more generally accessible, than any other technique except the most routine forms of ir or NMR spectroscopy and x-ray crystallography. Given the increased specialization of quantum-mechanical calculations, it is important to keep in mind that they also provide a comprehensive framework for interpretation of the whole set of properties of a material, and reveal the properties of matter at a level often unattainable through experiment.

9.6. Epilog: Theoretical geochemistry and the Earth and environmental sciences

The closing years of the 1980s have seen a greatly increased awareness on the part of scientists and of the public of the importance of understanding "Earth systems" (i.e., those materials and processes involved when the Earth undergoes chemical and physical change). This awareness has been brought about by the threat of irreversible changes in the atmosphere and hydrosphere, changes that may themselves threaten the survival of many life forms. Linked with these broadly environmental issues are concerns related to the energy and raw material needs of a rapidly growing world population. Here, again, those "Earth systems" that lead to the formation and concentration of fossil fuels and of metalliferous, industrial, and chemical minerals are the focus of study, as are systems associated with the environmental disruption caused by the exploitation and utilization of such resources. There can be little doubt that these environmental and resource issues represent the great challenge to scientists in the 1990s, and may well dominate both the scientific and political agenda, worldwide, well into the twenty-first century.

The thesis of this book has been that quantum mechanics provides the fundamental theoretical framework within which Earth materials and systems involving these materials may be understood. Quantum-chemical calculations tested against experimental (chiefly spectroscopic) studies lead to models that can be successfully refined both by improvements in experimentation and theoretical methodology. As we have shown, such models can enable predictions to be made of the structure, properties, and physico-chemical behavior of minerals and related materials. Such properties may themselves be of intrinsic interest to those working in materials science. However, the ultimate geochemical objective is to develop larger-scale models that quantitatively describe and hence may predict the behavior of Earth systems. As noted in the Preface to this text, recent years have seen the welcome growth of an interdisciplinary approach to such problems in which the traditional boundaries between the chemical, physical, biological, and geological sciences break down and the Earth is viewed as a whole. As should be evident from this book, quantum mechanics has a central role in our attempts to understand the Earth.

APPENDIX A
SYMBOLS, UNITS, CONVERSION FACTORS, AND CONSTANTS

Many symbols, units, and constants are defined as they are introduced in the text. Those more commonly used are given here.

Symbols

χ	an atomic orbital
ϕ	a molecular orbital (MO)
Ψ	a (complete) many-electron wave function
α, β	spin wave functions
H	the Hamiltonian operator
ρ	electron density
ζ	Slater orbital exponent
V	potential energy
Z	nuclear charge
μ	dipole moment
ν	frequency
λ	wavelength

$$\nabla^2 = \frac{\partial^2}{\partial x^2} + \frac{\partial^2}{\partial y^2} + \frac{\partial^2}{\partial z^2}$$

Atomic units (a.u.), the use of which simplifies many equations in quantum mechanics because mass is expressed as a multiple of electron mass m_e (so the mass of the electron is taken as unity), charge as a multiple of the proton's charge e, length as a multiple of the Bohr radius a_0, and energy in multiples of twice the ionization potential of the ground-state hydrogen atom (27.21 eV or one hartree, although the energy itself is sometimes used, 13.6 eV or one rydberg). Hence:

Quantity		*Symbol*	*Value in SI Units*
1 a.u. of mass		m_e	9.109×10^{-31} kg
"	length	a_0	5.292×10^{-11} m
"	charge	e	1.602×10^{-19} C
"	energy	$e^2/4\pi\varepsilon_0 a_0$	27.21 eV; 2625 kJ mol^{-1}
"	velocity	c	2.998×10^8 m s^{-1}

A consequence of the use of these units is that $h = 1$, $\mu_B = \frac{1}{2}$, and $R_H = \frac{1}{2}$. They may be augmented by the choice of $c = 1$ for the speed of light. Use of a.u. eliminates many of the constants in the Schrödinger equation.

Conversion table for frequency and energy units used in spectroscopy

	1 Hz ≡	**1 cm^{-1} ≡**	**1 J mol^{-1} ≡**	**1 eV ≡**
Hz	1	2.9979×10^{10}	2.5053×10^{9}	2.4182×10^{14}
cm^{-1}	3.3356×10^{-11}	1	8.3567×10^{-2}	8.0663×10^{3}
J mol^{-1}	3.9915×10^{-10}	11.9660	1	9.6522×10^{4}
eV	4.1353×10^{-15}	1.2397×10^{-4}	1.0360×10^{-5}	1

Constants (values in SI units)

e	electron charge, -1.602×10^{-19} C
m	electronic mass (at rest), 9.110×10^{-31} kg
c	velocity of light (in vacuo), 2.998×10^{8} m s^{-1}
h	Planck's constant, 6.626×10^{-34} J s
$\hbar$	(Planck's constant)/2π, 1.055×10^{-34} J s
μ_B	Bohr magneton, 9.274×10^{-2} J T^{-1}
μ_N	Nuclear magneton, 5.051×10^{-27} J T^{-1}
N_A	Avogadro constant, 6.022×10^{23} mol^{-1}
k	Boltzmann constant, 1.381×10^{-23} J K^{-1}
F	Faraday constant, 9.649×10^{4} C mol^{-1}
R	gas constant, 8.314 J K^{-1} mol^{-1}
a_0	Bohr radius, 0.529 Å
R_H	Rydberg constant (for hydrogen atom), 1.096776×10^{7} m^{-1}

Units and Conversion Factors (all SI units or permitted non-SI units except those marked with an asterisk)

Length	micrometer (μm) = 10^{-6} m
	nanometer (nm) = 10^{-9} m
	angstrom (Å) = 10^{-10} m
	picometer (pm) = 10^{-12} m
	*Bohr (a_0) = 0.529×10^{-10} m
Temperature	kelvin (K) (0°C = 273.2 K)
Pressure	pascal (Pa) = 0.98×10^{-5} atm (atmosphere)
	*atmosphere 1 atm = 1.013×10^{5} Pa (or N m^{-2})
	*bar = 10^{5} Pa
	*kilobar (kbar) = 10^{8} Pa

Dipole moment	*debye (D) = 3.334×10^{-30} C m
Magnetic flux density	gauss (G) = 10^{-4} T (tesla)
Frequency (ν)	*cycle per second = 1 Hz (hertz)
Electrical charge	coulomb (C)
Entropy (S)	*eu = cal $g^{-1} \cdot C^{-1}$ (= 4184 J kg^{-1} K^{-1})
Relative permittivity (ε)	*dielectric constant (= 1)
Energy	*calorie (cal; thermochemical) = 4.184 J (joule)
	electronvolt (eV) = 1.602×10^{-19} J
	electronvolt per molecule = 96.48 kJ mol^{-1}
	*erg = 10^{-7} J
	wave number (cm^{-1}) = 1.986×10^{-23} J
	*hartree (H) = 27.212 eV (= 43.594×10^{-19} J)
	*rydberg (Ry) = 13.606 eV (= 0.5 hartree)

APPENDIX B

EXPERIMENTAL METHODS FOR OBTAINING INFORMATION ON STRUCTURE AND BONDING

Method (Acronym)	Experimental basis	Information obtainable	References (end of table)
Auger electron spectroscopy (AES)	Sample under vacuum irradiated with photons causing ejection of electrons from core orbitals. Energies and intensities of Auger electrons that are ejected by a process of internal conversion are then measured in the spectrometer	Binding energies of core and valence electrons (and chemical compositions of surface layers)	Chang (1974); see Section 2.2.1
Angle-resolved photoelectron spectroscopy (ARPES)	Study of the various types of photoelectron spectra as a function of angle (see XPS, UPS)		
Bremsstrahlung isochromat spectroscopy (BIS)	The sample is exposed to an electron beam of known energy. The electrons undergo transitions to empty states in the conduction band, emitting a photon (also known as inverse photoelectron spectroscopy, IPES)	Details of the energies of empty (conduction-band) energy levels	
Brillouin scattering	The scattering of light by acoustic modes (see Section 2.4.1) on interaction with crystals is called Brillouin scattering. From measuring the change in frequency of the light scattered in particular directions, the velocities of the acoustic modes and hence the elastic constants can be determined. The experiment involves a laser light source and a spectrometer to analyze the scattered light	Used to determine the elastic constants of crystals (that may be subject to different *T*, *P*, etc.)	Cardona and Güntherodt (1989)

Coherent anti-stokes Raman spectroscopy (CARS)	A form of Raman Spectroscopy giving very intense spectra with intensity patterns and selection rules different from those of the conventional (see Raman spectroscopy)		
Compton scattering	The Compton effect is the inelastic scattering of a photon by an electron. When radiation is Compton scattered, the emerging beam is Doppler broadened because of the motion of the target electrons. Analysis of this broadened line shape, the Compton profile, provides detailed information about the electron momentum distribution in the scatterer	Used to test the quantum-mechanical description of the electrons involved in bonding in solids (the effect being particularly sensitive to the slower-moving outer electrons).	Cooper (1985)
Conversion electron Mössbauer spectroscopy (CEMS)	Electrons emitted as a byproduct of the Mössbauer effect (see later in table) are detected	Shallow escape depth of electron provides information on the nature (oxidation state, spin state, coordination, etc.) of the Mössbauer-active isotope in the surface layer	Tricker (1981), Berry (1985); see Section 2.5.3
Cathodoluminescence spectroscopy (CL)	See Luminescence spectroscopy		
Correlation spectroscopy (COSY)	A two-dimensional NMR technique (see NMR spectroscopy)		
Cross-polarization magic-angle-spinning NMR spectroscopy (CP-MAS)	A method for narrowing lines in NMR spectra and obtaining data for nuclei of low natural abundance (see NMR spectroscopy)		
Delays alternating with nutations for tailored excitation (DANTE)	An approach used in NMR spectroscopy to obtain resonances due to one set of chemically equivalent nuclei (see NMR spectroscopy)		

Method (Acronym)	Experimental basis	Information obtainable	References (end of table)
Diffuse reflectance spectroscopy (DRS)	Absorption of "light" energy in the near-ir–visible–near-uv region by a finely powdered sample is measured from light reflected back off a powder surface	Approximate variation of the absorption coefficient (k) with wavelength. Information on absorption edge and energies of electron transitions (*d-d*, charge transfer, etc.)	Wendlandt and Hecht (1966); see Section 2.3.2
e,2*e* spectroscopy	High-energy electron-impact ionization with complete determination of the collision kinematics	Information about character of molecular orbitals and electron distributions	Moore et al. (1982)
Electron diffraction	Monochromatic beam of electrons diffracted on passing through thin and very small fragment of crystalline material (in an electron microscope). Angles and intensities of diffracted beam record photographically	Information on symmetry and (approximate) crystal structure of material	Andrews et al. (1971); see Section 2.1.3
Electron-energy-loss spectroscopy (EELS or ELS)	A highly monochromated beam of low-energy (1–10 eV) electrons is reflected from a solid surface, and the energy of the scattered electrons is analyzed. Some of the incident electrons can lose a discrete amount of energy upon reflection associated with excitation of a vibration at the surface	A very sensitive method of surface analysis (detection to $\sim$0.1% of a monolayer over area of $\sim$1 mm^2) and the study of molecular interactions on solid surfaces	Weinberg (1985), Egerton (1986)
Electron microscopy	Monochromatic electrons focused to a very fine beam that interacts with sample to produce electron diffraction (see above) or images of various kinds and degrees of resolution	In addition to information on crystal symmetry and structure, inhomogeneities, defects, and variations in fine structure of materials can be studied at resolutions down to the level of unit cells, or even individual atoms	Zussman (1977); see Section 2.1.3

Electron–electron double resonance (ELDOR)	An ESR double-resonance experiment enabling hyperfine splittings to be measured in complex spectra (see ESR spectroscopy)		
Electron–nuclear double resonance (ENDOR)	A form of ESR experiment involving observation of the spectrum while irradiating nuclear spin transitions (see ESR spectroscopy)		
Electron transmission spectroscopy (ETS)	Involves measuring the transparency of a gas to an electron beam as a function of energy	Measures gas-phase electron affinities corresponding to electron capture into low-lying unoccupied molecular orbitals (i.e., the energy of the anion state arising from electron capture)	Giordan et al. (1986)
Electron paramagnetic resonance	See Electron spin resonance (ESR)		
Electron spectroscopy for chemical analysis (ESCA)	A term used to cover photoelectron spectroscopy (PES); both x-ray photoelectron spectroscopy (XPS) and ultraviolet photoelectron spectroscopy (UPS); see individual entries for XPS and UPS		
Electron spin resonance (ESR)	Absorption of microwave radiation in the presence of an external magnetic field by molecules, atoms, or ions possessing electrons with unpaired spins. The energy of this absorption is measured, and any fine structure associated with it is studied	Fingerprint identification of species such as paramagnetic impurities in diamagnetic materials. Information on stereochemistry and bonding of such species	Atherton (1973), McWhinnie (1985); see Section 2.6.1
Electronic absorption spectroscopy	Absorption of "light" energy in the near-ir–visible–near-uv region on transmission through a liquid or "translucent" solid phase (including single crystals) is measured as a function of wavelength. Polarized light may be used when studying single crystals	Energies of electronic transitions involving valence electrons and including crystal field (*d*-*d*) transitions and color centers. Information on oxidation state, spin state, stereochemistry—particularly of transition-metal ions	Lever (1968), Burns (1970, 1985); see Section 2.3.1

Method (Acronym)	Experimental basis	Information obtainable	References (end of table)
Extended x-ray absorption fine structure (EXAFS)	Absorption of intense x radiation, usually from a synchrotron source, usually measured by intensity of transmission of a single beam as a function of energy (wavelength)	Nature of the local structure surrounding a particular atom in a solid	Teo and Joy (1981); Lee et al. (1981); Calas et al. (1984); see Section 2.2.3
Fourier-transform infrared (FTIR)	A rapid and efficient method of collecting high-quality infrared spectra (see Infrared spectroscopy)		
Inverse photoelectron spectroscopy (IPES)	The same as Bremsstrahlung isochromat spectroscopy (see BIS)		
Infrared spectroscopy (ir)	Infrared light is allowed to pass through a sample (gas, liquid, powdered solid, or single crystal), and the absorption of energy is measured as a function of wavelength. Reflection of infrared light may also be studied (from a powder or polished crystal surface) as a function of wavelength	Infrared light is absorbed through vibrations of the atoms or rotations of the molecular system. IR spectra give information on lattice dynamics, bond strengths, coordination, and polyhedral linkage in complex structures.	McMillan (1985); see Section 2.4.2
Internal reflection spectroscopy (IRS)	Light is introduced into an optically transparent solid medium at angles above the critical angle, and the intensity of the emerging radiation measured after it has suffered one, or often hundreds, of internal reflections	Used to study adsorbed molecules or thin films on the surfaces of solid materials, materials of lower refractive index outside the surface, or to study the surface itself (surface states)	Harrick and Beckmann (1974)
Ion microprobe (ion probe)	See Secondary ion mass spectrometry		

Ion neutralization spectroscopy (INS)	A solid surface is bombarded by low-energy ions that undergo Auger neutralization, ejecting Auger electrons from the surface; these electrons are energy analyzed	Data obtained are used to infer the density of states of valence electrons of surface atoms	Hagstrum (1972)
Ion scattering spectroscopy (ISS)	Ions of noble gases (He^+, Ar^+) accelerated to energies of 500 eV–3 keV are impacted (at 45° to the normal to the surface). Ions reflected at 90° are energy analyzed	Surface chemical analysis	Smith (1967)
Luminescence spectroscopy	Luminescence is the *emission* of light from a sample brought about by excitation in a number of ways: using electrons (cathodoluminescence) or protons (see PEOL), using uv or visible light (photoluminescence) or by heating (thermoluminescence). The variation of intensity of emission with wavelength is measured in each case to give a luminescence spectrum	Luminescence in minerals and related solids generally arises from impurity centers or defect centers. Luminescence spectroscopy enables impurities and defects to be identified and their coordination and electronic configuration pinpointed	Walker (1985)
Low-energy electron diffraction (LEED)	Electrons of uniform energy (~5–500 eV) are scattered from the surface of a single crystal. Those electrons that have lost no energy are selected and accelerated to a fluorescent screen where the diffraction pattern from the surface can be observed	Provides accurate information on the crystal structure of the surface layer of a solid single crystal (bond lengths and angles)	Lagally (1985)
Magic-angle spinning nuclear magnetic resonance (MAS-NMR)	See Nuclear magnetic resonance (NMR)		
Mössbauer spectroscopy	Resonant absorption of γ-rays from an appropriate source by a specific nucleus, the source γ-ray energy being modulated by making use of the Doppler effect	Determination of the oxidation state, spin state, coordination, and degree of covalence of bond of the atom with the Mössbauer-active nucleus (most commonly Fe, Sn, Sb, Te in mineralogical work)	Bancroft (1973), Maddock (1985); see Section 2.5.3

Method (Acronym)	Experimental basis	Information obtainable	References (end of table)
Neutron diffraction	Monochromatic beam of neutrons is diffracted by a crystal (or powdered crystalline material). Angles and intensities of diffracted beam recorded by a detector	Neutron beams have wavelengths ~1–3 Å and interact with nuclei in crystals rather than electrons; hence they suffer scattering by atoms with magnetic moments enabling magnetic structure of solids to be studied. Also can be used to determine structural positions of light elements or distinguish between atoms of neighboring atomic number in a structure (indistinguishable using x-rays)	Bacon (1962); see Section 2.1.2
Nuclear magnetic resonance (NMR)	Sample is placed in an external magnetic field. Resonant absorption of radio energy by transitions of nuclei of certain isotopes from ground to various excited states is studied. Applied to liquids, and more recently to solids, where rapid spinning of the sample inclined at an angle of 54.7° to the applied magnetic field (the "magic angle") greatly enhances resolution	Determination of local environment of particular atoms in a molecule or crystal structure (e.g., in mineralogical work, studies of the nuclei ^{29}Si, ^{27}Al are important in studying ordering in complex silicates)	Mehring (1983), McWhinnie (1985); see Section 2.5.2
Nuclear magnetic double resonance spectroscopy (NMDR)	An NMR spectrum obtained by irradiating with two radio frequencies, valuable in simplifying complex spectra (see NMR spectroscopy)		
Nuclear Overhauser spectroscopy (NOESY)	A two-dimensional NMR technique (see NMR spectroscopy)		

Nuclear quadrupole resonance (NQR)	Dependent on the interaction between the quadrupole moment of the nucleus and the electric-field gradients at the nucleus arising from the charge distribution in a *solid*. Resonant absorption of radio-frequency energy occurs when nuclei are excited to various higher-energy states related to these interactions. It is this resonant absorption that is studied	Determination of local environment of particular atoms in a solid. Applicable to ~130 isotopes (e.g., in mineralogy, studies of ^{27}Al applied to order–disorder phenomena; studies of As, Sb, and Bi isotopes in sulfosalts applied to structural investigations)	Marfunin (1979); see Section 2.5.1
Photoelectron spectroscopy (PES)	See X-ray photoelectron spectroscopy (XPS), uv photoelectron spectroscopy (UPS)		
Proton excited optical luminescence spectroscopy (PEOL)	Luminescence spectroscopy where the source of excitation is a beam of protons (see Luminescence spectroscopy)		
Proton-induced x-ray emission (PIXE)	A solid sample is bombarded with a beam of energetic protons, causing the emission of x-rays, characteristic of the elements present. May employ a microbeam (hence MICROPIXE)	Used chiefly for elemental analysis and microanalysis of solids (including analysis of trace elements)	Khan and Crumpton (1981)
Raman spectroscopy	Monochromatic light (in the visible or uv range) is directed through the sample (gas, liquid, crystal, or powder), which must be translucent. Light scattered at 90° or 180° is collected, analyzed, and recorded. The incident light commonly used in modern instruments is from a laser source and may be polarized. The Raman effect involves shifts of frequency of scattered light relative to that from the source	The energy changes observed in the Raman effect have to do with vibrations and rotations of the molecule under study or vibrations of the crystal lattice. Raman spectra can be used to identify particular molecules, or polyhedra in solids or polyhedral linkages (e.g., particular silicon–oxygen units in silicate glasses)	McMillan (1985); see Section 2.4.3
Reflectance spectroscopy	See Diffuse reflectance, Specular reflectance		

Method (Acronym)	Experimental basis	Information obtainable	References (end of table)
Reflection extended x-ray absorption fine-structure spectroscopy (ReflEXAFS)	The EXAFS technique but using radiation reflected at a low angle from the surface and hence giving data for the surface atomic layers (see EXAFS)	Provides accurate information on the crystal structure of the surface layer of a single crystal	Lagally (1985)
Reflection high-energy electron diffraction (RHEED)	The diffraction of electrons with high energies (30–70 keV) incident at very low angles (0.5°–4°) to a crystal surface such that they are reflected from it		
Raman-induced Kerr-effect spectroscopy (RIKES)	A two-color Raman experiment in which rotation of the plane of polarization of one beam is monitored as the frequency of the other beam is altered. Gives Raman data with enhanced sensitivity (see Raman spectroscopy)		
Resonance Raman spectroscopy (RRS)	Raman spectroscopy using an irradiation frequency that is absorbed by the sample and hence an enhanced signal (see Raman spectroscopy)		
Scanning electron microscopy (SEM)	A very finely focused beam of electrons rapidly scans across the surface of a solid sample to generate a "photographic" image of surface topography at very high magnification. System may be combined with facility for semiquantitative microanalysis of material at the surface	High-resolution, very high-magnification image of surface topography of a sample (with chemical analysis of areas of the surfaces). A very useful general technique for surface studies of solids	Nicol (1975)

Scanning Tunneling microscopy (STM)	A solid sample surface (under vacuum) is scanned by an ultrafine stylus tip with a very small voltage applied across the gap, which is just a few angstrom units wide. Vacuum tunneling of electrons occurs across the gap, and this effect is very sensitive to the width of the gap, providing a means of mapping the surface at a horizontal resolution of Å	Arrangements of atoms on the surface of a crystal can be determined. Surface species and the nature of bonding of these can be studied by examining voltage–current variations during scanning	Hansma and Tersoff (1987)
Secondary-ion mass spectrometry (SIMS)	A beam of primary ions with an energy in the range 5–20 keV bombards a small spot on the surface of a solid sample and positive and negative ions sputtered from the surface are analyzed in a mass spectrometer	Surface chemical and isotopic analysis of very small areas; depth profile analysis	McCrea (1974)
Soft-x-ray appearance potential spectroscopy (SXAPS)	A solid surface is bombarded with monochromatic electrons, and small but abrupt changes in the resulting total x-ray emission intensity are detected as the energy of the electrons is varied	Identification of elements present in the surface region; relatively simple technique but one that is relatively insensitive to many elements	Houston and Park (1972)
Specular reflectance spectroscopy	Light (uv–visible–near-ir radiation) reflected back from a flat, highly polished surface of a solid measured in intensity as a function of varying wavelength. Measurements can be made using plane-polarized light, at normal incidence, and on oriented faces of single crystals	Manipulation of the raw data can provide accurate information on variation of optical constants (in particularly, *k*, the absorption coefficient) with wavelength. This yields information on the band edge and on the electronic structure of solids (particularly metals and semiconductors) in the valence region	Wendlandt and Hecht (1966); see Section 2.3.2
Surface extended x-ray-absorption fine structure (SEXAFS)	EXAFS applied to surfaces (see EXAFS, ReflEXAFS)		

Method (Acronym)	Experimental basis	Information obtainable	References (end of table)
Surface-enhanced Raman spectroscopy (SERS)	Raman spectroscopy of adsorbed species on surfaces (see Raman spectroscopy)		
Ultraviolet (uv) photoelectron spectroscopy (UPS)	A solid sample under vacuum is irradiated with a monochromatic beam of ultraviolet light (typically 21.22 eV). Less tightly bound electrons in orbitals in the valence region are ejected. The kinetic energies of these ejected electrons are analyzed in an energy spectrometer and, after correction for the energy of the incident radiation and for instrumental effects, give the binding energies of the valence electrons in the solid	An ultraviolet photoelectron spectrum is a plot of electron binding energies versus intensity. It provides detailed information on the electronic structures of a solid in the valence region	Turner et al. (1970); see Section 2.2.1
Ultraviolet (–visible) spectroscopy	See Electron absorption spectroscopy, specular reflectance spectroscopy, diffuse reflectance spectroscopy		
X-ray-absorption near-edge structure (XANES)	Absorption of intense x-radiation from a synchrotron source interacting with a sample is studied, usually by measuring transmission intensity. Specifically, the variations in absorption around and above the absorption edge that display complex fine structure in a molecular or condensed phase are studied	Detailed information on the electronic structure in the valence region, electronic configuration, energetics of virtual orbitals, etc.	Calas et al. (1984); see Section 2.2.3
X-ray-absorption spectroscopy (XAS)	Can be undertaken (as formerly) by measuring the intensity of absorption of x-rays by a sample placed between a detector and standard x-ray source; now largely superseded by the techniques of Extended x-ray-absorption fine structure (EXAFS) and X-ray-absorption near-edge structure (XANES). See entries for these		

X-ray emission spectroscopy (XES)	Bombardment of a solid sample (under vacuum) by a beam of x-rays or of electrons causes ejection of electrons from core orbitals. X-rays emitted from the sample when higher-energy electrons relax to fill core vacancies are detected and a spectrum recorded of their energies and intensities	Determination of the relative energies of electrons in various core- and valence-region orbitals. Transitions are subject to selection rules; so that contributions of various "atomic orbitals" to "molecular orbitals" in the valence region can be assessed	Agarwal (1979), Urch (1985); see Section 2.2.2
X-ray diffraction (XRD)	A monochromatic beam of x-rays is diffracted by a single crystal (or powdered crystalline material). Angles and intensities of the diffracted beam are recorded photographically or by a detector	Information on the crystal symmetry and structure; detailed determination of crystal structures, detailed three-dimensional information on the distribution of electron density in a crystalline material	Stout and Jensen (1966), Nuffield (1966); see Section 2.1.1
X-ray photoelectron spectroscopy (XPS)	A solid sample (under vacuum) is irradiated with a monochromatic beam of x-rays. Electrons in core- and valence-region orbitals are ejected. The kinetic energies of these ejected electrons are analyzed in an energy spectrometer and, after correction for the energy of the incident radiation and for instrumental effects, give the binding energies of core and valence electrons in the solid	An x-ray photoelectron spectrum is a plot of electron binding energies versus intensity. It provides detailed information on the electronic structure of a solid in the core and valence regions	Brundle and Baker (1979), Urch (1985); see Section 2.2.1

Agarwal, B.K. (1979). *X-ray Spectroscopy*. Berlin: Springer–Verlag.

Andrews, K.W., D.J. Dyson, and S.R. Keown (1971). *Interpretation of Electron Diffraction Patterns* (2nd ed.). London: Hilger.

Atherton, N.M. (1973). *Electron Spin Resonance*. London: Halsted Press.

Bacon, G.E. (1962). *Neutron Diffraction* (2nd ed.). Oxford: Oxford Univ. Press.

Bancroft, G.M. (1973). *Mössbauer Spectroscopy*. New York: McGraw Hill.

Berry, F.J. (1985). In: *Chemical Bonding and Spectroscopy in Mineral Chemistry* (F.J. Berry and D.J. Vaughan, eds.). London: Chapman and Hall.

Brundle, C.R., and A.D. Baker (1979). *Electron Spectroscopy: Theory, Techniques, and Applications*. New York: Academic Press.

Burns, R.G. (1970). *Mineralogical Applications of Crystal Field Theory*. Cambridge: Cambridge Univ. Press.

Burns, R.G. (1985). In: *Chemical Bonding and Spectroscopy in Mineral Chemistry* (F.J. Berry and D.J. Vaughan, eds.) London: Chapman and Hall.

Calas, G., W.A. Bassett, J. Petiau, M. Steinberg, D. Tchoubar, and A. Zarka (1984). *Phys. Chem. Mineral.* **11,** 17–36.

Cardona, M., and G. Güntherodt (1989). *Light Scattering in Solids V.* Berlin: Springer–Verlag.

Chang, C.C. (1974). In: *Characterization of Solid Surfaces* (P.F. Kane and G.R. Larrabee, eds.). New York: Plenum Press.

Cooper, M.J. (1985). Compton scattering and electron momentum determination. *Rep. Prog. Phys.* **48,** 415–81.

Egerton, R.F. (1986). *Electron Energy Loss Spectroscopy in the Electron Microscope.* New York: Plenum Press.

Hagstrum, H.D. (1972). *Science* **178,** 275–82.

Hansma, P.K., and J. Tersoff (1987). *J. Appl. Phys.* **61,** R1–R23.

Harrick, N.J., and K.H. Beckmann (1974). In: *Characterization of Solid Surfaces* (P.F. Kane and G.R. Larrabee, eds.). New York: Plenum Press.

Houston, J.E., and R.L. Park (1972). *Solid State Commun.* **10,** 91–94.

Jordan, K.D., and P.D. Burrow (1978). *Acc. Chem. Res.* **11,** 341.

Khan, M.R., and D. Crumpton (1981). *CRC Critical Reviews in Analytical Chemistry* **11,** 103 and 161.

Lagally, M.G. (1985). In: *Methods of Experimental Physics,* Vol. 22, *Solid State Physics: Surfaces* (R.L. Park and M.G. Lagally, eds.). Orlando: Academic Press.

Lee, P.A., P.H. Citrin, P. Eisenberger, and B.M. Kincaid (1981). *Rev. Mod. Phys.* **53,** 769–806.

Lever, A.B.P. (1968). *Inorganic Electronic Spectroscopy*. Amsterdam: Elsevier.

Maddock, A.G. (1985). In: *Chemical Bonding and Spectroscopy in Mineral Chemistry* (F.J. Berry and D.J. Vaughan, eds.). London: Chapman and Hall.

Marfunin, A.S. (1979). *Spectroscopy, Luminescence and Radiation Centers in Minerals*. New York: Springer–Verlag.

McCrea, J.M. (1974). In: *Characterization of Solid Surfaces* (P.F. Kane and G. Larrabee, eds.). New York: Plenum Press.

McMillan, P. (1985). In: *Microscopic to Macroscopic, Reviews in Mineralogy,* Vol. 14. Washington: Mineralogical Soc. of America.

McWhinnie, W.R. (1985). In: *Chemical Bonding and Spectroscopy in Mineral Chemistry* (F.J. Berry and D.J. Vaughan, eds.). London: Chapman and Hall.

Mehring, M. (1983). *Principles of High Resolution NMR in Solids*. New York: Springer–Verlag.

Moore, J.H., J.A. Tossell, and M.A. Coplan (1982). *Acc. Chem. Res.* **15,** 1982, 192–98.

Nicol, A.W. (ed.) (1975). *Physicochemical Methods of Mineral Analysis*. New York: Plenum.

Nuffield, E.W. (1966). *X-ray Diffraction Methods*. New York: Wiley.

Smith, D.P. (1967). *J. Appl. Phys.* **38,** 340–47.

Stout, G.H., and L.H. Jensen (1968). *X-ray Structure Determination*. New York: MacMillan.

Teo, B.K., and D.C. Joy (1981). *EXAFS Spectroscopy.* New York: Plenum Press.

Tricker, M.J. (1981). In: *Mössbauer Spectroscopy and its Chemical Applications* (J.G. Stevens and G.K. Shenoy, eds.). Adv. in Chemistry Series, Washington: Amer. Chem. Soc.

Turner, D.W., C. Baker, A.D. Baker, and C.R. Brundle (1970). *Molecular Photoelectron Spectroscopy.* New York: Wiley–Interscience.

Urch, D.S. (1985). In: *Chemical Bonding and Spectroscopy in Mineral Chemistry* (F.J. Berry and D.J. Vaughan, eds.). London: Chapman and Hall.

Walker, G. (1985). *Ibid.*

Weinberg, W.H. (1985). In: *Methods of Experimental Physics* (Vol. 22) *Solid State Physics: Surfaces* (R.L. Park and M.G. Lagally, eds.). Orlando: Academic Press.

Wendlandt, W.W., and H.G. Hecht (1966). *Reflectance Spectroscopy.* New York: Wiley–Interscience.

Zussman, J. (ed.) (1977). *Physical Methods in Determinative Mineralogy.* New York: Academic Press.

APPENDIX C

QUANTUM-MECHANICAL (AND RELATED) CALCULATIONAL METHODS AND TERMINOLOGY

Method (acronym)	**Brief description**	**Reference (main reference list)**
Ab initio (or *ab initio* SCF)	A general term used to refer to calculations "from first principles," often describing Hartree–Fock calculations with no integral approximations and with self-consistent charge distributions	Hehre et al. (1986); see Section 3.2
Ab initio pseudopotential	Band-theoretical method replacing core electrons by pseudopotentials, using density-functional electron exchange and correlation, a plane-wave basis, and a self-consistent charge distribution	Cohen (1984); see Section 3.11
AM1	Latest version of parametrized MNDO-level approximate SCF method (see MNDO)	Dewar et al. (1985)
Angular overlap model (AOM)	An approximate (non-SCF) molecular-orbital method involving extensive parametrization of the required integrals and with the overlap integral represented as a simple product of radial and angular terms	Burdett (1980)
Augmented plane wave (APW)	A band-theoretical method employing density-functional theory, a composite basis set, and a "muffin-tin" potential	Moruzzi et al. (1977); see Section 3.11
Band theory	A general term used to describe a calculation in which the potential and the wave function have translational symmetry and the entire periodic solid is considered	Ashcroft and Mermin (1976)
Basis set	The set of mathematical functions used to expand the molecular orbitals in a Hartree–Fock–Roothaan calculation	See Section 3.2
Configuration interaction (CI)	A high-level calculation based on Hartree–Fock theory in which the HF determinants are mixed so as to describe the dynamic correlation of electrons	Szabo and Ostlund (1989); see Section 3.3

Complete neglect of differential overlap (CNDO)	An approximate or semiempirical Hartree–Fock molecular-orbital method, utilizing approximate electron repulsion integrals and some Hamiltonian matrix elements to solve approximate HF equations and iterate to self-consistency	Pople and Beveridge (1970); see Section 3.7
"ΔSCF" (delta self-consistent field)	Calculation of ionization potentials as differences of total energies of neutral molecules and cations	See Section 3.5
Density-functional theory (DF)	Evaluation of total energy by focusing on the total electron density. Typically the exchange and correlation energy is expressed as a reasonably simple function of the electron density	von Barth (1986), Srivastava and Weaire (1987); see Section 3.9
Discrete variational (DV or DV-$X\alpha$)	A density-functional method for molecular systems with Slater orbital bases and no (or little) potential averaging	Baerends et al. (1973); see Section 3.9
Extended Hückel (molecular-orbital) theory (EHMO or EHT)	An approximate Hartree–Fock molecular-orbital method involving extensive parametrization (all Hamiltonian matrix elements parametrized to fit experimental data)	Hoffman and Lipscomb (1962): see Section 3.7
Empirical (or approximate) methods	Methods that approximate quantum-mechanical integrals and/or incorporate experimental data to simplify computation and improve agreement with experiment	
Full-potential linearized augmented plane wave (FLAPW)	An APW method in which the energy dependence of the basis functions is linearized and no potential averaging is used	Jansen and Freeman (1984); see Section 3.11
Hartree–Fock (theory) (HF) (restricted HF, RHF for closed shells; unrestricted HF, UHF for open shells)	A method in which a many-electron wave function is written as an antisymmetric product of one-electron orbitals. The instantaneous electron–electron repulsion is replaced by interaction with the time-averaged densities of the other electrons	Levine (1983); see Sections 3.1, 3.2
Hartree–Fock–Roothaan (theory) (HFR)	HF theory with expansion of the MOs in a finite basis set. The equation to be solved is now a matrix equation for the expansion coefficients	See Section 3.2
Intermediate neglect of differential overlap (INDO)	An approximate or semiempirical Hartree–Fock molecular-orbital method in which electron repulsion integrals and some Hamiltonian matrix elements are approximated and the approximate Hartree–Fock equations solved and integrated to self-consistency	Pople and Beveridge (1970); see Section 3.7

Method (acronym)	Brief description	Reference (main reference list)
Korringa–Kohn–Rostoker (KKR) method	A band-theoretical method employing density-functional theory, a composite basis set, and a "muffin-tin" potential	See Section 3.11
Linear band structure	Methods in which the energy dependence of atomic basis functions is approximated through linearization	Andersen (1975)
Linear combination of atomic orbitals (LCAO)	A term used to refer to a Hartree–Fock–Roothaan calculation, often applied to calculations with small bases	
LCAO-$X\alpha$	A density-functional molecular calculation with an analytic nuclear-centered basis set (typically Gaussian)	Sambe and Felton (1975); see Section 3.9
Local-density approximation (LDA)	DF schemes in which the exchange and correlation potential is a function of the local electron density (or spin density)	von Barth (1986); see Section 3.9
Local Density Functional (LDF)	Similar to LDA	
Linear muffin-tin orbital (LMTO)	Density-functional band calculation with "muffin-tin" orbitals as basis with their energy dependence linearized	Skriver (1984); see Section 3.9
Many-body perturbation theory (MBPT)	A method for incorporating correlation using perturbation theory with the difference of HF and exact electron repulsion as the perturbation	Szabo and Ostlund (1989), Cederbaum et al. (1980); see Section 3.3
Modified electron gas (MEG)	A method using model non-self-consistent charge densities and exchange and correlation energies from a free-electron-gas density functional	Gordon and Kim (1972); see Section 3.12
Modified neglect of differential overlap (MNDO)	An approximate or semiempirical Hartree–Fock molecular-orbital method in which some of the Hamiltonian matrix elements are parametrized to give agreement with experiment	Dewar et al. (1985) for newest version; see Section 3.7

Molecular-orbital theory (MO theory)	Any method representing the many-electron wave function for a molecule as an antisymmetrized product of one-electron orbitals	
Minimum basis set (MBS)	Hartree–Fock–Roothaan calculation in which each occupied atomic orbital of an atom is represented by one mathematical function with variable coefficient in the molecular orbitals	
Multiple-scattering self-consistent-field $X\alpha$ (MS-SCF-$X\alpha$)	A density-functional molecular method with Slater's local exchange approximation, "muffin-tin" averaging of the potential, and a composite basis	Johnson (1975); see Section 3.10
Perturbation theory	A general method for obtaining approximate solutions to a difficult problem based on the exact solutions of a simpler one	Levine (1983); see Section 3.3
Pseudopotential (PP)	Replacement of the orthogonality relation of core and valence electrons by an effective potential applied to the valence shell	See Section 3.11
Potential-Induced breathing (PIB)	A modification of the modified electron-gas method that incorporates the effect on the environment (described by an array of point charges) on the properties of the anion	Mehl et al. (1986); see Section 3.12
Self-consistent field (SCF)	Any method in which the electron density is evaluated by an iterative process	
Scattered-wave (SW) method	Same as multiple-scattering SCF-$X\alpha$ method	
Tight-binding method	Band-theoretical method using a LCAO expansion of the delocalized Bloch orbital (often with integral approximations)	Bullett (1980); see Section 3.11
Valence-shell electron-pair repulsion (VSEPR) model	A simple model based on the idea that the most favorable packing of pairs of electrons in the valence shell of a central atom dictates the bond angles and relative bond lengths in molecules. Generally expressed in the form of a set of rules	Gillespie (1972), Burdett (1980)
$X\alpha$	Density-functional scheme employing Slater's local-density functional for exchange and correlation	

REFERENCES

Abragam, A., and B. Bleaney (1970). *Electron Paramagnetic Resonance of Transition Metal Ions*. Oxford: Oxford Univ. Press.

Abraham, R., and G. H. Grant (1988). A molecular mechanics study of the Si–O bond and alkyl silanes. *J. Comp. Chem.* **9**, 709–18.

Adams, I., J. M. Thomas, and G. M. Bancroft (1972). An ESCA study of silicate minerals. *Earth Plan. Sci. Lett.* **16**, 429–32.

Adams, W. H. (1962). Orbital theories of electronic structure. *J. Chem. Phys.* **37**, 2009–18.

Ahrens, L. H. (1952). The use of ionization potentials. Part 1. Ionic radii of the elements. *Geochim. Cosmochim. Acta* **2**, 155–69.

Ahrens, L. H. (1953). The use of ionization potentials. Part 2. Anion affinity and geochemistry. *Geochim. Cosmochim. Acta* **3**, 1–29.

Ahrens, L. H. (1965). *Distribution of the Elements in Our Planet*. New York: McGraw-Hill.

Aida, M., and G. Nagata (1986). An *ab initio* MO study on the disulfide bond: properties concerning the characteristic S–S dihedral angle. *Theor. Chim. Acta* **70**, 73–80.

Akaogi, M., N. L. Ross, P. McMillan, and A. Navrotsky (1984). The Mg_2SiO_4 polymorphs (olivine, modified spinel, spinel)—thermodynamic properties from oxide melt solution calorimetry, phase relations, and models of lattice vibrations. *Amer. Mineral.* **69**, 499–512.

Akimoto, S., and M. H. Manghnani (1982) (Eds.) *High Pressure Research in Geophysics*. Boston: D. Reidel Publ. Co.

Alberti, A., and G. Vezzalini (1978). Madelung energies and cation distributions in olivine-type structures. *Zeit. Krist.* **147**, 167–75.

Albright, T. A., J. K. Burdett, and M. H. Whangbo (1985). *Orbital Interactions in Chemistry*. New York: Wiley.

Al-Kadier, M. A., C. Tolon, and D. S. Urch (1984). Photoelectron and x-ray spectroscopy of minerals. Part 1. Electronic structure of forsterite (magnesium orthosilicate). *J. Chem. Soc., Far. Trans.* 2, **80**, 669–79.

Allan, D. A., and M. P. Teter (1987). Nonlocal pseudopotentials in molecular-dynamical density-functional theory: application to SiO_2. *Phys. Rev. Lett.* **59**, 1136–39.

Allen, L. C. (1972). The shape of molecules. *Theor. Chim. Acta* **24**, 117–31.

Allinger, N. L. (1976). Calculation of molecular structure and energy by force-field methods. *Adv. Phys. Org. Chem.* **13**, 1–82.

Allred, A. L. (1961). Electronegativity values from thermochemical data. *J. Inorg. Nucl. Chem.* **17**, 215–21.

Almlof, J., K. Faegri, Jr., B. E. R. Schilling, and H. P. Luthi (1984). An investigation of correlation effects in transition-metal sandwich complexes. Hartree–Fock studies on a series of metallocenes. *Chem. Phys. Lett.* **106**, 266–70.

Almlof, J., and P. R. Taylor (1987). General contraction of Gaussian basis sets. I. Atomic natural orbitals for first- and second-row atoms. *J. Chem. Phys.* **86**, 4070–77.

Amini, M., S. Mitra, and R. W. Hockney (1981). Molecular dynamics study of boron trioxide. *Phys. C* **14**, 3689–700.

Amos, R. A. (1986). Structures, harmonic frequencies and infrared intensities of the dimers of H_2O and H_2S. *Chem. Phys.* **104**, 145–51.

Amthauer, G., and G. Rossman (1984). Mixed valence of iron in minerals with cation clusters. *Phys. Chem. Min.* **11**, 37–51.

Andersen, O. K. (1975). Linear methods in band theory. *Phys. Rev.* **B12**, 3060–83.

Anderson, G. M., and C. W. Burnham (1983). Feldspar solubility and the transport of aluminium under metamorphic conditions. *Amer. J. Sci.* **283A**, 283–97.

Anderson, J. S., and J. S. Ogden (1969). Matrix isolation studies of group IV oxides. I. Infrared spectra and structures of SiO, Si_2O_2, and Si_3O_3. *J. Chem. Phys.* **51**, 4189–96.

Anderson, O. L. (1986). Properties of iron at the Earth's core conditions. *Geophys. J.R. Astron. Soc.* **84**, 561–79.

Andrews, K. W., D. J. Dyson, and S. R. Keown (1971). *Interpretation of Electron Diffraction Patterns* (2nd ed.). Hilger.

Angell, C. A., and D. M. Gruen (1967). Octahedral and tetrahedral coordination states of cobalt (II) in molten zinc chloride–aluminum chloride mixtures. *J. Inorg. Nucl. Chem.* **29**, 2243–47.

Arndt, U. W., and B. T. M. Willis (1966). *Single Crystal Diffractometry*. Cambridge: Cambridge Univ. Press.

Ashcroft, N. W., and N. D. Mermin (1976). *Solid State Physics*. New York: Holt, Rinehart and Winston.

Atherton, N. M. (1973). *Electron Spin Resonance*. London: Halstead Press.

Bacon, G. E. (1962). *Neutron Diffraction* (2nd ed.) Oxford: Oxford Univ. Press.

Bader, R. F. W. (1964). Binding regions in polyatomic molecules and electron density distributions. *J. Amer. Chem. Soc.* **86**, 5070.

Bader, R. F. W. (1985). Atoms in molecules. *Acc. Chem. Res.* **18**, 9–15.

Bader, R. F. W., R. J. Gillespie, and P. J. MacDougall (1988). A physical basis for the VSEPR model of molecular geometry. *J. Amer. Chem. Soc.* **110**, 7329–36.

Bader, R. F. W., and T. T. Nguyen-Dang (1981). Quantum theory of atoms in molecules—Dalton revisited. *Adv. Quantum Chem.* **14**, 63–124.

Bader, R. F. W., T. T. Nguyen-Dang, and Y. Tal (1979). Quantum topology of molecular charge distributions. II. Molecular structure and its change. *J. Chem. Phys.* **70**, 4316–29.

Baerends, E. J., D. E. Ellis, and P. Ross (1973). Self-consistent molecular Hartree–Fock–Slater calculations. I. The computational procedure. *Chem. Phys.* **2**, 41–51.

Baes, C. F., Jr., and R. E. Mesmer (1981). The thermodynamics of cation hydrolysis. *Amer. J. Sci.* **281**, 935–62.

Bagawan, A. O., R. Muller-Fiedler, C. E. Brion, E. R. Davidson, and C. Boyle (1988). The valence orbitals of NH_3 by electron momentum spectroscopy: quantitative comparisons using Hartree–Fock limit and correlated wavefunctions. *Chem. Phys.* **120**, 335–57.

Balzarotti, A., F. Antonangeli, R. Girlanda, and G. Martino (1984). Electronic energy levels of αAl_2O_3 from *L*-edge photoabsorption of aluminum and small-cluster CNDO calculation. *Phys. Rev.* **B29**, 5903–8.

Balzarotti, A., and A. Bianconi (1976). Electronic structure of aluminum oxide as determined by x-ray photoemission. *Phys. Stat. Sol.* **B76**, 689–94.

Bancroft, G. M. (1973). *Mössbauer Spectroscopy: An Introduction for Inorganic Chemists and Geochemists.* New York: McGraw-Hill.

Bancroft, G. M., S. Aksela, H. Aksela, K. H. Tan, B. W. Yates, L. L. Coatsworth, and J. S. Tse (1986). Shape resonances above the Si 2*p* threshold in SiF_4. *J. Chem. Phys.* **84**, 5–9.

Barandiaran, Z., L. Seijo, S. Huzinaga, and M. Klobukowski (1986). Structure and properties of transition-metal compounds. A systematic study of basis set effects in *ab initio* SCF calculations. *Int. J. Quant. Chem.* **29**, 1047–58.

Bargeron, C. B., M. Avinor, and H. A. Drickamer (1971). The effect of pressure on the spin state of iron (II) in manganese (IV) sulfide. *Inorg. Chem.* **10**, 1338–39.

Barnes, H. L. (1979). Solubilities of ore minerals. In: *Geochemistry of Hydrothermal Ore Deposits,* 2nd ed. (H. L. Barnes, ed.) New York: Wiley–Interscience.

Barnes, H. L., and H. Ohmoto (eds.) (1990). *Hydrothermal Processes: Applications to Ore Genesis.* D. Reidel.

Barone, V., P. Bucci, F. Lelj, and N. Russo (1981). An *ab initio* reinvestigation of the geometric and electronic structure of boron trioxide. *J. Molec. Struc.* **76**, 29–35.

Bartell, L. S., L. S. Su, and H. You (1970). Lengths of phosphorous–oxygen and sulfur–oxygen bonds. An extended Hückel molecular orbital examination of Cruickshanks $d\pi$-$d\pi$ picture. *Inorg. Chem.* **9**, 1903–12.

Barthelmehs, K. L., G. V. Gibbs, and M. B. Boisen, Jr. (1990). Bond length and bonded radii variations in sulfide molecules and crystals containing main group elements: a comparison with oxides. *Amer. Mineral* **74**, 620–26.

Bassett, P. J., and D. R. Lloyd (1969). He(I) resonance photoelectron spectra of group IV tetrafluorides. *Chem. Phys. Lett.* **3**, 22–24.

Bassett, W. A., H. Shimizu, and E. M. Brody (1982). Pressure dependence of elastic moduli of forsterite by Brillouin scattering in the diamond cell. In: *High Pressure Research in Geophysics, Adv. in Earth and Planet Sci.* S. Akimoto and M. H. Manghnani, eds. **12**, 115–24.

Batra, A. P., J. P. Hernandez, and L. M. Slifkin (1976). Crystal-field effects and the migration of transition-metal ions in AgCl. *Phys. Rev. Lett.* **36**, 876–78.

Baur, W. H. (1970). Bond length variation and distorted coordination polyhedra in organic crystals. *Trans. Amer. Cryst. Assoc.* **6**, 129–55.

Baur, W. H. (1971). The prediction of bond-length variations in silicon–oxygen bonds. *Amer. Mineral.* **56**, 1573–99.

Baur, W. H., E. Tillmanns, and W. Hofmeister (1983). Topological analysis of crystal structures. *Acta. Cryst.* **B44**, 669–73.

Bell, P. M., and H. K. Mao (1972). Crystal field studies of lunar samples. *Ann. Rept. Geophys. Lab. Yrbk.* **71**, 480–89.

Bernard, J. E., and A. Zunger (1987). Electronic structure of ZnS, ZnSe, ZnTe and their pseudobinary alloys. *Phys. Rev.* **B36**, 3199–228.

Bernholc, Z., and N. A. W. Holzwarth (1983). Local spin-density description of multiple metal–metal bonding: Mo_2 and Cr_2. *Phys. Rev. Lett.* **50**, 1451–54.

Berry, F. J. (1985). Mineral Surfaces and the chemical bond. In: *Chemical Bonding and Spectroscopy in Mineral Chemistry* (F. J. Berry and D. J. Vaughan, eds.) London: Chapman and Hall.

Berry, F. J., and D. J. Vaughan (1985). *Chemical Bonding and Spectroscopy in Mineral Chemistry.* London: Chapman and Hall.

Berry, R. S., S. A. Rice, and J. Ross (1980). *Physical Chemistry.* New York: Wiley.

Bethe, H. (1929). Termaufspaltung in Kristallen (Splitting of terms in crystals). *Ann. Phys.* **3**, 133–206.

Bianconi, A. (1979). Core excitons and inner shell resonances in surface soft x-ray absorption (SSXA) spectra. *Surf. Sci.* **89**, 41–50.

Bianconi, A. (1981). X-ray absorption near edge spectra (XANES) and their application to local structure determination. In: *EXAFS for Inorganic Systems* (C. D. Garner and S. S. Hasnain, eds.) SERC Daresburg Laboratory, pp. 13–26.

Bianconi, A. (1988). XANES spectroscopy. In: *X-ray Absorption.* E. D. Doningsberg and R. Prins, eds. New York: Wiley, pp. 573–662.

Bianconi, A., and R. S. Bauer (1980). Evidence of SiO at the Si–oxide interface by surface soft x-ray absorption near-edge spectroscopy. *Surf. Sci.* **99**, 76–86.

Birch, F. (1952). Elasticity and constitution of the Earth's interior. *J. Geophys. Res.* **51**, 227–86.

Birle, J. D., G. V. Gibbs, P. B. Moore, and J. V. Smith (1968). Crystal structures of natural olivines. *Amer. Mineral.* **53**, 807–24.

Bish, D. L., and C. W. Burnham (1984). Structure energy calculations on optimum distance model structures: application to the silicate olivines. *Amer. Mineral.* **69**, 1102–9.

Bither, T. A., R. J. Bouchard, W. H. Cloud, P. C. Donohue, and W. J. Siemons (1968). Transition metal pyrite dichalcogenides. High pressure synthesis and correlation of properties. *Inorg. Chem.* **7**, 2208–20.

Bloch, A. N., and G. C. Schatteman (1981). Quantum defect orbital radii. In: *Structure and Bonding in Crystals.* Vol. I (M. O'Keefe and A. Navrotsky, eds.) New York: Academic Press, pp. 49–72.

Bloss, F. D. (1971). *Crystallography and Crystal Chemistry: An Introduction.* New York: Holt, Rinehart and Winston.

Bodeur, S., I. Nenner, and P. Millie (1986). Resonances in photoabsorption spectra of SiF_4, $Si(CH_3)_4$, and $SiCl_4$ near the silicon K edge. *Phys. Rev.* **A34**, 2986–97.

Boness, D. A., and J. M. Brown (1990). The electronic band structure of iron, sulfur and oxygen at high pressure and the earth's core. *J. Geophys. Res.* **95B**, 21721–30.

Boness, D. A., J. M. Brown, and A. K. McMahan (1986). The electronic thermodynamics of iron under Earth core conditions. *Phys. Earth Planet. Int.* **42**, 227–40.

Boon, J. A., and W. F. Fyfe (1972). The coordination number of ferrous ions in silicate glasses. *Chem. Geol.* **10**, 287–98.

Bopp, P. (1987). Molecular dynamics computer simulations of solvation in hydrogen bonded systems. *Pure Appl. Chem.* **59**, 1071–82.

Bottinga, Y., and D. F. Weill (1972). The viscosity of magmatic silicate liquids: a model for calculation. *Amer. J. Sci.* **272**, 438–75.

Bouchard, R. J., P. A. Russo, and A. Wold (1965). Preparation and electrical properties of some thiospinels. *Inorg. Chem.* **4**, 685–88.

Bowen, N. L. (1928). *The Evolution of the Igneous Rocks*. Princeton.

Boyd, R. J., S. C. Choi, and C. C. Hale (1984). Electronic and structural properties of borazine and related molecules. *Chem. Phys. Lett.* **112**, 136–41.

Boyer, L. L. (1981). First-principles equation-of-state calculations for alkali halides. *Phys. Rev.* **B23**, 3673–85.

Boyer, L. L. (1983). Bonding and equation of states for MgO. *Phys. Rev.* **B27**, 1271–75.

Boys, S. F. (1950). Electronic wave functions I. A general method of calculation for the stationary states of any molecular system. *Proc. Roy. Soc. (Lond.)* **A200**, 542–54.

Boys, S. F., and F. Bernardi (1970). The calculation of small molecular interactions by the difference of separate total energies. Some procedures with reduced errors. *Mol. Phys.* **19**, 553–66.

Bozek, J. D., G. M. Bancroft, and K. H. Tan (1990). Resonances in the silicon *L* core level cross sections characterized by photoabsorption spectroscopy and MS-$X\alpha$ calculations. *Chem. Phys.* **145**, 131–52.

Braga, M., S. K. Lie, C. A. Taft, and W. A. Lester, Jr. (1988). Electronic structure, hyperfine interactions, and magnetic properties for octahedral iron sulfides. *Phys. Rev.* **B38**, 10837–51.

Bragg, W. H. (1930). The structures of silicates. *Zeits. für Krist.* **74**, 237–305.

Brawer, S. A., and W. S. White (1975). Raman spectroscopic investigation of silicate glasses. I. The binary alkali silicates. *J. Chem. Phys.* **63**, 2421–32.

Briggs, D., and M. P. Seah (1980). *Practical Surface Analysis by Auger and X-ray Photoelectron Spectroscopy*. New York: John Wiley & Sons.

Brinker, C. J., R. J. Kirkpatrick, D. R. Tallant, B. C. Bunker, and B. Montez (1988). NMR confirmation of strained "defects" in amorphous silica. *J. Noncryst. Solids* **99**, 418–28.

Brion, D., J. Hayer, and J. J. Predoli (1980). Characterization by ESCA of surface compounds of fine pyrite during the flotation process. *Fine Part. Process., Proc. Int. Symp.*, Vol. 1, 544–47 (AIME, P. Somasundaran, ed.).

Brown, G. E., and G. V. Gibbs (1970). Stereochemistry and ordering in the tetrahedral portion of silicates. *Amer. Mineral.* **55**, 1587–607.

Brown, I. D. (1981). The bond-valence method: an empirical approach to chemical structure and bonding. In: *Structure and Bonding in Crystals* (M. O'Keeffe and A. Navrotsky, eds.) New York: Academic Press.

Bruckner, R., H. U. Chan, H. Goretzki, and M. Sammet (1980). XPS measurements and structural aspects of silicate and phosphate glasses. *J. Noncryst. Solids* **42**, 49.

Brundle, C. R., M. B. Robin, H. Basch, M. Pinsky, and A. Bond (1970). Experimental and theoretical comparison of the electronic structure of the ethylene and diborane. *J. Amer. Chem. Soc.* **92**, 3863–66.

Brytov, I. A., Y. N. Romaschenko, K. I. Konashenok, and Y. A. Obolenskiy (1984). The relationship between magnesium x-ray K and $L_{2,3}$ spectra and the structure and composition of minerals. *Geochem. Int.* No. 6, 53–61.

Buckingham, A. D. (1986). The structure and properties of the water molecules. In: *Water and Aqueous Solutions* (G. W. Nelson and J. E. Enderby, eds.) Bristol: Adam Hilger, pp. 1–10.

Buckley, A. N., and R. Woods (1983). An x-ray photoelectron spectroscopic investigation of the tarnishing of bornite. *Aust. J. Chem.* **36**, 1793–804.

Buckley, A. N., and R. Woods (1984). An x-ray photoelectron spectroscopic study of the oxidation of chalcopyrite. *Aust. J. Chem.* **37**, 2403–13.

Buerger, M. J. (1960). *Crystal Structure Analysis.* New York: Wiley.

Bukowinski, M. S. T. (1976a). On the electronic structure of iron at core pressures. *Phys. Earth Planet, Int.* **13**, 57–66.

Bukowinski, M. S. T. (1976b). The effect of pressure on the physics and chemistry of potassium. *Geophys. Res. Letts.* **3**, 491–93.

Bukowinski, M. S. T. (1980). Effect of pressure on bonding in MgO. *J. Geophys. Res.* **85**, 285–92.

Bukowinski, M. S. T. (1982). Pressure effects on bonding in calcium oxide: comparison with magnesium oxide. *J. Geophys. Res.* **87B**, 303–19.

Bukowinski, M. S. T. (1985). First principles equations of state of MgO and CaO. *Geophys. Res. Lett.* **12**, 536–39.

Bukowinski, M. S. T., and L. Knopoff (1976). Electronic transition in iron and properties of the core. *Geophys. Res. Lett.* **3**, 45–48.

Bukowinski, M. S. T., and G. H. Wolf (1985). Equation of state and stability of fluorite-structured SiO_2. *J. Geophys. Res.* **B91**, 4704–10.

Bullett, D. W. (1980). The renaissance and quantitative development of the tight binding method. In: *Solid State Physics, Adv. in Research and Applications,* Vol. 35 (F. Seitz, H. Ehrenreich, and D. Turnbull, eds.), pp. 129–214.

Bullett, D. W. (1982). Electronic structure of 3*d* pyrite- and marcasite-type sulphides. *J. Phys. C.* **15**, 6163–74.

Bullett, D. W. (1987). Applications of atomic-orbital methods to the structure and properties of complex transition-metal compounds. *Phys. Chem. Mineral.* **14**, 485–91.

Bullett, D. W., and W. G. Dawson (1986). Bonding relationships in some ternary and quaternary phosphide and tetrahedrite structures $(Ag_6M_4P_{12})M_6'$, $Cu_{12+x}Sb_4S_{13}$, $Cu_{14-x}Sb_4S_{13}$, $Ln_6Ni_6P_{17}$. *J. Phys. C* **19**, 5837–47.

Burdett, J. K. (1979). Application of "molecular" theories to the structure of the crystalline state. *Nature* **279**, 121–25.

Burdett, J. K. (1980). *Molecular Shapes.* New York: Wiley–Interscience.

Burdett, J. K. (1984). Theoretical challenges in understanding the structures of solids. *J. Phys. Chem.* **87**, 4368–75.

Burdett, J. K. (1988). Perspectives in structural chemistry. *Chem. Rev.* **88**, 3–30.

Burdett, J. K., and D. C. Caneva (1985). Energetic description of solids in terms of small fragments. *Inorg. Chem.* **24**, 3866–73.

Burdett, J. K., and S. Lee (1983). Peierls distortions in two and three dimensions and the structures of *AB* solids. *J. Am. Chem. Soc.* **105**, 1079.

Burdett, J. K., and T. J. McLarnan (1982). Geometrical and electronic links among the structures of MX_2 solids: structural enumeration and electronic stability of pyrite-like systems. *Inorg. Chem.* **21**, 1119–28.

Burdett, J. K., and T. J. McLarnan (1984). An orbital interpretation of Pauling's rules. *Amer. Mineral.* **69**, 601–21.

Burdett, J. K., G. D. Price, and S. L. Price (1981). The factors influencing solid state structure. An interpretation using pseudopotential radii structure maps. *Phys. Rev.* **B24**, 2903–12.

Burkert, U., and N. L. Allinger (1982). *Molecular Mechanics,* ACS Monograph 177, American Chemical Society, Washington, D.C.

Burnham, C. W., Y. Ohasi, S. S. Hafner, and D. Virgo (1971). Cation distribution and atomic thermal vibrations in an iron-rich orthopyroxene. *Amer. Mineral.* **56**, 850–76.

Burns, R. G. (1970). *Mineralogical Applications of Crystal Field Theory.* Cambridge: Cambridge Univ. Press.

Burns, R. G. (1981). Intervalence transitions in mixed valence minerals of iron and titanium. *Ann. Rev. Earth Planet. Sci.* **9**, 345–83.

Burns, R. G. (1985). Electronic spectra of minerals. In: *Chemical Bonding and Spectroscopy in Mineral Chemistry* (F. J. Berry and D. J. Vaughan, eds.) London: Chapman and Hall, pp. 63–101.

Burns, R. G. (1989). Spectral mineralogy of terrestrial planets: scanning their surfaces remotely. In: *Spectroscopic Studies of Minerals: Principles, Applications, and Advances* (D. J. Vaughan, ed.) *Mineral. Mag.* **53**, 135–51.

Burns, R. G., and V. M. Burns (1979). Manganese oxides. In: *Marine Minerals. Min. Soc. Amer. Reviews in Mineralogy* **6**, 1–46.

Burns, R. G., and W. S. Fyfe (1964). Site preference energy and selective uptake of transition metal ions from a magma. *Science* **144**, 1001–3.

Burns, R. G., and W. S. Fyfe (1967a). Trace element distribution rules and their significance. *Chem. Geol.* **2**, 89–104.

Burns, R. G., and W. S. Fyfe (1967b). Crystal field theory and the geochemistry of transition elements. In: *Researches in Geochemistry* (P. H. Abelson, ed.) New York: Wiley.

Burns, R. G., and F. E. Huggins (1973). Visible absorption spectra of a Ti^{3+} fassaite from the Allende meteorite: a discussion. *Amer. Mineral.* **58**, 955–61.

Burns, R. G., and D. J. Vaughan (1970). Interpretation of the reflectivity behaviour of ore minerals. *Amer. Mineral.* **55**, 1576–86.

Burns, R. G., and D. J. Vaughan (1975). Polarized electronic spectra. In: *Infrared and Raman Spectroscopy of Lunar and Terrestrial Minerals* (C. Karr, Jr., ed.) New York: Academic Press.

Bursten, B. E., J. R. Jensen, D. J. Gordon, P. M. Treichel, and R. F. Fenske (1981). Electronic structure of transition-metal nitrosyls. $X\alpha$-SW and configuration interaction calculations of the valence ionization potentials of $Co(CO)_3NO$ and $Mn(CO)_4NO$. *J. Amer. Chem. Soc.* **103**, 5226–31.

Busing, W. R. (1981). WMIN, a computer program to model molecules and crystals in terms of potential energy functions. Oak Ridge: Oak Ridge National Laboratory.

Buss, D. D., and N. J. Parada (1970). Calculation of the optical constants of lead telluride from augmented-plane-wave k·p energy bands. *Phys. Rev.* **B1**, 2692–99.

Cade, P. E., K. D. Sales, and A. C. Wahl (1966). Electronic structure of diatomic molecules. III. A. Hartree–Fock wavefunctions and energy quantities for $N_2(X\,^1\varepsilon_g{}^+)$ and $N_2{}^+$ ($X\,^2\varepsilon_g{}^+$, $A\,^2\pi_u$, $B\,^2\varepsilon_u{}^+$) molecular ions. *J. Chem. Phys.* **44**, 1973–2003.

Calabrese, A., and R. G. Hayes (1975). Valence-level studies of some first and second row oxyanions by x-ray photoelectron spectroscopy. *J. Electron Spectrosc.* **6**, 1–16.

Calais, J.-L. (1977). Band structure of transition metal compounds. *Adv. in Physics* **26**, 847–85.

Car, R., and M. Parrinello (1985). Unified approach for molecular dynamics and density-functional theory. *Phys. Rev. Lett.* **55**, 2471–74.

Car, R., and M. Parrinello (1988). Structural, dynamic, and electronic properties of amorphous silicon: an *ab initio* molecular dynamics study. *Phys. Rev. Lett.* **60**, 204–7.

Cardona, M., and D. L. Greenaway (1964). Optical properties and band structure of group IV-VI and group V materials. *PHys. Rev.* **133**, A1685–97.

Cardona, M., and G. Harbeke (1965). Optical properties and band structure of wurtzite-type crystals and rutile. *Phys. Rev.* **137**, A1467–76.

Carlsson, A. E., N. W. Ashcroft, and A. R. Williams (1984). Properties of SiO_2 in a high-pressure fluorite structure phase. *Geophys. Res. Lett.* **11**, 617–19.

Cartling, B. G. (1975). Localized description of the electronic structure of covalent semiconductors. I. Perfect crystals. *J. Phys. C; Solid State Phys.* **8**, 3171–82.

Case, D. A. (1982). Electronic structure calculations using the $X\alpha$ method. *Ann. Rev. Phys. Chem.* **33**, 151–71.

Case, D. A., and M. Karplus (1976). The calculation of one-electron properties from $X\alpha$ multiple scattering wavefunctions. *Chem. Phys. Lett.* **39**, 33–38.

Castleman, A. W. (1987). Clusters: bridging the gas and condensed phases. *Acc. Chem. Res.* **19**, 413–19.

Castleman, A. W., Jr., and R. G. Keesee (1986). Ionic clusters. *Chem. Rev.* **86**, 589–618.

Catlow, C. R. A., C. M. Freeman, and R. L. Royle (1985). Recent studies using simulation techniques. *Physica B&C* **131**, 1–12.

Catlow, C. R. A., and W. C. Mackrodt (1982). Theory of simulation methods for lattice and defect energy calculations in crystals. In: *Lecture Notes in Physics,* Vol. 166, *Computer Simulation of Solids* (C. R. A. Catlow and W. C. Mackrodt, eds.) Berlin: Springer-Verlag, pp. 3–20.

Catlow, C. R. A., and A. M. Stoneham (1983). Ionicity in solids. *J. Phys.* **C16**, 4321–38.

Catlow, C. R. A., J. M. Thomas, S. C. Parker, and D. A. Jefferson (1982). Simulating silicate structure and the structural chemistry of pyroxenoids. *Nature* **295**, 658–62.

Causa, M., R. Dovesi, C. Pisani, and C. Roetti (1986a). Electronic structure and stability of different crystal phases of MgO. *Phys. Rev.* **B33**, 1308–16.

Causa, M., R. Dovesi, C. Pisani, and C. Roetti (1986b). Electron charge density and electron momentum distribution in magnesium oxide. *Acta Cryst.* **B42**, 247–53.

Causa, M., R. Dovesi, C. Pisani, and C. Roetti (1986c). *Ab initio* Hartree–Fock study of the MgO(001) surface. *Surf. Sci.* **175**, 551–60.

Causa, M., R. Dovesi, C. Roetti, E. Kotomin, and V. R. Saunders (1987). A periodic *ab initio* Hartree–Fock calculation on corundum. *Chem. Phys. Lett.* **140**, 120–23.

Cederbaum, L. S., W. Domcke, J. S. Shirmer, and W. von Niessen (1980). Many-body effects in valence and core photoionization of molecules. *Phys. Scripta* **21**, 481–91.

Cederbaum, A., J. Schirmer, W. Domcke, and W. Von Niessen (1977). Complete breakdown of the quasiparticle picture for inner valence electrons. *J. Phys.* **B10**, L549–53.

Ceperley, D. M., and B. J. Alder (1980). Ground state of the electron gas by a stochastic method. *Phys. Rev. Lett.* **45**, 566–69.

Chakoumakos, B. C., and G. V. Gibbs (1986). Theoretical molecular orbital study of silanol–water interactions. *J. Phys. Chem.* **90**, 996–98.

Chakoumakos, B. C., R. J. Hill, and G. V. Gibbs (1981). A molecular orbital study of rings in silicates and siloxanes. *Am. Mineral.* **66**, 1237–49.

Chandrasekhar, J., D. C. Spellmeyer, and W. J. Jorgensen (1984). Energy component analysis for dilute aqueous solutions of Li^+, Na^+, F^-, and Cl^- ions. *J. Amer. Chem. Soc.* **106**, 903–10.

Chang, K. J., and M. O. Cohen (1984a). Theoretical study of BeO: Structural and electronic properties. *Solid State Comm.* **50**, 487–91.

Chang, K. J., and M. O. Cohen (1984b). High-pressure behaviour of MgO: structural and electronic properties. *Phys. Rev.* **B30**, 4774–81.

Chantry, G. W., and R. A. Plane (1960). Raman intensities of the A_1 lines of oxyanions. *J. Chem. Phys.* **32**, 319–21.

Charnock, J. M., C. D. Garner, R. .A. D. Pattrick, and D. J. Vaughan (1989a). Coordination sites of metals in tetrahedrite minerals determined by EXAFS. *Journ. Solid State Chem.* **82**, 271–89.

Charnock, J. M., C. D. Garner, R. A. D. Pattrick, and D. J. Vaughan (1989b). EXAFS and Mössbauer spectroscopic study of Fe-bearing tetrahedrites. *Mineral. Mag.* **53**, 193–99.

Charnock, J., C. D. Garner, R. A. D. Pattrick, and D. J. Vaughan (1990). An EXAFS study of thiospinel minerals. *Amer. Mineral.* **75**, 247–55.

Chelikowsky, J. R. (1977). An oxygen pseudopotential: application to the electronic structure of ZnO. *Solid State Comm.* **22**, 351–54.

Chelikowsky, J. .R., and J. K. Burdett (1986). Ionicity and the structural stability of solids. *Phys. Rev. Lett.* **56**, 961–64.

Chelikowsky, J. R., and S. G. Louie (1984). First principles linear combination of atomic orbitals methods for the cohesive and structural properties of solids: Application to diamond. *Phys. Rev.* **B29**, 3470–81.

Chelikowsky, J. R., and M. Schluter (1977). Electron states in α-quartz: a self-consistent pseudopotential calculation. *Phys. Rev.* **B15**, 4020–29.

Cheng, H. P., and D. E. Ellis (1989). First-principles potentials in modeling structure and thermodynamics of Fe-Ni alloys. *Phys. Rev.* **B39**, 12469–83.

Chianelli, R. R. (1983). Catalysis by transition metal sulfides. In: *Surface Properties and Catalysis by Non-Metals.* (J. P. Bonnelle et al., eds.) Dordecht, Netherlands: D. Reidel Co., pp. 361–78.

Chiang, T. C., J. A. Knapp, M. Aono, and D. E. Eastman (1980). Angle-resolved photoemission, valence band dispersion, $E(\mathbf{k})$ and electron hole lifetimes for GaAs. *Phys. Rev.* **B21**, 3513–22.

Ching, W. Y., R. A. Murray, D. J. Lam, and B. W. Veal (1983). Comparative studies of electronic structures of sodium metasilicate and α and β phases of sodium disilicate. *Phys. Rev.* **B28**, 4724–35.

Chisholm, M. H. (1985). Analogies between alkoxides and oxide structures in the chemistry of molybdenum and tungsten. *J. Solid State Chem.* **57**, 120–33.

Chong, D. P., and Y. Takahata (1977). Vibrational structure in diatomic photoelectron spectra: application to CS, PN, SiO and P_2. *J. Electron Spectrosc. Relat. Phenom.* **10**, 137–45.

Chornay, D. J., M. A. Coplan, J. A. Tossell, J. H. Moore, E. J. Baerends, and A. Rozendaal (1985). Valence electron momentum density in $Cr(CO)_6$ from (*e*,2*e*) spectroscopy and SCF-MO calculations. *Inorg. Chem.* **24**, 877–82.

Chou, S. H., J. Guo, and D. E. Ellis (1986). Electronic structure and x-ray absorption spectra of wustite $Fe_{1-x}O$. *Phys. Rev.* **B34**, 12–24.

Chou, J. S. Y., and K. D. Jordan (1987). Use of the $X\alpha$ method for the characterization of temporary negative ions of benzene and substituted benzenes. *J. Phys. Chem.* **91**, 5578–82.

Christ, C. L., and J. R. Clark (1977). A crystal-chemical classification of borate structures with emphasis on hydrated borates. *Phys. Chem. Minerals* **2**, 59–88.

Christou, G., K. S. Hagen, J. K. Bashkin, and R. H. Holm (1985). The clusters $[Co_8S_6(SPh)_8]^{4-5-}$: preparations, properties and structural relationship of near cubic $Co_8(\mu_4 - S)_6$ cores to the clusters in synthetic pentlandite. *Inorg. Chem.* **24**, 1010–18.

Chung, U. W., W. J. Lo, and G. A. Somorjai (1977). Low energy electron diffraction and electron spectroscopy studies of the clean (110) and (100) titanium dioxide (rutile) crystal surfaces. *Surf. Sci.* **64**, 588.

Ciraci, S., and I. P. Batra (1983). Electronic structure of α-alumina and its defect states. *Phys. Rev.* **B28**, 982–92.

Clarke, T. A., and E. N. Rizkalla (1976). X-ray photoelectron spectroscopy of some silicates. *Chem. Phys. Lett.* **37**, 523–26.

Clementi, E., and H. Popkie (1972). Study of the structure of molecular complexes. I. Energy surface of a water molecule in the field of a lithium positive ion. *J. Chem. Phys.* **57**, 1077–94.

Coehoorn, R., C. Haas, J. Dijkstra, C. J. F. Flipse, R. A. de Groot, and A. Wold (1987). Electronic structure of $MoSe_2$, MoS_2, and WSe_2. I. Band structure calculations and photoelectron spectroscopy. *Phys. Rev.* **B35**, 6195–206.

Cohen, A. J., and R. G. Gordon (1975). Theory of the lattice energy, equilibrium structure, elastic constants, and pressure-induced phase transitions in alkali-halide crystals. *Phys. Rev.* **B12**, 3228–41.

Cohen, A. J., and R. G. Gordon (1976). Modified electron-gas study of the stability, elastic properties, and high-pressure behavior of MgO and CaO crystals. *Phys. Rev.* **B14**, 4593–605.

Cohen, M. L. (1979). The pseudopotential panacea. *Physics Today* July, 40–47.

Cohen, M. L. (1984). Electronic structure of solids. *Phys. Rep.* **110**, 293–309.

Cohen, M. L., and T. K. Bergstresser (1966). Band structures and pseudopotential form factors for fourteen semiconductors of the diamond and zincblende structures. *Phys. Rev.* **141**, 789–96.

Cohen, M. L., P. J. Lin, D. M. Rossler, and W. C. Walker (1967). Ultraviolet optical properties and electronic band structure of MgO. *Phys. Rev.* **155**, 992–96.

Cohen, R. E. (1987). Calculation of elasticity and high pressure instabilities in corundum and stishovite with the potential induced breathing model. *Geophys. Res. Lett.* **14**, 37–40.

Cohen, R. E., L. L. Boyer, and M. J. Mehl (1987). Theoretical studies of charge relaxation effects on the statics and dynamics of oxides. *Phys. Chem. Minerals* **14**, 294–302.

Colburn, E. A., J. M. Dyke, E. P. F. Lee, A. Morris, and I. R. Trickle (1978). The vacuum ultraviolet photoelectron spectrum of the SiO($^1\Sigma^+$) molecule. *Molec. Phys.* **35**, 873–82.

Connor, J. A., M. Considine, and I. H. Hillier (1978). Low energy photoelectron spectra of solids: photoelectron spectra of carbonate, phosphite, sulfate, triborate and ethanoate ions. *J. Chem. Soc. Faraday Trans. II.* **74**, 1285–91.

Connor, J. A., I. H. Hillier, V. R. Saunders, and M. Barber (1972). On the bonding of the ions PO_4^{3-}, SO_4^{2-}, ClO_3^- and CO_3^{2-} as studied by x-ray spectroscopy and *ab initio* SCF-MO calculations. *Molec. Phys.* **23**, 81–90.

Cook, M., and M. Karplus (1987). Electronic correlation and density-functional methods. *J. Phys. Chem.* **91**, 31–37.

Coombs, P. C., J. F. DeNatale, P. J. Hood, D. K. McElfresh, R. S. Worfman, and J. F. Schackleford (1985). The nature of the Si–O–Si bond angle distribution in vitreous silica. *Phil. Mag.* **B51**, L39–41.

Costa Lima, M. T., and C. Senemaud (1976). Electronic distribution of SiO by x-ray spectroscopy. *Chem. Phys. Lett.* **40**, 157–59.

Cotton, F. A. (1971). *Chemical Applications of Group Theory.* New York: John Wiley & Sons.

Cowley, A. H. (1979). UV photoelectron spectroscopy in transition metal chemistry. *Progress in Inorganic Chemistry,* Vol. 26 (S. J. Lippard, ed.), pp. 45–160.

Craig, J. R., and D. J. Vaughan (1981). *Ore Microscopy and Ore Petrography.* New York: Wiley–Interscience.

Crerar, D., S. Wood, S. Brantley, and A. Bocarsly (1985). Chemical controls on solubility of ore-forming minerals in hydrothermal solutions. *Canad. Mineral.* **23**, 333–52.

Cronemeyer, D. C. (1952). Electrical and optical properties of rutile single crystals. *Phys. Rev.* **87**, 876–86.

Cruickshank, D. W. J. (1961). The role of 3*d*-orbitals in π-bonds between (a) silicon, phosphorus, sulphur or chlorine and (b) oxygen or nitrogen. *J. Chem. Soc.* 5486–504.

Cruickshank, D. W. J. (1985). A reassessment of $d\pi$-$d\pi$ bonding in tetrahedral oxyanions of second-row atoms. *J. Molec. Struct.* **130**, 177–91.

Curtis, L. A., J. W. Halley, J. Hauptman, and A. Rahman (1987). Nonadditivity of *ab initio* pair potentials for molecular dynamics of multivalent transition metal ions in water. *J. Chem. Phys.* **86**, 2319–27.

Cuthbert, J. D., and H. E. Petch (1963). NMR studies of hydrated sodium tetraborate minerals. I. Boron–oxygen polyions in borax and tincalconite. *J. Chem. Phys.* **38**, 1912–19.

Cynn, H., D. G. Isaak, R. E. Cohen, M. F. Nicol, and D. L. Anderson (1990). A high-pressure phase transition of corundum predicted by the potential induced breathing model. *Amer. Mineral.* **75**, 439–42.

Dalven, R. (1969). A review of the semiconductor properties of PbTe, PbSe, PbS and PbO. *Infrared Phys.* **9**, 141–84.

Das, T. P., and E. L. Hahn (1958). *Nuclear Quadrupole Resonance Spectroscopy.* New York: Academic Press.

DaSilva, J. R. G., D. G. Pinatti, C. E. Anderson, and M. L. Rudeen (1974). A refinement of the structure of vitreous silica. *Phil. Mag.* **31**, 713–17.

Davidson, E. R., and D. Feller (1984). Molecular properties of water. *Chem. Phys. Lett.* **104**, 54.

Davidson, E. R., and D. Feller (1986). Basis set selection for molecular calculations. *Chem. Rev.* **86**, 681–96.

Day, K. L., and B. Donn (1978). Condensation of nonequilibrium phases of refractory silicates from the vapor. *Science* **202**, 307–8.

DeAlti, G., P. Decleva, and A. Lisini (1982). On the validity on the $X\alpha$ method in the computation of ionization potentials: a comparison of the results for small molecules. *Chem. Phys.* **66**, 425–43.

DeAlti, G., P. Decleva, and A. Sgamellotti (1978). An MS-$X\alpha$ study of the photoelectron spectra and bonding in the fluorosilanes. *Chem. Phys.* **35**, 283–92.

Deer, W. A., R. A. Howie, and J. Zussman (1966). *An Introduction to the Rock-Forming Minerals.* New York: Wiley.

Deer, W. A., R. A. Howie, and J. Zussman (1978). *Rock Forming Minerals, Vol. 2A: Single Chain Silicates.* London: Longmans.

Deer, W. A., R. A. Howie, and J. Zussman (1982). *Rock Forming Minerals, Vol. 1A: Orthosilicates.* London: Longmans.

Deer, W. A., R. A.. Howie, and J. Zussman (1986). *Rock Forming Minerals, Vol. 1B: Disilicates and Ring Silicates.* London: Longmans.

de Groot, R. A., and C. Haas (1975). MST-$X\alpha$ calculations on molybdenum disulphide and some related compounds. *Solid State Commun.* **17**, 887–90.

de Jong, B. H. W. S., K. D. Keefer, G. E. Brown, Jr., and C. M. Taylor (1981). Polymerization of silicate and aluminate tetrahedra in glasses, melts and aqueous solutions. III. Local silicon environments and internal nucleation in silicate glasses. *Geochim. Cosmochim. Acta* **45**, 1291–308.

Delley B., A. J. Freeman, and D. E. Ellis (1983). Metal–metal bonding in Cr–Cr and Mo–Mo dimers: Another success of local spin-density theory. *Phys. Rev. Lett.* **50**, 488–91.

Dempsey, E. (1969). The calculation of Madelung potentials for faujasite-type zeolites. I. *J. Phys. Chem.* **73**, 3660–68.

Dent Glasser, L. S. (1979). Non-existent silicates. *Zeit. Krist.* **149**, 291–305.

Derbenwick, G. F. (1970). Stanford Electronic Laboratories Technical Rept. No. 5220-2.

Devine, R. A. B., R. Dupree, I. Farnan, and J. J. Capponi (1987). Pressure-induced bond-angle variation in amorphous SiO_2. *Phys. Rev.* **B35**, 2560–62.

Dewar, M. J. S., and C. Jie (1987). AM1 calculations for compounds containing silicon. *Organomet.* **6**, 1486–90.

Dewar, M. J. S., and W. Thiel (1977). Ground states of molecules. 38. The MNDO method. Approximations and parameters. *J. Amer. Chem. Soc.* **99**, 4899.

Dewar, M. J. S., E. G. Zoebisch, E. F. Healy, and J. P. Stewart (1985). Development and use of quantum mechanical molecular models. 76. AM1: a new general purpose quantum mechanical molecular model. *J. Amer. Chem. Soc.* **107**, 3902–9.

Didziulis, S. V., S. L. Cohen, K. D. Butcher, and E. I. Solomon (1988). Variable photon energy photoelectron spectroscopic studies of covalent bonding in $3d^{10}$ transition-metal compounds. *Inorg. Chem.* **27**, 2238–50.

Dietz, E. R. (1983). Scattered-wave calculations of the phosphorus L X-ray emission spectrum of ligand-substituted phosphorus oxyanions. *J. Phys.* **B16**, 4593–9.

Dikov, Y. P., E. I. Debolsky, Y. N. Romashchenko, S. P. Dolin, and A. A. Levin (1977). Molecular orbitals of $Si_2O_7^{6-}$, $Si_3O_{10}^{8-}$, etc. and mixed $(B,Al,P,Si)_m$ applied to clusters and x-ray spectroscopy data of silicates. *Phys. Chem. Mineral.* **1**, 27–41.

Dikov, Y. P., V. I. Rekharsky, G. L. Gutzev. S. P. Dolin, and A. A. Levin (1986). Model investigation of electronic structure of some silicate clusters by DVM-$X\alpha$. *Phys. Chem. Mineral.* **13**, 48–60.

Dikov, Y. P., Y. N. Romaschenko, I. A. Brytov, and V. V. Nemoskhalenko (1976). X-ray spectral investigation of silicates. I. Structure of the $L_{II,III}$ band of silicon. *Sov. Phys. Dokl.* **20**, 595–97.

Dill, D., and J. L. Dehmer (1974). Electron–molecule scattering and molecular photoionization using the multiple scattering method. *J. Chem. Phys.* **61**, 693–99.

Dirac, P. A. M. (1929). Quantum mechanics of many-electron systems. *Proc. Roy. Soc. (London)* **123A**, 714.

DiStefano, T. H., and D. E. Eastman (1971). Photoemission measurements of the valence levels of amorphous SiO_2. *Phys. Rev. Lett.* **27**, 1560–62.

Ditchfield, R. (1974). Self-consistent perturbation theory of diamagnetism: a gauge-invariant LCAO method for NMR shifts. *Molec. Phys.* **27**, 789–807.

Dixon, D. A., and D. O. Marynick (1977). Inversion barriers of AsH_3 and SeH_3^+. *J. Am. Chem. Soc.* **99**, 6101–3.

Dodd, C. G., and G. L. Glenn (1969). A survey of chemical bonding in silicate minerals by x-ray emission spectroscopy. *Amer. Mineral.* **54**, 1299–311.

Dollase, D. W. (1980). Optimum distance model of relaxation around substitutional defects. *Phys. Chem. Mineral.* **6**, 295–304.

Domashevskaya, E. P., V. A. Terekhov, L. N. Marshakova, Y. Ugai, V. I. Nefedov, and N. P. Sergushin (1976). Participation of *d* electrons of metals of groups I, II and III in chemical bonding with sulfur. *J. Electron Spectros. Relat. Phenom.* **9**, 261–67.

Dovesi, R., C. Pisani, C. Roetti, M. Causà, and V. R. Saunders (1988). CRYSTAL88. An *ab initio* all-electron LCAO-Hartree–Fock program for periodic systems, Quantum Chemistry Program Exchange, Indiana University.

Dovesi, R., C. Pisani, C. Roetti, and B. Silvi (1987). The electronic structure of α-quartz: A periodic Hartree–Fock calculation. *J. Chem. Phys.* **86**, 6967–71.

Downs, J. .W., and G. V. Gibbs (1987). An exploratory examination of the electron density and electrostatic potential of phenakite. *Amer. Mineral* **72**, 769–77.

Draganjac, M., and T. B. Rauchfuss (1985). Transition metal polysulfides: coordination compounds with purely inorganic chelate ligands. *Angew. Chem. Int. Ed. Engl.* **24**, 742–57.

Drago, R. S. (1977). *Physical Methods in Chemistry.* Philadelphia: Saunders & Co.

Drickamer, H. G., and C. W. Frank (1973). *Electronic Transitions and the High Pressure Chemistry and Physics of Solids.* London: Chapman and Hall.

Duff, K. J. (1974). Calibration of the isomer shifts for ^{57}Fe. *Phys. Rev.* **B9**, 66–72.

Duff, K. J., K. C. Mishra, and T. P. Das (1981). *Ab initio* determination of ^{57}Fe^{m} quadrupole moment from Mössbauer data. *Phys. Rev. Lett.* **46**, 1611–14.

Duffy, J. A., and M. D. Ingram (1971). Establishment of an optical scale for Lewis basicity in inorganic oxyacids, molten salts and glasses. *J. Amer. Chem. Soc.* **93**, 6448–54.

Duffy, J. A., and M. D. Ingram (1976). An interpretation of glass chemistry in terms of the optical basicity concept. *J. Noncryst. Solids* **21**, 373–410.

Duke, C. B. (1983). Structural chemistry of the cleavage faces of compound semiconductors. *J. Vac. Sci. Technol.* **B1**, 732–35.

Duncan, J. F., and P. W. R. Wigley (1963). The electronic structure of the iron atoms in complex iron cyanides. *J. Chem. Soc.* 1020–25.

Dunlap, B. I., J. W. D. Connolly, and J. R. Sabin (1979a). On some approximations in applications of $X\alpha$ theory. *J. Chem. Phys.* **71**, 3396–402.

Dunlap, B. I., J. W. D. Connolly, and J. R. Sabin (1979b). On first-row diatomic molecules and local density models. *J. Chem. Phys.* **71**, 4993–99.

Dupree, E., and R. F. Pettifer (1984). Determination of the Si–O–Si bond angle distribution in vitreous silica by magic angle spinning NMR. *Nature* **308**, 523–25.

Dyar, M. D. (1985). A review of Mössbauer data on inorganic glasses: the effects of composition on iron valency and coordination. *Amer. Mineral.* **70**, 304–16.

Eckelt, P. (1967). Energy band structures of cubic ZnS, ZnSe, ZnTe and CdTe (Korringa–Kohn–Rostoker method). *Phys. Status Solidi* **23**, 307–12.

Edwards, A. H., and W. B. Fowler (1985). Semiempirical molecular orbital techniques applied to silicon dioxide: MINDO3. *J. Phys. Chem. Solids* **46**, 841–57.

Edwards, J. O., G. C. Morrison, V. F. Ross, and J. W. Schulltz (1955). The structure of the aqueous borate ion. *J. Am. Chem. Soc.* **77**, 266–68.

Effenberger, H., A. Kirfel, and G. Will (1983). Untersuchungen zur electron endichteverteilung im dolomit, CaMg(CO$_3$)$_2$. *Tschermaks Mineral. Petrogr. Mitt.* **31**, 151–64.

Eggleston, C. M., and M. F. Hochella, Jr. (1990). Scanning tunneling microscopy of sulfide surfaces. *Geochim. Cosmochim. Acta* **54**, 1511–17.

Ellis, D. E., G. A. Benesh, and E. Byrom (1979). Self-consistent embedded-cluster model for magnetic impurities: Fe, Co, and Ni in β'-NiAl. *Phys. Rev.* **B20**, 1198–207.

Ellis, D. E., D. Geunzburger, and H. B. Jansen (1983). Electric field gradient and electronic structure of linear-bonded halide compounds. *Phys. Rev.* **B28**, 3697–705.

Ellis, E., D. W. Johnson, A. Breeze, P. M. Magee, and P. G. Perkins (1979). The electronic structure and optical properties of oxide glasses. I. SiO_2, $Na_2O:SiO_2$ and $Na_2O:CaO:SiO_2$. *Phil. Mag.* **B40**, 105–24.

Embrey, P. G., and A. J. Criddle (1978). Error problems in the two media method of deriving the optical constants *n* and *k* from measured reflectances. *Amer. Mineral.* **63**, 853–62.

Engelhardt, G., and R. Radeglia (1984). A semiempirical quantum chemical rationalization of the correlation between Si–O–Si angles and ^{29}Si NMR chemical shifts in silica polymorphs and framework aluminosilicates. *Chem. Phys. Lett.* **108**, 271–74.

Ermler, W. C., and A. D. McLean (1980). The effects of basis set quality and configuration mixing in *ab initio* calculations of the ionization potentials of the nitrogen molecule. *J. Chem. Phys.* **73**, 2297–303.

Ernst, C. A., A. L. Allred, M. A. Ratner, M. D. Newton, G. V. Gibbs, J. W. Moskowitz, and S. Toiol (1981). Bond angles in disiloxane: a pseudopotential electronic structure study. *Chem. Phys. Lett.* **81**, 425–29.

Euwema, R. N., G. G. Wepfer, T. Surratt, and D. L. Wilhite (1974). Hartree–Fock calculations for crystalline Ne and LiF. *Phys. Rev.* **B9**, 5249–56.

Evans, H. T., Jr. (1970). Lunar troilite: crystallography. *Science* **167**, 621–23.

Evans, H. T., Jr. (1971). Crystal structure of low chalcocite. *Nature* **232**, 69–70.

Falk, M., H. T. Flakus, and R. J. Boyd (1986). An *ab initio* SCF calculation of the effect of water–anion and water–cation interactions on the vibrational frequencies of water. *Spectrochim. Acta* **42A**, 175–80.

Fantoni, R., A. Giardini-Guidoni, R. Tiribelli, R. Cambi, and M. Rosi (1986). Ionization potentials and electron momentum distributions for SiF_4 valence-shell orbitals: an (*e*,2*e*) spectroscopic investigation and Green's function study. *Chem. Phys. Lett.* **128**, 67–75.

Farberovich, O. V., S. I. Kurganskii, and E. P. Domashevskaya (1980). Problems of the OPW method. II. Calculation of the band structure of zinc sulfide and cadmium sulfide. *Phys. Stat. Solidi* **B97**, 631–40.

Ferreira, L. G., A. A. Mbaye, and A. Zunger (1988). Chemical and elastic effects on isostructural phase diagrams: The ε-*G* approach. *Phys. Rev.* **B37**, 10547–68.

Field, R. W., A. Lagerquist, and I. Renhorn (1976). The low lying electronic states of SiO. *Phys. Scripta* **14**, 298–319.

Fink, M. J., K. J. Haller, R. West, and J. J. Michl (1984). Tetramesitylcyclodisiloxane: a cyclic siloxane with an unusual structure. *J. Amer. Chem. Soc.* **106**, 822–23.

Fischer, B., R. A. Pollak, T. H. DiStefano, and W. D. Grobman (1977). Electronic structure of SiO_2, $Si_xGe_{1-x}O_2$, and GeO_2 from photoemission spectroscopy. *Phys. Rev.* **B15**, 3193–99.

Fischer, D. W. (1972). X-ray band spectra and MO structure of rutile, TiO_2. *Phys. Rev.* **B5**, 4219–26.

Fjeldberg, T., G. Gundersen, T. Jonvik, H. M. Seip, and S. Saebo (1980). *Ab initio* studies of some trivalent boron compounds with boron–oxygen and boron–nitrogen bonds. *Acta. Chem. Scand.* **A34**, 547–65.

Fleischer, U., M. Schindler, and W. Kutzelnigg (1987). Magnetic properties in terms of localized quantities. VI. Small hybrides, fluorides and homonuclear molecules of phosphorous and silicon. *J. Chem. Phys.* **86**, 6337–47.

Fluck, E., and D. Weber (1975). Röntgen-photoelektron in spektroskopie und ihre anwendungen der phosphorchemie (German). *Pure Appl. Chem.* **44**, 373–91.

Folkerts, W., G. A. Sawatzky, C. Haas, R. A. de Groot, and F. U. Hillebrecht (1987). Electronic structure of some 3*d* transition-metal pyrites. *J. Phys. C* **20**, 4135–44.

Folmer, J. C. W., and F. Jellinek (1980). The valence of copper in sulphides and selenides: an x-ray photoelectron spectroscopy study. *J. Less Common Metals* **76**, 153–62.

Fomichev, V. A., T. M. Zimkina, and I. I. Zhukova (1969). Investigation of the energy structure of MgO by ultrasoft x-ray spectroscopy. *Sov. Phys. Solid State* **10**, 2421–27.

Forty, A. J. (1983). The structure and chemistry of crystal surfaces. *Contemp. Phys.* **24**, 271–99.

Fowler, W. B. (1981). Implications of an ionic model for SiO_2. *J. Phys. Chem. Solids* **42**, 623–29.

Freidman, S. P., and V. A. Gubanov (1983). Electronic structure of the 3*d* metal monosulphides by the $X\alpha$ discrete variational method. *J. Phys. Chem. Sol.* **44**, 187–94.

Freuh, A. J., Jr. (1954). The use of zone theory in problems of sulfide mineralogy. *Geochim. Cosmochim. Acta* **6**, 79–89.

Freund, F. (1981). Mechanism of the water and carbon dioxide solubility of oxides and silicates and the role of O^-. *Contrib. Mineral. Petrol.* **76**, 474–82.

Friedrich, H., B. Pittel, P. Rabe, W. H. E. Schwarz, and B. Sonntas (1980). Overlapping core to valence and core to Rydberg transitions and resonances in the XUV spectra of SiF_4. *J. Phys. B. (Atom. Molec. Phys.)* **13**, 25–30.

Fripiat, J. G., P. Galet, J. Delhallo, J. M. Andre, J. B. Nagy, and E. G. Derouane (1985). A nonempirical molecular orbital study of the siting and pairing of aluminium in ferrierite. *Phys. Chem.* **89**, 1932–37.

Fujimori, A., M. Saeki, N. Kimizuka, M. Taniguchi, and S. Suga (1986). Photoemission satellites and electronic structure of Fe_2O_3. *Phys. Rev.* **B34**, 7318–28.

Fujino, K., S. Sasaki, Y. Takeguchi, and R. Sadanaga (1981). X-ray determination of electron distributions in forsterite, fayalite and tephroite. *Acta. Cryst.* **B37**, 513–18.

Fyfe, C. A., G. C. Gobbi, J. S. Hartman, R. E. Lenkinski, J. H. O'Brien, E. R. Beangre, and M. A. R. Smith (1982). High resolution solid state MAS spectra of ^{29}Si, ^{27}Al, ^{11}B and other nuclei in inorganic systems using a narrow bore 400 MHz high resolution NMR spectrometer. *J. Mag. Res.* **47**, 168–73.

Fyfe, W. S. (1954). The problem of bond type. *Amer. Mineral.* **39**, 991–1005.

Gaffney, E. S., and T. J. Ahrens (1970). Stability of mantle minerals from lattice calculations and shock wave data. *Phys. Earth Planet. Inter.* **3**, 305–12.

Gaffney, J. S., and D. L. Anderson (1973). Effect of low-spin Fe^{2+} on the composition of the lower mantle. *J. Geophys. Res.* **78**, 7005–14.

Gajhede, M. (1985). *Ab initio* electric field gradient calculations for a series of oxygen-containing boron compounds. *Chem. Phys. Lett.* **120**, 266–71.

Gajhede, M., S. Larsen, and S. Retrup (1986). Electron density of orthoboric acid determined by x-ray diffraction at 105 K and *ab initio* calculations. *Acta. Cryst.* **B42**, 545–52.

Galeener, F. L. (1982a). Planar rings in glasses. *Solid State Comm.* **44**, 1037–40.

Galeener, F. L. (1982b). Planar rings in vitreous silica. *J. Non-Cryst. Solids* **49**, 53–62.

Garofalini, S. H. (1983). A molecular dynamic simulation of the vitreous silica surface. *J. Chem. Phys.* 2069–72.

Garofalini, S. H. (1984a). Defect species on vitreous silica-*a* molecular dynamics simulation. *J. Noncryst. Solids* **63**, 337–45.

Garofalini, S. H. (1984b). Molecular dynamics simulation of the frequency spectrum of amorphous silica. *J. Chem. Phys.*, 3189–92.

Geisinger, K., and G. V. Gibbs (1981). SiSSi and SiOSi bonds in molecules and solids: a comparison. *Phys. Chem. Minerals* **7**, 204–10.

Geisinger, K. L., G. V. Gibbs, and A. Navrotsky (1985). A molecular orbital study of bond length and angle variations in framework structures. *Phys. Chem. Minerals* **11**, 266–83.

Geisinger, K. L., M. A. Spackman, and G. V. Gibbs (1987). Exploration of structure, electron density distribution and bonding in coesite with Fourier and pseudoatom refinement methods using single-crystal x-ray diffraction data. *J. Phys. Chem.* **91**, 3237–44.

Geissberger, A. E., and P. J. Bray (1983). Determination of structure and bonding in amorphous SiO_2 using ^{17}O NMR. *J. Non-Cryst. Solids* **54**, 121–37.

Gerard, A., P. Imbert, H. Prange, F. Varret, and M. Wintenberger (1972). Fe^{2+} impurities, isolated and in pairs, in ZnS and CdS studied by the Mössbauer effect. *J. Phys. Chem. Solids* **32**, 2091–100.

Gerstein, B. C. (1973). Chemistry, bands, bonds and solids, a translator's notes. *J. Chem. Edu.* **50**, 316–22.

Giaquinta, P. V., M. P. Tosi, and N. H. March (1983). Coordination chemistry and ionic solvation in divalent metal halide aqueous solutions. *Phys. Chem. Liq.* **13**, 1–24.

Gibbs, G. V. (1982). Molecules as models for bonding in silicates. *Amer. Mineral.* **67**, 421–50.

Gibbs, G. V., L. W. Finger, and M. B. Boisen, Jr. (1987). Molecular mimicry of the bond length–bond strength variations in oxide crystals. *Phys. Chem. Minerals* **14**, 327–31.

Gibbs, G. V., E. P. Meagher, M. D. Newton, and D. K. Swanson (1981). A comparison of experimental and theoretical bond length and angle variations for minerals, inorganic solids and molecules. In: *Structure and Bonding in Crystals,* Vol. I (M. O'Keeffe and A. Navrotsky, eds.) New York: Academic Press, pp. 195–226.

Gibbs, G. V., E. P. Meagher, J. V. Smith, and J. J. Pluth (1977). Molecular orbital calculations for atoms in the tetrahedral frameworks of zeolites. *ACS Symposium Series,* No. 40, *Molecular Sieves-II* (J. R. Katzer, ed.). ACS, pp. 19–29.

Gignac, W. J., R. S. Williams, and S. P. Kowalczyk (1985). Valence- and conduction-band structure of the sapphire (1102) surface. *Phys. Rev.* **B32**, 1237–42.

Gilbert, T. L. (1972). Multiconfiguration self-consistent-field theory for localized orbitals. I. The orbital equation. *Phys. Rev.* **A6**, 580–600.

Gilbert, T. L., W. J. Stevens, H. Schrenk, M. Yoshimine, and P. S. Gagus (1973). Chemical bonding effects in the oxygen $K\alpha$ x-ray emission bands of silica. *Phys. Rev.* **B8**, 5977–98.

Gillespie, R. J. (1960). Bond angles and the spatial correlation of electrons. *J. Amer. Chem. Soc.* **82**, 5978–83.

Gillespie, R. J. (1972). *Molecular Geometry.* London: Van Nostrand–Rheinhold.

Gimarc, B. M. (1979). *Molecular Structure and Bonding, The Qualitative Molecular Orbital Approach.* New York: Academic Press.

Giordan, J. C., J. H. Moore, and J. A. Tossell (1986). Anion states of organometallic molecules and their ligands. *Acc. Chem. Res.* **19**, 281–86.

Goddard, W. A. (1985). Theoretical chemistry comes alive: full partner with experiment. *Science* **227**, 917–23.

Godwal, B. K., S. K. Sikka, and R. Chidambaram (1983). Equation of state theories of condensed matter up to about 10 TPa. *Phys. Rept.* **102**, 121–97.

Gofman, M. M., V. A. Andreev, and V. I. Nefedov (1986). Relative intensities in x-ray photoelectron spectra. Part XI. Calculation of photoionization cross sections for valence levels of SiF_4. *J. Electron Spectrosc. Relat. Phenom.* **37**, 375–87.

Goldschmidt, V. M. (1926). *Geochemische Verteilungsgesetze der Elemente.* Oslo: Skrifter Norske Videnskaps Akad Oslo I. Mat-Naturv. Kl.

Goldschmidt, V. M. (1932). *Zeit. Phys. Chem.* **B17**, 172.

Goldschmidt, V. M. (1937). The principles of distribution of chemical elements in minerals and rocks. *J. Chem. Soc. Lond.,* 655–73.

Goldschmidt, V. M. (1954). *Geochemistry.* London: Oxford Univ. Press.

Goodgame, M. M., and W. A. Goddard III (1982). Nature of Mo–Mo and Cr–Cr multiple bonds: a challenge for the local-density approximation. *Phys. Rev. Lett.* **48**, 135–38.

Goodgame, M. M., and W. A. Goddard III (1985). Modified generalized valence-bond method: a simple correction for the electron correlation missing in generalized valence-bond wave functions: prediction of double-well states for Cr_2 and Mo_2. *Phys. Rev. Lett.* **54**, 661–64.

Goodenough, J. B. (1967). Description of transition metal compounds: application to several sulfides. In: *Propriétés Thermodynamiques Physiques et Structurales des Dérivés Semi-metalliques.* Paris: Centre National de la Recherche Scientifique, pp. 263–92.

Goodenough, J. B. (1969). Descriptions of outer *d* electrons in thiospinels. *J. Phys. Chem. Solids* **30**, 261–80.

Goodenough, J. B. (1971). Metallic oxides. *Prog. Solid State Chem.* **5**, 145–399.

Goodenough, J. B. (1972). Energy bands in TX_2 compounds with pyrite, marcasite and arsenopyrite structures. *J. Solid State Chem.* **5**, 144–52.

Gopalakrishnan, J., T. Murugesan, M. S. Hegde, and C. N. R. Rao (1979). Study of transition-metal monosulfides by photoelectron spectroscopy. *J. Phys. C. (Solid State Phys.)* **12**, 5255–61.

Gordon, R. C., and Y. S. Kim (1972). Theory for the forces between closed shell atoms and molecules. *J. Chem. Phys.* **56**, 3122–33.

Goto, T., R. J. Ahrens, G. R. Rossman, and Y. Syono (1980). Absorption spectrum of shock compressed Fe^{2+} bearing MgO and the radiative conductivity of the lower mantle. *Phys. Earth Plan. Int.* **22**, 277–88.

Graddon, D. P. (1968). *An Introduction to Coordination Chemistry* (2nd ed.) Oxford: Pergamon.

Grandke, T., L. Ley, and M. Cardona (1978). Angle-resolved uv photoemission and electronic band structures of the lead chalcogenides. *Phys. Rev.* **B18**, 3847–71.

Grant, F. A. (1959). Properties of rutile (titanium dioxide). *Rev. Mod. Phys.* **31**, 646–74.

Grant, J. T. (1982). Surface analysis with Auger electron spectroscopy. *Appl. Surf. Sci.* **13**, 35–62.

Greaves, G. N., A. Fontaine, P. Lagarde, and D. Raoux (1981). Local structure around sodium in glass. In: *EXAFS for Inorganic Systems* (C. D. Garner and S. S. Hasnain, eds.) SERC Daresbury Laboratory Publication.

Greenwood, N. N., and T. C. Gibb (1971). *Mössbauer Spectroscopy.* New York: McGraw-Hill.

Gresch, R., W. Muller-Warmuth, and H. Dutz (1979). X-ray photoelectron spectroscopy of sodium phosphate glasses. *J. Noncryst. Solids* **34**, 127–36.

Griffith, W. P. (1969). Raman studies on rock-forming minerals. Part I. Orthosilicates and cyclosilicates. *J. Chem. Soc. A,* 1372–77.

Griffith, W. P. (1975). Raman spectroscopy of terrestrial minerals. In: *Infrared and Raman Spectroscopy of Lunar and Terrestrial Minerals* (C. Karr, Jr., ed.). New York: Academic Press.

Grigoras, S., and T. H. Lane (1987). *Ab initio* calculations on the effect of polarization functions of disiloxane. *J. Comput. Chem.* **8**, 84–93.

Grimsditch, M. (1984). Polymorphism in amorphous SiO_2. *Phys. Rev. Lett.* **52**, 2379.

Griscom, D. L. (1977). The electronic structure of SiO_2: A review of recent spectroscopic and theoretical advances. *J. Noncryst. Solids* **24**, 155–234.

Griscom, D. L. (1978). Borate glass structure. In: *Borate Glasses: Structure, Properties and Applications* (L. D. Pye, V. D. Frechett, and N. J. Kreidl, eds.) New York: Plenum.

Guenzburger, D., B. Maffeo, and M. O. DeSiquiera (1977). Electronic structure and related properties of ferrocyanide ion calculated by the SCF-$X\alpha$ scattered wave method. *J. Phys. Chem. Solids* **38**, 35–39.

Guenzburger, D., E. M. B. Saitovitch, M. A. DePaoli, and H. Manelo (1984). On the photofragmentation of $Fe(CO)_5$. II. Molecular orbital studies of $Fe(CO)_n$, $1 \geq n \geq 5$. *J. Chem. Phys.* **80**, 735–44.

Gunnarsson, O., J. Harris, and R. O. Jones (1977). Density functional theory and molecular binding. I. First-row diatomic molecules. *J. Chem. Phys.* **67**, 3970–79.

Gupta, A., and J. A. Tossell (1981). A theoretical study of bond distances, x-ray spectra and electron density distributions in borate polyhedra. *Phys. Chem. Mineral.* **7**, 159–64.

Gupta, A., and J. A. Tossell (1983). Quantum mechanical studies of distortions and polymerization of borate polyhedra. *Amer. Mineral.* **68**, 989–95.

Gupta, A., D. K. Swanson, J. A. Tossell, and G. V. Gibbs (1981). Calculation of bond distances, one-electron energies and electron density distributions in first-row tetrahedral hydroxy and oxyanions. *Amer. Mineral.* **66**, 601–9.

Gurr, G. E., P. W. Montgomery, C. D. Knutson, and B. T. Gorres (1970). The crystal structure of trigonal diboron trioxide. *Acta. Cryst.* **B26**, 906–15.

Hall, M. B. (1986). Charge densities in simple molecules and metal complexes. *Chem. Scripta* **26**, 389–94.

Hall, M. B., M. F. Guest, I. H. Hillier, D. R. Lloyd, A. F. Orchard, and A. W. Potts (1972). On the assignment of the He I photoelectron spectrum of silicon tetrafluoride. *J. Electron. Spectrosc. Relat. Phenom.* **1**, 497–99.

Ham, F. S., and G. A. Slack (1971). Infra-red absorption and luminescence spectra of Fe^{2+} in cubic ZnS: role of the Jahn-Teller coupling. *Phys. Rev.* **48**, 777–95.

Hamajima, T., T. Kambara, K. I. Gondaira, and T. Oguchi (1981). Self-consistent electronic structures of magnetic semiconductors by a discrete variational $X\alpha$ calculation III. Chalcopyrite $CuFeS_2$. *Phys. Rev.* **B24**, 3349–53.

Harris, S. (1982). Study of the electronic structure of first and second row transition metal sulfides using SCF-SW-$X\alpha$ cluster calculations. *Chem. Phys.* **67**, 229–37.

Harris, S., and R. R. Chianelli (1984). Catalysis by transition metal sulfides: the relation between calculated electronic trends and HDS activity. *J. Catalysis* **86**, 400–12.

Harrison, W. (1976). Surface reconstruction on semiconductors. *Surf. Sci.* **55**, 1–19.

Harrison, W. (1980). *Electronic Structure and the Properties of Solids.* San Francisco: W.H. Freeman & Co.

Hartmann, E., and R. Szargan (1979). SCF-$X\alpha$ SW calculation of chemical shifts of x-ray and electron emission lines and relaxation properties of SiX_4 molecules. *Chem. Phys. Lett.* **68**, 175–78.

Hasnain, S. S. (1981). Instrumentation for EXAFS and facilities at the SRS. In: *EXAFS for Inorganic Systems* (C. D. Garner and S. S. Hasnain, eds.). SERC Daresbury Laboratory Publication.

Hass, E. C., P. G. Mezey, and P. J. Plath (1981). A nonempirical molecular orbital study on Lowenstein's rule and zeolite composition. *J. Molec. Struct.* **76**, 389–99.

Hathaway, K. B., H. J. F. Jansen, and A. J. Freeman (1985). Total-energy local-spin-density approach to structural and electronic properties of ferromagnetic iron. *Phys. Rev.* **B31**, 7603–11.

Hawthorne, F. C. (1988) (ed.) *Spectroscopic Methods in Mineralogy and Geology. Reviews in Mineralogy,* Vol. 18. Min. Soc. America.

Hay, P. J., and W. R. Wadt (1985). *Ab initio* effective core potentials for molecular calculations, potentials for the transition metal atoms Sc to Hg. *J. Chem. Phys.* **82**, 270–83 [and two following papers].

Hayashi, Y. (1968). Sci. Rep. Thoku Univ. Ser. 1:51:43 (reproduced in Joyner and Hercules, 1980).

Haycock, D., M. Casrai, and D. S. Urch (1978). Electronic structure of molybdenum disulphide: angle resolved x-ray spectroscopy. *Japan J. Appl. Phys.* **17**, 138–40.

Hazen, R. M. (1976). Effects of temperature and pressure on the crystal structure of forsterite. *Amer. Mineral.* **61**, 1280–93.

Hazen, R. M., and L. W. Finger (1982). *Comparative Crystal Chemistry.* New York: Wiley.

Hazen, R. H., H. K. Mao, and P. M. Bell (1977). *Proc. 8th Lunar Sci. Conf.,* Oxford: Pergamon Press.

Hedelman, S., and W. N. Mitchell (1968). Some new diffuse and specular reflectance accessories for the Cary models 14 and 15 spectrophotometer. In:

Modern Aspects of Reflectance Spectroscopy (W. Wendlandt, ed.) New York: Plenum Press.

Hedin, L., and B. I. Lundquist (1971). Explicit local exchange-correlation potentials. *J. Phys. C. (Solid St. Phys.)* **4**, 2064–83.

Hehre, W. J., L. Radom, P. V. R. Schleyer, and J. A. Pople (1986). *Ab Initio Molecular Orbital Theory.* New York: Wiley.

Heicklen, J., and V. Knight (1964). The infrared spectrum of SiF_4. *Spectrochim. Acta* **20**, 295–98.

Heijser, W., A. Th. van Kessel, and E. J. Baerends (1976). Self-consistent molecular Hartree–Fock–Slater calculations. IV. On electron densities, spectroscopic constants and proton affinities of some small molecules. *Chem. Phys.* **16**, 371–79.

Heine, V. (1980). Electronic structure from the point of view of the local atomic environment. *Solid State Physics: Advances in Research and Applications,* Vol. 35 (F. Seitz, D. Turnbull, and H. Ehrenreich, eds.). New York: Academic Press, p. 1.

Heinzinger, K. (1985). Computer simulations of aqueous electrolyte solutions. *Physica* **131B&C**, 196–216.

Helgeson, H. C., and D. H. Kirkham (1974). Theoretical prediction of the thermodynamic behaviour of aqueous electrolytes at high pressures and temperatures, I. Summary of the thermodynamic/electrostatic properties of the solvent. *Amer. J. Sci.* **274**, 1089–198.

Hemley, R. J., and R. G. Gordon (1985). Theoretical study of solid NaF and NaCl at high pressures and temperatures. *J. Geophys. Res.* **B90**, 7803–13.

Hemley, R. J., M. D. Jackson, and R. G. Gordon (1985). First principles theory for the equations of state of minerals at high temperature and pressure. *Geophys. Res. Lett.* **12**, 247–50.

Hemley, R. J., M. D. Jackson, and R. G. Gordon (1987). Theoretical study of the structure, lattice dynamics, and equations of state of perovskite-type $MgSiO_3$ and $CaSiO_3$. *Phys. Chem. Mineral.* **14**, 2–12.

Hemley, R. J., H. K. Mao, P. M. Bell, and B. O. Mysen (1986). Raman spectroscopy of SiO_2 glass at high pressure. *Phys. Rev. Lett.* **57**, 747–54.

Hemstreet, L. A., Jr. (1975). Cluster calculations of the effect of single vacancies on the electronic properties of PbS. *Phys. Rev.* **B11**, 2260–70.

Henrich, V. E. (1979). Ultraviolet photoemission studies of molecular adsorption on oxide surfaces. *Prog. Surf. Sci.* **9**, 143–64.

Henrich, V. E. (1983). The nature of transition-metal–oxide surfaces. *Prog. Surf. Sci.* **14**, 175–200.

Henrich, V. E. (1985). The surfaces of metal oxides. *Rep. Prog. Phys.* **48**, 1481–541.

Henrich, V. E. (1987). Electron spectroscopic studies of perfect and defect metal oxide surfaces. *Phys. Chem. Mineral.* **14**, 396–400.

Henrich, V. E., G. Dresselhaus, and H. J. Zeiger (1980). Energy-dependent electron-energy-loss spectroscopy: Application to the surface and bulk electronic structure of MgO. *Phys. Rev.* **B22**, 4764–75.

Henrich, V. E., and R. L. Kurtz (1981). Surface electronic structure of TiO_2: atomic geometry, ligand coordination, and the effect of adsorbed hydrogen. *Phys. Rev.* **B23**, 6280–87.

Herman, F., R. L. Kortum, C. D. Kuglia, and J. L. Shay (1967). In: II-VI *Semi-*

conducting Compounds, 1967 International Conference (D. G. Thomas, ed.) New York: W.A. Benjamin, Inc., p. 503.

Herman, F., R. L. Kortum, I. B. Ortenburger, and J. P. Van Dyke (1968). Relativistic band structure of GeTe, SnTe, PbTe, PbSe and PbS. *J. Physique (Paris)* **29**, C4–C62.

Hermansson, K., J. Lindgren, and H. Agren (1986). Theoretical studies of IR intensities of $Zn^{2+}OH_2$ and $Mg^{2+}OH_2$. *Molec. Phys.* **57**, 857–63.

Hess, A. C., P. F. McMillan, and M. O'Keeffe (1986). Force fields for SiF_4 and H_4SiO_4: *ab initio* molecular orbital calculations. *J. Phys. Chem.* **90**, 5661–65.

Hess, A. C., P. F. McMillan, and M. O'Keeffe (1987). *Ab initio* force field of the S_4 conformation of H_4SiO_4. *J. Phys. Chem.* **91**, 1395–96.

Hess, A. C., P. F. McMillan, and M. O'Keeffe (1988). Torsional barriers and force fields in H_4TO_4 molecules and molecular ions (T = C, B, Al, Si). *J. Phys. Chem.* **92**, 1785–91.

Hildenbrand, D. L. (1972). Gaseous equilibrium Ge + SiO = GeO + Si and the dissociation energy of SiO. *High Temp. Sci.* **4**, 244–47.

Himpsel, F. J. (1983). Angle-resolved measurements of the photoemission of electrons in the study of solids. *Adv. Phys.* **32**, 1–51.

Hinchliffe, A. (1988). *Computational Quantum Chemistry.* New York: Wiley.

Hinkel, V., H. Haak, C. Mariani, L. Sarba, K. Horn, and N. E. Christensen (1989). Investigation of the bulk band structure of IV-VI compound semiconductors PbSe, PbTe. *Phys. Rev.* **B40**, 5549–56.

Hirshfeld, F. L., and S. Rzotkiewicz (1974). Electrostatic binding in the first row AH and A_2 diatomic molecules. *Molec. Phys.* **27**, 1319–43.

Hobza, P., J. Sauer, G. Morgeneyer, J. Hurych, and R. Zahradnik (1981). Bonding ability of surface sites in silica and their effect on hydrogen bonds. A quantum-chemical and statistical thermodynamics treatment. *J. Phys. Chem.* **85**, 4061–67.

Hoffman, R. (1963). An extended Hückel theory. I. Hydrocarbons. *J. Chem. Phys.* **39**, 1397–412.

Hoffman, R. (1982). Building bridges between inorganic and organic chemistry. *Angew. Chem. (Int. Ed. Engl.)* **21**, 711–24.

Hoffman, R. (1986). The close ties between organometallic chemistry, surface science and the solid state. *Pure Appl. Chem.* **58**, 481–94.

Hoffman, R., and W. N. Lipscomb (1962). Theory of polyhedral molecules. I. Physical factorization of the secular equation. II. A crystal field model. *J. Chem. Phys.* **36**, 2179–95.

Hohenberg, P., and W. Kohn (1964). Inhomogenous electron gas. *Phys. Rev.* **B136**, 864–71.

Hohl, D., R. O. Jones, R. Car, and M. Parrinello (1988). Structure of sulfur clusters using simulated annealing: S_2 to S_{13}. *J. Chem. Phys.* **89**, 6823–35.

Hosono, H. H. Kawazoe, and T. Kanazaw (1979). ESR and optical absorption of Cu^{2+} in Na_2O–SiO_2 glasses. *J. Noncryst. Solids* **33**, 103–15.

Hotokka, M., and P. Pyykkö (1989). An *ab initio* study of bonding trends in the series BO_3^{3-}, CO_3^{2-}, NO_3^- and O_4 (D_{3h}). *Chem. Phys. Lett.* **157**, 415–18.

Hubner, K. P. (1972). Constants of diatomic molecules. In: *Amer. Inst. Phys. Handbook.* New York: McGraw-Hill.

Hufner, S., and G. K. Wertheim (1973). X-ray photoelectron band structure of some transition metal compounds. *Phys. Rev.* **B8**, 4857–67.

Huheey, J. E. (1983). *Inorganic Chemistry: Principles of Structure and Reactivity.* 3rd ed. New York: Harper and Row.

Hulliger, F., and E. Mooser (1965). Semiconductivity in pyrite, marcasite and arsenopyrite phases. *J. Phys. Chem. Solids* **26**, 429–33.

Huntress, W., Jr., and L. Wilson (1972). An ESCA study of lunar and terrestrial minerals. *Earth Plan. Sci. Lett.* **15**, 59–64.

Hybertsen, M. S., and S. G. Louie (1987). Theory and calculation of quasiparticle energies and band gaps. *Comments Cond. Mat. Phys.* **5**, 223–47.

Ibach, H. (ed.) (1977). *Electron Spectroscopy for Surface Analysis.* Berlin: Spinger–Verlag.

Iguchi, Y. (1974). Silicon $L_{2,3}$ emission and photoelectric yield spectra of Mg_2SiO_4, Fe_2SiO_4, and Ni_2SiO_4. *Phys. Fem.* **9**. Suppl. 51, 162–63.

Iishi, K. (1978). Lattice dynamics of forsterite. *Amer. Mineral.* **63**, 1198–208.

Irish, D. E. (1971). Vibrational spectral studies of electrolyte solutions and fused salts. In: *Ionic Interactions: from dilute solutions to fused salts,* Vol. 2 (S. Petrrucci, ed.), New York: Academic, pp. 188–258.

Izumitani, T., and S. Hirota (1985). Fundamental absorption of glasses in the vacuum ultraviolet region. *J. Non-Cryst. Sol.* **73**, 255–63.

Jackson, M. D., and G. V. Gibbs (1988). A modeling of the coesite and feldspar framework structure types of silica as a function of pressure using modified electron gas methods. *J. Phys. Chem.* **92**, 540–45.

Jackson, M. D., and R. G. Gordon (1988a). Electron-gas theory of some phases of magnesium oxide. *Phys. Rev.* **B38**, 5654–60.

Jackson, M. D., and R. G. Gordon (1988b). MEG investigation of low pressure silica-shell model for polarization. *Phys. Chem. Mineral.* **16**, 212–20.

Jameson, C. J., and A. K. Jameson (1988). Absolute shielding scale for ^{29}Si. *Chem. Phys. Lett.* **149**, 300–5.

Janes, N., and E. Oldfield (1986). Oxygen-17 NMR study of bonding in silicates; The *d*-orbital controversy. *J. Amer. Chem. Soc.* **108**, 5743–53.

Jansen, H. J. F., and A. J. Freeman (1984). Total-energy full-potential linearized augmented-plane-wave method for bulk solids: Electronic and structural properties of tungsten. *Phys. Rev.* **B30**, 561–69.

Jeanloz, R., T. J. Ahrens, H. K. Mao, and P. M. Bell (1979). *B*1–*B*2 transition in calcium oxide from shock-wave and diamond-cell experiments. *Science* **206**, 829–30.

Jeanloz, R., and A. B. Thompson (1983). Phase transitions and mantle discontinuities. *Rev. Geophys. Space Phys.* **21**, 51–74.

Jellison, G. E., Jr., L. W. Panek, P. J. Bray, and G. B. Rouse, Jr. (1977). Determination of structure and bonding in vitreous B_2O_3 by means of ^{10}B, ^{11}B and ^{17}O NMR. *J. Chem. Phys.* **66**, 802–12.

Jen, J. S., and M. R. Kalinowski (1989). An ESCA study of the bridging to nonbridging oxygen ratio in sodium silicate glass and the correlations to glass density and refractive index. *J. Noncryst. Solids* **38–39**, 21–26.

Jensen, W. B. (1980). *The Lewis Acid-Base Concepts: An Overview.* New York: Wiley.

Joffre, J., P. Geneste, and D. A. Lerner (1986). A quantum chemical study of site modeling for the adsorption and desulfurization of thiophene. *J. Catalysis* **97**, 543.

John, I. G., G. B. Bacskay, and N. S. Hush (1980). Finite field method calculations. VI. Raman scattering activities, infrared absorption intensities and higher order moments: SCF and CI calculations for the isotopic derivatives of H_2O and SCF calculations for CH_4. *Chem. Phys.* **51**, 49–60.

Johnson, K. H. (1973). Scattered-wave theory of the chemical bond. *Adv. Quant. Chem.* **7**, 143–85.

Johnson, K. H. (1975). Quantum Chemistry. *Ann. Rev. Phys. Chem.* **26**, 39.

Johnson, M. L., and R. Jeanloz (1983). A Brillouin-zone model for compositional variation in tetrahedrite. *Amer. Mineral.* **68**, 220–26.

Jolly, W. L. (1983). Analysis of $p\pi \rightarrow p\pi$ bonding in halogen compounds of silicon, germanium, and tin. *Chem. Phys. Lett.* **100**, 546–48.

Jonas, A. E., G. K. Schweitzer, F. A. Grimm, and T. A. Carlson (1972). The photoelectron spectra of the tetrafluoro and tetramethyl compounds of the group IV elements. *J. Electron Spectrosc. Relat. Phenom.* **1**, 29–66.

Jones, W., J. M. Thomas, R. K. Thorpe, and M. J. Tricker (1978). Conversion electron Mössbauer spectroscopy and the study of surface properties and reactions. *Appl. Surf. Sci.* **1**, 388–407.

Joyner, D., and D. Hercules (1980). Chemical bonding and electronic structure of B_2O_3, H_3BO_3 and BN; an ESCA, Auger, SIMS and SXS study. *J. Chem. Phys.* **72**, 1095–108.

Julg, A., and D. Letoquart (1978). Modifications of certain properties of carbonate and nitrate ions due to the influence of the crystalline environment. *Nouv. J. Chim.* **1**, 261–63.

Kahn, A. (1983). Semiconductor surface structures. *Surf. Sci. Reports* **3**, 193–300.

Kane, P. F., and G. R. Larrabee (1974). *Characterisation of Solid Surfaces*. New York: Plenum Press.

Kawazoe, H., H. Hosono, and T. Kanazawa (1978a). Electronic structure and properties of oxide glasses (I) π-electron distribution of alkali borate glass networks. *J. Noncryst. Solids* **29**, 159–71.

Kawazoe, H., H. Hosono, and T. Kanazawa (1978b). Electronic structure and properties of oxide glasses (II). Basicity measured by copper (II) ion probe in Na_2O-P_2O_5, K_2O-B_2O_3 and K_2SO_4-$ZnSO_4$ glasses. *J. Noncryst. Solids* **29**, 173–86.

Keller, P. R., J. W. Taylor, F. A. Grimm, P. Senn, T. A. Carlson, and M. O. Krause (1983). Angle-resolved photoelectron measurements on the $2p$ orbitals of Si in SiF_4 and $Si(CH_3)_4$ in the gas phase. *Chem. Phys.* **74**, 247–51.

Kenton, A. C., and M. W. Ribarsky (1981). *Ab initio* calculations on hydrogen-bonded silicon clusters. *Phys. Rev.* **B23**, 2897–910.

Keys, J. D., J. L. Horwood, T. M. Baleshta, L. J. Cabri, and D. C. Harris (1968). Iron–iron interaction in iron-containing zinc sulfide. *Canad. Mineral.* **9**, 453–67.

Khan, M. A. (1976). Energy bands in pyrite-type crystals. *J. Phys. Ser. C.* **9**, 81–94.

Khanna, R. K., D. D. Stranz, and B. Donn (1981). A spectroscopic study of intermediates in the condensation of refractory smokes: matrix isolation experiments on SiO. *J. Chem. Phys.* **74**, 2108–15.

Kiefer, S. W. (1979). Thermodynamics and lattice vibrations of Minerals. I. Mineral heat capacities and their relationships to simple lattice vibrational models. *Rev. Geophys. Space Phys.* **17**, 1–19.

Kinase, W., M. Tanaka, and H. Nomura (1979). Birefringence of $CaCO_3$ and electronic polarizabilities of the constituent ions. *J. Phys. Soc. Jpn.* **47**, 1375–76.

Kirfel, A., G. Will, and R. F. Stewart (1983). The chemical bonding in lithium metaborate, $LiBO_2$. Charge densities and electrostatic properties. *Acta. Cryst.* **B39**, 175–85.

Kistenmacher, H., H. Popkie, and C. Clementi (1974). Study of the structure of molecular complexes. VIII. Small clusters of water molecules surrounding Li^+, Na^+, K^+, F^- and Cl^-. *J. Chem. Phys.* **61**, 800–15.

Kitaura, K., C. Satoko, and K. Morokuma (1979). Total energies of molecules with the local density functional approximation and Gaussian basis sets. *Chem. Phys. Lett.* **65**, 206–11.

Klein, M. L. (1985). Computer simulation studies of solids. *Ann. Rev. Phys. Chem.* **36**, 525–48.

Kohn, W., and L. J. Sham (1965). Self-consistent equations including exchange and correlation effects. *Phys. Rev.* **A140**, 1133–38.

Kollman, P. A., and I. D. Kuntz (1972). Studies of cation hydration. *J. Amer. Chem. Soc.* **94, 9237–38.**

Konig, E. (1971). The nephelauxitic effect: calculation and accuracy of interatomic repulsion parameters in cubic high spin d^2, d^3, d^7, and d^8 systems. *Struct. Bonding* **9**, 175–211.

Konijnendijk, W. L., and J. M. Stevels (1976). The structure of borosilicate glasses studied by Raman scattering. *J. Noncryst. Solids* **20**, 193–224.

Konovalov, S. P., and V. G. Solomonik (1983). Theoretical study of the electronic and geometric structure, force fields and vibrational spectra of free BO_2^-, NO_3^- and CO_3^{2-} ions. *Russ. J. Phys. Chem.* **57**, 384–86.

Koopmans, T. (1933). Uber die Zuordnung von wellenfunktinen und eigenwerten zu den einzelnen elecktronen eines atoms. *Physica* **1**, 104–13.

Koput, J. (1990). *Ab initio* study of the molecular structure and potential energy surface of disiloxane. *Chem. Phys.* **148**, 299–308.

Koster, A. S., and H. Mendel (1970). X-ray *K* emission spectra and energy levels of compounds of 3*d* transition metals. I. Oxides. *J. Phys. Chem. Solids* **31**, 2511–22.

Koto, K., and N. Morimoto (1975). Superstructure investigation of bornite, Cu_5FeS_4, by the modified partial Patterson function. *Acta Cryst.* **31B**, 2268–73.

Kowalczyk, S. P., F. R. McFeely, L. Ley, V. T. Gritsyna, and D. A. Shirley (1977). The electronic structure of $SrTiO_3$ and some simple related oxides (MgO, Al_2O_3, SrO, TiO_2). *Solid State Comm.* **23**, 161–69.

Kroner, J., D. Nolle, and H. Noth (1973). Photoelectron spectroscopic investigations on boron compounds. I. Orbital sequence and charge densities of methylthio and methyoxyboranes. *Zeit. fur Naturforsch.* **28b**, 416–25.

Kruh, R. .F., and C. L. Standley (1962). An x-ray diffraction study of aqueous zinc chloride solutions. *Inorg. Chem.* **1**, 941–43.

Kudo, T., and S. Nagase (1985). Theoretical study on the dimerization of silanone and the properties of the polymeric products $(H_2SiO)_n$ ($n = 2, 3$, and 4). Comparison with dimers of $(H_2SiS)_2$ and $(H_2CO)_2$. *J. Amer. Chem. Soc.* **107**, 2589–95.

Kuharski, R. A., and P. J. Rossky (1984). Quantum mechanical contributions to the structure of liquid water. *Chem. Phys. Lett.* **103**, 357–62.

Kumazawa, M., and O. L. Anderson (1969). Elastic moduli, pressure derivatives, and temperature derivatives of single crystal olivine and single crystal forsterite. *Journ. Geophys. Rs.* **74**, 5961–72.

Kunz, A. B., and G. T. Surratt (1978). A self-consistent energy band study of FeO, CoO, and NiO. *Solid State Comm.* **25**, 9–12.

Kuroda, Y., and Y. Iguchi (1971). A soft x-ray study of olivines. *Min. Soc. Japan Spec. Pap.* **1**, 247–49.

Kutzelnigg, W. (1984). Chemical bonding in higher main group elements. *Angew. Chem. Int.* (Engl. Ed.) **23**, 272–95.

Kutzler, F. W., C. R. Natoli, D. K. Misemer, S. Doniach, and K. O. Hodgson (1980). Use of one electron theory for the interpretation of near edge structure of K-shell x-ray absorption spectra of metal complexes. *J. Chem. Phys.* **73**, 3274–88.

Lad, R. J., and V. E. Henrich (1989). Photoemission study of the valence-band electronic structures in Fe_xO, Fe_3O_4, and α-Fe_2O_3 single crystals. *Phys. Rev.* **B39**, 13478–85.

Ladd, M. F. C. (1980). Charge distributions in polyatomic ions, and their relationships with cohesive energies of ionic crystals. *Theoret. Chim. Acta.* **54**, 157.

Langell, M. A., and S. L. Bernasek (1979). Transition metal compound surfaces. *Prog. Surf. Sci.* **9**, 165–89.

Langer, K., and K. R. Fentrup (1979). Automated microscope-absorption-spectrophotometry of rock-forming minerals in the range 40000–5000 cm^{-1} (250–2000 μm). *J. Microscopy* **116**, 311–20.

Langhoff, S. R., and J. O. Arnold (1979). Theoretical study of the $X\ {}^1\Sigma^+$, $A\ {}^1\Pi$, $C\ {}^1\Sigma^-$, and $E\ {}^1\Sigma^+$ states of the SiO molecule. *J. Chem. Phys.* **70**, 852–63.

Lasaga, A. (1982). Optimization of CNDO for molecular orbital calculations on silicates. *Phys. Chem. Mineral.* **8**, 36–46.

Lasaga, A. C., and R. T. Cygan (1982). Electronic and ionic polarizabilities of silicate minerals. *Amer. Mineral.* **67**, 328–34.

Lasaga, A. C., and G. V. Gibbs (1987). Applications of quantum mechanical potential surfaces to mineral physics calculations. *Phys. Chem. Mineral.* **14**, 107–17.

Lasaga, A. C., and G. V. Gibbs (1990). *Ab initio* quantum mechanical calculations on water–rock interactions: absorption and hydrolysis reactions. *Am. J. Sci.* **290**, 263–95.

Lauer, S., A. X. Trautwein, and F. G. Harris (1984). Electronic structure calculations, photoelectron spectra, optical spectra and Mössbauer parameters for the pyrites MS_2 (M = Fe, Co, Ni, Cu, Zn). *Phys. Rev.* **B29**, 6774.

Laughlin, R. B. (1980). Optical absorption edge of SiO_2. *Phys. Rev.* **B22**, 3021–29.

Lauterbur, P. C. (1958). Anisotropy of the ^{13}C chemical shift in calcite. *Phys. Rev. Lett.* **1**, 343–44.

Lazzeretti, P., and R. Zanasi (1980). Theoretical determination of the magnetic properties of HI, H_2S, PH_3 and SiH_4 molecules. *J. Chem. Phys.* **72**, 6768–76.

Leckey, R. C. G. (1976). Subshell photoionization cross sections for the elements for Al *Kα* radiation. *Phys. Rev.* **A13**, 1043–51.

Lee, C. Y., J. A. McCammon, and P. J. Rossky (1984). The structure of liquid water at an extended hydrophobic surface. *J. Chem. Phys.* **80**, 4448–55.

Levien, L., C. T. Prewitt, and D. J. Weidner (1980). Structure and elastic properties of quartz at pressure. *Amer. Mineral.* **65**, 920–30.

Levine, I. N. (1983). *Quantum Chemistry.* Boston, MA: Allyn and Bacon.

Lewis, G. N. (1923). *Valence and the Structure of Atoms and Molecules.* New York: Amer. Chem. Soc. Mono. Series.

Lewis, J., D. Schwarzenbach, and H. D. Flack (1982). Electric field gradients and charge density in corundum, α-Al_2O_3. *Acta. Cryst.* **A38**, 733–39.

Ley, L., R. A. Pollak, F. R. McFeely, S. P. Kowalczyk, and D. A. Shirley (1974). Total valence band densities of states of III-V and II-VI compounds from x-ray photoemission spectroscopy. *Phys. Rev.* **B9**, 600–21.

Li, E. K., K. H. Johnson, D. E. Eastman, and J. L. Freeouf (1974). Localized and bandlike valence electron states in FeS_2 and NiS_2. *Phys. Rev. Lett.* **32**, 470–72.

Liberman, D. A. (1978). Self-consistent field electronic structure calculations for compressed magnesium oxide. *J. Phys. Chem. Solids* **39**, 255–57.

Lie, S. K., M. Braga, and C. A. Taft (1988). Electronic structure, hyperfine interactions, and radial densities in the Fe^{1+} tetrahedral sulfide as calculated by the multiple-scattering method. *Phys. Rev.* **B38**, 4382–87.

Lin, T. C., and C. A. Angell (1984). Electronic spectra and coordination of Ni^{2+} in potassium borate glass and melt to 1000°C. *J. Amer. Ceram. Soc.* **67**, C33–34.

Lippmaa, E., M. Mägi, A. Samoson, M. Tarmak, and G. Engelhardt (1980). Structural studies of silicates by solid state high resolution ^{29}Si NMR. *J. Amer. Chem. Soc.* **102**, 4889–93.

Lipscomb, W. N. (1966). The chemical shift and other second-order magnetic and electric properties of small molecules. *Adv. Magn. Reson.* **2**, 137–224.

Liu, S.-B., J. F. Stebbins, E. Schneider, and A. Pines (1988). Diffusive motion in alkali silicate melts: an NMR study at high temperature. *Geochim. Cosmochim. Acta* **52**, 527–38.

Lloyd, D. R., and P. J. Roberts (1975). Photoelectron spectra of halides VII. Variable temperature He(I) and He(II) studies of CF_4, SiF_4, and GeF_4. *J. Electron Spectrosc. Relat. Phenom.* **1**, 325–30.

Lo, B. W. N. (1973). The polarizabilities of planar nitrate, carbonate and borate anions in crystal. *J. Phys. Chem. Solids* **34**, 513–20.

Loeffler, B. M., R. G. Burns, J. A. Tossell, D. J. Vaughan, and K. H. Johnson (1974). Charge transfer in lunar materials: interpretation of ultraviolet–visible spectral properties of the Moon. *Proc. 5th Lunar Sci. Conf.* **3**, 3007–16.

Losch, W., and A. J. Monhemius (1976). An AES study of a copper–iron sulphide mineral. *Surf. Sci.* **60**, 196–210.

Louisnathan, S. J., and G. V. Gibbs (1972a). The effect of tetrahedral angles on

Si–O bond overlap populations for isolated tetrahedra. *Amer. Mineral.* **57**, 1614–42.

Louisnathan, S. J., and G. V. Gibbs (1972b). Variation of Si–O distances in olivines, sodamelilite and sodium metasilicate as predicted by semi-empirical molecular orbital calculations. *Amer. Mineral.* **57**, 1643–63.

Low, W., and M. Weger (1960). Paramaagnetic resonance and optical spectra of divalent iron in cubic fields. *Phys. Rev.* **118**, 1130–36.

Lowenhaupt, D. E., and D. K. Smith (1974). The high temperature crystal structure of Ag_2S. II. *Abstr. Summer Mtg. Amer. Cryst. Assoc. Penn State Univ.*, p. 265.

Lowenstein, W. (1954). The distribution of aluminum in the tetrahedra of silicates and aluminates. *Amer. Mineral.* **39**, 92–96.

Lukehart, C. M. (1985). *Fundamental Transition Metal Organometallic Chemistry*. Monterey, Calif.: Brooks/Cole.

Mabilia, M., R. A. Pearlstein, and A. J. Hopfinger (1987). Molecular modelling of zeolite structure. 1. Properties of the sodalite cage. *J. Amer. Chem. Soc.* **109**, 7960–68.

Maciel, G. E., L. Simeral, and J. J. H. Ackerman (1977). Effect of complexation of zinc (II) on zinc-67 chemical shifts. *J. Phys. Chem.* **81**, 263–67.

Mackrodt, W. C. (1988). Atomistic simulation of oxide surfaces. *Phys. Chem. Mineral.* **15**, 228–37.

Mackrodt, W. C., and R. F. Stewart (1979). Defect properties of ionic solids, I. Point defect energies based on modified electron-gas potentials. *J. Phys. C. (Solid State Phys.)* **12**, 431–49.

Maddock, A. G. (1985). Mössbauer spectroscopy in mineral chemistry. In: *Chemical Bonding and Spectroscopy in Mineral Chemistry* (F. J. Berry and D. J. Vaughan, eds.) London: Chapman and Hall.

Madix, R. J., J. L. Solomon, and J. Stohr (1988). The orientation of the carbonate anion on Ag(110). *Surf. Sci.* L253–59.

Magi, M., E. Lippmaa, A. Samoson, G. Engelhardt, and A. R. Grimmer (1984). Solid-state high resolution silicon-29 chemical shifts in silicates. *J. Phys. Chem.* **88**, 1518–22.

Malkin, V. G., O. V. Gritsenko, and G. M. Zhidomirov (1988). ^{29}Si NMR: A new approach to the analysis of chemical shift variations. *Chem. Phys. Lett.* **152**, 44–49.

Mammone, J. F., H. K. Mao, and P. M. Bell (1981). Equations of state of CaO under static pressure conditions. *Geophys. Res. Letts.* **8**, 140–42.

Manghnani, M. H., and S. Akimoto (1977) (eds.). *High Pressure Research—Application to Geophysics*. New York: Academic Press.

Manghnani, M. H., and Y. Syono (1987) (eds.). *High Pressure Research in Mineral Physics*. Tokyo: Amer. Geophys. Union/Terra Publishing Co.

Mao, H. K., and P. M. Bell (1973). Polarized crystal field spectra of the moon. In: *Analytical Methods Developed for Application to Lunar Sample Analysis. Amer. Soc. Test. Mater. Spec. Tech. Pub.* **539**, 100–19.

Marfunin, A. S. (1979). *Spectroscopy, Luminescence and Radiation Centers in Minerals*. Berlin: Springer-Verlag.

Marfunin, A. S., A. N. Platonov, and V. E. Fedorov (1968). Optical spectrum of Fe^{2+} in sphalerite. *Soviet Phys. Solid State* **9**, 2847–48.

Maruthe, V. R., and A. Trautwein (1983). Calculation of charge density, electric field gradient and internal magnetic field at the nuclear site using molecular orbital cluster theory. In: *Advances in Mössbauer Spectroscopy* (B. V. Thosar, ed.), pp. 398–449.

Matsukawa, T., M. Obashi, S. Nakai, and C. Sugiura (1978). The *K* absorption spectra of FeS_2, CoS_2 and NiS_2. *Jap. Journ. Appl. Phys.* **17**, Suppl. 17-2, 184–86.

Matsui, M. (1988). Molecular dynamics study of $MgSiO_3$ perovskite. *Phys. Chem. Mineral.* **16**, 234–38.

Matsui, M., M. Akaogi, and T. Matsumoto (1987). Computational model of the structural and elastic properties of the ilmenite and perovskite phases of $MgSiO_3$. *Phys. Chem. Mineral.* **14**, 101–6.

Matsui, Y., and K. Kawamura (1984). Computer simulation of structures of silicate melts and glasses. In: *Materials Science of the Earth's Interior* (I. Sunagawa, ed.) Tokyo: Terra, pp. 3–23.

Mavroides, J. G., D. E. Tehernev, J. A. Kafalas, and D. F. Kolesar (1975). *Mater. Res. Bull.* **10**, 1023–30.

Mazalov, L. N., V. D. Yumatov, and G. N. Dolenko (1979). Structure of the molecular orbitals in organic phosphates and polyphosphates. *J. Struct. Chem.* **21**, 14–22.

McFeely, F. R., S. Kowalczyk, L. Ley, R. A. Pollack, and D. A. Shirley (1973). High-resolution x-ray photoemission spectra of PbS, PbSe, and PbTe valence bands. *Phys. Rev.* **B7**, 5228–36.

McKay, J. M., and V. E. Henrich (1984). Structure of valence and conduction bands in nickel (II) oxide. *Phys. Rev. Lett.* **53**, 2343–46.

McLarnan, T. J., R. J. Hill, and G. V. Gibbs (1979). A CNDO/2 molecular orbital study of shared tetrahedral edge conformations in olivine-type compounds. *Aust. J. Chem.* **32**, 949–59.

McMillan, P. F. (1981). A structural study of aluminosilicate glasses by Raman spectroscopy. Unpub. Ph.D. Thesis, Arizona State Univ.

McMillan, P. F. (1984a). Structural studies of silicate glasses and melts—applications and limitations of Raman spectroscopy. *Amer. Mineral.* **69**, 622–44.

McMillan, P. (1984b). A Raman spectroscopy study of glasses in the system CaO–MgO–SiO_2. *Amer. Mineral.* **69**, 645–59.

McMillan, P. (1985). Vibrational spectroscopy in the mineral sciences. In: *Microscopic to Macroscopic—Atomic Environments to Thermodynamic Properties. Reviews in Mineralogy,* Vol. **14** (S. W. Kieffer and A. Navrotsky, eds.), pp. 9–63.

McMillan, P. F., and A. C. Hess (1988). Symmetry, group theory and quantum mechanics. In: *Spectroscopic Methods in Mineralogy and Geology* (F. C. Hawthorne, ed.) MSA, pp. 11–61.

McMillan, P., and B. Piriou (1983). Raman spectroscopic studies of silicate and related glass structure: a review. *Bull. de Mineral.* **106**, 57–75.

McMillan, P., A. Putnis, and M. A. Carpenter (1984). A Raman spectroscopic study of Al–Si ordering in synthetic magnesium cordierite. *Phys. Chem. Mineral.* **10**, 256–60.

McWhinnie, W. R. (1985). Electron spin resonance and nuclear magnetic resonance applied to minerals. In: *Chemical Bonding and Spectroscopy in Mineral Chemistry* (F. J. Berry and D. J. Vaughan, eds.) London: Chapman and Hall.

Meads, R. E., and D. J. Malden (1975). Electron spin resonance in natural kaolinites containing iron (3^+) and other transition metal ions. *Clay Mineral.* **10**, 313–45.

Meagher, E. P. (1980). Stereochemistry and energies of single two-repeat silicate chains. *Amer. Mineral.* **65**, 746–55.

Meagher, E. P., J. A. Tossell, and G. V. Gibbs (1979). A CNDO/2 molecular orbital study of the silica polymorphs quartz, cristobalite and coesite. *Phys. Chem. Mineral.* **4**, 11–21.

Mehl, M. J., R. E. Cohen, and H. Krakauer (1988). Linearized augmented plane wave electronic structure calculations for MgO and CaO. *J. Geophys. Res.* **93**, 8009–22.

Mehl, M. J., R. E. Cohen, H. Krakauer, and R. Rudd (1987). LAPW study of the high pressure behaviour of stoichiometric FeO. *EOS* **68**, 1455.

Mehl, M. J., R. J. Hemley, and L. L. Boyer (1986). Potential-induced breathing model for the elastic moduli and high pressure behavior of the cubic alkaline earth oxides. *Phys. Rev.* **B33**, 8685–96.

Meier, R., and T. K. Ha (1980). A theoretical study of the electronic structure of disiloxane [$(SiH_3)_2O$] and its relation to silicates. *Phys. Chem. Mineral.* **6**, 37–46.

Michalske, T. A., and B. C. Bunker (1984). Slow fracture model based on strained silicate structures. *J. Appl. Phys.* **56**, 2686–93.

Miller, A., A. Mackinnon, and D. Weaire (1981). Beyond the binaries—the chalcopyrite and related semiconducting compounds. *Solid State Physics* **36**, 119–75.

Mitchell, K. A. R. (1973). Low energy electron diffraction. *Contemp. Phys.* **14**, 251.

Mitra, S. K., M. Amini, D. Fincham, and R. W. Hockney (1981). Molecular dynamics simulation of silicon dioxide glass. *Phil. Mag.* **B43**, 365–72.

Miyamoto, M., H. Takeda, K. Fujino, and Y. Takeuchi (1982). The ionic compressibilities and radii estimated for some transition metals in olivine structures. *Mineral. Journ.* **11**, 172–79.

Miyoshi, E., and Y. Sakai (1988). Applications of the model potential method to transition metal compounds. *J. Comp. Chem.* **9**, 719–27.

Mizukami, S., A. Ohtani, N. Kawai, and E. Ito (1975). High pressure x-ray diffraction studies on β- and α-Mg_2SiO_4. *Phys. Earth Plan. Ints.* **10**, 177–82.

Moller, C., and M. S. Plesset (1934). Note on an approximation treatment for many electron systems. *Phys. Rev.* **46**, 618–22.

Moore, J. H., J. A. Tossell, and M. A. Coplan (1982). Electronic structure of molecules by *(e,2e)* spectroscopy. *Accts. Chem. Res.* **15**, 192–98.

Mooser, E., and W. B. Pearson (1959). On the crystal chemistry of normal valence compounds. *Acta Cryst.* **12**, 1015–22.

Mortier, W. J., J. Sauer, J. A. Lercher, and H. Noller (1984). Bridging and terminal hydroxyls. A structural chemical and quantum chemical discussion. *J. Phys. Chem.* **88**, 905–12.

Moruzzi, V. L., A. R. Williams, and J. F. Janak (1977). Local density theory of metallic cohesion. *Phys. Rev.* **B15**, 2854–57.

Mott, N. F. (1974). *Metal–Insulator Transitions*. London: Taylor and Francis.

Mozzi, R. L., and B. E. Warren (1969). The structure of vitreous silica. *J. Appl. Crystallogr.* **2**, 164–72.

Mozzi, R. L., and B. E. Warren (1970). The structure of vitreous born oxide. *J. Appl. Cryst.* **3**, 251–57.

Mueller, C. M., and U. Scherz (1980). Cluster calculations of transition metal impurities in semiconductors. *Proc. Int. Conf. Phys. Semicond. 15th*, 275–78.

Muhlhausen, C., and R. G. Gordon (1981). Electron-gas theory of ionic crystals, including many-body effects. *Phys. Rev.* **B23**, 900–23.

Mulla, D. J., P. F. Low, J. H. Cushman, and D. J. Diestler (1984). A molecular dynamics study of water near silicate surfaces. *J. Colloid Interfac. Sci.* **100**, 576–80.

Muller, A., and E. Diemann (1987). Polysulfide complexes of metals. *Adv. Inorg. Chem.* **31**, pp. 89–122, (H. J. Erndew and A. G. Sharpe, eds.) New York: Academic Press.

Müller, J. E., R. O. Jones, and J. Harris (1983). Density functional calculations for H_2O, NH_3, and CO_2 using localized muffin-tin orbitals. *J. Chem. Phys.* **79**, 1874–84.

Muller, A., H. Seidel, and W. Rittner (1967). Elecktronen absorptions spektren and HMO-rechung von trichalkogenocarbonationem. *Spectr. Acta* **A23**, 1616–26.

Mulliken, R. S. (1955). Electronic population analysis on LCAO-MO molecular wave functions. I. *J. Chem. Phys.* **23**, 1833–40.

Mulliken, R. S. (1962). Criteria for the construction of good self-consistent-field molecular orbital wave functions, and the significance of LCAO-MO population analysis. *J. Chem. Phys.* **36**, 3428–39.

Mulliken, R. S., and W. B. Pearson (1969). *Molecular Complexes.* New York: Wiley Interscience.

Murdoch, J. B., J. F. Stebbins, and I. S. E. Carmichael (1985). High-resolution ^{29}Si NMR study of silicate and aluminosilicate glasses: the effect of network-modifying cations. *Amer. Mineral.* **70**, 332–43.

Mysen, B. O. (1983). The structure of silicate melts. *Ann. Rev. Earth Planet. Sci.* **11**, 75–97.

Mysen, B. O., and D. Virgo (1985). Iron-bearing silicate melts: relations between pressure and redox equilibria. *Phys. Chem. Mineral.* **12**, 191–200.

Mysen, B. O., D. Virgo, E.-R. Neumann, and F. A. Seifert (1985). Redox equilibria and the structural states of ferric and ferrous iron in melts in the system CaO-MgO-Al_2O_3-SiO_2-Fe-O: relationships between redox equilibria, melt structure and liquidus phase equilibria. *Amer. Mineral.* **70**, 317–31.

Mysen, B. O., D. Virgo, and F. A. Seifert (1982). The structure of silicate melts: implications for chemical and physical properties of natural magma. *Rev. Geophys. Space Phys.* **20**, 353–83.

Nada, R., C. R. A. Catlow, R. Dovesi, and C. Pisani (1990). An *ab initio* Hartree–Fock study of α-quartz and stishovite. *Phys. Chem. Mineral.* **17**, 353–62.

Nagel, S. (1985a). Nuclear quadrupole interaction and chemical bonding. MS-$X\alpha$ cluster calculation for Cu_2O. *J. Phys. Chem. Solids* **46**, 743–56.

Nagel, S. (1985b). Cluster calculation of electronic structure and hyperfine interactions for α-Fe_2O_3. *J. Phys. Chem. Solids* **46**, 905–19.

Nagel, S. (1985c). Cluster calculation of electronic structure and quadrupole interaction in α-Al_2O_3. *J. Phys. C (Solid St. Phys.)* **18**, 3673–85.

Nakai, I., Y., Sugitani, K. Nagashima, and Y. Niwa (1978). X-ray photoelectron spectroscopic study of copper minerals. *J. Inorg. Nucl. Chem.* **40**, 789–91.

Nakatsuji, H. (1983). Cluster expansion of the wavefunction. Valence and Rydberg excitations, ionization and inner-valence ionizations of CO_2 and N_2O studied by the SAC and SAC CI theories. *Chem. Phys.* **75**, 425–41.

Nakatsuji, H., K. Kanda, K. Endo, and T. Yonezawa (1984). Theoretical study of the metal chemical shift in nuclear magnetic resonance Ag, Cd, Cu and Zn complexes. *J. Amer. Chem. Soc.* **106**, 4653–60.

Narbutt, K. I. (1974). X-ray $K\alpha_{1,2}$ and $K\beta$ spectra of sulfur atoms contained in minerals and certain chemical compounds. *Izv. Akad. Nauk. SSSR Ser. Fiz.* **38**, 104–13.

Navrotsky, A. (1987). High pressure transitions in silicates. *Prog. Solid State Chem.* **17**, 53–86.

Navrotsky, A., K. L. Geisinger, P. McMillan, and G. V. Gibbs (1985). The tetrahedral framework in glasses and melts—inferences from molecular orbital calculations and implications for structure, thermodynamics and physical properties. *Phys. Chem. Mineral.* **11**, 284–98.

Navrotsky, A., R. Hon, D. F. Weill, and D. J. Henry (1980). Thermochemistry of glasses and liquids in the systems $CaMgSi_2O_6$-$CaAl_2SiO_6$-$NaAlSi_3O_8$, SiO_2-$CaAl_2Si_2O_8$-$NaAlSi_3O_8$ and SiO_2-Al_2O_3-CaO-Na_2O. *Geochim. Cosmochim. Acta* **44**, 1409–33.

Nemnonov, S. A., and S. S. Mikhailova (1974). X-ray $K\beta$ spectra of sulfur in Ni, Cu and Zn monosulfides. *Izv. Akad. Nauk. SSSR Ser. Fiz.* **38**, 56–58.

Newton, M. D., and G. V. Gibbs (1980). *Ab initio* calculated geometries and charge distributions for H_4SiO_4 and $H_6Si_2O_7$ compared with experimental values for silicates and siloxanes. *Phys. Chem. Mineral.* **6**, 221–46.

Newton, M. D., M. O'Keeffe, and G. V. Gibbs (1980). *Ab initio* calculation of interatomic force constants in $H_6Si_2O_7$ and the bulk modulus of α-quartz and α-cristobalite. *Phys. Chem. Mineral.* **6**, 305–12.

Nguyen, M. T. (1986). The structure and bonding of the lithium metaborate ($LiBO_2$) molecule. An *ab initio* study. *J. Molec. Struct. (Theochem.)* **136**, 371–79.

Nicholls, C., and D. S. Urch (1975). X-ray emission and photoelectron spectra from magnesium oxide: a discussion of the bonding based on the unit Mg_4O_4. *J. Chem. Soc. Dalton,* 2143–48.

Nicholls, C., and D. S. Urch (1976). The bonding in magnesium oxide. A discussion based on x-ray emission and x-ray photoelectron spectra. *J. Molec. Struct.* **31**, 327–36.

Nickel, E. H. (1968). Structural stability of minerals with the pyrite, marcasite, arsenopyrite and loellingite structures. *Canad. Mineral.* **9**, 311–21.

Nickel, E. H. (1970). The application of ligand field concepts to an understanding of the structural stabilities and solid solution limits of sulfides and related minerals. *Chem. Geol.* **5**, 233–41.

Nieuwpoort, W. C., D. Post, and P. Th. van Duijnen (1978). Calibration constant for Fe Mössbauer isomer shifts derived from *ab initio* self-consistent-field calculations on octahedral FeF_6 and $Fe(CN)_6$ clusters. *Phys. Rev.* **B17**, 91–98.

Nithianandam, V. J., and S. E. Schnatterly (1988). Soft x-ray emission and inelastic electron scattering study of the electronic excitations in amorphous and crystalline silicon dioxide. *Phys. Rev.* **B38**, 5547–53.

Nitsan, U., and T. J. Shankland (1976). Optical properties and electronic structure of mantle silicates. *Geophys. J. Roy. Astr. Soc.* **45**, 59–87.

Norman, J. G., Jr. (1976). Non-empirical vs. empirical choices for overlapping-sphere radii ratios in SCF-$X\alpha$-SW calculations on ClO_4^-, and SO_2. *Molec. Phys.* **31**, 1191–98.

Norman, M. R., and A. J. Freeman (1986). Model supercell local-density calculations of the 3*d* excitation spectra of nickel monoxide. *Phys. Rev.* **B33**, 8896–98.

Nucho, R. N., and A. Madhukar (1980). Electronic structure of SiO_2: α-quartz and the influence of local disorder. *Phys. Rev.* **B21**, 1576–88.

Oberhammer, H., W. Zeil, and G. Fogarsi (1973). The molecular structure of cyclic methylsiloxanes. *J. Molec. Struct.* **18**, 309–18.

Oddershede, J. (1978). Propagator methods. In: *Ab Initio Methods in Quantum Chemistry. II.* (K. P. Lawley, ed.) New York: Wiley.

Ohashi, Y., and C. W. Burnham (1972). Electrostatic and repulsive energies of the *M*1 and *M*2 cation sites in pyroxenes. *J. Geophys. Res.* **77**, 5761–66.

Ohnishi, S. (1978). A theory of the pressure-induced high-spin–low-spin transition of transition metal oxides. *Phys. Earth Planet. Int.***17**, 130–39.

Ohsawa, A., H. Yamamoto, and H. Watanabe (1974). X-ray photoelectron spectra of valence elections in FeS_2, CoS_2 and NiS_2. *J. Phys. Soc. Jap.* **37**, 568.

Ohtani, E., F. Taulelle, and C. A. Angell (1985). Al^{3+} coordination changes in liquid aluminosilicates under pressure. *Nature* **314**, 78–81.

O'Keeffe, M., and G. V. Gibbs (1984). Defects in amorphous silica: *ab initio* MO calculations. *J. Chem. Phys.* **81**, 876–79.

O'Keeffe, M., and G. V. Gibbs (1985). *Ab initio* MO calculations on cyclodisiloxanes and other Si–*X*–Si–*X* rings and the problem of "silica-w." *J. Phys. Chem.* **89**, 4574–77.

O'Keeffe, M., and P. F. McMillan (1986). The Si–O–Si force field: *Ab initio* MO calculations. *J. Phys. Chem.* **90**, 541–42.

O'Keeffe, M., M. D. Newton, and G. V. Gibbs (1980). *Ab initio* calculation of interatomic force constants in $H_6Si_2O_7$ and the bulk modulus of α-quartz and α-cristobalite. *Phys. Chem. Min.* **6**, 305–12.

O'Keeffe, M, C. L. Shavers, and B. G. Hyde (1981). Cation packing and molar volume in oxides and nitrides with the wurtzite structure. *J. Solid State Chem.* **39**, 265–67.

Oldfield, E., and R. J. Kirkpatrick (1985). High-resolution nuclear magnetic resonance of inorganic solids. *Science* **227**, 1537–44.

O'Malley, P. J., and J. Dwyer (1988). *Ab initio* molecular orbital calculations on the siting of aluminum in the Theta-1 framework: some general guidelines governing the site preferences of aluminum in zeolites. *Zeolites* **8**, 317–21.

O'Nions, R. K., and D. G. W. Smith (1973). Bonding in silicates: an assessment of bonding in orthopyroxene. *Geochim. Cosmochim. Acta* **37**, 249–57.

Orchin, M., and H. H. Jaffé (1971). *Symmetry, Orbitals and Spectra.* New York: Wiley-Interscience.

Orgel, L. E. (1966). *An Introduction to Transition Metal Chemistry: Ligand Field Theory.* London: Methuen.

Ottonello, G. (1987). Energies and interactions in binary (*Pbnm*) orthosilicates: a born parameterization. *Geochim. Cosmochim. Acta* **51**, 3119–35.

Pacansky, J., and K. Hermann (1978). *Ab initio* SCF calculations on molecular silicon dioxide. *J. Chem. Phys.* **69**, 963–67.

Pantelides, S., and W. A. Harrison (1975). Structure of the valence band of zincblende-type semiconductors. *Phys. Rev.* **B11**, 3006–21.

Pantelides, S. T., D. J. Mickish, and A. B. Kunz (1974). Electronic structure and properties of magnesium oxide. *Phys. Rev.* **B10**, 5203–12.

Paques-Ledent, M., and P. Tarte (1973). Vibrational studies of olivine-type compounds. I. The IR and Raman spectra of the isotopic species of Mg_2SiO_4. *Spectrochim. Acta* **29A**, 1007–16.

Park, K. T., K. Terakara, and Y. Matsui (1988). Theoretical evidence for a new ultra-high-pressure phase of SiO_2. *Nature* **336**, 670–72.

Paschalis, E., and A. Weiss (1969). Hartree–Fock-Roothaan wave functions, electron density distributions, diamagnetic susceptibility, dipole polarizability and antishielding factor for ions in crystals. *Theoret. Chim. Act.* **13**, 381–403.

Paschina, G., G. Piccaluga, G. Pinna, and M. Magini (1983). Chloro-complexes formation in a $ZnCl_2$–$CdCl_2$ aqueous solution: An x-ray diffraction study. *J. Chem. Phys.* **78**, 5745–52.

Pate, B. B. (1986). The diamond surface: atomic and electronic structure. *Surf. Sci.* **165**, 83–142.

Pauling, L. (1927). The sizes of ions and the structure of ionic crystals. *J. Amer. Chem. Soc.* **49**, 765–90.

Pauling, L. (1929). The principles determining the structure of complex ionic crystals. *J. Amer. Chem. Soc.* **51**, 1010–26.

Pauling, L. (1960). *The Nature of the Chemical Bond.* 3rd ed., New York: Cornell University Press.

Pauling, L. (1970). Crystallography and chemical bonding of sulfide minerals. *Mineral. Soc. Amer. Spec. Paper* **3**, 125–31.

Pauling, L. (1979). Diamagnetic anisotropy of the carbonate ion in calcite, aragonite, strontianite and witherite and of other non-cyclic planar aromatic groups with resonance structures. *Zeit. Krist.* **150**, 155–61.

Pavlychev, A. A., A. S. Vinogradov, and T. M. Zimkina (1982). Discontinuities of the continuous-absorption cross section for molecules near the threshold for inner-electron-shell ionization. *Opt. Spectrosco. (USSR)* **52**, 139–43.

Pearson, R. G. (1963). Hard and soft acids and bases. *J. Amer. Chem. Soc.* **85**, 3533–39.

Pearson, R. G. (1988). Absolute electronegativity and hardness: application to inorganic chemistry. *Inorg. Chem.* **27**, 734–40.

Pen'kov, I. N., and I. A. Safin (1963). Nuclear quadrupole resonance (NQR) in realgar. *Dokl. Akad. Nauk. SSSR* **153**, 642–49.

Perdew, J. P., and A. Zunger (1981). Self-interaction correction to density-functional approximations for many-electron systems. *Phys. Rev.* **B23**, 5048–79.

Perry, D. L., and J. A. Taylor (1986). X-ray photoelectron and Auger spectroscopic studies of Cu_2S and CuS. *J. Mater. Sci. Lett.* **5**, 384–86.

Perry, W. B., and W. J. Jolly (1974a). Valence electron binding energies of some silicon compounds from x-ray photoelectron spectroscopy. *J. Electron Spectrosc. Relat. Phenom.* **4**, 219–32.

Perry, W. B., and W. J. Jolly (1974b). Correlation of core electron binding energies with charge distributions for compounds of carbon, silicon and germanium. *Inorg. Chem.* **13**, 1211–17.

Pettifer, R. F., R. Dupree, I. Farnan, and U. Sternberg (1988). NMR determinations of Si–O–Si bond angle distributions in silica. *J. Noncryst. Solids* **106**, 408–12.

Philipp, H. R. (1971). Optical properties of non-crystalline Si, SiO, SiO_x, and SiO_2. *J. Phys. Chem Solids* **32**, 1935–45.

Phillips, J. C. (1970). Ionicity of the chemical bond in crystals. *Rev. Mod. Phys.* **42**, 317–56.

Pickett, W. E. (1989). Electronic structure of the high-temperature oxide superconductors. *Rev. Mod. Phys.* **61**, 433–512.

Pickett, W. E., and C. S. Wang (1984). Local-density approximation for dynamical correlation corrections to single-particle excitations in insulators. *Phys. Rev.* **B30**, 4719–33.

Pietro, W. J., and W. J. Hehre (1983). Molecular orbital theory of the properties of inorganic and organometallic compounds. 3. STO-3G basis sets for first- and second-row transition metals. *J. Comp. Chem.* **4**, 241–351.

Piller, H. (1977). *Microscope Photometry.* Berlin: Springer–Verlag.

Piriou, B., and P. McMillan (1983). The high-frequency vibrational spectra of vitreous and crystalline orthosilicates. *Amer. Mineral.* **68**, 426–43.

Pisani, C. (1987). Hartree–Fock *ab initio* approaches to the solution of some solid-state problems: state of the art and prospects. *Int. Rev. Phys. Chem.* **6**, 367–84.

Pisani, C., R. Dovesi, and C. Roetti (1988). Hartree–Fock *ab initio* treatment of crystalline systems. *Lecture notes in Chemistry,* Vol. 48 (G. Berthier et al., eds.) Berlin: Springer–Verlag.

Pittel, B., W. H. E. Schwarz, P. Rabe, H. Freidrich, and B. Sonntag (1979). DESY Report SR-79/16.

Pitzer, K. S. (1979). Relativistic effects on chemical properties. *Acc. Chem. Res.* **12**, 271–76.

Platonov, A. N., and A. S. Marfunin (1968). Optical absorption spectra of sphalerite. *Geochem. Internat.* **5**, 245–59.

Podloucky, R., and J. Redinger (1984). A theoretical study of Compton scattering for magnesia. I. Momentum density, Compton profiles and B functions. *J. Phys. C* **16**, 6955–69.

Pople, J. A. (1975). Some deficiencies of MINDO3 semiempirical theories. *J. Am. Chem. Soc.* **97**, 5306–8.

Pople, J. A., and D. L. Beveridge (1970). *Approximate Molecular Orbital Theory.* New York: McGraw–Hill.

Pople, J. A., M. Head-Gordon, and K. Raghavachari (1987). Quadratic configuration interaction. A general technique for determining electron correlation energies. *J. Chem. Phys.* **87**, 5968–75.

Post, J. E., and C. W. Burnham (1986). Ionic modeling of mineral structures and energies in the electron gas approximation: TiO_2 polymorphs, quartz, forsterite, diopside. *Amer. Mineral.* **71**, 142–50.

Power, L. F., and H. A. Fine (1976). The iron–sulfur system. I. The structure and physical properties of the compounds of the low temperature phase fields. *Min. Sci. Engng.* **8**, 106–28.

Press, M. R., and D. E. Ellis (1987). Defect clusters in $Fe_{1-x}O$. *Phys. Rev.* **B35**, 4438–54.

Prewitt, C. T., and V. Rajamani (1974). Electron interactions and chemical bonding in sulfides. *Min. Soc. Amer. Reviews in Mineralogy,* Vol. 1 (P. H. Ribbe, ed.), PR1–41.

Prewitt, C. T., and R. D. Shannon (1968). Crystal structure of a high-pressure form of B_2O_3. *Acta. Cryst.* **B24**, 869–74.

Price, G. D., and S. C. Parker (1984). Computer simulations of the structural and physical properties of the olivine and spinel polymorphs of Mg_2SiO_4. *Phys. Chem. Mineral.* **10**, 209–16.

Prutton, M., J. A. Walker, M. R. Welton-Cook, R. C. Felton, and J. A. Ramsey (1979). LEED studies of the structures of the (100) surfaces of divalent metal oxides. *Surf. Sci.* **89**, 95–101.

Pulay, P. (1977). Direct use of the gradient for investigating molecular energy surfaces. In: *Applications of Electronic Structure Theory* (H. F. Schaefer III, ed.) New York: Plenum, pp. 153–85.

Putnis, A., and J. D. C. McConnell (1980). *Principles of Mineral Behaviour.* Oxford: Blackwells.

Pye, L. D., V. D. Frechette, and N. J. Kreidl (eds.) (1978). *Borate glasses: structure, properties and applications.* New York: Plenum.

Pykko, P., and J. P. Desclaux (1979). Relativity and the periodic system of the elements. *Acc. Chem. Res.* **12**, 276–81.

Pytkowicz, R. M. (1983). *Equilibria, Nonequilibria and Natural Waters. I.* New York: Wiley–Interscience.

Rabii, S., and R. H. Lasseter (1974). Band structure of PbTe and trends in the Pb chalcogenides. *Phys. Rev. Lett.* **33**, 703–5.

Radom, L. (1976). Structures of simple anions from *ab initio* molecular orbital calculations. *Aust. J. Chem.* **29**, 1635–40.

Raghavachari, K. (1986). Theoretical study of small silicon clusters: Equilibrium geometries and electronic structures of Si_n ($n=2$–7, 10). *J. Chem. Phys.* **84**, 5672–86.

Raine, G. P., H. F. Schaefer III, and R. C. Haddon (1983). The dimers of carbon monoxide and carbon monosulfide. Chemically bound triplet electronic ground states. *J. Am. Chem. Soc.* **105**, 194–98.

Rajamani, V., and C. T. Prewitt (1973). Crystal chemistry of natural pentlandites. *Canad. Mineral.* **12**, 178–87.

Rajamani, V., and C. T. Prewitt (1975). Refinement of the structure of Co_9S_8. *Canad. Mineral.* **13**, 75–78.

Ramaker, D. E., J. S. Murday, N. H. Turner, G. Moore, M. G. Lagally, and J. Houston (1979). Calculated and measured Auger line shapes in SiO_2. *Phys. Rev.* **B19**, 5375–87.

Ramberg, H. (1952). Chemical bonds and distribution of cations in silicates. *J. Geol.* **60**, 331–55.

Ramberg, H. (1953). Relationships between heats of reaction among solids and properties of the constituent ions, and some geochemical implications. *J. Geol.* **61**, 318–52.

Ravenak, W., J. W. M. Jacobs, and A. Van der Avoird (1983). Hartree–Fock–

Slater LCAO calculation of the Mössbauer parameters of some antimony compounds. *Chem. Phys.* **78**, 391–404.

Redinger, J., and K. Schwarz (1981). Electronic charge distribution of the polarizable O_2^- ion in MgO and CaO in contrast to the F-ion in NaF. *Z. Phys.* **B40**, 269–76.

Redondo, A., W. A. Goddard, III, C. A. Swarts, and T. C. McGill (1981). Oxidation of silicon surfaces. *J. Vac. Sci. Tech.* **19**, 498–501.

Reeder, R. J. (ed.) (1983). *Carbonates: Mineralogy and Chemistry. Reviews in Mineralogy,* Vol. 11, Min. Soc. America.

Rhodin, T. N., and G. Ertl (1979). *The Nature of the Surface Chemical Bond.* North-Holland.

Ribbe, P. (ed.) (1974). *Sulfide Mineralogy. Reviews in Mineralogy,* Vol. 1, Mineral. Soc. Amer.

Richards, G. (1979). Third age of quantum chemistry. *Nature* **78**, 507.

Ringwood, A. E. (1955). The principles governing trace element distribution during magmatic crystallization. *Geochim. Cosmochim. Acta* **7**, 189–202.

Ringwood, A. E. (1984). The Earth's core: its composition, formation and bearing upon the origin of the Earth. *Proc. Roy. Soc. Lond.* **A395**, 1–46.

Robin, M. .B. (1985). Antibonding σ^* orbitals in molecular spectroscopy. *Can. J. Chem.* **63**, 2032–43.

Roothaan, C. C. J. (1951). New developments in molecular orbital theory. *Rev. Mod. Phys.* **23**, 69–89.

Rosasco, G. J., and E. Roedder (1979). Application of a new Raman microprobe spectrometer to nondestructive analysis of sulfate and other ions in individual phases in fluid inclusions in minerals. *Geochim. Cosmochim. Acta* **43**, 1907–15.

Rosch, N., W. G. Klemperer, and K. H. Johnson (1973). On the use of overlapping spheres in the SCF-$X\alpha$ scattered-wave method. *Chem. Phys. Lett.* **23**, 149–54.

Rosenberg, M., F. Martino, A. W. Reed, and P. Eisenberger (1978). Compton profile studies of amorphous and single crystal SiO_2. *Phys. Rev.* **B18**, 844–50.

Rosenquist, T. (1954). A thermodynamic study of the iron, cobalt and nickel sulfides. *J. Iron Steel Inst.* **176**, 37–57.

Rössler, U., and M. Lietz (1966). Band structure of cubic and hexagonal ZnS augmented-plane-wave (APW) method. *Phys. Stat. Solid.* **17**, 579–604.

Rossman, G. R. (1988). Optical spectroscopy. In: *Spectroscopic Methods in Mineralogy and Geology* (F. C. Hawthorne, ed.) *Reviews in Mineralogy,* Vol. 18, Min. Soc. Amer.

Runciman, W. A., D. Sengupta, and M. Marshall (1973). The polarized spectra of iron in silicates. I. Enstatite. *Amer. Mineral.* **58**, 444–50.

Rye, R. R., and J. E. Houston (1983). Auger spectra of tetrahedral halides and hydrides. *J. Chem. Phys.* **78**, 4321–29.

Sakka, S., and J. D. MacKenzie (1969). High pressure effects on glass. *J. Noncryst. Solids* **1**, 107–42.

Sakka, S., and K. Matusita (1976). Studies of binary silicate glasses based on the Si $K\alpha$ and Si $K\beta$ emission x-rays. *J. Noncryst. Solids* **22**, 57–66.

Sakkopoulos, S., E. Vitoratus, and T. Argureas (1984). Energy band diagram for pyrrhotite. *J. Phys. Chem. Solids* **45**, 923–28.

Salahub, D. R., R. P. Messmer, and K. H. Johnson (1976). Ionization potentials and bond lengths for CO, N_2, and F_2 using the SCF-$X\alpha$-SW method: A study of the effect of overlapping spheres. *Molec. Phys.* **31**, 529–34.

Sambe, H., and R. H. Felton (1975). A new computational approach to Slater's SCF-$X\alpha$ equation. *J. Chem. Phys.* **62**, 1122–26.

Sanders, M. J., M. Leslie, and C. R. A. Catlow (1984). Interatomic potentials for SiO_2. *J. Chem. Soc., Chem. Comm.* 1271–73.

Sano, M., and H. Yamatera (1982). *Ab initio* MO study of $[M(H_2O)_6]^{n+}$ ions. In: *Ions and Molecules in Solution* (N. Tanaka, H. Ohtaki, and R. Tamamushi, eds.) *Studies in Physical and Theoretical Chemistry,* Vol. 27, pp. 109–16. Amsterdam: Elsevier.

Sasaki, T., and H. Adachi (1980a). Calculations of photoelectron spectra for tetrahedral oxyanions by the Hartree–Fock–Slater model. *J. Electron. Spectrosc.* **19**, 261–71.

Sasaki, T., and H. Adachi (1980b). Calculations of XPS spectra for oxyanions and related compounds by the discrete-variational-$X\alpha$ method. *Int. J. Quantum Chem.* **18**, 227–35.

Sasaki, S., K. Fujino, Y. Takeuchi, and R. Sadmaga (1980). On the estimation of atomic charges by the x-ray method for some oxides and silicates. *Acta Cryst.* **A36**, 904–15.

Sasaki, S., Y. Takeuchi, K. Fujiho, and S. Akimoto (1982). Electron-density distributions of three orthopyroxenes $Mg_2Si_2O_6$, $Co_2Si_2O_6$ and $Fe_2Si_2O_6$. *Zeit. Krist.* **158**, 279–97.

Sato, K. (1984). Reflectivity spectra and optical constants of pyrites (FeS_2, CoS_2 and NiS_2) between 0.2 and 4.4 eV. *J. Phys. Soc. Japan* **53**, 1617–20.

Sauer, J. (1983). Molecular structure of orthosilicic acid and importance of p-d π bonding. An *ab initio* molecular orbital study. *Chem. Phys. Lett.* **97**, 275–78.

Sauer, J. (1989). Molecular models in *ab initio* studies of solids and surfaces: from ionic crystals and semiconductors to catalysts. *Chem. Rev.* **89**, 199–255.

Sauer, J., H. Haberlandt, and G. Pacchion (1986). Bonding of water ligands to copper and nickel atoms: crucial role of intermolecular electron correlation. *J. Phys. Chem.* **90**, 3051–52.

Sauer, J., P. Hobza, and R. Zahradnitk (1980). Quantum chemical investigation of interaction sites in zeolites and silica. *J. Phys. Chem.* **84**, 3318–26.

Sawaryn, A., L. P. Aldridge, R. Blas, V. R. Maruthe, and A. X. Trautwein (1986). *Ab initio, $X\alpha$* and IEHT MO calculations of Mössbauer spectroscopy parameters for iron carbonyls. *Hyperfine Int.* **29**, 1303–6.

Sawatzky, G. A., and J. W. Allen (1984). Magnitude and origin of the band gap in nickel (II) oxide. *Phys. Rev. Lett.* **53**, 2339–42.

Sawatzky, G. A., J. M. D. Coey, and A. H. Morrish (1969). Mössbauer study of electron hopping in the octahedral sites of Fe_2O_3. *J. Appl. Phys.* **40**, 1402–3.

Schaefer, H. F., III (1972). *The Electronic Structure of Atoms and Molecules: A Survey of Rigorous Quantum Mechanical Results.* Reading, Mass.: Addison–Wesley.

Schaefer, H. F., III (1981). Approaching the Hartree–Fock limit for organotransition metal complexes. *J. Molec. Struct. Theochem.* **76**, 117–35.

Schaefer, H. F., III (1982). The silicon–carbon double bond: a healthy rivalry between theory and experiment. *Acc. Chem. Res.* **15**, 283–90.

Schaefer, H. F., III (1984). *Quantum Chemistry: The Development of Ab Initio Methods in Molecular Electronic Structure Theory.* Oxford: Clarendon Press.

Schlegel, A., and P. Wachter (1976). Optical properties, phonons and electronic structure of iron pyrite (FeS_2). *J. Phys.* **C9**, 3363–69.

Schmidt, M. W., J. A. Boatz, K. K. Baldridge, S. Koseki, M. S. Gordon, S. T. Elbert, and B. Lam (1987). *QCPE Bull.* **I**, 115.

Schofield, J. H. (1976). Hartree–Fock subshell photoionization cross-sections at 1254 and 1487 eV. *J. Electron Spectrosc. Relat. Phenom.* **8**, 129–37.

Schoolar, R. B., and J. R. Dixon (1965). Optical constants of lead sulfide in the fundamental absorption edge region. *Phys. Rev.* **137**, A667–70.

Schramm, S., and E. Oldfield (1984). High resolution oxygen 17 NMR of solids. *J. Amer. Chem. Soc.* **106**, 2502–6.

Schreyer, W. (1982) (ed.). *High Pressure Researches in Geoscience: Behaviour and Properties of Earth Materials at High Pressures and Temperatures.* Stuttgart: E Schweizerbart'sche Verlagsbuchhandlung.

Schwarz, K. (1972). Optimization of the statistical exchange parameter α for the free atoms H through Nb. *Phys. Rev.* **B5**, 2466–68.

Schwarz, K. (1974). Optimized statistical exchange parameters α for atoms with higher *Z. Theoret. Chim. Acta* **34**, 225–31.

Schwarz, K. (1987). Band theoretical studies of the electronic structure of oxides. *Phys. Chem. Mineral.* **14**, 315–19.

Schwarz, W. H. E. (1975). Continuous change from valence to Rydberg type states. An example of XUV spectroscopy. *Chem. Phys.*, 157–64.

Schwarz, W. H. E., P. Valtazanos, and K. Ruedenberg (1985). Electron difference densities and chemical bonding. *Theor. Chim. Acta* **68**, 471–506.

Sellers, H., J. E. Boggs, A. Nemukhin, and J. Almlof (1981). The molecular structure and computed vibrational spectrum of B_2O_3. *J. Molec. Struct. (Theochem.)* **85**, 195–205.

Selvaray, U., K. J. Rao, C. N. R. Rao, J. Klinowski, and J. M. Thomas (1985). MASS NMR as a probe of Si–O–Si angles in lithium silicate glasses. *Chem. Phys. Lett.* **114**, 24–27.

Sette, F., J. Stohr, and A. P. Hitchcock (1984). Correlation between intramolecular bond lengths and *K*-shell σ-shape resonances in gas-phase molecules. *Chem. Phys. Lett.* **110**, 517–20.

Seward, T. M. (1981). Metal complex formation in aqueous solutions at elevated temperatures and pressures. In: *Nobel Symposium on the Chemistry and Geochemistry of Solutions at High Temperatures and Pressures* (F. Wickman and D. Rickard, eds.), *Phys. Chem. Earth* **13–14**, 113–32.

Seward, T. M. (1984). The formation of lead (II) chloride complexes to 300°C: a spectrophotometric study. *Geochim. Cosmochim. Acta* **48**, 121–34.

Shaffer, P. T. B. (1969). A review of the structure of silicon carbide. *Acta Cryst.* **B25**, 477–81.

Shangda, X., G. Changxin, L. Libin, and D. E. Ellis (1987). Electronic structure of alumina and ruby. *Phys. Rev.* **B35**, 7671–79.

Shannon, R. D. (1981). Bond distances in sulfides and a preliminary table of sulfide crystal radii. In: *Structure and Bonding in Crystals II* (M. O'Keeffe and A. Navrotsky, eds.), New York: Academic Press, pp. 53–70.

Sherman, D. M. (1984). The electronic structures of manganese oxide minerals. *Amer. Mineral.* **69**, 788–99.

Sherman, D. M. (1985a). The electronic structures of Fe^{3+} coordination sites in iron oxides: applications to spectra, bonding, and magnetism. *Phys. Chem. Mineral.* **12**, 161–75.

Sherman, D. M. (1985b). SCF-$X\alpha$-SW MO study of Fe–O and Fe–OH chemical bonds: applications to the Mössbauer spectra and magnetochemistry of hydroxyl bearing Fe^{3+} oxides and silicates. *Phys. Chem. Mineral.* **12**, 311–14.

Sherman, D. M. (1987a). Molecular orbital (SCF-$X\alpha$-SW) theory of metal–metal charge transfer processes in minerals. I. Application to Fe^{2+}-Fe^{3+} charge transfer and electron delocalization in mixed valence iron oxides and silicates. *Phys. Chem. Mineral.* **14**, 355–63.

Sherman, D. M. (1987b). Molecular orbital (SCF-$X\alpha$-SW) theory of metal–metal charge transfer processes in minerals. II. Application to Fe^{2+}-Ti^{4+} charge transfer transitions in oxides and silicates. *Phys. Chem. Mineral.* **14**, 364–67.

Sherman, D. M. (1990). Chemical bonding and the incorporation of potassium into the earth's core. *Geophys. Res. Lett.* **17**, 693–96.

Shuey, R. T. (1975). *Semiconducting Ore Minerals. Developments in Economic Geology,* No. 4, Amsterdam: Elsevier.

Silvi, B., and E. Bernard (1987). On the determination of atom–atom potentials in silicates from quantum chemical calculations. *Chem. Geol.* **62**, 125–30.

Simons, G., and A. N. Bloch (1973). Pauli force model potential for solids. *Phys. Rev.* **B7**, 2754–61.

Simunek, A., and G. Wiech (1984). Angle-dependent x-ray sulfur *K*-emission bands and electronic structure of SnS_2 and MoS_2. *Phys. Rev.* **D30**, 923–30.

Skriver, H. L. (1984). *The LMTO Method Muffin-Tin Orbitals and Electronic Structure.* Berlin: Springer–Verlag.

Slater, J. C. (1951). A simplification of the Hartree–Fock method. *Phys. Rev.* **81**, 385–90.

Slater, J. C. (1965). *Quantum Theory of Molecules and Solids,* Vol. 2. New York: McGraw–Hill.

Slater, J. C. (1968). Average energy of states of given multiplets in atoms. *Phys. Rev.* **165**, 655–58.

Slater, J. C. (1974a). *Quantum Theory of Molecules and Solids,* Vol. 4. New York: McGraw–Hill.

Slater, J. C. (1974b). *The self-consistent field method for atoms, molecules and solids.* New York: McGraw–Hill.

Slater, J. C. (1975). *Solid State and Molecular Theory: A Scientific Biography.* New York: Wiley.

Smit, T. J. M., W. C. Nieuwpoort, and C. Haas (1978). The electronic structure of CuCl: An "*ab initio*" Hartree–Fock SCF-MO study of the $CuCl_4^{3-}$ cluster. *J. Phys. Chem. Solids* **39**, 1095–98.

Smith, G. S., and K. Langer (1982). Single crystal spectra of olivines in the range 40,000–50,000 cm^{-1} at pressures up to 200 kbars. *Amer. Mineral.* **67**, 343.

Smith, V. H., Jr. (1977). Theoretical determination and analysis of electronic charge distributions. *Physica Scripta* **15**, 147–62.

Smith, V. H., Jr., and J. R. Sabin (1978). The Compton profile as a criterion for the choice of a local exchange parameter α. *J. Phys. B. (Atom Molec. Phys.)* **11**, 385–89.

Snyder, L. C. (1976). Quantum chemical calculations to model borate glass electronic structure and properties. In: *Borate Glass* (L. D. Pye et al., eds.), pp. 151–65.

Snyder, L. C., G. E. Peterson, and C. R. Kurkjian (1976). Molecular orbital calculations of quadrupolar coupling of ^{11}B in molecular models of glasses. *J. Chem. Phys.* **64**, 1569–73.

Snyder, L. C., and K. Raghavachari (1984). *Ab initio* quantum chemical study of the dimerization of silicon monoxide. *J. Chem. Phys.* **80**, 5076–79.

Snyder, L. C., and Z. Wasserman (1980). On the structure and stability of pyramidal B_2O_3. *J. Chem. Phys.* **73**, 998–99.

Sontum, S. F., D. A. Case, and M. Karplus (1983). $X\alpha$ multiple scattering calculations on iron (II) porphine. *J. Chem. Phys.* **79**, 2881–92.

Soppe, W., C. van der Marel, W. F. van Gunsteren, and H. W. den Hartog (1988). New insights into the structure of B_2O_3 glass. *J. Noncryst. Solids* **103**, 201–9.

Soules, T. F. (1979). A molecular dynamic calculation of the structure of sodium silicate glasses. *J. Chem. Phys.* **71**, 4570–78.

Soules, T. F. (1980). A molecular dynamic calculation of the structure of B_2O_3 glass. *J. Chem. Phys.* **73**, 4032–36.

Spackman, M. A., and E. N. Maslen (1986). Chemical properties from the promolecule. *J. Phys. Chem.* **90**, 2020–27.

Srivastava, G. P., and D. Weaire (1987). The theory of the cohesive energies of solids. *Adv. Phys.* **36**, 463–517.

Stebbins, J. F. (1987). Identification of multiple structural species in silicate glasses by ^{29}Si NMR. *Nature* **330**, 465–67.

Stebbins, J. F., and P. McMillan (1989). Five- and six-coordinated Si in $K_2Si_4Si_4O_9$ glass quenched from 1.9 GPa and 1200°C. *Amer. Mineral.* **74**, 965–68.

Stebbins, J. F., J. B. Murdoch, E. Schneider, I. S. E. Carmichael, and A. Pines (1985). A high temperature high resolution NMR study of ^{23}Na, ^{27}Al and ^{29}Si in molten silicates. *Nature* **314**, 250–52.

Stenkamp, L. Z., and E. R. Davidson (1973). An ICSCF investigation of Walsh's Rules. *Theor. Chim. Acta* **30**, 283–314.

Sternberg, V. (1988). Theory of the influence of the second coordination sphere on the chemical shift. *Molec. Phys.* **63**, 249–67.

Stewart, R. F., and M. A. Spackman (1981). Charge density distributions. In: *Structure and Bonding in Crystals* (M. O'Keeffe and A. Navrotsky, eds.) Vol. 1, pp. 279–98.

Stizza, S., I. Davoli, and M. Benfatto (1987). X-ray absorption spectroscopy in compressed vitreous silica and vanadium pentoxide gel. *J. Noncryst. Solids* **95 & 96**, 327–34.

St. John, J., and A. N. Bloch (1974). Quantum-defect electronegativity scale for non-transition elements. *Phys. Rev. Lett.* **33**, 1095–98.

Stout, G. H., and L. H. Jensen (1972). *X-ray Structure Determination.* London: McMillan.

Strens, R. G. J. (1969). The nature and geophysical importance of spin-pairing of iron (II). In: *The Application of Modern Physics to the Earth and Planetary Interiors* (S. K. Runcorn, ed.) New York: Academic Press.

Strens, R. G. J. (1976). Behaviour of iron compounds at high pressure. In: *The Physics and Chemistry of Minerals and Rocks*. (R. G. J. Strens, ed.) London: Wiley.

Stromberg, A., U. Wahlgren, L. Pettersson, and P. E. M. Siegbahn (1984). On the role of 3*d* orbitals in sulfur. *Chem. Phys.* **89**, 323–28.

Stukel, D. J., R. N. Euwema, T. C. Collins, F. Herman, and R. L. Kortum (1969). Self-consistent orthogonalized-plane-wave and empirically refined orthogonalized-plane-wave energy band models for cubic ZnS, ZnSe, CdS, and CdSe. *Phys. Rev.* **179**, 740–51.

Suffritti, G. B., and A. Gamba (1987). Theoretical studies on zeolites. *Int. Rev. Phys. Chem.* **6**, 229–314.

Suga, S., K. Inoue, M. Taniguchi, S. Shin, M. Seki, K. Sato, and T. Teranishi (1983). Vacuum ultraviolet reflectance spectra and band structures of pyrites (FeS_2, CoS_2 and NiS_2) and NiO measured with synchrotron radiation. *J. Phys. Soc. Japan* **52**, 1848–56.

Sugiura, C., Y. Gohshi, and I. Suzuki (1974). Sulfur $K\beta$ x-ray emission spectra and electronic structures of some metal sulfides. *Phys. Rev.* **B10**, 338–43.

Sugiura, C., I. Suzuki, J. Kashiwakura, and Y. Gohshi (1976). Sulfur K x-ray emission bands and valence band structures of transition metal disulfides. *J. Phys. Japan* **40**, 1720–24.

Sunagawa, I. (1984) (ed.). *Materials Science of the Earth's Interior.* Dordrecht, Netherlands: Reidel.

Surratt, G. T., R. N. Euwema, and D. L. Wilhite (1973). Hartree–Fock lattice constant and bulk modulus of diamond. *Phys. Rev.* **B8**, 4019–25.

Susak, N. J. (1981). *Spectra, Thermodynamics and Molecular Chemistry of Some Divalent Transition Metal Chloro-Complexes in Hydrothermal Solution at 300°C,* Ph.D. Thesis. Princeton, New Jersey: Princeton University.

Susak, N. J., and D. A. Crerar (1984). Factors controlling mineral zoning in hydrothermal ore deposits. *Econ. Geol.* **77**, 476–82.

Svane, A., and E. Antoncik (1986). Theoretical investigation of the ^{67}Zn Mössbauer isomer shifts in zinc chalcogenides. *Phys. Rev.* **B33**, 7462–73.

Swope, R. J., and J. W. Downs (1988). An experimental determination of the electron density and electrostatic potential of dandurite. *EOS-Trans. Amer. Geophys. Union* **69**, 499.

Symons, M. (1978). *Chemical and Biochemical Aspects of Electron Spin Resonance Spectroscopy.* Wokingham: Van Nostrand Reinhold.

Szabo, A., and N. S. Ostlund (1989). *Modern Quantum Chemistry: Introduction to Advanced Electronic Structure Theory.* New York: MacMillan.

Tabor, D. (1981). Solid Surfaces: their atomic, electronic and macroscopic properties. *Contemp. Phys.* **22**, 215.

Tachikawa, H., T. Ichikawa, and H. Yoshida (1990). Geometrical structure and electronic states of the hydrated Ti(III) ion. An *ab initio* CI study. *J. Amer. Chem. Soc.* **112**, 982–87.

Tafto, J., and J. Zhu (1982). Electron energy-loss near edge structure (ELNES), a potential technique in the studies of local atomic arrangements. *Ultramicro.* **9**, 349–54.

Tang Kai, A., H. Annersten, and T. Ericsson (1980). Molecular orbital (MS$X\alpha$)

calculations of *s*-electron densities of tetrahedrally coordinated ferric iron: comparison with experimental isomer shifts. *Phys. Chem. Minerals* **5**, 343–49.

Taniguchi, K., and B. L. Henke (1976). Sulfur, $L_{II,III}$ emission spectra and molecular orbital studies of sulfur compounds. *J. Chem. Phys.* **64**, 3021–35.

Tegeler, E., N. Koscuch, G. Wiech, and A. Faessler (1980). Molecular orbital analysis of the CO_3^{2-} ion by studies of the anisotropic x-ray emission of its components. *J. Electron Spectrosc.* **18**, 23–28.

Teo, B. K., and D. C. Joy (eds.) (1981). *EXAFS Spectroscopy*. New York: Plenum Press.

Terakura, K., A. R. Williams, T. Oguchi, and J. Kübler (1984a). Transition-metal monoxides: band or Mott insulators. *Phys. Rev. Lett.* **52**, 1830–33.

Terakura, K., T. Oguchi, A. R. Williams, and J. Kübler (1984b). Band theory of insulating transition-metal monoxides: band-structure calculations. *Phys. Rev.* **B30**, 4734–47.

Thiel, W. (1978). The most stable CNDO/2 water dimer. *Theoret. Chem. Acta* **48**, 357–59.

Timken, K. C., S. E. Schramm, R. J. Kirkpatrick, and E. Oldfield (1987). Solid-state oxygen-17 nuclear magnetic resonance spectroscopic studies of alkaline earth metasilicates. *J. Phys. Chem.* **91**, 1054–58.

Timken, H. K. C., N. Janes, G. L. Turner, S. L. Lambert, L. B. Welsh, and E. Oldfield (1986). Solid-state oxygen-17 nuclear magnetic resonance spectroscopic studies of zeolites and related systems. 2. *J. Am. Chem. Soc.* **108**, 7236–41.

Timofeeva, T. V., I. L. Dubchak, V. G. Dashevsky, and Y. T. Struchkov (1984). Flexibility of siloxane rings and rigidity of ladder-like siloxane polymers; interpretation on the basis of atom–atom potential functions. *Polyhedron* **3**, 1109–19.

Tosi, M. P. (1964). Cohesion of ionic solids in the Born model. *Solid State Phys.* **16**, 1–120.

Tossell, J. A. (1973). Molecular orbital interpretation of x-ray emission and ESCA spectral shifts in silicates. *J. Phys. Chem. Solids* **34**, 307–19.

Tossell, J. A. (1975a). The electronic structures of Mg, Al and Si in octahedral coordination with oxygen from SCF $X\alpha$ calculations. *J. Phys. Chem. Solids* **36**, 1273–80.

Tossell, J. A. (1975b). The electronic structures of silicon, aluminum and magnesium in tetrahedral coordination with oxygen from SCF-$X\alpha$ MO calculations. *J. Amer. Chem. Soc.* **97**, 4840–44.

Tossell, J. A. (1976a). Electron structure of iron-bearing oxidic minerals at high pressure. *Amer. Mineral.* **61**, 130–44.

Tossell, J. A. (1976b). SCF-$X\alpha$ studies of the electronic structures of C, Si and Ge oxides. *J. Phys. Chem. Solids* **37**, 1043–50.

Tossell, J. A. (1977a). A comparison of silicon–oxygen bonding in quartz and magnesium olivine from x-ray spectra and molecular orbital calculations. *Amer. Mineral.* **62**, 136–41.

Tossell, J. A. (1977b). SCF-$X\alpha$ scattered wave MO studies of the electronic structure of ferrous iron in octahedral coordination with sulfur. *J. Chem. Phys.* **66**, 5712–19.

Tossell, J. A. (1977c). Theoretical studies of valence orbital binding energies in solid ZnS, ZnO, and ZnF_2. *Inorg. Chem.* **16**, 2944–49.

Tossell, J. A. (1978a). Self-consistent field $X\alpha$ study of one-electron energy levels in Fe_3O_4. *Phys. Rev.* **B17**, 484–87.

Tossell, J. A. (1978b). Theoretical studies of the electronic structure of copper in tetrahedral and triangular coordination with sulfur. *Phys. Chem. Minerals* **2**, 225–36.

Tossell, J. A. (1979). Calculations of bond distances and cohesive energies for gaseous halides using the modified electron gas ionic model. *Chem. Phys. Lett.* **67**, 359–64.

Tossell, J. A. (1980a). Calculation of *L* x-ray emission energies and intensities in PO_4^{3-} and ClO_4^{-}. *Inorg. Chem.* **19**, 3228–30.

Tossell, J. A. (1980b). Calculation of bond distances and heats of formation for BeO, MgO, SiO_2, TiO_2, FeO, and ZnO using the ionic model. *Amer. Mineral.* **65**, 163–73.

Tossell, J. A. (1980c). Theoretical study of structures, stabilities and phase transitions in some metal dihalide and dioxide polymorphs. *J. Geophys. Res.* **85**, 6456–60.

Tossell, J. A. (1981). Structures and cohesive properties of hydroxides and fluorides calculated using the modified electron gas ionic model. *Phys. Chem. Mineral.* **7**, 15–19.

Tossell, J. A. (1983). A qualitative molecular orbital study of the stability of polyanions in mineral structures. *Phys. Chem. Mineral.* **9**, 115–23.

Tossell, J. A. (1984a). Correlation of ^{29}Si nuclear magnetic resonance chemical shifts in silicates with orbital energy differences obtained from x-ray spectra. *Phys. Chem. Mineral.* **10**, 137–41.

Tossell, J. A. (1984b). A qualitative MO model for bridging bond angle variations in minerals. *Phys. Chem. Mineral.* **11**, 81–84.

Tossell, J. A. (1984c). A reinterpretation of the electronic structures of $FeAs_2$ and related minerals. *Phys. Chem. Mineral.* **11**, 75–80.

Tossell, J. A. (1985a). *Ab initio* SCF MO and modified electron gas studies of electron deficient anions and ion pairs in mineral structures. *Physica* **131B&C**, 283–89.

Tossell, J. A. (1985b). Quantum mechanical models and methods in mineralogy. In: *Chemical Bonding and Spectroscopy in Mineral Chemistry* (F. J. Berry and D. J. Vaughan, eds.) London: Chapman and Hall, pp. 1–30.

Tossell, J. A. (1986). Studies of unoccupied molecular orbitals of the B–O bond by molecular orbital calculations, x-ray absorption near edge, electron transmission and NMR spectroscopy. *Amer. Mineral.* **71**, 1170–77.

Tossell, J. A. (1987). Quantum mechanical studies of Si–O and Si–F bonds in molecules and minerals. *Phys. Chem. Mineral.* **14**, 320–26.

Tossell, J. A. (1989). Quantum mechanical studies of the structures, stabilities, vibrational spectra and Zn NMR spectra of $ZnCl_n^{2-n}$ species in aqueous solutions. *EOS, Trans. Amer. Geophys. Union* **70**, 352.

Tossell, J. A. (1990a). Calculations of the structures, stabilities, Raman and Zn NMR spectra of $ZnCl_n(OH_2)_a^{2-n}$ species in aqueous solution. *J. Phys. Chem.* **95**, 366–71.

Tossell, J. A. (1990b). Calculation of NMR shieldings and other properties of three and five coordinate Si, three coordinate O and some siloxane and boroxol ring compounds. *J. Noncryst. Solids* **120**, 13–19.

Tossell, J. A. (1990c). *Ab initio* calculation of the structures, Raman frequencies and Zn NMR spectra of tetrahedral complexes of Zn^{2+}. *Chem. Phys. Lett.* **169**, 145–49.

Tossell, J. A. (1991). Calculation of the effect of deprotonation of the Si NMR shielding for the series $Si(OH)_4$ to SiO_4^{4-}. *Phys. Chem. Mineral.* **17**, 654–60.

Tossell, J. A., G. E. Brown, Jr., and G. A. Waychunas (1985a). Studies of the unoccupied molecular orbitals of tetrahedral oxyanions. TO_4^{n-}, and related molecules by x-ray absorption near edge spectroscopy (XANES) and multiple-scattering (MS) $X\alpha$ molecular orbital calculations, *GSA Ann. Meeting Abst.*

Tossell, J. A., and J. W. Davenport (1984). MS-$X\alpha$ calculation of the elastic electron scattering cross sections and x-ray absorption spectra of CX_4 and SiX_4 (X=H, F, Cl). *J. Chem. Phys.* **80**, 813–21.

Tossell, J. A., and G. V. Gibbs (1976). Molecular orbital studies of angular distortions resulting from tetrahedral edge sharing in silicon oxides, sulfides and hydrides. *J. Molec. Struct.* **35**, 273–87.

Tossell, J. A., and G. V. Gibbs (1977a). A molecular orbital study of shared-edge distortions in linked polyhedra. *Amer. Mineral.* **61**, 287–94.

Tossell, J. A., and G. V. Gibbs (1977b). Molecular orbital studies of geometries and spectra of minerals and inorganic compounds. *Phys. Chem. Mineral.* **2**, 21–58.

Tossell, J. A., and G. V. Gibbs (1978). The use of molecular orbital calculations on model systems for the prediction of bridging-bond-angle variations in siloxanes, silicates, silicon nitrides and silicon sulfides. *Acta. Cryst.* **A34**, 463–72.

Tossell, J. A., and P. Lazzeretti (1986). *Ab initio* calculations of ^{29}Si NMR chemical shifts for some gas phase and solid state silicon fluorides and oxides. *J. Chem. Phys.* **84**, 369–74.

Tossell, J. A., and P. Lazzeretti (1987a). *Ab initio* calculation of oxygen nuclear quadrupole coupling constants and oxygen and silicon NMR shielding constants in molecules containing Si–O bonds. *Chem. Phys.* **112**, 205–12.

Tossell, J. A., and P. Lazzeretti (1987b). *Ab initio* calculation of the ^{31}P–($2a+b$–5) shielding tensor for the series PO_aF_b, $a+b=4$ and for HPO_4^{2-}. *Chem. Phys. Lett.* **140**, 37–40.

Tossell, J. A., and P. Lazzeretti (1988a). Calculation of NMR parameters for bridging oxygens in H_3T–$OT'H_3$ linkages (T, T' = Al, SiP), for oxygen in SiH_3O^-, SiH_3OH, and SiH_3OMg^+ and for bridging fluorine in $H_3SiFSiH_3^+$. *Phys. Chem. Mineral.* **15**, 564–69.

Tossell, J. A., and P. Lazzeretti (1988b). *Ab initio* calculation on the refractive indices and related properties of $CaCO_3$. *Phys. Rev.* **B15**, 5694–98.

Tossell, J. A., and P. Lazzeretti (1988c). *Ab initio* calculation of B and O nuclear quadrupole coupling constants in NMR shielding constants in molecular models for B_2O_3 glass. *J. Noncryst. Solids* **99**, 267–75.

Tossell, J. A., and P. Lazzeretti (1990). Calculation of the structure, vibrational spectra, and polarizability of boroxine, $H_3B_3O_3$, a model for boroxol rings in vitreous B_2O_3. *J. Phys. Chem.* **94**, 1723–24.

Tossell, J. A., J. H. Moore, and J. C. Giordan (1985b). Energies of Π acceptor orbitals in SiH_4, PH_3, H_2S and their permethylated derivatives. *Inorg. Chem.* **24**, 1100–3.

Tossell, J. A., and D. J. Vaughan (1981). Relationships between valence orbital binding energies and crystal structures in compounds of copper, silver, gold, zinc, cadmium and mercury. *Inorg. Chem.* **20**, 3333–40.

Tossell, J. A., and D. J. Vaughan (1987). Electronic structure and the chemical reactivity of the surface of galena. *Canad. Mineral.* **25**, 381–92.

Tossell, J. A., D. J. Vaughan, and J. K. Burdett (1981). Pyrite, marcasite and arsenopyrite type minerals: crystal chemical and structural principles. *Phys. Chem. Minerals* **7**, 177–84.

Tossell, J. A., D. J. Vaughan, and K. H. Johnson (1973a). Electronic structure of ferric iron octahedrally coordinated to oxygen. *Nature (Phys. Sci.)* **244**, 42–45.

Tossell, J. A., D. J. Vaughan, and K. H. Johnson (1973b). X-ray photoelectron, x-ray emission and UV spectra of SiO_2 calculated by the SCF-$X\alpha$ scattered wave method. *Chem. Phys. Lett.* **20**, 329–34.

Tossell, J. A., D. J. Vaughan, and K. H. Johnson (1974). The electronic structure of rutile, wustite and hematite from molecular orbital calculations. *Amer. Mineral.* **59**, 319–34.

Tossell, J. A., D. S. Urch, D. J. Vaughan, and G. Weich (1982). The electronic structure of $CuFeS_2$, chalcopyrite, from x-ray emission and x-ray photoelectron spectroscopy and $X\alpha$ calculations. *J. Chem. Phys.* **77**, 77–82.

Townes, C. H., and B. P. Dailey (1949). Determination of electron structure of molecules from nuclear quadrupole effects. *J. Chem. Phys.* **17**, 782–96.

Tricker, K. J., L. A. Ash, and W. Jones (1979). On the anomalous inertness to oxidation of the surface regions of vivianite: a ^{57}Fe conversion electron and transmission Mössbauer study. *J. Inorg. Nucl. Chem.* **41**, 891–93.

Tse, J. S., M. L. Klein, and I. R. McDonald (1984). Lattice vibrations of ices Ih, VIII, and IX. *J. Chem. Phys.* **81**, 6124–29.

Tsukada, M., J. Adachi, and C. Satoko (1983). Theory of electronic structure of oxide surfaces. *Prog. Surf. Sci.* **14**, 113–74.

Tsuneyuki, N., M. Tsukada, H. Aoki, and V. Matsui (1988). First-principles interatomic potential of silica applied to molecular dynamics. *Phys. Rev. Lett.* **61**, 869–87.

Tsutsumi, K., H. Nakamomri, and S. K. Ichikawa (1976). X-ray Mn *K* emission spectra of manganese oxides and manganates. *Phys. Rev.* **B13**, 929–33.

Tung, Y. W., and M. L. Cohen (1969). Relativistic band structure and electronic properties of SnTe, GeTe, and PbTe. *Phys. Rev.* **180**, 823–26.

Turner, G. L., K. A. Smith, R. J. Kirkpatrick, and E. Oldfield (1986). Boron-11 nuclear magnetic resonance spectroscopic study of borate and borosilicate minerals and a borosilicate glass. *J. Mag. Res.* **67**, 544–50.

Uchida, N., T. Maekawa, and T. Yokokawa (1985). An application of MNDO calculation to borate polyhedra. *J. Noncryst. Solids* **74**, 25–36.

Uchida, N., T. Maekawa, and T. Yokokawa (1986). MNDO studies of basicity of borate glasses. *J. Noncryst. Solids* **85**, 290–308.

Ugliengo, P., V. Saunders, and E. Garrone (1990). Silanol as a model for the free hydroxyl of amorphous silica: *ab initio* calculations of the interaction with water. *J. Phys. Chem.* **94**, 2260–67.

Underhill, P. R., and T. E. Gallon (1982). The surface defect peak in the electron energy loss spectrum of MgO (100). *Solid State Commun.* **43**, 9–11.

Urano, T., T. Kanji, and M. Kaburagi (1983). Surface structure of MgO (001) surface studied by LEED. *Surf. Sci.* **134**, 109–21.

Urch, D. S. (1971). X-ray emission spectroscopy. *Quart. Rev. (Chem. Soc.)* **25**, 343.

Urch, D. S. (1985). X-ray spectroscopy and chemical bonding in minerals. In: *Chemical Bonding and Spectroscopy in Mineral Chemistry* (F. J. Berry and D. J. Vaughan, eds.) London: Chapman and Hall.

van der Heide, H., R. Helle, C. F. Van Brugen, and C. Haas (1980). X-ray photoelectron sectra of 3*d* transition metal pyrites. *J. Solid State Chem.* **33**, 17–25.

Vassiliou, M. S., and T. J. Ahrens (1981). Hugoniot equation of state of periclase above 200 GPa. *Geophys. Res. Lett.* **8**, 729–32.

Vaughan, D. J. (1971). *Aspects of Structure and Bonding in the Iron Sulphides and Related Minerals*. D.Phil. Thesis, University of Oxford.

Vaughan, D. J., and R. G. Burns (1971). Mineral chemistry and bonding of pentlandite and mackinawite. *Geol. Soc. Amer. Ann. Mtg.*, Vol. 3, 737 (abstr.), Boulder, Colorado.

Vaughan, D. J., R. G. Burns, and V. M. Burns (1971). Geochemistry and bonding of thiospinel minerals. *Geochim. Cosmochim. Acta* **35**, 365–81.

Vaughan, D. J., and J. R. Craig (1978). *Mineral Chemistry of Metal Sulfides*. Cambridge: Cambridge University Press.

Vaughan, D. J., and J. R. Craig (1985). The crystal chemistry of iron–nickel thiospinels. *Amer. Mineral.* **70**, 1036–43.

Vaughan, D. J., and M. S. Ridout (1971). Mössbauer studies of some sulphide minerals. *J. Inorg. Nucl. Chem.* **33**, 741–47.

Vaughan, D. J., and J. A. Tossell (1973). Molecular orbital calculations on beryllium and boron oxyanions: interpretation of x-ray emission, ESCA, and NQR spectra and of the geochemistry of beryllium and boron. *Amer. Mineral.* **58**, 765–70.

Vaughan, D. J., and J. A. Tossell (1978). Major transition metal oxide minerals: their electronic structures and the interpretation of mineralogical properties. *Canad. Mineral.* **16**, 159–68.

Vaughan, D. J., and J. A. Tossell (1980). The chemical bond and the properties of sulfide minerals: I. Zn, Fe and Cu in tetrahedral and triangular coordinations with sulfur. *Canad. Mineral.* **18**, 157–63.

Vaughan, D. J., and J. A. Tossell (1981). Electronic structure of thiospinel minerals: results from MO calculations. *Amer. Mineral.* **66**, 1250–53.

Vaughan, D. J., and J. A. Tossell (1983). Electronic structures of sulfide minerals—theory and experiment. *Phys. Chem. Minerals* **9**, 253–62.

Vaughan, D. J., J. A. Tossell, and K. H. Johnson (1974). The bonding of ferrous iron to sulphur and oxygen: a comparative study using SCF-$X\alpha$ scattered wave molecular orbital calculations. *Geochim. Cosmochim. Acta* **38**, 993–1005.

Vaughan, D. J., J. A. Tossell, and C. J. Stanley (1987). The surface properties of bornite. *Min. Mag.* **51**, 285–93.

Verhoogen, J. (1958). Physical properties and bond type in Mg-Al oxides and silicates. *Amer. Mineral.* **43**, 552–79.

Versluis, L., and T. Ziegler (1988). The determination of molecular structures by density functional theory. The evaluation of analytical energy gradients by numerical integration. *J. Chem. Phys.* **88**, 322–28.

Vetrivel, R., C. R. A. Catlow, and E. A. Colbourn (1988). Nonempirical quantum chemical calculations on ZSM-5 zeolites. I. Bronsted acid sites. *Proc. Roy. Soc.* **A417**, 81–94.

Virgo, D., and S. S. Hafner (1969). Fe^{2+}-Mg^{2+} order–disorder in heated orthopyroxenes. *Mineral. Soc. Amer. Spec. Pap.* **2**, 67–81.

Virgo, D., and S. S. Hafner (1970). Fe^{2+}, Mg order disorder in natural orthopyroxenes. *Amer. Mineral.* **55**, 201–23.

Virgo, D., and B. O. Mysen (1985). The structural state of iron in oxidized *vs* reduced glasses at 1 atm: a ^{57}Fe Mössbauer study. *Phys. Chem. Mineral.* **12**, 65–76.

Vladov, Ch., M. Neshev, L. Petrov, and D. Shopov (1983). In: *Proc. 5th Interat. Symp. on Heterogeneous Catalysis*, Part II. Varna, p. 479

von Barth, U. (1986). Applications of density functional theory to atoms, molecules and solids. *Chem. Scripta* **26**, 449–61.

von Barth, U., and L. Hedin (1972). A local exchange-correlation potential for the spin polarized case: I. *J. Phys. C Solid State Phys.* **5**, 1629–42.

Wagner, C. F., D. E. Passoja, H. F. Hillery, T. G. Kinisky, H. A. Six, W. T. Jansen, and J. A. Taylor (1982). Auger and photoelectron line energy relationships in aluminium–oxygen and silicon oxygen compounds. *J. Vac. Sci. Tech.* **21**, 933–44.

Walch, P. F., and D. E. Ellis (1973). One-electron interpretation of optical absorption and soft-x-ray data in MgO. *Phys. Rev.* **B8**, 5920–33.

Walker, L. R., G. K. Wertheim, and V. Jaccarino (1961). Interpretation of the Fe^{57} isomer shift. *Phys. Rev. Lett.* **6**, 98–100.

Wang, C. S., and B. M. Klein (1981). First-principles electronic structure of Si, Ge, GaP; GaAs, ZnS, and ZnSe. I. Self-consistent energy bands, charge densities, and effective masses. *Phys. Rev.* **B24**, 3393–416.

Ward, J. C. (1970). The structure and properties of some iron sulfides. *Rev. Pure Appl. Chem.* **20**, 175–206.

Wasastjerna, J. A. (1923). Radii of ions. *Soc. Sci. Fenn Comm. Phys. Nat.* **1**, 1–25.

Waseda, Y., and J. M. Toguri (1977). The structure of molten binary silicate systems CaO-SiO_2 and MgO-SiO_2. *Metall. Trans.* **8B**, 563–68.

Waseda, Y., and J. M. Toguri (1978). The structure of the molten FeO-SiO system. *Metall. Trans.* **9B**, 595–601.

Watson, R. E., and A. J. Freeman (1960). Crystalline field and spin polarization effects on electron densities and magnetic form factors. *Phys. Rev.* **120**, 1134–41.

Waychunas, G. A., G. E. Brown, Jr., C. W. Ponader, and W. E. Jackson (1988). Evidence from x-ray absorption for network-forming Fe^{2+} in molten alkali silicates. *Nature* **332**, 251–53.

Weber, J., and M. Geoffrey (1979). Potential energy surfaces and the multiple scattering (MS) $X\alpha$ method: a new study of the cases of H_2O and NH_3. *J. Molec. Struct.* **51**, 141–44.

Weber, T. A., and F. H. Stillinger (1983). Molecular dynamics study of ice crystallite melting. *J. Phys. Chem.* **87**, 4277–81.

Weiden, N., and H. Rager (1985). The chemical shift of the ^{29}Si nuclear magnetic resonance in a synthetic single crystal of Mg_2SiO_4. *Z. Naturforsch.* **40A**, 126–30.

Weider, D., and U. Sherz (1985). Self-consistent-field cluster calculations of nickel (2+) centers in cubic zinc sulfide, cadmium sulfide, and zinc selenide in the CNDO approximation. *Phys. Rev.* **B32**, 5273–79.

Weisser, O., and S. Landa (1973). *Sulfide Catalysts: Their Properties and Applications.* Oxford: Pergamon Press.

Weissmann, R., and K. Muller (1981). Auger electron spectroscopy—a local probe for solid surfaces. *Surf. Sci. Reports* **105**, 251–309.

Wells, A. F. (1975). *Structural Inorganic Chemistry* (4th Ed.). Oxford: Clarendon.

Welsh, I. D., and P. M. Sherwood (1989). Photoemission and electronic structure of FeOOH: distinguishing between oxide and oxyhydroxide. *Phys. Rev.* **B40**, 6386–92.

Welton-Cook, M. R., and W. Berndt (1982). A LEED study of the MgO (100) surface: identification of a finite rumple. *J. Phys. C: Solid State Phys.* **15**, 5691–710.

Welz, D., and M. Rosenberg (1987). Electronic band structure of tetrahedral iron sulfides. *J. Phys. C* **20**, 3911–24.

Wendlandt, W. W., and H. G. Hecht (1966). *Reflectance Spectroscopy.* New York: Interscience.

Weng, X., and P. Rez (1989). Multiple-scattering approach to oxygen K near-edge structures in electron-energy-loss spectroscopy of alkali earths. *Phys. Rev.* **B39**, 7405–11.

Werner, H. J., P. Psmus, and M. Grimm (1982). *Ab initio* calculations of radiative transition probabilities in the $X\,{}^1\Sigma^+$ state of SiO and the $X\,{}^2\Sigma^+$ and $A\,{}^2\Pi$ states of SiO^+. *Chem. Phys.* **73**, 169–78.

Wertheim, G. (1964). *Mössbauer Effect: Principles and Applications.* New York: Academic Press.

Wertheim, G. K., F. J. DiSalvo, and D. N. E. Buchanan (1973). Valence bands of layer structure transition metal chalcogenides. *Solid State Comm.* **13**, 1228.

West, R. H., and J. E. Castle (1982). The correlation of the Auger parameter with refractive index: an XPS study of silicates using Zr $L\alpha$ radiation. *Surf. Interface Anal.* **4**, 68–75.

Whangbo, M-H., R. Hoffman, and R. B. Woodward (1978). Conjugated one and two dimensional polymers. *Proc. Roy. Soc. London* **A366**, 23–46.

White, J. C. (ed.) (1985). *Applications of Electron Microscopy in the Earth Sciences.* Mineral. Assoc. Canada Short Course Notes II.

Wiech, G., and E. Z. Kurmaev (1985). X-ray emission bands and electronic structure of crystalline and amorphous silica (SiO_2). *J. Phys. C* **18**, 4393–402.

Wijeyesekera, S. D., and R. Hoffman (1983). Marcasites and arsenopyrites: structure, bonding and electrical properties. *Inorg. Chem.* **22**, 3287–300.

Williams, A. R., J. Kübler, and C. D. Gelatt, Jr. (1979). Cohesive properties of metallic compounds: augmented-spherical-wave calculations. *Phys. Rev.* **B19**, 6094–118.

Williams, G. L., G. M. Bancroft, M. G. Bown, and A. C. Turnock (1971). Anomalous Mössbauer spectra of *C2/c* clinopyroxenes. *Nature (Phys. Sci.)* **230**, 149–51.

Wilson, J. A. (1972). Systematics of the breakdown of Mott insulation in binary transition metal compounds. *Adv. Phys.* **21**, 143–98.

Wilson, J. A., and A. D. Yoffe (1969). The transition metal dichalcogenides. Discussion and interpretation of the observed opitcal, electrical and structural properties. *Adv. Phys.* **18**, 193–335.

Wilson, T. M. (1970). Electronic structure of the first row transition metal compounds. *Int. Journ. Quantum Chem. Symp.* **3**, 757–74.

Wolf, G. H., and M. S. T. Bukowinski (1985). *Ab initio* structural and thermoelastic properties of orthorhombic $MgSiO_3$ perovskite. *Geophys. Res. Letts.* **12**, 809–12.

Wolf, G. H., and M. S. T. Bukowinski (1987). Theoretical study of the structural properties and equations of state of $MgSiO_3$ and $CaSiO_3$ perovskites: implications for lower mantle composition. In: *High Pressure Research in Mineral Physics* (M. Manghnani and Y. Syono, eds.) Tokyo: Amer. Geophys. Union/Terra Pub. Co.

Wolf, G. H., and M. S. T. Bukowinski (1988). Variational stabilization of the ionic charge densities in the electron-gas theory of crystals: applications to MgO and CaO. *Phys. Chem. Mineral.* **15**, 209–20.

Wolf, G. H., and R. Jeanloz (1985). Lattice dynamics and structural distortions of $CaSiO_3$ and $MgSiO_3$ perovskites. *Geophys. Lett.* **12**, 413–16.

Wolff, R., and R. Radeglia (1980). Zur theoretischen interpretation tetrakoordinierter zentralatome. *Z. Phys. Chem. (Leipzig)* **261**, 726–44.

Wolfram, T. (1981). Chemisorption and surface electronic properties of the *d*-band oxides. *J. Vac. Sci. Technol.* **18**, 428–32.

Wood, B. J., and R. .G. J. Strens (1972). Calculation of crystal field splittings in distorted coordination polyhedra: Spectra and thermodynamic properties of minerals. *Min. Mag.* **38**, 909–17.

Wood, P. R., and D. S. Urch (1976). Valence band x-ray emission spectra of manganese in various oxidation states. *J. Chem. Soc. (Dalton)*, 2472–76.

Wood, S. A. (1985). *Some Aspects of the Physical Chemistry of Hydrothermal Ore-Forming Solutions*, Ph.D. Thesis. Princeton, New Jersey: Princeton University.

Woodcock, L. V. (1975). Molecular dynamics calculations on molten ionic salts. In: *Adv. in Molten Salt Chem.* (J. Braunstein, G. Mamantov, and G. P. Smith, eds.) New York: Plenum, pp. 1–74.

Woodcock, L. V., C. A. Angell, and P. Cheeseman (1976). Molecular dynamics studies of the vitreous state: simple ionic systems and silica. *J. Chem. Phys.* **65**, 1565–77.

Xu, Y, and W. Y. Ching (1988a). Comparison of charge density distribution and electronic bonding in α-SiO_2 and β-Si_3N_4. *Physica* **B150**, 32–36.

Xu, Y., and W. Y. Ching (1988b). Total energy calculation in α-SiO_2 and β-Si_3N_4. *Materials Research Society Symposium Proceedings* **105** (SiO_2 and its Interfaces), 181–86.

Yagi, T., H. K. Mao, and P. M. Bell (1982). Hydrostatic compression of perovskite-type $MgSiO_3$. In: *Advances in Physical Geochemistry*, Vol. 2 (S. K. Saxena, ed.) New York: Springer–Verlag, pp. 317–25.

Yamashita, J., and S. Asano (1970). Electronic state of doubly charged oxygen negative ion in MgO. *J. Phys. Soc. Japan* **28**, 1143–50.

Yamashita, J., and S. Asano (1983a). Cohesive properties of alkali halides and simple oxides in the local-density formalism. *J. Phys. Soc. Jpn.* **52**, 3506–13.

Yamashita, J., and S. Asano (1983b). Cohesive properties of 3*d* transition-metal monoxides. *J. Phys. Soc. Jpn.* **52**, 3514–19.

Yarmoshenko, Yu. M., V. M. Cherkashenko, and E. Z. Kurmaev (1983). The anisotropy of x-ray emission spectra for $2H$-MoS_2 single crystals. *J. Elect. Spect. Related Phenom.* **32**, 103–12.

Yasaitis, J. A., and R. Kaplow (1972). Structure of amorphous silicon monoxide. *J. Appl. Phys.* **43**, 995–1000.

Yates, B. W., K. H. Tan, G. M. Bancroft, L. L. Coatsworth, and J. S. Tse (1985). Photoelectron study of the valence levels of CF_4 and SiF_4 from 20 to 100 eV. *J. Chem. Phys.* **83**, 4906–15.

Yin, L. I., S. Ghose, and I. Adler (1971). Core binding energy difference between bridging and nonbridging oxygen atoms in a silicate chain. *Science* **173**, 633–34.

Yin, M. T., and M. L. Cohen (1982). Theory of *ab initio* pseudopotential calculations. *Phys. Rev.* **B25**, 7403–11.

Zang, Z. G., M. B. Boisen, Jr., L. W. Finger, and G. V. Gibbs (1985). Molecular mimicry of the geometry and charge density distribution of polyanions in borate minerals. *Amer. Mineral.* **70**, 1238–47.

Zdrazil, M., and J. Sedlacek (1977). Quantum chemical model of the adsorption of thiophene during hydroesulphurization. *Collect. Czech. Chem. Commun.* **42**, 3133–43.

Zemann, J. (1981). Zür sterochimie der karbonate. *Fortschr. Mineral.* **59**, 95–116.

Zemel, J. N., J. D. Jensen, and R. B. Schoolar (1965). Electrical and optical properties of epitaxial films of PbS, PbSe, PbTe, and SnTe. *Phys. Rev.* **140**, A330–42.

Zhu, J. K., D. Li, J. Li, and Y. K. Pan (1983). Calculation of photoelectron spectra of group IV tetrachlorides and carbon tetrahalides by SCF-$X\alpha$-SW method. *Theoret. Chim. Acta* **63**, 223–33.

Zobetz, E. (1982). Über die gestalt von BO_3^- gruppen. *Zeit. fur Krist.* **160**, 81–92.

Zonnevylle, M. C., R. Hoffmann, and S. Harris (1988). Thiophene hydrodesulfurization on MoS_2; theoretical aspects. *Surface Sci.* **199**, 320–60.

Zunger, A., and M. L. Cohen (1978). Density-functional pseudopotential approach to crystal phase stability and electronic structure. *Phys. Rev. Lett.* **41**, 53–56.

Zunger, A., and A. J. Freeman (1978). Local-density self-consistent energy-band structure of cubic cadmium sulfide. *Phys. Rev.* **B17**, 4850–63.

INDEX